INVESTIGATION OF CHARGE AND SPIN PERSISTENT CURRENT CHARACTERISTICS AND TOPOLOGICAL ASPECTS OF PSEUDOSPIN-1 α-T_3 LATTICE SYSTEMS

A Thesis Submitted
in Partial Fulfillment of the Requirements
for the Degree of
DOCTOR OF PHILOSOPHY
By

MIJANUR ISLAM
Roll No - 196121109
Supervisor : Prof. SAURABH BASU

Department of Physics
Indian Institute of Technology Guwahati
Guwahati-781039, Assam, India
January, 2025

ABSTRACT

We study prototype of a pseudospin-1 fermionic α-T_3 model, which smoothly interpolates between graphene ($\alpha = 0$) and a dice lattice ($\alpha = 1$). For $\alpha \in [0 : 1]$, the band structure features a flat band at zero energy separating two linearly dispersive Dirac cones. We explore persistent charge and spin transport in an α-T_3 quantum ring (QR) analytically in presence of a magnetic field, and systematically examine how different spin-orbit couplings (SOC) (both Haldane and Rashba types) impact Aharonov-Bohm oscillations and persistent currents in the spin and charge sectors. We also include (topological) defects to assess spintronic applications of our ring setup. We broaden our perspectives and examine an α-T_3 system as an electron pump, a gedanken experiment contemplated by Laughlin to demonstrate quantum Hall effect. Interestingly, the Fano factor reveals distinct transport regimes, demonstrating ballistic, Poissonian and diffusive behaviour for different values of α. Next, to shed light on the topological properties, we consider phases and phase transitions therein solely impacted by the electron-phonon coupling in the spin-orbit coupled α-T_3 bulk and ribbon systems. Our model demonstrates multiple topological phase transitions shown via the presence (or absence) of chiral and helical edge modes in semi-infinite ribbon geometries which are further evidenced by computing the $\mathbb{Z}$ and $\mathbb{Z}_2$ invariants.

Dedicated to my beloved parents, family, and friends

&

the memory of my late grandparents

ACKNOWLEDGEMENTS

I would like to express my heartfelt appreciation to everyone who, directly or indirectly, supported and encouraged me in pursuing my Ph.D. This journey has been the realization of a dream I envisioned long ago, back in class 7.

First and foremost, I extend my deepest gratitude to my supervisor, Prof. Saurabh Basu, for his invaluable guidance, unwavering support, and profound expertise throughout my research journey. His steadfast commitment to academic excellence and insightful feedback have been pivotal in shaping the direction and substance of my work. Despite his busy schedule, he has generously devoted his time and effort to mentor me, for which I am profoundly grateful. One of the most important lessons I have learned from him during these years is his remarkable ability to present ideas concisely, along with his exceptional time management, dedication, and commitment. I am privileged to be a member of his research group. I sincerely hope to embody these qualities in my own career moving forward.

I would also like to express my sincere gratitude to the chairman of my doctoral committee, Prof. Subharadip Ghosh, and to the committee members, Dr. Pankaj Kumar Mishra and Prof. Ashwini Kumar Sharma, for reviewing my progress annually and providing insightful feedback and invaluable suggestions. I am equally thankful to all the HoDs, as well as the faculty, technical, and non-technical staff of the department of Physics, for their unyielding support and friendly demeanor whenever it was needed.

My heartfelt appreciation goes to our collaborators Dr. Sudipta Koley, Dr. Priyadarshini Kapri, Dr. Tutul Biswas, Dr. Kuntal Bhattacharyya, and Ms. Srijata Lahiri. Their invaluable contributions, expertise, and enthusiasm have greatly enriched my research and broadened my perspectives. In particular, I am deeply grateful to Dr. Sudipta Koley for his guidance during my early phase. I also want to express my gratitude to Dr. Priyadarshini Kapri for being both a collaborator and a mentor during the initial stages of my research. A special acknowledgment goes to Dr. Tutul Biswas. I have learned a great deal from him, and his significant contributions have sharpened my scientific skills, polished my approach to research, and played a pivotal role in shaping my work while deepening my understanding of the subject.

I would like to thank my seniors Dr. Priyanka Sinha, Dr. Shilpi Roy, Dr. Sayan Mondal, Dr. Kuntal Bhattacharyya, and my juniors Dipendu, Srijata, Koustav, Shreya, and Gourab for their invaluable support, constant encouragement, and the many useful and unuseful discussions that made this journey memorable. I am also grateful to Dr. Sudin Ganguly for the enriching interactions during my Ph.D journey. I am especially thankful to Shilpi di and Priyanka di for their exceptional support, motivation, and mentorship. Their enduring guidance and the warmth with which they treated me like a younger brother made my research journey not only productive but also enjoyable.

I am immensely grateful to the Indian Institute of Technology Guwahati for its captivating beauty and for providing me with the most exciting, memorable, and transformative period of my life. I would like to thank to the staff of the library and computer center at IIT Guwahati for their invaluable support and for providing excellent research facilities that greatly contributed to my work. I also extend my heartfelt appreciation to the Government of India and the Council of Scientific and Industrial Research (CSIR) for their invaluable financial support throughout this journey.

I feel fortunate to have had friends like Himangshu, Sunil, Shantanu, Chinmoy, Lipika, and Seshadri, whose camaraderie made my research years unforgettable. Campus life would not be so easy and enjoyable without their presence. A special thanks to my RS-3 and RS-4 labmates for fostering a welcoming and enjoyable lab environment. I also wish to extend my gratitude to Debu da, Rajnandan da, Sanu, Vishal, Anjishnu da, Anirudh, and all the cricket field friends, seniors, and juniors who brought excitement and joy to life both on and off the cricket field at IITG.

My heartfelt thanks also go to Shamim, Nasir bhai, and Amit, whose incredible contributions made my hostel life truly delightful.

I express my sincere gratitude to the mess workers, medical staff, bus drivers, security guards, cleaning crew, and the staff at nearby eateries for their indispensable roles in making my time at IITG enjoyable and comfortable.

Most importantly, I am deeply grateful to all my family members, and in particular, my parents Jamirul Islam and Manju Khatun, my uncles Jakirul and Jahedul, my aunts Reshma and Amina, my brothers Mostafijur, Rezwan, and Jiyad, my sister Jiniya, and my sister-in-law Remim for their persistent love and encouragement throughout my academic journey. Words cannot fully convey my gratitude for their constant support and the role they have played in my success. A very special thanks goes to Rehena, for her resolute understanding through every good and bad day, month, and year. I cannot thank her enough for being by my side in every possible way, as my best friend and my loving wife. I am profoundly indebted to my late grandparents for their unconditional love and support. Their steadfast belief in me and their guidance shaped the person I am today. If they were alive, I am certain they would have been even prouder than I am to see this achievement.

I would like to thank all my teachers for their support and encouragement to pursue my dreams over the years. In particular, I am deeply thankful to Dr. Biraj Kumar Barman, Mr. Santanu Chowdhury, Mr. Gokul Chandra Paul, Mr. Rabati Mohan Sarkar, Mr. Bablu Mondal, Dr. Md. Abdul Khan, Dr. Gahul Amin, Dr. Pradip Kumar Chottopadhyay, Dr. Prasenjit Thakur, Mr. Palash Patra, and most importantly, Mr. Habibur Rahaman, whose guidance and inspiration during my school years profoundly influenced my passion for studying and learning physics.

My heartfelt thanks go to my childhood friends Sakib, Abinash, Sabed, and Tajidul, who have been a constant source of support and guidance since primary school. Their readiness to lend a helping hand and offer valuable advice has meant a great deal to me.

I am also grateful to my college and off-campus friends, especially Tauhuratul, Masuda, Noor, Evana, Sahanur, Moumita, Tamim, Urmi, Suman, Faruk, Debjani, Shamik, Tanmoy, Tanima, Salty, and Sanjay, for their support and for making my leisure moments more memorable and enjoyable.

Finally, I want to take a moment to thank myself for striving to be the best version of who I can be and for always aiming to embody the values of humanity above all else.

Guwahati, January 2025
Mijanur Islam

DISCLAIMER

The bibliography included in this thesis is not exhaustive but comprises of the references that were thoroughly consulted during the course of this work. I sincerely apologize for any inadvertent omissions of research papers, review articles, or other scientific documents relevant to the focus of this thesis that should have been cited. Additionally, for illustrative purposes, some figures in this thesis have been adapted from other sources and are properly cited.

DECLARATION

This is to certify that the thesis entitled "*INVESTIGATION OF CHARGE AND SPIN PERSISTENT CURRENT CHARACTERISTICS AND TOPOLOGICAL ASPECTS OF PSEUDOSPIN-1 α-T_3 LATTICE SYSTEMS*", submitted by me to the *Department of Physics, Indian Institute of Technology Guwahati*, for the award of the degree of Doctor of Philosophy, is a bonafide work carried out by me under the supervision of Prof. Saurabh Basu. The content of this thesis, in full or in parts, have not been submitted to any other University or Institute for the award of any degree or diploma. The research work has been conducted between January, 2020 to January, 2025. In accordance with standard scientific reporting practices, appropriate acknowledgments have been provided wherever the work references findings from other studies.

Mijanur Islam

Mijanur Islam

Department of Physics,

Indian Institute of Technology Guwahati,

Guwahati-781039, Assam, India.

Date: 18.04.2025

CERTIFICATE

This is to certify that the thesis entitled "*INVESTIGATION OF CHARGE AND SPIN PERSISTENT CURRENT CHARACTERISTICS AND TOPOLOGICAL ASPECTS OF PSEUDOSPIN-1 α-T_3 LATTICE SYSTEMS*", submitted by Mr. Mijanur Islam (Roll No. 196121109), a research scholar in the *Department of Physics*, *Indian Institute of Technology Guwahati*, for the award of the degree of Doctor of Philosophy, is a record of an original research work carried out by him under my supervision and guidance. In my opinion, the thesis has fulfilled all requirements as per the regulations of the institute and reached the standard needed for submission. The results embodied in this thesis have not been submitted to any other University or Institute for the award of any degree or diploma.

Prof. Saurabh Basu

Professor,

Department of Physics,

Indian Institute of Technology Guwahati,

Guwahati-781039, Assam, India.

Date: 18/4/25

LIST OF PUBLICATIONS

The following are described in this thesis:

Publications in journal:

1. *Effect of magnetic field on the electronic properties of an α-T_3 quantum ring*

   M. Islam, T. Biswas, and S. Basu

   • Phys. Rev. B **108**, 085423 (2023) • e-Print: arXiv:2304.08830

2. *Spin and charge persistent currents in a Kane Mele α-T_3 quantum ring*

   M. Islam and S. Basu

   • J. Phys.: Condens. Matter **36**, 135301 (2024) • e-Print: arXiv:2308.06804

3. *Screw dislocation in a Rashba spin-orbit coupled α-T_3 Aharonov-Bohm quantum ring*

   M. Islam and S. Basu

   • Sci. Rep. **14**, 11232 (2024) • e-Print: arXiv:2310.14169

4. *Electron-phonon coupling induced topological phase transition in an α-T_3 Haldane-Holstein model*

   M. Islam, K. Bhattacharyya, and S. Basu

   • Phys. Rev. B **110**, 045426 (2024) • e-Print: arXiv:2408.14367

5. *Holstein polaron in a pseudospin-1 quantum spin Hall system: first and second order topological phase transitions*

   K. Bhattacharyya, S. Lahiri, **M. Islam**, and S. Basu

   • Phys. Rev. B **110**, 235432 (2024) • e-Print: arXiv:2408.14367

6. *Conductance properties of an α-T_3 Corbino disk*

   M. Islam and S. Basu

   • Accepted in J. Phys.: Condens. Matter (2025) • e-Print: arXiv:2409.20395

The following are not described in this thesis:

Publication in journal:

1. *Transport properties of the parent $LaNiO_2$*

   M. Islam, S. Koley, and S. Basu

   • Eur. Phys. J. B **94**, 187 (2021) • e-Print: arXiv:2106.00632

2. *Electrical and thermal transport through α-T_3 NIS junction*

   M. Islam and P. Kapri

   • J. Phys.: Condens. Matter **35**, 105301 (2022) • e-Print: arXiv:2209.06021

Conference Attended

1. Participated in the Webinar on "**Atomistic Modelling and Simulation of Materials**," organized by Department of Metallurgical and Materials Engineering, IIT Kharagpur on 30th and 31st May, 2021.

2. Oral presentation at "**3rd National Conference on Frontiers of Modern Physics (NCFMP-2021)**," organized by the Department of Physics, School of basic and Applied Sciences, Adamas University held on 26th and 27th November, 2021.

3. Flash talk and poster presentation at the "**4th PRL Conference on Condensed Matter Physics (PRL CCMP-2023)**," held at Physical Research Laboratory, Ahmedabad from 6th-8th February, 2023.

4. Oral presentation at "**International Conference on Frontiers in Pure and Applied Physics (ICFPAP-2024)**," held at the Department of Physics, USTM from 29th February-2nd March, 2024.

5. Oral presentation at "**7th Annual Conference on Quantum Condensed Matter (QMAT 2024)**," held at the Department of Physics, IIT Guwahati from 20th-23rd December, 2024.

CURRICULUM VITAE

Mijanur Islam was born on 15th January 1996, in West Bengal, India. He did his B.Sc. with Physics Honors in 2017 from Alipurduar College under University of North Bengal and his M.Sc in physics in 2019 from the University of North Bengal. He had enrolled in the Ph.D. program at the Indian Institute of Technology Guwahati in 2020 (January). He had qualified for Graduate Aptitude Test in Engineering (GATE) in 2020, CSIR-UGC NET in 2018, and Joint Admission test for Masters (JAM) in 2017. He has earned the Senior Research Fellowship in 2022 by Indian Institute of Technology Guwahati.

Contents

List of Figures

List of Tables

ABBREVIATIONS AND NOTATIONS

MBE :	molecular beam epitaxy
2DEG :	two dimensional electron gas
QR :	quantum ring
AB :	Aharonov-Bohm
TRS :	time reversal symmetry
SOC :	spin-orbit coupling
ISOC :	intrinsic spin-orbit coupling
RSOC :	Rashba spin-orbit coupling
LL :	Landau level
NN :	nearest neighbour
NNN :	next nearest neighbour
TD :	topological defect
CB :	conduction band
VB :	valence band
FB :	flat band
dFB :	distorted flat band
BZ :	Brillouin zone
TKNN :	Thouless, Kohmoto, Nightingale, and den Nijs
QAHE :	quantum anomalous Hall effect
TI :	topological insulator
e-ph :	electron-phonon
LFT :	Lang-Firsov transformation
QHE :	quantum Hall effect
QSHE :	quantum spin Hall effect
WCC :	Wannier charge center
HWCC :	hybrid Wannier charge center
WF :	Wannier function
TPT :	topological phase transition

α : ratio between the hopping amplitudes

B_0 : magnetic field

R : radius of the ring

Φ : magnetic flux

Φ_0 : flux quantum

ϕ_{ij} : Haldane flux

$\mathcal{M}$: Semenoff mass

λ : strength of the ISOC

λ_R : strength of the RSOC

λ_{eph} : strength of the e-ph coupling

j : persistent current

j_S : equilibrium spin current

ζ : valley index

m : total angular momentum quantum number

n : band index

β : Φ/Φ_0

b^z : Burgers vector

η : $b^z/2\pi$

G : conductance

μ : induced dipole moment

j_{b^z} : Burgers current

F : Fano factor

ϕ^B : Berry phase

Ω : Berry curvature

C : Chern number

$\mathbb{Z}_2$: $\mathbb{Z}_2$ invariant

σ_{xy} : anomalous Hall conductivity

Chapter 1

Introduction

1.1 General Perspectives on Research in 2D Materials

REcent advancements in nanotechnology have enabled researchers to fabricate and manufacture low-dimensional nanoscale or mesoscale structures, with high control, which are promising new nano-electronic devices with remarkable characteristics, including high performance, high speed data transfer rate, and other novel properties. In addition parallel efforts have been performed to improve computational power, increase transmit rate, and data storage. Over the last two decades the development in fabrication techniques provides the possibility to experimentally realize mesoscopic dimensions. The well-known techniques are the molecular beam epitaxy (MBE), lithography technique [1–4] which are widely used in the fabrication of nano-structured materials. A familiar example is realization of a two dimensional electron gas, 2DEG (a thin layer of charges) at the interfaces of two semiconducting heterostructures, such as, GaAs/GaAlAs, where the mean free path of electrons are measured to be about 10 μm and hence justifies the term *'mesoscopic transport'*. The miniaturization of devices has sparked tremendous excitement, extending beyond a single area of interest and being recognized as a multidisciplinary field of research.

Fabrication of micro and nano sized structures such as quantum dots, wires, and rings has made it possible for physicists to examine new ideas in electronic devices. These small size devices act as artificial atoms with spectra and shell structures similar to those of real atoms [5]. In this thesis we have chosen quantum rings (one of the systems under focus) for two main reasons. First, quantum rings (QRs) display interesting phenomena, such as persistent currents [6–10] which are not found in dots or wires. The basic difference between the ring geometry and a quantum dot is the excluded central disk region wich confines the electron in a ring to a narrow channel. This compact, periodic geometry can allow dynamics not found in any other low dimensional systems [11]. Second, it has been possible to experimentally create extremely small rings. These nano rings can be fabricated either by dry etching [12] or by MBE techniques to foster self assembled InGaAs/GaAs rings with the size of $\sim 30\ nm$ [13].

Furthermore, earlier in the 1980s and 1990s, the Aharonov-Bohm (AB) effect and the persistent currents were observed in metallic rings (e.g., Au, Cu) [8, 9, 14] and GaAs-based two-dimensional electron gas systems [15–18]. In 1999, Morpurgo et al. [19] provided experimental evidence of the spin Berry phase by interpreting peak splitting in Fourier spectra of AB oscillations. The spin Berry phase, linked to spin-orbit interactions, became a focus of both theoretical and experimental studies. Fuhrer et al. [20] in 2000s used an atomic force microscope to fabricate quantum rings on AlGaAs/GaAs surfaces, resolving addition energy spectra and magnetic field-dependent oscillations [21]. Lorke et al. [13, 22, 23] created few-electron quantum rings from self-assembled InAs dots, studying their quantum states using far infrared and capacitance spectroscopy. Warburton et al. [24] analyzed single InAs QRs via photoluminescence, revealing singlet-triplet splitting and other spectral features. Yang et al. [25] observed interference effects due to the spin Berry phase in AB conductance oscillations.

Recently, the most promising material of the century, graphene [26–28] has garnered significant attention in the study of QR systems, both theoretically and experimentally [29–31]. This is mainly due to its unique properties, such as the involvement of linearly dispersive 'massless' Dirac fermions [32, 33], possible topological phases originating from the violation of time reversal symmetry (TRS) [34], the manifestation of AB oscillations in the presence of a magnetic field [29–31, 35, 36] etc. In the graphene QR, the persistent currents are induced by the breaking of TRS [35]. Additionally, the confinement of electrons in the ring structure leads to the controlled lifting of valley degeneracy in the presence of a magnetic field [37]. Studies have also shown evidence of broken valley degeneracy [38] and an interplay between valley polarization and electron-electron interaction [37] in graphene QRs. Numerous investigations have been conducted in recent years to understand the microscopic details of graphene QRs under external magnetic fields, with and without invoking spin-orbit interactions [39–46]. It is demonstrated

that a graphene QR has potential application in future optoelectronic [47] and interferometric [48] devices.

The persistent current is a current flowing around a ring which is constant in time and which is not driven by an external power source. As such, it is a thermal equilibrium property of the ring system. While persistent currents are usually associated with superconductors, quantum mechanics allows, for such a current to exist in resistive materials as well. In QRs, we can have same persistent currents too despite their origin being different. Theoretically, persistent currents in QRs have been known for some time [49, 50] and they have also been measured experimentally using SQUIDs [51]. For the persistent current in a ring of resistive material to be measurable, the ring must be at low temperature ($\lesssim 1$ K) and small ($\lesssim 1\ \mu m$). Further, the violation of the surface inversion symmetry may induce a special type of spin-orbit coupling (SOC), which is known as the Rashba spin-orbit coupling (RSOC) [52]. The RSOC originates due to an effective electric field originating from the potential gradient across the interface [53, 54]. The RSOC has great importance in the emerging field of spintronics for fabricating novel devices at very small length scales and is very central to our discussion. The possibility of being able to tune the RSOC strength by an external gate voltage or other techniques offers an additional significance [55, 56]. Recently, in Ref. [57] it is shown how a double gated structure and a solid electrolyte surrounding the gates have been used to obtain an enhanced RSOC strength. A large number of devices have been proposed based on spin-orbit interaction, for example, the spin field effect transistor [58], and several spin interference based devices [59, 60]. In two dimensional systems, owing to its surface inversion asymmetry, RSOC is found to have large values and hence produces unignorable effects in quantum transport. Since we are going to be interested in conductance properties of two dimensional lattice systems, the RSOC will be an important component for most of our studies. The inversion symmetry is broken inside the plane, leading to asymmetric spin branches. The separation of the spin branches results in distinct velocities of the two spins, leading to a spin persistent currents. We shall discuss them in details in the latter chapters.

Additionally, defects exist almost in every material and could be a central topic of further research. Defects appear due to imperfections in material growth processes, which are almost inevitable and they are especially robust against small perturbations. Further, there are kinds of defects where the arrangement or configuration of the defects cannot be smoothly transformed into a simple or uniform state without a phase transition. These one is called topological defects. The relevance of such defects to spintronic applications has sparked interest in topological defects on the dynamics of the (spinful) carriers [61, 62]. The interaction of the topological defect with the carriers in a spin-orbit coupled environment leads to impact on the spin dynamics, and

thus could aid in designing spintronic devices through dislocation engineering [63]. Although spintronic research has predominantly focused on defect-free materials, however, defects, due to their ability to couple with the magnetic moments could prove their utility in design of spintronic devices. Furthermore, curvature, which has been proposed as a tool for enhancing electronic nanodevice design, complements the prospects of defects in applications, such as, device fabrication etc [64].

Let us also include a distinct but related to the one dimensional QR and talk about a two dimensional Corbino disk with a finite width (as opposed to the ring) with an external field threading the system. A Corbino disk was contemplated to show quantized Hall effect and gained relevance after the discovery of the quantum Hall effect in 2D MOSFET structures [65]. It was shown in Ref. [66] that in the rectangular geometry, with the characteristic sizes much larger than the electron magnetic length, the quantized Hall current may be expressed as the difference between diamagnetic currents flowing along the two edges (see also Ref. [67]). When in a state of thermodynamic equilibrium the chemical potential of these edges is the same, the edge currents cancel each other and the total one caused by the applied external magnetic field is zero. However, the annular geometry of the Corbino disk represents a practical realization of the cylinder geometry suggested by Laughlin for the gedanken experiment explaining quantum Hall effect. The sizes of the disk in Ref. [68] are assumed to be macroscopic, i.e., its inner and outer radii along with the width of the ring strongly exceeds the electron magnetic length. Further, recent studies have extensively investigated various quantum transport phenomena in graphene Corbino disks as well, both experimentally [69–72] and theoretically [73–75]. The edge-free geometry of the disk enables transport studies via evanescent waves in nanoscale graphene systems [76]. At zero magnetic field, the conductance of ultraclean ballistic disks as a function of the carrier concentration [71] aligns well with the basic mode-matching analysis described in Ref. [77]. Further, in presence of a non-zero magnetic field, periodic (approximately sinusoidal) magnetoconductance oscillations have been predicted [78, 79], yet experimental confirmation of this intriguing quantum interference phenomenon is still lacking. Recently, the authors of Ref. [75] demonstrated that a Corbino graphene disk, when pierced by a current carrying solenoid, can exhibit Aharonov-Bohm type conductance oscillations. They also found that these oscillations are more pronounced in the presence of an electrostatic potential, which breaks cylindrical symmetry and introduces mode mixing. In this thesis, in latter chapter we will present one such annular geometry, that is the Corbino disk which is contemplated by Laughlin as an electron pump that shows generation of radial (Hall) current as the enclosed flux quantum changes. The undergoing studies in the applications of graphene Corbino disks are replaced by α-T_3 disks which align well with the focus of this thesis.

Let us provide a brief note on the quantum Hall effect and its relation to topology. In 1879, Edwin Hall conducted the first experiment that demonstrated the existence of moving charges in metals [80]. A century later, during the 1980s, significant advancements occurred in the field of transport and topological studies with the discovery of the integer quantum Hall effect by Klaus von Klitzing [65] and fractional quantum Hall effect by Tsui, Störmer, and Gossard [81]. Unlike the classical Hall effect, which shows a linear dependence on the magnetic field, Klitzing [65] observed that Hall conductivity exhibits quantized plateaus measured in units of (e^2/h) across a wide range of magnetic fields. This quantization arises from the discretization of the energies of the cyclotron orbits into macroscopically degenerate flat bands known as the Landau levels (LLs) [82, 83]. Immediately following these discoveries, researchers recognized that Hall quantization has topological implications. Specifically, the conductance is facilitated by modes that are localized at the edges of the sample while the bulk remains perfectly insulating. This distinct behavior of the 'bulk' and 'edge' modes had not been observed before and marks the inception of what we now refer to as topological insulators (TIs). In 1982, the connection between the quantized Hall conductance and the topology was elucidated by Thouless, Kohmoto, Nightingale, and den Nijs. This connection can be characterized by a topological invariant, known as TKNN invariant [84], for example, Chern number is one of the TKNN invariant. The Chern number corresponds to the quantized value of Hall conductivity, σ_{xy} in units of e^2/h ($\sigma_{xy} = Ce^2/h$, C being the Chern number). Furthermore, these topological states can be understood by the bulk-boundary correspondence, which means that the properties of the boundary modes can be derived from the behavior of the bulk states. In addition to the Hall effect induced by magnetic fields, researchers have attempted to observe similar phenomena in the absence of magnetic fields, which is referred to as the quantum anomalous Hall effect (QAHE). This effect relies solely on the breaking of TRS in the system [85–88] which yields a transverse (Hall) current. The concept of QAHE was first introduced by Haldane [34] in a two-dimensional honeycomb lattice (a paradigmatic model for graphene), where a complex next-nearest-neighbor (NNN) hopping equivalent to a threaded flux through the honeycomb plaquette (also known as Haldane flux) breaks the TRS. In this model, the properties of the electronic bands are associated with a topological invariant called the Chern number [89–92]. The topology of a band is often characterized by different quantities, including the Berry phase, Berry connection, Berry curvature, and the previously mentioned Chern number all leading to identical description. This topological invariant can take a non-zero value when TRS is broken, resulting in quantized plateaus in the anomalous Hall conductivity, and can be perceived via the presence (or absence) of chiral edge modes in semi-infinite geometries, such as ribbons. Further, incorporating the real spin degrees of freedom of the electrons, and without violating the TRS, the conventional (charge) Hall conductivity becomes zero. However, in this scenario, the spin Hall conductivity remains

non-zero. Such systems are characterized by a topological invariant known as the $\mathbb{Z}_2$ invariant, which leads to the emergence of helical (instead of chiral) edge modes in a nanoribbon.

Following Haldane's pioneering research in 1988 [34], there has been a significant interest in identifying comparable topological phases within various two-dimensional model systems. These include structures such as the Lieb lattice [93–95], checkerboard lattice [96], and Kagomé lattice [97–99], buckled lattice [100], acoustic systems [101], as well as the dice lattice, among others [102, 103], etc. Notably, experimental implementations of the Haldane model have been successfully demonstrated in two-dimensional honeycomb configurations, such as Fe-based ferromagnetic insulators like $XFe_2(PO_4)_2$, where X can be K, Cs, or La [104], the interface between the two trivial ferromagnetic insulators EuO and GdN [105] etc. Moreover, advancements in cold atomic systems that facilitated formation of optical lattices created by standing-wave laser beams [106–108]), have opened up new avenues for exploring these intriguing non-trivial topological phases. Examples include optical honeycomb [109] and dice lattices [110], which further enrich the study of topological phenomena.

It is of general interest to assess the role of interactions on the topological features. In particular, electron-electron interaction is of interest, however due to lack of any credible formalism, other than large scale numarics, the progress is limited. Nevertheless, other kinds of interaction may be included. For example, the electron-phonon (e-ph) interaction has been proven to deliver promising discoveries in solids [111–113] starting from the inducing superconductivity [114–116], transport in 3D materials [117], low-dimensional polaronic effects [118–121], charge density wave [122–124] formation in solids to the Fermi-polarons in ultracold gases [125–127], Peierls transition [128–130], topological signatures in novel systems [131–133] etc. More recently, Bose polaron [134–136], phonon-induced Floquet topological phases [137, 138], and several others have been actively investigated. In a polar or ionic crystal, when an electron propagates through the lattice, it distorts the structure of the lattice. As a result, a net polarization potential arises due to the interaction between the electron and the oscillating lattice, which can lead to the trapping of the electron. The quasiparticles generated from this interaction are characterized as electrons dressed with phonon clouds, commonly referred to as polarons. Depending on the strength of the e-ph interaction, the polarons can be self-trapped (strong coupling limit) or delocalized (weak coupling limit). In a tight binding system, the electron is found to be strongly bound to its own lattice site, and that electron can participate in forming the polaron by interacting with the onsite phonons. Therefore the radius of the polaron in such narrow-band systems is short-ranged and does not spread over extended region in the lattice. The polarons in such systems are often called as the '*small polarons*' or the *Holstein polarons* [139, 140]. The

polaron formation in tight binding systems can be realized through an interaction between the "extra" fermionic impurity and the phonons in the system.

Let us now put all these physical phenomena in a single thread for putting things in perspective for this thesis. Thus, we should be talking about prototype systems (or materials) where these phenomena can be observed. Graphene is one such material consisting of a single layer of carbon atoms arranged in a honeycomb lattice, as illustrated in Fig. 1.1(a). Since the experimental discovery of graphene in 2004 [141] by Novoselov and Geim, as a two-dimensional crystal, a novel area of research has emerged [142]. For low-energy, the tight binding Hamiltonian can be effectively expressed as $H = \hbar v_F \mathbf{S} \cdot \mathbf{k}$, or more generally the Dirac-Weyl equation with pseudospin S = 1/2, pseudospin here means sublattice degrees of freedom. Further, in the low-energy spectrum, the electrons act like a two-dimensional gas of massless Dirac fermions, following a relativistic linear dispersion relation ($E = \hbar v_F k$), although the Fermi velocity ($v_F \approx 10^6 m/s$) is much small than (10^{-3} times) the speed of light [143]. This unique behavior has earned a term 'pseudorelativistic' and enabled studies of various transport phenomena, including Klein tunneling (perfect transmission through potential barriers) [144–146], quantum interference phenomena localized within the material (capabilities that traditional electron systems cannot achieve) [147] etc. Furthermore, graphene exhibits an unconventional quantum Hall effect [148–151], characterized by a half-integer spacing in the Hall quantization. This phenomenon is a direct consequence of the unusual Berry phase of π found in graphene.

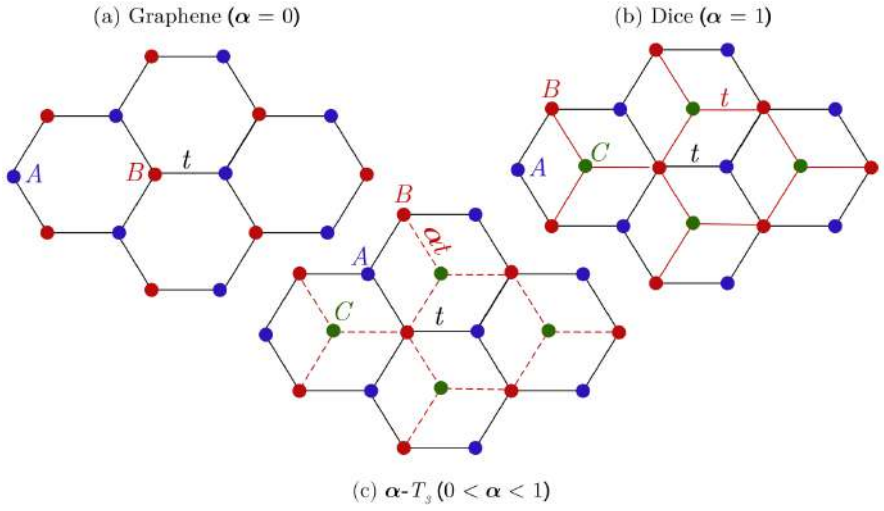

Figure 1.1: The figure depicts the α-T_3 lattice at the center, (c), flanked by the graphene honeycomb lattice (its $\alpha = 0$ limit) on the left, (a) and the dice lattice (its $\alpha = 1$ limit) on the right, (b). In the graphene lattice, each unit cell contains two atoms located at sites A (blue) and B (red), connected by a hopping parameter t. In the α-T_3 and dice lattices, an additional site C (green) is located at the center of each hexagon and connected with the B sites only. For the dice lattice, site C is connected to the B sites via the hopping parameter t, while in the α-T_3 lattice, the connection is governed by a variable hopping parameter αt. Notably, there is no hopping between the A and C sites in any of the lattices.

On the other hand, there exists an interesting variant of the honeycomb structure of graphene with T_3 symmetry, usually known as the dice lattice, as shown in Fig. 1.1(b) [152–155]. Here, the honeycomb lattice is augmented by an extra site located at the center of each hexagon. Three inequivalent sites in a unit cell effectively introduce an enlarged subspace spanned by pseudospin S = 1 fermion. It can be described by the same Dirac-Weyl Hamiltonian as graphene in this enlarged subspace. On the experimental font, it has been argued that a particular arrangement of three counterpropagating pairs of laser beams can produce an optical dice lattice [156] in the cold atomic environment. It has further been proposed that a dice lattice can be fabricated in a heterostructure of cubic lattices, namely, $SrTiO_3/SrIrO_3/SrTiO_3$ [157] along the (111) direction. A number of studies [158–160] have explored the properties of general pseudospin S lattices, arising from the generalized Dirac-Weyl Hamiltonian, and provide insights into lattices with pseudospin S = 1/2, 1 and beyond.

Recently, proposal for a more generalized two-dimensional Dirac material, called the α-T_3 lattice [161] emerged. A unit cell of the α-T_3 lattice comprises of three non-equivalent lattice sites as shown in Fig. 1.1(c). The hopping strength between the A and B sites is t, while the sites B and C are connected through a hopping strength αt. The strength of α may be considered as a tunable parameter and it demonstrates a smooth changeover with the variation of the parameter α from graphene ($\alpha = 0$) (Fig. 1.1(a)) to the dice lattice ($\alpha = 1$) (Fig. 1.1(b)). The electronic dispersion of the α-T_3 lattice with $\alpha = 1/\sqrt{3}$ can be realized in a $Hg_{1-x}Cd_xTe$ quantum well corresponding to a certain critical doping [162]. Within the nearest-neighbor tight-binding framework, the low-energy spectrum of the α-T_3 lattice near a particular valley, governed by the Dirac-Weyl Hamiltonian with an enlarged pseudospin (S > 1/2), comprises of three bands, with two dispersive bands (linearly dispersing in momentum) and a zero-energy flat band. All the six band-touching points (the so called Dirac points) in the first Brillouin zone lie on the flat band. Due to the α-T_3 lattice's crystal structure allows it to exhibit so many noteworthy characteristics, it has been the subject of extensive research recently [163–169]. When it is perfectly flat, due to the zero group velocity, the presence of a dispersionless flat band in the α-T_3 may not contribute to electronic transport, but it can offer intriguing physics for quantum transport [170–172] and topology. A good number of physical quantities, such as the Berry phase-dependent direct current (DC) Hall conductivity [163], dynamical optical conductivity [163], magneto-optical conductivity, the Hofstadter butterfly [164, 173], Berry-phase modulated valley-polarized magnetoconductivity [174], the photoinduced valley and electron–hole symmetry breaking [175] in the α-T_3 lattice have been studied recently. Further, other properties, such as the conductivity [166, 176], super-Klein tunneling [177–179], gap generation and flat band catalysis [180, 181], non-linear optical response [182], topological phase transition [183–186], electronic and optical

properties under radiation [187, 188], Weiss oscillations [174], zitterbewegung [189], plasmons [190, 191], Ruderman-Kittel-Kasuya-Yosida (RKKY) interaction [192, 193], minimal conductivity [166], spin-Hall phase transition [186], and the thermoelectric performance of a nanoribbon [194] of α-T_3 lattice have also been explored. Moreover, nontrivial topology [195, 196], the diamagnetic [197] (at $\alpha = 0$) to paramagnetic [152, 153] (at $\alpha = 1$) transition in the orbital magnetic responses of the lattice have also been reported. Furthermore, recently a number of studies have been done on the α-T_3 lattice using Blonder–Tinkham–Klapwijk (BTK) formalism, for example, an α-T_3 NS [198], NIS junction [199], pure cross Andreev reflections in superconducting hybrid junctions [200]. Interesting physics can also arise from the α-T_3 lattice in the presence of time periodic external radiations [172, 201, 202] etc.

Motivated by the above scenario, we wish to explore the transport and topological aspects of pseudospin-1 α-T_3 crystal lattices. We shall study both charge and spin persistent currents in QRs made with α-T_3 lattice with various SOCs and in presence of external magnetic field and defects. Later, we will see how the e-ph coupling is intimately related to topological phases of matter, which in turn affects the conducting properties and the edge modes of the system.

In the following, we shall provide brief descriptions of the essential ingradients (which may be systems, formalism, or phenomena) that have extensively discussed in the thesis.

1.2 Quantum Ring

A quantum ring is a nanostructure in which electrons are confined in a ring like geometry, allowing unique quantum effects to dominate their behavior. The ring will be assumed to be strictly one dimensional and has a static potential variation. There is typically a desired radius to width ratio for quantum rings to observe quantum interference effects and ensure well defined quantized energy levels. To observe quantum effects such as the Aharonov-Bohm (AB) effect, the radius (R) of the ring must be on a mesoscopic scale, meaning it should be large enough to allow an electron to encircle it coherently, but small enough that quantum coherence is maintained [203]. The width (W) of the ring, which is the distance between the inner and outer edges, must be narrow enough to ensure that the electron wavefunctions primarily circulate along the ring without occupying a large cross sectional area. This confinement strengthens quantized energy levels and reduces unwanted scattering effects. If the ring is too wide relative to the radius, multiple electron paths can interfere in complex ways, making the quantum interference effects harder to interpret. A narrower width generally ensures a more straightforward single mode electron transport around the ring. For clear quantum effects, the radius to width ratio is often

set to be higher ($R \gg W$). This ratio provides a balance where, the electrons are confined to the ring path with minimal cross sectional area interference and the phase coherence around the ring is preserved for clearer AB oscillations and energy quantization. An electron traversing the ring behaves exactly like an electron in a periodic structure, where the potential variation in one period is the same as that in one circuit around the ring. The schematic representation of an ideal one-dimensional (1D) ring is illustrated in Fig. 1.2.

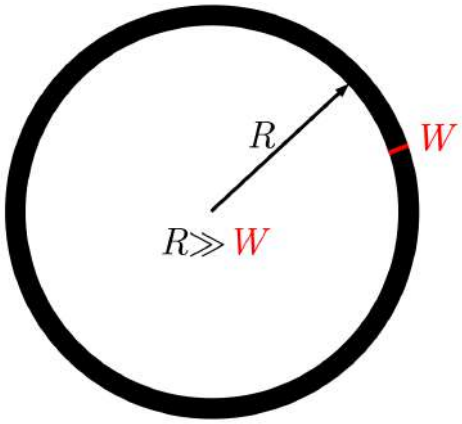

Figure 1.2: A schematic of an ideal one-dimensional quantum ring, characterized by a radius R that is much larger than its width W ($R \gg W$).

1.3 Aharonov-Bohm Effect

In classical mechanics, a charged particle is not influenced by the electromagnetic fields in regions where the fields are zero. For a long time, it was assumed the same held true in quantum mechanics. However, in 1959, Aharonov and Bohm [204] conceptualized that the vector potential can affect the quantum behavior of a particle even in regions where the field is absent. This remarkable finding indicates that the potentials are more fundamental than the fields, a phenomenon commonly referred to as the Aharonov-Bohm effect.

To illustrate this effect, we consider a modified double-slit-like experiment, as shown in Figure 1.3. In this experiment, a beam of coherent charged particles (charge q) is emitted from a source region (A). The beam is split into two parts, which then recombine after passing through the slits. A detector is placed in region B to measure the resulting interference pattern. Additionally, a long solenoid containing a constant magnetic flux is placed behind the middle wall, ensuring that each part of the beam passes on opposite sides of the solenoid [205].

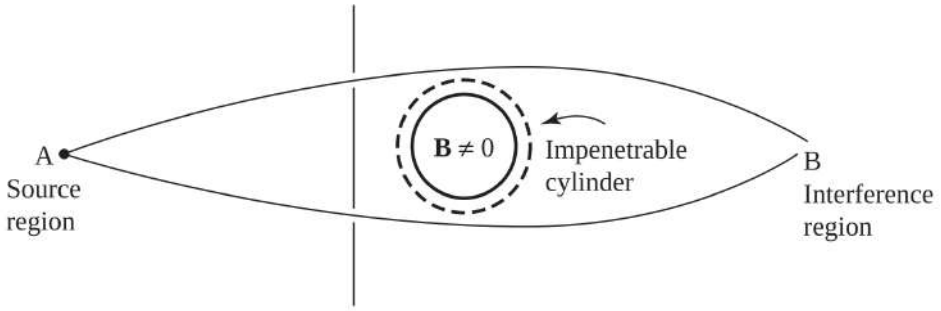

Figure 1.3: Sketch of the setup for the Aharonov-Bohm effect. In order for the magnetic field to approximately vanish outside the solenoid, we take the solenoid to be very large in the direction perpendicular to the image plane. Image taken from Ref. [205].

We are all familiar with the results of the double-slit experiment, while let us express the calculation more clearly as a path integral. We can present it as follows,

$$\begin{aligned} \sum_{\text{paths}} e^{iS/\hbar} &= \sum_{\text{paths, slit1}} e^{iS/\hbar} + \sum_{\text{paths, slit2}} e^{iS/\hbar} \\ &\sim \quad e^{ikL_1} \quad + \quad e^{ikL_2} \end{aligned} \tag{1.1}$$

where S represents the action, L_1 and L_2 are the path lengths through the two respective slits to any point being measured on the output screen, and k denotes the wavevector of the incoming wave.

The Lagrangian of a charged particle in a general electromagnetic (EM) field is given by,

$$\mathcal{L} = \frac{m}{2}\dot{\vec{r}}^2 + q(\dot{\vec{r}} \cdot \vec{A} - V) \tag{1.2}$$

where m, q, and $\dot{\vec{r}}$ are mass, charge, and velocity of the particle respectively, whereas $\vec{A}$ and V denote the vector and scalar potentials respectively. When there is no EM field present, we return to the original double-slit experiment, and we refer to the action in this scenario as S_0. Introducing a magnetic field into the Lagrangian can alter the action by,

$$S \to S_0 + q\int \vec{A} \cdot \dot{\vec{r}}\, dt = S_0 + q\int \vec{A} \cdot\ d\vec{l}. \tag{1.3}$$

Now returning to the double-slit experiment, in the presence of the vector potential the probability amplitude to find the particle at some point on the detector is proportional to [206],

$$\sum_{\text{paths, slit1}} exp\left(i\frac{S_0}{\hbar} + i\frac{q}{\hbar}\int \vec{A} \cdot d\vec{l}\right) + \sum_{\text{paths, slit2}} exp\left(i\frac{S_0}{\hbar} + i\frac{q}{\hbar}\int \vec{A} \cdot d\vec{l}\right). \tag{1.4}$$

The physically important quantity is the difference in accumulated phases between the two paths. This is given by,

$$exp\left(\frac{iq}{\hbar}\int_{\text{slit1}}\vec{A}\cdot d\vec{l} - \int_{\text{slit2}}\vec{A}\cdot d\vec{l}\right)c = exp\left(\frac{iq}{\hbar}\oint\vec{A}\cdot d\vec{l}\right), \tag{1.5}$$

where the integral is taken over a loop that traverses forward through slit 1 and then returns backward through slit 2.

Using Stoke's theorem, we can write the exponent in Eq. (1.5) as,

$$\frac{iq}{\hbar}\oint\vec{A}\cdot d\vec{l} = \frac{iq}{\hbar}\int_{\text{enc}}(\vec{\nabla}\times\vec{A})\cdot d\vec{S} = \frac{iq}{\hbar}\int_{\text{enc}}\vec{B}\cdot d\vec{S} = \frac{iq}{\hbar}\Phi_{\text{enc}} \tag{1.6}$$

where Φ_{enc} is the flux enclosed in the loop. Thus, there is a measurable relative phase shift between the two paths given by $\frac{iq}{\hbar}\Phi_{\text{enc}}$. This phase shift leads to a change in the interference pattern observed on the screen. It is important to note that although the original Lagrangian may not appear particularly gauge invariant, the final result (after integrating around the complete path) is indeed gauge independent.

An important point regarding the AB effect is that if Φ_{enc} is an integer multiple of the elementary flux quantum Φ_0 $(= h/q)$, then the phase shift becomes an integer multiple of 2π and is effectively equivalent to having no phase shift at all.

1.4 Persistent Currents

The persistent current studied in this thesis is an equilibrium property of the system. It occurs in mesoscopic systems, like a ring or a loop, where the wave function is phase coherent around the loop. The magnetic flux through the ring induces a phase in the wave function due to the AB effect as discussed earlier. When there is a magnetic flux threading the ring, it can affect the energy levels of the system.

We consider the simplest possible model for the 1D ring into which an electron of mass m and charge $-e$ is revoling around. We parametrize the ring by the coordinate u and circumference L, as shown in Fig. 1.4. The time-independent Schrödinger equation for the Hamiltonian $\vec{H} = \vec{p}^2/2m$ is,

$$-\frac{\hbar^2}{2m}\frac{d^2\psi_n}{du^2} = \epsilon_n\psi_n \tag{1.7}$$

with the wavefunction ψ_n subjected to the boundary condition,

$$\psi_n(u+L) = \psi_n(u). \tag{1.8}$$

The eigenfunctions and eigenenergies indexed by integer n are,

$$\psi_n(u) = \frac{1}{\sqrt{L}}\, exp\left(2\pi i n \frac{u}{L}\right) \quad \text{and} \quad \epsilon_n = \frac{h^2}{2mL^2} n^2. \tag{1.9}$$

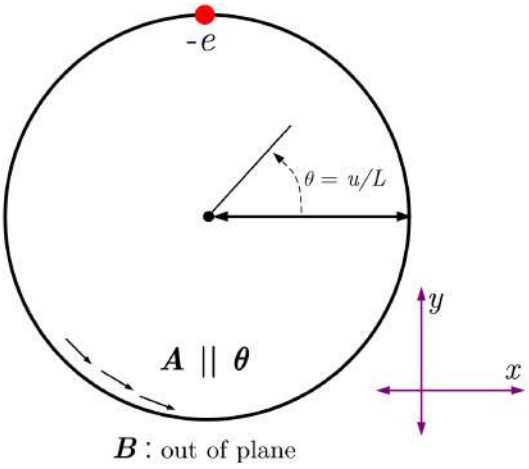

Figure 1.4: A perfect one-dimensional ring. The figure shows the orientation relative to an applied magnetic field of a perfect, one-dimensional ring of radius $L/2\pi$ to which a particle with charge -e is confined. The applied magnetic field B is parallel to the $\hat{z}$ direction and points out of the plane. The vector potential $\vec{A}$ chosen in the text is tangent everywhere to the ring and parallel to the cylindrical unit vector $\hat{\theta}$.

Now, let us consider the effects of an external magnetic field $\vec{B}$ to the system. We choose the coordinates so that the ring lies in the xy-plane and is centered at the origin. We assume that the magnetic field $\vec{B} = B\hat{z}$ is parallel to the z-axis.

In the presence of a magnetic field, the Hamiltonian becomes $\vec{H} = (\vec{p} - q\vec{A})^2/2m$, where $\vec{A}$ is the vector potential of the magnetic field satisfying $\vec{B} = \nabla \times \vec{A}$. Further, we shall use $q = -e$ throughout the thesis.

For $\vec{B} = B\hat{z}$, we can write $\vec{A} = -\frac{B}{2}(y\hat{x} - x\hat{y})$. Defining cylindrical coordinates (r, θ) and corresponding unit vectors $(\hat{r}, \hat{\theta})$ satisfying,

$$\begin{aligned} &x = r\cos\theta, \quad y = r\sin\theta, \quad r = \sqrt{x^2+y^2}, \quad \theta = \tan^{-1}(y/x), \\ &\hat{r} = \cos\theta\hat{x} + \sin\theta\hat{y}, \quad \text{and} \quad \hat{\theta} = -\sin\theta\hat{x} + \cos\theta\hat{y}. \end{aligned} \tag{1.10}$$

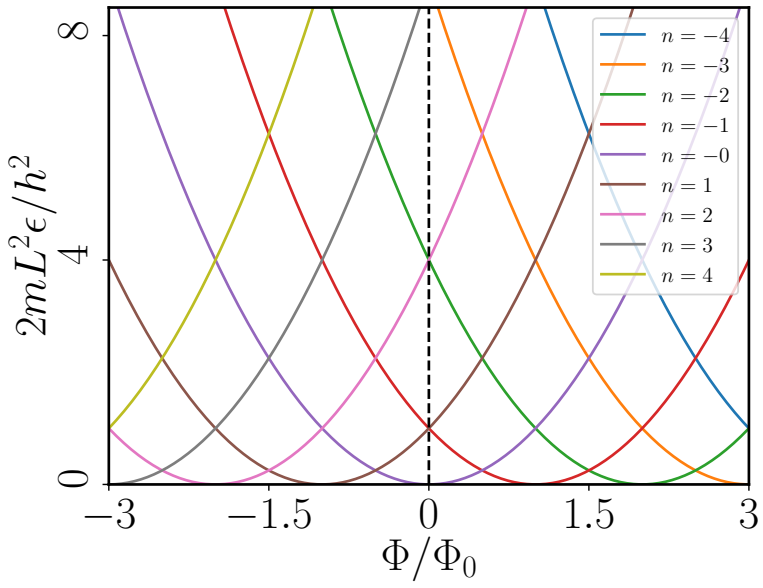

Figure 1.5: Eigenenergies of a perfect one-dimensional ring. The figure shows the first few eigenenergies ϵ_n. The dashed line marks the point $\Phi = 0$.

We can write $\vec{A} = Br\hat{\theta}/2$. Confined to $r = L/2\pi$ along the ring, we can also write $\vec{A} = \Phi\hat{\theta}/L$ where $\Phi = \pi r^2 B$ is the flux enclosed by the ring. The coordinate $u = L\theta/2\pi$ follows the ring in a circle about the origin, and thus the derivative d/du, which is everywhere tangent to the ring, is always parallel to $\hat{\theta}$. Thus, in the presence of $\vec{B}$, the 1D time-independent Schrödinger equation parametrized by u becomes,

$$\frac{1}{2m}\left(-i\hbar\frac{d}{du} + e\frac{\Phi}{L}\right)\psi_n = \epsilon_n\psi_n. \tag{1.11}$$

The eigenfunctions ψ_n are again given by Eq. (1.9) with the eigenenergies now,

$$\begin{aligned}\epsilon_n &= \frac{1}{2m}\left(\frac{2\pi\hbar}{L}n + e\frac{\Phi}{L}\right)^2 \\ &= \frac{\hbar^2}{2mR^2}\left(n + \frac{\Phi}{\Phi_0}\right)^2,\end{aligned} \tag{1.12}$$

where we have introduced the flux quantum $\Phi_0 = h/e$. The energies ϵ_n are plotted as a function of flux Φ in Fig. 1.5. The eigenenergy ϵ_n of the n^{th} eigenstate is parabola. Further, the energy spectrum is symmetric under both $\Phi \to -\Phi$ and $\Phi \to \Phi + \Phi_0$.

The persistent current is discussed using an idealized Aharonov-Bohm flux ϕ threading the ring but not penetrating the linewidth of the ring itself. It is possible to attain all of the results given here for the 1D, perfect ring using this idealized flux. We now find the current associated with each eigenstate. A particle moving at velocity v around a ring of circumference L makes one round trip in time $\Delta t = L/v$. If the particle has charge $-e$, then the average current,

the charge passing any given point of the ring per unit time averaged over one period, is $i = -e/\Delta t = -ev/L$. The velocity of such a charged particle in a magnetic field can be written as $v = (p + eA)/m$. Then, for the system we are considering, the velocity v_n associated with the n^{th} eigenstate as given in Eq. (1.9) satisfies,

$$\begin{aligned} v_n\psi_n(u) &= \frac{(p+eA)}{2m}\psi_n(u) \\ &= \frac{1}{m}\bigg(-i\hbar\frac{d}{du} + e\frac{\Phi}{L}\bigg)\bigg(\frac{1}{\sqrt{L}}exp\big(2\pi in\frac{u}{L}\big)\bigg) \\ &= \frac{\hbar}{mR}\bigg(n + \frac{\Phi}{\Phi_0}\bigg)\psi_n(u), \end{aligned} \tag{1.13}$$

yielding a current given by,

$$\begin{aligned} i_n &= -\frac{e}{L}v_n \\ &= -\frac{e\hbar}{2\pi mR^2}\bigg(n + \frac{\Phi}{\Phi_0}\bigg) \end{aligned} \tag{1.14}$$

We note that in terms of the energy ϵ_n given in Eq. (1.12) the current i_n may be written as,

$$i_n = -\frac{\partial\epsilon_n}{\partial\Phi}. \tag{1.15}$$

This is the definition of the persistent current. We shall revisit it later and extensively use it in our calculations.

1.5 Topological Defects

A topological defect (TD) is a disruption or an irregularity in the crystalline order or structure of a material arrangement, which gives rise to broken symmetries. These defects are essentially misaligned regions in an otherwise ordered system and often form during fabrication. TDs, as the name suggests are stable, meaning their effect cannot be removed or modified by continuous transformations of the surrounding order without drastically modifying (such as cutting or tearing) them. TDs can vary depending on the dimensionality and nature of the system, here the primary types of TDs observed in various fields, including condensed matter physics are listed in Table 1.1.

As our system is purely 1D and posseses crystalline symmetry, screw dislocation is one of the natural types of TD may present in our system, we will elaborate this in a later chapter of the thesis. Further, in the framework of geometric theory of defects [207, 208], elastic deformations induced by topological defects in continuous media are described using a metric. These theory

Dimension	Defects	Example	Description
0D	Point defects	Monopoles	In spin systems
1D	Line defects	Vortices Screw dislocation	In superfluids In crystalline materials
2D	Surface defects	Domain walls Grain boundaries	In ferromagnetic materials In polycrystalline materials
3D	Volume defects	Textures Solitons	In skyrmions Soliton in field theory

Table 1.1: Example of different topological defects in different dimensions.

bears a resemblance to the theory of three-dimensional gravity. Within this geometric formalism, the continuous elastic medium is represented as a Riemann–Cartan manifold, where the curvature and torsion are associated with disclinations and dislocations, respectively, present in the medium. Consequently, the Burgers vector (measures the magnitude and direction of dislocation) and the Frank angle (the angle that characterizes the orientation of the Burgers vector relative to the dislocation line) are respectively analogous to torsion and curvature. The impact of topological defects on the quantum dynamics of electrons/holes in a crystal has been explored in various physical scenarios [61, 62]. Theoretical descriptions of quantum dynamics within a medium containing dislocations have been undertaken for quite some time. For instance, Kawamura [209] and Bausch, Schmitz, and Turski [210, 211] investigated the scattering of a single particle within dislocated media using a distinct approach. They demonstrated that the equation describing the scattering of a quantum particle by a screw dislocation follows the AB form. The AB effect has also been explored using the Katanaev–Volovich approach in media with a dislocation, as seen in Refs. [212, 213], and in the presence of dislocations, as observed in Refs. [62, 214]. In Ref. [215], Aurell probed deeper into the influence of dislocations on the properties of quantum dots. More recently, the study of the impact of topological defects in mesoscopic systems has been conducted in Ref. [63], particularly with regard to a quantum dot in presence of a dislocation.

1.6 Corbino Disk

The Corbino disk was proposed by O. M. Corbino, an Italian physicist, in 1911. He designed this disk-shaped geometry to study electrical conductivity and magnetic field effects in materials, specifically to investigate the influence of a magnetic field on radial current flow in a

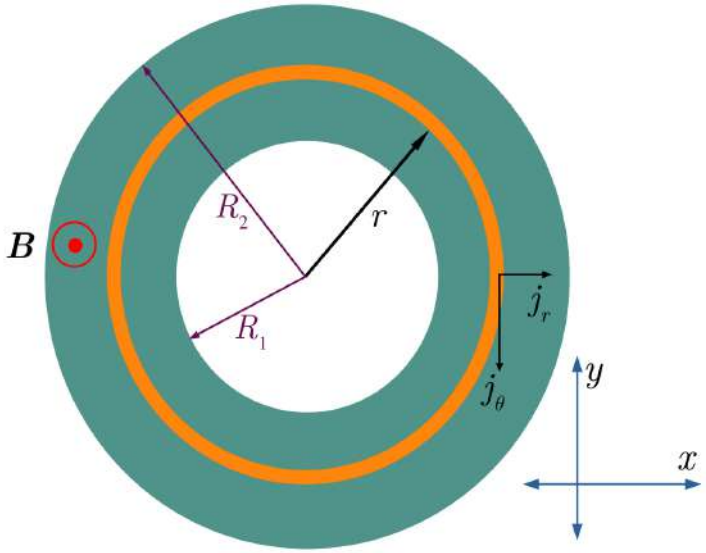

Figure 1.6: A Corbino disk with inner radius R_1 and outer radius R_2, subjected to an external magnetic field B oriented perpendicular to the plane of the disk.

circular conductor. A Corbino disk is a circular, ring-shaped electronic device as shown in Fig. 1.6 used to study the electrical properties of materials in the absence of edge currents, which makes it distinct from other common geometries. It consists of a conductive disk (or a thick ring) with a central circular electrode and an outer circular electrode. This design means that current flows radially across the ring, creating a unique current path compared to straight-line or rectangular geometries. When a magnetic field is applied perpendicular to the disk, circular currents and radially dependent magnetoresistance effects arise. Because the edges of the disk are circular rather than linear, this setup avoids the influence of edge states that are present in other geometries, like the Hall bar. In a Corbino disk, resistance changes as a function of the applied magnetic field, giving insight into the magnetoresistance of the material. This can reveal information about carrier mobility, density, and scattering mechanisms. Magnetoconductance and magnetoresistance oscillations can also be observed, especially in high-mobility materials such as graphene or 2DEGs in semiconductors.

The Corbino disk geometry is often used to study the quantum Hall effect (QHE) without interference from edge currents. Generally, in systems that show QHE, quantized Hall conductance is observed in a planar geometry. Analogously, this disk system is also an ideal candidate for investigating the Hall voltages as the external field threading the vacant region in changed by the flux quantum. In graphene-based systems, the Corbino disk is particularly useful for examining the unique properties of the Dirac fermions, as well as phenomena like magnetoconductance oscillations, and AB-type effects etc.

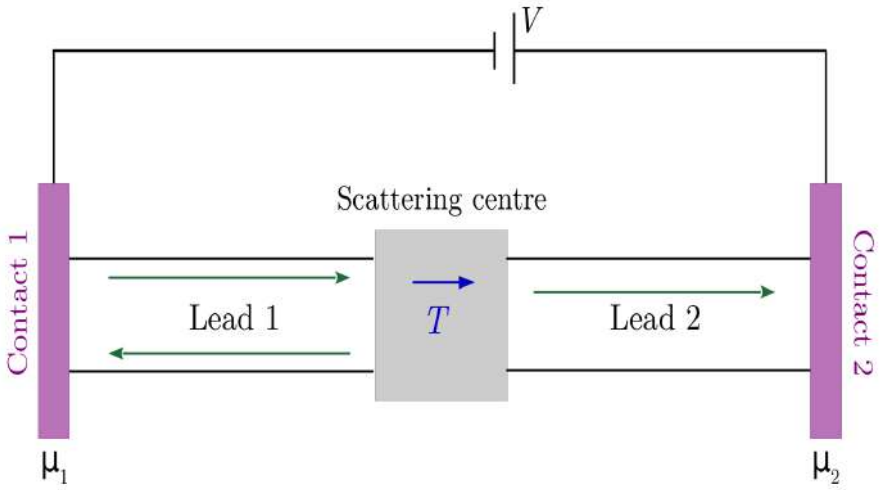

Figure 1.7: Coherent transport through a system with two leads, each with multiple propagating states.

1.7 Landauer-Büttiker Formula

This section provides an overview of the Landauer approach, which is an important technique in the physics of mesoscopic systems. The Landauer-Büttiker approach treats electron transport as a barrier transmission problem [216–219] [1]. In this framework, ohmic contacts are considered as reservoirs that inject and collect current, with the assumption that inelastic scattering occurs exclusively. A schematic representation of this concept is shown in Fig. 1.7. The measured conductances can be expressed as functions of the transmission probabilities at the Fermi level between the reservoirs.

The conduction in a macroscopic (2D) conductor is given by the Ohm's law as,

$$G = \frac{\sigma A}{L} \tag{1.16}$$

where A is cross section area of a conductor of length L having the conductivity of σ. This implies that as $A \to 0$, $G \to 0$, indicating that conductance vanishes in narrow conductors. Conversely, $G \to \infty$ for very small conductors (as $L \to 0$). These behaviours stem from the assumption that conductivity is uniform along the length of the conductor, a concept that breaks down at atomic scales where Ohm's law cease to hold. The failure in Ohm's law has been experimentally validated in quantum point contacts and atomic-sized wires, leading to the development of the Landauer formula [220, 221] to address these limitations which takes the

[1] Although in 1981 Fisher and Lee [216] were the first to derive the Landauer-Büttiker formula, it has become widespread practice in the literature to refer to a later article from 1985, co-authored by Büttiker and Landauer [217] (hence the name).

form,

$$G = \frac{2e^2}{h} MT \tag{1.17}$$

where T represents the average probability of an electron to be injected from one end and transmitted to the other end of the conductor and M is the number of the transverse modes.

When current flows between two leads having electrochemical potential differences μ_1 and μ_2 at zero temperature, there is no qualitative distinction between current and voltage probes. Büttiker proposed that all probes can be treated equivalently [222, 223]. In the linear response regime, the aforementioned equation (Eq. (1.17)) takes on the following form,

$$I = \frac{2e}{h} \overline{T}[\mu_1 - \mu_2]. \tag{1.18}$$

Here $\overline{T}(= |T|^2)$ is the product of the transmission probability per mode T at the Fermi energy and the number of modes M. By combining all the terminals (labelled by a and b) we get,

$$I_a = \frac{2e}{h} \sum_b \left[\overline{T}_{b \leftarrow a} \mu_a - \overline{T}_{n \leftarrow b} \mu_b \right]. \tag{1.19}$$

These arrows tell us that there is a backward electron transfer from the second subscript, that is, a note to the first one, that is b note (we shall drop them afterwards). We can rewrite Eq. (1.19) in the form (with $V_i = \mu_i / e$),

$$I_a = \sum_b \left[G_{ba} V_a - G_{ab} V_b \right] \tag{1.20}$$

where

$$G_{ba} = \frac{2e^2}{h} \overline{T}_{ba} = \frac{2e^2}{h} |T_{ba}|^2. \tag{1.21}$$

To ensure that the current becomes zero when the values of the chemical potential are equal [224], the transmission coefficient G satisfy the sum rules as follows,

$$\sum_b G_{ba} = \sum_a G_{ab} \tag{1.22}$$

Therefore, Eq. (1.20) becomes,

$$I_a = \sum_b G_{ab} \left[V_a - V_b \right]. \tag{1.23}$$

This is the Landauer- Büttiker formula for the conductance of a system. When the coupling to the leads is strong and the electrons can be treated as noninteracting (using a single particle

Hamiltonian) the Landauer-Büttiker formalism becomes a highly effective tool for understanding quantum transport phenomena [225–227].

1.8 Topological Considerations

Topology is a branch of mathematics that examines quantities of a system that remain invariant under continuous transformations, such as twistings, bending, stretching, cutting, and gluing. Tearing, however, is not allowed. These quantities are referred to as topological invariants, which are quantities associated with topological space that take on discrete values (usually normalized to be integer-valued) that do not change under continuous deformations of the space. One way to determine if two spaces are topologically equivalent to each other is to compare the values of these invariants. A classical example, one can transform a single hole donut into a coffee cup, but the number of holes (which is one in this case) remains the same, which is a topological invariant. Such invariants play a crucial role in distinguishing topological and trivial phases.

Topology in condensed matter physics is an emerging field that explores how certain properties of the materials remains unchanged under smooth deformations. These are robust even in presence of impurities or disorders. By deformations, one implies how the energy levels of a system changes under tuning of certain external parameters (e.g., an electric field). If the number of the energy levels below the Fermi level remain unaltered due to this deformation process, then the resultant system and the original one belong to the same topology class. If certain energy band (or bands) cross the Fermi level then the topological properties are disturbed, however if the resultant system still possesses a spectral gap, then the system has undergoing a topological phase transition.

In condensed matter systems, the role of topology first came into light after the discovery of integer quantum Hall effect [65]. As already stated, the plateaus are associated with topological invariants known as the Chern numbers [228, 229]. In this section, we shall see computation of such topological invariants from the band properties. However, we begin form Berry phase for a better understanding of the topological invariants.

1.8.1 Berry phase

In 1984, Michael Berry [230] introduced the concept of the Berry phase, which is a phase difference that occurs when a non-degenerate energy eigenstate of a quantum system experiences

adiabatic evolution along a closed path in parameter space. As the system reverts to its initial state, an extra phase emerges in conjunction with the dynamical phase, this geometrical phase, now known as the Berry phase or Berry-Pancharatnam phase. This phase holds importance in numerous physical systems, particularly in solid-state physics [231–233], due to several key characteristics, such as, its gauge invariance, which allows it to be measured experimentally via quantum interference experiments [234], its geometric aspect can be described as a line integral of the Berry curvature (analogous of Gaussian curvature in topology) across the surface encircled by the closed path, and finally it has relevance in differential geometry and gauge field theories [235]. Significantly, integrating the Berry curvature across closed surfaces yields topological values referred to as Chern numbers, which are fundamental to phenomena such as the quantized Hall plateaus observed in the quantum Hall effect [84, 231]. The closed surface is the first Brillouin zone (BZ) in our case.

1.8.2 Mathematical formulation of Berry phase

We shall follow the formalism presented in Refs. [231, 236, 237] to derive the Berry phase. We consider a physical system with the Hamiltonian $H(\mathbf{R})$ that is dependent on time via a set of parameters represented by vector $\mathbf{R} = (R_1, R_2, R_3, ...)$ where $R_i = R(t)$. Along a closed path $\mathcal{C}$ in parameter space, the parameters $R(t)$ vary slowly, causing the Hamiltonian to evolve adiabatically in time. One can obtain the instantaneous wavefunctions $|n(\mathbf{R})\rangle$ of $H(\mathbf{R})$, which serve as the orthonormal basis, by digonalizing $H(\mathbf{R})$ at each point $\mathbf{R}$ as,

$$H(\mathbf{R})|n(\mathbf{R})\rangle = \epsilon_n(\mathbf{R})|n(\mathbf{R})\rangle. \tag{1.24}$$

According to the adiabatic theorem of quantum mechanics [238], a system that is initially prepared in one of its eigenstates, $|n(\mathbf{R}(0))\rangle$, will remain an instantaneous eigenstate of the Hamiltonian $H(\mathbf{R})$ during the adiabatic evolution in parameter space. Consequently, the only degree of freedom of quantum state is its phase which need not be zero. Here, we require that the basis function's phase be single-valued and smooth along path $\mathcal{C}$ in the parameter space [231]. Therefore, after time t the wavefunction will be in the state,

$$|\Psi_n(t)\rangle = e^{-i\gamma(t)}|n(\mathbf{R})\rangle \tag{1.25}$$

having acquired a phase $\gamma(t)$. The evolution of the wavefunction can be described by the time-dependent Schrödinger equation,

$$i\hbar\frac{\partial}{\partial t}\Psi(t) = H(\mathbf{R})\Psi(t) \tag{1.26}$$

substituting Eq. (1.25) in Eq. (1.26) and taking the scalar product with $|n(\mathbf{R})\rangle$ on both side and using the orthonormality $\langle n(\mathbf{R})|n(\mathbf{R})\rangle = 1$, we find,

$$\epsilon_n(\mathbf{R}) - i\hbar\langle n(\mathbf{R})|\frac{d}{dt}|n(\mathbf{R})\rangle = \hbar\frac{d}{dt}\gamma(t). \tag{1.27}$$

The phase $\gamma(t)$ can be obtained by integrating Eq. (1.27) with respect to time as,

$$\gamma(t) = \frac{1}{\hbar}\int_0^t \epsilon_n(\mathbf{R}(t'))dt' - i\int_0^t \langle n(\mathbf{R}(t'))|\frac{d}{dt}|n(\mathbf{R}(t'))\rangle dt', \tag{1.28}$$

where the first term is the usual dynamical phase factor, and the second term is a geometric phase known as the Berry phase. The Berry phase is given as,

$$\phi^{\mathrm{B}} = -i\int_0^t \langle n(\mathbf{R}(t'))|\frac{d}{dt}|n(\mathbf{R}(t'))\rangle dt'. \tag{1.29}$$

For a closed path, $\mathbf{R}(t)$ parametrizes a cyclic, adiabatic process. The chain rule for derivatives use to eliminate the explicit time dependency of Eq. (1.29), and we get,

$$\phi^{\mathrm{B}} = -i\oint_{\mathcal{C}} \langle n(\mathbf{R})|\nabla_{\mathbf{R}}|n(\mathbf{R})\rangle \cdot d\mathbf{R}. \tag{1.30}$$

We shall use this expression to compute Berry phase. The quantity in the integrand is known as the Berry connection which is denoted by $\mathcal{A}$, that is,

$$\mathcal{A} = i\langle n(\mathbf{R})|\nabla_{\mathbf{R}}|n(\mathbf{R})\rangle. \tag{1.31}$$

One can also compute the curl of $\mathcal{A}$, which can be denoted by Ω, and is known as the Berry curvature,

$$\Omega = \nabla \times \mathcal{A}. \tag{1.32}$$

In a condensed matter system, the Bloch wave vector of a Hamiltonian is used to compute Berry connection, which further helps to compute the Berry phase and the Berry curvature [239]. The calculations of Berry curvature are illustrated in the next section.

1.8.3 Berry curvature

Berry curvature can be viewed as a representation showing how much the *ground* (the wavefunction of a quantum system) twists or changes as one move in different directions. It describes how the wavefunction of the system changes when specific parameters, like the position or momentum of a particle, are altered. Let us consider a 2D parameter space, so that we have vectors $|\Psi_\lambda\rangle$ as a function of $\lambda = (\lambda_x, \lambda_y)$. Then the definition of the Berry connection in Eq. (1.31) naturally generalizes to that of a 2D vector $\mathcal{A}(\lambda) = (\mathcal{A}_x, \mathcal{A}_y)$ via,

$$\mathcal{A}_\mu(\lambda) = i\langle\Psi_\lambda|\partial_\mu\Psi_\lambda\rangle \tag{1.33}$$

where $\partial_\mu = \partial/\partial\lambda_\mu$ and the Berry phase expression of Eq. (1.30) can be written as a line integral around the loop, i.e.,

$$\phi^{\mathrm{B}} = \oint \mathcal{A}\cdot d\lambda \tag{1.34}$$

Then the Berry curvature $\Omega(\lambda)$ is simply defined as the Berry phase per unit area in (λ_x, λ_y) space. Thus, we can think as Berry connection $\equiv$ vector potential and Berry curvature $\equiv$ magnetic field. In a continuum framework, it becomes just the curl of the Berry potential as shown in Eq. (1.32).

Now we show the Berry curvature for a 2D system whose band structure lies in the k_x - k_y plane. Therefore, the Berry curvature is a function of k_x and k_y which is given by,

$$\Omega = [\nabla\times\mathcal{A}]_z = \frac{\partial\mathcal{A}_y}{\partial k_x} - \frac{\partial\mathcal{A}_x}{\partial k_y}. \tag{1.35}$$

Since $\mathcal{A}$ is independent of k_z, only z-component of Ω is non-zero. Now, using Eq. (1.33) we can simplify the above expression as,

$$\begin{aligned}
\Omega_z &= \frac{\partial\mathcal{A}_y}{\partial k_x} - \frac{\partial\mathcal{A}_x}{\partial k_y} \\
&= i\frac{\partial}{\partial k_x}\langle\Psi_\lambda(\mathbf{k})|\frac{\partial}{\partial k_y}\Psi_\lambda(\mathbf{k})\rangle - [x\longleftrightarrow y] \\
&= i\left\langle\frac{\partial}{\partial k_x}\Psi_\lambda(\mathbf{k})\middle|\frac{\partial}{\partial k_y}\Psi_\lambda(\mathbf{k})\right\rangle + i\left\langle\Psi_\lambda(\mathbf{k})\middle|\frac{\partial^2}{\partial k_x\partial k_y}\Psi_\lambda(\mathbf{k})\right\rangle - [x\longleftrightarrow y] \\
&= i\left\langle\frac{\partial}{\partial k_x}\Psi_\lambda(\mathbf{k})\middle|\frac{\partial}{\partial k_y}\Psi_\lambda(\mathbf{k})\right\rangle - i\left\langle\frac{\partial}{\partial k_y}\Psi_\lambda(\mathbf{k})\middle|\frac{\partial}{\partial k_x}\Psi_\lambda(\mathbf{k})\right\rangle \quad \left[\text{using } \frac{\partial^2}{\partial k_x\partial k_y} = \frac{\partial^2}{\partial k_y\partial k_x}\right] \\
&= \mathrm{Im}\sum_{\lambda'\neq\lambda}\big\langle\nabla\Psi_\lambda(\mathbf{k})\big|\Psi_{\lambda'}(\mathbf{k})\big\rangle\times\big\langle\Psi_{\lambda'}(\mathbf{k})\big|\nabla\Psi_\lambda(\mathbf{k})\big\rangle.
\end{aligned} \tag{1.36}$$

Last line is obtained via inserting a complete set of states, namely, $\sum_{\lambda'} \big|\Psi_{\lambda'}(\mathbf{k})\big\rangle\big\langle\Psi_{\lambda'}(\mathbf{k})\big| = \mathrm{I}$. Now, to calculate $\big\langle\Psi_{\lambda'}(\mathbf{k})\big|\nabla\Psi_{\lambda}(\mathbf{k})\big\rangle$, we begin with,

$$\begin{aligned} H(\mathbf{R})\big|\Psi_\lambda(\mathbf{k})\big\rangle &= E_\lambda\big|\Psi_\lambda(\mathbf{k})\big\rangle \\ \Rightarrow \nabla[H(\mathbf{R})\big|\Psi_\lambda(\mathbf{k})\big\rangle] &= \nabla[E_\lambda\big|\Psi_\lambda(\mathbf{k})\big\rangle] \\ \Rightarrow \nabla H\big|\Psi_\lambda(\mathbf{k})\big\rangle + H\big|\nabla\Psi_\lambda(\mathbf{k})\big\rangle &= \nabla E_\lambda\big|\Psi_\lambda(\mathbf{k})\big\rangle + E_n\big|\nabla\Psi_\lambda(\mathbf{k})\big\rangle \\ \Rightarrow \big\langle\Psi_{\lambda'}(\mathbf{k})\big|\nabla H\big|\Psi_\lambda(\mathbf{k})\big\rangle + \big\langle\Psi_{\lambda'}(\mathbf{k})\big|H\big|\nabla\Psi_\lambda(\mathbf{k})\big\rangle &= E_\lambda\big\langle\Psi_{\lambda'}(\mathbf{k})\big|\nabla\Psi_\lambda(\mathbf{k})\big\rangle \\ \Rightarrow \big\langle\Psi_{\lambda'}(\mathbf{k})\big|\nabla\Psi_\lambda(\mathbf{k})\big\rangle &= \frac{\big\langle\Psi_{\lambda'}(\mathbf{k})\big|\nabla H\big|\Psi_\lambda(\mathbf{k})\big\rangle}{E_\lambda - E_{\lambda'}}. \end{aligned} \tag{1.37}$$

Therefore, from Eq. (1.36) we get,

$$\Omega_z^\lambda(\mathbf{k}) = i\sum_{\lambda'\neq\lambda} \frac{\big\langle\Psi_\lambda(\mathbf{k})\big|\nabla H\big|\Psi_{\lambda'}(\mathbf{k})\big\rangle \times \big\langle\Psi_{\lambda'}(\mathbf{k})\big|\nabla H\big|\Psi_\lambda(\mathbf{k})\big\rangle}{(E_\lambda - E_{\lambda'})^2}. \tag{1.38}$$

The summation includes all the eigensolutions except for the one with the degeneracy. The advantage of the summation formula is that it can be evaluated under any choice of gauge since the wave function involved does not undergo any differentiation. This property is particularly useful when performing numerical computations.

1.8.4 Chern number ($\mathbb{Z}$ invariant)

The Chern number provides understanding into the topological features of materials and supports the categorization of phases that are not explained by traditional symmetry breaking. In a condensed matter system, the Chern number relates to a specific band, and if it is non-zero, the system is referred to as a Chern insulator or a topological insulator. The Chern insulator exhibits topological characteristics, including quantized Hall conductivity, non-zero edge current, and so on. Nevertheless, in order to attain these non-trivial phases, it is essential to break the TRS and ensure that there must be a gap in the dispersion spectrum to prevent any degeneracy (as degeneracies can lead to divergences in the Berry curvature as shown in Eq. (1.38)). In the quantum Hall effect, the Hall conductivity is quantized in units of e^2/h, and is directly proportional to the Chern number of the occupied bands. The quantization is due to the topological attributes of the system, with the Chern number being a fundamental parameter in detailing this effect. Further, systems having non-zero Chern number exhibit robust edge states as a result of the bulk-boundary correspondence. This principle asserts that the topological characteristics of the bulk (Chern number) determine the presence of conducting states along the edges, which are protected even in presence of impurities or defects. The Chern number is defined as a sum of

the Berry curvature for a system residing on a torus. In a 2D system, the BZ exhibits a toroidal geometry, as the momenta possess periodicity (say, 2π), making k_x equivalent to $k_x + 2\pi$, and k_y equivalent to $k_y + 2\pi$. Consequently, the integration of Berry curvature over the first BZ provides the Chern number as,

$$C = \frac{1}{2\pi} \iint_{\mathrm{BZ}} \Omega_z^{\lambda}(\mathbf{k})\, dk_x dk_y \tag{1.39}$$

where $\Omega_z^{\lambda}(\mathbf{k})$ can be obtained from Eq. (1.38). We have used Eq. (1.39) to compute Chern numbers in all of the systems we considered.

1.8.5 $\mathbb{Z}_2$ topological invariant

This section covers the calculation of a different topological invariant referred to as the $\mathbb{Z}_2$ invariant, which characterizes the quantum spin Hall (QSH) phase of a system. In contrast to the Chern insulators, these systems exhibit quantized spin Hall conductivity and spin-filtered edge currents in a ribbon geometry, whereas the charge sector conductivity disappears. For a spin Hall insulating phase to arise, TRS must be preserved in the system. We discuss these non-trivial phases in more detail later in the context of the Kane-Mele model.

To describe the topological properties of this system, the Wannier charge centers (WCCs) (which is known as the center of charge in a unit cell) are employed. The electronic ground state in periodic crystalline solids is naturally described by extended Bloch functions $|\psi_{n\mathbf{k}}\rangle$, or the cell-periodic versions $|u_{n\mathbf{k}}\rangle = e^{-i\mathbf{k}\cdot\mathbf{r}}|\psi_{n\mathbf{k}}\rangle$, labeled by the band n and crystal momentum $\mathbf{k}$. Further, the WCC can be thought of as the expectation value of the position operator for a basis represented by Wannier functions (WFs). These WFs are a set of orthogonal functions indexed by a lattice position, say $\mathbf{R}$, $w_n(\mathbf{r}-\mathbf{R}) = \langle \mathbf{r}|W_n(\mathbf{R})\rangle$, and maximally localized about that point with respect to all relevant spatial dimensions, which can be obtained from the Bloch states by a Fourier transformation as,

$$|W_n(\mathbf{R})\rangle = \frac{V}{(2\pi)^d} \int_{BZ} e^{-i\mathbf{k}.\mathbf{R}}|\psi_{n\mathbf{k}}\rangle\, d^d k, \tag{1.40}$$

where d and V represent the dimensionality of the $\mathbf{k}$-space and the volume of the real space primitive unit cell respectively, and the integral is taken over the first BZ. On the other hand, a convenient strategy for a 2D QSH may be to construct a "hybrid Wannier functions" (HWFs), which are localized along one direction, say along $\hat{x}$ (Wannier like in 1D), and delocalized along

the other directions, namely, $\hat{y}$ and $\hat{z}$ (Bloch like in 2D) [240, 241] which read as,

$$|W_n^H(R_x, k_y, k_z)\rangle = \frac{a_x}{(2\pi)} \int_{-\pi/a_x}^{\pi/a_x} e^{-ik_x R_x a_x} |\psi_{n\mathbf{k}}\rangle \, dk_x. \tag{1.41}$$

Here, a_x is the lattice constant along the x direction. Thus, the HWF can be thought of as a WF of a 1D system, coupled to the external parameters k_y and k_z. With the help of the evolution of HWFs around a closed loop in the BZ, the adiabatic, unitary evolution of the occupied Bloch bands can be described.

A geometric interpretation in terms of the Zak phase [242] can be given to illustrate WCCs. To do this, a Berry potential is introduced for the lattice periodic part of the Bloch functions as,

$$\mathcal{A}_n(\mathbf{k}) = i\langle u_{n\mathbf{k}}|\nabla_{\mathbf{k}}|u_{n\mathbf{k}}\rangle. \tag{1.42}$$

In 1D, WCCs can be redefined in terms of Berry potential using the transformations between Wannier and Bloch representations of Ref. [243] as,

$$\overline{x}_n = \frac{ia_x}{(2\pi)} \int_{-\pi/a_x}^{\pi/a_x} \langle u_{n\mathbf{k}}|\partial_{k_x}|u_{n\mathbf{k}}\rangle \, dk_x = \frac{a_x}{(2\pi)} \int_{-\pi/a_x}^{\pi/a_x} \mathcal{A}_n(k_x) \, dk_x. \tag{1.43}$$

Similarly, for our 2D system, we can construct the hybrid WCC (HWCC), which can be represented as the expectation value of the position operator, $\hat{\mathbf{X}}$, with respect to the HWFs (see Eq. (1.41)) as,

$$\langle x_n(k_y, k_z)\rangle = \langle W_n^H(R_x, k_y, k_z)|\hat{\mathbf{X}}|W_n^H(R_x, k_y, k_z)\rangle. \tag{1.44}$$

By the modern theory of polarization [244–246], the HWCC can be interpreted in terms of the Berry phase, $\phi_n^{\mathrm{B}}(k_y, k_z)$ as,

$$\langle x_n(k_y, k_z)\rangle = \frac{\phi_n^{\mathrm{B}}(k_y, k_z)}{2\pi} = \frac{1}{2\pi} \int_0^{2\pi} \mathcal{A}_n(k_x, k_y, k_z) dk_x, \tag{1.45}$$

where we have taken $a_x = 1$ without any loss of generality.

Since our 2D model lies in the x-y plane, we can define a k-vector in the momentum space as $\mathbf{k} = k_{\hat{b}_1}\hat{b}_1 + k_{\hat{b}_2}\hat{b}_2$ and characterize the $\mathbb{Z}_2$ invariant by employing the hybrid Wannier transformation along $\hat{b}_1$ and studying its evolution as a function of the remaining momentum, that is $k_{\hat{b}_2}$, where $\mathbf{b_1}$ and $\mathbf{b_2}$ are the reciprocal lattice vectors and are given as,

$$\mathbf{b_1} = (-\frac{2\pi}{\sqrt{3}a_0}, \frac{2\pi}{3a_0}) \quad \text{and} \quad \mathbf{b_2} = (\frac{2\pi}{\sqrt{3}\mathrm{a}_0}, \frac{2\pi}{3\mathrm{a}_0}). \tag{1.46}$$

Therefore, we can now compute the HWCC in the direction a_1 as a function of $k_{\hat{b}_1}$, which can be mathematically formulated as $\langle r_{n,\hat{a}_1}(k_{\hat{b}_2})\rangle = \langle W_n^H(R_{\hat{a}_1}, k_{\hat{b}_2})|\hat{\mathbf{X}}|W_n^H(R_{\hat{a}_1}, k_{\hat{b}_2})\rangle$, and assumes a form,

$$\langle r_{n,\hat{a}_1}(k_{\hat{b}_2})\rangle = \frac{\phi_n^{\mathrm{B}}(k_{\hat{b}_2})}{2\pi} = \frac{1}{2\pi}\oint \mathcal{A}_n^{\hat{b}_1}(k_{\hat{b}_1}, k_{\hat{b}_2})dk_{\hat{b}_1}, \tag{1.47}$$

with $\mathcal{A}_n^{\hat{b}_1}(k_{\hat{b}_1}, k_{\hat{b}_2}) = i\langle u_{n\mathbf{k}}|\frac{\partial}{\partial k_{\hat{b}_1}}|u_{n\mathbf{k}}\rangle$.

The interpretation of the $\mathbb{Z}_2$ invariant in terms of the HWCC goes as follows. It is defined as the number of individual HWCC crossed by an arbitrary line traversing half the BZ, modulo 2 [246]. If the line intersects an even (odd) number of HWCCs while traversing through half the BZ, the $\mathbb{Z}_2$ invariant is zero (non-zero), assuring a topologically trivial (nontrivial) phase.

1.9 Topological Insulators

The concept of a topological insulator (TI) has appeared in the condensed matter physics relatively recently, that is around the first decade of the 21st century. Topological insulators are a new class of materials which are characterized by a bulk band gap like an ordinary band insulator (see Fig. 1.8(a)), while have protected conducting states at their edge in the case of two-dimensional TI or at the surface for three-dimensional TI (see Fig. 1.8(b)) The most important feature of TI is that its behavior is independent of its specific geometry and the conductive edge (surface) states in a TI are topologically protected that results in characteristic energy bands that continuously connect the bulk conduction with those of the valence bands. The existence of topological phases in TIs depends on various symmetries, such as time-reversal symmetry, chiral symmetry, and particle-hole symmetry. This relationship gives rise to a classification framework, often referred to as the "periodic table of topological insulators and superconductors", as outlined in Appendix A. For example, the time-reversal symmetry is represented by the operator Θ, with $\Theta^2 = \pm 1$ represent the presence of TRS, while $\Theta^2 = 0$ implies the absence of TRS. The topological phases in each symmetry class are denoted by the invariants $\mathbb{Z}$, $\mathbb{Z}_2$, and zero, correspondingly, the TIs can be classified into a $\mathbb{Z}$ (Chern insulator) or $\mathbb{Z}_2$ index insulators. The Chern number, C is actually a $\mathbb{Z}$ invariant and is used widely in this thesis.

Our work is based on two different class of systems. One is the class A (see Appendix A) Haldane model [34], which is characterized by the non-zero Chern number that denotes chiral edge modes. The two-dimensional system that shows quantum Hall state, belongs to this symmetry class. The other one we have studied is the Kane-Mele model [248] which belongs to class AII (see Apendix A) symmetry and has odd (even) $\mathbb{Z}_2$ topological invariant. This in turn implies the

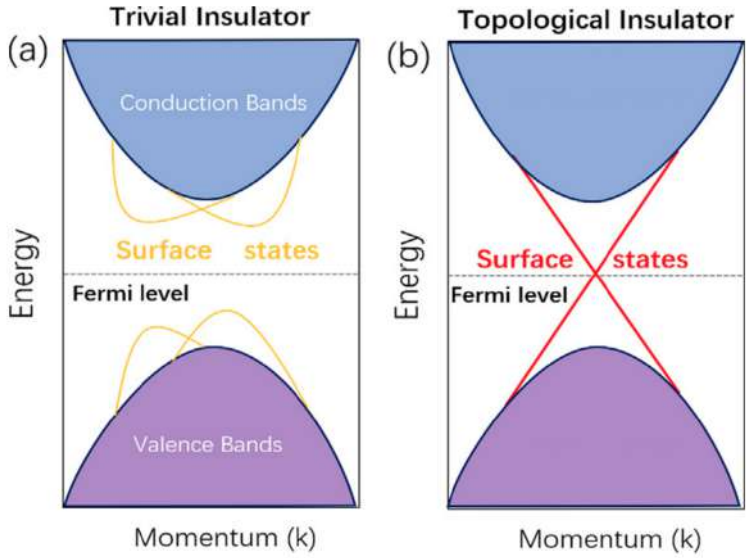

Figure 1.8: Schematic diagram of comparison between (a) a trivial insulator and (b) a topological insulator. The surface states of a trivial insulator are insulating, whereas those of a topological insulator are metallic and are protected by topological invariants. Figure courtesy Ref. [247].

presence of the helical edge modes in a system with open boundaries and demonstrates quantum spin Hall phase.

1.10 Spin-Orbit Coupling

Spin-orbit coupling (SOC) refers to the interaction between the spin of a particle and its orbital motion, resulting in shifts in energy levels due to the interplay between the spin of electron and the magnetic field produced by the nucleus. In this section, we present a straightforward derivation of SOC. Since electric and magnetic fields transform under Lorentz transformations between inertial frames [249], an electron that moves through the electric field of the nucleus experiences a magnetic field from its own frame of reference. The interaction between the electron's spin and this magnetic field arising from its orbital motion can be expressed as,

$$H_{int} = -\vec{\mu}_e \cdot \vec{B} \tag{1.48}$$

where $\vec{\mu} = -g\mu_B\vec{S}$ is the magnetic moment of the self rotating electron with g, gyromagnetic ratio and μ_B, Bohr magneton,

$$H_{int} = g\mu_B\vec{S} \cdot \vec{B}. \tag{1.49}$$

Since $\vec{B} = \frac{1}{2}\frac{\vec{E}\times\vec{v}}{c^2\sqrt{1-v^2/c^2}}$, $\vec{E}$ is related to the electric potential ,$\frac{1}{2}$ is Thomas correction factor and $\sqrt{1-v^2/c^2}$ is the relativistic factor, the energy corresponding to interaction term gives,

$$\begin{aligned} H_{SO} &= g\mu_B \frac{\vec{E}\times\vec{v}}{2c^2\sqrt{1-v^2/c^2}} \cdot \vec{S} \\ &= \frac{ge\hbar}{8mc^2}\frac{\vec{E}\times\vec{v}}{\sqrt{1-v^2/c^2}} \cdot \vec{\sigma} \quad \left(\text{putting } \vec{S} = \frac{\sigma}{2} \text{ and } \mu_B = \frac{e\hbar}{2m}\right) \\ &= \frac{ge\hbar}{4mc^2}\frac{\vec{E}\times\vec{v}}{\sqrt{1-v^2/c^2}} \cdot \vec{\sigma} \quad \left(\text{with } g = 2\right) \\ &= -\frac{e\hbar}{4m_e^2c^2}\vec{\sigma}\cdot\vec{p}\times\vec{\nabla}V \end{aligned} \tag{1.50}$$

where m_e is the effective electron mass, c denotes the velocity of light, σ is the Pauli spin matrix, p is the momentum, and $\vec{E}$ is given by $\vec{E} = -\vec{\nabla}V$, where V is the electric potential. From the above expression it is understood that if a charged particle moves through a potential gradient, then SOC emerges. In crystals, the above form may be approximated by,

$$H_{SO} = \zeta_{SO}\vec{L}\cdot\vec{S} \tag{1.51}$$

where ζ_{SO} is the interaction strength, $\vec{L}$ represents the orbital angular momentum operator and $\vec{S}$ denotes the spin angular momentum operator [250]. The corresponding energies of this Hamiltonian are non degenerate. Hence, the SOC leads to the formation of energy sub levels that exhibit different energies depending on the orientation of the total angular momentum vector. This phenomenon is known as fine structure splitting.

There are different types of SOC depending on its orgin, such as, impurities in the conduction layer, which serve as a primary source of SOC in metallic systems. Absence of crystal inversion symmetry, wherein an electron experiences an asymmetry in the crystal potential due to the lack of bulk inversion symmetry. This can lead to spin splitting in the conduction band and is referred to as the Dresselhaus spin-orbit interaction [251, 252]. Lack of surface inversion symmetry in the confinement potential of electrons, which can occur in a quantum well or a heterostructure. When the motion of an electron is confined to two dimensions, such as in quantum wells, an asymmetric confinement potential can give rise to another type of SOC known as the Rashba spin-orbit coupling (RSOC) [52]. This will be explained in more detail in the following section.

1.10.1 Rashba spin-orbit coupling

In solids, quasi-free electrons are largely unaffected by the strong attraction of the nuclei of their host atoms. Nevertheless, these electrons can still encounter electric fields or potential gradients as a result of internal effects. When subjected to a strong electric field or potential gradient, the phenomenon of SOC can arise. If a potential gradient occurs across an interface due to structural inversion asymmetry, it leads to the formation of a specific type of spin-orbit coupling referred to as Rashba spin-orbit coupling, named after its discoverer, E. I. Rashba [52]. The significance of RSOC cannot be overstated, it provides a unique opportunity to manipulate the asymmetry in the confinement potential through electrostatic methods. This means that we can finely tune the strength of RSOC by adjusting an external gate voltage, making it a versatile tool in semiconductor technology. Additionally, the strength of RSOC varies with the crystal composition in quantum wells and is largest in narrow-gap III-V semiconductors like InAs and InGaAs etc. In the following, we shall delve deeper into RSOC using a continuum model.

The Rashba Hamiltonian for a two-dimensional electron gas (2DEG) can be described via the following form [52],

$$H_R = \lambda_R(\vec{\sigma} \times \vec{p}) \cdot \hat{z} \tag{1.52}$$

where $\lambda_R = -\frac{ge\hbar\vec{E}}{8m_e^2c^2}$ is the strength of the RSOC, $\vec{\sigma}$ is a vector of Pauli spin matrices, $\vec{E} = -\vec{\nabla}V$ is electric field along $\hat{z}$ direction, and $\vec{p} = -i\hbar\vec{\nabla}$ is the momentum operator. In the absence of any Zeeman coupling and elastic scattering, the total Hamiltonian is given by,

$$H = \frac{p^2}{2m} + \lambda_R(\vec{\sigma} \times \vec{p}) \cdot \hat{z} = \frac{p_x^2 + p_y^2}{2} + \lambda_R(\sigma_x p_y - \sigma_y p_x). \tag{1.53}$$

The energy spectrum of the Hamiltonian yields the form [253, 254],

$$E(\mathbf{k}) = \frac{\hbar^2\mathbf{k}^2}{2m} \pm \lambda_R\hbar|\mathbf{k}| \tag{1.54}$$

where $|\mathbf{k}| = \sqrt{k_x^2 + k_y^2}$ is the modulus of electron momentum and the $\pm$ sign refers for two different spin-filtered bands. The associated wavevectors of the Hamiltonian corresponding to the bands are given by,

$$\psi_\pm = \frac{e^{i(k_x x + k_y y)}}{\sqrt{2}} \begin{pmatrix} 1 \\ \pm ie^{-i\vartheta} \end{pmatrix} \tag{1.55}$$

where $\vartheta = \tan^{-1}(k_y/k_x)$. From Eq. (1.55) it is easily understood the spin states are orthogonal to the direction of motion. When an electron traverses in the x-direction, the spinor component of the wavevector assumes the form $(1, \pm i)$, implying that the spin-$\uparrow$ and spin-$\downarrow$ are entangled in

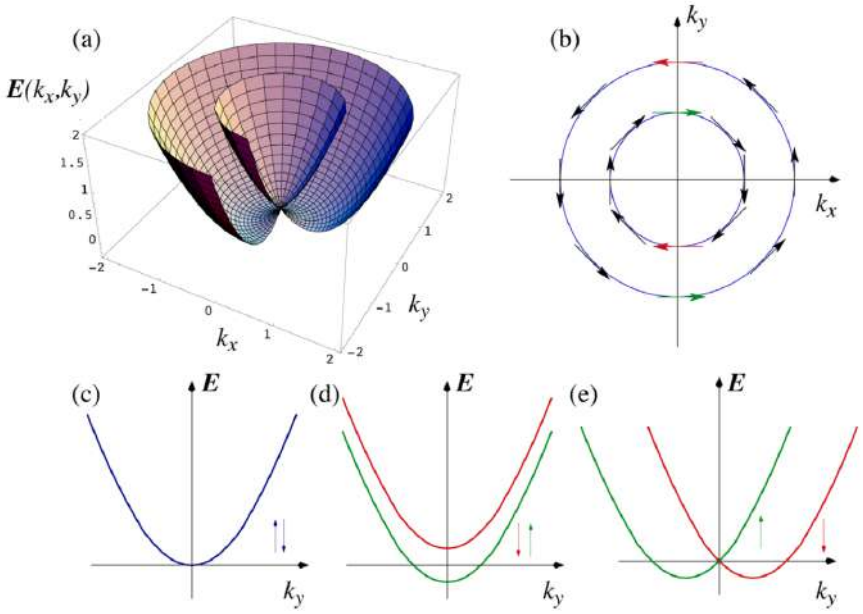

Figure 1.9: (a) Three-dimensional energy spectrum of 2DEG with Rashba Spin-Orbit Coupling (RSOC) included. (b) Fermi energy contours presented in the $k_x - k_y$ plane. (c) Energy spectra for a free electron without the influence of either RSOC or Zeeman energy. The energy spectra for an electron subjected to a magnetic field (Zeeman splitting) are shown in (d), while (e) depicts the energy spectra in the presence of RSOC. Figure courtesy Ref. [254].

the y-direction. In contrast, when the electron moves along the y-direction, the wavevectors take the form $(1, \pm 1)$, indicating that the spin-$\uparrow$ and spin-$\downarrow$ states are confined within the x-direction (see Fig. 1.9).

Fig. 1.9(a) depicts the three dimensional energy spectra corresponding to Eq. (1.54). While Fig. 1.9(b) demonstrates the Fermi energy with the spin states. In Figs. 1.9(c)-1.9(e), the spectra of the 2DEG are shown as a function of k_y while k_x is taken at zero. Fig. 1.9(c) is related to the case $\lambda_R = 0$, where there is no splitting of energy between the spins, that is, the bands are degenerate and coincide with each other. The degeneracies are lifted in presence of an external magnetic field, B and the splitting is known as the Zeeman splitting and the gap separating spin-$\uparrow$ and spin-$\downarrow$ bands is equal to $g\mu_B B$ (see Fig. 1.9(d)). The case with non-zero λ_R is shown in Fig. 1.9(e), where the spin degeneracy is lifted except at $k_y = 0$, however, it does not open any gap.

1.11 Anomalous Hall Conductivity

The anomalous Hall effect (AHE) is a phenomenon that occurs in certain materials where an electric current produces a transverse voltage (perpendicular to the current) even without an external magnetic field, resulting in what is known as anomalous Hall conductivity. The term

'anomalous' is used to differentiate it from the original Hall effect (or conductivity), which is caused by the presence of a magnetic field. The AHE typically manifests in ferromagnetic and other materials having strong SOC, and it is influenced by the material's intrinsic electronic structure and magnetic properties. Anomalous Hall conductivity is observed to be non-zero when the system possesses a non-zero Chern number. In our studies, to understand topological properties of an α-T_3 model we have not incorporated any external magnetic field (unlike the transport studies pertained in QR), allowing us to focus solely on anomalous Hall conductivity. To compute it, we first obtain the Berry curvature, $\Omega_z^n(k_x, k_y)$ of a system using Eq. (1.38), and then use the formula as given by [231, 255],

$$\sigma_{xy} = \frac{\sigma_0}{2\pi} \sum_n \int_{occupied} \frac{dk_x dk_y}{(2\pi)^2} \, f[E_n(k_x, k_y)] \, \Omega_z^n(k_x, k_y) \tag{1.56}$$

where $E_n(k_x, k_y)$ denotes the electronic energy of the nth band and $\sigma_0 = e^2/h$. $f[E]$ is the Fermi-Dirac distribution function which reads as,

$$f[E] = \frac{1}{1 + e^{(E-E_F)/k_B T}} \tag{1.57}$$

where E_F is the Fermi energy, k_B is the Boltzmann constant, and T is the temperature. It should be noted that the integration is carried out over the occupied states only, that is, only the states below the Fermi level, E_F are taken into account and the summation in Eq. (1.56) is taken over all the bands therein.

1.12 Haldane Model

The Haldane model is a fundamental concept in condensed matter physics, proposed by physicist F. Duncan M. Haldane in 1988 [34]. It describes a two-dimensional honeycomb lattice model of electrons, similar to graphene, which consists of two sublattices (A and B). Each unit cell contains two atoms, and each atom on a sublattice is connected to three nearest neighbors from the opposite sublattice as shown in Fig. 1.10. This model includes a complex next-nearest-neighbor (NNN) hopping between atoms on the same sublattice, which is crucial for understanding topological phases of matter, particularly the quantum Hall effect. The complex phase in NNN hopping introduces a chiral motion that mimics the effect of an external magnetic field and breaks time-reversal symmetry, even without a net magnetic flux passing through the lattice. This chiral hopping term breaks the TRS and causes non-zero Hall conductivity, which is essential for the formation of topologically protected edge states. However, it maintains the inversion symmetry. The Hamiltonian governing the system in the presence of such hopping

can be expressed as follows,

$$H = -\left[t\sum_{\langle i,j\rangle} c_i^\dagger c_j + t_H \sum_{\langle\langle i,j\rangle\rangle} e^{i\phi_{ij}} c_i^\dagger c_j + h.c.\right] + \mathcal{M}\sum_i \xi_i c_i^\dagger c_i \tag{1.58}$$

where first term is the electron hopping between the A and B sites with the real nearest-neighbor (NN) hopping amplitude t. The summation of $\langle i, j\rangle$ runs over the NN sites with indices i and j, and $c_{i,j}^\dagger$ ($c_{i,j}$) is the creation (annihilation) operator of electrons on the corresponding A and B sites denoted by i and j indices, respectively. The second term is the complex NNN hopping of electrons $\langle\langle i, j\rangle\rangle$ (double angular brackets denote the NNN hopping are to distinguished from the single ones that stand for NN hopping) between A-B-A or B-A-B representing the spin-orbit coupling proposed by Haldane with the hopping amplitude t_H and phase ϕ_{ij}. The phase ϕ_{ij} acquires a positive (negative) value when the electron hops in the anticlockwise (clockwise) direction depending on the orientation of the two nearest neighbour bonds and can be computed from the relation of $\text{sgn}(\mathbf{d}_{ik} \times \mathbf{d}_{kj})_z$. Here $\mathbf{d}_{ik}$ is a vector that connects site i to its NN site j. The term $e^{\phi_{ij}}$ breaks the TRS since it flips the direction of the hoppings. The last term is the staggered onsite potential (also known as Semenoff mass $\mathcal{M}$) that differs between sublattices. ξ_i takes values $+1$ and -1 depending on the A and B sublattices respectively.

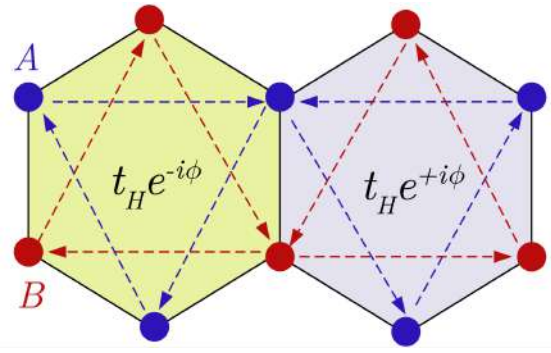

Figure 1.10: Two-dimensional honeycomb lattice model of electrons with two sublattices A (blue dot) and B (red dot). The direction dependent complex NNN hopping are shown by the corresponding arrows. For NNN hopping in the clockwise (counter-clockwise) direction ϕ is negative (positive).

In the absence of the complex hopping term, the model features Dirac points (gapless points) in its band structure located at the corners of the BZ. When the complex hopping is introduced, it opens a gap at the Dirac points, leading to insulating behavior in the bulk while allowing conductive states at the edges. The model exhibits nontrivial topological properties, characterized by a non-zero Chern number. By tuning parameters such as the phase ϕ_{ij}, staggered potential $\mathcal{M}$, and hopping amplitudes t and t_H, the model can transition between topological and trivial insulating phases. Due to the nontrivial Chern number, the system supports edge states that

are protected by topology, making them robust against certain types of disorder and imperfections. The Haldane model is one of the first theoretical frameworks to demonstrate a QAHE, where quantized Hall conductance is observed without the need for an external magnetic field. The QAHE arises from intrinsic magnetism within the system along with the complex hopping terms.

We will thoroughly explore this model to study the transport as well as the topological properties of our α-T_3 lattice in this thesis.

1.12.1 Phase diagram: Chern number

We introduce the onsite potential $\mathcal{M}$ to explore the interplay between topological phases governed by $\mathcal{M}$ and the Haldane flux ϕ. Consequently, we derive the Chern number phase diagram in the $\mathcal{M}$-ϕ plane, as illustrated in Fig. 1.11. The region enclosed by the blue curves in the $\phi > 0$ domain corresponds to the $C = +1$ phase, while the analogous region in the $\phi < 0$ domain represents the $C = -1$ phase. Areas outside the blue boundary indicate the trivial insulating regime with $C = 0$. Notably, a semi-metallic phase exists between the trivial and non-trivial regimes, demarcated by the blue curve. The equation describing these boundary curve are given by,

$$\mathcal{M}/t_H = \pm 3\sqrt{3}\sin\phi \tag{1.59}$$

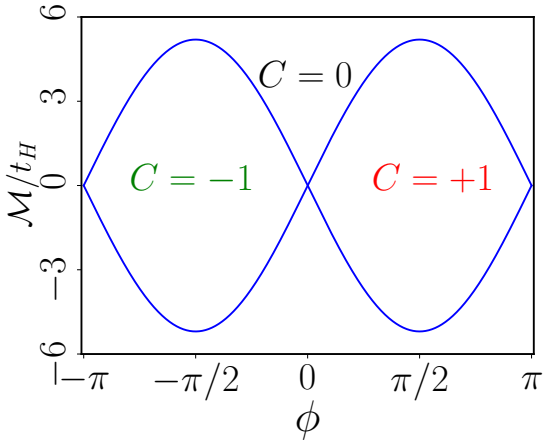

Figure 1.11: The phase diagram of the Haldane model is illustrated, where the blue boundary regions for $\phi > 0$ and $\phi < 0$ are denoted as $C = +1$ and $C = -1$ phases, respectively, the area outside this boundary represents a trivial insulating phase with $C = 0$.

1.13 Kane-Mele Model

The generation of spin currents is a subject of significant interest in solid state systems. Ref. [256] have demonstrated that the spin-Hall effect can be observed in doped semiconductors in the presence of the SOC, where a spin current flows perpendicular to an applied electric field. Kane and Mele [257] proposed that at sufficiently low energies a single plane of graphene could exhibit the QSH effect owing to an energy gap generated by the SOC. This model extends the Haldane model via incorporating spin-orbit coupling and time-reversal symmetry, providing the first theoretical description of QSH insulator. The SOC introduces a coupling between the spin of the electrons and their orbital motion, resulting in a complex hopping term between NNNs. This SOC term effectively breaks the spin symmetry while preserving time-reversal symmetry. The tight binding Hamiltonian for the Kane-Mele model on a honeycomb lattice is given by,

$$H = \Big[-t \sum_{\langle i,j\rangle\sigma} c^{\dagger}_{i\sigma} c_{j\sigma} + i\lambda_{SO} \sum_{\langle\langle i,j\rangle\rangle\sigma} \nu_{ij} c^{\dagger}_{i\sigma} \sigma_z c_{j\sigma} + i\lambda_R \sum_{\langle i,j\rangle\sigma} c^{\dagger}_{i\sigma} (\vec{\sigma} \times \hat{D}_{ij}) \cdot \hat{z} c_{j\sigma} + h.c. \Big] + \lambda_{\rm v} \sum_i \xi_i c^{\dagger}_{i\sigma} c_{i\sigma} \tag{1.60}$$

where the first term is the NN hopping which was already discussed in Haldane model. Here the operator $c^{\dagger}_{i\sigma}$ consists of two spinors. The second term represents the NNN hopping with the quantity ϕ_{ij} is replaced by $\frac{\pi}{2}\nu_{ij}$. This means that the flux is taken to be $\pi/2$, and the magnitude of ν_{ij} follows the same rule described by ϕ_{ij} in the Haldane model (see the description of Eq. (1.58)). It may be noticed that a z-component of the Pauli matrix, σ_z is added in the NNN hopping term which represents the real spin degree of freedom of electrons. Due to this σ_z term the flux takes opposite signs corresponding to the two different spins, namely, $+\pi/2$ for $\uparrow$-spin and $-\pi/2$ for $\downarrow$-spin. This term is now called the intrinsic spin-orbit coupling term as it couples the electron spin σ_z with the chirality of the electron ν_{ij} with the strength λ_{SO}. The third term is the NN Rashba spin-orbit coupling term with the strength λ_R. Further, $\vec{\sigma} = (\sigma_x, \sigma_y, \sigma_z)$ denotes the Pauli matrix vector and $\hat{D}_{ij}$ is the unit vector that connects the site i to its NN site j (direction is from site i to site j). The last term is the staggered sublattice potential as discussed in Eq. (1.58). For $\lambda_R = 0$, the Kane-Mele Hamiltonian can be written as a sum of Haldane Hamiltonian of two different spins, that is,

$$H_{\rm KM} = H^{\uparrow}_{\rm Haldane}(\phi = +\frac{\pi}{2}) + H^{\downarrow}_{\rm Haldane}(\phi = -\frac{\pi}{2}). \tag{1.61}$$

For the quantum spin Hall effect to occur, the requirement is of the presence of gapless edge states which are able to conduct, although the bulk remains insulating. Kane and Mele has shown spin-filtered metallic edge states are present in their model. They have shown that the gapless edge states are present irrespective of the Rashba term and are robust against disorder

or any perturbation that preserves the TRS which ensures that edge states for spin-↑ and spin-↓ electrons propagate in opposite directions, creating a helical edge state configuration. Thus these gapless edge states characterize a novel topological state which is distinct from an ordinary insulator. It has a profound impact on shaping the research on transport properties and topological materials and potential applications in electronics and quantum technologies which we will explore in details in this thesis.

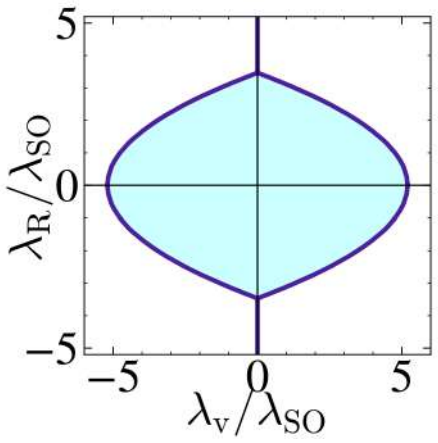

Figure 1.12: The phase diagram of the Kane-Mele model is depicted, with the colored region indicating the spin Hall phase characterized by $\mathbb{Z}_2 = 1$. In contrast, the white region corresponds to the trivial insulating phase, where $\mathbb{Z}_2 = 0$.

1.13.1 Phase diagram: $\mathbb{Z}_2$ invariant

Despite the similarity of the bands for each spin to the Haldane model, they exhibit unique behavior. Due to the complex next-nearest-neighbor (NNN) hopping phases of $\phi = +\pi/2$ and $-\pi/2$ for ↑- and ↓-spins, respectively, the spins acquire opposite masses at the Dirac points. This results in spin-dependent Chern numbers, denoted as C_ν, with $C_\uparrow = +1$ and $C_\downarrow = -1$. The total Chern number, $\sum_{\nu=\uparrow,\downarrow} C_\nu = 0$, is conserved due to time-reversal symmetry. However, the difference between the Chern numbers is non-zero, indicating the presence of another topological invariant known as the $\mathbb{Z}_2$ invariant. Such systems are classified as $\mathbb{Z}_2$ topological insulators. The difference between the Chern numbers for spin-↑ and spin-↓ electrons is given by $C_s = C_\uparrow - C_\downarrow = 2$. The $\mathbb{Z}_2$ invariant can be calculated using $C_s/2 \mod 2$, which equals 1 [258, 259]. When the staggered sublattice potential λ_v and Rashba spin-orbit coupling (SOC) λ_R are introduced, the previous method of computing the $\mathbb{Z}_2$ invariant becomes inapplicable. The Rashba term couples the spin and sublattice degrees of freedom, making it impossible to calculate $C_\uparrow$ and $C_\downarrow$ separately. Instead, we employ the method outlined in Sec. 1.8.5 to compute the $\mathbb{Z}_2$ invariant for various values of λ_R and λv, as shown in Fig. 1.12. The region enclosed

by the curve (shaded in blue) corresponds to a $\mathbb{Z}_2$ invariant of 1, while it vanishes outside this region. Thus, the system exhibits a non-trivial spin Hall insulating phase ($\mathbb{Z}_2 = 1$) within the curve and transitions to a trivial insulating phase ($\mathbb{Z}_2 = 0$) outside.

1.14 Lang-Firsov Transformation

Let us consider the classical canonical transformation applied to systems with strong electron-phonon (e-ph) coupling of the Holstein type. This approach was introduced by Lang and Firsov [260] to systematically explore the perturbation theory related to the mobility of small-radius polarons. They successfully captured a significant portion of the short-range e-ph interactions, allowing them to gather infinite series for the transformed operators during the Hamiltonian transformation. The authors [260] simplified the Hamiltonian of the system by restricting the contribution of the e-ph interaction to the local electron variables as,

$$H = \sum_{m} \epsilon a_m^\dagger a_m + \sum_{m,g} t_g a_{m+g}^\dagger a_m + \sum_{\mathbf{k}} \hbar\omega_{\mathbf{k}} \left(b_{\mathbf{k}}^\dagger b_{\mathbf{k}} + \frac{1}{2} \right) + \sum_{m,\mathbf{k}} \hbar\omega_{\mathbf{k}} a_m^\dagger a_m \left(U_{m,\mathbf{k}} b_{\mathbf{k}}^\dagger + U_{m,\mathbf{k}}^* b_{\mathbf{k}} \right) \tag{1.62}$$

where $a_m^\dagger$ (a_m) are operators of creation (annihilation) of an electron at a site m, $b_{\mathbf{k}}^\dagger$ ($b_{\mathbf{k}}$) are creation (annihilation) operators of a phonon with quasi momentum $\mathbf{k}$, ϵ is the ground state electron energy, the parameter t_g characterizes the hopping energy from site g to m and vice versa, $U_{m,\mathbf{k}}$ is the e-ph interaction parameter and $\omega_{\mathbf{k}}$ is the phonon mode frequency.

According to the Lang-Firsov transformation (LFT), the canonical transformation $\tilde{H} = e^S H e^{-S}$ of the Hamiltonian (1.62) with the unitary operator S in the form,

$$S = \sum_{m,\mathbf{k}} a_m^\dagger a_m \left(U_{m,\mathbf{k}} b_{\mathbf{k}}^\dagger - U_{m,\mathbf{k}}^* b_{\mathbf{k}} \right), \tag{1.63}$$

leads to a new Hamiltonian,

$$\tilde{H} = \sum_{m} a_m^\dagger a_m (\epsilon - \Delta) + \sum_{\mathbf{k}} \hbar\omega_{\mathbf{k}} \left(b_{\mathbf{k}}^\dagger b_{\mathbf{k}} + \frac{1}{2} \right) + \sum_{m,g} \hat{\Upsilon}_{m,g} t_g a_{m+g}^\dagger a_m \tag{1.64}$$

which describes the energy of polarons, lattice oscillators, and their residual interaction. Here, $\Delta = \sum_{\mathbf{k}} \hbar\omega_{\mathbf{k}} |U_{m,\mathbf{k}}|^2$ is the polaron shift of the atomic energy of the ground states of charge carriers and $\hat{\Upsilon}_{m,g} = \exp\left[\sum_{\mathbf{k}} (b_{\mathbf{k}}^\dagger \Delta_{m,m+g,\mathbf{k}} - b_{\mathbf{k}} \Delta_{m,m+g,\mathbf{k}}^*) \right]$ is the renormalization of the hopping integral, it depends on the strength of the e-ph coupling, $\Delta_{m,m+g,\mathbf{k}} = U_{m,\mathbf{k}} - U_{m+g,\mathbf{k}}$. In the transformed Hamiltonian, the contribution characterizing the interaction of electrons at different

sites through the exchange of virtual phonons is discarded, since it is less than the Coulomb correlations of electrons not taken into account in the original model.

1.15 α-T_3 Structure

The crystal structure of α-T_3 lattice is depicted in Fig. 1.13(a). The α-T_3 lattice is defined as a special honeycomb like structure with sublattices A (blue) and B (red) occupying the hexagonal vertices and there is an additional inequivalent site present at the center (C sublattice) of each hexagonal honeycomb lattice (HCL) of graphene structure. That additional C site is connected only with one of the two sublattices A or B sites of the honeycomb lattice. Further, a unit cell of the α-T_3 lattice consists of three inequivalent lattice sites. Two of these, usually known as *rim* sites (A and C sublatices), both the *rim* sites are connected to the three nearest neighbors (NNs) thus has the coordination number 3. The remaining lattice site is called a *hub* site (B sublattice), and is connected to six NNs, providing a coordination number of 6. This configuration creates a bipartitite lattice structure with two distinct types of sites. The lattice can be thought as a variant of the HCL of graphene. The center atom C is connected with B sublattices via hopping amplitude denoted as αt, while the hopping amplitude between sublattices A and B is represented as t. Here α is a dimensionless real parameter that denotes the ratio of the hopping amplitudes. The α-T_3 model exhibits an $\alpha \rightarrow 1/\alpha$ duality. With the continuous tuning of the parameter $\alpha \in [0:1]$, the α-T_3 lattice provides an interpolation between the honeycomb structure of graphene ($\alpha = 0$) and the dice lattice ($\alpha = 1$). For $\alpha = 0$, the atoms at site C are uncoupled from the atoms at site B, and we recover a lattice analogous to the honeycomb lattice of graphene with an inert C sublattice. For $\alpha = 1$ the hopping parameter between the A and B sites is identical to that of the hopping parameter between the B and C sites, and we recover the dice lattice.

The Bravais lattice vectors for the lattice are shown in Fig. 1.13(b). They are given as,

$$\begin{aligned} \mathbf{a_1} &= \frac{a}{2}(-\sqrt{3}, 3), \\ \mathbf{a_2} &= \frac{a}{2}(\sqrt{3}, 3) \end{aligned} \tag{1.65}$$

where a is the lattice constant, as indicated in Fig. 1.13(a) and the magnitude of the lattice vectors are $|\mathbf{a_1}| = |\mathbf{a_2}| = \sqrt{3}a$. The bond length between two atoms is measured as $a = 1.42\mathring{A}$.

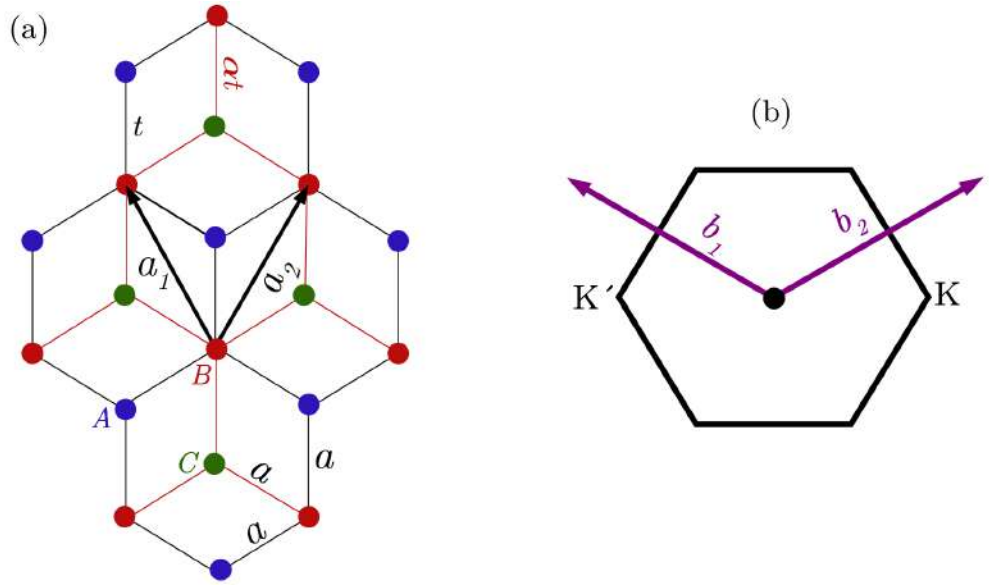

Figure 1.13: (a) Real space lattice structure of α-T_3 lattice with sublattices A (blue), B (red), and C (green). The lattice translation vectors are a_1 and a_2. The hopping between sublattice A and B is t and between B and C is αt, where a is the lattice constant. (b) Hexagonal Brillouin zone of the α-T_3 lattice and the reciprocal lattice vectors are b_1 and b_2. Two inequivalent points in the Brillouin zone are K and K′.

The nearest neighbour vectors that point to the A sites from the B sites can be written as,

$$\begin{aligned}
\delta_{\mathbf{1}}^{\mathbf{A}} &= (0, -a) = -\left(\frac{\mathbf{a_1} + \mathbf{a_2}}{3}\right), \\
\delta_{\mathbf{2}}^{\mathbf{A}} &= \frac{a}{2}(\sqrt{3}, 1) = \delta_{\mathbf{1}}^{\mathbf{A}} + \mathbf{a_2}, \\
\delta_{\mathbf{3}}^{\mathbf{A}} &= \frac{a}{2}(-\sqrt{3}, 1) = \delta_{\mathbf{1}}^{\mathbf{A}} + \mathbf{a_1}
\end{aligned} \tag{1.66}$$

in terms of the original lattice parameters, as well as the Bravais lattice vectors. Similarly, the nearest neighbour vectors that point to the C sites from the B sites take the form,

$$\begin{aligned}
\delta_{\mathbf{1}}^{\mathbf{C}} &= -\delta_{\mathbf{1}}^{\mathbf{A}}, \\
\delta_{\mathbf{2}}^{\mathbf{C}} &= -\delta_{\mathbf{2}}^{\mathbf{A}}, \\
\delta_{\mathbf{3}}^{\mathbf{C}} &= -\delta_{\mathbf{3}}^{\mathbf{A}}.
\end{aligned} \tag{1.67}$$

In the reciprocal space, the lattice translation vectors are denoted by,

$$\begin{aligned}
\mathbf{b_1} &= \frac{2\pi}{3}\left(-\frac{1}{\sqrt{3}}, \frac{1}{3}\right), \\
\mathbf{b_2} &= \frac{2\pi}{3}\left(\frac{1}{\sqrt{3}}, \frac{1}{3}\right).
\end{aligned} \tag{1.68}$$

The first Brillouin zone (FBZ) of the reciprocal lattice is bounded by the planes bisecting the vectors to the nearest reciprocal lattice points. The six points are located at the corners of the

FBZ where only two are of importance, that are, K and K′ . They are called Dirac points (generally known as valleys), owing to the Dirac-like low energy dispersion of the electrons, and their coordinates in the reciprocal space are given by, K= $\left(\frac{4\pi}{3\sqrt{3}a}, 0\right)$ and K′ = $\left(-\frac{4\pi}{3\sqrt{3}a}, 0\right)$, respectively, as depicted in figure 1.13(b).

1.15.1 Tight binding Hamiltonian of the α-T_3 lattice

A simple tight-binding model can be utilized to characterize the properties of the lattice. A tight-binding model assumes that electrons are tightly bound to their respective atoms and allowed to hop from site to site via a hopping parameter.

We can write a tight-binding Hamiltonian for the α-T_3 lattice using the nearest neighbour vectors in Eqs. (1.66) and (1.67), which does not consider spin and the onsite interaction between electrons, is expressed as [161],

$$\begin{aligned} H &= -t \sum_{\delta_{\mathbf{i}}^{\mathbf{A}}, n} \left(b_n^\dagger a_{n+\delta_{\mathbf{i}}^{\mathbf{A}}} + h.c. \right) - \alpha t \sum_{\delta_{\mathbf{i}}^{\mathbf{C}}, n} \left(b_n^\dagger c_{n+\delta_{\mathbf{i}}^{\mathbf{C}}} + h.c. \right) \\ &= -t \sum_{\delta_{\mathbf{i}}^{\mathbf{A}}, \delta_{\mathbf{i}}^{\mathbf{C}}, n} \left(b_n^\dagger a_{n+\delta_{\mathbf{i}}^{\mathbf{A}}} + \alpha b_n^\dagger c_{n+\delta_{\mathbf{i}}^{\mathbf{C}}} + h.c. \right) \end{aligned} \tag{1.69}$$

where n indexes over all of the N lattice sites in the lattice (the B sites). Here $h.c.$ stands for Hermitian conjugate. $(a^\dagger, b^\dagger, c^\dagger)$ and (a, b, c) are the creation and the annihilation operators at A, B, C sites respectively. Thus, for example, $b_n^\dagger$ creates an electron at the sublattice site B located at n and $a_{n+\delta_{\mathbf{i}}^{\mathbf{A}}}$ annihilates an electron at one of the nearest neighbour A sites with the index $n + \delta_{\mathbf{i}}^{\mathbf{A}}$.

All the creation and annihilation operators can be transformed to momentum space, for example,

$$\begin{aligned} b_n^\dagger &= \frac{1}{\sqrt{N}} \sum_{\mathbf{k}} e^{i\mathbf{k}\cdot n} b_{\mathbf{k}}^\dagger, \\ a_{n+\delta^{\mathbf{A}}} &= \frac{1}{\sqrt{N}} \sum_{\mathbf{k}'} e^{-i\mathbf{k}'\cdot(n+\delta^{\mathbf{A}})} a_{\mathbf{k}'} \end{aligned} \tag{1.70}$$

These transformations will allow us to write the Hamiltonian in terms of the momentum space operators and we can diagonalize the Hamiltonian to calculate the energy dispersions. Substituting Eq. (5.16) in Eq. (1.69) and using,

$$\frac{1}{N} \sum_{\mathbf{k}} e^{(\mathbf{k}-\mathbf{k}')\cdot n} = \delta_{\mathbf{k},\mathbf{k}'}, \tag{1.71}$$

the Hamiltonian can now be transformed as,

$$H = -t\sum_{\mathbf{k}}\left(f(\mathbf{k})b^{\dagger}_{\mathbf{k}}a_{\mathbf{k}} + h.c.\right) - \alpha t\sum_{\mathbf{k}}\left(f^{*}(\mathbf{k})b^{\dagger}_{\mathbf{k}}c_{\mathbf{k}} + h.c.\right). \tag{1.72}$$

The unit cell of α-T_3 lattice consists of three sublattices A, B, and C, therefore it will be useful to express the Eq. (1.72) in terms of a spinor $\Psi^{\dagger} = \left(a^{\dagger}_{\mathbf{k}}, b^{\dagger}_{\mathbf{k}}, c^{\dagger}_{\mathbf{k}}\right)$ as,

$$H = \sum_{\mathbf{k}}\Psi^{\dagger}H(\mathbf{k})\Psi. \tag{1.73}$$

Now the Hamiltonian in the momentum space is given as,

$$H(\mathbf{k}) = \begin{pmatrix} 0 & f(\mathbf{k}) & 0 \\ f^{*}(\mathbf{k}) & 0 & f(\mathbf{k})\tan\varphi \\ 0 & f^{*}(\mathbf{k})\tan\varphi & 0 \end{pmatrix} \tag{1.74}$$

where $\alpha = \tan\varphi$ and $f(\mathbf{k}) = -t(1 + e^{i\mathbf{k}\cdot\mathbf{a_1}} + e^{i\mathbf{k}\cdot\mathbf{a_2}})$. Rescaling the Hamiltonian by $\cos\varphi$, we get the momentum space Hamiltonian for the α-T_3 model as,

$$H(\mathbf{k}) = \begin{pmatrix} 0 & f(\mathbf{k})\cos\varphi & 0 \\ f^{*}(\mathbf{k})\cos\varphi & 0 & f(\mathbf{k})\sin\varphi \\ 0 & f^{*}(\mathbf{k})\sin\varphi & 0 \end{pmatrix}. \tag{1.75}$$

1.15.2 Band structure of the α-T_3 lattice

The energy eigenvalues of the Hamiltonian in Eq. (1.75) consist of three distinct bands and are given by,

$$\epsilon = 0, \pm|f(\mathbf{k})| \tag{1.76}$$

where

$$|f(\mathbf{k})| = t\sqrt{3 + 4\cos\left(\frac{3ak_y}{2}\right)\cos\left(\frac{\sqrt{3}ak_x}{2}\right) + 2\cos\left(\sqrt{3}ak_x\right)}. \tag{1.77}$$

The energy dispersion described above (see Eq. (1.76)) is the same as that of the conduction and valence bands in graphene, in addition the α-T_3 lattice features an extra band, specifically, a dispersionless flat band that intersects the other two bands at the Dirac points located at K= $\left(\frac{4\pi}{3\sqrt{3}a}, 0\right)$ and K′ $= \left(-\frac{4\pi}{3\sqrt{3}a}, 0\right)$ in the Brillouin zone. A schematic of the three bands of the α-T_3 lattice is shown in Fig. 1.14. All three bands are present for the full range of $\alpha \neq 0$.

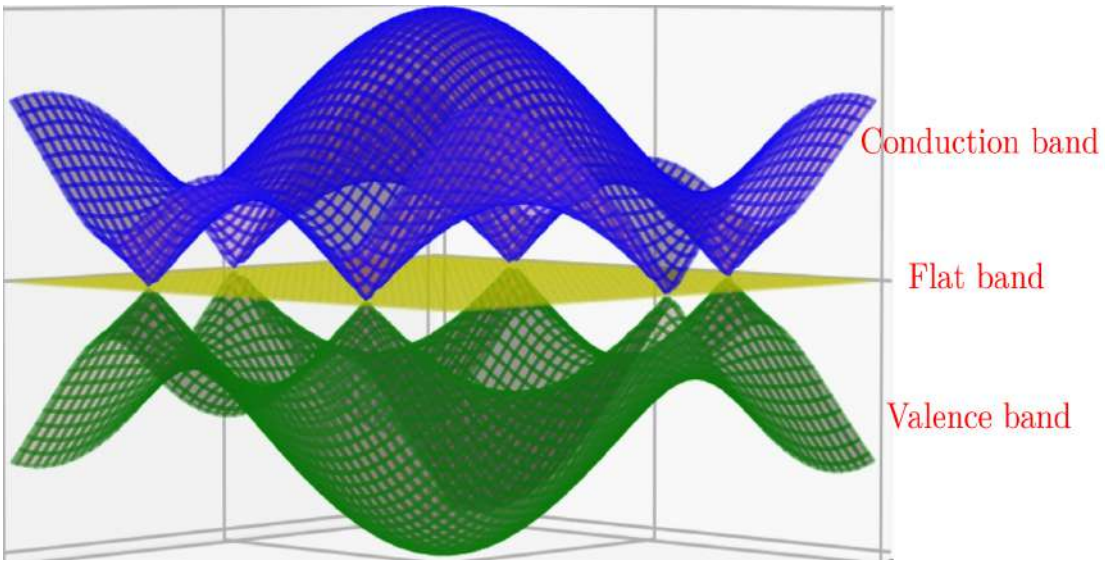

Figure 1.14: The band structure of the α-T_3 lattice, which consists of conduction band, valence band, and zero energy flat band.

1.15.3 Low-energy Hamiltonian of the α-T_3 lattice

The low energy Hamiltonian of the α-T_3 lattice can be obtained by expanding $f(\mathbf{k})$ upto first order in momenta about the Dirac points $\mathrm{K} = \left(\frac{4\pi}{3\sqrt{3}a}, 0\right)$ and $\mathrm{K}' = \left(-\frac{4\pi}{3\sqrt{3}a}, 0\right)$ such that $\mathbf{k} \to \mathbf{k} + \mathbf{K}(\mathbf{K}')$ and $|\mathbf{k}| \ll |\mathbf{K}(\mathbf{K}')|$ and given by,

$$\begin{aligned} f(\mathbf{k}+\mathbf{K}) &= \frac{3at}{2}(k_x + ik_y) = \hbar v_F(k_x + ik_y), \\ f(\mathbf{k}+\mathbf{K}') &= \frac{3at}{2}(-k_x + ik_y) = \hbar v_F(-k_x + ik_y). \end{aligned} \tag{1.78}$$

where the Fermi velocity v_F is given by $v_F = \frac{3at}{2\hbar}$. Combining those two we can write the linearized version of $f(\mathbf{k})$ as,

$$f(\mathbf{k}) = \hbar v_F(\zeta k_x + ik_y) \tag{1.79}$$

where $\zeta = \pm 1$ is the valley index for K $(+1)$, and K$'$ (-1) valleys respectively. The momentum $\mathbf{k}$ is now measured from the Dirac points (K, K$'$) in the two dimensional Brillouin zone. We will use this convention whenever we are working in the low-energy approximation throughout the thesis.

Finally, at low-energies, the tight binding Hamiltonian in Eq. (1.75) becomes,

$$H(\mathbf{k}) = \begin{pmatrix} 0 & f(\mathbf{k})\cos\varphi & 0 \\ f^*(\mathbf{k})\cos\varphi & 0 & f(\mathbf{k})\sin\varphi \\ 0 & f^*(\mathbf{k})\sin\varphi & 0 \end{pmatrix} = \hbar v_F \mathbf{S}\cdot\mathbf{k}. \tag{1.80}$$

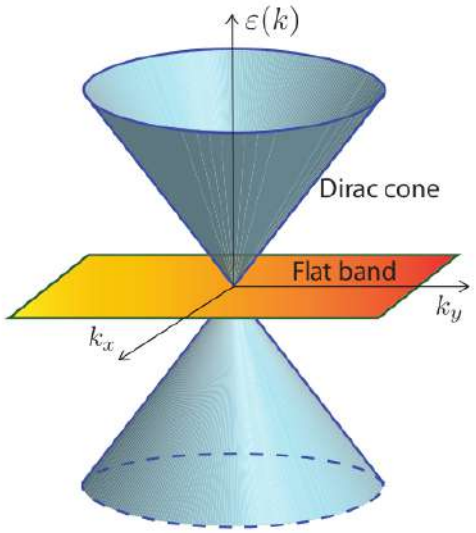

Figure 1.15: Low-energy dispersion of the α-T_3 lattice near a single K point. The cones representing the linearly dispersing valence and conduction bands, along with a dispersionless flat band at zero energy intersecting the Dirac point. Figure courtesy Ref. [161].

The x and y components of the pseudospin operator $\mathbf{S}$ associated with the α-T_3 lattice are given by,

$$S_x = \zeta \begin{pmatrix} 0 & \cos\varphi & 0 \\ \cos\varphi & 0 & \sin\varphi \\ 0 & \sin\varphi & 0 \end{pmatrix} \quad \text{and} \quad S_y = -i \begin{pmatrix} 0 & \cos\varphi & 0 \\ -\cos\varphi & 0 & \sin\varphi \\ 0 & -\sin\varphi & 0 \end{pmatrix}, \tag{1.81}$$

respectively. This linearized version of the α-T_3 Hamiltonian (Eq. (1.80)) known as Dirac-Weyl Hamiltonian with pseudospin-S and the low-energy dispersion around the Dirac points becomes,

$$\varepsilon_{\mathbf{k}} = 0, \pm\hbar v_F |\mathbf{k}|. \tag{1.82}$$

Two linearly dispersing bands (Dirac cones) with energy $\varepsilon_{\mathbf{k},\mathbf{s}} = s\hbar v_F \mathbf{k}$, where $s = \pm 1$ corresponds to the conduction and valence band respectively. These bands intersect with a dispersionless flat band with zero energy, as illustrated in Fig. 1.15. Notably, the energy band structure is independent of α. The low-energy excitation in the α-T_3 lattice obeys relativistic energy dispersion and exhibits massless fermionic behavior similar to graphene ($S = 1/2$), while are theoretically characterized by the generic Dirac-Weyl Hamiltonian [155, 158] with pseudospin-S.

1.15.4 Low-energy eigenfunctions of the α-T_3 lattice

The low-energy eigenvectors of the low-energy Hamiltonian can be obtained from Eq. (1.80) associated with each of the three eigenvalues. For the flat band, the wavefuction is,

$$|\Psi_0\rangle = \begin{pmatrix} \sin\varphi e^{i\phi_{\mathbf{k}}} \\ 0 \\ -\cos\varphi e^{-i\phi_{\mathbf{k}}} \end{pmatrix}. \tag{1.83}$$

For the other two bands, the wavefunctions are,

$$|\Psi_s\rangle = \frac{1}{\sqrt{2}} \begin{pmatrix} \cos\varphi e^{i\phi_{\mathbf{k}}} \\ s \\ \sin\varphi e^{-i\phi_{\mathbf{k}}} \end{pmatrix}, \tag{1.84}$$

with $s = \pm 1$ for the conduction and the valence band, respectively. Here, $\phi_{\mathbf{k}}$ is the angle associated with momentum $\mathbf{k}$ in two dimensional Brillouin zone such that $f(\mathbf{k}) = |f(\mathbf{k})|e^{i\phi_{\mathbf{k}}}$ with $f(\mathbf{k})$ given in Eq. (1.79). Throughout the study of α-T_3 lattice we will use the low energy Hamiltonian in Eq. (1.80) and corresponding eigenfuctions (Eqs. (1.83) and (1.84)).

1.15.5 Berry phase of an α-T_3 lattice

We follow the method prescribed in Ref [161] to determine the Berry phase for the α-T_3 lattice. The Berry phase in the α-T_3 lattice continuously changes with the parameter α. To compute the Berry phase we begin with Eq. (1.30) and utilize the wavefunctions for the conduction and the valence bands in K valley from Eq. (1.84). Since the momentum $\mathbf{k}$ is considered to be a parameter in the two-dimensional Brillouin zone, we can write,

$$\phi_{\mathrm{K}}^{\mathrm{B}} = -i\oint_{\mathcal{C}} \langle n(\mathbf{R})|\nabla_{\mathbf{R}}|n(\mathbf{R})\rangle \cdot d\mathbf{R} = -\frac{i}{2}\oint_{\mathcal{C}} \begin{pmatrix} \cos\varphi e^{-i\phi_{\mathbf{k}}} & s & \sin\varphi e^{i\phi_{\mathbf{k}}} \end{pmatrix} \nabla_{\mathbf{k}} \begin{pmatrix} \cos\varphi e^{i\phi_{\mathbf{k}}} \\ s \\ \sin\varphi e^{-i\phi_{\mathbf{k}}} \end{pmatrix} \cdot d\mathbf{k}. \tag{1.85}$$

After taking the derivative we obtain,

$$\phi_{\mathrm{K}}^{\mathrm{B}} = -\frac{i}{2}\oint_{\mathcal{C}} \begin{pmatrix} \cos\varphi e^{-i\phi_{\mathbf{k}}} & s & \sin\varphi e^{i\phi_{\mathbf{k}}} \end{pmatrix} \begin{pmatrix} i\cos\varphi e^{i\phi_{\mathbf{k}}}\nabla_{\mathbf{k}}\phi_{\mathbf{k}} \\ 0 \\ -i\sin\varphi e^{-i\phi_{\mathbf{k}}}\nabla_{\mathbf{k}}\phi_{\mathbf{k}} \end{pmatrix} \cdot d\mathbf{k}, \tag{1.86}$$

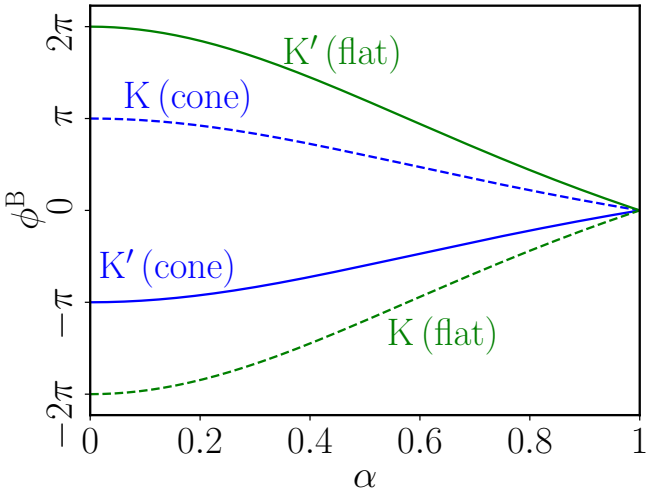

Figure 1.16: The Berry phase of the α-T_3 lattice is a function of α, decreasing steadily with increasing α and approaching zero as $\alpha \to 1$.

which may further be simplified to acquire a form,

$$\phi_{\mathrm{K}}^{\mathrm{B}} = -\frac{i}{2}\left(i\cos^2\varphi - i\sin^2\varphi\right)\oint_{\mathcal{C}} d\phi_{\mathbf{k}}. \tag{1.87}$$

The integral over $\phi_{\mathbf{k}}$ comes out to be 2π, therefore the Berry phase is obtained as,

$$\phi_{\mathrm{K}}^{\mathrm{B}} = \pi\cos 2\varphi. \tag{1.88}$$

Similarly, the Berry phase for the K′ valley introduce a negative sign (since the K′ valley is left-handed we get $\oint_{\mathcal{C}} d\phi_{\mathbf{k}} = -2\pi$). Therefore, in general the Berry phase for the Dirac cones at the K ($\zeta = 1$) and K′ ($\zeta = -1$) valleys can be expressed as,

$$\phi_{\zeta}^{\mathrm{B}} = \zeta\pi\cos 2\varphi = \zeta\pi\left(\frac{1-\alpha^2}{1+\alpha^2}\right) \tag{1.89}$$

in terms of the original parameter α. This expression shows a continuous variation as a function of α. It is non-topological [176], indicating that the Berry phase changes smoothly as the lattice is deformed from one limiting case to another. Specifically, it transitions from graphene, where $\phi_{\mathrm{K}}^{\mathrm{B}} = \zeta\pi$ to the dice lattice, where $\phi_{\mathrm{K}}^{\mathrm{B}} = 0$ as the parameter α is varies from 0 to 1. Furthermore, for the flat band at both the K and K′ valleys, using the wavefunction given in Eq. (1.83), a similar analysis yields a Berry phase of,

$$\phi_{0,\zeta}^{\mathrm{B}} = -2\zeta\pi\cos 2\varphi = -2\zeta\pi\left(\frac{1-\alpha^2}{1+\alpha^2}\right). \tag{1.90}$$

The variation of the Berry phase as a function of α is depicted in Fig. 1.16.

1.16 Organisation of the Thesis

The main objective of this thesis lies in studying the transport and topological properties of α-T_3 lattice systems within the framework of a tight-binding model in the presence of an external magnetic field, SOC (intrinsic and Rashba), topological defects, and studying topology in presence of e-ph couplings. In the following, we present a more elaborate plan of the thesis by including a description of the various problems that have been tackled in the form of different chapters of the thesis. We proceed with a brief description in the context of each one by one. We have a total of eight chapters in the thesis. We organize the thesis as follows.

In ***chapter* 2**, we consider a quantum ring of a certain radius which is built from a sheet of the α-T_3 lattice and solve for its spectral properties in presence of an external magnetic field. We also calculate the persistent current which exhibits quantum oscillations as a function of the magnetic field with a period of one flux quantum. We have also explored the effect of a staggered mass term (that breaks the sublattice symmetry) in the Hamiltonian. In presence of the field, each of the flat band levels becomes dispersive. Finally, we also see the effect of the mass term on the behaviour of the persistent current, which shows periodicity of one flux quantum.

In ***chapter* 3**, we conduct a study of different persistent currents in a spin-orbit coupled α-T_3 fermionic QR. In particular, we have considered effects of Haldane-like intrinsic (ISOC) and Rashba spin-orbit couplings (RSOC) that are both inherent to two dimensional quantum structures and yield interesting consequences. It is noted that the flat bands demonstrate dispersive behaviour, and hence is able to contribute to the transport properties only for finite ISOC. Moreover, RSOC yields spin-split bands, thereby contributing to spin-resolved currents. The charge and the spin-polarized persistent currents are hence computed in presence of these spin-orbit couplings. The persistent currents in both the charge and the spin sectors oscillate as a function of the magnetic field with a period equal to the flux quantum, although they now depend upon the spin-orbit coupling parameters. Interestingly, the ISOC distorts the current profiles, owing to the distribution of the flat band caused by it, whereas RSOC alone preserves the flat band and hence a perfect periodicity of the current characteristic is maintained. Further, we have explored the role played by the parameter α in our entire analysis to enable studies while interpolating from graphene to a dice lattice.

In ***chapter* 4**, we investigate the effect of a topological defect, such as a screw dislocation in an α-T_3 AB QR and scrutinized the effects of an external transverse magnetic field and RSOC therein. The screw dislocation yields an effective flux which reshape the periodic oscillations

in the persistent current in both charge and spin sectors, with a period equal to one flux quantum. Moreover, they suffer a phase shift proportional to the degree of dislocation, and include scattering effects due to the dislocation present in the system. Such tunable oscillation of the spin persistent current highlights applications of our system as potential spintronic devices. Additionally, the presence of the distortion induces a chirality effect, giving rise to an additional chiral current even in the absence of an external field.

In ***chapter* 5**, we investigate an α-T_3 lattice in the form of a Corbino disk, characterized by inner and outer radii, threaded by a tunable magnetic flux. Our results reveal periodic Aharonov-Bohm oscillations in the conductance, reminiscent of the utility of the Corbino disk as an electron pump. Further, these results are strongly influenced by parameters, such as, doping level, ratio of the inner and outer radii, magnetic flux, and α. Additionally, complex quantum interference effect resulting in the possible emergence of higher harmonic modes and split-peak structures in the conductance, become prominent for smaller α values and larger ratios of the radii. Further, the Fano factor reveals distinct transport regimes for the carriers, transitioning from Poissonian to pseudo-diffusive for $\alpha < 1$, and from ballistic to pseudo-diffusive at the dice limit ($\alpha = 1$). Thus, this setup serves as a fertile ground for studying the generation of quantum Hall current and Aharonov-Bohm oscillations in a flat band system, alongwith demonstrating intricate appearance of higher harmonics in the electron transport.

In ***chapter* 6**, we present impelling evidence of topological phase transitions (TPTs) induced by e-ph coupling in an α-T_3 Haldane-Holstein model. The e-ph coupling has been incorporated via the Lang-Firsov transformation which adequately captures the polaron physics in the high frequency (anti-adiabatic) regime, and yields an effective Hamiltonian through zero phonon averaging at $T = 0$. While exploring the signature of phase transitions driven by polaron and its interplay with the parameter α. The topological insulator characterized by edge modes, finite Chern number, and Hall conductivity, and the system undergoes a spectral gap closing transition. Further, the critical coupling strength depends upon α.

In ***chapter* 7**, we propose the occurrence of a QSH and a TPT driven by e-ph coupling in a pseudospin-1 fermionic system on an α-T_3 lattice. Our model is formulated in the spirit of the Kane-Mele model modified by the Holstein Hamiltonian (accounting for the e-ph interaction). It is shown that the system possesses topologically nontrivial phases up to a critical e-ph coupling, and are characterized by the helical QSH edge states along with a non-zero $\mathbb{Z}_2$ invariant for a certain range of α.

We conclude in ***chapter* 8** by summarizing the important results obtained in our thesis. We also include a brief outlook on the possible extension of the thesis work.

Chapter 2

Persistent Current in an α-T_3 Quantum Ring

WE examine a quantum ring with a specific radius constructed from a sheet of the α-T_3 lattice and analyze its spectral properties in the presence of an external magnetic field. The energy spectrum includes a conduction band, a valence band, and a zero-energy flat band, each characterized by discrete energy levels that correspond to the angular momentum quantum number. Additionally, we calculate the persistent current, which displays quantum oscillations as a function of the magnetic field, with a periodicity of one flux quantum occurring at a particular Dirac point.

2.1 Introduction

Electronic properties of lower dimensional materials (two and below) with various geometries have continued to fascinate the scientific community over the years. Among such structures quantum rings (QRs) are widely celebrated due to their enormous potential in device applications. Previously QRs have been realized in semiconductor materials by growing quantum dots and then transforming them to ringlike structures [13], depleting a two-dimensional electron gas

using the electric field effect or local oxidation techniques [18, 20, 262–264], atom manipulation [265] by cryogenic scanning tunneling microscopy to assemble individual atomic rings on a semiconductor surface [266], etc. The QRs can be employed for implementing logic gate functions [267, 268], have the possibility for designing and controlling propagation of electrons in a tunable periodic potential [266], QR structures have more advantages in applications of LED devices and laser diodes [269, 270], spin filters [271], etc.

Recently we have witnessed a tremendous quest for the practical device applications of graphene QRs [29, 30, 40, 41]. Graphene QRs have also been synthesized by thermal hydrolysis process. Also, graphene QR has a great potential for electronic field-effect transistors, hybrid solar cell devices, optoelectronic devices [47], and graphene-based electron interferometer [48]. Furthermore, lots of studies have been done in recent years to understand the microscopic details of the graphene QR in presence of an external magnetic field with and without spin-orbit interactions [28, 35–39, 42–45, 272–275].

Motivated by the above prospects of the quantum ring, we study the electronic properties of an ideal QR made with α-T_3 lattice in this chapter. Before going into more complicated systems, we intend to see how the energy spectrum evolves as we migrate from graphene ($\alpha = 0$) to dice lattice ($\alpha = 1$) for a bare α-T_3 QR. Further, to obtain the analytical expressions for the energy levels and wavefunctions, we first derive the closed ring Hamiltonian by performing the proper coordinate mapping for an α-T_3 lattice. However, to exploit the symmetry of the system, we shall resort to cylindrical coordinates which involve certain subtleties in constructing a Hermitian Hamiltonian and we shall follow the approach of Meijer [203]. Using such a Hamiltonian, it is possible to describe several aspects of the α-T_3 QR without the additional complications coming from the edge effect and without having the problem of the finite width of the QR. Additionally, the inclusion of an external magnetic field would facilitate studies on the evolution of the spectral properties, the persistent current, and the interplay of the Aharonov-Bohm effect therein. With such a motivation, we consider an α-T_3 ring in presence of external magnetic field and study various properties as a function of α, which is a parameter in this chapter. Finally, we have also studied the effect of a mass term (distinct for the three sublattices) on the spectral properties and the features of the corresponding persistent current.

The chapter is organized in the following way. In Sec. 2.2 we discuss the formalism of the α-T_3 ring. The energy spectra are discussed in Sec. 2.3 and the persistent current in Sec. 2.4. In Sec. 2.5, we discuss the effect of a mass term on the energy spectra as well as on the persistent current of the ring. We summarize our results in Sec. 2.6.

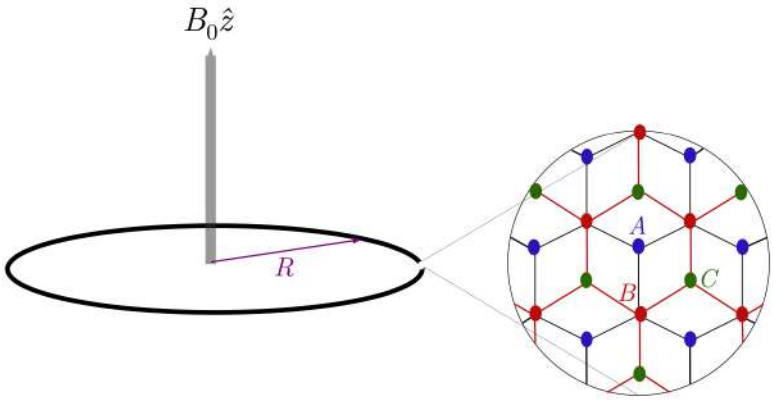

Figure 2.1: A schematic diagram of the α-T_3 ring of radius R subjected to a transverse magnetic field $\boldsymbol{B} = B_0\hat{z}$. The structure of the α-T_3 lattice is depicted in the zoomed portion. A, B, and C lattice sites are shown by blue, red, and green dots, respectively.

2.2 α-T_3 QR Formalism

We consider a ring of radius R, in the x-y plane, made from the α-T_3 lattice as depicted in Fig. 2.1. The geometric structure of the α-T_3 lattice is shown in the zoomed portion of Fig. 2.1. A unit cell contains three inequivalent lattice sites, namely, A, B, and C. The sites A and B form the honeycomb structure (graphene) with the nearest neighbour hopping parameter t. The central site C is connected with only the three surrounding B sites via hopping αt where $0 < \alpha \leq 1$.

Additionally, the ring is also subjected to a perpendicular magnetic field $\boldsymbol{B} = B_0\hat{z}$, where B_0 is a constant. In the vicinity of a particular valley (K or K′) characterized by the index ζ that can take values ± 1, the low energy excitations in the α-T_3 lattice can be described by the following Dirac-Weyl Hamiltonian,

$$H^{\zeta} = v_F(\zeta\pi_x S_x + \pi_y S_y), \tag{2.1}$$

where v_F is the Fermi velocity and π_x and π_y are the components of the canonical momentum operator defined via $\boldsymbol{\pi} = \boldsymbol{p} + e\boldsymbol{A}$, where $\boldsymbol{p}$ denotes the in-plane mechanical momentum operator and $\boldsymbol{A}$ is the vector potential. Here, x and y components of the pseudospin operator $\boldsymbol{S}$ associated with the α-T_3 lattice are given by,

$$S_x = \begin{pmatrix} 0 & \cos\varphi & 0 \\ \cos\varphi & 0 & \sin\varphi \\ 0 & \sin\varphi & 0 \end{pmatrix} \quad \text{and} \quad S_y = -i\begin{pmatrix} 0 & \cos\varphi & 0 \\ -\cos\varphi & 0 & \sin\varphi \\ 0 & -\sin\varphi & 0 \end{pmatrix}, \tag{2.2}$$

respectively, with $\tan\varphi = \alpha$, implying that a tunability for graphene to dice lies in the parameter φ. The third, namely, the z-component of $\boldsymbol{S}$ can be directly obtained from the commutation relation $[S_x, S_y] = iS_z$.

Further, in general, the vector potential $\boldsymbol{A}$ corresponding to a uniform magnetic field $\boldsymbol{B}$ is given by $\boldsymbol{A} = \frac{1}{2}(\boldsymbol{B} \times \boldsymbol{r})$, where $\boldsymbol{r}$ is the position vector. Since $\boldsymbol{B} = B_0\hat{z}$, we choose $\boldsymbol{A}$ in the symmetric gauge as $\boldsymbol{A} = B_0(-y\hat{x} + x\hat{y})$. For our problem it the more convenient to write $\boldsymbol{A}$ in the polar coordinates (r, θ) as $\boldsymbol{A} = \frac{1}{2}rB_0\hat{\theta}$.

We can rewrite the Hamiltonian in Eq. (2.1) using Eq. (2.2) as,

$$H^{\zeta} = v_F \begin{pmatrix} 0 & \{\zeta(p_x + eA_x) - i(p_y + eA_y)\}\cos\varphi & 0 \\ \{\zeta(p_x + eA_x) + i(p_y + eA_y)\}\cos\varphi & 0 & \{\zeta(p_x + eA_x) - i(p_y + eA_y)\}\sin\varphi \\ 0 & \{\zeta(p_x + eA_x) + i(p_y + eA_y)\}\sin\varphi & 0 \end{pmatrix}. \tag{2.3}$$

Now we transform $v_F(p_x + eA_x - ip_y - ieA_y)$ into the polar coordinates (r, θ) using the transformations as follows,

$$\begin{aligned} & v_F(p_x + eA_x - ip_y - ieA_y) \\ &= v_F\Big(-i\hbar\frac{\partial}{\partial x} - \frac{eB_0y}{2} + i^2\hbar\frac{\partial}{\partial y} - i\frac{eB_0x}{2}\Big) \\ &= v_F\Big[-i\hbar\big(\cos\theta\frac{\partial}{\partial r} - \frac{\sin\theta}{r}\frac{\partial}{\partial\theta}\big) - \frac{eB_0r\sin\theta}{2} - \hbar\big(\sin\theta\frac{\partial}{\partial r} + \frac{\cos\theta}{r}\frac{\partial}{\partial\theta}\big) - i\frac{eB_0r\cos\theta}{2}\Big] \\ &= \hbar v_F\Big[-i\big(\cos\theta - i\sin\theta\big)\frac{\partial}{\partial r} - \big(\cos\theta - i\sin\theta\big)\frac{1}{r}\frac{\partial}{\partial\theta} - \frac{ieB_0r}{2\hbar}\big(\cos\theta - i\sin\theta\big)\Big] \\ &= \hbar v_F\, e^{-i\theta}\Big[-i\frac{\partial}{\partial r} - \frac{1}{r}\frac{\partial}{\partial\theta} - \frac{ieB_0r}{2\hbar}\Big]. \end{aligned} \tag{2.4}$$

To derive the third line from the second line of the above equation, we have used $x = r\cos\theta$, $y = r\sin\theta$, $\frac{\partial}{\partial x} = \cos\theta\frac{\partial}{\partial r} - \frac{\sin\theta}{r}\frac{\partial}{\partial\theta}$, and $\frac{\partial}{\partial y} = \sin\theta\frac{\partial}{\partial r} + \frac{\cos\theta}{r}\frac{\partial}{\partial\theta}$. Similarly, $v_F(p_x + eA_x + ip_y + ieA_y)$ becomes $\hbar v_F\, e^{i\theta}(-i\frac{\partial}{\partial r} + \frac{1}{r}\frac{\partial}{\partial\theta} + \frac{ieBr}{2\hbar})$. The components of the vector potential $A_r = 0$ and $A_\theta = \frac{Br}{2}$.

Therefore, the Hamiltonian in cylindrical coordinates becomes,

$$H^{\zeta} = v_F(\mathbf{p} + e\mathbf{A})_{cyl} \cdot \mathbf{S}_{cyl}, \tag{2.5}$$

with $\mathbf{p} = (p_r, p_\theta)$, $\mathbf{A} = (A_r, A_\theta)$ and $S = (S_r, S_\theta)$, where $p_r = -i\hbar\frac{\partial}{\partial r}$, $p_\theta = -i\hbar\frac{1}{r}\frac{\partial}{\partial\theta}$, and the pseudospin components takes the form,

$$S_r = \begin{pmatrix} 0 & e^{-i\theta}\cos\varphi & 0 \\ e^{i\theta}\cos\varphi & 0 & e^{-i\theta}\sin\varphi \\ 0 & e^{i\theta}\sin\varphi & 0 \end{pmatrix}, \text{ and } S_\theta = \begin{pmatrix} 0 & -ie^{-i\theta}\cos\varphi & 0 \\ ie^{i\theta}\cos\varphi & 0 & -ie^{-i\theta}\sin\varphi \\ 0 & ie^{i\theta}\sin\varphi & 0 \end{pmatrix}. \tag{2.6}$$

After doing the transformations the final Hamiltonian at the two valleys (say K and K′) in the polar coordinates assumes a form,

$$H^\zeta = \hbar v_F \begin{pmatrix} 0 & e^{-i\zeta\theta}(-i\zeta\frac{\partial}{\partial r} - \frac{1}{r}\frac{\partial}{\partial\theta} - \frac{ieB_0 r}{2\hbar})\cos\varphi & 0 \\ e^{i\zeta\theta}(-i\zeta\frac{\partial}{\partial r} + \frac{1}{r}\frac{\partial}{\partial\theta} + \frac{ieB_0 r}{2\hbar})\cos\varphi & 0 & e^{-i\zeta\theta}(-i\zeta\frac{\partial}{\partial r} - \frac{1}{r}\frac{\partial}{\partial\theta} - \frac{ieB_0 r}{2\hbar})\sin\varphi \\ 0 & e^{i\zeta\theta}(-i\zeta\frac{\partial}{\partial r} + \frac{1}{r}\frac{\partial}{\partial\theta} + \frac{ieB_0 r}{2\hbar})\sin\varphi & 0 \end{pmatrix}. \tag{2.7}$$

The Hamiltonian H^ζ in Eq. (2.1) commutes with the z-component of the total angular momentum operator defined as: $J_z = L_z + S_z$, where $L_z = -i\hbar\frac{\partial}{\partial\theta}$ is the orbital angular momentum operator and S_z is the pseudospin operator (see Appendix B for details). This makes it feasible to use the total angular momentum to be a good quantum number to characterize the energy levels. In polar coordinates, the eigenstates of Eq. (2.7) are given by,

$$\psi(r,\theta) = \begin{pmatrix} \chi_1(r)e^{iw\theta} \\ \chi_2(r)e^{im\theta} \\ \chi_3(r)e^{iq\theta} \end{pmatrix} \tag{2.8}$$

where w, m, and q are the angular momentum labels and χ_is denote the amplitudes corresponding to the three sublattices. Moreover, we consider a strictly one-dimensional (1D) ring of radius R such that the radial part is frozen in the eigensolution [26, 38, 203, 276]. For the sake of the hermiticity of the Hamiltonian in ring geometry, one should make the replacements $r \to R$ and $\frac{\partial}{\partial r} \to -\frac{1}{2R}$. These replacements are also obvious because the radial momentum vanishes in the strict 1D limit (see Appendix C for details).

Further, solving $H^\zeta\psi(r,\theta) = E\psi(r,\theta)$ at K valley ($\zeta = 1$), we obtain,

$$\begin{aligned} &\hbar v_F e^{-i\theta}\cos\varphi(-i\frac{\partial}{\partial r} - \frac{1}{r}\frac{\partial}{\partial\theta} - \frac{ieB_0 r}{2\hbar})\chi_2(r)e^{im\theta} = E\chi_1(r)e^{iw\theta} \\ &\Rightarrow i\hbar v_F\cos\varphi(\frac{1}{2R} - \frac{m}{R} - \frac{eB_0 R}{2\hbar})\chi_2(R)e^{i(m-1)\theta} = E\chi_1(R)e^{iw\theta} \\ &\Rightarrow -E\chi_1(R) - i\frac{\hbar v_F}{R}(m + \beta - \frac{1}{2})\chi_2(R)\cos\varphi = 0 \end{aligned} \tag{2.9}$$

with the condition $w = (m-1)$. Where $\beta = \frac{eB_0R^2}{2\hbar}$ can be expressed as $\beta = \Phi/\Phi_0$ with $\Phi = \pi R^2 B_0$ being the magnetic flux threading the ring and $\Phi_0 = h/e$ the quantum of magnetic flux. Further,

$$\hbar v_F e^{i\theta}\cos\varphi(-i\frac{\partial}{\partial r}+\frac{1}{r}\frac{\partial}{\partial\theta}+\frac{ieB_0r}{2\hbar})\chi_1(r)e^{iw\theta}+\hbar v_F e^{-i\theta}\sin\varphi(-i\frac{\partial}{\partial r}-\frac{1}{r}\frac{\partial}{\partial\theta}-\frac{ieB_0r}{2\hbar})\chi_3(r)e^{iq\theta}=E\chi_2(r)e^{im\theta}$$
$$\Rightarrow i\hbar v_F\cos\varphi(\frac{1}{2R}+\frac{w}{R}+\frac{eB_0R}{2\hbar})\chi_1(R)e^{i(w+1)\theta}+i\hbar v_F\sin\varphi(\frac{1}{2R}-\frac{q}{R}-\frac{eB_0R}{2\hbar})\chi_3(R)e^{i(q-1)\theta}=E\chi_2(R)e^{im\theta}$$

$$\Rightarrow i\frac{\hbar v_F}{R}(m+\beta-\frac{1}{2})\chi_1(R)\cos\varphi - E\chi_2(R) - i\frac{\hbar v_F}{R}(m+\beta+\frac{1}{2})\chi_3(R)\sin\varphi = 0 \quad (2.10)$$

with the condition $w = m-1$ and $q = m+1$. Finally one gets,

$$\begin{aligned}
&\hbar v_F e^{i\theta}\sin\varphi(-i\frac{\partial}{\partial r}+\frac{1}{r}\frac{\partial}{\partial\theta}+\frac{ieB_0r}{2\hbar})\chi_2(r)e^{im\theta}=E\chi_3(r)e^{iq\theta}\\
&\Rightarrow i\hbar v_F\sin\varphi(\frac{1}{2R}+\frac{m}{R}+\frac{eB_0R}{2\hbar})\chi_2(R)e^{i(m+1)\theta}=E\chi_3(R)e^{in\theta} \qquad (2.11)\\
&\Rightarrow i\frac{\hbar v_F}{R}(m+\beta+\frac{1}{2})\chi_2(R)\sin\varphi - E\chi_3(R)=0
\end{aligned}$$

with the condition $q = m+1$. Similarly, at the other valley K′ ($\zeta = -1$) the conditions are $w = m+1$ and $q = m-1$. Combining them, we obtain the following conditions that should be valid, namely,

$$w = m-\zeta \quad \text{and} \quad q = m+\zeta. \qquad (2.12)$$

Thus, the eigenstates of H^ζ can be obtained as,

$$\psi^{m\zeta}(R,\theta) = \begin{pmatrix}\chi_1(R)e^{i(m-\zeta)\theta}\\ \chi_2(R)e^{im\theta}\\ \chi_3(R)e^{i(m+\zeta)\theta}\end{pmatrix}, \qquad (2.13)$$

where the integer m is the only independent total angular momentum quantum number (w and q depends on m through Eq. (2.12)). Therefore, the Hamiltonian corresponding to an ideal α-T_3 ring is given by,

$$H^\zeta_{\text{ring}} = \frac{\hbar v_F}{R}\begin{pmatrix}0 & -i(m+\beta-\frac{\zeta}{2})\cos\varphi & 0\\ i(m+\beta-\frac{\zeta}{2})\cos\varphi & 0 & -i(m+\beta+\frac{\zeta}{2})\sin\varphi\\ 0 & i(m+\beta+\frac{\zeta}{2})\sin\varphi & 0\end{pmatrix}. \qquad (2.14)$$

We obtain the energy spectrum as,

$$E^{m\zeta}_{\text{FL}} = 0 \quad \text{and} \quad E^{m\zeta}_{\pm} = \pm\frac{\hbar v_F}{R}\Delta^\zeta_m(\alpha,\beta). \qquad (2.15)$$

Here, $\Delta_m^{\zeta}(\alpha,\beta)$ is defined as,

$$\Delta_m^{\zeta}(\alpha,\beta)=\sqrt{(m+\beta)^2+\frac{1}{4}-\zeta(m+\beta)\frac{1-\alpha^2}{1+\alpha^2}}. \tag{2.16}$$

The energy spectrum in Eq. (2.15) of the α-T_3 ring consists of a zero energy flat band, $E_{\rm FL}$ alongwith a number of discrete levels in the conduction band, E_+ and the valence band, E_-.

The normalized wavefunctions corresponding to $E_{\pm}^{m\zeta}$ at a particular valley are obtained as,

$$\Psi_{\pm}^{m\zeta}(R,\theta)=\frac{e^{im\theta}}{\sqrt{2}\Delta_m^{\zeta}}\begin{pmatrix}\mp\left(m+\beta-\frac{\zeta}{2}\right)\cos\phi\, e^{-i\zeta\theta}\\ i\Delta_m^{\zeta}\\ \pm\left(m+\beta+\frac{\zeta}{2}\right)\sin\phi\, e^{i\zeta\theta}\end{pmatrix}. \tag{2.17}$$

Additionally, we obtain the wave function associated with $E_{\rm FL}^{m\zeta}$ as,

$$\Psi_{\rm Fl}^{m\zeta}(R,\theta)=\frac{e^{im\theta}}{\Delta_m^{\zeta}}\begin{pmatrix}\left(m+\beta+\frac{\zeta}{2}\right)\sin\phi\, e^{-i\zeta\theta}\\ 0\\ \left(m+\beta-\frac{\zeta}{2}\right)\cos\phi\, e^{i\zeta\theta}\end{pmatrix}. \tag{2.18}$$

It is interesting to note that that the flat band contains infinite number degenerate levels [see Eq. (2.18)], that is, any value of the quantum number m yields a valid solution.

2.3 Energy Spectra of a QR

2.3.1 Without magnetic field ($B_0 = 0$)

The energy levels as function of ring radius R for $\alpha = 0$ (i.e. graphene), $\alpha = 0.5$, and $\alpha = 1$ (i.e. dice lattice) at both the K and K′ valleys of α-T_3 quantum ring are shown in Fig. 2.2, with $-5 \leq m \leq -1$ (red curves), $1 \leq m \leq 6$ (blue curves), and $m = 0$ (green curves). Further, for nonzero values of α, there are three energy bands with the zero energy flat band (as shown by the cyan lines in Fig. 2.2) and the dispersive valence and conduction bands. In the absence of the external magnetic field ($B_0 = 0$), the energy branches of the valence and conduction band at both the valleys have $1/R$ dependency and approach $E \to 0$ for very large radii as can be seen from Eq. (2.15). However, the scenario for large radii depends on the m values. Certain degeneracies are present which we shall discuss in the following paragraph. Moreover, we observe $E^{\zeta}(m) = E^{-\zeta}(-m)$ as it should be, since energy levels are even in m at zero magnetic field.

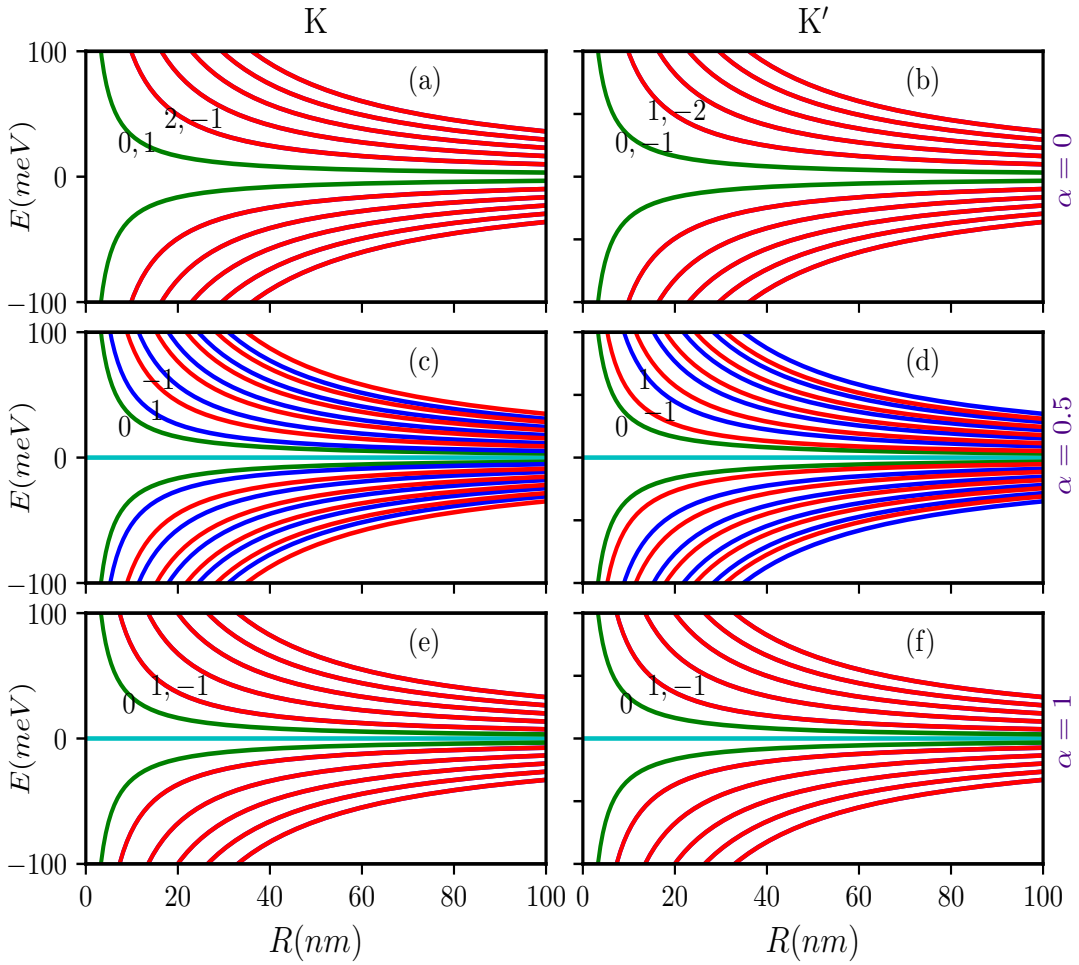

Figure 2.2: The energy levels of the α-T_3 quantum ring (QR) are shown as a function of the ring radius R in the absence of an external magnetic field ($B_0 = 0$). The energy levels are categorized by the angular momentum quantum number m, with $m = -5, ..., -1$ (red), $m = 0$ (green), and $m = 1, ..., 5$ (blue). The plots are presented for three values of α, namely, $\alpha = 0$ (a, b), $\alpha = 0.5$ (c, d), and $\alpha = 1$ (e, f). The two columns represent the energy levels in the two distinct valleys, namely, the K valley (left column) and the K′ valley (right column). Quantum numbers corresponding to specific energy levels are labeled for clarity.

Again, the zero field energy spectra at the K valley for different values of α are shown in Fig. 2.3 in a different context, that is, we shall see the m dependence of the energy levels. One can easily verify the results of the graphene quantum ring by setting $\alpha = 0$ in Eqs. (2.15) and (2.16). In this case, Δ_m^ζ depends on the valley as $\Delta_m^\zeta = |m - \zeta/2|$. Thus, at the K valley, the energy levels with $m = 0$ and $m = 1$ are degenerate, and so are levels with $m = 2$ and $m = -1$, $m = 3$ and $m = -2$,... Similarly, the energy levels with $m = 0$ and $m = -1$, $m = 1$ and $m = -2$, $m = 2$ and $m = -3$,... are degenerate at the K′ valley which also can be realized in Fig. 2.2(a) and (b). However, in the other limit ($\alpha = 1$), Δ_m^ζ becomes valley independent, as $\Delta_m^\zeta = \sqrt{m^2 + 1/4}$. Therefore, the energy level with $m = 0$ is nondegenerate and the levels corresponding to $m = \pm 1, \pm 2, ...$ are degenerate at both the valleys (see Fig. 2.2(e) and (f)).

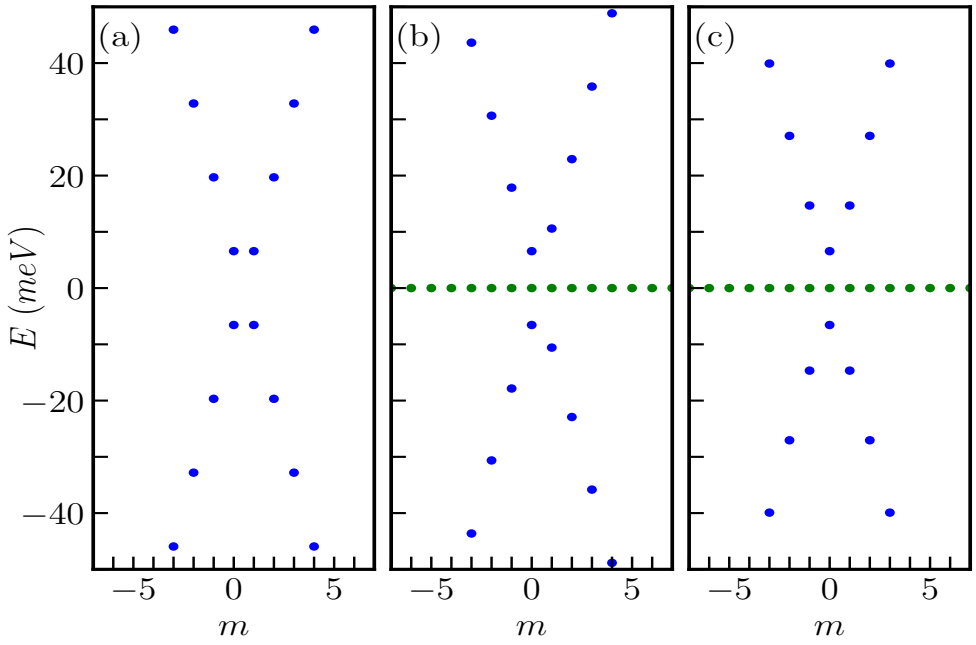

Figure 2.3: Zero magnetic field energy levels of the α-T_3 ring as a function of the quantum number m for (a) $\alpha = 0$, (b) $\alpha = 0.5$, and (c) $\alpha = 1$ at K valley. Here, we consider $R = 50$ nm. The $\alpha = 0$ case in (a) represents the quantum ring made of graphene, that is without an atom sitting in the center of the hexagon. The flat band is missing in this case.

Furthermore, at an intermediate value of α in the range $[0 : 1]$, say, $\alpha = 0.5$, all the energy levels are nondegenerate (see Fig. 2.2(c) and (d)). Here, only the $m = 0$ level is valley independent, while all the other levels depend on the valley in a complicated manner according to Eq. (2.16).

2.3.2 With magnetic field ($B_0 \neq 0$)

Now, let us discuss the case when the α-T_3 ring is threaded by a perpendicular magnetic flux. In this case, we find $\Delta_m^\zeta = |m + \beta - \zeta/2|$ and $\Delta_m^\zeta = \sqrt{(m+\beta)^2 + 1/4}$ for $\alpha = 0$ and $\alpha = 1$, respectively. In the case of a graphene ring ($\alpha = 0$), it is understood that the energy levels with $m = -\beta$ and $m = 1 - \beta$, $m = 2 - \beta$ and $m = -1 - \beta$, $m = 3 - \beta$ and $m = -2 - \beta$,... at the K valley, and that with $m = -\beta$ and $m = -1 - \beta$, $m = 1 - \beta$ and $m = -2 - \beta$, $m = 2 - \beta$ and $m = -3 - \beta$,... at the K$'$ valley are degenerate for β to be an integer. In the other limiting case, that is, $\alpha = 1$, Δ_m^ζ does not depend on the valley index ζ. Here, for integer value of β, the energy level with $m = -\beta$ is nondegenerate and the energy levels with $m = \pm 1 - \beta, \pm 2 - \beta, ...$ are degenerate. For intermediate value of α, no such degeneracy exists. These facts are clearly shown in Fig. 2.4. When β deviates from being an integer, all the energy levels becomes nondegenerate for all values of α.

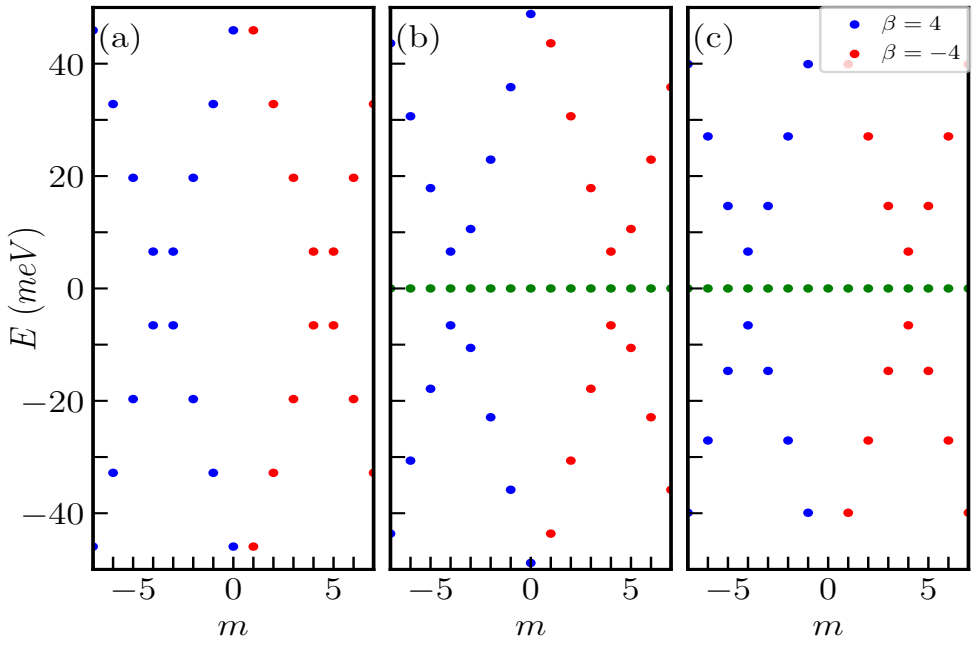

Figure 2.4: The energy levels of the α-T_3 ring at K valley as a function of the quantum number m for (a) $\alpha = 0$, (b) $\alpha = 0.5$, and (c) $\alpha = 1$ when the magnetic field is such that $\beta = \pm 4$. Here, we consider $R = 50\ nm$. The $\alpha = 0$ case in (a) represents the quantum ring made of graphene, that is without an atom sitting in the center of the hexagon. Thus, the flat band is missing here.

The band gap tuning with magnetic field of this type of systems can attract a lot of attention in the absorption and emission spectra studies, where the lowest energy gap results in strong signal in experiments. Stimulated by this, let us define the energy gap, ΔE^{ζ} at a particular valley ζ given by, $\Delta E^{\zeta} = E_{+}^{m\zeta} - E_{-}^{m\zeta}$. The minimum value of ΔE at the K valley is plotted as a function of β in Fig. 2.5. ΔE oscillates periodically with β with the oscillation period being $\beta = 1$. This happens since the minimum magnetic field required to transfer an electron from one angular momentum state to the subsequent angular momentum state is such that $\beta = 1$. For $\alpha = 0$ (Fig. 2.5(a)) and $\alpha = 1$ (Fig. 2.5(c)), ΔE is symmetric about $\beta = 0$. However, ΔE is not symmetric about $\beta = 0$ for an intermediate value, such as, $\alpha = 0.5$ (Fig. 2.5(b)). Also note that the energy gap at $\beta = 0$ (zero magnetic field) is independent of α.

In order to ascertain the size dependence of the energy eigenvalues of the ring, let us discuss how they depend on the radius, R. It is clear from Eq. (2.16) that Δ_m^{ζ} is independent of R in the absence of the magnetic field which leads to the $1/R$-dependence of the energy levels irrespective of the value of α as mentioned earlier. The above scenario is altered significantly in the presence of a magnetic field. In Fig. 2.6, we have shown the R-dependence of a few energy levels for both valleys considering $B_0 = 5$T for a few values of α, namely, $\alpha = 0$ (Fig. 2.6(a) and (b)), $\alpha = 0.5$ (Fig. 2.6(c) and (d)), and $\alpha = 1$ (Fig. 2.6(e) and (f)). Comparing the left and the right panels of Fig. 2.6 we conclude that all the energy levels become valley dependent

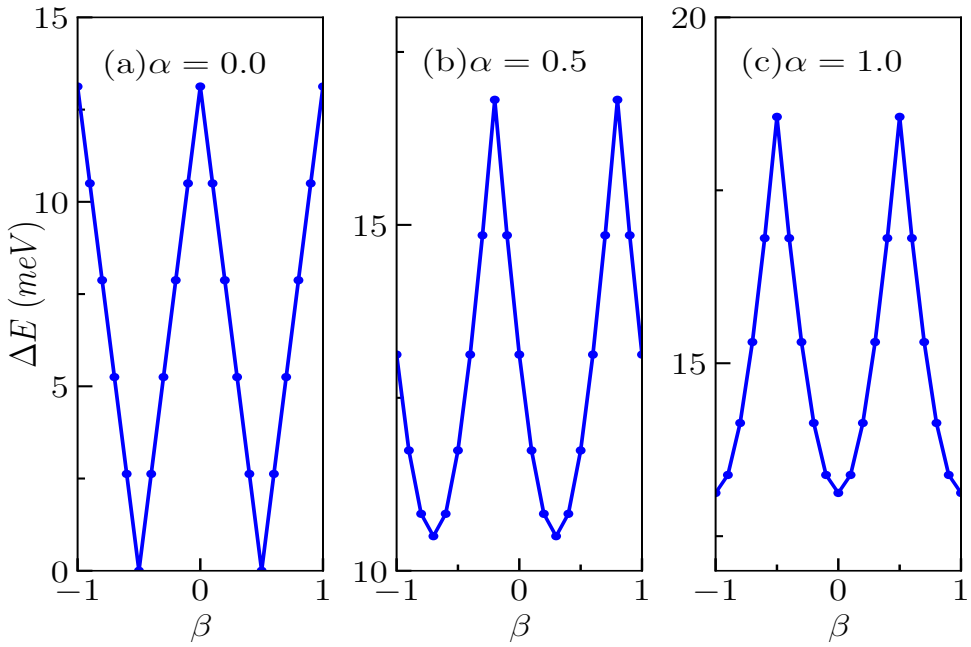

Figure 2.5: The minimum value of the energy gap $\Delta E = E_+^m - E_-^m$ at the K valley as a function of β for (a) $\alpha = 0$, (b) $\alpha = 0.5$, and (c) $\alpha = 1$. Here, we consider $R = 50\ nm$.

(except at $\alpha = 1$) in presence of the magnetic field. Further, for $\alpha = 0$ the energy branches with $m = 0$ and $m = -1, -2, ..., -5$ (negative m values) touch each other at the Fermi level, while the band gap between the branches with $m = 1, 2, 3$ (positive m values) increases with increasing m for the K valley. On the other hand at the K$'$ valley, the energy branches with $m = -1, -2, ..., -5$ (negative m values) touch each other at the Fermi level, while the band gap between the branches with $m = 0$ and $m = 1, 2, 3$ (positive m values) increases with m. It is observed that in presence of magnetic field, the relation between the angular momentum label m at K and K$'$ valley can be thought as $m_{\mathbf{K}'} = m_{\mathbf{K}} - 1$ that is, the role played by $m = 0$ at K valley is now played by $m = -1$ at K$'$ valley. While for the $\alpha \neq 0$ cases it is clear that at both the valleys the band gap increases with $m = 0$ and $m = 1, 2, 3$ (positive m values) with increase in the angular momentum quantum number m. However, the band gap between the branches with $m = -1, -2, ..., -5$ (negative m values) decreases with the increase of m. This features can be confirmed via Fig. 2.7 where we have shown the band gap energy as a function of the total angular momentum quantum number m. It is observed that at both the valleys the band gap increases as we increase the value of m from negative to positive value for all non zero values of α. For $\alpha = 0$ that is, graphene at K valley there is a band touching upto $m = 0$ and band gap increases with increasing m (Fig. 2.7(a)), while at K$'$ valley, the band touching happens upto $m = -1$ and then the band gap increases with the increase in m (Fig. 2.7(b)). Furthermore, form Fig. 2.6 we can also observe that each of the levels show a non-monotonic behaviour as a function of the radius R. In the limit of small R, all the energy levels vary inversely with R.

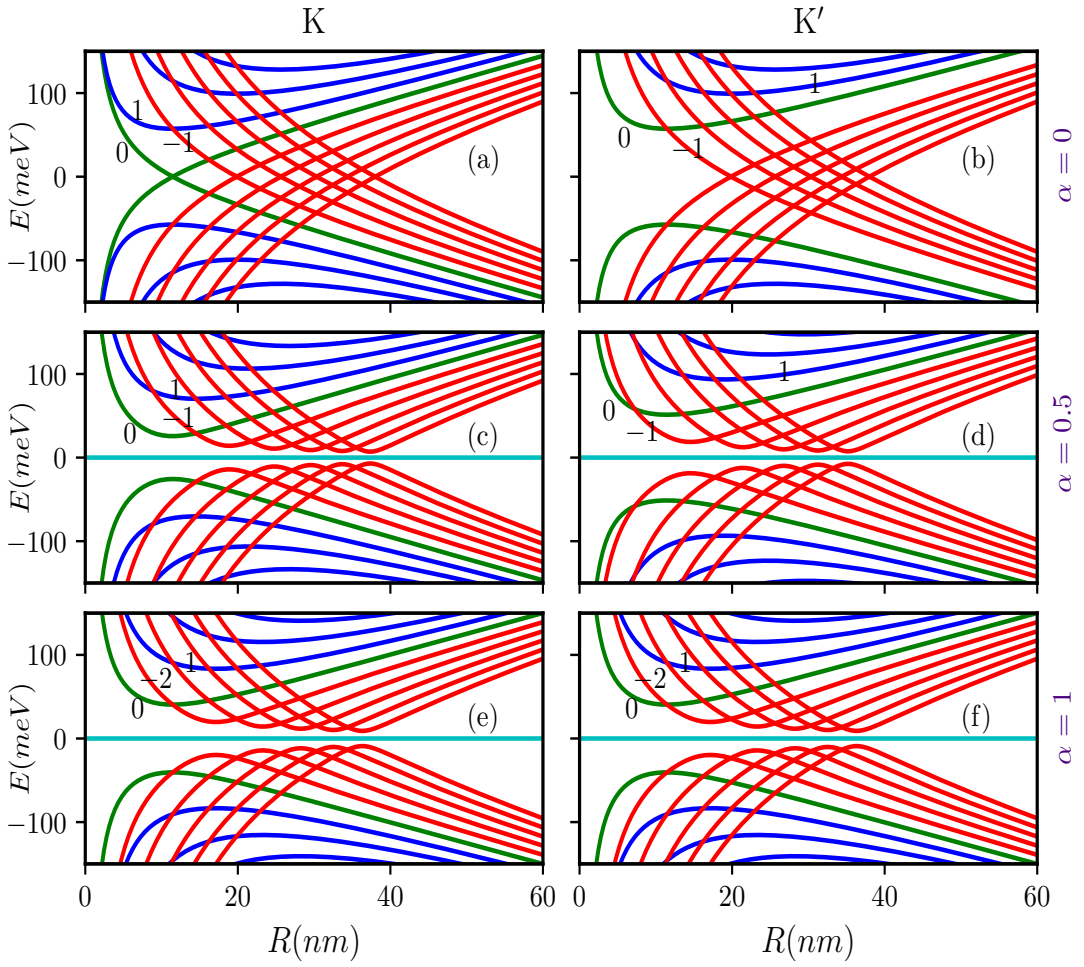

Figure 2.6: The energy levels of the α-T_3 quantum ring (QR) are shown as a function of the radius R in the presence of an external magnetic field, $B_0 = 5$T. The energy levels are categorized by the angular momentum quantum number m, with $m = -5, ..., -1$ (red), $m = 0$ (green), and $m = 1, 2, 3$ (blue). The plots are presented for three values of α, namely, $\alpha = 0$ (a, b), $\alpha = 0.5$ (c, d), and $\alpha = 1$ (e, f). The two columns represent the energy levels in the two distinct valleys, namely, the K valley (left column) and the K′ valley (right column). Quantum numbers corresponding to specific energy levels are labeled for clarity.

On the other hand, the energy scales as, $E \sim |ev_F B_0 R|/2$, in limit of large R. However, the criteria of R being "large" depends on m which can be understood in the following way.

The energy level attains an extremum (minimum for conduction band and maximum for valence band) at a particular value of R, namely $R = R_0$, which can be obtained by setting,

$$\left.\frac{dE_{\pm}^{m\zeta}}{dR}\right|_{R=R_0} = 0. \tag{2.19}$$

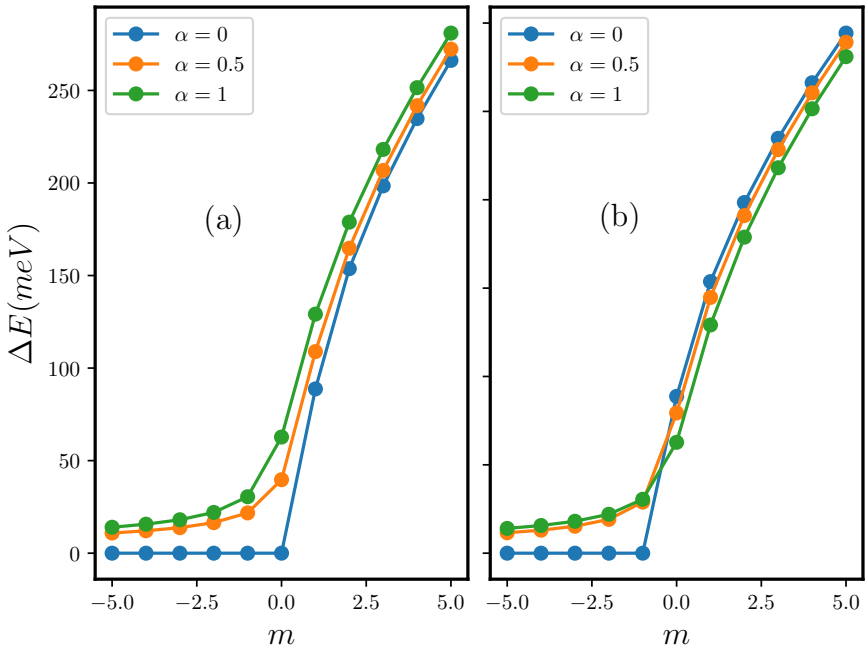

Figure 2.7: Energy gap for different angular momentum quantum number for a magnetic field $B_0 = 5$T (a) for K valley, and (b) for K$'$ valley.

Using Eq. (2.15) and Eq. (2.19), we find R_0 as,

$$R_0 = \sqrt{2}l_0\left(m^2 - m\zeta\frac{1-\alpha^2}{1+\alpha^2} + \frac{1}{4}\right)^{\frac{1}{4}}, \tag{2.20}$$

where $l_0 = \sqrt{\hbar/(eB_0)}$ is the magnetic length. For a fixed B_0, R_0 mainly depends on m, ζ and α. In the two limiting cases, namely, $\alpha = 0$ and $\alpha = 1$, we have $R_0 = l_0\sqrt{2m-\zeta}$ and $R_0 = \sqrt{2}l_0(m^2 + 1/4)^{1/4}$, respectively. For a given magnetic field, R_0 scales with m as, $R_0 \propto \sqrt{|m|}$ when m is large enough. This feature is shown in Fig. 2.8(a) where we present the radius dependence of a few positive energy levels with relatively large m, namely, $m = -50, -40, -30, -20, -10, 10, 20, 30, 40, 50$ at K valley for $\alpha = 0.5$ and $B_0 = 5$T. It is clear that the condition, for which one can consider R being "large", depends on m explicitly. More specifically, for an arbitrarily large value of R, we can always find a value of m which corresponds to the energy minimum. The scaling of the minimum energy with m depends on the sign of m also. For instance, $E_{min} \propto 1/\sqrt{|m|}$ when m is negative. On the other hand, for positive m, we have $E_{min} \propto \sqrt{m}$. These scaling features of E_{min} are depicted in Fig. 2.8(b) and Fig. 2.8(c). Therefore, the low energy states at the K valley are actually the states characterized by large negative m values. It is also worthy to mention here that by reversing the sign of either the valley index ζ or the magnetic field $\boldsymbol{B}$, one can have $E_{min} \propto 1/\sqrt{m}$ for $m > 0$ and $E_{min} \propto \sqrt{|m|}$ for $m < 0$. The results for other values of α are not shown here. We

have confirmed that other non zero values of α yield qualitatively similar results.

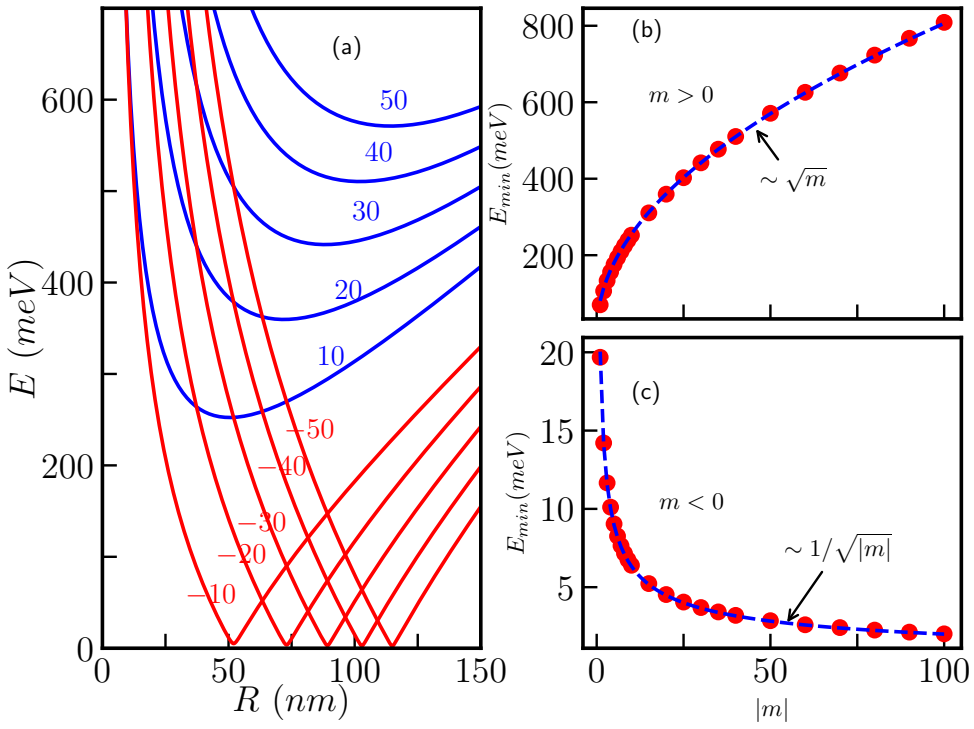

Figure 2.8: (a) Dependence of energy levels on the radius R of the α-T_3 ring at K valley considering large m values. We consider $B_0 = 5$T and $\alpha = 0.5$. (b) Minimum value of the energy as a function of m considering $m > 0$. Here, we find $E_{min} \sim \sqrt{m}$. (c) Minimum value of the energy as a function of m when $m < 0$. In this case, we obtain $E_{min} \sim 1/\sqrt{|m|}$.

The energy levels as function of the external magnetic flux (β) are shown in Fig. 2.9 at both the K and K′ valleys for a QR with $\alpha = 0$ (Figs. 2.9(a) and (b)), $\alpha = 0.50$ (Figs. 2.9(c) and (d)), and $\alpha = 1.00$ (Figs. 2.9(e) and (f)) for $-5 \leq m \leq -1$ (red curves), $1 \leq m \leq 5$ (blue curves), and $m = 0$ (green curves). For $\alpha = 0$, the magnetic flux dependency of the spectra appears as,

$$E = \pm \frac{\hbar v_F}{R}\left(m + \beta - \frac{\zeta}{2}\right) \tag{2.21}$$

which implies that the energies are linearly dependent on the external magnetic flux β (Figs. 2.9(a) and (b)). However, it is clear that, at any finite β, $E^{\zeta} \neq E^{-\zeta}$. Thus, the valley degeneracy is lifted. For $\alpha = 0.5$ the magnetic field dependency of the spectra can be obtained as,

$$E^2 - \frac{\hbar^2 v_F^2}{R^2}\left[(m + \beta + \frac{\zeta}{2})^2 \sin^2\varphi + (m + \beta - \frac{\zeta}{2})^2 \cos^2\varphi\right] = 0 \tag{2.22}$$

as shown in Figs. 2.9(c) and (d). Here also it is observed that, at any finite β, $E^{\zeta} \neq E^{-\zeta}$, again with the valley degeneracy being lifted. For $\alpha = 1$ the relation can be express as,

$$E^2 - \frac{\hbar^2 v_F^2}{2R^2}\left[(m + \beta + \frac{\zeta}{2})^2 + (m + \beta - \frac{\zeta}{2})^2\right] = 0 \tag{2.23}$$

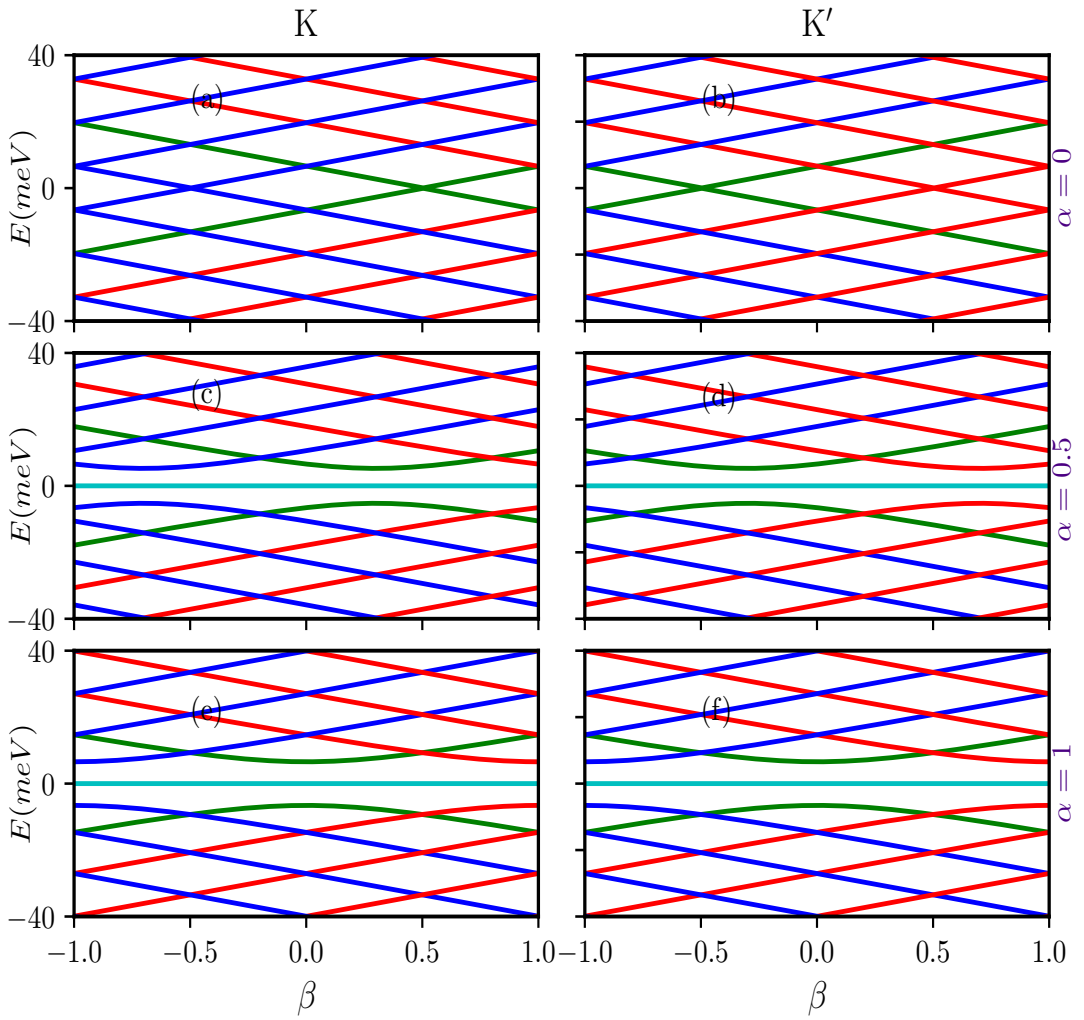

Figure 2.9: Energy levels as function magnetic flux β for (a, b) $\alpha = 0$, (c, d) $\alpha = 0.5$, and (e, f) $\alpha = 1$ quantum ring with the total angular momentum quantum number $-2 \leq m \leq -3$ (red curves), $1 \leq m \leq 3$ (blue curves), and $m = 0$ (green curves). Since the energy levels are periodic with respect to the magnetic flux, the calculations are confined to the regime $-1 \leq \beta \leq 1$.

as depicted in Figs. 2.9(e) and (f). Hence, we can find that, at any finite β, $E^{\zeta} = E^{-\zeta}$. Here, the valley degeneracy is protected. Thus, for nonzero α we can see that the energy has a hyperbolic dependence on the applied magnetic flux with minima at,

$$\beta = -m - \frac{\zeta}{2}(\sin^2\varphi - \cos^2\varphi) = -m + \frac{\zeta}{2}\cos 2\varphi \tag{2.24}$$

and a gap of,

$$\begin{aligned}\Delta E &= E_+ - E_- \\ &= \frac{2\hbar v_F}{R}\sqrt{(m+\beta+\frac{\zeta}{2})^2\sin^2\varphi + (m+\beta-\frac{\zeta}{2})^2\cos^2\varphi} \\ &= \frac{\hbar v_F}{R}\sin 2\varphi.\end{aligned} \tag{2.25}$$

Therefore, the energy gap increases with α, For $\alpha = 0$ the spectra are gapless, for $\alpha = 0.5$ magnitude of the spectral gap is $0.8\frac{\hbar v_F}{R}$, and for $\alpha = 1$ that is, for a dice QR the gap is $\frac{\hbar v_F}{R}$. We summarize these results in table 2.1.

$\boldsymbol{\alpha}$	$\boldsymbol{\Delta E}$	**valley degeneracy**
0	0	broken
0.5	$0.8\frac{\hbar v_F}{R}$	broken
1	$\frac{\hbar v_F}{R}$	protected

Table 2.1: Summary of α, ΔE, and valley degeneracies in presence of magnetic field.

2.4 Persistent Current

We consider the behaviour of the persistent current in the α-T_3 ring. The persistent current is the equilibrium current flowing along the angular direction in a QR when threaded by a magnetic flux. A proper knowledge of the current aids in quantifying the energy spectrum near the Fermi energy. This current can be calculated using the relation, $j_{x(y)} = \hbar v_F[\Psi^\dagger S_{x(y)}\Psi]$ (we set $\hbar = 1$ for the rest of the chapter). Using this definition, the radial and the angular currents are further obtained as $j_r = v_F[\Psi^\dagger S_r\Psi]$ and $j_\theta = v_F[\Psi^\dagger S_\theta\Psi]$, respectively. Here, S_r and S_θ are given in Eq. (2.6). The radial current can be calculated using Eq. (2.17) as,

$$\begin{aligned}
&(j_r)_\zeta = v_F[\psi^\dagger S_r\psi] \\
&\Rightarrow (j_r)_\zeta = -\frac{v_F e^{im\theta}}{\sqrt{2}\Delta_m^\zeta}\psi^\dagger \begin{pmatrix} 0 & e^{-i\theta}\cos\varphi & 0 \\ e^{i\theta}\cos\varphi & 0 & e^{-i\theta}\sin\varphi \\ 0 & e^{i\varphi}\sin\theta & 0 \end{pmatrix} \begin{pmatrix} (m+\beta-\frac{\zeta}{2})\cos\varphi e^{-i\theta} \\ i\Delta_m^\zeta \\ -(m+\beta+\frac{\zeta}{2})\sin\varphi e^{i\theta} \end{pmatrix} \\
&\Rightarrow (j_r)_\zeta = \frac{v_F}{2{\Delta_m^\zeta}^2}\begin{pmatrix}(m+\beta-\frac{\zeta}{2})\cos\varphi e^{i\theta} & -i\Delta_m^\zeta & -(m+\beta+\frac{\zeta}{2})\sin\varphi e^{-i\theta}\end{pmatrix}\begin{pmatrix} i\Delta_m^\zeta\cos\varphi e^{-i\theta} \\ (m+\beta-\frac{\zeta}{2})\cos^2\varphi - (m+\beta+\frac{\zeta}{2})\sin^2\varphi \\ i\Delta_m^\zeta\sin\varphi e^{i\theta}\end{pmatrix} \\
&\Rightarrow (j_r)_\zeta = \frac{v_F}{2{\Delta_m^\zeta}^2}\Big[\cancel{i\Delta_m^\zeta(m+\beta-\tfrac{\zeta}{2})\cos^2\varphi} - \cancel{i\Delta_m^\zeta(m+\beta-\tfrac{\zeta}{2})\cos^2\varphi} + \cancel{i\Delta_m^\zeta(m+\beta+\tfrac{\zeta}{2})\sin\varphi} - \cancel{i\Delta_m^\zeta(m+\beta+\tfrac{\zeta}{2})\sin\varphi}\Big] \\
&\Rightarrow (j_r)_\zeta = 0.
\end{aligned} \tag{2.26}$$

Thus, for the case of an ideal ring we have vanishing radial current $j_r = 0$. Further, the angular current becomes,

$$
\begin{aligned}
&(j_\theta)_\zeta = v_F[\psi^\dagger S_\theta \psi] \\
&\Rightarrow (j_\theta)_\zeta = -\frac{v_F e^{im\theta}}{\sqrt{2}\Delta_m^\zeta}\psi^\dagger \begin{pmatrix} 0 & -ie^{-i\theta}\cos\varphi & 0 \\ ie^{i\theta}\cos\varphi & 0 & -ie^{-i\theta}\sin\varphi \\ 0 & -ie^{i\varphi}\sin\theta & 0 \end{pmatrix} \begin{pmatrix} (m+\beta-\frac{\zeta}{2})\cos\varphi e^{-i\theta} \\ i\Delta_m^\zeta \\ -(m+\beta+\frac{\zeta}{2})\sin\varphi e^{i\theta} \end{pmatrix} \\
&\Rightarrow (j_\theta)_\zeta = \frac{v_F}{2{\Delta_m^\zeta}^2}\begin{pmatrix} (m+\beta-\frac{\zeta}{2})\cos\varphi e^{-i\theta} & -i\Delta_m^\zeta & -(m+\beta+\frac{\zeta}{2})\sin\varphi e^{i\theta} \end{pmatrix} \begin{pmatrix} \Delta_m^\zeta\cos\varphi e^{-i\theta} \\ i(m+\beta-\frac{\zeta}{2})\cos^2\varphi + i(m+\beta+\frac{\zeta}{2})\sin^2\varphi \\ -\Delta_m^\zeta\sin\varphi e^{i\theta} \end{pmatrix} \\
&\Rightarrow (j_\theta)_\zeta = \frac{v_F}{\Delta_m^\zeta}\left((m+\beta-\frac{1}{2})\cos^2\varphi + (m+\beta+\frac{1}{2})\sin^2\varphi\right).
\end{aligned}
\tag{2.27}
$$

Thus, we calculate the angular current at a particular valley as (writing $(j_\theta)_\zeta = j_\zeta$,

$$j_\zeta = \frac{v_F}{2\Delta_m^\zeta}\left[2\zeta(m+\beta) - \frac{1-\alpha^2}{1+\alpha^2}\right]. \tag{2.28}$$

The total angular current is composed of the contributions from the two valleys, namely,

$$j = j_{\mathbf{K}} + j_{\mathbf{K}'}. \tag{2.29}$$

The expression for the persistent current given in Eq. (2.28) can also be obtained using the following definition, namely, $j = -\sum_{m,\zeta}\frac{\partial E}{\partial \Phi}$ within the framework of the linear response theory, where the sum runs over all the occupied states. In Fig. 2.10, we show variation of the persistent current with β for different values of α. The persistent current is periodic in β with a period, $\beta = 1$. However, the oscillation pattern of the current corresponding to $\alpha = 0$ is completely different than that for $\alpha = 1$. Furthermore, the individual contributions arising from different valleys are exactly equal and opposite in both the graphene and dice lattice, that is, $\alpha = 0$ and $\alpha = 1$ (see Fig. 2.10(a) and (c)) which causes the total persistent current to vanish. The persistent current also vanishes at individual valleys when $\beta = 0$ (no magnetic field) for $\alpha = 1$. The case for an intermediate α that is, $0 < \alpha < 1$ is more interesting. Here, the currents from individual valleys do not compensate each other which results in a nonvanishing total persistent current. It is also noteworthy that the current at a particular valley does not vanish even when β is equal to zero, which gives rise to a total nonvanishing current corresponding to zero magnetic flux as illustrated in Fig. 2.10(b). So the opposite chirality of the electrons at the other valley is indispensable.

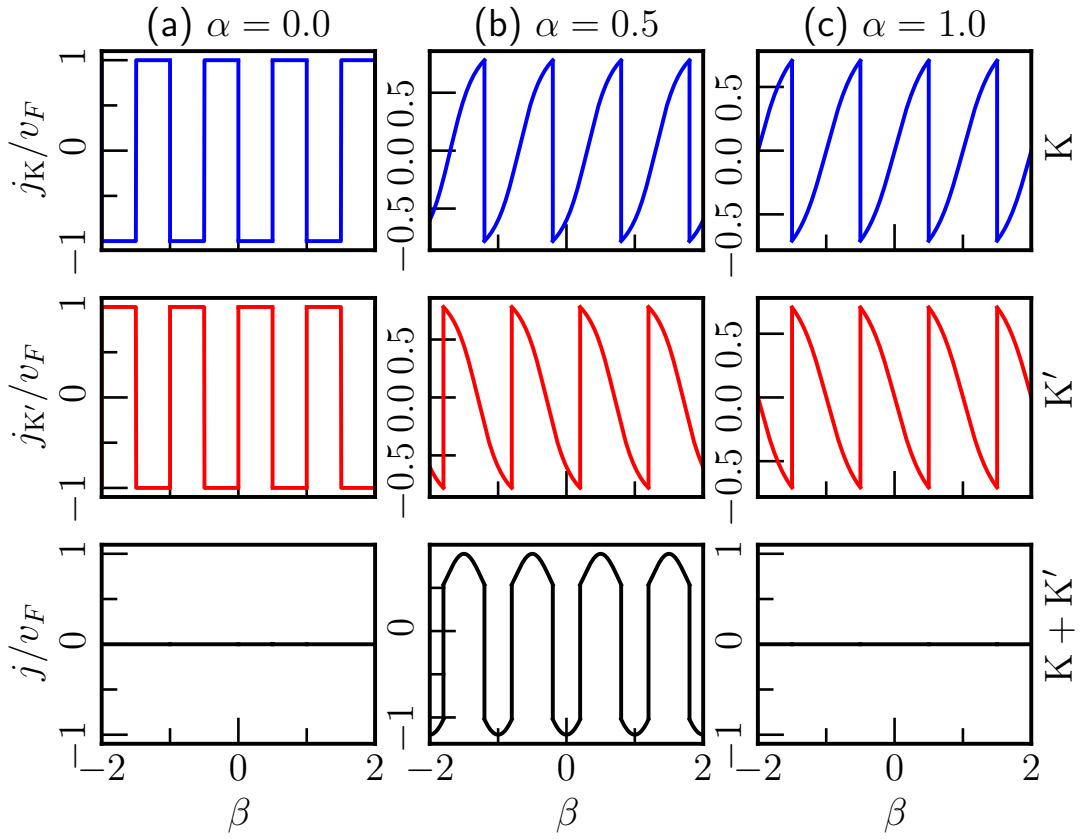

Figure 2.10: Persistent current as a function of $\beta = \Phi/\Phi_0$. (a) column for $\alpha = 0$, (b) column for $\alpha = 0.5$, and (c) column for $\alpha = 1$. Similarly, first row is for K valley, second row for K′-valley, and the third one is for the total of the two valleys.

2.5 A Staggered Mass in the α-T_3 Lattice

The mass of Dirac fermions in graphene is a fascinating subject that bridges various domains of physics. It encompasses phenomena such as the quantum Hall effect [34, 257], quantum transport, and practical applications like bandgap engineering in graphene-based devices [277]. In pristine graphene, Dirac fermions are massless [142, 150]. However, they can acquire different types of masses depending on the symmetry-breaking mechanisms that disrupt the equivalence between the two carbon atoms in the hexagonal unit cell (A and B atoms). For instance, an inversion symmetry-breaking potential, characterized by an energy shift of $+\delta$ on the A atoms and $-\delta$ on the B atoms [278–280], introduces a perturbation ($\delta\sigma_z$) that opens a bandgap of $E_g = |2\delta|$ [281, 282]. Interestingly, the mass term (δ) can take either positive or negative values, depending on the sign of the potential energy applied to one sublattice. A spatial variation in the sign of δ gives rise to intriguing phenomena, including the formation of domain walls where δ vanishes. At these domain walls, a topologically protected one-dimensional conducting

channel, hosting Weyl fermions as midgap states, can emerge. Such channels are thought to arise due to lattice mismatch between graphene and h-BN [283].

In this section, we explore the effect of the staggered mass induced by an inversion-symmetry-breaking potential in the α-T_3 lattice. Similar to graphene, the α-T_3 lattice possesses a hexagonal structure but features three sublattices (A, B, and C atoms). We investigate how this staggered mass impacts the persistent current in the α-T_3 lattice, highlighting its resemblance to graphene while emphasizing the unique effects introduced by its lattice structure.

2.5.1 Formalism

In this section, we are interested to see the effect of staggered mass term [180, 284] on the low energy spectrum of the α-T_3 ring,

$$\mathcal{M} = \begin{pmatrix} \delta & 0 & 0 \\ 0 & 0 & 0 \\ 0 & 0 & -\delta \end{pmatrix}. \tag{2.30}$$

Note that $\mathcal{M}$ can be thought to break the sublattice symmetry by including a different onsite potential at each of the A, B, and C sublattices. Now, following the same procedure as stated in Sec. 2.2 the effective Hamiltonian for the α-T_3 ring in presence of an external magnetic flux becomes,

$$H_\delta^\zeta = \frac{\hbar v_F}{R} \begin{pmatrix} \delta_0 & -i(m+\beta-\frac{\zeta}{2})\cos\varphi & 0 \\ i(m+\beta-\frac{\zeta}{2})\cos\varphi & 0 & -i(m+\beta+\frac{\zeta}{2})\sin\varphi \\ 0 & i(m+\beta+\frac{\zeta}{2})\sin\varphi & -\delta_0 \end{pmatrix}, \tag{2.31}$$

where $\delta_0 = R\delta/(\hbar v_F)$. The energy eigenvalues are obtained as,

$$E_n^{m\zeta} = 2\sqrt{\frac{P_m^\zeta}{3}}\cos\left[\frac{1}{3}\cos^{-1}\left(\frac{3Q_m^\zeta}{2P_m^\zeta}\sqrt{\frac{3}{P_m^\zeta}}\right) - \frac{2\pi n}{3}\right], \tag{2.32}$$

where $n = 0$, 1, and 2 are associated with the conduction band, the (distorted) flat band, and the valence band, respectively. Here,

$$P_m^\zeta = \frac{\hbar^2 v_F^2}{R^2}\left(\delta_0^2 + {\Delta_m^\zeta}^2\right)$$

and

$$Q_m^{\zeta} = \delta \frac{\hbar^2 v_F^2}{R^2} \left[\frac{1-\alpha^2}{1+\alpha^2} \left\{ (m+\beta)^2 + \frac{1}{4} \right\} - \zeta(m+\beta) \right].$$

The normalized wavefunctions can be written in the form,

$$\Psi_n^{m\zeta}(R,\theta) = N_n^{\zeta} e^{im\theta} \begin{pmatrix} -i\frac{\hbar v_F}{R}\left(m+\beta-\frac{\zeta}{2}\right)(E_n^{m\zeta}+\delta)\cos\varphi\, e^{-i\zeta\theta} \\ E_n^{m\zeta\,2} - \delta^2 \\ i\frac{\hbar v_F}{R}\left(m+\beta+\frac{\zeta}{2}\right)(E_n^{m\zeta}-\delta)\sin\varphi\, e^{i\zeta\theta} \end{pmatrix}, \tag{2.33}$$

with

$$N_n^{\zeta} = \frac{1}{\sqrt{\frac{\hbar^2 v_F^2}{R^2}[(E_n^{m\zeta}+\delta)^2\left(m+\beta-\frac{\zeta}{2}\right)^2\cos^2\varphi + (E_n^{m\zeta}-\delta)^2\left(m+\beta+\frac{\zeta}{2}\right)^2\sin^2\varphi] + (E_n^{m\zeta\,2}-\delta^2)^2}}.$$

2.5.2 The energy spectrum

Without magnetic field ($B_0 = 0$)

For graphene ($\alpha = 0$), as previously mentioned, the onsite potential introduces a bandgap of magnitude $|2\delta$ (which will be discussed in detail in the next section). However, the other features remain largely unchanged. Our primary focus is on the $\alpha > 0$ cases. In Figs. 2.11 and 2.12, we have shown the radius dependence of the zero field energy levels at both valleys for $\alpha = 0.5$ and $\alpha = 1$, respectively. We have considered two different values of the mass term, namely, $\delta = 50\,meV$ and $\delta = 100\,meV$. Typically, we consider $\delta \ll t$ (t is taken as $1eV$). The effect of the mass term in the energy spectrum is mainly two fold. Firstly, it introduces gap(s) in the spectrum that is, gap between the conduction band and the flat band and that between the flat band and the valence band. Secondly, it makes the flat band ($n = 1$) dispersive that is, a nonzero group velocity is now associated with each of the levels and hence all will contribute to the transport properties of the system. We shall see it later. The energy levels having small m values corresponding to $n = 0$, $n = 1$, and $n = 2$ merge to values equal to δ, 0, and $-\delta$, respectively in the limit of large R as evident from Figs. 2.11 and 2.12. This merging of the levels is also true for large m in the case of $\alpha = 1$, which we shall discuss in the next paragraph. In the small R limit, the energy levels belonging to $n = 0$ and $n = 2$ are inversely proportional to R irrespective of α ($\alpha = 0.5$ and 1). However, the levels associated with $n = 1$ deviate significantly from the $1/R$ dependence for both values of α. For a given n value, the energy levels at the K valley are related to those at the K′ valley as $E_n^{m(+\zeta)} = E_n^{-m(-\zeta)}$. Thus, the

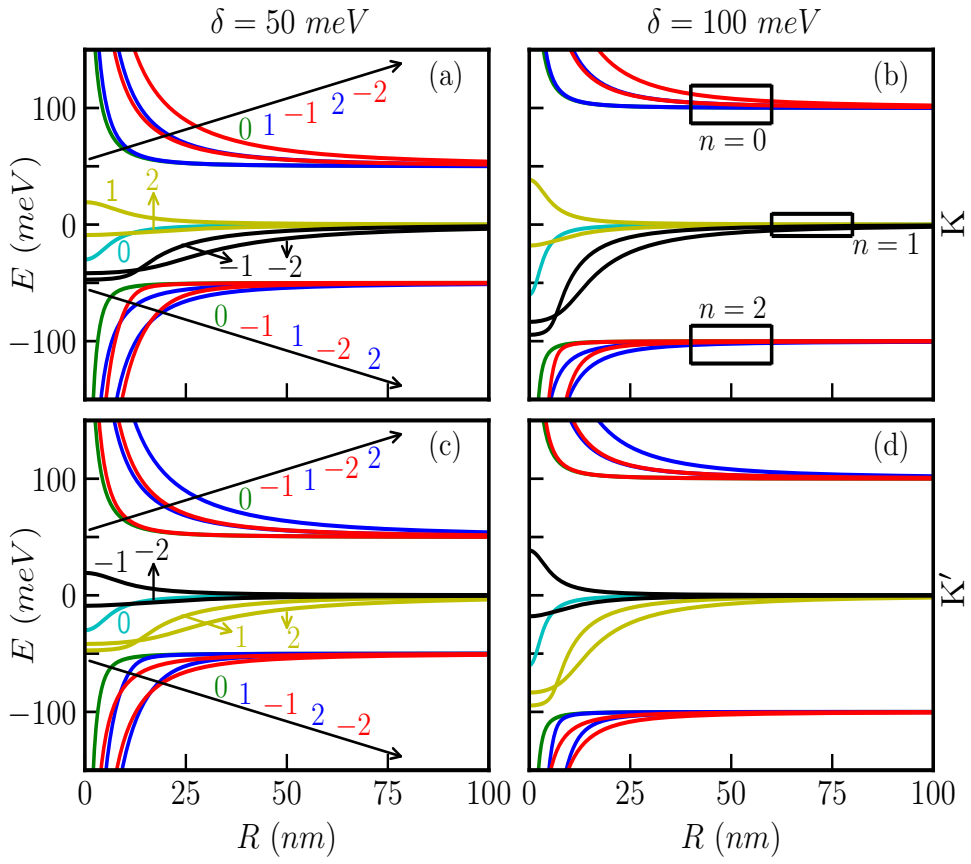

Figure 2.11: Zero field energy levels as a function of radius R for $\alpha = 0.5$ at both valleys considering $\delta = 50\,meV$ and $\delta = 100\,meV$.

scenario is identical at the other valley except that m reverses its sign. When $\alpha = 1$ (Fig. 2.12), we have $E_0^{m(+\zeta)} = -E_2^{-m(+\zeta)}$ at a particular valley ζ which is in direct contrast to the earlier results obtained corresponding to $\delta = 0$ (see Sec. 2.3.1). In the flat band ($n = 1$), we find that the level with $m = 0$ remains flat with zero energy, and the other levels satisfy $E_1^{m(+\zeta)}) = -E_1^{-m(+\zeta)}$. In the case of $\alpha = 0.5$ (Fig. 2.11), the above mentioned features are absent. In addition, the $m = 0$ level in the flat band is no longer flat. It shifts down towards negative energy at small values of R. By inspecting both Figs. 2.11 and 2.12, one can also comment that all the energy levels are non-degenerate for all values of α except for $\alpha = 0$ and this can be attributed to the presence of the mass term δ. Thus, the staggered mass is an important quantity to consider. Here, we would like to point out some features of the zero field energy spectrum in the limit of large m. In the case of $\alpha = 1$, we have $\Delta_m^\zeta \sim m$, $P_m^\zeta \sim \hbar^2 v_F^2 m^2/R^2$, and $Q_m^\zeta \sim -\zeta\hbar^2 v_F^2 \delta m/R^2$ when m is large. Let us now define a quantity $\mathcal{I}^\zeta$ such as,

$$\mathcal{I}^\zeta = \frac{3Q_m^\zeta}{2P_m^\zeta}\sqrt{\frac{3}{P_m^\zeta}}. \tag{2.34}$$

For large m, we obtain $\mathcal{I}^{\zeta} \sim -3\sqrt{3}\zeta R\delta/(2\hbar v_F m^2)$. Considering typical values of the param-

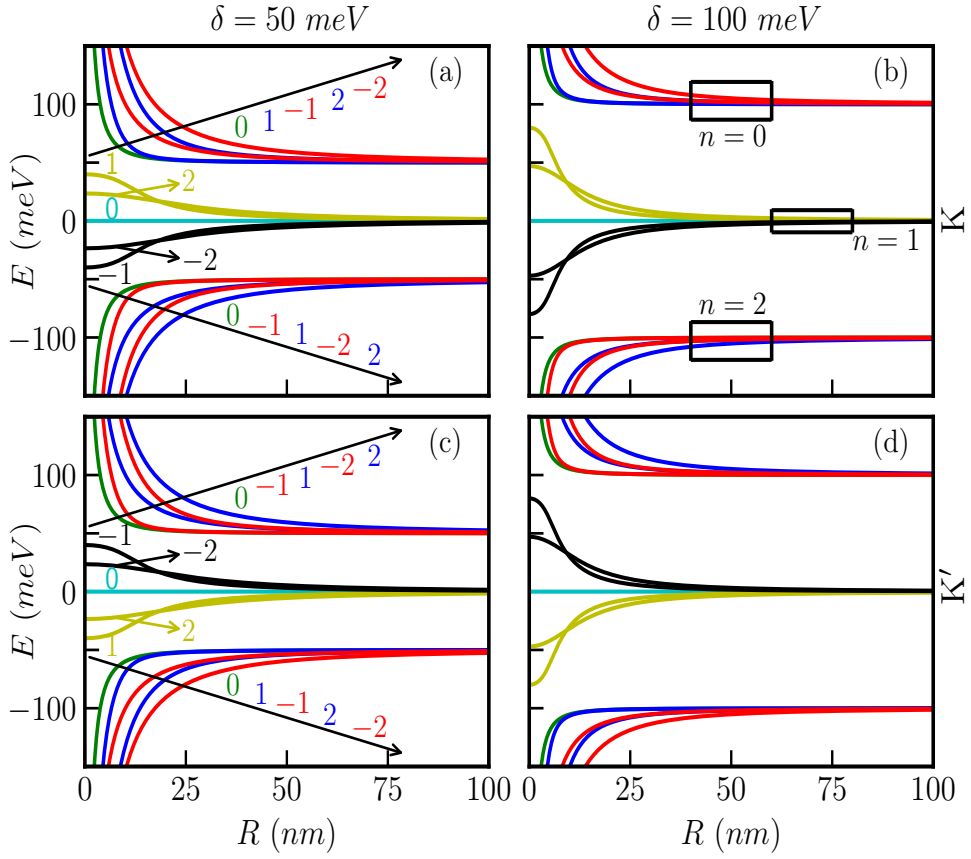

Figure 2.12: Zero field energy levels as a function of radius R for $\alpha = 1$ at both valleys considering $\delta = 50\,meV$ and $\delta = 100\,meV$.

eters: $R = 200$ nm, $\delta = 50\,meV$, and $m = 30$, one can verify that $3\sqrt{3}\zeta R\delta/(2\hbar v_F m) < 1$. Therefore, we have $\mathcal{I}^{\zeta} \to 0$ when m is sufficiently large. From Eq. (2.32), we find the energy levels when R is large enough,

$$E_n^{m\zeta} \sim \frac{2\delta}{\sqrt{3}} \cos\left(\frac{\pi}{6} - \frac{2\pi n}{3}\right). \tag{2.35}$$

It is now obvious from Eq. (2.35) that $E_0^{m\zeta} \to \delta$, $E_1^{m\zeta} \to 0$, and $E_2^{m\zeta} \to -\delta$. In other words, the levels with large m belonging to $n = 0$, $n = 1$, and $n = 2$ also merge at values δ, 0, and $-\delta$, respectively for large R corresponding to $\alpha = 1$. However, the scenario is different for $\alpha = 0.5$. In this case, one obtains $\mathcal{I}^{\zeta} \sim 9\sqrt{3}R\delta/(10\hbar v_F m)$ for large m. For the parameter values chosen earlier, we have $\mathcal{I}^{\zeta} < 1$. It is now straightforward to obtain the energy spectrum in limit of large R as,

$$E_n^{m\zeta} \sim \frac{2\delta}{\sqrt{3}} \cos\left(\vartheta_0 - \frac{2\pi n}{3}\right), \tag{2.36}$$

where ϑ_0 depends on R, δ, and m explicitly as $\vartheta_0 = \frac{1}{3}\cos^{-1}(\mathcal{I}^{\zeta})$.

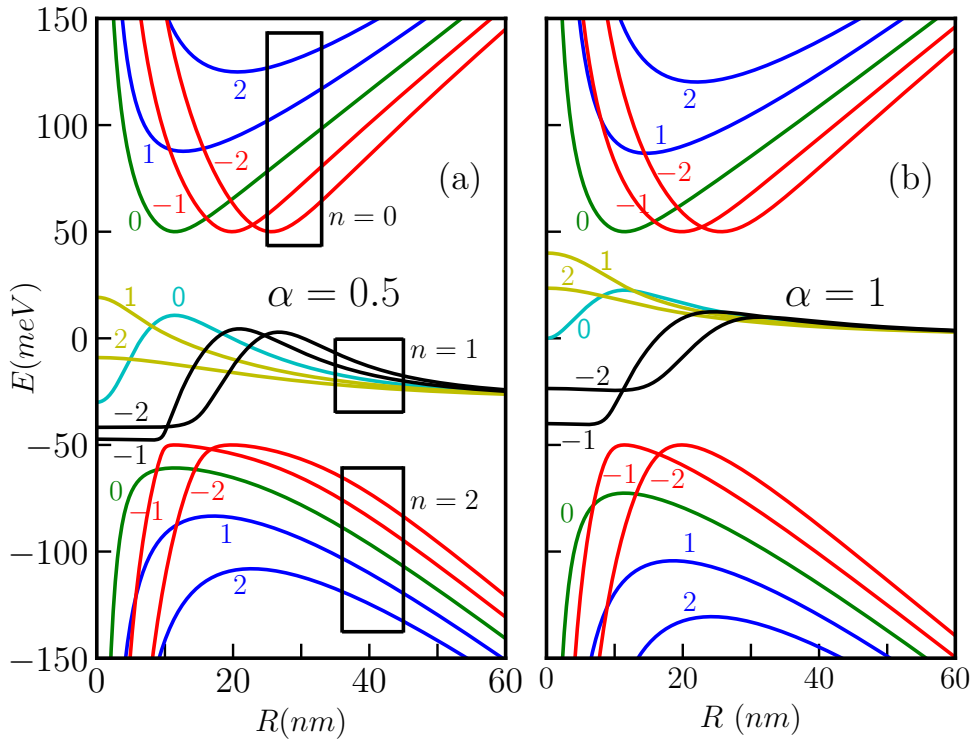

Figure 2.13: Finite field energy levels at K valley as a function of R in presence of the mass term $\delta = 50\ meV$ for (a) $\alpha = 0.5$ and (b) $\alpha = 1$. Here, we consider $B_0 = 5$T.

With magnetic field ($B_0 \neq 0$)

In Fig. 2.13, we show the R dependence of the energy levels having small m values at the K valley in presence of a magnetic field, where we have chosen, $B_0 = 5$T. The qualitative features of the energy spectrum deviate significantly from the zero magnetic field case. Here, all the energy levels are non-degenerate for all values of α. Unlike the $B_0 = 0$ case, one observes that, $E_0^m \neq -E_2^{-m}$, $E_1^m \neq -E_1^{-m}$, and a distortion of the $m = 0$ flat band energy level for $\alpha = 1$ (Fig. 2.13(b)). In addition, the levels in the $n = 1$ band merge with zero energy at large values of R. However, this is not the scenario for intermediate values of α, namely, $\alpha = 0.5$ (Fig. 2.13(a)), where the levels in the dispersive flat band do not merge to zero energy at large R. The energy levels in the conduction band as well as in the valence band depend on R in a similar fashion as in the case of $\delta = 0$ (see Fig. 2.6). The energy levels as a function of the external magnetic flux are shown in Fig. 2.14 for a quantum ring with a particular radius and mass, namely, $R = 10\ nm$ and $\delta = 50meV$. We consider three different vales of α, namely, $\alpha = 0$, $\alpha = 0.5$, and $\alpha = 1$ for both the K and the K′ valleys. It can be observed that for $\alpha = 0$, at both the valleys we can find that $E_+^{m(+\zeta)} = -E_-^{m(+\zeta)}$, here '+' and '−' refers the conduction

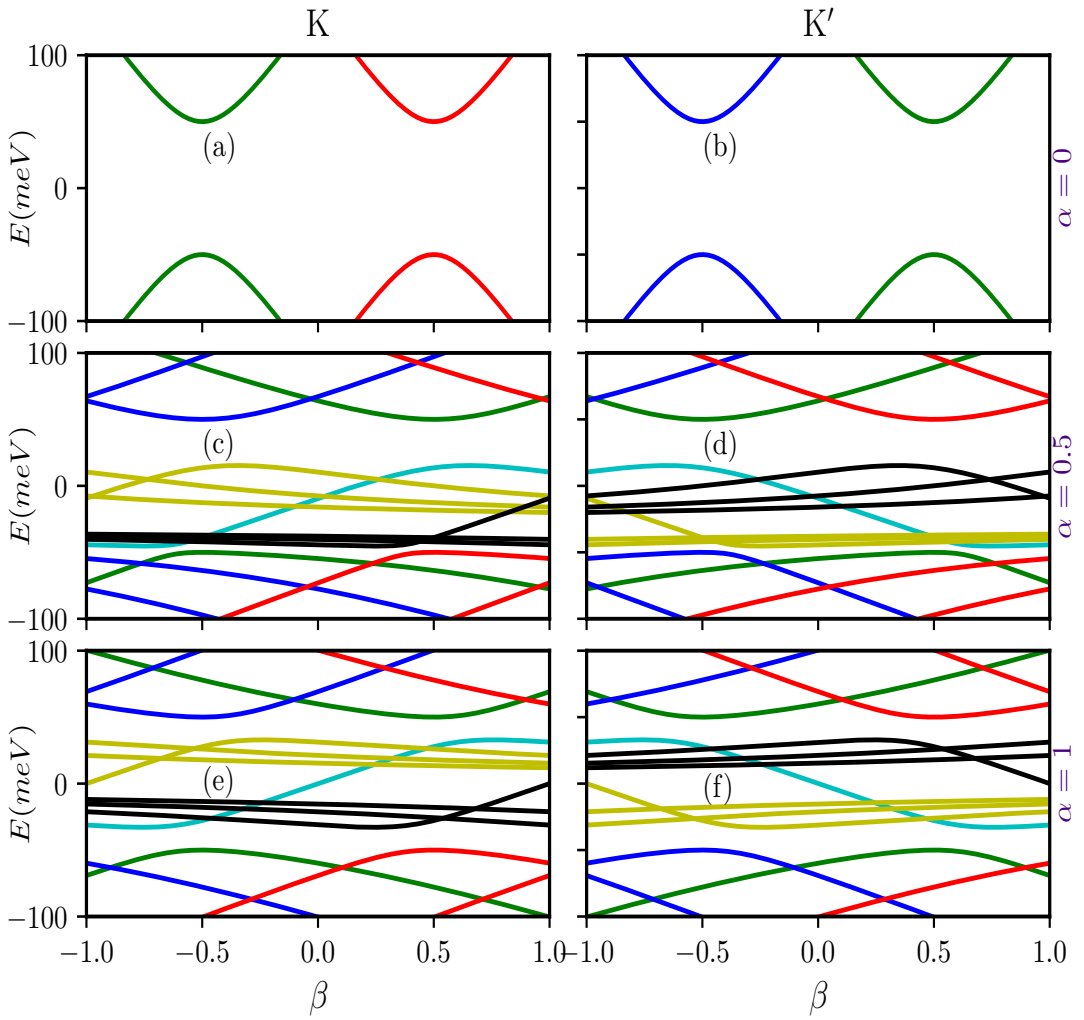

Figure 2.14: The energy levels of the α-T_3 quantum ring (QR) are shown as a function of the magnetic flux β for three values of α, namely, (a, b) $\alpha = 0$, (c, d) $\alpha = 0.5$, and (e, f) $\alpha = 1$. The total angular momentum quantum numbers are represented as follows, for $\alpha = 0$, $m = 0$ (green curves), $m = 1$ (blue curves), and $m = -1$ (red curves). For the valence and conduction bands at $\alpha > 0$, $m = -1, -2$ (red curves), $m = 1, 2$ (blue curves), and $m = 0$ (green curves). For the distorted flat band, $m = 0$ (cyan curves), $m = 1, 2, 3$ (yellow curves), and $m = -1, -2, -3$ (black curves). The two columns represent the two distinct valleys, namely, the K valley (left column) and the K′ valley (right column). An onsite potential of $\delta = 50\, meV$ is taken here. Since the energy levels are periodic with respect to the magnetic flux, the calculations are confined to the regime $-1 \leq \beta \leq 1$.

and valence bands correspondingly. Further, the magnetic flux dependency of the spectra can be rewritten as,

$$E^2 - \frac{\hbar^2 v_F^2}{R}\left[(m + \beta - \frac{\zeta}{2})^2 + \delta^2\right] = 0. \tag{2.37}$$

Unlike the massless case ($\delta = 0$) the energies are no longer linearly dependent on the external magnetic flux β, rather they follow hyperbolic dependency on the applied flux (Figs. 2.14(a) and (b)). For nonzero α we can see that the energy deviates from their hyperbolic dependency on the applied magnetic flux. These situations are significantly alters from their without mass

counterpart. Moreover, for any value of $\alpha \neq 0$, $E^{m,\Phi}_{\zeta,\uparrow}(n) \neq -E^{m,\Phi}_{\zeta,\uparrow}(n)$, the valence-conduction band symmetry is broken due to the mass term. However, for any α, there is no valley degeneracy present. Thus, it leads to non-zero valley current we shall discuss them in the subsequent subsection.

2.5.3 Persistent current

Here, we study the effect of the mass term on the behaviour of the persistent current. The persistent current at a particular valley and at a particular band now acquires the following form,

$$j^{\zeta}_{n} = 2v_F \frac{\hbar v_F}{R} N^{\zeta 2}_{n} \left(E^{m\zeta 2}_{n} - \delta^2\right) \left[(m+\beta)E^{m\zeta}_{n} + \delta(m+\beta)\frac{1-\alpha^2}{1+\alpha^2} - \frac{\zeta\delta}{2} - \frac{\zeta E^{m\zeta}_{n}}{2}\frac{1-\alpha^2}{1+\alpha^2}\right] \quad (2.38)$$

The persistent current at a particular valley is calculated from the contributions from the conduction band ($n = 0$) and the distorted flat band ($n = 1$) as,

$$j_{\zeta} = j^{n=0}_{\zeta} + j^{n=1}_{\zeta}. \quad (2.39)$$

The total angular current comprising of contributions from both the valleys is given by, $j = j_{\mathbf{K}} + j_{\mathbf{K}'}$. It is worthy to mention that the distortion of the energy levels in the flat band gives rise to finite persistent current unlike the case corresponding to no mass term ($\delta = 0$). In Fig. 2.15, we show the variation of the persistent current with β considering $\delta = 50\ meV$ corresponding to a ring radius $R = 10\ nm$. The introduction of the mass term completely changes the oscillation pattern of the persistent current from the case of $\delta = 0$ (see Fig. 2.10). The currents at different valleys are no longer equal and opposite which result in a nonvanishing total persistent current for all values of α. Further, the current at a particular valley, as well as the total current oscillates periodically in β with the periodicity $\beta = 1$. Here, the total persistent current at $\beta = 0$ (no magnetic field) is zero for all values of $\alpha \neq 0$.

2.6 Summary

In summary, we have investigated the properties of an α-T_3 QR. Particularly, we are interested in the behavior of the energy spectrum, the persistent current and the size dependencies of the spectral features as one interpolates between graphene ($\alpha = 0$ and the dice lattice ($\alpha = 1$). Ignoring the radial dependence of the ring allows to overlook the boundary effects. We list a number of observations in the following. Confinement of the carriers in the ring leads to

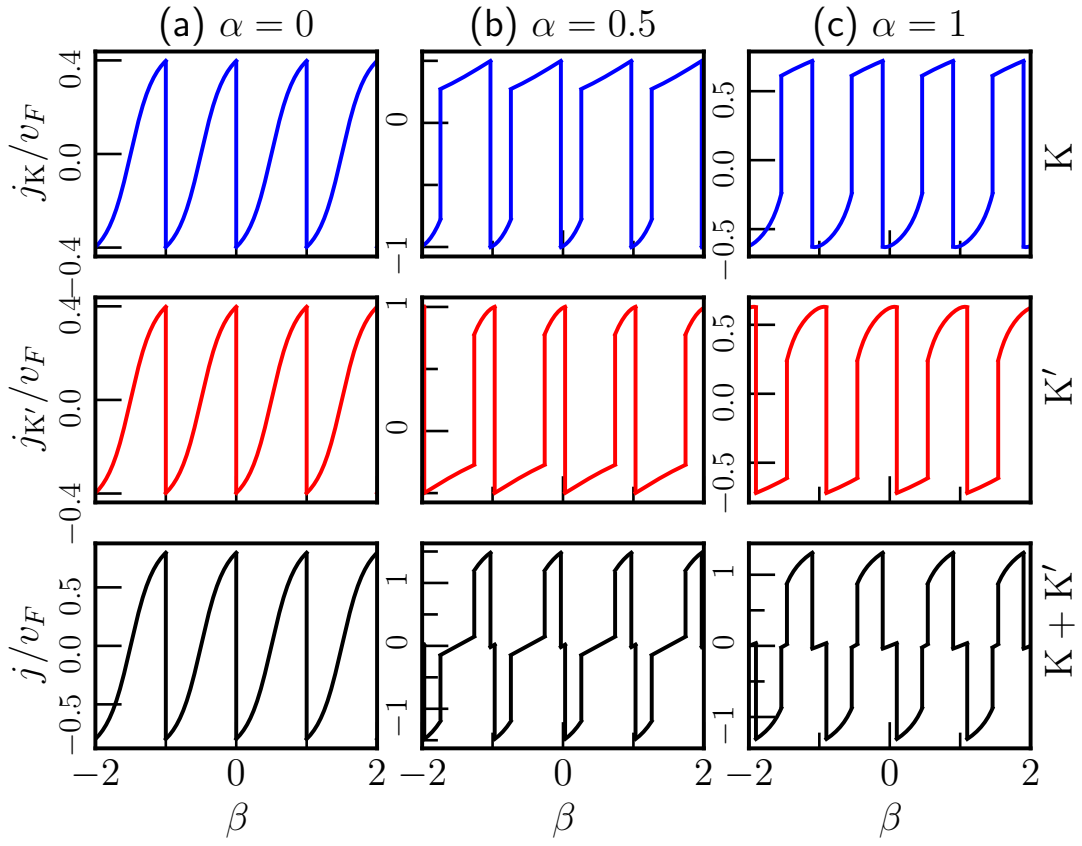

Figure 2.15: Persistent current as a function of $\beta = \Phi/\Phi_0$. (a) column for $\alpha = 0$, (b) column for $\alpha = 0.5$ and (c) column for $\alpha = 1$. Similarly, first row is for K valley, second row for K′-valley, and the third one is for the total of the two valleys. Here, we have considered the mass term $\delta = 50\ meV$ and the radius $R = 10\ nm$.

energy quantization characterized by the angular momentum quantum number m. As a result, we obtain discrete levels corresponding to both the conduction and the valence bands. However, the flat band consists of a huge number of zero energy degenerate levels which is insensitive to an applied magnetic field. In the zero field case, all the energy levels in the conduction or the valence band depend inversely on the radius (R) of the ring independent of values of α. Furthermore, there is a degeneracy in the energy levels corresponding to $\alpha = 0$. However, for an intermediate value of α, namely, $0 < \alpha < 1$, the energy levels become non-degenerate. Interestingly, this degeneracy is restored in the case of $\alpha = 1$ except for $m = 0$ level. It is also found that the valley degeneracy is broken for all values of α such that $\alpha \neq 1$. When the ring is subjected to a perpendicular magnetic field, the energy levels follow a substantial deviation from their typical $1/R$-dependence. In the large R limit the energy level scales as $E \sim R$, while at small R, it still behaves as $1/R$. The minimum energy gap between the conduction and the valence bands oscillates periodically as a function of the magnetic flux Φ with a period equal to one flux quantum Φ_0. We also calculate the persistent current which exhibits Φ_0 periodic oscillations at individual valleys, reminiscent of the Aharonov-Bohm oscillations. The total

persistent current comprising of both the valley vanishes for both $\alpha = 0$ and $\alpha = 1$ as a consequence of exact compensation of the contributions from two valleys. But when $0 < \alpha < 1$, the total current is nonzero and it undergoes Φ_0 periodic oscillations. Interestingly, we observe a nonzero persistent current at zero magnetic field. We have also discussed the effect of staggered mass term in the energy spectra. In absence of the magnetic field, the mass term makes the flat band dispersive in the small R limit except for the $m = 0$ band corresponding to $\alpha = 1$. A magnetic field alters the situation significantly by making all the levels in the flat band dispersive for all values of $\alpha \neq 0$. With the mass term, the persistent current is again periodic with a period of one flux quantum, but the oscillation pattern is completely different from the previous case (zero mass). However, there is a finite contribution coming from the distorted flat band in the persistent current. Finally, the total current is non-zero for all values of α.

Chapter 3

Persistent Currents in the Spin-Orbit Coupled α-T_3 Quantum Ring: Effects of Intrinsic and Rashba terms

---

We have investigated the properties of a spin-orbit-coupled α-T_3 pseudospin-1 fermionic quantum ring in detail. Our study includes the energy spectrum, persistent currents in both the charge and spin sectors, and their dependence on size. Furthermore, these properties are influenced by the spin-orbit couplings, the magnetic field, and the lattice parameter α. By tuning these parameters, we can manipulate the persistent currents, making them a controllable physical measurement in our system.

3.1 Introduction

Motivated by the promising prospects of the quantum rings (QRs), in this chapter we present analytical results for the energy levels of an ideal ring of pseudospin-1 α-T_3 lattice. We consider the bare Dirac Hamiltonian, augmented by either the intrinsic or the Rashba spin-orbit coupling

(SOC) terms or both. Specifically, we may focus on the Kane-Mele model on a ring which can be considered as two copies of the Haldane model with different Haldane fluxes for the two spins. The Haldane term is often referred to as the intrinsic SOC (ISOC). While studying topology, we shall call it as the Haldane term, for now, we continue denoting it as ISOC. In addition, we may consider the Rashba SOC which obeys all the symmetries that a parent α-T_3 ring has can be controlled by an external electric field [257] that breaks the mirror symmetry with respect to the α-T_3 plane, while the intrinsic coupling can be enhanced through edge heavy-atom functionalization [285]. The above discussion can be extended for an α-T_3 QR in presence of an external magnetic field and study the behaviour of the persistent currents.

We start by obtaining a ring Hamiltonian of radius R in polar coordinate. We handle subtleties regarding the hermiticity of the Hamiltonian and exclude additional complexities arising from the edge effects for the finite QR. Consequently, we obtain the analytical expressions for the energy spectrum and the corresponding wave functions as a function of the ring radius and an external magnetic field. Particularly, motivated by our studies in Chapter 2, we intend to see how the energy spectrum evolves as we approach the dice limit ($\alpha = 1$) starting from the graphene ($\alpha = 0$). Further, the inclusion of an external field would facilitate studies on the evolution of the spectral properties, the persistent current, and the interplay of the Aharonov-Bohm (AB) effect. Notably, we can tune the charge persistent currents, valley currents, and spin equilibrium currents via the parameters, α, the strength of the Rashba, and the intrinsic SOCs, allowing an interplay of these parameters and measurable quantities such as the currents in the spin, charge, and valley sectors.

A brief note on the choice of the spin-orbit coupling parameters will add a motivation to the results presented below. Through tight-binding calculations, it has been demonstrated that the numerical magnitude of ISOC is approximately 10 to 20 times smaller than that of RSOC [286]. Moreover, recent research has indicated that in cases where the both couplings are present and have comparable magnitudes, a mixing of the radial states occur. Conversely, when one of these couplings dominates, the system exhibits non-overlap of the radial states [287]. Several investigations have been conducted on the pseudospin-1 α-T_3 and dice lattices, utilizing an ISOC strengths within the range varying between $0.01t$ and $0.1t$ [102, 103, 186], and RSOC strengths within a range of roughly $0.1t$ to t [157, 288, 289]. Additionally, the typical value for the nearest-neighbor hopping parameter in graphene is $t = 2.7eV$ [290]. In our calculations, we shall adopt $t = 1eV$ everywhere, and to explore the effects of ISOC and RSOC, we shall employ two distinct sets of parameter values, namely, ISOC to have values $0.05t, 0.1t$, and RSOC to be $0.5t, 0.8t$. However, other values of t, $\tilde{\lambda}$, and λ_R, for example, lower values of t, $\tilde{\lambda}$, and λ_R have been considered by us, and found that they do not significantly alter the qualitative nature of our

results. Instead, they mainly introduce minor quantitative difference, and hence have skipped presenting them in the thesis.

The organization of this chapter is as follows. In Sec. 3.2, we discuss the various properties of pseudospin-1 α-T_3 QR in presence of intrinsic SOC including the energy spectrum and the persistent currents. Similar results for the Rashba SOC are given in Sec. 3.3. In Sec. 3.4, we present the results for a Hamiltonian along with both the intrinsic and the Rashba SOCs including the energy spectrum as well as the persistent currents of the ring. We summarize our results in Sec. 3.5. To give a structure to the preceding discussion we have included results in the absence and presence of an external magnetic field for each of the cases in different subsections. The energy level diagrams are presented as a function of the radius of the QR in presence and absence of the external field. Physical quantities such as the persistent currents are also investigated as a function of the external flux.

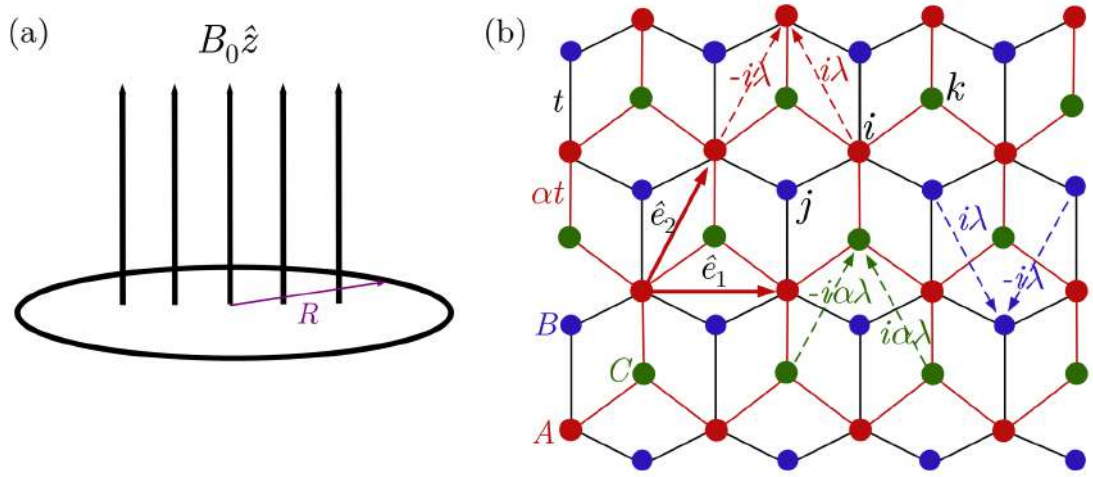

Figure 3.1: (a) Schematic diagram of the α-T_3 QR of radius R subjected to a perpendicular magnetic field $B = B_0\hat{z}$. (b) Lattice structure of the α-T_3 lattice. Here, A, B, and C lattice sites are shown by red, blue, and green dots respectively. The dashed arrows represent the hopping among the next nearest neighbouring (NNN) atoms, such as B-A-B or C-B-C or A-B-A or B-C-B. $\hat{e}_1$ and $\hat{e}_2$ are the lattice unit vectors.

3.2 Pseudospin-1 α-T_3 QR with ISOC

We consider a ring of radius R, in the x-y plane, made from the pseudospin-1 α-T_3 lattice as depicted in Fig. 3.1(a). The α-T_3 lattice structure is schematically shown in Fig. 3.1(b). The hopping energy between the A and B sites is t, while the hopping energy between the sites B and C is αt. Including the intrinsic spin-orbit coupling, the α-T_3 lattice Hamiltonian is given by [34, 186],

$$H=\sum_{\langle ij\rangle}tc^{\dagger}_{i\sigma}c_{j\sigma}+\sum_{\langle ik\rangle}\alpha tc^{\dagger}_{i\sigma}c_{k\sigma}+\frac{i\lambda}{3\sqrt{3}}\sum_{\langle\langle ij\rangle\rangle\sigma\sigma'}\nu_{ij}c^{\dagger}_{i\sigma}\sigma_z c_{j\sigma'}+\frac{i\alpha\lambda}{3\sqrt{3}}\sum_{\langle\langle ik\rangle\rangle\sigma\sigma'}\nu_{ik}c^{\dagger}_{i\sigma}\sigma_z c_{k\sigma'} \quad (3.1)$$

where $c^{\dagger}_{i,j,k}(c_{i,j,k})$ is the creation (annihilation) operator of electrons on the corresponding A, B, and C sites denoted by j, i, and k indices, respectively. The first term is the electron hopping between the A and B sites, while the second one is that between the B and C sites. The summations of $\langle ij\rangle$ and $\langle ik\rangle$ run over the nearest neighbour (NN) sites A-B (B-C). The third term is the next nearest neighbour (NNN) hopping of electrons $\langle\langle ij\rangle\rangle$ (double angular brackets denote the NNN hopping are to distinguish from the single ones that stand for NN hopping) between A-B-A or B-A-B representing the spin-orbit coupling proposed by Kane and Mele in graphene [257], λ is the SOC strength. ν_{ij} $(\nu_{ik})=1$ for the NNN hopping to be anticlockwise and ν_{ij} $(\nu_{ik})=-1$ (depending on the orientation of the two nearest neighbour bonds the electron traverses in going from site j to i) if it is clockwise with respect to the positive z axis (which is perpendicular to the lattice xy plane), σ_z,σ, and σ' are the real spin Pauli operators. The last term describes the SOC due to the introduction of the central C atoms into the graphene lattice, that is, the C-B-C and B-C-B NNN hoppings are feasible (A-C-A and C-A-C are neglected). $\alpha\lambda$ is the corresponding SOC strength (similar to αt), so that putting $\alpha=0$ reproduces all the results for graphene.

In the Bloch representation, the above lattice Hamiltonian can be transformed into a continuum one. Therefore, the total low-energy Hamiltonian around the Dirac points are governed by a pseudospin-1 Dirac-Weyl Hamiltonian of the form,

$$H(\sigma)=\hbar v_F\begin{pmatrix}0&(\zeta p_x-ip_y)\cos\varphi&0\\(\zeta p_x+ip_y)\cos\varphi&0&(\zeta p_x-ip_y)\sin\varphi\\0&(\zeta p_x+ip_y)\sin\varphi&0\end{pmatrix}-\zeta\sigma\tilde{\lambda}\begin{pmatrix}\cos\varphi&0&0\\0&\sin\varphi-\cos\varphi&0\\0&0&-\sin\varphi\end{pmatrix} \quad (3.2)$$

where $\tan\varphi=\alpha$, p_x and p_y donate the in-plane mechanical momentum operator, $\zeta=\pm1$, representing the K (K′) valley index, $\tilde{\lambda}=\lambda/\cos\varphi$, and $\hbar v_F=\sqrt{3}at/2\cos\varphi$, while σ denotes the real spin degrees of freedom. The Hamiltonian in Eq. (3.2) can be expressed in the polar (r,θ) coordinates as,

$$H(\sigma)=\begin{pmatrix}-\zeta\sigma\tilde{\lambda}\cos\varphi&\hbar v_F e^{-i\theta}(-i\zeta\frac{\partial}{\partial r}-\frac{1}{r}\frac{\partial}{\partial\theta})\cos\varphi&0\\\hbar v_F e^{i\theta}(-i\zeta\frac{\partial}{\partial r}+\frac{1}{r}\frac{\partial}{\partial\theta})\cos\varphi&\zeta\sigma\tilde{\lambda}(\cos\varphi-\sin\varphi)&\hbar v_F e^{-i\theta}(-i\zeta\frac{\partial}{\partial r}-\frac{1}{r}\frac{\partial}{\partial\theta})\sin\varphi\\0&\hbar v_F e^{i\theta}(-i\zeta\frac{\partial}{\partial r}+\frac{1}{r}\frac{\partial}{\partial\theta})\sin\varphi&\zeta\sigma\tilde{\lambda}\sin\varphi\end{pmatrix}. \quad (3.3)$$

The eigenstates of H are obtained as,

$$\Psi_\sigma(r,\theta) = \begin{pmatrix} \chi_{1\sigma}(r)e^{i(m-\zeta)\theta} \\ \chi_{2\sigma}(r)e^{im\theta} \\ \chi_{3\sigma}(r)e^{i(m+\zeta)\theta} \end{pmatrix}, \tag{3.4}$$

where the integer m labels the orbital angular momentum quantum number and $\chi_{i\sigma}$s denote the amplitudes corresponding to the three sublattices. We follow the earlier approach employed for an ideal one dimensional quantum ring by freezing the radial part, $r = R$ in the eigensolutions. Therefore, the Hamiltonian corresponding to an ideal α-T_3 ring is given by,

$$H(\sigma) = \begin{pmatrix} -\zeta\sigma\tilde{\lambda}\cos\varphi & -i\frac{\hbar v_F}{R}\frac{\zeta}{2}\cos\varphi & 0 \\ i\frac{\hbar v_F}{R}(m-\frac{\zeta}{2})\cos\varphi & \zeta\sigma\tilde{\lambda}(\cos\varphi-\sin\varphi) & -i\frac{\hbar v_F}{R}(m+\frac{\zeta}{2})\sin\varphi \\ 0 & i\frac{\hbar v_F}{R}(m+\frac{\zeta}{2})\sin\varphi & \zeta\sigma\tilde{\lambda}\sin\varphi \end{pmatrix} \tag{3.5}$$

The energy eigenvalues are obtained as,

$$E^m_{\zeta,\sigma}(n) = 2\sqrt{-\frac{P}{3}}\cos\left[\frac{1}{3}\cos^{-1}\left(\frac{3Q}{2P}\sqrt{-\frac{3}{P}}\right) - \frac{2\pi n}{3}\right] \tag{3.6}$$

where n = 0, 1, and 2 are associated with the conduction band (CB), the (distorted) flat band (dFB), and the valence band (VB), respectively. Here P and Q are given by,

$$P = \frac{\tilde{\lambda}^2}{2}\sin 2\varphi - \tilde{\lambda}^2 - \frac{\hbar^2 v_F^2}{R^2}\left[N^2\sin^2\varphi + M^2\cos^2\varphi\right]$$

and

$$Q = \frac{\zeta\sigma\tilde{\lambda}}{2}\sin 2\varphi\left[\tilde{\lambda}^2(\cos\varphi-\sin\varphi) + \frac{\hbar^2 v_F^2}{R^2}\left(M^2\cos\varphi - N^2\sin\varphi\right)\right]$$

respectively. The normalized spinor wavefunctions are given by,

$$\Psi^{m\zeta}_{n,\sigma}(R,\theta) = N^\zeta_{n,\sigma}\, e^{im\theta}\begin{pmatrix} -i\frac{\hbar v_F}{R}M\left(E^m_{\zeta,\sigma} - \zeta\sigma\tilde{\lambda}\sin\varphi\right)\cos\varphi\, e^{-i\zeta\theta} \\ \left(E^m_{\zeta,\sigma} + \zeta\sigma\tilde{\lambda}\cos\varphi\right)\left(E^m_{\zeta,\sigma} - \zeta\sigma\tilde{\lambda}\sin\varphi\right) \\ i\frac{\hbar v_F}{R}N\left(E^m_{\zeta,\sigma} + \zeta\sigma\tilde{\lambda}\cos\varphi\right)\sin\varphi\, e^{i\zeta\theta} \end{pmatrix}, \tag{3.7}$$

with

$$N^\zeta_{n,\sigma} = \frac{1}{\sqrt{\frac{\hbar^2 v_F^2}{R^2}\left[M^2\left(E^m_{\zeta,\sigma}-\zeta\sigma\tilde{\lambda}\sin\varphi\right)^2\cos^2\varphi + N^2\left(E^m_{\zeta,\sigma}+\zeta\sigma\tilde{\lambda}\cos\varphi\right)^2\sin^2\varphi\right] + \left(E^m_{\zeta,\sigma}+\zeta\sigma\tilde{\lambda}\cos\varphi\right)^2\left(E^m_{\zeta,\sigma}-\zeta\sigma\tilde{\lambda}\sin\varphi\right)^2}},$$

where $M = (m - \frac{\zeta}{2})$ and $N = (m + \frac{\zeta}{2})$. One can easily verify that, when there is no SOC, that is, $\tilde{\lambda} = 0$, the eigenvalues of Eq. (3.6) can be directly simplified onto the eigenvalues of the parent α-T_3 QR with one zero energy mode (as discussed in Chapter 2). When $\tilde{\lambda} \neq 0$, we get three energy bands for one kind of spin. The energy dispersions around the Dirac points (K or K′) for a particular value of α (intermediate to graphene and dice), namely, $\alpha = 0.4$ are plotted in Fig. 3.2.

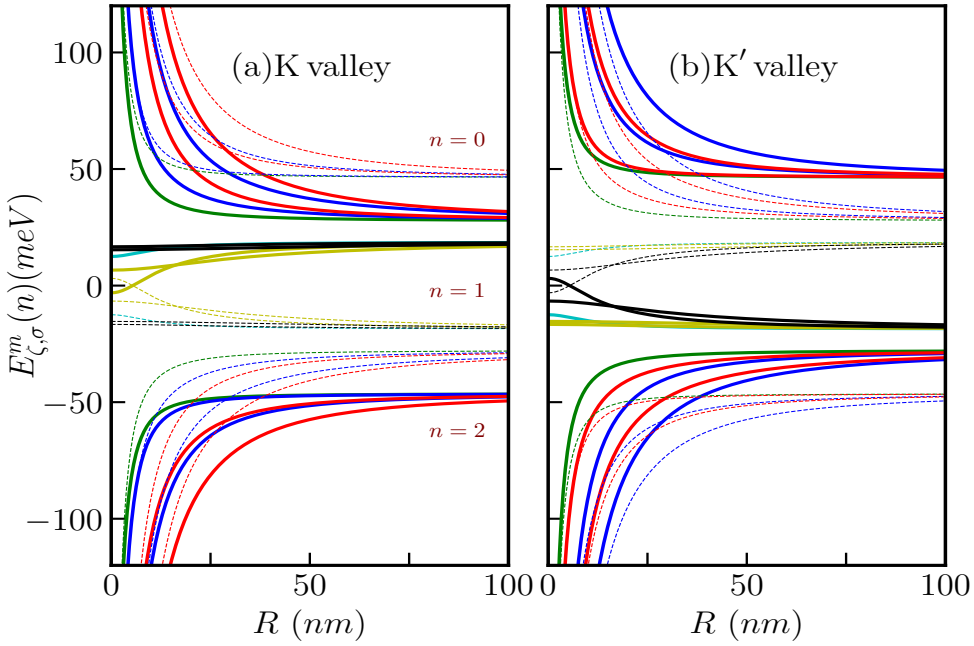

Figure 3.2: The spin-resolved band structures $E^m_{\zeta,\sigma}(n)$ vs R of the α-T_3 quantum ring for the (a) K valley and (b) K′ valley in absence of an external field. $n = 0, 1$, and 2 denote the CB, dFB, and VB respectively. The solid and the dashed lines in each panel are for spin-↑ and spin-↓ bands respectively. The parameters are taken as $\tilde{\lambda} = 0.05t$, $t = 1eV$, and $\alpha = 0.4$. For the VB and CB, the angular momentum quantum numbers are chosen as $m = 0$ (green curves), $m = -1, -2$ (red curves) and $m = 1, 2$ (blue curves). For the dFB, the corresponding values are $m = 0$ (cyan curves), $m = -1, -2$ (black curves) and $m = 1, 2$ (yellow curves). These values and notations will be consistently used in the subsequent figures of this section.

3.2.1 Without magnetic field ($B_0 = 0$)

The energies as a function of ring radius R at the K valley is shown in Fig. 3.2(a) and the same at the K′ valley is presented in Fig. 3.2(b) with $m = 0$ (green curves), $m = -1, -2$ (red curves) and $m = 1, 2$ (blue curves) for the valence and the conduction bands. Further, for distorted flat bands with $m = 0$ (cyan curves), $m = -1, -2$ (black curves) and $m = 1, 2$ (yellow curves). It is seen that for $n = 1$, the original dispersionless flat band is no longer flat, instead, it becomes distorted. That is, a non-zero group velocity may be associated with this band electrons. Hence, the $n = 1$ band electrons will start contributing to the transport

properties of the system. Moreover, the $n = 1$ band shifts away from the band center ($E = 0$) and the bands for opposite spin species move in opposite directions (as indicated by dashed and solid lines in each panel), resulting in formation of spin polarized bands. However, it is worth noting that the spin polarizations for the K and K′ valleys are opposite. This certainly implies that the time-reversal symmetry remains unchanged. The spin-valley splitting of the α-T_3 band structure bears resemblance to those observed in transition metal dichalcogenide materials, such as, MoS_2 [291], where the two valleys exhibit opposite spin splitting, while the system overall maintains a time-reversal symmetry. This intriguing spin-valley dependent band structure can be experimentally observed through spin-valley selective circular dichroism [292], a phenomenon in which the responses of the left and the right handed circularly polarized lights differ. For the graphene ($\alpha = 0$) or the dice lattice ($\alpha = 1$), the energy bands retain the spin and the valley degeneracy, that is, $E_{\zeta\sigma} = E_{\bar{\zeta}\bar{\sigma}}$ with $\bar{\sigma} = -\sigma$ and $\bar{\zeta} = -\zeta$ in Eq. (3.6), because the particle-hole symmetry remains invariant, although the inversion symmetry is broken.

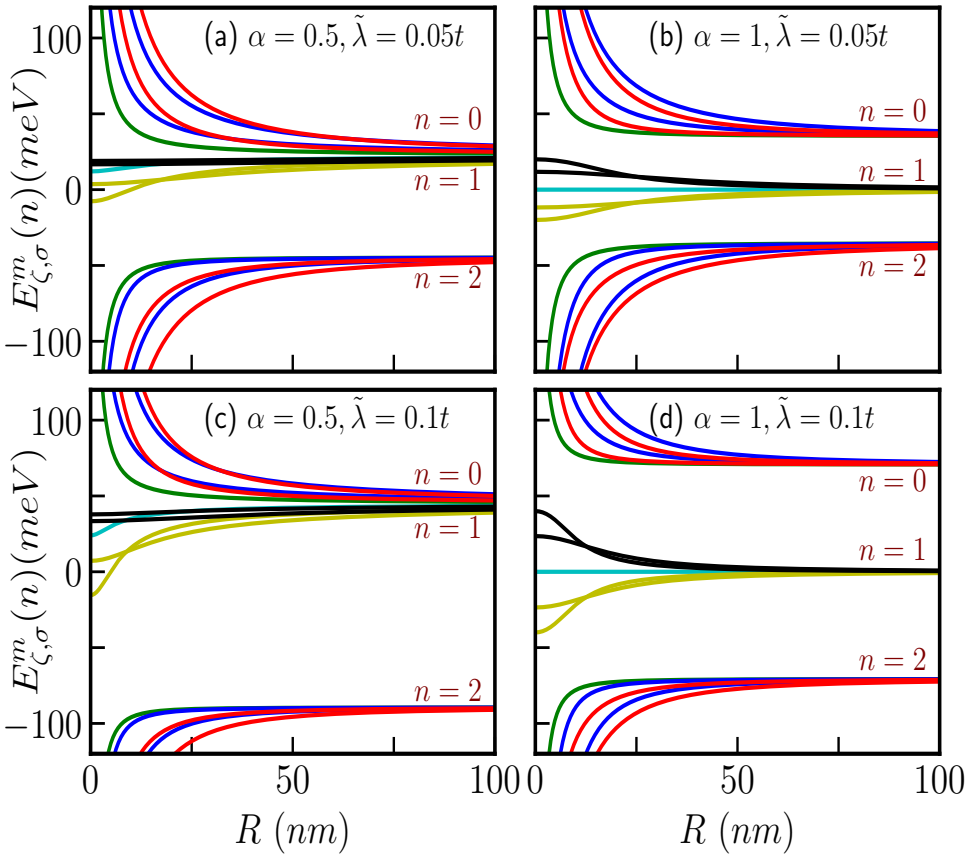

Figure 3.3: The energy dispersion in absence of magnetic field as a function of R at the K valley of the α-T_3 quantum ring corresponding to the α and ISOC values (a) $\alpha = 0.5$, $\tilde{\lambda} = 0.05t$, (b) $\alpha = 1$, $\tilde{\lambda} = 0.05t$, (c) $\alpha = 0.5$, $\tilde{\lambda} = 0.1t$, and (d) $\alpha = 1$, $\tilde{\lambda} = 0.1t$ and $t = 1eV$ are shown. The indices $n = 0, 1$, and 2 denote the CB, dFB, and VB respectively.

In Fig. 3.3, we present the energy bands at a particular valley (say, K valley) and for ↑-spin

only, by considering two different cases, namely, $\alpha = 0.5$ and $\alpha = 1$, corresponding to two values of the ISOC term, namely, $\tilde{\lambda} = 0.05t$ and $\tilde{\lambda} = 0.1t$. The purpose is to observe how the band structure changes with α and responds to the SOC parameter $\tilde{\lambda}$. Let us first discuss the $\alpha = 0$ (graphene) case [28]. In this scenario, there is no $n = 1$ band (distorted flat band) for all values of m (as (distorted) flat band comes for $\alpha \neq 0$ only), while all the branches of CB ($n = 0$) and the VB ($n = 2$) display a 1/R dependence in the small radius limit, whereas, the energies marge at some values, namely, $E_{\zeta,\sigma} \to \pm\tilde{\lambda}$ for large radii (see Fig. 3.4(a)). Notably, the criterion for large R differs for different values of m. Additionally, the branches are two-fold degenerate with $m = (0, 1), (2, -1), (3, -2)$ and so on. It is worth mentioning that all the energy levels are non-degenerate for all values of α, except for $\alpha = 0$. Further, at the K valley, as we increase α, the distortion increases in the limit of small radius. However, in the large R limit, some interesting features emerge as stated in the following. In the range $0 < \alpha \leq 0.5$, the dFB ($n = 1$) shifts away from the band center towards the CB ($n = 0$), and this shift increases with α. The $n = 1$ bands merge to a value $\alpha\tilde{\lambda}$ and the $n = 0$ band merge to $(1 - \alpha)\tilde{\lambda}$ at the large R limit. On the other hand, for α to be in the range $0.5 < \alpha \leq 1$, the shift decreases with increasing α. Again, the $n = 1$ bands merge to a value $(1 - \alpha)\tilde{\lambda}\cos\varphi$ and the $n = 0$ band merge at $\alpha\tilde{\lambda}\cos\varphi$ in the large R limit. While the energy levels corresponding to $n = 2$ merge at $-\tilde{\lambda}\cos\varphi$ in the limit of large R, irrespective the value of α. We summarize the results in Table 3.1. More details are shown Fig. 3.4 where we depict the results for varies values of α. However, at the K$'$ valley, the dFBs shift towards the VB ($n = 2$) and the bands corresponding to $n = 0$ merge to a value $\tilde{\lambda}\cos\varphi$ at the large R limit (see solid curves in Fig. 3.2(b)).

	$0 < \alpha \leq 0.5$	$0.5 < \alpha \leq 1$
Bands	Marging energy	Marging energy
$n = 0$	$\alpha\tilde{\lambda}$	$\alpha\tilde{\lambda}\cos\varphi$
$n = 1$	$(1 - \alpha)\tilde{\lambda}$	$(1 - \alpha)\tilde{\lambda}\cos\varphi$
$n = 2$	$-\tilde{\lambda}\cos\varphi$	$-\tilde{\lambda}\cos\varphi$

Table 3.1: Summary of different marging energy values for distinct bands at large radii in absence of magnetic field.

In Figs. 3.3(a), (c) we show the results for $\alpha = 0.5$ with $\tilde{\lambda} = 0.05t$ and $\tilde{\lambda} = 0.1t$, respectively. Inside the dFB ($n = 1$), the degree of distortion increases with increasing $\tilde{\lambda}$ and the bands characterized by $m = 0$ (cyan curves) and $m = 1, 2, ..$ (yellow curves) exhibit large distortion. In contrast, the energy bands with $m = -1, -2, ..$(black curves) remain nearly dispersionless. In addition, we find the following interesting results for the dice lattice $\alpha = 1$ (see Figs. 3.3(b),

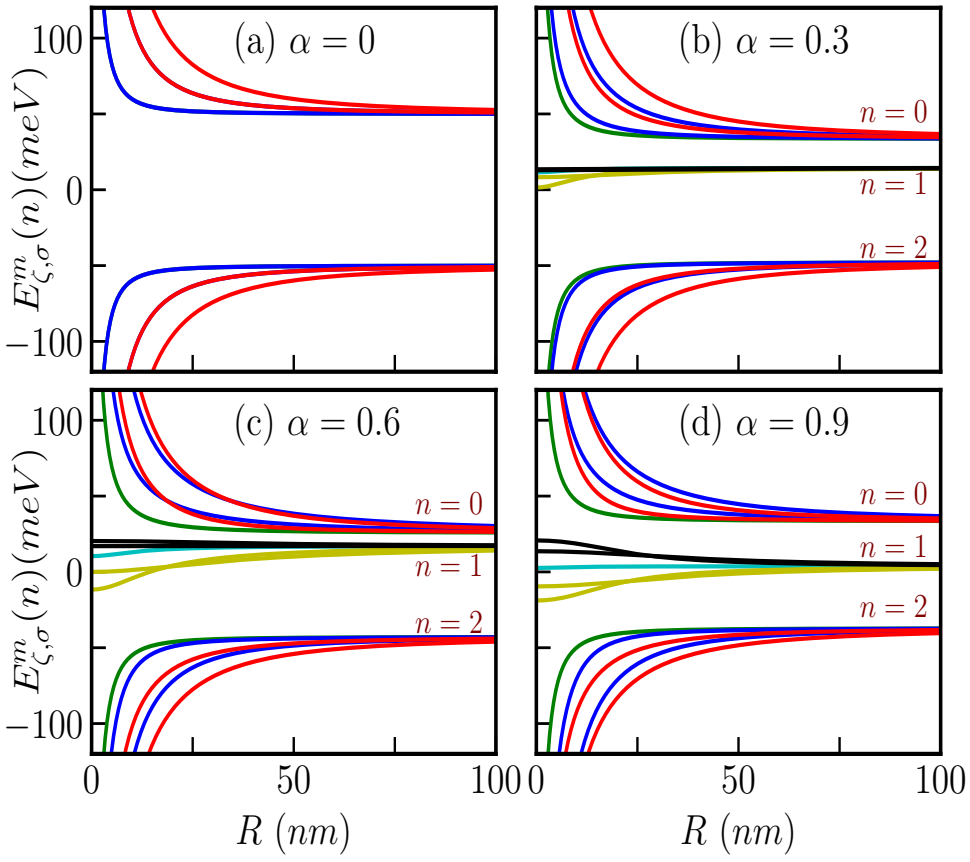

Figure 3.4: Evolution of the spin-↑ and K valley energy dispersion as a function of R of the α-T_3 QR for different values of α. The parameters are taken as $\tilde{\lambda} = 0.05t$ and $t = 1eV$. Panels (a), (b), (c), and (d) denote $\alpha = 0, 0.3, 0.6$, and 0.9 respectively.

(d)). In the limit of small radii, all the branches of VB and CB vary as 1/R. Further, the branches are non-degenerate. Inside the $n = 1$ dFB, we find the level with $m = 0$ remains flat at $E = 0$. From Eq. (3.6), it may be noted that the other levels satisfy, $E^m_{\zeta,\sigma}(1) = -E^{-m}_{\zeta,\sigma}(1)$. Further, we have $E^m_{\zeta,\sigma}(0) = -E^{-m}_{\zeta,\sigma}(2)$ which are in direct contrast to the results for the bare case ($\tilde{\lambda} = 0$). Here, only the ↑-spin and the K valley band structures are plotted, moreover, others for the ↓-spin and the K′ valley are essentially the same.

3.2.2 In presence of magnetic field ($B_0 \neq 0$)

Persistent equilibrium currents provide valuable information about the energy spectrum of a system near the Fermi energy. Although such currents are typically small and are detected through the magnetic moment they generate [293], some recent experiments have shown promising results by employing dense arrays of rings on a cantilever, which enhances the magnetic signal

and allows for both current measurements and the use of the setup as a sensitive magnetometer. The Corbino disk geometry, which can be fabricated with high precision using innovative techniques [294] involving nanoparticle manipulation and hydrogenation of open bonds, is particularly suitable for studying persistent currents. We study that in a later chapter.

To study the persistent currents and the effects of the magnetic field on the energy spectra, we include a magnetic flux threading the ring in the transverse direction, ($\mathbf{B} = B_0\hat{z}$, where B_0 is a constant). This is incorporated in the Hamiltonian in Eq. (3.5), which assumes a form,

$$H^{\Phi}(\sigma) = \begin{pmatrix} -\zeta\sigma\tilde{\lambda}\cos\varphi & -i\frac{\hbar v_F}{R}\left(m-\frac{\zeta}{2}+\frac{\Phi}{\Phi_0}\right)\cos\varphi & 0 \\ i\frac{\hbar v_F}{R}\left(m-\frac{\zeta}{2}+\frac{\Phi}{\Phi_0}\right)\cos\varphi & \zeta\sigma\tilde{\lambda}\left(\cos\varphi-\sin\varphi\right) & -i\frac{\hbar v_F}{R}\left(m+\frac{\zeta}{2}+\frac{\Phi}{\Phi_0}\right)\sin\varphi \\ 0 & i\frac{\hbar v_F}{R}\left(m+\frac{\zeta}{2}+\frac{\Phi}{\Phi_0}\right)\sin\varphi & \zeta\sigma\tilde{\lambda}\sin\varphi \end{pmatrix} \tag{3.8}$$

where $\Phi = \pi R^2 B_0$ is the magnetic flux, and Φ_0 is the usual flux quantum. Owing to the magnetic field present, the modifications to the spectra can be written as,

$$E^{m,\Phi}_{\zeta,\sigma}(n) = 2\sqrt{-\frac{P_\Phi}{3}}\cos\left[\frac{1}{3}\cos^{-1}\left(\frac{3Q_\Phi}{2P_\Phi}\sqrt{-\frac{3}{P_\Phi}}\right)-\frac{2\pi n}{3}\right] \tag{3.9}$$

where n = 0, 1, and 2 described earlier. Here, the quantities P_Φ and Q_Φ are denoted by,

$$P_\Phi = \frac{\tilde{\lambda}^2}{2}\sin 2\varphi - \tilde{\lambda}^2 - \frac{\hbar^2 v_F^2}{R^2}\left[N_\Phi^2\sin^2\varphi + M_\Phi^2\cos^2\varphi\right]$$

and

$$Q_\Phi = \frac{\zeta\sigma\tilde{\lambda}}{2}\sin 2\varphi\left[\tilde{\lambda}^2(\cos\varphi-\sin\varphi) + \frac{\hbar^2 v_F^2}{R^2}\left(M_\Phi^2\cos\varphi - N_\Phi^2\sin\varphi\right)\right]$$

with $M_\Phi = (m+\frac{\Phi}{\Phi_0}-\frac{\zeta}{2})$, $N_\Phi = (m+\frac{\Phi}{\Phi_0}-\frac{\zeta}{2})$. Thus the quantities M_Φ and N_Φ include Φ, namely the flux.

The normalized spinor wavefunctions for the up and down spin are given by,

$$\Psi^{m\zeta\Phi}_{n,\sigma}(R,\theta) = N^{\zeta,\Phi}_{n,\sigma}\, e^{im\theta}\begin{pmatrix} -i\frac{\hbar v_F}{R}M_\Phi\left(E^{m,\Phi}_{\zeta,\sigma}-\zeta\sigma\tilde{\lambda}\sin\varphi\right)\cos\varphi\, e^{-i\zeta\theta} \\ \left(E^{m,\Phi}_{\zeta,\sigma}+\zeta\sigma\tilde{\lambda}\cos\varphi\right)\left(E^{m,\Phi}_{\zeta,\sigma}-\zeta\sigma\tilde{\lambda}\sin\varphi\right) \\ i\frac{\hbar v_F}{R}N_\Phi\left(E^{m,\Phi}_{\zeta,\sigma}+\zeta\sigma\tilde{\lambda}\cos\varphi\right)\sin\varphi\, e^{i\zeta\theta} \end{pmatrix}, \tag{3.10}$$

with,

$$N^{\zeta,\Phi}_{n,\sigma} = \frac{1}{\sqrt{\frac{\hbar^2 v_F^2}{R^2}\left[M_\Phi^2\left(E^{m,\Phi}_{\zeta,\sigma}-\zeta\sigma\tilde{\lambda}\sin\varphi\right)^2\cos^2\varphi + N_\Phi^2\left(E^{m,\Phi}_{\zeta,\sigma}+\zeta\sigma\tilde{\lambda}\cos\varphi\right)^2\sin^2\varphi\right] + \left(E^{m,\Phi}_{\zeta,\sigma}+\zeta\sigma\tilde{\lambda}\cos\varphi\right)^2\left(E^{m,\Phi}_{\zeta,\sigma}-\zeta\sigma\tilde{\lambda}\sin\varphi\right)^2}}.$$

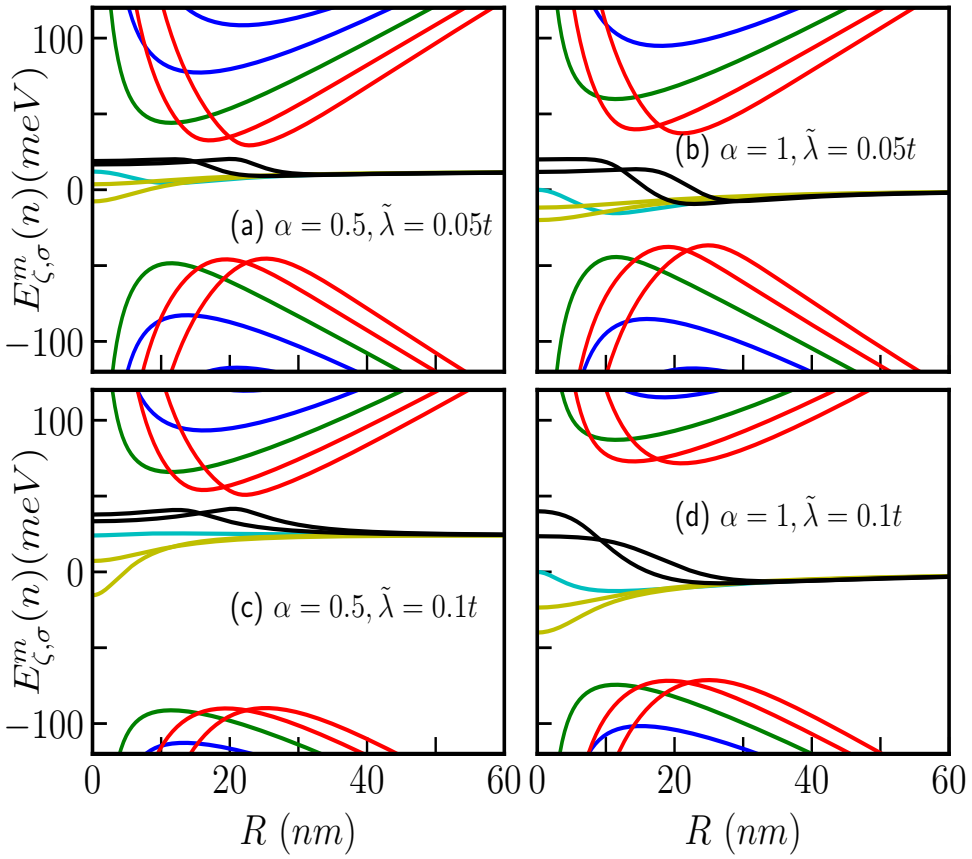

Figure 3.5: The energy spectra as a function of ring radius R of the α-T_3 quantum ring at K valley in presence of external magnetic field of $B_0 = 5$T for (a) $\alpha = 0.5$, $\tilde{\lambda} = 0.05t$, (b) $\alpha = 1$, $\tilde{\lambda} = 0.05t$, (c) $\alpha = 0.5$, $\tilde{\lambda} = 0.1t$, and (d) $\alpha = 1$, $\tilde{\lambda} = 0.1t$ and $t = 1eV$ taken. $n = 0, 1$, and 2 denote the CB, distorted FB, and VB respectively.

The qualitative features of the energy spectrum deviate significantly from the case corresponding to zero magnetic field. In contrast to the $B_0 = 0$ situation, we observe that all energy levels are non-degenerate for all values of α. Additionally, we find that $E^{m,\Phi}_{\zeta,\sigma}(1) \neq -E^{-m,\Phi}_{\zeta,\sigma}(1)$, $E^{m,\Phi}_{\zeta,\sigma}(0) \neq -E^{-m,\Phi}_{\zeta,\sigma}(2)$, where the number inside the parenthesis denotes $n = 0, 1, 2$. Furthermore, there is distortion of the $m = 0$ flat band energy level for $\alpha = 1$. In addition, the flat band energy levels merge with zero energy at large values of R. However, this is not the scenario for intermediate values of α. As $\alpha \neq 0$, the zero energy modes merge at some finite (positive) energy values depending upon the value of α in the large R limit. Again, each of the levels of the VB and CB exhibits a non-monotonic behaviour as a function of the radius R. The energy levels attain an extremum for a given value of the quantum number m (minimum for the conduction band and maximum for the valence band) at a particular value of R. However, positions of these extrema depend on the value of m. For a particular m, in the limit of small R, all the energy levels vary inversely as R. On the other hand, the energy scales as, $E \sim R$ in the limit of large R. More detailed results are provided in the Fig. 3.5.

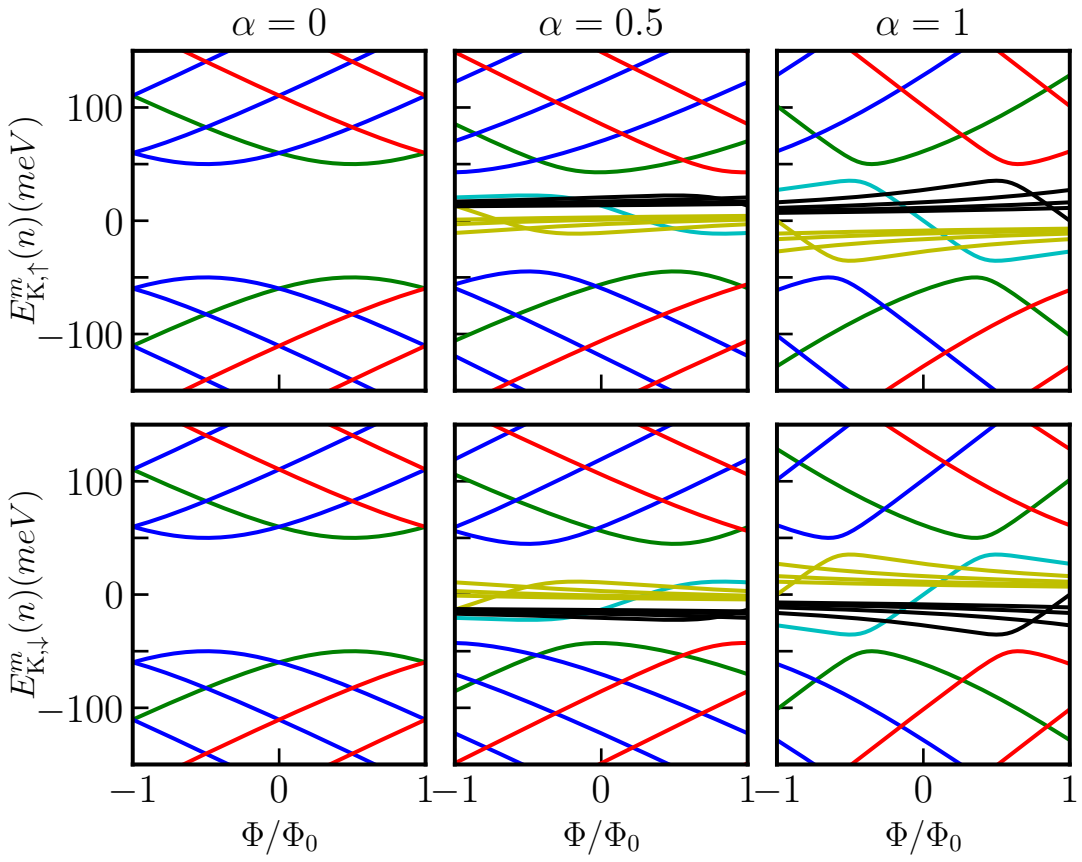

Figure 3.6: Energy $E^{m,\Phi}_{\mathrm{K},\sigma}(n)$ as a function of external magnetic flux Φ/Φ_0 at K valley for different values of α with $R = 10\ nm$. Plots in the upper panel are for $\uparrow$-spin and the lower panel are for $\downarrow$-spin bands. The parameters are taken as $\tilde{\lambda} = 0.05t$ and $t = 1eV$.

The energy levels as a function of the external magnetic flux are shown in Fig. 3.6 and Fig. 3.7 for a quantum ring with a particular radius and ISOC value, namely, $R = 10\ nm$ and $\tilde{\lambda} = 0.05t$. We consider two cases, for a particular valley (say, K valley) with both $\uparrow$- and $\downarrow$- spins, and for a particular spin (say $\uparrow$-spin) involving both the K and the K$'$ valleys. It can be observed that for $\alpha = 0$ at K valley, $E^{m,\Phi}_{\mathrm{K},\uparrow}(n) = E^{m,\Phi}_{\mathrm{K},\downarrow}(n)$ (see Fig. 3.6(a)), thus it will possess zero spin current (we shall discuss it later). From Fig. 3.6, it is observed that for non-zero α, we get, $E^{m,\Phi}_{\mathrm{K},\uparrow}(0) = -E^{m,\Phi}_{\mathrm{K},\downarrow}(2)$, $E^{m,\Phi}_{\mathrm{K},\uparrow}(2) = -E^{m,\Phi}_{\mathrm{K},\downarrow}(0)$ and for the distorted flat band, we have $E^{m,\Phi}_{\mathrm{K},\uparrow}(1) = -E^{m,\Phi}_{\mathrm{K},\downarrow}(1)$. Moreover, for any intermediate α ($0 < \alpha < 1$), for the $\uparrow$-spin, the $n = 1$ bands are shifted towards $n = 0$ CBs, while the $\downarrow$-spin bands are shifted towards the $n = 2$ VBs, as discussed earlier. For the dice case ($\alpha = 1$), the $n = 1$ bands are equally spaced from both the CBs and VBs.

Moving on to Fig. 3.7, we observe following the interesting aspects. For any value of α such that $\alpha < 1$, $E^{m,\Phi}_{\zeta,\uparrow}(n) \neq E^{m,\Phi}_{-\zeta,\uparrow}(n)$ since the time reversal symmetry (TRS) is broken by the external magnetic field. However, for the dice lattice we can see $E^{m,\Phi}_{\zeta,\uparrow}(n) = E^{m,\Phi}_{-\zeta,\uparrow}(n)$ for all

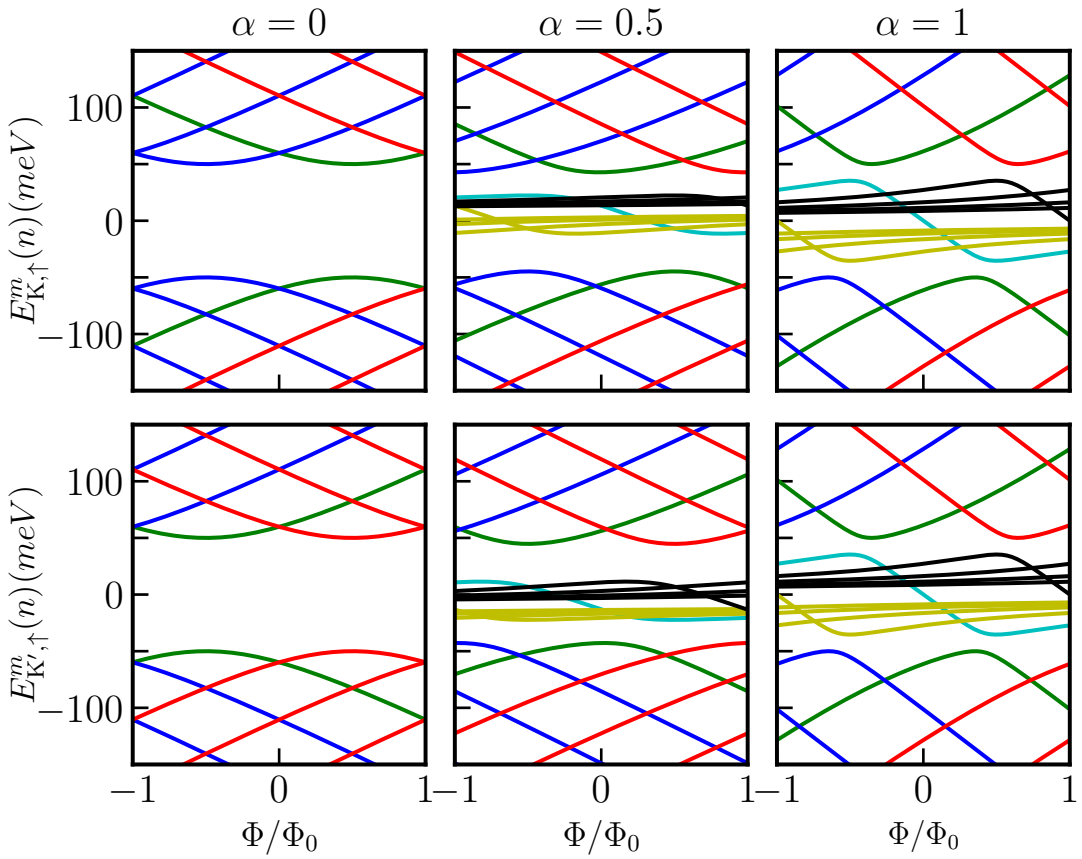

Figure 3.7: Energy $E^{m,\Phi}_{\zeta,\uparrow}(n)$ as a function of external magnetic flux Φ/Φ_0 for $\uparrow$-spin bands for different values of α with $R = 10\ nm$. Plots in the upper panel are for K valley and the lower panel are for K$'$ valley. The parameters are taken as $\tilde{\lambda} = 0.05t$ and $t = 1eV$.

the bands, thus it leads to zero valley current (we shall discuss later). Also, for any intermediate α ($0 < \alpha < 1$) the $\uparrow$-spin bands of the $n = 1$ bands are shifted towards $n = 0$ bands (CBs), while the $\downarrow$-spin bands are shifted towards the $n = 2$ bands (VBs) in the K$'$ valley as discussed earlier. Again for the dice case ($\alpha = 1$), the $n = 1$ bands are equally spaced with respect to the CBs and VBs for both the valleys.

3.2.3 Persistent currents

Charge persistent current

Let us delve into the topic of persistent currents. The persistent current is the equilibrium current that flows along the angular (θ) direction in a QR when threaded by a magnetic flux. This current can be calculated using the relation, $j_{x(y)} = \hbar v_F[\Psi^\dagger S_{x(y)}\Psi]$ (we set $\hbar = 1$ for the rest of the chapter), where $S_{x,y}$ denote the x and y components of the pseudospin operator. Using this

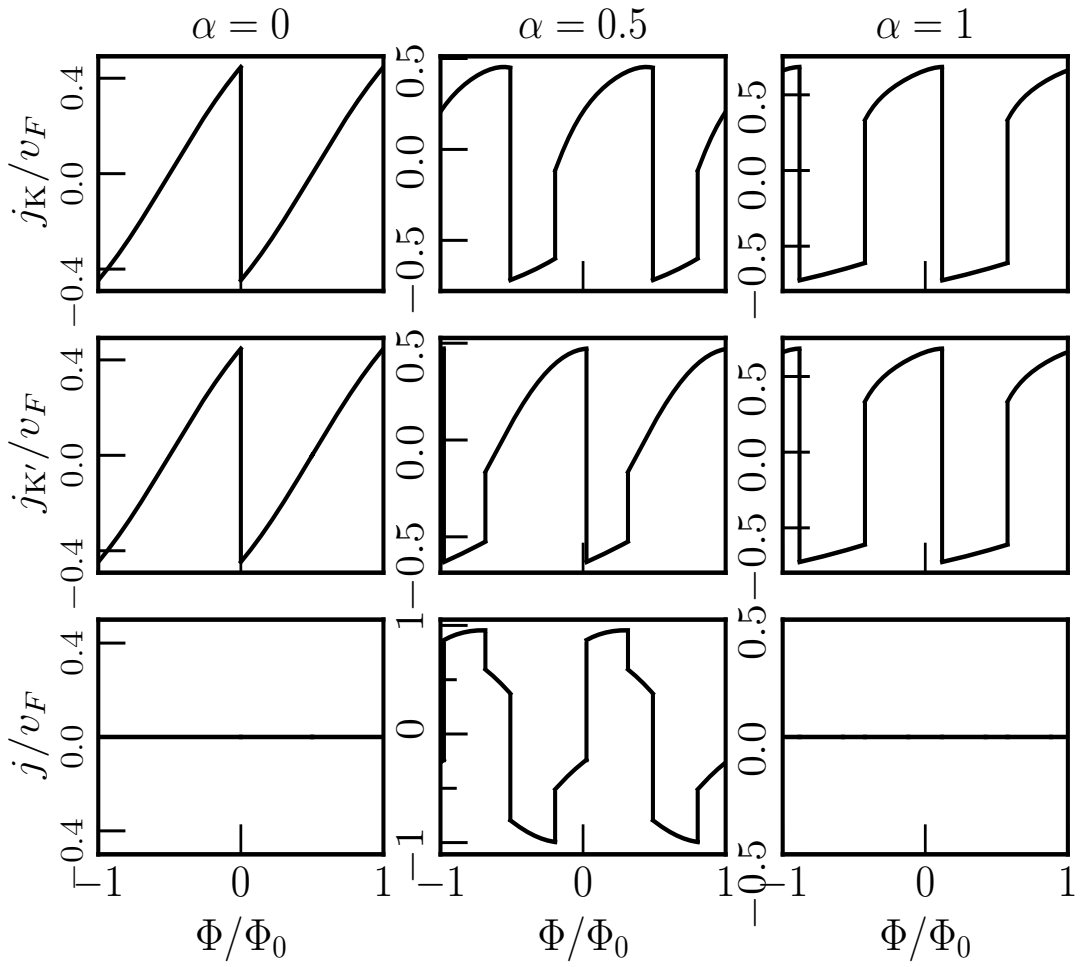

Figure 3.8: The charge persistent currents as a function of external magnetic flux Φ/Φ_0 for $\uparrow$-spin bands are shown. Upper row is for the K valley, middle row is for the K$'$ valley, and the lower row shows the valley current. Here we have considered $\tilde{\lambda} = 0.05t$, $t = 1eV$, and $R = 10$ nm. We have shown results for three different α values, namely, $\alpha = 0, 0.5$ and 1.

definition, the radial and the angular currents are further obtained as $j_r = v_F[\Psi^\dagger S_r \Psi]$ and $j_\theta = v_F[\Psi^\dagger S_\theta \Psi]$, respectively. Here, S_r and S_θ are given by $S_r = S_x \cos\theta + S_y \sin\theta$ and $S_\theta = -S_x \sin\theta + S_y \cos\theta$, respectively. Along a particular direction ($r = R$) of the α-T_3 ring, although the radial current vanishes (as proved in the previous chapter), we can calculate the angular current at a particular valley as well as for a particular spin. The analytical expression for the charge persistent current is derived as follows,

$$\begin{aligned} j_n^\zeta =& 2v_F \frac{\hbar v_F}{R} \big(N_{n,\sigma}^{\zeta,\Phi}\big)^2 \big(E_{\zeta,\sigma}^{m,\Phi}(n) + \zeta\sigma\tilde{\lambda}\cos\varphi\big)\big(E_{\zeta,\sigma}^{m,\Phi}(n) - \zeta\sigma\tilde{\lambda}\sin\varphi\big)\times \\ & \Big[M_\Phi\big(E_{\zeta,\sigma}^{m,\Phi}(n) - \zeta\sigma\tilde{\lambda}\sin\varphi\big)\cos^2\varphi + N_\Phi\big(E_{\zeta,\sigma}^{m,\Phi}(n) + \zeta\sigma\tilde{\lambda}\cos\varphi\big)\sin^2\varphi\Big]. \end{aligned} \tag{3.11}$$

The net persistent current at a particular valley is calculated by considering the contributions from the valence band ($n = 2$) and the distorted flat band ($n = 1$) via, $j_\zeta = j^\zeta_{n=2} + j^\zeta_{n=1}$. It is worthy to mention that the distortion of the energy levels in the flat band gives rise to a finite persistent current. From Fig. 3.7 it is observed that the low-energy state comprises of different m values for a range of the scaled flux, Φ/Φ_0. Using this low-energy state from Fig. 3.7, we illustrate the variation of the persistent currents as a function of Φ/Φ_0 with $\tilde{\lambda} = 0.05t$ and $R = 10\ nm$ in Fig. 3.8. The inclusion of the spin-orbit coupling term alters the oscillation pattern of the persistent current compared to bare ($\tilde{\lambda} = 0$) case. In the upper panel of Fig. 3.8 we display the persistent current due to the $\uparrow$-spin at the K valley, while in the middle panel, we show the same at the K$'$ valley. The currents at different valleys are no longer equal, except for the cases $\alpha = 0$ and $\alpha = 1$. Moreover, the persistent current at a specific valley oscillates periodically with Φ/Φ_0, with the periodicity $\Phi/\Phi_0 = 1$. Though the oscillation pattern varies with the parameter α, the oscillation period remains independent of α. Additionally, we observe a finite persistent current at a specific valley when $\Phi = 0$ (no magnetic field) for all values of α.

We further introduce a quantity called the valley current as,

$$j = j_Q(\zeta = 1) - j_Q(\zeta = -1) \tag{3.12}$$

where ζ denotes the valley index. In this context, we find that the persistent current corresponding to the two extreme cases ($\alpha = 0$ and $\alpha = 1$) are equal, resulting in zero valley current for graphene and the dice lattice. However, for an intermediate value of α (say, $\alpha = 0.5$), we observe an oscillatory valley current with the oscillation period of $\Phi/\Phi_0 = 1$. Furthermore, the oscillation pattern of the valley current depends on the parameter α.

Equilibrium spin current

Now, we turn our attention to calculation of the equilibrium spin currents. We define the equilibrium spin current as,

$$j_S = j^\zeta_n(\sigma = 1) - j^\zeta_n(\sigma = -1) \tag{3.13}$$

where $\sigma = \pm 1$ denotes $\uparrow$- and $\downarrow$-spins. As mentioned earlier, for non-zero α, the spin resolved energy levels are not the same within a range of flux in unit of Φ/Φ_0, thus potentially leading to passage of spin currents. To investigate this, we first calculate the persistent current for both the $\uparrow$-spin and $\downarrow$-spin bands at a particular valley, using the same procedure as mentioned above. In the upper panel of Fig. 3.9, we show the persistent current for $\uparrow$-spin, while in the middle panel, we show the same for $\downarrow$-spin at the K valley. We observe that both the $\uparrow$-spin and $\downarrow$-spin

persistent currents oscillate with Φ/Φ_0 with a periodicity of $\Phi/\Phi_0 = 1$ for all values of α. Thus, this result is distinct from the valley current. Additionally, the currents corresponding to different spins are no longer equal, except when $\alpha = 0$. The latter yields a zero spin current (j_S) for $\alpha = 0$. Further, for non-zero α, we observe oscillatory equilibrium spin currents with the oscillation period of $\Phi/\Phi_0 = 1$. However, the oscillation pattern of the equilibrium spin currents are affected by the value of α, as shown in the lower panel of Fig. 3.9.

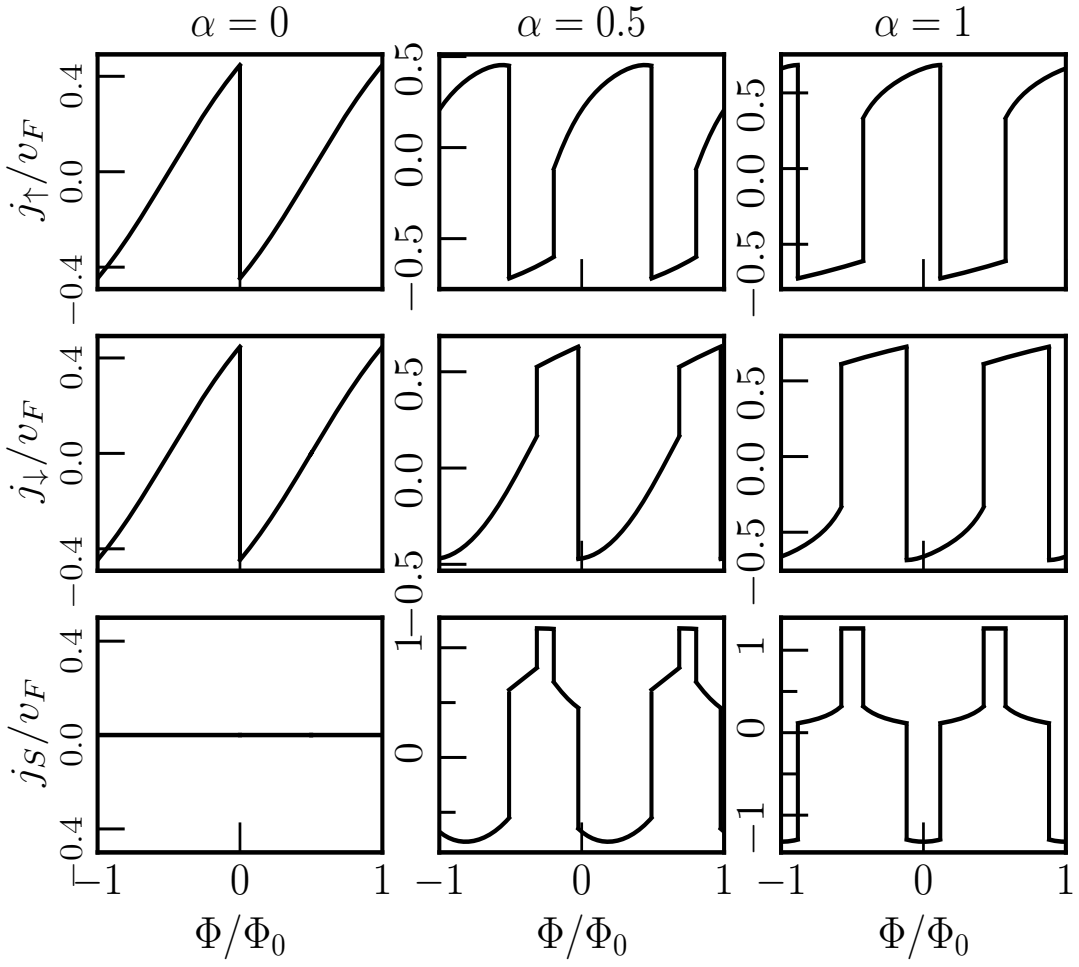

Figure 3.9: The persistent currents as a function of Φ/Φ_0 are shown. Plots in the upper row are for the $\uparrow$-spin, middle row for the $\downarrow$-spin of K valley, and the bottom row contain the equilibrium spin currents (calculated using Eq. (3.13)) at the same valley. Here we have considered $\tilde{\lambda} = 0.05t$, $t = 1eV$, and $R = 10\ nm$. We have shown for three different α values, namely, $\alpha = 0, 0.5$ and 1.

3.3 Pseudospin-1 α-T_3 QR with RSOC

Here we consider the system to have Rashba SOC. The corresponding Hamiltonian can be written as, $H = H_0 + H_R$, where H_0 is the tight-binding term, and H_R is the Rashba spin-orbit

coupling term. We write the Hamiltonian as,

$$H = -\sum_{\langle ij\rangle\sigma} t c^{\dagger}_{i\sigma} c_{j\sigma} - \sum_{\langle ik\rangle\sigma} \alpha t c^{\dagger}_{i\sigma} c_{k\sigma} - \sum_{\langle ij\rangle\sigma\sigma'} i\lambda_R c^{\dagger}_{i\sigma} (\hat{D}_{ij}\cdot\vec{\sigma})_{\sigma\sigma'} c_{j\sigma'} - \sum_{\langle ik\rangle\sigma\sigma'} i\alpha\lambda_R c^{\dagger}_{i\sigma} (\hat{D}_{ik}\cdot\vec{\sigma})_{\sigma\sigma'} c_{k\sigma'} + \Big(h.c.\Big) \tag{3.14}$$

where the first and second terms and the notations have described earlier in Sec. 3.2. Further, the Rashba SOC induced by electric fields due to a gradient of the crystal potential [157, 288, 289]. Where $\vec{\sigma} = (\sigma_x, \sigma_y, \sigma_z)$ is the Pauli matrix vector, $\hat{D}_{ij}$ ($\hat{D}_{ik}$) is the unit vector along the direction of the cross product $\vec{E}_{ij} \times \vec{r}_{ij}$ ($\vec{E}_{ik} \times \vec{r}_{ik}$) of the electric field $\vec{E}_{ij}$ ($\vec{E}_{ik}$) and displacement $\vec{r}_{ij}$ ($\vec{r}_{ik}$) for the bond ij (ik). λ_R is the strength of Rashba SOC between the A and the B sites while $\alpha\lambda_R$ is that between the B and the C sites. Here we ignore the complex NNN hopping (ISOC = 0). In momentum space, the Hamiltonian of the α-T_3 lattice becomes,

$$H = \begin{pmatrix} 0 & -t\gamma^{*}_{\mathrm{k}} & 0 & 0 & -i\lambda_R\gamma^{*}_{\mathrm{k}+} & 0 \\ -t\gamma_{\mathrm{k}} & 0 & -\alpha t\gamma^{*}_{\mathrm{k}} & i\lambda_R\gamma_{\mathrm{k}-} & 0 & i\alpha\lambda_R\gamma^{*}_{\mathrm{k}+} \\ 0 & -\alpha t\gamma_{\mathrm{k}} & 0 & 0 & -i\alpha\lambda_R\gamma_{\mathrm{k}-} & 0 \\ 0 & -i\lambda_R\gamma^{*}_{\mathrm{k}-} & 0 & 0 & -t\gamma^{*}_{\mathrm{k}} & 0 \\ i\lambda_R\gamma_{\mathrm{k}+} & 0 & i\alpha\lambda_R\gamma^{*}_{\mathrm{k}-} & -t\gamma_{\mathrm{k}} & 0 & -\alpha t\gamma^{*}_{\mathrm{k}} \\ 0 & -i\alpha\lambda_R\gamma_{\mathrm{k}+} & 0 & 0 & -\alpha t\gamma_{\mathrm{k}} & 0 \end{pmatrix} \tag{3.15}$$

where we have defined $\gamma_{\mathrm{k}} = 1 + e^{ik_1} + e^{ik_2}$ and $\gamma_{\mathrm{k}\pm} = 1 + e^{i(k_1 \pm 2\pi/3)} + e^{i(k_2 \pm 4\pi/3)}$. Further, the components are along the axes indicated in Fig. 3.1(b) as $k_i = \vec{k}.\hat{\mathrm{e}}_i$. The annihilation operator basis is $(c_{1\mathrm{k}\uparrow}, c_{2\mathrm{k}\uparrow}, c_{3\mathrm{k}\uparrow}, c_{1\mathrm{k}\downarrow}, c_{2\mathrm{k}\downarrow}, c_{3\mathrm{k}\downarrow})$. In the vicinity of a Dirac point (namely, K), the Hamiltonian corresponding to an ideal α-T_3 ring is given by,

$$H = \frac{\hbar v_F}{R} \begin{pmatrix} 0 & -i(m+\frac{1}{2})\cos\varphi e^{\frac{i\pi}{3}} & 0 & 0 & -\frac{\lambda_R}{t}(m+\frac{1}{2})\cos\varphi e^{\frac{i\pi}{3}} & 0 \\ i(m+\frac{1}{2})\cos\varphi e^{-\frac{i\pi}{3}} & 0 & -i(m-\frac{1}{2})\sin\varphi e^{\frac{i\pi}{3}} & \frac{\lambda_R}{t}(m-\frac{1}{2})\cos\varphi e^{\frac{i\pi}{3}} & 0 & -\frac{\lambda_R}{t}(m+\frac{1}{2})\sin\varphi e^{-\frac{i\pi}{3}} \\ 0 & i(m-\frac{1}{2})\sin\varphi e^{-\frac{i\pi}{3}} & 0 & 0 & -\frac{\lambda_R}{t}(m-\frac{1}{2})\sin\varphi e^{-\frac{i\pi}{3}} & 0 \\ 0 & \frac{\lambda_R}{t}(m-\frac{1}{2})\cos\varphi e^{-\frac{i\pi}{3}} & 0 & 0 & i(m-\frac{1}{2})\cos\varphi e^{-\frac{i\pi}{3}} & 0 \\ -\frac{\lambda_R}{t}(m+\frac{1}{2})\cos\varphi e^{-\frac{i\pi}{3}} & 0 & \frac{\lambda_R}{t}(m-\frac{1}{2})\sin\varphi e^{\frac{i\pi}{3}} & -i(m-\frac{1}{2})\cos\varphi e^{\frac{i\pi}{3}} & 0 & i(m+\frac{1}{2})\sin\varphi e^{-\frac{i\pi}{3}} \\ 0 & -\frac{\lambda_R}{t}(m+\frac{1}{2})\sin\varphi e^{\frac{i\pi}{3}} & 0 & 0 & -i(m+\frac{1}{2})\sin\varphi e^{\frac{i\pi}{3}} & 0 \end{pmatrix} \tag{3.16}$$

where $\tan\varphi = \alpha$ and $\hbar v_F = \frac{3at}{2}\cos\varphi$. The eigenstates of the ring Hamiltonian can be obtained as,

$$\psi(R,\theta) = \begin{pmatrix} \chi_{1\uparrow}(R)e^{i(m+1)\theta} \\ \chi_{2\uparrow}(R)e^{im\theta} \\ \chi_{3\uparrow}(R)e^{i(m-1)\theta} \\ \chi_{1\downarrow}(R)e^{i(m-1)\theta} \\ \chi_{2\downarrow}(R)e^{im\theta} \\ \chi_{3\downarrow}(R)e^{i(m+1)\theta} \end{pmatrix} \tag{3.17}$$

where the integer m labels the orbital angular momentum quantum number and χ_i's denote the amplitudes corresponding to the three sublattices. Here, we investigate the behaviour at a given value of radius r, namely $r = R$, such that the radial dependence is frozen in the eigensolutions. Finally, we obtain the energy spectrum as,

$$\begin{aligned} E_1 &= 0 \\ E_2 &= \kappa\frac{\epsilon}{2}\sqrt{(1+4m^2-4m\frac{1-\alpha^2}{1+\alpha^2})(1+\frac{\lambda_R^2}{t^2})} \\ E_3 &= \kappa\frac{\epsilon}{2}\sqrt{(1+4m^2)(1+\frac{\lambda_R^2}{t^2}\frac{1-\alpha^2}{1+\alpha^2})+4m(\frac{\lambda_R^2}{t^2}+\frac{1-\alpha^2}{1+\alpha^2})} \end{aligned} \tag{3.18}$$

where $\kappa = \pm 1$ is the particle-hole index and $\epsilon = \frac{\hbar v_F}{R}$. E_1 is the zero energy flat band, E_2 is the $\uparrow$-spin energy band and E_3 is the $\downarrow$-spin band respectively.

3.3.1 Without magnetic field ($B_0 = 0$)

The energy spectra at the K valley in presence of Rashba SOC are expressed in Eq. (3.18). Fig. 3.10 displays the energies as a function of the ring radius, R, for various values of α and λ_R. One can easily verify the results of the α-T_3 quantum ring without the RSOC term by setting $\lambda_R = 0$ in Eq. (3.18). Here, we have considered two scenarios, namely, $\lambda_R = 0.5t$ and $\lambda_R = 0.8t$ corresponding to $\alpha = 0.5$ and 1 (since our results align with the existing findings for graphene ($\alpha = 0$), we intentionally exclude the $\alpha = 0$ cases from subsequent discussions). We have plotted only the $m = -1$, 0, and 1 bands represented by red, green, and blue curves, respectively. When $\lambda_R = 0$, the system exhibits three bands, with one being totally flat band. However, with a non-zero λ_R the original three bands split into six spin-split bands, including two non-dispersive flat bands and four dispersive bands as described by Eq. (3.18). From Fig. 3.10, it is evident that all the energy branches have a $1/R$ dependence and approach $E \to 0$ for very large values of the radii, irrespective of the value of α. Additionally, the dispersive bands remain non-degenerate, in contrast to the case of the pseudospin-1 α-T_3 QR without SOC. Moreover, the dispersive $\uparrow$-spin and $\downarrow$-spin bands split as well. Specifically, for $m = 0$, the energies are given by,

$$E_2 = \frac{\kappa\epsilon}{2}\sqrt{1+\frac{\lambda_R^2}{t^2}} \quad \text{and} \quad E_3 = \frac{\kappa\epsilon}{2}\sqrt{1+\frac{\lambda_R^2}{t^2}\frac{1-\alpha^2}{1+\alpha^2}}. \tag{3.19}$$

It can be observed that the $\uparrow$-spin energy band, E_2 is independent of α, while the $\downarrow$-spin band, E_3 has a dependency on α. Consequently, the splitting between the $m = 0$ bands (green curves

in Fig. 3.10) increases with increasing values of α. Whereas, the splitting between the bands with $m = -1$ (red curves in Fig. 3.10) and $m = 1$ (blue curves in Fig. 3.10) decreases as α increases. Furthermore, the energy splitting decreases with the increase of $|m|$ values for all values of α. In addition to that, the energy splitting increases with λ_R increasing. An intriguing observation is that for $\alpha = 1$, that is, the dice lattice, the energies are obtain as,

$$E_2 = \frac{\kappa\epsilon}{2}\sqrt{(1+4m^2)(1+\frac{\lambda_R^2}{t^2})} \quad \text{and} \quad E_3 = \frac{\kappa\epsilon}{2}\sqrt{1+4m^2+4m\frac{\lambda_R^2}{t^2}}. \tag{3.20}$$

Thus, E_2 is a even function of m, making it two-fold degenerate with $m = \pm1, \pm2, \pm3, ...$ etc. On the other hand, the E_3 band is an odd function of m, resulting in it being non-degenerate as illustrated in Figs. 3.10(b) and 3.10(d).

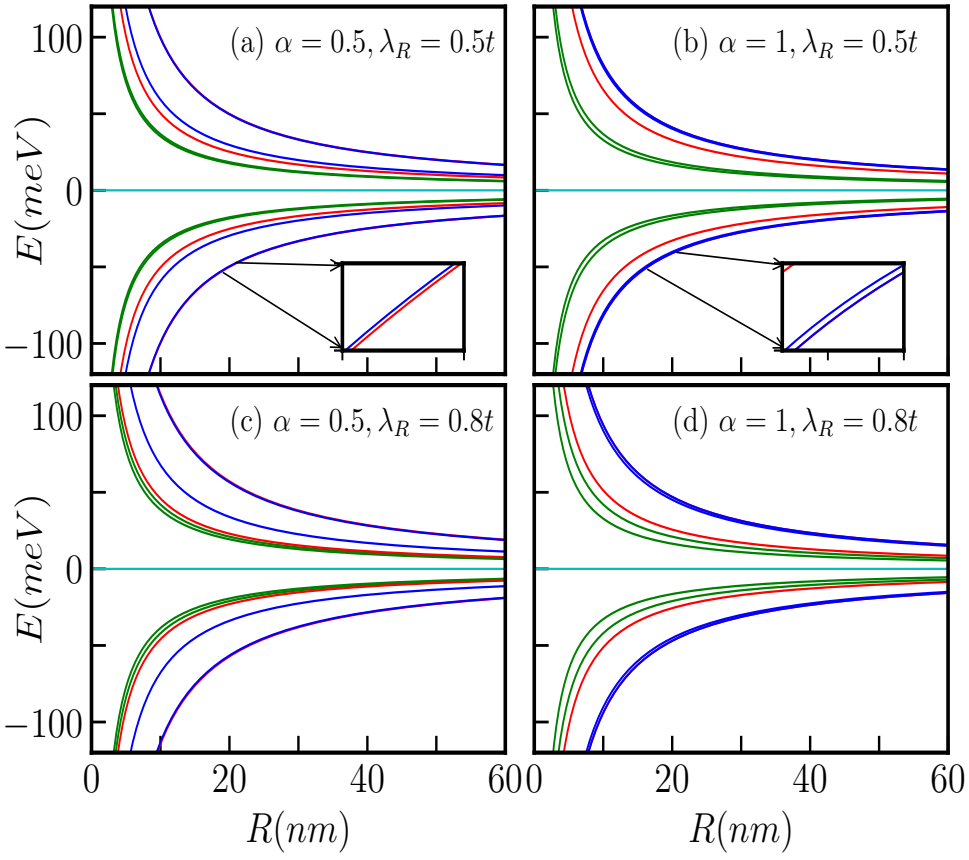

Figure 3.10: The energy levels in the absence of an external field with $m = -1$ (red curves), 0 (green curves), and 1 (blue curves) of the α-T_3 quantum ring as a function of ring radius R in presence of only RSOC are shown. (a) for $\alpha = 0.5$, $\lambda_R = 0.5t$, (b) for $\alpha = 1$, $\lambda_R = 0.5t$, (c) for $\alpha = 0.5$, $\lambda_R = 0.8t$, and (d) for $\alpha = 1$, $\lambda_R = 0.8t$. We have taken $t = 1eV$. In the insets, we show the zoomed version for the same

3.3.2 In presence of magnetic field ($B_0 \neq 0$)

Now let us discuss the case when the pseudospin-1 α-T_3 ring is threaded by a perpendicular magnetic field $\mathbf{B} = B_0\hat{z}$. The spectrum of the system is modified by the field flux as follows,

$$\begin{aligned} E_1(\Phi) &= 0 \\ E_2(\Phi) &= \kappa\frac{\epsilon}{2}\left\{\left[1+4(m+\beta)^2-4(m+\beta)\frac{1-\alpha^2}{1+\alpha^2}\right]\left(1+\frac{\lambda_R^2}{t^2}\right)\right\}^{\frac{1}{2}} \\ E_3(\Phi) &= \kappa\frac{\epsilon}{2}\left\{\left[1+4(m+\beta)^2\right]\left(1+\frac{\lambda_R^2}{t^2}\frac{1-\alpha^2}{1+\alpha^2}\right)+4(m+\beta)\left(\frac{\lambda_R^2}{t^2}+\frac{1-\alpha^2}{1+\alpha^2}\right)\right\}^{\frac{1}{2}} \end{aligned} \tag{3.21}$$

where $\beta = \Phi/\Phi_0$ with $\Phi = \pi R^2 B_0$ is magnetic flux through the ring and Φ_0 is the usual flux quantum. The Zeeman coupling has been neglected at small enough values of the field. The addition of a magnetic field, represented by a U(1) minimal coupling with flux Φ threading the ring, breaks the time reversal symmetry allowing for the emergence of persistent charge currents [6] which we shall discuss later.

In Fig. 3.11, we show the dependence of a few energy levels on the ring radius, R, considering $B_0 = 5$T for the two aforementioned cases i.e., $\lambda_R = 0.5t$ with $\alpha = 0.5, 1$, and $\lambda_R = 0.8t$ with $\alpha = 0.5, 1$. Each level exhibits a non-monotonic behaviour as a function of the radius R. The energy levels attain an extremum (minimum for conduction band and maximum for valence band) at a particular value of R. However, the positions of these extrema depend on the values of m, α and λ_R explicitly. In the limit of small R, all the energy levels vary inversely with R. On the other hand, the energy scales as, $E \sim |R|$ that is in limit of large R. Additionally, for a fixed magnetic field and for large m, the extrema points depend on R as $R \propto \sqrt{|m|}$ irrespective of α. Thus, the concept of large radii differs for different values of m. Consequently, for negative values of m, the extrema points of the energy exhibit a scaling behaviour, namely, $E_{min} \propto 1/\sqrt{|m|}$, resulting in a diminishing of the spectral gap with increasing $|m|$. Conversely, for positive values of m, the energy extrema scales as, $E_{min} \propto \sqrt{m}$. Furthermore, from Eq. (3.21), it is evident that in presence of a magnetic field, the energy splitting between the bands of the $m = 0$ level as well as the $m \neq 0$ levels decreases with the increase in the values of the parameters α and λ_R. Again, from Eq. (3.21) it is noted that for $\alpha < 1$, there are two points where the spin bands cross each other as a function of R for $m = 0$ and $m = -1, -2, -3, ...$ etc. bands, whereas there is only one band crossing point for $m = 1, 2, 3...$ values. These crossings

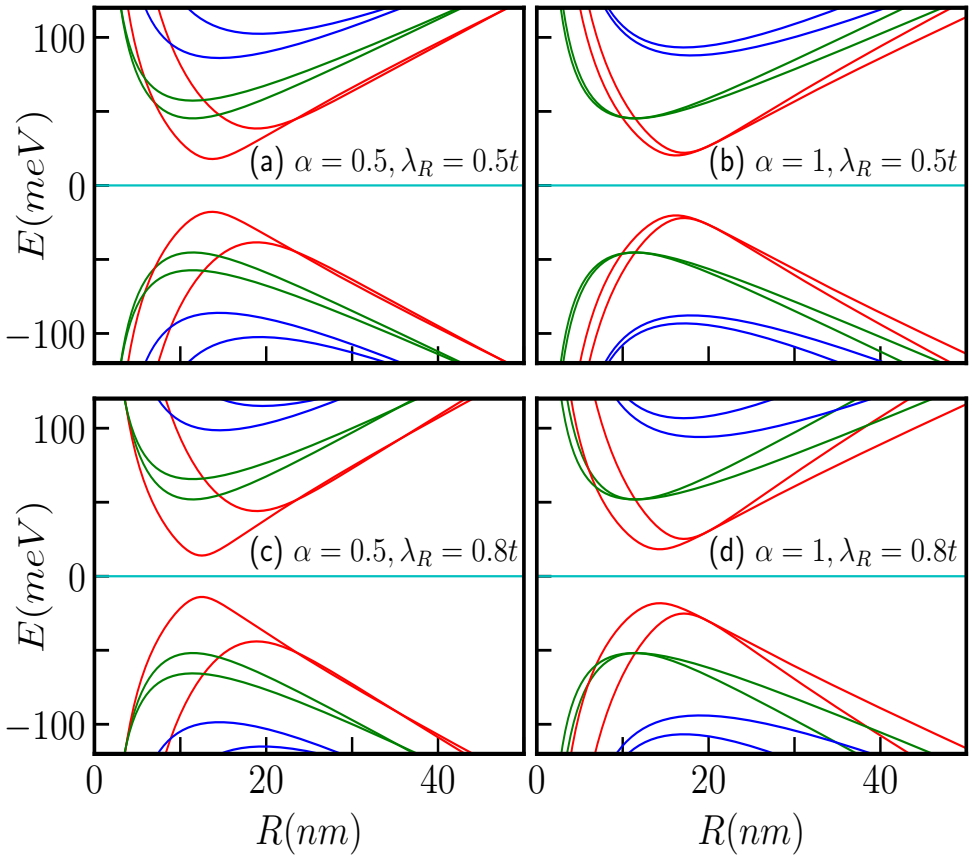

Figure 3.11: Energy levels with $m = -1$ (red curves), 0 (green curves), and 1 (blue curves) of the α-T_3 quantum ring as a function of ring radius R in presence of an external magnetic field of magnitude $B_0 = 5$T (a) for $\alpha = 0.5$, $\lambda_R = 0.5t$, (b) for $\alpha = 1$, $\lambda_R = 0.5t$, (c) for $\alpha = 0.5$, $\lambda_R = 0.8t$, and (d) for $\alpha = 1$, $\lambda_R = 0.8t$ and $t = 1eV$ taken.

obey the following equation,

$$\frac{\lambda_R^2}{t^2}\left[1+4(m+\beta)^2-4(m+\beta)\right]-\frac{\lambda_R^2}{t^2}\frac{1-\alpha^2}{1+\alpha^2}\left[1+4(m+\beta)^2+4(m+\beta)\right]-8(m+\beta)\frac{1-\alpha^2}{1+\alpha^2}=0. \tag{3.22}$$

Eq. (3.22) can be checked against the plots shown in Figs. 3.11(a) and 3.11(c).

Now, for the dice lattice case ($\alpha = 1$), the above mentioned condition requires $m + \beta = 1/2$, which implies that along the radius R, the band crossing point occurs at $R = \sqrt{2}l_0\sqrt{(\frac{1}{2} - m)}$, where $l_0 = \sqrt{\hbar/(eB_0)}$ is the magnetic length. Consequently, there is only one band crossing point for $m = 0$ and $m = -1, -2, -3, ..$ etc. bands. Furthermore, band crossing is prohibited for m to be positive as there are no real values of R for $m > 0$, indicating that the corresponding spin bands do not cross each other as illustrated in Figs. 3.11(b) and 3.11(d) by the blue curves.

The energy levels as a function of the external magnetic flux ($\beta = \Phi/\Phi_0$) are depicted in Fig. 3.12 for a quantum ring with $R = 10\ nm$, considering different cases, namely, (a) $\alpha = 0.5$, $\lambda_R = 0.5t$, (b) $\alpha = 1$, $\lambda_R = 0.5t$, (c) $\alpha = 0.5$, $\lambda_R = 0.8t$, and (d) $\alpha = 1$, $\lambda_R = 0.8t$. The

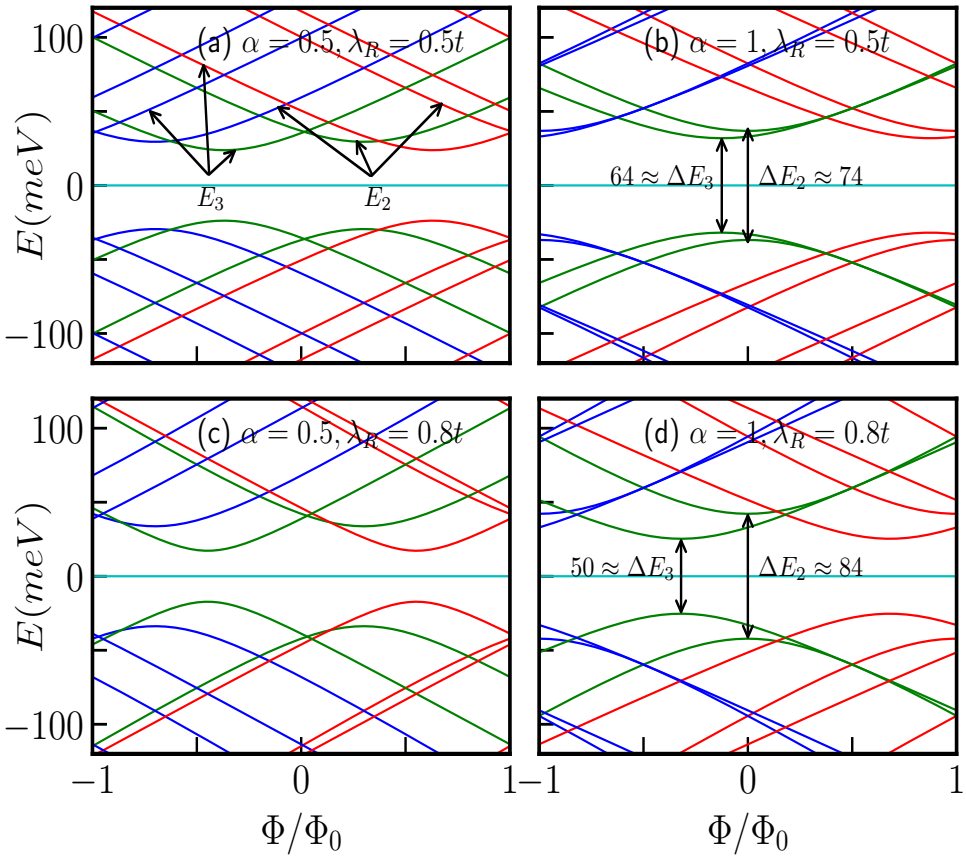

Figure 3.12: Energy levels as function of external magnetic flux Φ/Φ_0 for (a) for $\alpha = 0.5$, $\lambda_R = 0.5t$, (b) for $\alpha = 1$, $\lambda_R = 0.5t$, (c) for $\alpha = 0.5$, $\lambda_R = 0.8t$, and (d) for $\alpha = 1$, $\lambda_R = 0.8t$ with $R = 10\ nm$ are shown. We have taken $t = 1eV$, and total angular momentum quantum numbers are denoted by $m = -1, -2$ (red curves), $m = 0$ (green curves), and $m = 1, 2$ (blue curves).

curves are represented by red, green, and blue colors corresponding to $m = -1$, $m = 0$, and $m = 1$, respectively. The magnetic field dependence of the energy spectra become evident when we rewrite Eq. (3.21) as,

$$E_2^2 - \frac{\epsilon^2}{4}\big[1 + 4(m+\beta)^2 - 4(m+\beta)\frac{1-\alpha^2}{1+\alpha^2}\big](1 + \frac{\lambda_R^2}{t^2}) = 0, \tag{3.23}$$

and

$$E_3^2 - \frac{\epsilon^2}{4}\big[\big(1 + 4(m+\beta)^2\big)(1 + \frac{\lambda_R^2}{t^2}\frac{1-\alpha^2}{1+\alpha^2}) + 4(m+\beta)(\frac{\lambda_R^2}{t^2} + \frac{1-\alpha^2}{1+\alpha^2})\big] = 0. \tag{3.24}$$

Thus, the energies display a hyperbolic dependence on the applied magnetic field, exhibiting extrema at the flux values given by,

$$\frac{\Phi}{\Phi_0} = -m + \frac{1}{2}\left(\frac{1-\alpha^2}{1+\alpha^2}\right) \tag{3.25}$$

for ↑-spin band E_2, which is independent of the strength of the Rashba coupling, but depends on the values of m and the parameter α. For the dice lattice ($\alpha = 1$), the extrema occur at $\frac{\Phi}{\Phi_0} = -m$. However, the extrema for the ↓-spin band E_3 occur at

$$\frac{\Phi}{\Phi_0} = -m - \frac{1}{2}\left(\frac{\frac{\lambda_R^2}{t^2} + \frac{1-\alpha^2}{1+\alpha^2}}{1 + \frac{\lambda_R^2}{t^2}\frac{1-\alpha^2}{1+\alpha^2}}\right), \tag{3.26}$$

showing a dependency on the strength of Rashba SOC, α and m. For the dice lattice ($\alpha = 1$), the extrema are obtained at $\frac{\Phi}{\Phi_0} = -m - \frac{1}{2}\frac{\lambda_R^2}{t^2}$. The energy gaps at the extrema points are given by,

$$\Delta E_2 = \frac{2\epsilon\alpha}{1+\alpha^2}\sqrt{1 + \frac{\lambda_R^2}{t^2}} \quad \text{and} \quad \Delta E_3 = \frac{2\epsilon\alpha}{1+\alpha^2}\sqrt{\frac{1 - \frac{\lambda_R^4}{t^4}}{1 + \frac{\lambda_R^2}{t^2}\frac{1-\alpha^2}{1+\alpha^2}}}. \tag{3.27}$$

Therefore, it is observed that for a fixed value of Rashba coupling, the energy gaps for both the spin bands increase with increase in α. However, the minimum energy gap for both the spin bands is independent of m. Also the ↓-spin bands, namely, E_3 have lower energy than the ↑-spin bands (E_2). The ↑-spin E_2 and ↓-spin E_3 bands are illustrated in the Fig. 3.12(a). For the dice lattice case, and for $\lambda_R = 0.5t$, the energy gaps are obtained as, $\Delta E_2 \approx 74\ meV$ and $\Delta E_3 \approx 64\ meV$ (with $t = 1\ eV$) which can be verified from the Fig. 3.12(b). Furthermore, from Fig. 3.12 it is evident that $E_2(m) \neq E_2(-m)$ and $E_3(m) \neq E_3(-m)$, indicating the existence of finite spin currents.

3.3.3 Persistent currents

Charge persistent current

The charge persistent current in the low-energy state can be calculated using the linear response formula, $j_Q = -\sum_{m,\kappa}\frac{\partial E}{\partial \Phi}$ (the other definition, namely, $\hbar v_F \Psi^\dagger S \Psi$ yields identical results), where the sum refers to all (and only) the occupied states (for the valence band ($\kappa = -1$)) and the m values are chosen carefully to perform the summation. Since the current is periodic in Φ/Φ_0 with a period of 1 (that is $\Phi = \Phi_0$), we restrict the discussion to the window $-1 \leq \Phi/\Phi_0 \leq 1$. The analytical form for the charge current is,

$$j^{\kappa}_{Q,\lambda_R} = -\frac{\epsilon^2\kappa}{2\Phi_0}\sum_m \frac{(1+\frac{\lambda_R^2}{t^2})\left[2(m+\frac{\Phi}{\Phi_0}) - \frac{1-\alpha^2}{1+\alpha^2}\right]}{E_2(\Phi)} - \frac{\epsilon^2\kappa}{2\Phi_0}\sum_m \frac{2(m+\frac{\Phi}{\Phi_0})(1+\frac{\lambda_R^2}{t^2}\frac{1-\alpha^2}{1+\alpha^2}) + (\frac{\lambda_R^2}{t^2} + \frac{1-\alpha^2}{1+\alpha^2})}{E_3(\Phi)}. \tag{3.28}$$

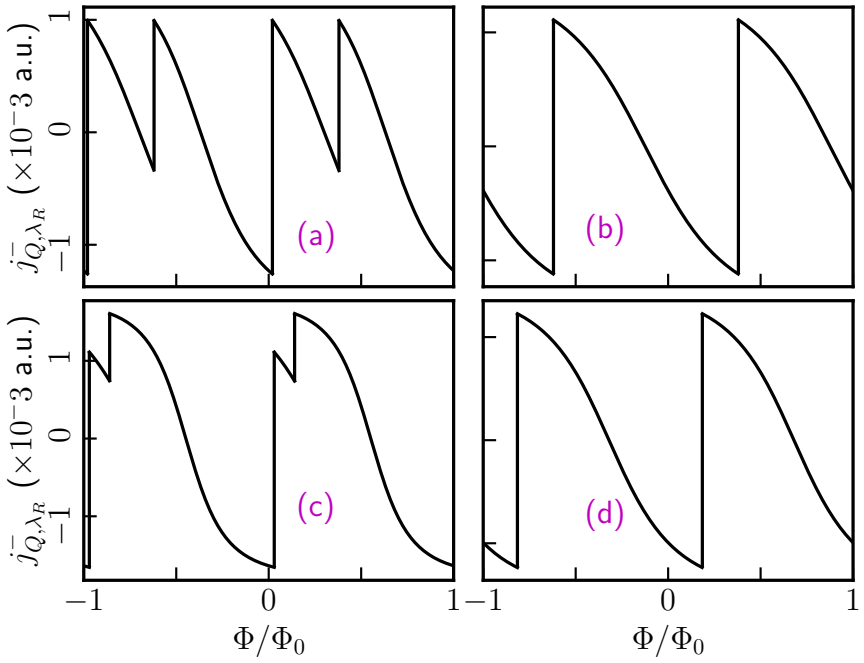

Figure 3.13: The charge persistent currents as a function of external magnetic flux for the low-energy state for (a) $\alpha = 0.5$, $\lambda_R = 0.5t$, (b) $\alpha = 1$, $\lambda_R = 0.5t$, (c) $\alpha = 0.5$, $\lambda_R = 0.8t$, and (d) $\alpha = 1$, $\lambda_R = 0.8t$ are shown. The ring has a radius, $R = 10\ nm$ and $t = 1eV$ taken.

The spin branches closest to the Fermi energy exhibit non-monotonic behaviour, resulting in two distinct contributions to the charge current coming from the $\uparrow$-spin and $\downarrow$-spin components. Since we are calculating the current contributions arising from the low-energy states, it is clear from Fig. 3.12 that for a certain range of Φ/Φ_0, only one energy state labelled by a particular value of m is present. Hence, the sum in Eq. (3.28) comprises of only one value of m. We have computed the current taking the contributions from both the spin branches and the results are depicted in Fig. 3.13 for (a) $\alpha = 0.5$, $\lambda_R = 0.5t$, (b) $\alpha = 1$, $\lambda_R = 0.5t$, (c) $\alpha = 0.5$, $\lambda_R = 0.8t$, and (d) $\alpha = 1$, $\lambda_R = 0.8t$, for a particular ring radius, namely, $R = 10\ nm$. The asymmetric structure of the spectral features between the two spin branches allows for the possibility of a net spin current, as we shall see below. For all values of α, the persistent currents oscillate periodically with Φ/Φ_0, with a periodicity of $\Phi/\Phi_0 = 1$. Fig. 3.13 illustrates that the persistent currents can be tuned by adjusting the parameter α for a fixed value of the Rashba coupling (λ_R). Moreover, the charge persistent currents can be manipulated via λ_R for a fixed α, since the Rashba parameter can be controlled by a gate voltage. In contrast, the intrinsic spin-orbit coupling ($\tilde{\lambda}$) cannot be tuned by applying external fields. However, experimental evidence has shown that the intrinsic spin-orbit coupling strength can still be manipulated via carbon hybridization technique and may contribute in tuning the charge persistent current [295].

Equilibrium spin current

We shall now study equilibrium spin currents. In contrast to the formalism for obtaining the charge current, one can obtain the spin currents by accounting for distinct velocities for different spin branches. Thus, we define equilibrium spin current as,

$$j_S = j_Q(\uparrow) - j_Q(\downarrow). \tag{3.29}$$

We have calculated the equilibrium spin currents following the procedure discussed earlier.

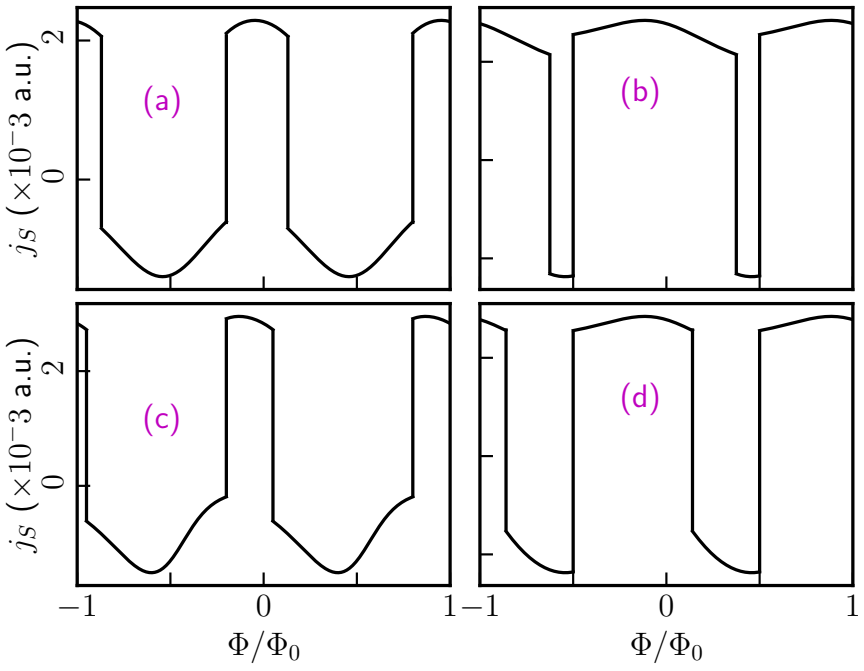

Figure 3.14: The equilibrium spin currents as a function of external magnetic flux for (a) $\alpha = 0.5$, $\lambda_R = 0.5t$, (b) $\alpha = 1$, $\lambda_R = 0.5t$, (c) $\alpha = 0.5$, $\lambda_R = 0.8t$, and (d) $\alpha = 1$, $\lambda_R = 0.8t$ are shown. The ring has a radius of $R = 10\ nm$ and $t = 1eV$ taken.

The peculiar separation of the spin branches results in velocity differences between the two spin projections, giving rise to a spin current, as shown in Fig. 3.14. The figure illustrates a significant spin current for small values of the flux, which can be attributed to the large charge current originating from a single spin branch.

The striking feature is that the magnitude as well as the pattern of the spin currents depend upon the parameters α and the strength of the Rashba coupling (λ_R). We present results for (a) $\alpha = 0.5$, $\lambda_R = 0.5t$, (b) $\alpha = 1$, $\lambda_R = 0.5t$, (c) $\alpha = 0.5$, $\lambda_R = 0.8t$, and (d) $\alpha = 1$, $\lambda_R = 0.8t$ for a ring of radius, $R = 10\ nm$. The presence of the Rashba coupling breaks inversion symmetry (in addition to the σ_z symmetry) in the plane even for small λ_R. The symmetry breaking determines the spin labelling of the energy branches that take part in yielding

the spin currents. Additionally, the spin currents exhibit periodic behaviour with Φ/Φ_0, with a periodicity equal to one flux quantum.

3.4 Pseudospin-1 α-T_3 QR with ISOC in Addition with RSOC

We add the Rashba SOC term to the Hamiltonian in Eq. (3.1) of the pseudospin-1 fermionics. Thus, we are dealing with a Kane-Mele Hamiltonian with a Rashba term for pseudospin-1 α-T_3 QR. The resulting Hamiltonian is,

$$H = t\sum_{\langle ij\rangle} c^{\dagger}_{i\sigma}c_{j\sigma} + \alpha t\sum_{\langle ik\rangle} c^{\dagger}_{i\sigma}c_{k\sigma} + \frac{i\lambda}{3\sqrt{3}}\sum_{\langle\langle ij\rangle\rangle\sigma\sigma'}\nu_{ij}c^{\dagger}_{i\sigma}\sigma_z c_{j\sigma'} + \frac{i\alpha\lambda}{3\sqrt{3}}\sum_{\langle\langle ik\rangle\rangle\sigma\sigma'}\nu_{ik}c^{\dagger}_{i\sigma}\sigma_z c_{k\sigma'}$$
$$+\lambda_R\sum_{\langle ij\rangle\sigma\sigma'} ic^{\dagger}_{i\sigma}(\hat{D}_{ij}\cdot\vec{\sigma})_{\sigma\sigma'}c_{j\sigma'} + \alpha\lambda_R\sum_{\langle ik\rangle\sigma\sigma'} ic^{\dagger}_{i\sigma}(\hat{D}_{ik}\cdot\vec{\sigma})_{\sigma\sigma'}c_{k\sigma'} + \Big(h.c.\Big). \tag{3.30}$$

All the terms and notations have described earlier in Sec. 3.2 and Sec. 3.3. Thus, in the vicinity of a Dirac point (namely, K), the Hamiltonian corresponding to an ideal α-T_3 ring is given by,

$$H = \begin{pmatrix}
-\tilde{\lambda}\cos\varphi & -i\epsilon(m+\frac{1}{2})\cos\varphi e^{\frac{i\pi}{3}} & 0 & 0 & -\frac{\epsilon\lambda_R}{t}(m+\frac{1}{2})\cos\varphi e^{\frac{i\pi}{3}} & 0 \\
i\epsilon(m+\frac{1}{2})\cos\varphi e^{-\frac{i\pi}{3}} & \tilde{\lambda}(\cos\varphi-\sin\varphi) & -i\epsilon(m-\frac{1}{2})\sin\varphi e^{\frac{i\pi}{3}} & \frac{\epsilon\lambda_R}{t}(m-\frac{1}{2})\cos\varphi e^{\frac{i\pi}{3}} & 0 & -\frac{\epsilon\lambda_R}{t}(m+\frac{1}{2})\sin\varphi e^{-\frac{i\pi}{3}} \\
0 & i\epsilon(m-\frac{1}{2})\sin\varphi e^{-\frac{i\pi}{3}} & \tilde{\lambda}\sin\varphi & 0 & -\frac{\epsilon\lambda_R}{t}(m-\frac{1}{2})\sin\varphi e^{-\frac{i\pi}{3}} & 0 \\
0 & \frac{\epsilon\lambda_R}{t}(m-\frac{1}{2})\cos\varphi e^{-\frac{i\pi}{3}} & 0 & \tilde{\lambda}\cos\varphi & i\epsilon(m-\frac{1}{2})\cos\varphi e^{-\frac{i\pi}{3}} & 0 \\
-\frac{\epsilon\lambda_R}{t}(m+\frac{1}{2})\cos\varphi e^{-\frac{i\pi}{3}} & 0 & \frac{\epsilon\lambda_R}{t}(m-\frac{1}{2})\sin\varphi e^{\frac{i\pi}{3}} & -i\epsilon(m-\frac{1}{2})\cos\varphi e^{\frac{i\pi}{3}} & -\tilde{\lambda}(\cos\varphi-\sin\varphi) & i\epsilon(m+\frac{1}{2})\sin\varphi e^{-\frac{i\pi}{3}} \\
0 & -\frac{\epsilon\lambda_R}{t}(m+\frac{1}{2})\sin\varphi e^{\frac{i\pi}{3}} & 0 & 0 & -i\epsilon(m+\frac{1}{2})\sin\varphi e^{\frac{i\pi}{3}} & -\tilde{\lambda}\sin\varphi
\end{pmatrix}. \tag{3.31}$$

The eigenstates of the ring Hamiltonian can be obtained as,

$$\psi(R,\theta) = \begin{pmatrix}
\chi_{1\uparrow}(R)e^{i(m+1)\theta} \\
\chi_{2\uparrow}(R)e^{im\theta} \\
\chi_{3\uparrow}(R)e^{i(m-1)\theta} \\
\chi_{1\downarrow}(R)e^{i(m-1)\theta} \\
\chi_{2\downarrow}(R)e^{im\theta} \\
\chi_{3\downarrow}(R)e^{i(m+1)\theta}
\end{pmatrix}. \tag{3.32}$$

We have described all the terms and the notations earlier.

3.4.1 Without magnetic field ($B_0 = 0$)

The electronic energy spectra at the K valley as a function of the ring radius R of the system, via varying both λ and λ_R, have been obtained via numerical diagonalization of Eq. (3.30) and are

shown in Fig. 3.15. When both the Rashba coupling (λ_R) and the intrinsic spin-orbit coupling ($\tilde{\lambda}$) are considered, the energy bands for spin-$\uparrow$ and spin-$\downarrow$ states become distinguishable for any value of m. Consequently, in this case we get pairs of conduction ($n = 0$), distorted flat ($n = 1$), and valence ($n = 2$) bands, one for each spin. In Fig. 3.15, we have plotted the energy spectra for two different α values, namely, $\alpha = 0.5$ (Fig. 3.15(a)) and $\alpha = 1$ (Fig. 3.15(b)) with $m = 0$ (green curves), 1 (blue curves), and -1 (red curves). The parameters used in the calculations are $\tilde{\lambda} = 0.05t$ and $\lambda_R = 0.5t$. Notably, the energy levels are now non-degenerate for all values of α. It is worth mentioning that for all values of α, and for small radii, all the branches of the VB and CB vary as $1/R$. Within the CB and VB, the energy splitting between the spin bands corresponding to a specific m value increases with α in the range namely, $0 < \alpha \leq 0.5$.

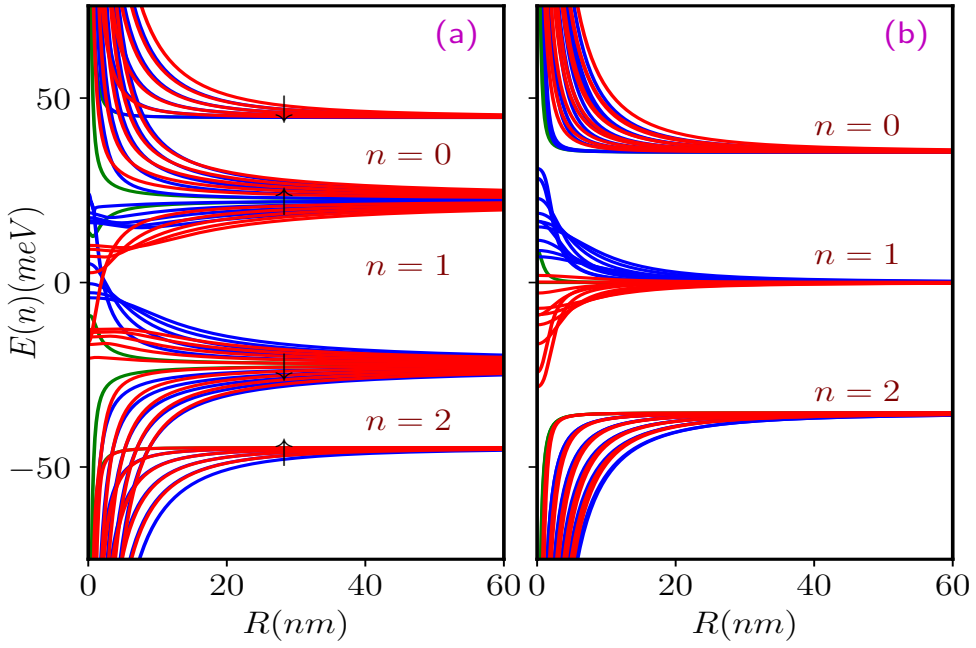

Figure 3.15: The energy spectra as a function of the ring radius R of the α-T_3 quantum ring at K valley for (a) $\alpha = 0.5$, and (b) $\alpha = 1$. $n = 0, 1$, and 2 denote the CB, distorted FB, and VB respectively. The parameters are taken as $\tilde{\lambda} = 0.05t$, $\lambda_R = 0.5t$, and $t = 1eV$. Our results with $-5 \leq m \leq 5$ are shown, here positive values of m are shown by red curves, $m = 0$ shown by green curves, and negative values are shown by red curves.

However, as α increases within the range $0.5 < \alpha \leq 1$, the energy separation between the spin bands decreases. Additionally, regardless of the value of α, the energy separation diminishes as the magnitude of m ($|m|$) increases. Within the distorted $n = 1$ band, the degree of distortion increases as α increases in the small radius limit. A finite gap exists between the $\uparrow$- and $\downarrow$-spin bands of the $m = 0$ band. This gap increases with α in the range $0 < \alpha \leq 0.5$, while it decreases in the range $0.5 < \alpha \leq 1$. This non-monotonicity is an interesting feature of our study. Furthermore, the energy separation between the $\uparrow$- and $\downarrow$-spin bands decreases as α and $|m|$ increases. Moreover, certain spin bands intersect at a particular value of the radius of the

ring, as depicted in Fig. 3.15(a). As we increase α, the crossing point gradually shifts towards larger values of R. In the limit $\alpha = 1$, the $\downarrow$-spin band of $m = 0$ remains flat at zero energy, and the spin bands converge at large values of R as shown in Fig. 3.15(b). Furthermore, in the regime of large radii, we observe intriguing features in the energy spectra, which we shall discuss below.

As we increase α in the range $0 < \alpha \leq 0.5$, a distinct separation between the spin branches of a specific band (VB, dFB, or CB) becomes evident, and this separation becomes more prominent as α increases. Specifically, the $\uparrow$-spin bands of the distorted flat band ($n = 1$) migrate away from the band center ($E = 0$) and move closer to the $\uparrow$-spin bands of the conduction band ($n = 0$). The $\uparrow$-spin energy bands of $n = 1$ band (distorted FB) merge to a value of $\alpha\tilde{\lambda}$, while the $\uparrow$-spin bands of the $n = 0$ band converge to a value given by $(1-\alpha)\tilde{\lambda}$ in the limit of large R. It is important to note that the specific criteria for considering R as "large" vary, in a sense they depend upon the value of m. Conversely, the $\downarrow$-spin bands of $n = 1$ shift towards the $\downarrow$-spin bands of $n = 2$ (VB). Again they merge to a value $-\alpha\tilde{\lambda}$ and $-(1-\alpha)\tilde{\lambda}$ respectively. For more detailed information, we present the same results for different values of α in Fig. 3.16. Fig. 3.15(a) illustrates the results for $\alpha = 0.5$ where $\uparrow$-spin bands of $n = 0$ and $n = 1$ merge to a value $\tilde{\lambda}/2$, while the $\downarrow$-spin bands merge to $-\tilde{\lambda}/2$. Additionally, the $\downarrow$-spin bands corresponding to $n = 0$ merge to a value $\tilde{\lambda}\cos\varphi$ in the large R limit, while the $\uparrow$-spin bands of the $n = 2$ merge to $-\tilde{\lambda}\cos\varphi$ as depicted in Fig. 3.15(a). For example, to quote some numbers, corresponding to $\alpha = 0.5$, the $\uparrow$-spin branches of the VB ($n = 2$) merge to a value $-45\ meV$, while the $\downarrow$-spin branches of the CB ($n = 0$) merge at $45\ meV$. These results match very well with our analytic results discussed above.

For the range $0.5 < \alpha \leq 1$, as we increase α, the separation between the spin branches for a specific band (VB, dFB or CB) diminishes, eventually leading to spin-mixed bands at $\alpha = 1$. In contrast to the previous scenario, in the current case, here the $\uparrow$-spin bands of the distorted flat band ($n = 1$) merge together at a value $(1-\alpha)\tilde{\lambda}$, while the $\downarrow$-spin bands merge to $-(1-\alpha)\tilde{\lambda}$ in the limit of large R. On the other hand, the $\uparrow$-spin and the $\downarrow$-spin branches of the $n = 0$ band merge to $\alpha\tilde{\lambda}\cos\varphi$ and $\tilde{\lambda}\cos\varphi$ respectively, while the $\uparrow$-spin and the $\downarrow$-spin branches of the $n = 2$ band merge to $-\tilde{\lambda}\cos\varphi$ and $-\alpha\tilde{\lambda}\cos\varphi$ respectively. Fig. 3.15(b) displays the results for the $\alpha = 1$ case where the spin bands corresponding to the $n = 1$ band merge together at zero energy and the spin bands of the $n = 0$ and $n = 2$ merge to $\pm\tilde{\lambda}/\sqrt{2}$ respectively, which are in accordance with the aforementioned explanations. We summarize the results in the Table 3.2.

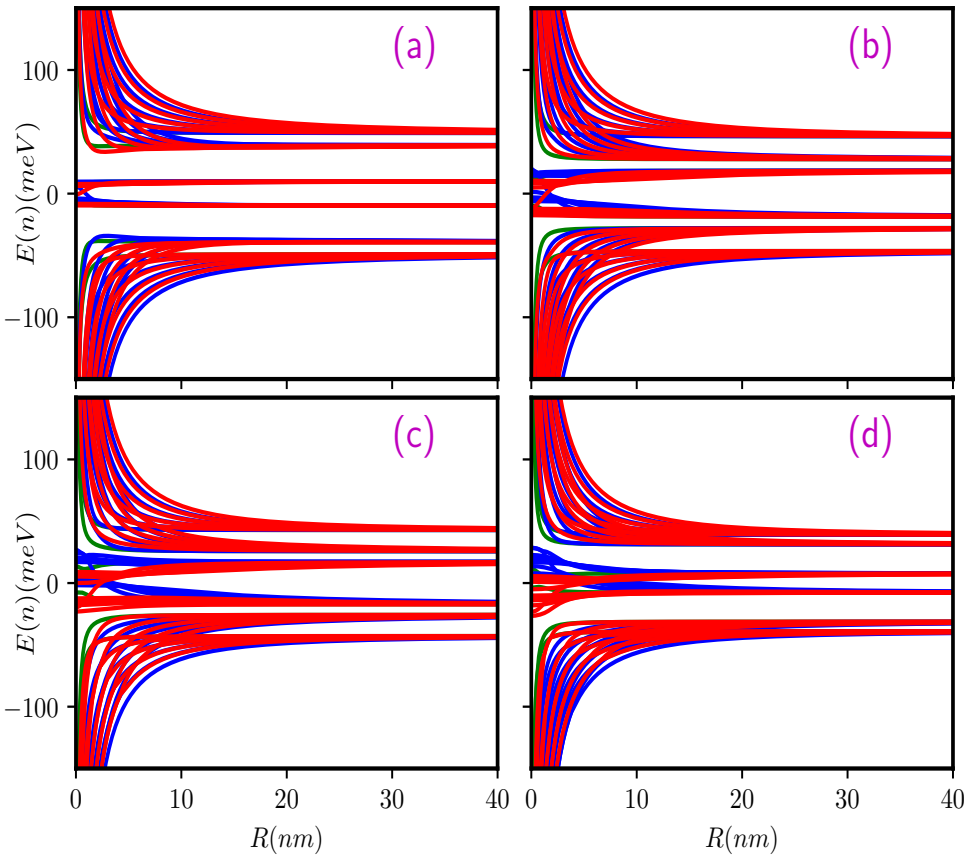

Figure 3.16: Evolution of the energy spectra as a function of ring radius R of the α-T_3 quantum ring at K valley in presence of both the ISOC and RSOC terms together for (a) $\alpha = 0.2$, (b) $\alpha = 0.4$, (c) $\alpha = 0.6$, and (d) $\alpha = 0.8$. The parameters are $\tilde{\lambda} = 0.05t$, $\lambda_R = 0.5t$, and $t = 1eV$. $n = 0, 1$, and 2 denote the CB, distorted FB, and VB respectively.

		$0 < \alpha \leq 0.5$	$0.5 < \alpha \leq 1$
Bands	Spin-resolved bands	Marging energy	Marging energy
$n = 0$	$\uparrow$-spin	$(1-\alpha)\tilde{\lambda}$	$\alpha\tilde{\lambda}\cos\varphi$
$n = 0$	$\downarrow$-spin	$\tilde{\lambda}\cos\varphi$	$\tilde{\lambda}\cos\varphi$
$n = 1$	$\uparrow$-spin	$\alpha\tilde{\lambda}$	$(1-\alpha)\tilde{\lambda}$
$n = 1$	$\downarrow$-spin	$-\alpha\tilde{\lambda}$	$-(1-\alpha)\tilde{\lambda}$
$n = 2$	$\uparrow$-spin	$-\tilde{\lambda}\cos\varphi$	$-\tilde{\lambda}\cos\varphi$
$n = 2$	$\downarrow$-spin	$-(1-\alpha)\tilde{\lambda}$	$-\alpha\tilde{\lambda}\cos\varphi$

Table 3.2: Summary of different marging energy values of different spin branches at large radii in absence of magnetic field.

3.4.2 In presence of magnetic field ($B_0 \neq 0$)

Now, let us consider the case when the ring is subjected to a perpendicular magnetic field. The field significantly alters the above scenario. In Fig. 3.17, we show the dependence of several

energy levels on the ring radius (R) for two cases namely, $\alpha = 0.5$ and $\alpha = 1$, assuming a magnetic field strength of $B_0 = 5$T. Each level exhibits a non-monotonic behaviour as a function of R. Notably, the energy levels of the CB ($n = 0$) and VB ($n = 2$) attain inflection points (minimum for CB and maximum for VB) at specific values of R. However, the locations of these points depend on the values of m, α, $\tilde{\lambda}$, and λ_R, as shown in Fig. 3.17. In the limit of small R, all the energy levels vary inversely with R. On the other hand, the energy scales approximately linearly with R, in the limit of large R. It is worth mentioning that the criteria for considering R as "large" differ for different values of m. Furthermore, within the CB ($n = 0$) and VB ($n = 2$) for a particular value of m and α, the energy splitting between the spin branches decreases as R increases before reaching the inflection points. However, after reaching these points, the energy splitting between the spin bands increases with R (see Fig. 3.17(a)). Additionally, the energy splitting between the bands decreases as $|m|$ increases, for all values of α. Moreover, for a specific $|m|$ value, the energy splitting decreases as α increases, and eventually, the spin bands merge at the extremum point in the limit of $\alpha = 1$ as shown in the Fig. 3.17(b).

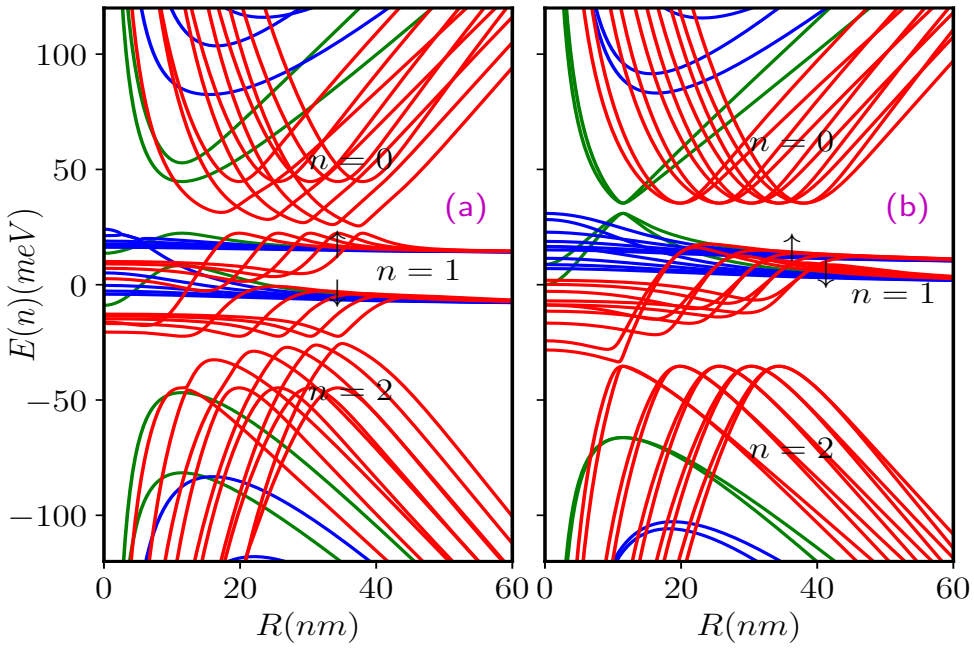

Figure 3.17: The energy spectra as a function of ring radius R of the α-T_3 quantum ring in presence of an external magnetic field of $B_0 = 5$T at K valley for (a) $\alpha = 0.5$, and (b) $\alpha = 1$. $n = 0, 1$, and 2 denote the CB, distorted FB, and VB respectively. The parameters are taken as $\tilde{\lambda} = 0.05t$, $\lambda_R = 0.5t$, and $t = 1eV$. m values are taken from -5 to 5 and positive values of m are shown by red curves, $m = 0$ shown by green curves, and negative values are shown by red curves.

Let us briefly discuss the behaviour of energy levels within the dFB ($n = 1$) considering to the choice of parameters m, R, and α. In the small R limit, and for a specific value of m, increasing α results in a greater degree of distortion within the dFB. Additionally, for a fixed value of α,

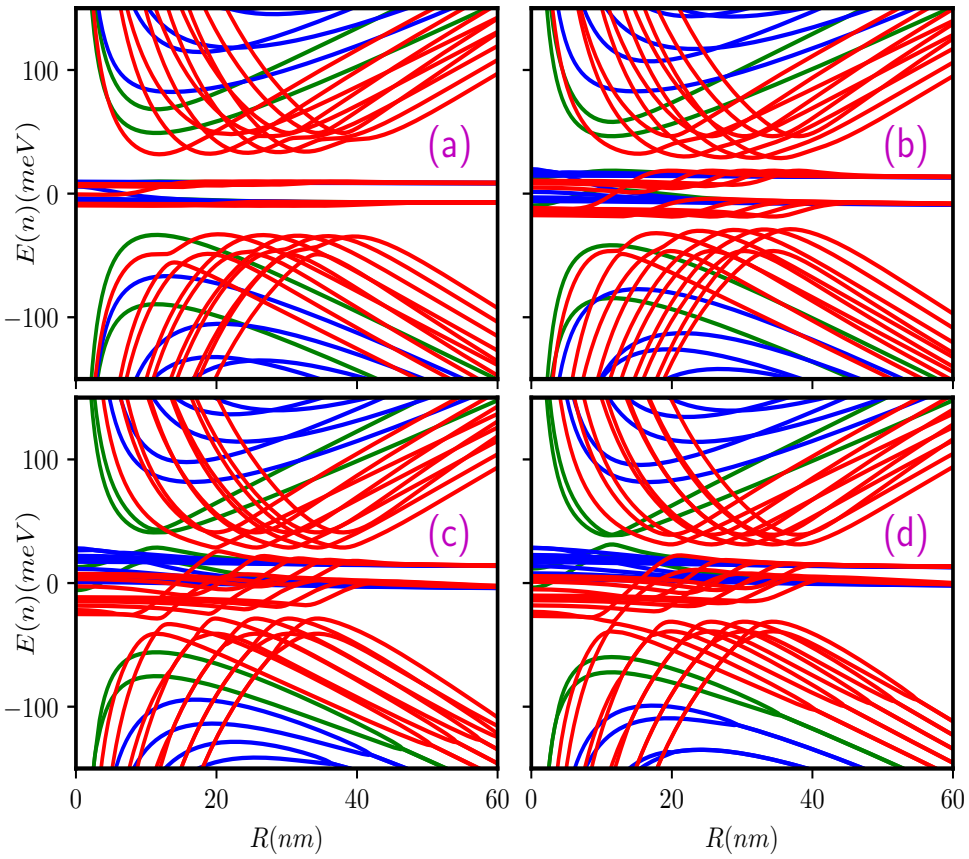

Figure 3.18: Evolution of the energy spectra as a function of ring radius R of the α-T_3 quantum ring at K valley in presence of external magnetic field of $B_0 = 5$T considering both the ISOC and RSOC terms together for (a) $\alpha = 0.2$, (b) $\alpha = 0.4$, (c) $\alpha = 0.6$, and (d) $\alpha = 0.8$. The parameters are taken as $\tilde{\lambda} = 0.05t$, $\lambda_R = 0.5t$, and $t = 1eV$. $n = 0, 1$, and 2 denote the CB, dFB, and VB respectively.

the distortion also increases with $|m|$ increase. Now, focusing on a fixed value of $|m|$, within the range of $0 < \alpha \leq 0.5$, an increase in α leads to an increase in the separation between the spin-$\uparrow$ and spin-$\downarrow$ bands. However, within the range of $0.5 < \alpha \leq 1$, the splitting between the spin bands decreases as α increases. Moreover, for a particular α value, in the small R limit, the energy separation increases with increasing $|m|$. On the other hand, in the large R limit, the spin-$\uparrow$ and spin-$\downarrow$ bands with different m values merge with each other, resulting in spin-split energy bands, which happens for any value of α. However, in the large R limit, the splitting between the spin bands increases as α increases in the other range, that is, $0 < \alpha \leq 0.5$, while the separation between the bands decreases as α increases within the range of $0.5 < \alpha \leq 1$. For more detailed information, we provide Fig. 3.18, which includes results for additional α values.

In Fig. 3.17(a), we illustrate the case for $\alpha = 0.5$. Here, for a fixed $|m|$, the energy splitting between the spin bands increases as R increases. The energy separation between the spin bands increases as $|m|$ increases in the small R limit. The $\uparrow$-spin bands of $n = 1$ shift towards the

$\uparrow$-spin bands of $n = 0$, and as m increases in the negative direction, they also move closer to each other. Similarly, the $\downarrow$-spin bands shift towards the $\downarrow$-spin bands of the $n = 2$, and as negative values of m increases, they move closer to each other. In Fig. 3.17(b), we depict the case for $\alpha = 1$. Here, the separation between the spin bands of $m = 0$ and negative values of m decreases with increasing R. Further, at a certain radius (inflection points), they touch each other. Subsequently, the band gap increases, leading to the emergence of spin-separated bands in the large R limit. However, for positive values of m no band touching occurs. Furthermore, the bands of the distorted FB with $m = 0$ shift towards the bands of CB with $m = 0$, and as the negative values of m increases, the shifting points move further apart. Conversely, the spin-$\downarrow$ band of the distorted FB with $m = -1$ shifts towards the bands of VB with $m = -1$, and as m increases towards the negative values, the shifting points also move further apart.

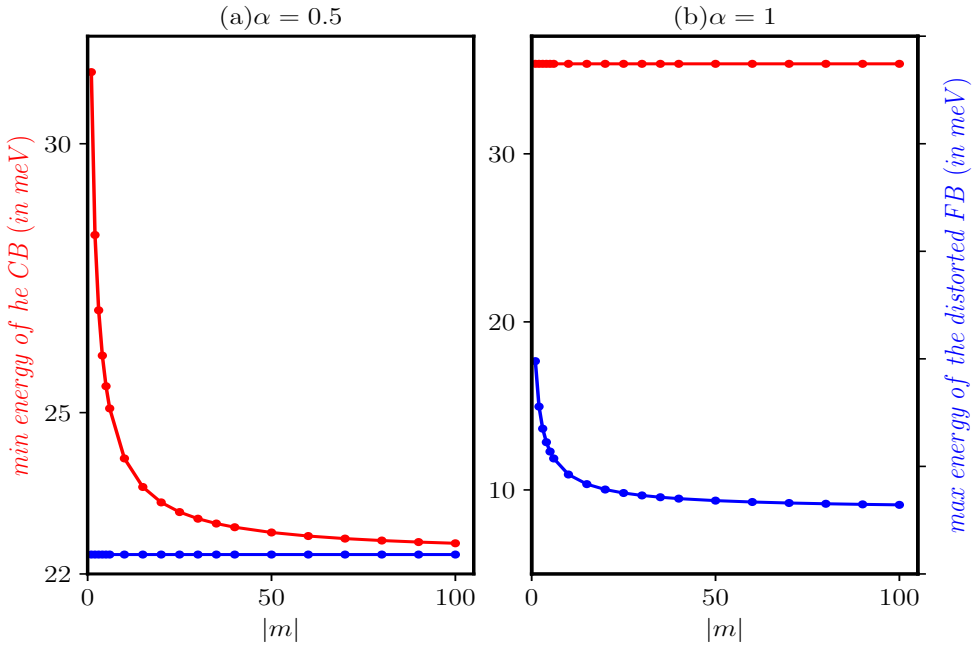

Figure 3.19: Minimum value of the conduction band energy levels and maximum value of the distorted flat band energy levels of the ring as a function of the quantum number $|m|$ for $\alpha = 0.5$ and $\alpha = 1$. Here, we consider the ring radius $R = 10nm$, $\tilde{\lambda} = 0.05t$, $\lambda_R = 0.5t$, $t = 1eV$, and the magnetic field is $B_0 = 5$T.

Notably, it is observed that there always exists a finite gap between the lowest point of the CB and the highest point of the dFB. The same holds true for the highest point of the VB and the lowest point of the dFB. Consequently, these energy levels will never mix with each other, even when R and $|m|$ attain very large values. To verify this, in Figure 3.19, we have depicted the minimum energy of the CB and the maximum energy of the dFB as a function of the quantum number $|m|$ for both $\alpha = 0.5$ and $\alpha = 1$. The results reveal a distinct gap between the minimum of the CB and the maximum of the dFB. Additionally, for $\alpha = 0.5$, the minimum energy of the

CB, and for $\alpha = 1$, the maximum energy of the dFB exhibits a behaviour that scales as $1/\sqrt{|m|}$. Notably, the maximum energy of the dFB for $\alpha = 0.5$ and the minimum energy of the CB for $\alpha = 1$ remain approximately constant.

3.4.3 Persistent current

Charge persistent current

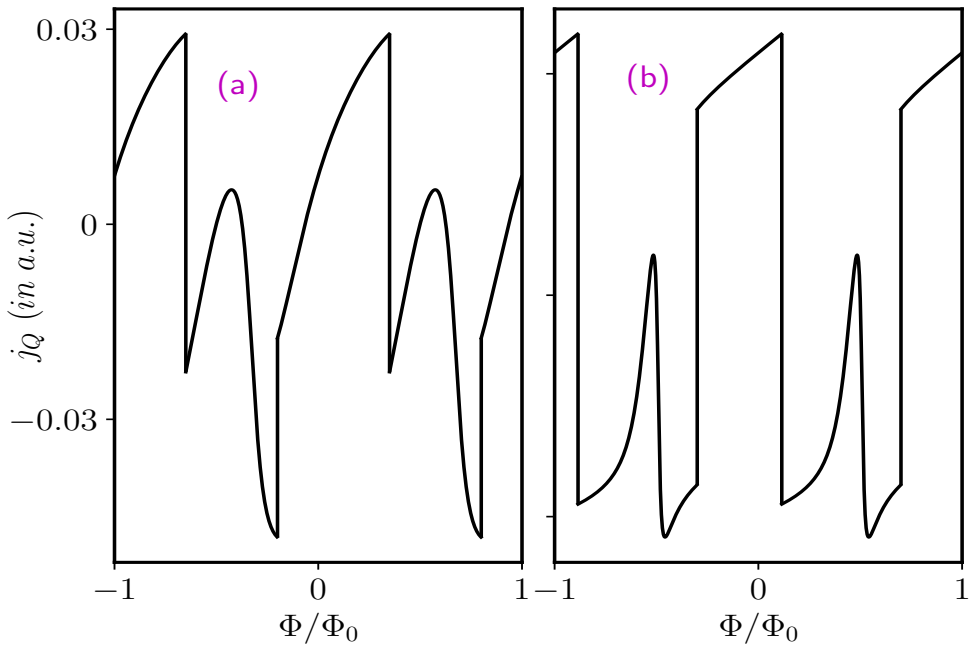

Figure 3.20: The charge persistent current as a function of external magnetic flux for the low-energy states in presence of both the ISOC and RSOC terms for (a) $\alpha = 0.5$ and (b) $\alpha = 1$. The radius of the ring is $10\ nm$ and the parameters are taken as $\tilde{\lambda} = 0.05t$, $\lambda_R = 0.5t$, and $t = 1eV$.

From Fig. 3.17, it is evident that the presence of an external field in this case causes the flat band to no longer remain flat, which in turn contributes to the transport properties of the system. To investigate the impact of the distorted flat band, we calculate the persistent currents. The charge persistent currents in the low-energy state can be determined using the linear response definition, $j_Q = -\sum_m \frac{\partial E}{\partial \Phi}$, where the summation is over the low-energy occupied states only. We confined our discussion in the range $-1 \leq \Phi/\Phi_0 \leq 1$, where the occupied states exist in the valence band and the distorted flat band. We follow the same procedure as stated in Secs. 3.2 and 3.3. The persistent currents then obtained as a combination of contributions from the valence band ($n = 2$) and the distorted flat band ($n = 1$) as, $j_Q = j_Q^{n=1} + j_Q^{n=2}$. It is noteworthy that the distortion of the energy levels in the flat band gives rise to finite persistent currents, in contrast to the case of Rashba SOC (in Sec. 3.3). In Fig. 3.20, we demonstrate the variation of

the persistent currents with Φ/Φ_0, for $\tilde{\lambda} = 0.05t$, $\lambda_R = 0.5t$, and $R = 10\ nm$ corresponding to two different cases, namely $\alpha = 0.5$ (Fig. 3.20(a)), and $\alpha = 1$ (Fig. 3.20(b)). The introduction of $\tilde{\lambda}$ and λ_R completely changes the oscillation pattern of the persistent currents from the case of $\tilde{\lambda} \neq 0$, $\lambda_R = 0$ (see Fig. 3.8) and $\tilde{\lambda} = 0$, $\lambda_R \neq 0$ (see Fig. 3.13). Furthermore, the currents exhibit periodic oscillations in Φ/Φ_0 with the periodicity $\Phi/\Phi_0 = 1$. The period of oscillation remains insensitive to the value of α. However, the oscillation pattern varies for different α values. Moreover, the charge persistent currents can be manipulated by λ_R, which is tunable via an external.

In many case, we have excluded the plots for graphene ($\alpha = 0$), as the results are known, which in some other cases, we have included them so as to underscore how the scenario evolves with the value of α.

Equilibrium spin current

Finally, we consider the equilibrium spin currents. We define the equilibrium spin currents as in Eq. (4.20), which combines charge current contributions from different spin-split labels. We have calculated this taking into account of the low-energy states of the separate spin branches. In this case, the inversion symmetry is broken inside the plane, leading to asymmetric spin branches. The peculiar separation of the spin branches results in velocity differences between the two spins, leading to a spin current, as illustrated in Fig. 3.21. We have consider two cases, $\alpha = 0.5$ (Fig. 3.21(a)) and $\alpha = 1$ (Fig. 3.21(b)), corresponding to the parameter values $\tilde{\lambda} = 0.05t$, $\lambda_R = 0.5t$, and $R = 10\ nm$. The figures depict a large spin current for small fluxes, which can be attributed to the large charge currents originating from the individual spin branches. These currents oscillate periodically in Φ/Φ_0, with the periodicity $\Phi = \Phi_0$. Furthermore, the pattern of oscillation varies for different α values, while the oscillation period remains independent of the values of α. The Rashba coupling originates from the broken inversion symmetry in the plane, and determines the spin labelling of the energy branches participating in the spin current. Additionally, the intrinsic SOC term makes the flat band dispersive, allowing it to contribute to the equilibrium spin currents. Furthermore, the equilibrium spin currents can also be manipulated by Rashba coupling and ISOC, as they are tunable via external field and edge functionalization.

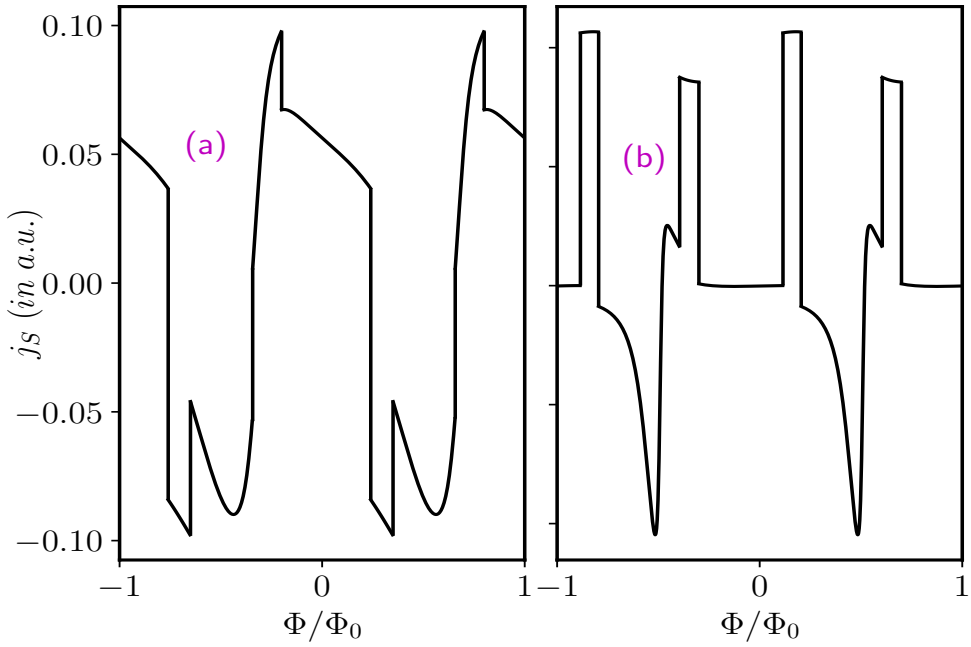

Figure 3.21: The equilibrium spin current as a function of external magnetic flux for the low-energy states considering both the ISOC and RSOC terms for (a) $\alpha = 0.5$ and (b) $\alpha = 1$. Again the ring radius is $10\ nm$ and the parameters are taken as $\tilde{\lambda} = 0.05t$, $\lambda_R = 0.5t$, and $t = 1eV$.

3.5 Summary

In this chapter we have thoroughly examined the electronic properties of the α-T_3 QR in presence of an external magnetic field, including the effects of Rashba and intrinsic spin-orbit couplings separately, as well as their combined effects. The key observations from our analyses include the following.

When only intrinsic spin-orbit coupling is present ($\tilde{\lambda} \neq 0$, $\lambda_R = 0$) and in the absence of a magnetic field, the flat band becomes dispersive for small ring radii, except for the $m = 0$ band corresponding to $\alpha = 1$ (dice limit). At large radii, the energy levels in the valence band (VB) and the conduction band (CB) converge to specific energy values determined by the parameters $\tilde{\lambda}$ and α. The introduction of the magnetic field makes all the levels in the flat band dispersive at all finite values of α ($\alpha \neq 0$). The energy levels in the VB and CB display significant deviations from their typical R dependence. The persistent currents exhibit Φ_0 periodic oscillations at the individual valleys, resembling Aharonov-Bohm oscillations. The valley currents, derived by combining charge current contributions from the two valleys, exist only for intermediate to graphene (pseudospin-1/2) and dice lattice (pseudospin-1), $0 < \alpha < 1$, while in the limiting cases that is, $\alpha = 0$ and $\alpha = 1$, they vanish. Equilibrium spin currents obtained from combining the charge current contributions from different spin labels also exist

for all values of $\alpha \neq 0$ (pseudospin-1 system) and exhibit Φ_0 periodic oscillations, with the oscillation pattern depending on α and $\tilde{\lambda}$.

As a second scenario, we have considered only Rashba spin-orbit coupling present ($\tilde{\lambda} = 0$, $\lambda_R \neq 0$). The inclusion of λ_R leads to six bands in the spectrum, including two non-dispersive flat bands and four dispersive spin-split VB and CB. The flat band consists of a large number of degenerate levels at zero-energy, which are insensitive to the applied magnetic field. In the absence of a magnetic field, all the energy levels in the CB and VB exhibit inverse dependence on the ring radius R, and are independent of α. Interestingly, the $\uparrow$-spin energy levels corresponding to $\alpha = 1$ is two-fold degenerate, except for the $m = 0$ level. However, the $\downarrow$-spin bands are non-degenerate for all values of α. When the ring is subjected to a perpendicular magnetic field, the energy levels deviate significantly from their typical R dependence, displaying a $1/R$ behaviour for small R and R behaviour for large R. The persistent currents show Φ_0 periodic oscillations, with distinct patterns for different α and λ_R values. We derived equilibrium spin currents, by combining the charge current contributions from different spin branches which display the same periodic behaviour.

As a final case, we have considered the effects of both spin-orbit couplings, namely, $\tilde{\lambda} \neq 0$ and $\lambda_R \neq 0$. In the absence of a magnetic field, all the flat bands become dispersive for small ring radii, except for the $m = 0$ $\downarrow$-spin band corresponding to $\alpha = 1$. The introduction of a magnetic field leads to all the levels of the flat band becoming dispersive for all $\alpha \neq 0$, with the VB and CB behaving with the ring radius R similar to the previous cases. Further, the persistent currents exhibit Φ_0 periodic oscillations with a pattern distinct from the previous cases. The equilibrium spin currents are non-zero as well for all values of α and display similar periodic behaviour with a distinct oscillatory pattern. The parameters α, $\tilde{\lambda}$, and λ_R are tunable in our work ($\tilde{\lambda}$, λ_R are experimentally tunable too), the persistent currents can be controlled by varying these parameters.

Chapter 4

Effects of Screw Dislocation in a Rashba Spin-Orbit Coupled α-T_3 Quantum Ring

---

Having studied the role of intrinsic and Rashba spin-orbit coupling, we resort to explore imperfection in a quantum ring. With such a motivation, we investigate the effect of a topological defect, such as a screw dislocation in an α-T_3 Aharonov-Bohm quantum ring and scrutinize the role of an external transverse magnetic field therein in this chapter. The screw dislocation introduces an effective flux that reshapes the periodic oscillations in the persistent current in both charge and spin sectors, with a period of one flux quantum. Moreover, these currents demonstrate a phase shift proportional to the degree of dislocation. Further, we have ascertained the role of scattering effects due to the dislocation present in the system. Such tunable oscillation of the spin persistent current highlights applications of our system as potential spintronic devices. Additionally, the presence of the distortion induces a chirality effect, giving rise to an additional chiral current even in the absence of an external field.

4.1 Introduction

A myriad of physical phenomena is induced by dislocations in experiments. For instance, the time-reversal symmetry-breaking superconducting state along the (110) lattice direction in Sr_2RuO_4 [296], the influence of screw dislocations on the mechanical response of complex layered materials [297, 298], etc. Further, the interplay between real-space topological lattice defects and the reciprocal space topology of energy bands, may result in one-dimensional topological modes bound to screw dislocations in three-dimensional topological insulators. Dislocation-induced helical modes [299], geometry-induced charge separation on a helicoidal ribbon [300, 301], and other phenomena further highlight the diverse effects produced by dislocations. Moreover, recent studies on position-dependent mass Schrödinger particles in space-like screw dislocations [302], as well as the application of quantum dots with screw dislocations in nonlinear optical [303], and magneto-optical specifications [304], have garnered significant attention in the scientific community dealing with quantum ring (QR) based devices.

Driven by the exciting possibilities offered by QRs, this study focuses onto the impact of a topological defect positioned at the center of the α-T_3 QR, in presence of a Rashba spin-orbit coupling (RSOC). The interplay of RSOC and topological defect on the energy spectra and transport will comprise of the important discussions made in this chapter. The inclusion of this topological defect is achieved in the Hamiltonian through a geometric route. Furthermore, our analyse involve into the dynamics of a charged particle constrained to navigate a QR with a fixed radius, all the while being influenced by the presence of this topological defect. Additionally, we incorporate the Rashba SOC term, which does not violate any of the symmetries of the parent α-T_3 ring. Notably, this term can be manipulated using an external electric field [257] or adding heavy adatoms, etc. that effectively breaks the mirror symmetry with respect to the α-T_3 plane. This discussion underscores the necessity for a comprehensive investigation into the behaviour of an α-T_3 QR with Rashba SOC and topological defect. To further elucidate the controllability of persistent currents, we incorporate an external magnetic field into our analyse. These explorations have sparked substantial research activity, particularly in the context of potential applications within the emerging field of spintronics. An intriguing avenue for further investigation involves the combination of Rashba SOC with dislocation in an α-T_3 QR to examine various properties. At the theoretical level, it is imperative to gain a deeper understanding of the cumulative effects of a robust electric field from SOC, confinement, and disorder potentials, such as the topological defect considered by us. These factors directly impact charge transport and the spin-related attributes of electrons.

This chapter is structured as follows. In Section 4.2, we present the model incorporating a topological defect. Section 4.3 provides an overview of the electronic properties of the system. The discussion of the persistent currents are presented in Section 4.4. The Burgers currents, including explicit formulas, is presented in various sub-sections of Section 4.6. Finally, our findings are summarized in Section 4.7.

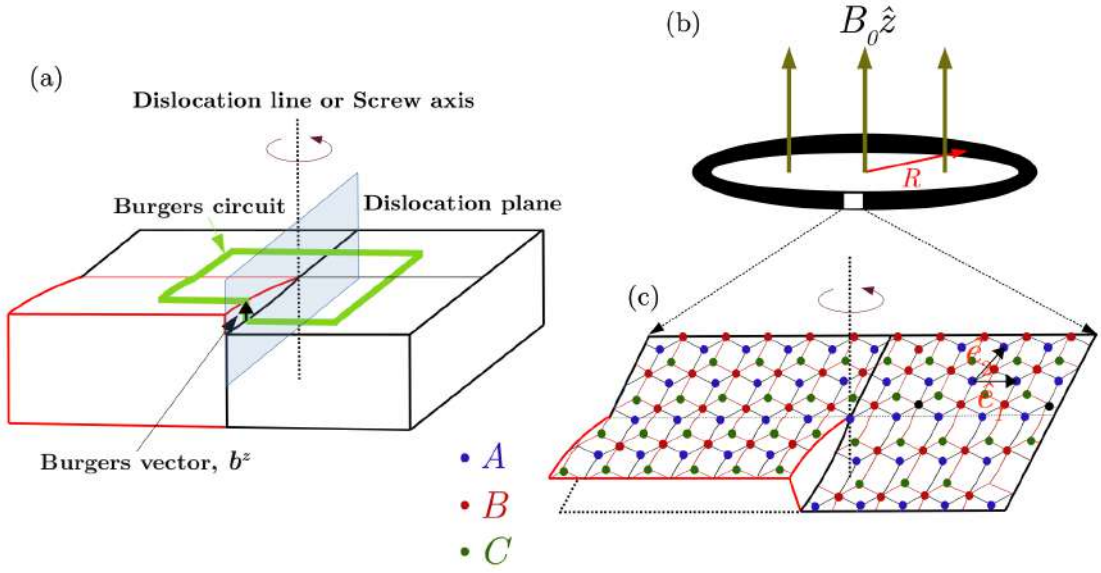

Figure 4.1: (a) Schematic diagram of a screw dislocation. Dislocation line, dislocation plane, Burgers circuit, and Burgers vector have shown in the figure. A counter-clockwise rotation is combined with a translation along the z-axis, resulting in a helical or spiral distortion. (b) A schematic diagram of the α-T_3 ring of radius R subjected to a transverse magnetic field $B = B_0\hat{z}$ and a screw dislocation. (c) Lattice structure of the α-T_3 lattice is shown in the zoomed portion. Here, A, B, and C lattice sites are shown by black, blue, and red dots respectively. Hopping amplitude between the A and B sublattice is t, while between B and C is αt. Black arrows labelled by $\hat{e}_1$ and $\hat{e}_2$ indicate the two translational vectors of the α-T_3 lattice. The lattice is subjected to a screw dislocation.

4.2 α-T_3 QR with Screw Dislocation in Addition with RSOC

In this section we shall investigate the dynamics of particles in a medium with a screw dislocation along the z direction as shown in Fig. 4.1. Before going to the details, let us briefly discuss the screw dislocation. A screw dislocation is a type of linear crystallographic defect or a dislocation within a crystal lattice. Dislocations cause disruptions in the regular arrangement of atoms in a crystal structure. Particularly, a screw dislocation is characterized by a helical or spiral distortion of the atomic planes around a central axis, known as the dislocation line. The dislocation line refers to the line along which the atomic arrangement in a crystal lattice is disrupted or distorted in a helical fashion. A dislocation plane is a theoretical surface or a plane that represents the boundary between two regions of a crystal lattice with different arrangements of

atoms. The dislocation plane is parallel to the dislocation line with the atomic planes on one side of the dislocation line are displaced relative to the planes on the other side. This displacement imparts a twisting or a screw-like distortion to the crystal lattice. Understanding the effects of screw dislocation is crucial in analysing and predicting the behaviour of materials, especially in the context of mechanical properties, deformation, and plasticity, however, they are not under focus in our work. The Burgers vector, denoted as b^z (see Fig. 4.1), represents the magnitude and direction of the lattice distortion associated with a dislocation. The Burgers circuit is a closed path around a dislocation line, and it is chosen in such a way that it encloses the dislocation and returns to the same lattice plane. The Burgers circuit provides information about the Burgers vector by examining the net translation of the crystal lattice around the dislocation. The displacement of the lattice planes along the Burgers circuit is equal to the Burgers vector.

In this case, the three-dimensional geometry of the medium, is characterized by non-trivial torsion which is identified with the surface density of the Burgers vector. Thus, the Burgers vector can be viewed as flux of torsion. The screw dislocation is described by the following metric, in cylindrical coordinates,

$$ds^2 = g_{ij}dx^i dy^j = dr^2 + (dz + \eta d\theta)^2 + r^2 d\theta^2. \tag{4.1}$$

Using usual notations, where $r > 0$, $0 \leqslant \theta \leqslant 2\pi$, and $-\infty \leqslant z \leqslant \infty$, and η is a parameter related to the Burgers vector b^z by $\eta = b^z/2\pi$. A screw dislocation on a crystal surface is illustrated in Fig. 4.1. The illustration depicts a continuous warping of the surface as the growth front advances in the anti-clockwise direction. This process results in the generation of a helix with a specific pitch through accretion. The growth spirals (or helices) are readily observed and have been experimentally found in many crystals. They can be measured precisely by multiple beam interferometry [305, 306]. In fact, several Burgers vectors may be found on a single crystal surface.

Further, when we make a measurement of a physical vector quantity, we require the components of the vector in the original flat space (the laboratory coordinates). For example, the expectation value of the momentum is obtained by using the momentum operator,

$$\begin{aligned} \hat{\mathbf{p}} &= -i\hbar\nabla = -i\hbar\hat{e}_i\zeta^{ij}\partial_j = -i\hbar\hat{e}_i\partial^i, \\ \langle p^i\rangle &= \langle\psi|\hat{p}^i|\psi\rangle, i = x, y, z, \end{aligned} \tag{4.2}$$

where $\zeta^{ij} = \delta^{ij}$ is the flat-space metric, and ψ is the wave function. If the wave function on the constrained surface is given, we transform the momentum operator as follows [307, 308],

$$\hat{p}^i = -i\hbar\partial^i = -i\hbar g^{\mu\nu}\frac{\partial x^i}{\partial \tilde{x}^\mu}\frac{\partial}{\partial \tilde{x}^\nu} = -i\hbar\tilde{\partial}^\mu x^i \tilde{\partial}_\mu. \tag{4.3}$$

The coordinate indices in the curved space are given by the Greek letters (μ, ν), and the curved space coordinates are denoted by $\tilde{x}^\mu$, with $\tilde{\partial}_\mu$ being the covariant derivative in the curved space. Concisely, the momentum operators for the metric given in Eq. (4.1) can be written in vector form as,

$$\begin{aligned} p^x &= -i\hbar\Big[\cos\theta\frac{\partial}{\partial r} - \frac{\sin\theta}{r}\frac{\partial}{\partial\theta} + \frac{\eta\sin\theta}{r}\frac{\partial}{\partial z}\Big], \\ p^y &= -i\hbar\Big[\sin\theta\frac{\partial}{\partial r} + \frac{\cos\theta}{r}\frac{\partial}{\partial\theta} - \frac{\eta\cos\theta}{r}\frac{\partial}{\partial z}\Big], \\ p^z &= -i\hbar\Big[\frac{\eta^2+r^2}{r^2}\frac{\partial}{\partial z} - \frac{\eta}{r^2}\frac{\partial}{\partial\theta}\Big]. \end{aligned} \tag{4.4}$$

We shall use these momenta to study the Rashba spin-orbit coupled Aharonov-Bohm α-T_3 ring in presence of a topological defect.

Now, we consider that the α-T_3 quantum ring system includes Rashba SOC. The corresponding Hamiltonian can be written as, $H = H_0 + H_R$, where H_0 is the tight-binding term, and H_R is the Rashba spin-orbit coupling term. We write the Hamiltonian as [309],

$$H = -t\sum_{\langle ij\rangle\sigma} c^\dagger_{i\sigma}c_{j\sigma} - \alpha t\sum_{\langle ik\rangle\sigma} c^\dagger_{i\sigma}c_{k\sigma} - i\lambda_R\sum_{\langle ij\rangle\sigma\sigma'} c^\dagger_{i\sigma}(\hat{D}_{ij}\cdot\vec{\sigma})_{\sigma\sigma'}c_{j\sigma'} - i\alpha\lambda_R\sum_{\langle ik\rangle\sigma\sigma'} c^\dagger_{i\sigma}(\hat{D}_{ik}\cdot\vec{\sigma})_{\sigma\sigma'}c_{k\sigma'} + \Big(h.c.\Big), \tag{4.5}$$

where $\sigma = \uparrow, \downarrow$, spin indices and i, j, and k are labels for the sites corresponding to A, B, and C sublattices respectively. The first term is the electron hopping between the A and B sites, while the second one is that between the B and C sites. The summation of $\langle ij\rangle$ ($\langle ik\rangle$) runs over the nearest neighbour sites of A-B (B-C). Further, the Rashba SOC induced by electric fields due to a gradient of the crystal potential [157, 288, 289], where $\vec{\sigma} = (\sigma_x, \sigma_y, \sigma_z)$ is the Pauli matrix vector, $\hat{D}_{ij}$ ($\hat{D}_{ik}$) is the unit vector along the direction of the cross product $\vec{E}_{ij}\times\vec{r}_{ij}$ ($\vec{E}_{ik}\times\vec{r}_{ik}$) of the electric field $\vec{E}_{ij}$ ($\vec{E}_{ik}$) and displacement $\vec{r}_{ij}$ ($\vec{r}_{ik}$) for the bond ij (ik). λ_R is the strength of Rashba SOC between the A and the B sites, while $\alpha\lambda_R$ is that between the B and the C sites.

In momentum space, the Hamiltonian of the α-T_3 lattice becomes,

$$H = \begin{pmatrix} 0 & -t\gamma_{\mathrm{k}}^{*} & 0 & 0 & -i\lambda_R\gamma_{\mathrm{k}+}^{*} & 0 \\ -t\gamma_{\mathrm{k}} & 0 & -\alpha t\gamma_{\mathrm{k}}^{*} & i\lambda_R\gamma_{\mathrm{k}-} & 0 & i\alpha\lambda_R\gamma_{\mathrm{k}+}^{*} \\ 0 & -\alpha t\gamma_{\mathrm{k}} & 0 & 0 & -i\alpha\lambda_R\gamma_{\mathrm{k}-} & 0 \\ 0 & -i\lambda_R\gamma_{\mathrm{k}-}^{*} & 0 & 0 & -t\gamma_{\mathrm{k}}^{*} & 0 \\ i\lambda_R\gamma_{\mathrm{k}+} & 0 & i\alpha\lambda_R\gamma_{\mathrm{k}-}^{*} & -t\gamma_{\mathrm{k}} & 0 & -\alpha t\gamma_{\mathrm{k}}^{*} \\ 0 & -i\alpha\lambda_R\gamma_{\mathrm{k}+} & 0 & 0 & -\alpha t\gamma_{\mathrm{k}} & 0 \end{pmatrix} \tag{4.6}$$

where $\gamma_{\mathrm{k}} = 1 + e^{ik_1} + e^{ik_2}$ and $\gamma_{\mathrm{k}\pm} = 1 + e^{i(k_1 \pm 2\pi/3)} + e^{i(k_2 \pm 4\pi/3)}$. The components are along the axes indicated in Fig. 4.1(c) as $k_i = \vec{k} \cdot \hat{\mathrm{e}}_i$. Our basis for writing this Hamiltonian is $(c_{1\mathrm{k}\uparrow}, c_{2\mathrm{k}\uparrow}, c_{3\mathrm{k}\uparrow}, c_{1\mathrm{k}\downarrow}, c_{2\mathrm{k}\downarrow}, c_{3\mathrm{k}\downarrow})$. In the vicinity of a Dirac point (namely, K), and taking the momentum correction (4.4) due to screw dislocation into account, the Hamiltonian (4.6) corresponding to an ideal α-T_3 ring is given by,

$$H_{ring} = \frac{\hbar v_F}{R} \begin{pmatrix} 0 & -i(m-k\eta+\frac{1}{2})\cos\varphi e^{\frac{i\pi}{3}} & 0 & 0 & -\frac{\lambda_R}{t}(m-k\eta+\frac{1}{2})\cos\varphi e^{\frac{i\pi}{3}} & 0 \\ i(m-k\eta+\frac{1}{2})\cos\varphi e^{-\frac{i\pi}{3}} & 0 & -i(m-k\eta-\frac{1}{2})\sin\varphi e^{\frac{i\pi}{3}} & \frac{\lambda_R}{t}(m-k\eta-\frac{1}{2})\cos\varphi e^{\frac{i\pi}{3}} & 0 & -\frac{\lambda_R}{t}(m-k\eta+\frac{1}{2})\sin\varphi e^{-\frac{i\pi}{3}} \\ 0 & i(m-k\eta-\frac{1}{2})\sin\varphi e^{-\frac{i\pi}{3}} & 0 & 0 & -\frac{\lambda_R}{t}(m-k\eta-\frac{1}{2})\sin\varphi e^{-\frac{i\pi}{3}} & 0 \\ 0 & \frac{\lambda_R}{t}(m-k\eta-\frac{1}{2})\cos\varphi e^{-\frac{i\pi}{3}} & 0 & 0 & i(m-k\eta-\frac{1}{2})\cos\varphi e^{-\frac{i\pi}{3}} & 0 \\ -\frac{\lambda_R}{t}(m-k\eta+\frac{1}{2})\cos\varphi e^{-\frac{i\pi}{3}} & 0 & \frac{\lambda_R}{t}(m-k\eta-\frac{1}{2})\sin\varphi e^{\frac{i\pi}{3}} & -i(m-k\eta-\frac{1}{2})\cos\varphi e^{\frac{i\pi}{3}} & 0 & i(m-k\eta+\frac{1}{2})\sin\varphi e^{-\frac{i\pi}{3}} \\ 0 & -\frac{\lambda_R}{t}(m-k\eta+\frac{1}{2})\sin\varphi e^{\frac{i\pi}{3}} & 0 & 0 & -i(m-k\eta+\frac{1}{2})\sin\varphi e^{\frac{i\pi}{3}} & 0 \end{pmatrix} \tag{4.7}$$

where $\tan\varphi = \alpha$ and $\hbar v_F = 3at/2\cos\varphi$. The eigenstates of the ring Hamiltonian can be obtained as,

$$\psi(R,\theta) = \begin{pmatrix} \chi_{1\uparrow}(R)e^{i\theta} \\ \chi_{2\uparrow}(R) \\ \chi_{3\uparrow}(R)e^{-i\theta} \\ \chi_{1\downarrow}(R)e^{-i\theta} \\ \chi_{2\downarrow}(R) \\ \chi_{3\downarrow}(R)e^{i\theta} \end{pmatrix} e^{im\theta}e^{ikz} \tag{4.8}$$

where the integer m labels the orbital angular momentum quantum number, k is the momentum along the z direction and χ_is denote the amplitudes corresponding to the three sublattices. Here, we investigate the electronic behaviour of the ring at a given value of radius r, namely $r = R$, such that the radial part is rendered frozen in the eigensolutions. To account for the hermiticity of the Hamiltonian in ring geometry, we made the replacements $r \to R$ and $\frac{\partial}{\partial r} \to -\frac{1}{2R}$ and

obtain the energy spectrum as,

$$\begin{aligned} E_1 &= 0 \\ E_2 &= \kappa\frac{\epsilon}{2}\left\{\left[1+4\big(m-k\eta\big)^2-4\big(m-k\eta\big)\frac{1-\alpha^2}{1+\alpha^2}\right]\left(1+\frac{\lambda_R^2}{t^2}\right)\right\}^{\frac{1}{2}} \\ E_3 &= \kappa\frac{\epsilon}{2}\left\{\left[1+4\big(m-k\eta\big)^2\right]\left(1+\frac{\lambda_R^2}{t^2}\frac{1-\alpha^2}{1+\alpha^2}\right)+4\big(m-k\eta\big)\left(\frac{\lambda_R^2}{t^2}+\frac{1-\alpha^2}{1+\alpha^2}\right)\right\}^{\frac{1}{2}} \end{aligned} \tag{4.9}$$

where κ $(=\pm 1)$ is the particle-hole index and $\epsilon = \frac{\hbar v_F}{R}$. E_1 is the zero energy flat band, E_2 and E_3 correspond to the energies for the $\uparrow$-spin and $\downarrow$-spin bands respectively. The energy spectra at the K valley in presence of Rashba SOC and screw dislocation are expressed in Eq. (4.9). Further, the scattering effects due to the presence of screw dislocation are included as follows. In fact, the phase shift suffered by a particle incoming with a momentum k and scattered with angular momentum quantum number m by a screw dislocation may be derived as follows. The detailed calculations are provided in Appendix D. The resulting phase shifts can be expressed as [310–312],

$$\delta_m(\vec{k}) = -\frac{\pi}{2}\left(|m+\frac{\vec{k}\cdot\vec{b^z}}{2\pi}|-|m|\right) = -\frac{\pi}{2}\left(|m+k\eta|-|m|\right). \tag{4.10}$$

This alteration in phase, induced by the presence of the screw dislocation, will have implications for the transport properties of the system. A detailed discussion on such effects will be presented in the subsequent sections.

4.3 Discussion on the Energy Spectrum

4.3.1 Without magnetic field ($B_0 = 0$)

In Figs. 4.2(a) and (b) we illustrate the energies as a function of the ring radius, R, for various values of α at fixed λ_R and $k\eta$ values. In this case, we have considered a particular value for the RSOC and screw dislocation, namely, $\lambda_R = 0.5t$ and $k\eta = 0.3$ corresponding to $\alpha = 0.5$ and 1, and plotted only the $m = -1$, 0, and 1 bands represented by red, green, and blue curves, respectively. When $\lambda_R = 0$, the system exhibits three bands, with one being a flat band. However, with a non-zero λ_R the original three bands split into six spin dependent bands, including two non-dispersive flat bands and four dispersive bands as described by Eq. (4.9). From Fig. 4.2, it is evident that all the energy branches have a $1/R$ dependence and approach $E \to 0$ for very large radii, irrespective of the value of α. Additionally, the dispersive bands

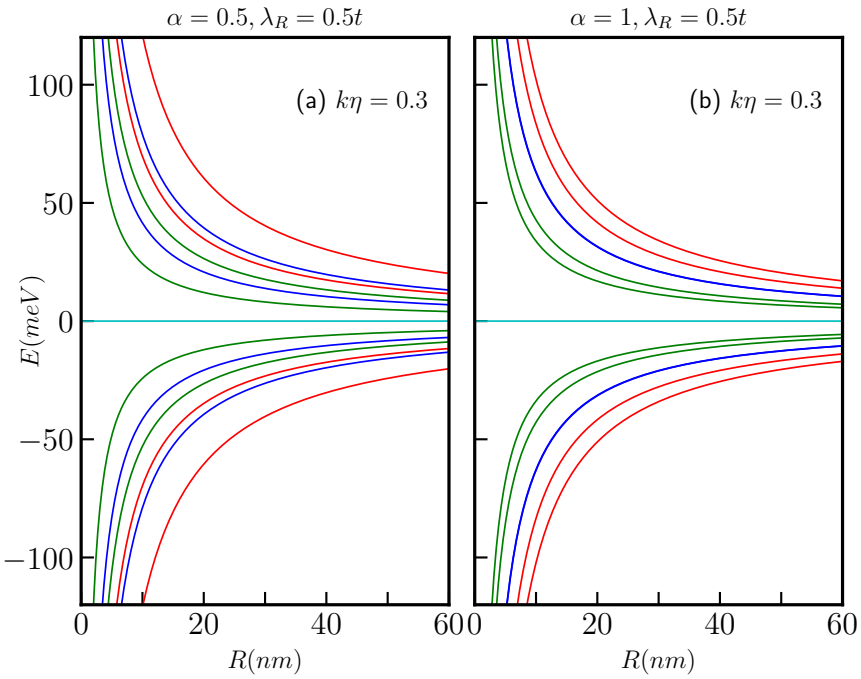

Figure 4.2: The spin-split energy spectra in the absence of a magnetic field for the α-T_3 AB ring are depicted as a function of the ring radius, R, for quantum numbers $m = 0$ (green curves), $m = 1$ (blue curves), and $m = -1$ (red curves) in the presence of a topological defect with a magnitude of $k\eta = 0.3$ are presented in panels (a) for $\alpha = 0.5$ and (b) for $\alpha = 1$. The Rashba coupling parameter is all the while set at $\lambda_R = 0.5t$. The flat band is represented using the cyan color, and this convention will be maintained throughout the rest of the chapter.

remain non-degenerate, in contrary to the case of the pseudospin-1 α-T_3 QR without SOC. The scenario involving a topological defect arises when we implement the transformation which renormalized the angular momentum quantum number, m via $m' \to (m - k\eta)$. Consequently, upon examining Eq. (4.9), it becomes apparent that, unlike the situation where $k\eta = 0$, all the energy levels for both $\uparrow$-spin and $\downarrow$-spin states, including the $m = 0$ bands, become dependent on the parameters α and λ_R. Hence, the splitting between the spin-split bands hinges on the presence of dislocations in the system, the parameter α, and the strength of the Rashba coupling, λ_R, as dictated by Eq. (4.9). Furthermore, for $\alpha = 1$, that is,for the dice lattice, the energies are given by,

$$E_2 = \frac{\kappa\epsilon}{2}\sqrt{[1 + 4(m - k\eta)^2](1 + \frac{\lambda_R^2}{t^2})} \tag{4.11}$$

and

$$E_3 = \frac{\kappa\epsilon}{2}\sqrt{1 + 4(m - k\eta)^2 + 4(m - k\eta)\frac{\lambda_R^2}{t^2}}. \tag{4.12}$$

It is worth noting that E_2 and E_3 are non-degenerate, in contrast to the case that deals without screw dislocation (Chapter 3, Sec. 3.3.1). Additionally, the quantum number m undergoes a shift that depends on η, which is associated with the Burgers vector. This shift is a manifestation

of the Aharonov-Bohm effect, akin to what is observed in the context of a one-dimensional quantum ring penetrated by a magnetic flux [20].

The energy levels as a function of the strength of the screw dislocation are presented in Fig. 4.3 for two distinct cases, namely, $\alpha = 0.5$ and $\alpha = 1$ (dice lattice). Moreover, Eq. (4.9) makes it clear that the dispersive energy levels exhibit a hyperbolic dependence on the screw dislocation. It is important to note that the energy spectrum depends on the Burgers vector, $b^z = 2\pi\eta$, as well as the radius, R of the ring, and hence associated with the geometry of the system.

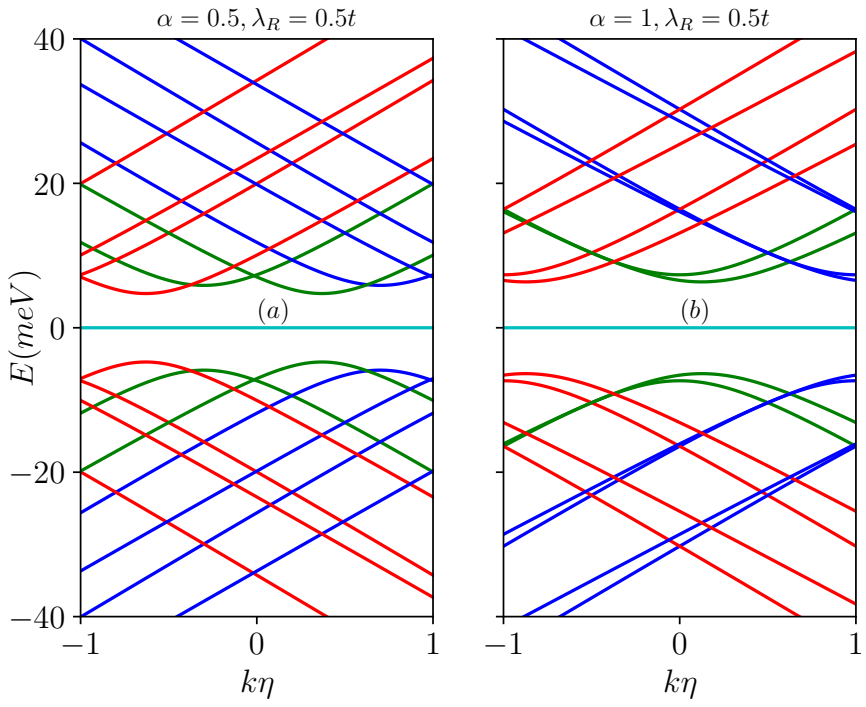

Figure 4.3: Energy levels in the absence of a magnetic field, as a function of the screw dislocation parameter $k\eta$, are depicted for (a) $\alpha = 0.5$ and (b) $\alpha = 1$, with a fixed ring radius of $R = 50\ nm$. The energy levels corresponding to different total angular momentum quantum numbers, namely $m = -1, -2$ (red curves), $m = 0$ (green curves), and $m = 1, 2$ (blue curves), are presented. The Rashba coupling parameter remains constant at $\lambda_R = 0.5t$.

Additionally, there are spin resolved energy extrema, with maxima in the valence bands and minima in the conduction bands. The positions of these extrema are determined by the strength of dislocation as follows. For the $\uparrow$-spin bands, the extrema are found at,

$$k\eta = m - \frac{1}{2}\left(\frac{1-\alpha^2}{1+\alpha^2}\right) \tag{4.13}$$

which is independent of λ_R. For the dice case ($\alpha = 1$), the extrema occur at $k\eta = m$. However, for the $\downarrow$-spin bands, the extrema occur at,

$$k\eta = m + \frac{1}{2}\left(\frac{\frac{\lambda_R^2}{t^2} + \frac{1-\alpha^2}{1+\alpha^2}}{1 + \frac{\lambda_R^2}{t^2}\frac{1-\alpha^2}{1+\alpha^2}}\right). \tag{4.14}$$

The expression above shows a dependency on λ_R and hence we shall observe an interplay between the dislocation and RSOC. In fact, this interplay gives rise to interesting consequences as we shall see later. Furthermore, for each value of m, a band crossing point exists for $\alpha < 1$. However, in the case of $\alpha = 1$, no band crossings occur, instead, the bands touch each other at certain specific $k\eta$ values, depending upon the parameter λ_R.

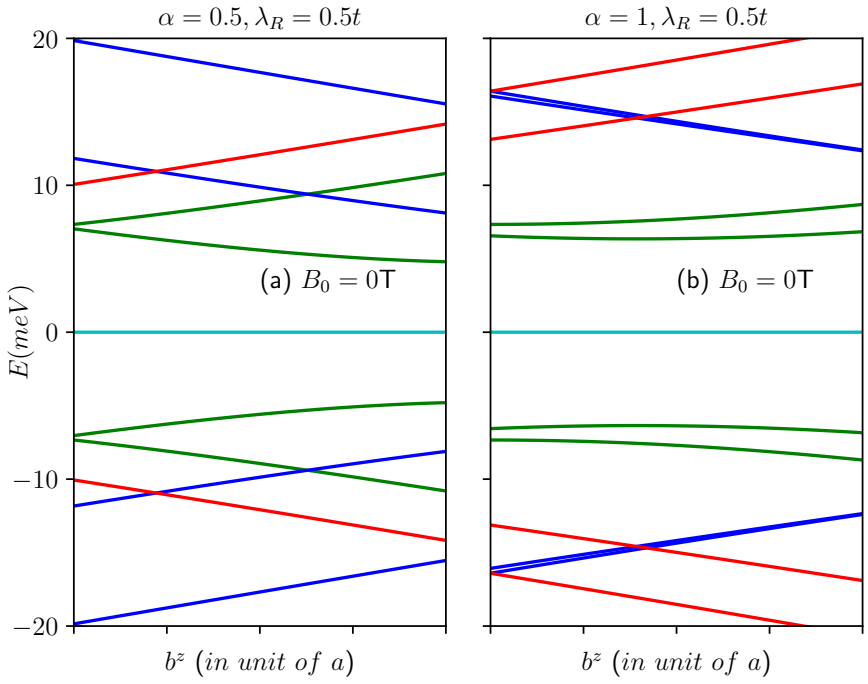

Figure 4.4: The energy spectra as a function of the Burgers vector in absence of magnetic field (a) for $\alpha = 0.5$ and (b) for $\alpha = 1$. The quantum number m ranges from -1 to 1. Positive values of m represented by blue curves, $m = 0$ depicted by green curves, and negative values by red curves. The Rashba coupling parameter remains constant at $\lambda_R = 0.5t$.

The energy levels as a function of the Burgers vector, b^z (in unit of the lattice constant) in the absence of a magnetic field are shown in Figs. 4.4(a) for $\alpha = 0.5$ and (b) for $\alpha = 1$. For a particular value of α, increasing b^z results in a linear increase in the conduction band energy levels corresponding to negative m values and a linear decrease in the energy levels for the positive values of m. Additionally, for $\alpha < 1$ (here $\alpha = 0.5$), the energy level of the $\uparrow$-spin in the $m = 0$ band increases, while that for the $\downarrow$-spin level decreases. Moreover, when $\alpha = 1$, the energy levels associated with the $m = 0$ bands decrease as b^z increases (shown in green curves in Fig. 4.4(b)). In the valence band, an opposite trend is observed where the energy levels for negative m decrease linearly, while the energy levels for positive m increase linearly. Furthermore, for $\alpha < 1$, the $\downarrow$-spin energy level of the $m = 0$ band increases, while that for the

$\uparrow$-spin level decreases. With increase in α, the energy difference between the spin-split bands diminishes (see Figs. 4.4(a) and (b)). However, it is worth noting that the $m = 0$ bands remain as the low-energy bands in the absence of a magnetic field. The scenario in presence of the magnetic field is described later.

4.3.2 With magnetic field ($B_0 \neq 0$)

Now let us discuss the case when the α-T_3 ring is threaded by a perpendicular magnetic field $\mathbf{B} = B_0\hat{z}$. The only non-zero component of the vector potential is $A_\theta = B_0 r/2$. Notice that, in the non-Euclidean metric of the dislocation, the vector potential that produces the uniform magnetic field is identical to the flat space (Euclidean) potential vector. The spectrum of the system is modified by the field as follows,

$$
\begin{aligned}
&E_1(\Phi) = 0 \\
&E_2(\Phi) = \kappa\frac{\epsilon}{2}\left\{\left[1 + 4\big(m - k\eta + \frac{\Phi}{\Phi_0}\big)^2 - 4\big(m - k\eta + \frac{\Phi}{\Phi_0}\big)\frac{1-\alpha^2}{1+\alpha^2}\right]\left(1 + \frac{\lambda_R^2}{t^2}\right)\right\}^{\frac{1}{2}} \\
&E_3(\Phi) = \kappa\frac{\epsilon}{2}\left\{\left[1 + 4\big(m - k\eta + \frac{\Phi}{\Phi_0}\big)^2\right]\left(1 + \frac{\lambda_R^2}{t^2}\frac{1-\alpha^2}{1+\alpha^2}\right) + 4\big(m - k\eta + \frac{\Phi}{\Phi_0}\big)\left(\frac{\lambda_R^2}{t^2} + \frac{1-\alpha^2}{1+\alpha^2}\right)\right\}^{\frac{1}{2}}
\end{aligned}
\tag{4.15}
$$

where $\Phi = \pi R^2 B_0$ is magnetic flux through the ring and Φ_0 is the usual flux quantum ($= h/e$). The Zeeman coupling has been neglected at small enough values of the field. The addition of a magnetic field, represented by a U(1) minimal coupling with flux Φ threading the ring, breaks the time reversal symmetry allowing for the emergence of persistent charge currents [6] which we shall discuss later.

Referring to Equation (4.15), we find that all of the previously discussed (in Chapter 3, Sec. 3.3.2) characteristics remain unaltered, except we may consider that m as an effective quantum number, let us call it as m' with $m' \to (m - k\eta)$ which has a shift in the m values by an amount of $k\eta$. The results are visually represented in Figs. 4.5(a) and (b), where we show the dependence of a few energy levels on the ring radius, R, considering $B_0 = 3$T for the two aforementioned cases that is, $\alpha = 0.5$ and 1 with $\lambda_R = 0.5t$ and the parameter $k\eta$ set to a modest value, namely, $k\eta = 0.3$. Again, for the case of $\alpha = 1$, the band crossing points emerge at $R = \sqrt{2}l_0\sqrt{\frac{1}{2} - (m - k\eta)}$, signifying a shift to the right as depicted in Fig. 4.5(b).

Furthermore, the conditions for the extremal points now becomes,

$$
\frac{\Phi}{\Phi_0} = -(m - k\eta) + \frac{1}{2}\left(\frac{1-\alpha^2}{1+\alpha^2}\right) \tag{4.16}
$$

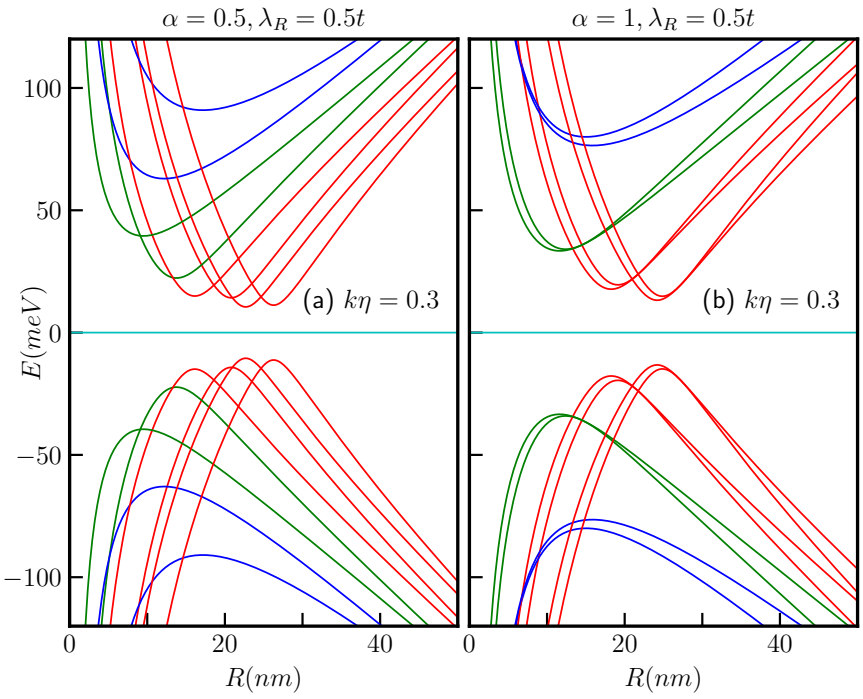

Figure 4.5: The energy spectra as a function of the ring radius R of the α-T_3 quantum ring under the influence of an external magnetic field with a strength of $B_0 = 3$T at the K valley are presented in panels (a) for $\alpha = 0.5$ and (b) for $\alpha = 1$, we introduce a screw dislocation with a magnitude of $k\eta = 0.3$. The parameters used in these calculations are $\lambda_R = 0.5t$ and $t = 1eV$. The quantum number m ranges from -2 to 2, with positive values of m represented by blue curves, $m = 0$ depicted by green curves, and negative values by red curves.

for $\uparrow$-spin band E_2, the extrema points are independent of the strength of the Rashba coupling, but depends on the values of m and the parameter α. However, the extrema for the $\downarrow$-spin band E_3 occur at,

$$\frac{\Phi}{\Phi_0} = -(m - k\eta) - \frac{1}{2}\left(\frac{\frac{\lambda_R^2}{t^2} + \frac{1-\alpha^2}{1+\alpha^2}}{1 + \frac{\lambda_R^2}{t^2}\frac{1-\alpha^2}{1+\alpha^2}}\right), \tag{4.17}$$

showing a dependency on the strength of Rashba SOC (λ_R), α and m. Thus, we can conclude that the location of the extremal points are also modified due to $m' \to (m - k\eta)$, resulting in a displacement of these extremal points by an amount equal to $k\eta$ in the positive direction, as illustrated in Figs. 4.6(a)-(d).

The energy gaps at the extrema points, that is, the minimum values of the gaps between the valence and the conduction bands are given by,

$$\begin{aligned} \Delta E_2 &= \frac{2\epsilon\alpha}{1+\alpha^2}\sqrt{1 + \frac{\lambda_R^2}{t^2}}, \\ \Delta E_3 &= \frac{2\epsilon\alpha}{1+\alpha^2}\sqrt{\frac{1 - \frac{\lambda_R^4}{t^4}}{1 + \frac{\lambda_R^2}{t^2}\frac{1-\alpha^2}{1+\alpha^2}}}. \end{aligned} \tag{4.18}$$

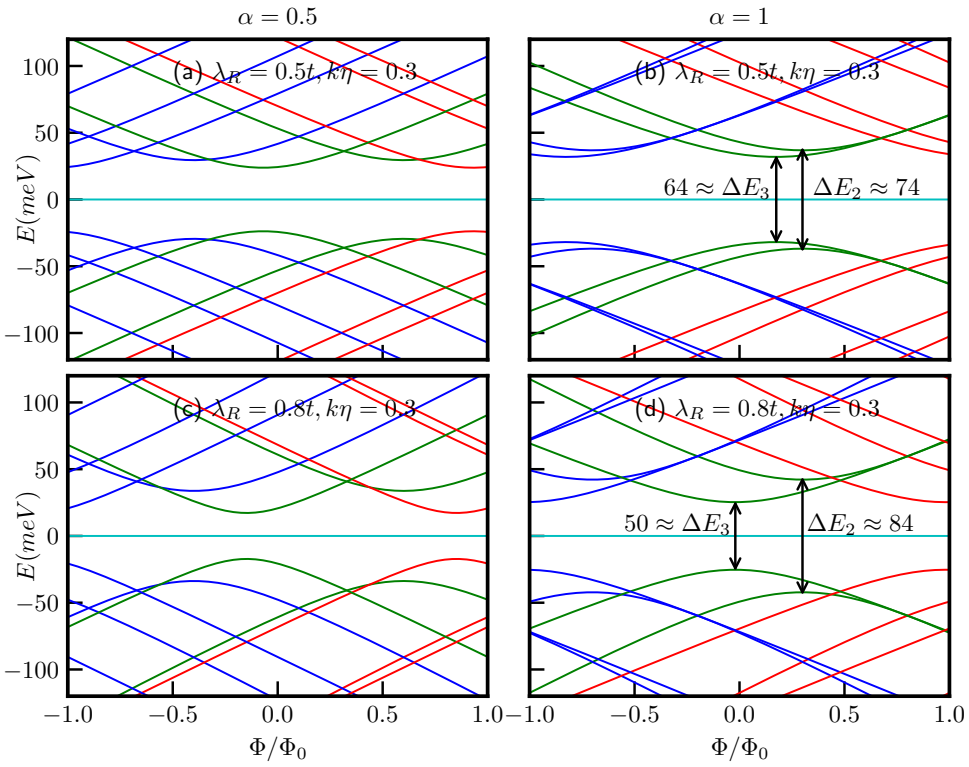

Figure 4.6: The energy levels as functions of the external magnetic flux Φ/Φ_0 with a fixed ring radius of $R = 10\ nm$, maintain the same conventions for the quantum number m as in the previous plots. We explore various combinations of α, λ_R, and $k\eta$ as follows: (a) $\alpha = 0.5$, $\lambda_R = 0.5t$, and $k\eta = 0.3$, (b) $\alpha = 1$, $\lambda_R = 0.5t$, and $k\eta = 0.3$, (c) $\alpha = 0.5$, $\lambda_R = 0.8t$, and $k\eta = 0.3$, and (d) $\alpha = 1$, $\lambda_R = 0.8t$, and $k\eta = 0.3$.

It is important to note that the energy gaps at these extremal points, as per Eq. (4.18), are not influenced by the presence of the topological defect ($k\eta$), their dependencies solely rely on the parameters α and λ_R. To demonstrate this, we have considered two values of λ_R, namely, $\lambda_R = 0.5t$ and $\lambda_R = 0.8t$. The energy gap values for the $\alpha = 1$ case are presented in the respective figures (see Fig. 4.6).

In this particular scenario, we are dealing with a one-dimensional quantum ring in the presence of a screw dislocation and Aharonov–Bohm flux. The energy spectrum displays a parabolic dependence on the Burgers vector, similar to its dependence on the magnetic flux. Upon analysing our findings, we could infer that a particle within a space featuring a topological defect behaves similarly to a particle in a Euclidean space in the presence of an effective magnetic flux threading the ring. This effective flux arises from a combination of two contributions, the first is of a topological nature stemming from the topological defect, while the other is due to the magnetic flux Φ. By adjusting the magnetic flux as an external fine-tuning parameter to counterbalance the topological contribution introduced by the defect, we can nullify the Aharonov–Bohm effect in the ring. In such cases, the energy spectrum resembles that of a particle moving in a quantum

ring in a space devoid of any magnetic flux. This is a very important result. Conversely, it provides a clue how the effects of a topological defect can be totally or partially compensated by an external field with regard to the observation of the AB effect. Further consequences on the spin and charge currents are elucidated below.

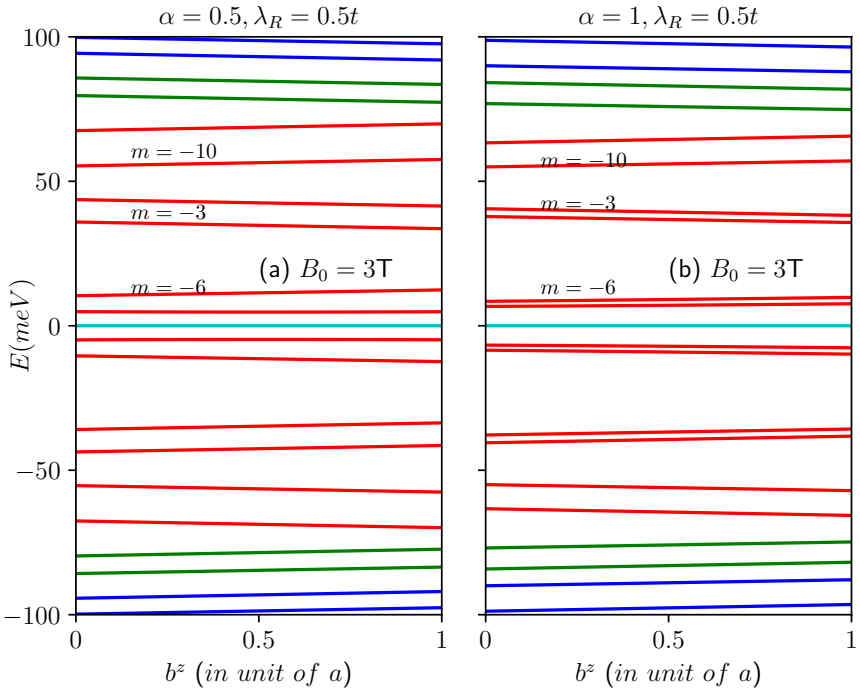

Figure 4.7: The energy spectra as a function of the Burgers vector in presence of magnetic field of $B_0 = 3$T (a) for $\alpha = 0.5$ and (b) for $\alpha = 1$. The quantum numbers are shown in the plots. Positive values of m represented by blue curves, $m = 0$ depicted by green curves, and negative values by red curves.

The energy levels as a function of the Burgers vector in presence of a magnetic field of $B_0 = 3$T are illustrated in Fig. 4.7(a) for $\alpha = 0.5$ and (b) for $\alpha = 1$. The plots show a deviation from the previous scenario corresponding to zero magnetic field. In this case, the energy levels of both the conduction and the valence bands remain nearly unchanged as a function of b^z. Notably, the $m = 0$ bands no longer represent the lowest energy states, instead, the negative m bands possess lower energy than the $m = 0$ bands in presence of the magnetic field. These bands contribute significantly to the transport properties of the system. As the quantum number m becomes more negative, the energy difference between the valence and the conduction bands decreases. Specifically, for $m = -6$, the system exhibits the minimum spectral gap. Subsequently, the gap between the conduction bands and valence bands increase with $|m|$, as illustrated in Figs. 4.7(a) and (b). Additionally, as α increases, the energy difference between the spin-split bands for negative m decreases, while that for the $m \geq 0$ bands increases. Thus, a screw dislocation, among other things, presents distinct spectral properties in presence and absence of an external magnetic field.

4.4 Persistent Currents

4.4.1 Charge persistent current

The charge persistent current in the low-energy state can be calculated using the linear response formula, $j_Q = -\sum_{m,\kappa} \frac{\partial E}{\partial \Phi}$, where the sum refers to all (and only) the occupied states (for the valence band ($\kappa = -1$)) and the m values are chosen carefully to perform the summation. Since the current is periodic in Φ/Φ_0 with a unit period (that is $\Phi = \Phi_0$), we restrict the discussion to the window $-1 \leq \Phi/\Phi_0 \leq 1$. The analytical form for the charge current is obtained as,

$$j_Q^{\kappa} = -\frac{\epsilon^2\kappa}{2\Phi_0}\sum_m \frac{(1+\frac{\lambda_R^2}{t^2})\left[2(m-k\eta+\frac{\Phi}{\Phi_0})-\frac{1-\alpha^2}{1+\alpha^2}\right]}{E_2(\Phi)} - \frac{\epsilon^2\kappa}{2\Phi_0}\sum_m \frac{2(m-k\eta+\frac{\Phi}{\Phi_0})(1+\frac{\lambda_R^2}{t^2}\frac{1-\alpha^2}{1+\alpha^2})+(\frac{\lambda_R^2}{t^2}+\frac{1-\alpha^2}{1+\alpha^2})}{E_3(\Phi)}. \tag{4.19}$$

The spin branches closest to the Fermi energy exhibit non-monotonic behaviour, resulting in two distinct contributions to the charge current coming from the $\uparrow$-spin and $\downarrow$-spin components. Since we are calculating the current contributions arising from the low-energy states, it is clear from Fig. 4.6 that for a certain range of Φ/Φ_0, only one energy state labelled by a particular value of m is present. Hence, the sum in Eq. (4.19) comprises of only one value of m. Furthermore, based on the observations in Fig. 4.6, we can discern that the low-energy states when $\alpha = 0.5$ encompass both the spin bands. Consequently, in our current calculations, we considered contributions from both the spin branches. In contrast, for the $\alpha = 1$ scenario, the low-energy state exclusively comprises the $\downarrow$-spin branches, and thus, we only have accounted for the contributions from the $\downarrow$-spin to compute the persistent current. The outcomes of these calculations are depicted in Fig. 4.8 for both $\alpha = 0.5$ and $\alpha = 1$, considering various combinations of λ_R and $k\eta$, all the while maintaining a fixed ring radius of $R = 10\ nm$.

To solely observe the effects of screw dislocation here we have also depicted the results of without dislocation ($k\eta = 0$). The asymmetric spectral features between the two spin branches allows for the possibility of a net spin currents, as we shall see below. For all values of α, the persistent currents oscillate periodically with Φ/Φ_0, with a periodicity of $\Phi/\Phi_0 = 1$. Figs. 4.8(a) and (b) illustrate that the persistent currents can be tuned by adjusting the parameter α for a fixed value of the Rashba coupling (λ_R). Moreover, the charge persistent currents can be manipulated via λ_R for a fixed α, (see Figs. 4.8(a), (c) and (e)) since the Rashba parameter can be controlled by a gate voltage. Further, it is worth noting the presence of a kink in the current profile when $\alpha < 1$. This kink arises because different spin bands contribute to the current, as indicated by the distinctions denoted by $\uparrow$ and $\downarrow$ for their respective spin bands. However, this kink phenomenon is absent for the dice lattice ($\alpha = 1$), as evident in Figs. 4.8(b), (d), and (f).

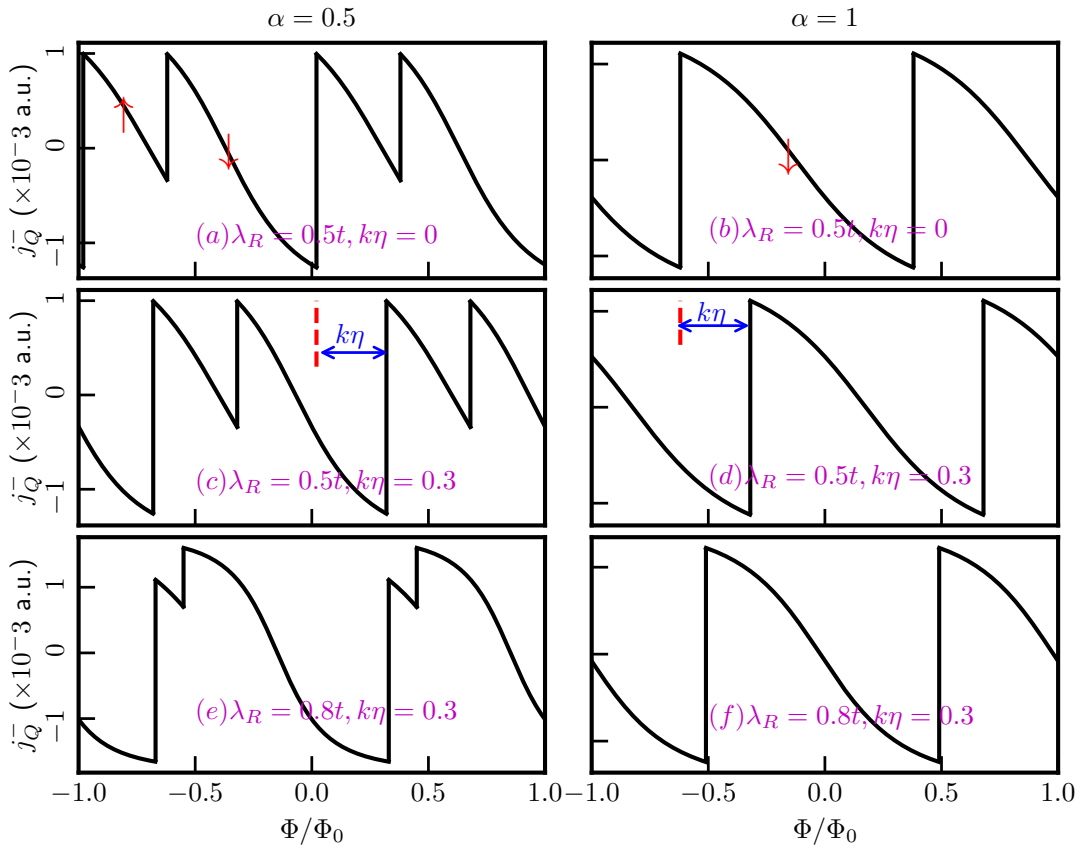

Figure 4.8: The charge persistent currents are plotted as functions of the external magnetic flux, considering the low-energy states without accounting for the topological defect, in panels (a) for $\alpha = 0.5$ and (b) for $\alpha = 1$, with $\lambda_R = 0.5t$. In panels (c) and (d), the same currents are presented in the presence of the screw dislocation term $k\eta = 0.3$, for $\alpha = 0.5$ and $\alpha = 1$ respectively. Panels (e) and (f) highlight the impact of the Rashba SOC as we increase the λ_R parameter to $0.8t$, while keeping $k\eta = 0.3$ fixed for $\alpha = 0.5$ and 1 respectively. In panels (a) and (b), the labels $\uparrow$ and $\downarrow$ denote the currents from the corresponding spin bands. In panels (c) and (d), the phase shift is represented by the blue arrows. Here, a.u. refers to arbitrary unit where we have considered $\hbar = e = v_F = 1$.

The reason being, in this case, only the $\downarrow$-spin bands contribute to the current, as mentioned earlier.

Furthermore, the topological defect plays a pivotal role in the behaviour of the charge current. As illustrated in Figure 4.8, we can observe that, for a fixed value of λ_R, the screw dislocation induces a phase shift in the current, regardless of the specific value of α. For example, every point of the current profile is shifted by the same amount as the strength of the topological defect as shown in the middle panel of Fig. 4.8. However, the topological defect does not influence the current profile itself. A desired shift in the current profile may be achieved via the controllable parameter $k\eta$. Further, the Rashba coupling, λ_R plays a role as well. The depth in the kink of the current profile decreases with the increasing λ_R (see bottom panel of Fig. 4.8). This can be understood from the lower panel of Figure 4.6, as the increase in λ_R results in a decrease

in the ↑-spin contribution in the low-energy state which occurs within a certain range of Φ/Φ_0. However, the overall oscillation period remains unaltered.

In summary, we can manipulate the persistent current profile by fine-tuning the Rashba coupling, and we have the ability to shift the phase of the current to suit our specific applications by adjusting the strength of the topological defect.

4.4.2 Equilibrium spin current

We shall now study equilibrium spin currents. In contrast to the formalism for obtaining the charge current, one can obtain the spin currents by accounting for distinct velocities for different spin branches. Thus, we define equilibrium spin current as,

$$j_S = j_Q(\uparrow) - j_Q(\downarrow). \tag{4.20}$$

We have calculated the equilibrium spin currents following the procedure discussed earlier. The peculiar separation of the spin branches results in differences of the velocities between the two spin projections, giving rise to a spin current, as shown in Fig. 4.9. The figure illustrates a significant spin current for small values of the flux, which can be attributed to the large charge current originating from a single spin branch.

The striking feature is that the magnitude as well as the pattern of the spin currents depend upon the parameters α and the strength of the Rashba coupling (λ_R). We present results for $\alpha = 0.5$, and $\alpha = 1$ with different values of λ_R and topological defect $k\eta$ for a ring of radius, $R = 10\ nm$. The presence of the Rashba coupling breaks inversion symmetry (in addition to the σ_z symmetry) in the plane even for small λ_R. The symmetry breaking determines the spin labelling of the energy branches that take part in yielding the spin currents. Additionally, the spin currents exhibit periodic behaviour with Φ/Φ_0, with a periodicity equal to one flux quantum, irrespective the value of α. This implies that the spin transport is insensitive to tuning of the A-C hopping. Similar to the case of charge persistent current, we also notice a phase shift introduced by the topological defect. The magnitude of this phase shift precisely corresponds to the strength of the defect.

To gain further insights, we present a color plot illustrating the equilibrium spin current (j_S) as a function of the strength of Rashba SOC and the topological defect in Fig. 4.10. The color map allows us to observe the interplay between these two parameters at a specific value of the magnetic flux, namely, $\Phi/\Phi_0 = 0.3$. Further, we have considered the angular momentum quantum number fixed at $m = 0$, which is most relevant for the flux used here. The observed behaviour

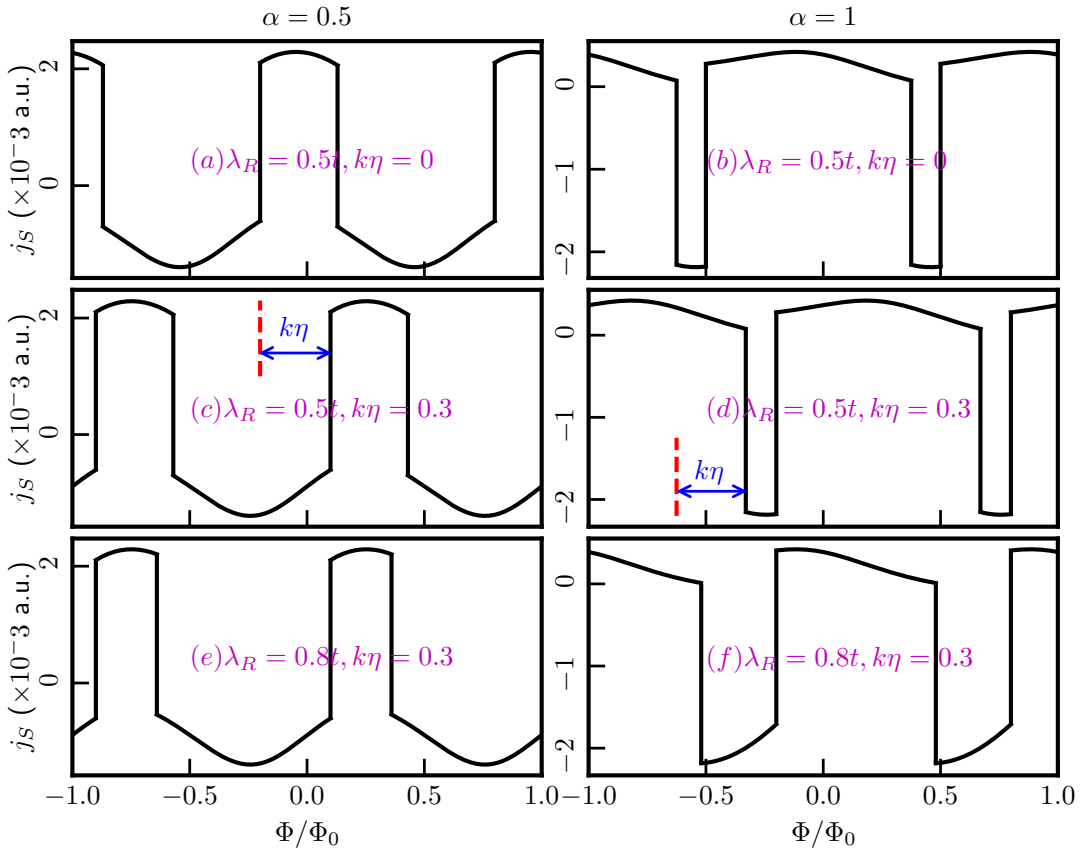

Figure 4.9: The equilibrium spin currents are plotted as functions of the external magnetic flux, considering the low-energy states without accounting for the topological defect, in panels (a) for $\alpha = 0.5$ and (b) for $\alpha = 1$, with $\lambda_R = 0.5t$. In panels (c) and (d), the same currents are presented in the presence of the screw dislocation term $k\eta = 0.3$, for $\alpha = 0.5$ and $\alpha = 1$ respectively. Panels (e) and (f) highlight the impact of the Rashba SOC as we increase the λ_R parameter to $0.8t$, while keeping $k\eta = 0.3$ fixed for $\alpha = 0.5$ and 1 respectively. In panels (c) and (d), the phase shift is represented by the blue arrows.

reveals that the spin persistent current oscillates between negative and positive values as we tune the strength of the topological defect for a fixed value of λ_R. For $\alpha < 1$ (see Figure 4.10(a)), we observe a significant variation as a function of the defect in the spin persistent current for all values of λ_R (in unit of t). In contrast, for $\alpha = 1$ (as depicted in Figure 4.10(b)), the variation is less pronounced for small values of λ_R, whereas it becomes more significant as we increase λ_R. Furthermore, the color map suggests that to achieve the maximum spin persistent current for a spintronic device, one requires a high value of λ_R and the strength of the topological defect to have close to 0.5. The role played by λ_R is known in literature, while that due to the topological defect and their interplay are less studied. It is also worth noting that the results are presented for a value $\Phi/\Phi_0 = 0.3$, however the qualitative nature of the plot remains consistent for other magnetic flux values and angular momentum quantum numbers (m). In practical applications, by fine-tuning external parameters such as magnetic flux, dislocation, and the strength

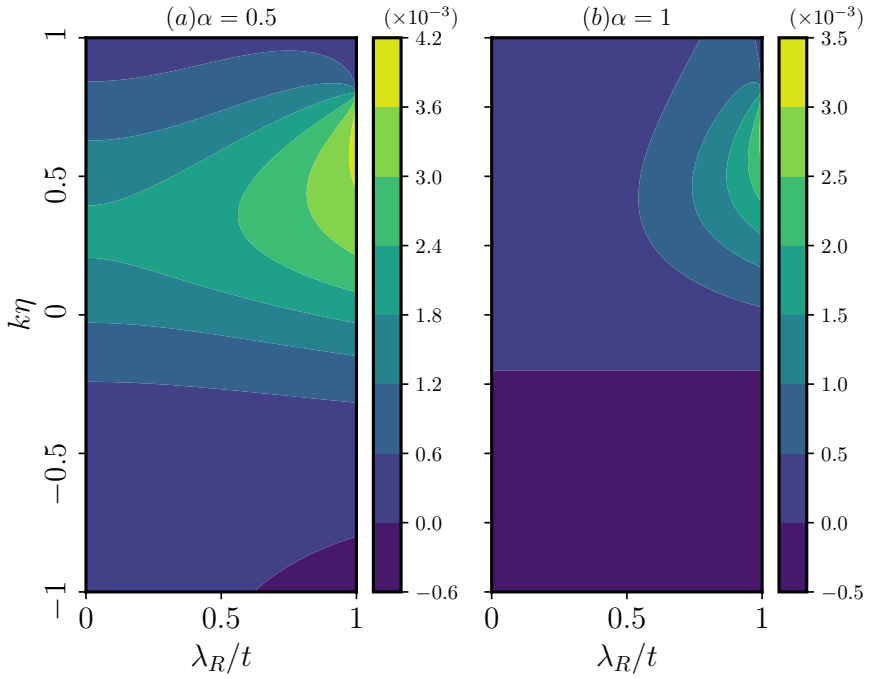

Figure 4.10: The equilibrium spin currents are plotted as functions of the strength of the Rashba SOC and the topological defect, considering a fixed magnetic flux, $\Phi/\Phi_0 = 0.3$, and angular momentum quantum number $m = 0$, panels (a) for $\alpha = 0.5$, and (b) for $\alpha = 1$.

of the Rashba SOC, one can tailor the spin current to suit specific device requirements. However, we have to note that the qualitative characteristics of the plot remain consistent even if $\lambda_R/t > 1$, that is, achieving maximum spin persistent current necessitates high values of λ_R and the strength of the topological defect ($k\eta$). Further, the detailed behaviour of the plots may vary depending on the quantum number m. As we increase the values of λ_R/t, different m values start contributing to the spin current.

These findings underscore the potential of α-T_3 quantum rings as key components for spintronic applications, where we can manipulate the performance of the devices by adjusting both the strength of the Rashba coupling and that of the topological defect.

4.5 Dipole Moment of the Ring: Applications to Spintronics

Continuing with the aforementioned studies, we now can compute the induced dipole moment of the α-T_3 ring. This is attributed to the persistent currents flowing in the charge and spin sectors circulating around the ring. By defining the induced dipole moment as the product of the charge current density (j_Q) or the spin current density (j_S) and the area of the quantum ring, denoted as μ, we may get useful information. In Figure 4.11, we illustrate the dipole moments for various scenarios, namely, $\uparrow$-spin charge current for $\alpha = 0.5$ (Fig. 4.11 (a)), $\uparrow$-spin charge

current for $\alpha = 1$ (Fig. 4.11 (b)), $\downarrow$-spin charge current for $\alpha = 0.5$ (Fig. 4.11 (c)), and $\downarrow$-spin charge current for $\alpha = 1$ (Fig. 4.11 (d)). Additionally, in Figure 4.11 (e) and (f), we display the total spin dipole moment for $\alpha = 0.5$ and $\alpha = 1$, respectively. The parameters $\lambda_R = 0.5t$ and $k\eta = 0.3$ are held constant throughout. It is apparent from Figure 4.11 that the dipole moments originating from different spin branches are neither uniform nor equivalent, instead, they exhibit oscillatory behavior with a period of Φ_0. Such charge and spin dipole moments have the prospects of inducing spin torque in the ring system, a key aspect in the realm of spintronic devices. Moreover, the ability to manipulate both the charge and spin persistent currents, along with the dipole moments, through parameters such as α, Φ, and λ_R, coupled with modulation by the degree of dislocation ($k\eta$), highlights the system's controllability. This opens up avenues for tailored applications in spintronics.

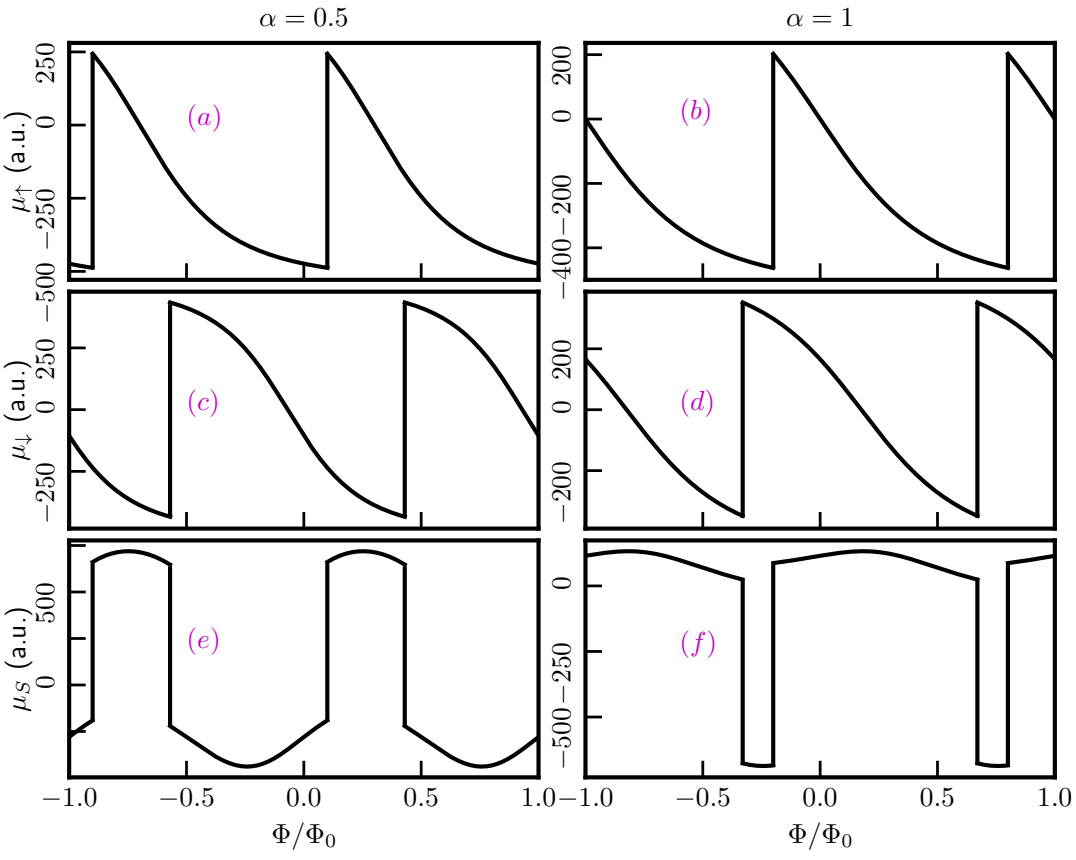

Figure 4.11: The induced dipole moments are plotted as function of the external magnetic flux, panels (a) for $\alpha = 0.5$, $\uparrow$-spin current, (b) for $\alpha = 1$, $\uparrow$-spin current, (c) for $\alpha = 0.5$, $\downarrow$-spin current, (d) for $\alpha = 1$, $\downarrow$-spin current, (e) for $\alpha = 0.5$, total spin current, and (f) for $\alpha = 1$, total spin current. The other parameters are taken as $\lambda_R = 0.5t$ and $k\eta = 0.3$.

4.6 Burgers Currents

4.6.1 Formalism

In general the Hamiltonian of the system in a screw dislocated medium given in Eq. (4.1) can be represented in the form,

$$\mathcal{H} = \frac{1}{2m\sqrt{g}}\big(-i\hbar\partial_i - \mathcal{A}_i\big)\sqrt{g}g^{ij}\big(-i\hbar\partial_j - \mathcal{A}_j\big) \tag{4.21}$$

where $\mathcal{A}_\mu(\mu = 0, x, y, z)$ denote the components of the gauge field. The non-Abelian potential $\mathcal{A}$ captures the effects (including the spin-orbit coupling) if one makes the following identifications where $\mathcal{A}_0 = -\frac{e\hbar}{mc}B^a\tau^a$ and $\mathcal{A}_{ind}$ is the screw dislocation induced vector potential (contained in the spatial coordinates x, y, z). B^a is the external magnetic field and $\tau^a = S^a/2$ are the generators of the SU(2) group corresponding to the spin-1 operator. The external magnetic field is in the z-direction. Further, even in absence of an external magnetic field, the screw dislocation effectively acts as an artificial gauge field that gives rise to a pseudo-magnetic field, $B_s = (\nabla \times \mathcal{A}_i)_z$ perpendicular to the α-T_3 lattice plane.

Following the formalism of Refs. [167, 313–315], due to this effective field $\mathcal{F}_{i0} = \partial_i\mathcal{A}_0 - \partial_t\mathcal{A}_i - i[\mathcal{A}_i, \mathcal{A}_0]$, there is a dissipative current j_i^a which is conjugate to the effective field. Calculating the time derivative of the expectation value of $\mathcal{H}$ (given in Eq. (4.21)) we find that,

$$\frac{d}{dt}\langle\mathcal{H}\rangle = \int dr\, j_i^a \mathcal{F}_{i0}^a. \tag{4.22}$$

Armed with a gauge invariant Hamiltonian and the variational definition of j_i^a, we are ready to calculate the equilibrium charge and spin currents induced by the screw dislocation. Following the same technique as earlier in the presence of an external magnetic field, one naturally expects an orbital response in the form of a diamagnetic current. This current is given by the derivative of the energy $E[\mathcal{A}_i^a](= \langle\mathcal{H}\rangle)$ with respect to $\mathcal{A}_i^a$. As $E[\mathcal{A}_i^a]$ is gauge invariant, it can depend only on the effective gauge field, namely,

$$\mathcal{F}_{ij} = \partial_i\mathcal{A}_j - \partial_j\mathcal{A}_i - i[\mathcal{A}_i, \mathcal{A}_j]. \tag{4.23}$$

A particular form of the invariant is determined by the symmetry of a particular system. Firstly, we assume that the external magnetic field is zero, i.e., $\mathcal{A}_0 = 0$. Since in the absence of $\mathcal{A}_i^a$ the system is rotationally invariant, the first spin-orbit (SO) correction to the energy must be

proportional to tr$(\mathcal{F}_{ij}\mathcal{F}_{ij})$ that is,

$$E_{\rm SO} = \frac{\lambda}{4}\int dr \mathcal{F}^a_{ij}\mathcal{F}^a_{ij}, \tag{4.24}$$

where λ is a constant (on dimensional grounds $\lambda \sim p_F^{D-2}/m$, where p_F is the Fermi momentum and $D > 1$ is the dimension of space). Thus, the current due to the effective field yields,

$$j^a_i = -\frac{\delta E_{\rm SO}}{\delta \mathcal{A}^a_i}. \tag{4.25}$$

We may define the current induced by the screw dislocation as the Burgers current which can be expressed as, $j_{b^z} = -\frac{\delta E_{\rm SO}}{\delta b^z}$. Further, the induced spin current, which we may define as the Burgers spin current, can also be written as, $j_{S,b^z} = j_{b^z}(\uparrow) - j_{b^z}(\downarrow)$. Eq. (4.23) is precisely the Yang-Mills magnetostatic equation. Intuitively, the results are analogous to the case of an external magnetic field. However, there is a difference in the spatial distribution of the currents induced by the screw dislocation.

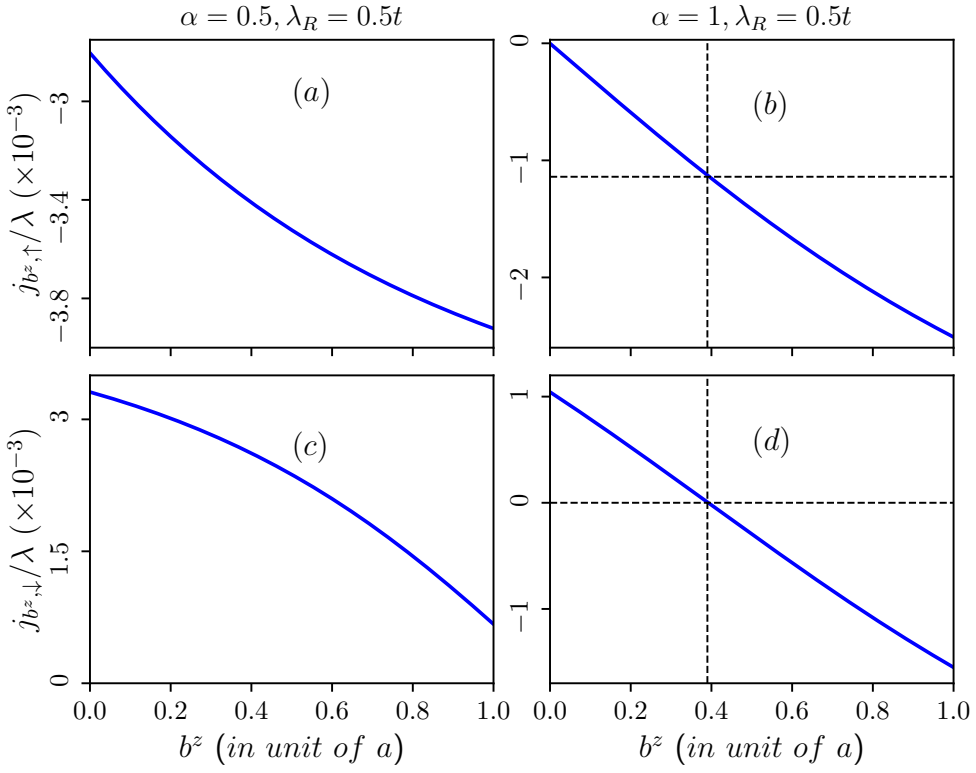

Figure 4.12: Burgers current as a function of the Burgers vector induced by the topological screw dislocation in absence of external magnetic field. Upper panel: corresponds to ↑-spin (a) for $\alpha = 0.5$ and (b) for $\alpha = 1$. Lower panel: corresponds to ↓-spin (c) for $\alpha = 0.5$ and (d) for $\alpha = 1$. The Rashba spin-orbit coupling parameter is taken as $\lambda_R = 0.5t$.

4.6.2 Burgers charge current

In Fig. 4.12, we depict the Burgers current for different spin sectors as a function of the Burgers vector corresponding to the lowest energy level of the valence band in the absence of an external magnetic field for $\alpha = 0.5$ (refer to Figs. 4.12(a) ($\uparrow$-spin) and (c) ($\downarrow$-spin), and for $\alpha = 1$ (Figs. 4.12(b) ($\uparrow$-spin) and (d) ($\downarrow$-spin)). These plots correspond to a fixed value of the Rashba spin-orbit coupling, namely, $\lambda_R = 0.5t$. Equation (4.9) reveals that even in the absence of an external magnetic field, there exists an effective field due to the topological defect represented by the screw dislocation. This effective field contributes to the generation of Burgers current. For the scenario without an external magnetic field and $\alpha = 0.5$ (refer to Fig. 4.12(a) and (c)), the Burgers current steadily decreases with an increase in the Burgers vector. Moreover, for $\alpha = 1$ and only for the $\uparrow$-spin branch (Fig. 4.12(b)), the Burgers current undergoes a sign change at an approximate value of $b^z \sim 0.4$ (in unit of the lattice constant). This change in sign (can be interpreted as a back flow) of the current is attributed to the behaviour of the energy spectrum. Since the spectral properties undergo a change in slope and the current being proportional to that, a sign change occurs. One can clearly see that the variation in the $\uparrow$-spin Burgers current, $j_{b^z,\uparrow}$, and the $\downarrow$-spin Burgers current, $j_{b^z,\downarrow}$ with respect to b^z are strikingly dissimilar and opposite in nature, rather than being equal and opposite, in the $\alpha = 0.5$ scenario. These currents depict two circulating spin currents moving in opposite directions within the ring, potentially resulting in a chirality effect even without an external magnetic field. However, for $\alpha = 1$, the situation significantly altered. Here, the chirality persists up to a certain threshold of screw dislocation ($b^z \sim 0.4$), beyond which both spin ($\uparrow$ and $\downarrow$) currents align in the same direction. Summarizing, the manifestation of the chiral current induced solely by the screw dislocation offers valuable insights with implications for future technological advancements.

Additionally, in Fig. 4.13, we depict the Burgers current as a function of the Burgers vector corresponding to the lowest energy level of the valence band in presence of an external magnetic field for $\alpha = 0.5$ (refer to Figs. 4.13(a) ($\uparrow$-spin) and (c) ($\downarrow$-spin) and $\alpha = 1$ (refer to Fig. 4.13(b) ($\uparrow$-spin) and (d) ($\downarrow$-spin)). In the presence of an external magnetic field, the bands corresponding to negative quantum number, and in particular $m = -6$ bands emerge as the lowest energy states, and these remain nearly constant with the Burgers vector. These plots are presented for a fixed value of the Rashba spin-orbit coupling ($\lambda_R = 0.5t$). In the presence of a magnetic field, the sign-change feature of the Burgers current is observed for $\alpha = 0.5$ only for the $\downarrow$-spin branch (refer to Fig. 4.13(c)), while there is a steady decrease in the Burgers current for $\alpha = 1$ (refer to Fig. 4.13(d)). Here, chirality persists only for $\alpha = 0.5$ up to a certain threshold of screw

dislocation ($b^z \sim 0.5$), beyond which both spin currents align in the same direction. However, for $\alpha = 1$ there is no chirality present in the system.

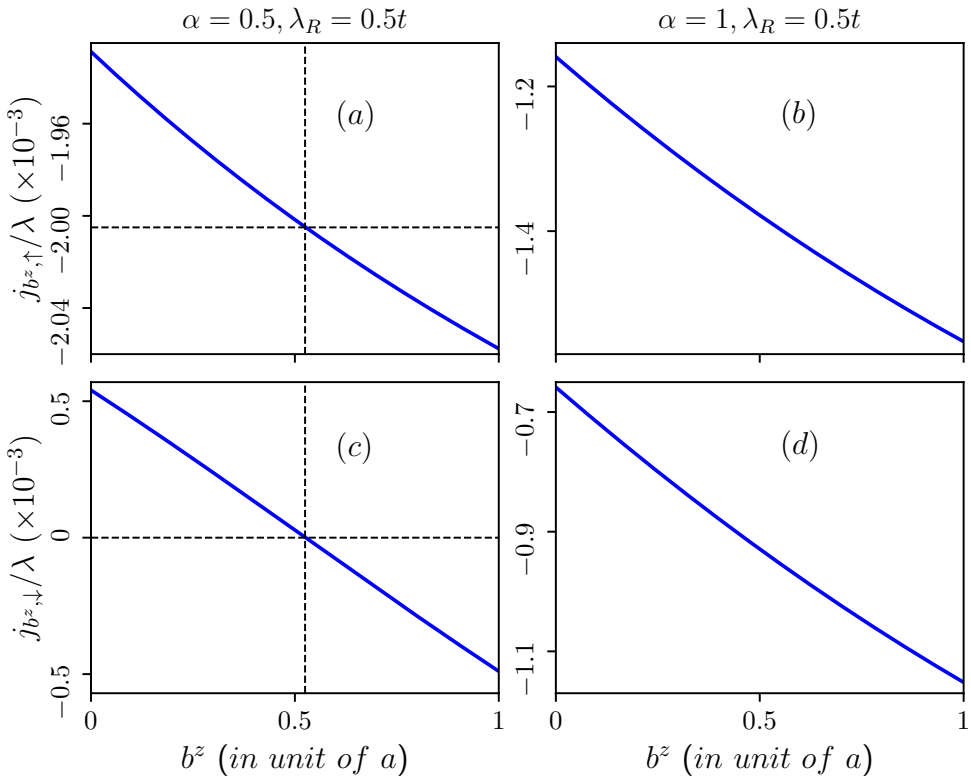

Figure 4.13: Burgers current as a function of the Burgers vector induced by the topological screw dislocation in presence of an external magnetic field of $B_0 = 3$T. Upper panel: corresponds to $\uparrow$-spin (a) for $\alpha = 0.5$ and (b) for $\alpha = 1$. Lower panel: corresponds to $\downarrow$-spin (c) for $\alpha = 0.5$ and (d) for $\alpha = 1$. The Rashba spin-orbit coupling parameter is taken as $\lambda_R = 0.5t$.

4.6.3 Burgers spin current

The Burgers spin current as a function of the Burgers vector for the scenarios mentioned above are illustrated in Fig. 4.14. The presence of the Rashba spin-orbit coupling in the system results in spin-split energy branches, leading to the emergence of Burgers spin current defined as the difference in Burgers current between the two spin branches. In the absence of an external magnetic field, we observe an initial increase in the Burgers spin current with the Burgers vector. Beyond a certain maximum value, it decreases for any value of α. Notably, the Burgers vector corresponding to the maximum Burgers spin current increases with higher values of α. For $\alpha = 1$, the maximum of j_{S,b^z} occurs at $b^z \sim 0.4$ (in unit of the lattice constant) (refer to Fig. 4.14(b)). Since the Burgers vector signifies the amount of screw dislocation in the system, maximizing the Burgers spin current would require large screw dislocations, and the behaviour

is more for large values of α. Moreover, the presence of an external magnetic field eliminates this upturn in j_{S,b^z}, as depicted in Figs. 4.14(c) and (d), where the Burgers spin current steadily decreases with increasing b^z.

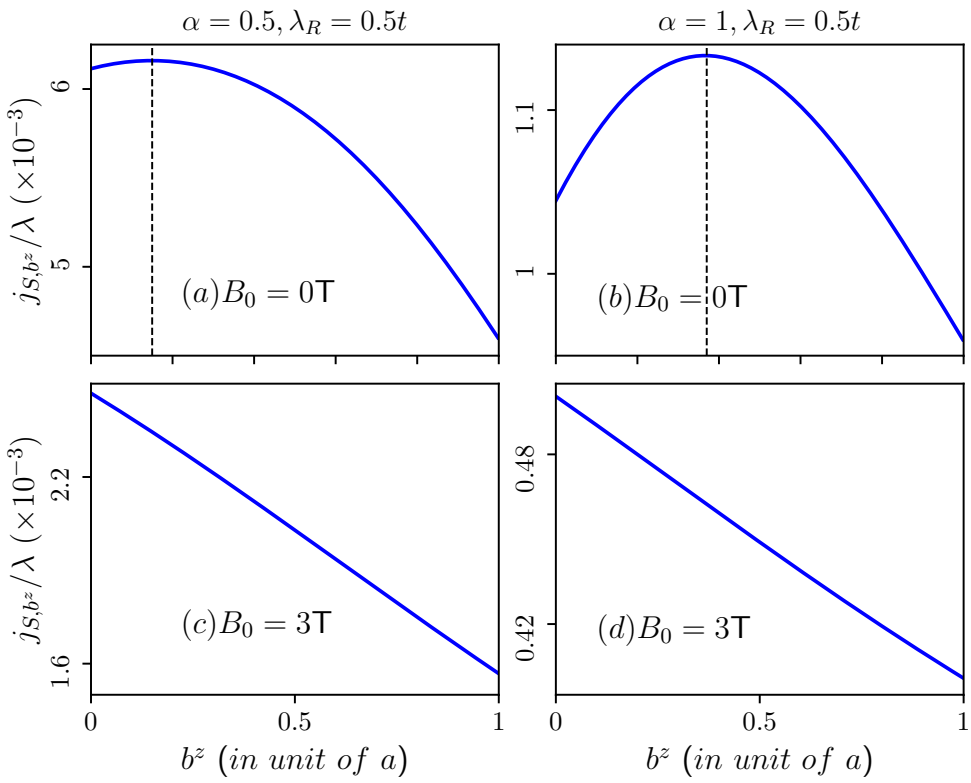

Figure 4.14: Burgers spin current as a function of the Burgers vector induced by the topological screw dislocation. Upper panel: in absence of external magnetic field (a) $\alpha = 0.5$ and (b) $\alpha = 1$. For $\alpha = 0.5$ maximum Burgers spin current occurs at $b^z \sim 0.15$ (in unit of lattice constant) and for $\alpha = 1$ maximum Burgers spin current occurs at $b^z \sim 0.4$ (in unit of lattice constant). Lower panel: in presence of external magnetic field of $B_0 = 3\mathsf{T}$ (c) $\alpha = 0.5$ and (d) $\alpha = 1$. The Rashba spin-orbit coupling parameter is taken as $\lambda_R = 0.5t$.

4.6.4 Burgers dipole moment

Another interesting contribution to the dipole moment may come from the chiral current in the spin sector which arise even in the absence of an external magnetic field. The dipole moment, as expected, shows a non-monotonic behaviour (shown in Fig. 4.15) as a function of the strength of the dislocation (i.e. b^z) which hints towards an efficient '*operating region*' for our system to yield large spin torque.

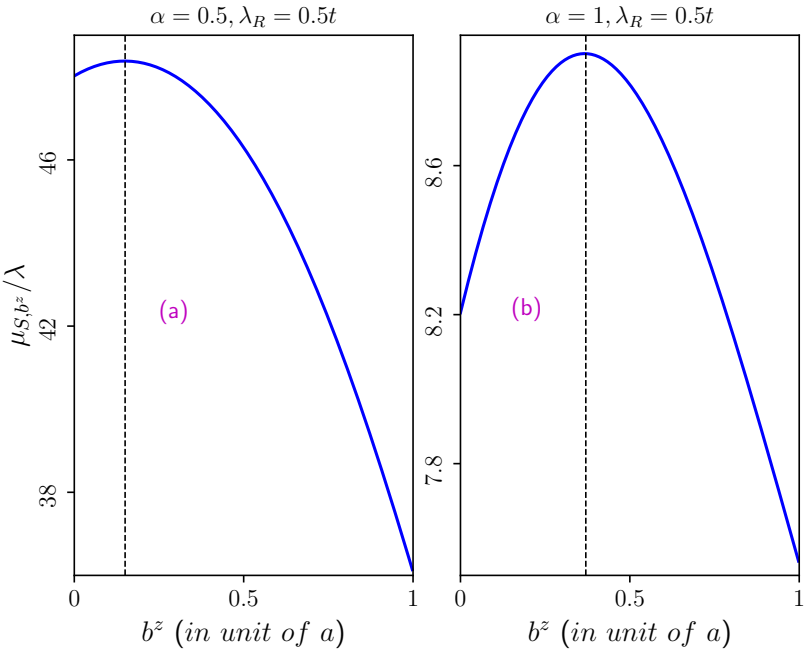

Figure 4.15: Burgers dipole moment as a function of the Burgers vector induced by the topological screw dislocation in absence of external magnetic field are shown. Here (a) for $\alpha = 0.5$ and (b) for $\alpha = 1$. The other parameters are taken as $\lambda_R = 0.5t$ and $k\eta = 0.3$.

4.7 Summary

In summary, we have conducted a comprehensive investigation of the properties of Rashba spin-orbit coupling in the context of an α-T_3 pseudospin-1 fermionic Aharonov-Bohm quantum ring, considering the presence of a special type of topological defect. Our exploration covered aspects such as the energy spectrum, persistent currents, their dependencies on (Rashba) spin-orbit coupling, screw dislocations, and magnetic fields. Even without the influence of an external magnetic field, the screw dislocation causes the degeneracy of the dice lattice to lift, although other aspects remain unchanged. Under the influence of a perpendicular magnetic field, the energy levels deviate significantly from their usual R-dependence, showcasing behaviours of $1/R$ for small R and R for larger R. The presence of the topological defect introduces an effect, effectively emulating a magnetic flux traversing the ring. This effective flux is the result of two contributions, one stemming from the topological nature of the defect and the other from the external magnetic flux.

The spin-split energy bands corresponding to different quantum number (m) exhibit distinct characteristics as a function of the Burgers vector in presence and absence of an external magnetic field. In the absence of an external magnetic field, the bands associated with quantum number $m = 0$ represent the lowest energy states. Additionally, the energy levels demonstrate a

nearly linear increase (or decrease) as a function of the Burgers vector. On the other hand, in the presence of an external magnetic field, the bands corresponding to negative quantum number emerge as the lowest energy states, and these remain nearly constant with the Burgers vector.

Furthermore, the persistent currents in both the spin and charge sectors exhibit periodic oscillations with a periodicity of Φ_0, featuring distinct patterns corresponding to different α and λ_R values. Notably, the presence of a topological defect shifts the phase of current oscillation by an amount equal to the strength of the defect. We have also derived equilibrium spin currents by combining the charge current contributions from different spin branches, underscoring the potential utility of our system in spintronic applications. Equilibrium spin currents are present for all α values, with a $\Phi = \Phi_0$ periodic behaviour. Similar to the charge persistent current, the presence of a topological defect shifts the phase of the oscillations in the spin current profile by an amount proportional to the defect.

The Burgers current exhibits an almost linear decrease with the Burgers vector, both in the presence and absence of an external magnetic field. However, without the external field, these current undergoes a sign change for $\alpha = 1$, whereas in the presence of the external magnetic field, this sign change occurs for $\alpha = 0.5$ at specific values of the Burgers vector. Additionally, the presence of distortion in the α-T_3 lattice induces a chirality effect within the system, giving rise to an additional chiral current even in the absence of an external magnetic field. Moreover, in the absence of an external magnetic field, the Burgers spin current initially increases with an increase in the Burgers vector. After attaining a maximum, the current decreases with further increase in b^z for all values of α. However, this phenomenon disappears in the presence of an external magnetic field.

In conclusion, by adjusting the parameters α, $k\eta$, Φ, and λ_R, we have comprehensively shown the ability to manipulate the persistent currents, rendering them as controllable features in our system. To emphasize the role of the α-T_3 ring system in spintronic devices, we have computed the induced dipole moment of the ring. Particularly, the contribution of the Burgers spin current yields useful information on the prospects of it being used for spintronic applications.

Chapter 5

Conductance Properties of α-T_3 Corbino Disks

In this work, we investigate an α-T_3 lattice in the form of a Corbino disk. Through analytic solutions of the stationary Dirac-Weyl equation, we compute the transmission probability of the carriers and hence obtain the conductance features for $0 < \alpha \leq 1$ which allows ascertaining the role of the flat band, alongwith scrutinizing the transport features from graphene to a dice lattice. Our results reveal periodic Aharonov-Bohm (AB) oscillations in the conductance, reminiscent of the utility of the Corbino disk as an electron pump.

5.1 Introduction

Two-dimensional (2D) Dirac materials owing to their massless fermionic dispersion and high electronic mobility have prospects providing the building block for future electronic devices. The striking electronic properties can be modified by nanostructuring and patterning, such as, manufacturing nanoribbons [316], nanorings [29], junctions [317], quantum dots (QDs) [318], QD arrays [319, 320]. Therefore, the transport properties heavily depend on the design of the geometry, its edge shape [321, 322] etc. Here, we present one such annular geometry called as

the Corbino disk which is contemplated by Laughlin as an electron pump that shows generation of radial (Hall) current as the enclosed flux quantum changes.

Recent studies have extensively investigated various quantum transport phenomena in graphene Corbino disks, both experimentally [69–72, 323] and theoretically [73–75, 77, 78, 324, 325]. The edge-free geometry of the disk enables transport studies via evanescent waves in nanoscale graphene systems [76]. At zero magnetic field, the conductance of ultraclean ballistic disks as a function of the carrier concentration [71] aligns well with the basic mode-matching analysis described in Ref. [77]. Further, in presence of a non-zero magnetic field, periodic (approximately sinusoidal) magnetoconductance oscillations have been predicted [73, 78], yet experimental confirmation of this intriguing quantum interference phenomenon is still lacking. Recently, the authors of Ref. [75] demonstrated that a Corbino graphene disk, when pierced by a current carrying solenoid, can exhibit Aharonov-Bohm (AB) type conductance oscillations. They also found that these oscillations are more pronounced in the presence of an electrostatic potential, which breaks cylindrical symmetry and introduces mode mixing. Furthermore, Refs. [326, 327] explored the effects of mass and wedge disclination on a graphene Corbino disk, revealing that the *mass* term can conspire to eliminate tunneling effects by creating points of zero transmission.

In recent years, a number of properties of lower-dimensional systems in the α-T_3 lattice have been investigated as discussed earlier. However, an α-T_3 Corbino disk and its transport properties are yet to be explored. Thus, studying the electronic properties of the α-T_3 Corbino disk presents an intriguing opportunity of examining the transmission coefficients and hence electrical conductance in presence of a threaded magnetic field or a solenoid. We will follow the Corbino disk setup proposed for graphene in Ref. [75]. Following a general introduction of the model, we have outlined a solution with a view to obtain the transport features of the α-T_3 Corbino disk.

The chapter is organized as follows. In Sec. 5.2, we introduce the α-T_3 model, discuss the method of mode-matching analysis for the system as shown in Fig. 5.1 and solve the eigenvalue problem for the α-T_3 Corbino disk. Next, in Sec. 5.3, the numerical computations of the transmission, conductance oscillations, and Fano factor are presented in Sec. 5.4. A comparison between graphene and α-T_3 Corbino disk is discussed in Sec. 5.5 The conclusions of the results are given in Sec. 5.6.

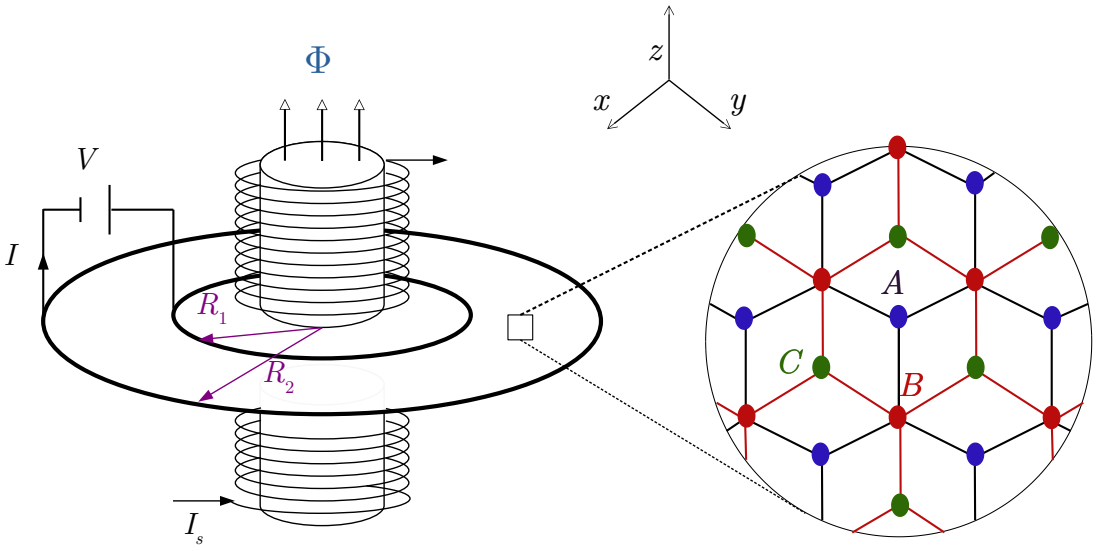

Figure 5.1: Schematic of an α-T_3 Corbino disk with inner radius R_1 and outer radius R_2, connected by two electrodes as shown by thick black circles. A voltage source (V) drives the current (I) through the disk. A long solenoid, carrying the current I_s, generates the flux Φ piercing the annular regime. The coordinate system is also shown. The structure of the α-T_3 lattice is depicted in the zoomed portion. A, B, and C sub lattice sites are shown by blue, red, and green dots, respectively. The hopping between the A and B sublattice is t and between the B and C is αt.

5.2 Formalism

Let us begin by considering a Corbino disk with an α-T_3 lattice geometry, and characterized by an inner radius R_1 and outer radius R_2 which are connected by two electrodes. A current-carrying long solenoid (to eliminate edge effects) penetrates the inner area of the disk, yielding a magnetic flux Φ_i threading the annular region.

Further, in the vicinity of a specific valley (say, the K-valley), the low energy excitations in the α-T_3 lattice can be described by the following Dirac-Weyl Hamiltonian

$$H = v_F(\pi_x S_x + \pi_y S_y) + U(r), \tag{5.1}$$

where v_F is the Fermi velocity and π_x and π_y are the components of the canonical momentum operator defined via $\boldsymbol{\pi} = \boldsymbol{p} + e\boldsymbol{A}$. Here, $\boldsymbol{p}$ denotes the in-plane mechanical momentum operator $(-i\hbar(\partial_x, \partial_y))$ and the vector potential $\boldsymbol{A}$. Here, the components of the pseudospin-1 operator $\boldsymbol{S}$

associated with the α-T_3 lattice are given by

$$S_x = \begin{pmatrix} 0 & \cos\varphi & 0 \\ \cos\varphi & 0 & \sin\varphi \\ 0 & \sin\varphi & 0 \end{pmatrix} \quad \text{and} \quad S_y = \begin{pmatrix} 0 & -i\cos\varphi & 0 \\ i\cos\varphi & 0 & -i\sin\varphi \\ 0 & i\sin\varphi & 0 \end{pmatrix}$$

with $\tan\varphi = \alpha$. The z-component of $\boldsymbol{S}$ can be directly derived from the commutation relation $[S_x, S_y] = iS_z$. Due to the circular symmetry, we adopt the symmetric gauge for the vector potential, expressed as

$$\boldsymbol{A} = (A_x, A_y) = \frac{\Phi}{2\pi}\left(-\frac{y}{r^2}, \frac{x}{r^2}\right). \tag{5.2}$$

We consider the case of a disk with an annular region pierced by a long solenoid, generating a flux Φ. Additionally, we assume that the electrostatic potential energy $U(r)$ depends only on the radial distance, $r = \sqrt{x^2 + y^2}$. Specifically, $U(r) = 0$ within the disk region $(R_1 < r < R_2)$ and $U(r) = U_\infty$ (will be set to infinity) outside this area. The Hamiltonian in equation (5.1) commutes with the z-component of the total angular momentum operator, defined as $J_z = L_z + S_z$, where $L_z = -i\hbar\frac{\partial}{\partial\theta}$ is the orbital angular momentum operator, and S_z is the pseudospin operator. The energy eigenfunctions at a particular valley (namely, K valley) can therefore be chosen as eigenstates of J_z, as

$$\psi_m(r,\theta) = \begin{pmatrix} \chi_{m,A}(r)e^{i(m-1)\theta} \\ \chi_{m,B}(r)e^{im\theta} \\ \chi_{m,C}(r)e^{i(m+1)\theta} \end{pmatrix}, \tag{5.3}$$

where m is an integer, the three spinor components (A, B, C) correspond to the sublattice degrees of freedom, with (r, θ) denotes the coordinates. The Dirac equation now can be written as $H_m(r)\chi_m(r) = E\chi_m(r)$, where $\chi_m(r) = [\chi_{m,A}(r), \chi_{m,B}(r), \chi_{m,C}(r)]^T$, and

$$H_m(r) = -i\hbar v_F S_x \partial_r + U(r) + \hbar v_F S_y \begin{pmatrix} \frac{m-1}{r} + \frac{e\Phi}{hr} & 0 & 0 \\ 0 & \frac{m}{r} + \frac{e\Phi}{hr} & 0 \\ 0 & 0 & \frac{m+1}{r} + \frac{e\Phi}{hr} \end{pmatrix}. \tag{5.4}$$

For a piecewise-constant potential energy $U(r)$ and in presence of a bias voltage, which implies a varying electron concentration (called as doping later) such that the electron energies satisfy $E > U(r)$, the eigenfunctions of $H_m(r)$ (equation 5.4) for the incoming waves (propagating from $r = 0$) and outgoing waves (propagating from $r = \infty$) are, up to a normalization constant,

given by

$$\chi_m^{inc} = \begin{pmatrix} -i\cos\varphi\chi_1(kr) \\ H_{\nu(m)}(kr) \\ -i\sin\varphi\chi_2(kr) \end{pmatrix} \quad \text{and} \quad \chi_m^{out} = \begin{pmatrix} -i\cos\varphi\chi_3(kr) \\ H_{\nu(m)}(kr) \\ -i\sin\varphi\chi_4(kr) \end{pmatrix} \tag{5.5}$$

where

$$\nu(m) = m + \frac{\Phi}{\Phi_0}, \tag{5.6}$$

$$\begin{aligned} \chi_{1/2}(kr) &= \frac{H^{(2)}_{\nu(m)-1}(kr) - H^{(2)}_{\nu(m)+1}(kr)}{2} \pm \frac{\nu(m)H^{(2)}_{\nu(m)}(kr)}{kr}, \\ \chi_{3/4}(kr) &= \frac{H^{(1)}_{\nu(m)-1}(kr) - H^{(1)}_{\nu(m)+1}(kr)}{2} \pm \frac{\nu(m)H^{(1)}_{\nu(m)}(kr)}{kr}, \end{aligned} \tag{5.7}$$

$H^{(1,2)}_{\nu}(\rho)$ is the Henkel function of the first and second kinds, and $k = |E - U(r)|/(\hbar v_F)$. The solution for the Eq. (5.4) pertaining to the disk area can be represented as

$$\chi_m^{(d)} = A_m\chi_m^{inc}(k_F r) + B_m\chi_m^{out}(k_F r), \qquad R_1 < r < R_2 \tag{5.8}$$

with A_m and B_m being arbitrary constants, and the Fermi wave vector is given by $k_F = |E|/(\hbar v_F)$.

The heavily doped (large bias voltage) α-T_3 leads are modeled via taking the limit of $U(r) = U_\infty \to \pm\infty$ for $r < R_1$ or $r > R_2$. The corresponding wave functions in different regimes can be expressed as

$$\chi_m^{(1)} = \frac{e^{\pm ik_\infty r}}{\sqrt{r}} \begin{pmatrix} \cos\varphi \\ 1 \\ \sin\varphi \end{pmatrix} + r_m \frac{e^{\mp ik_\infty r}}{\sqrt{r}} \begin{pmatrix} \cos\varphi \\ -1 \\ \sin\varphi \end{pmatrix}, \quad r < R_1 \tag{5.9}$$

$$\chi_m^{(2)} = t_m \frac{e^{\pm ik_\infty r}}{\sqrt{r}} \begin{pmatrix} \cos\varphi \\ 1 \\ \sin\varphi \end{pmatrix}, \quad r > R_2 \tag{5.10}$$

where we introduced reflection (transmission) amplitudes $r_m(t_m)$ and $k_\infty = |E - U_\infty|/(\hbar v_F) \to \infty$. To proceed with the computation, we recall some useful formulae of the Hankel functions,

namely,

$$H_{\nu+\tau}^{1/2}(kr) = \pm i H_{\nu}^{1/2}(kr), \quad H_{\nu}^{1/2}(kr) = [H_{\nu}^{2/1}(kr)]^{*}. \tag{5.11}$$

The mode-matching conditions, $\chi_m^{(1)}(R_1) = \chi_m^{(d)}(R_1)$ and $\chi_m^{(d)}(R_2) = \chi_m^{(2)}(R_2)$, enforcing the continuity of the wave functions at R_1, for the B sublattice [328],

$$\chi_{m,B}^{(1)}(R_1) = \chi_{m,B}^{(d)}(R_1) \tag{5.12}$$

and for the A and C sublattices,

$$\cos\varphi\chi_{m,A}^{(1)}(R_1) + \sin\varphi\chi_{m,C}^{(1)}(R_1) = \cos\varphi\chi_{m,A}^{(d)}(R_1) + \sin\varphi\chi_{m,C}^{(d)}(R_1). \tag{5.13}$$

Similarly, at R_2, for B sublattice,

$$\chi_{m,B}^{(d)}(R_2) = \chi_{m,B}^{(2)}(R_2) \tag{5.14}$$

and for the A and C sublattices,

$$\cos\varphi\chi_{m,A}^{(d)}(R_1) + \sin\varphi\chi_{m,C}^{(d)}(R_1) = \cos\varphi\chi_{m,A}^{(2)}(R_1) + \sin\varphi\chi_{m,C}^{(2)}(R_1). \tag{5.15}$$

Hence, we find the transmission probability for the mth mode to be given by

$$T_{\nu(m)} = |t_{\nu(m)}|^2 = \frac{4}{(kR_1)(kR_2)} \frac{\frac{4}{\pi^2} + [\mathfrak{D}_{\nu(m)}^{(1)}]^2}{[\mathfrak{D}_{\nu(m)}^{(2)}]^2 + [\mathfrak{D}_{\nu(m)}^{(3)}]^2 + [\mathfrak{D}_{\nu(m)}^{(4)}]^2 + [\mathfrak{D}_{\nu(m)}^{(5)}]^2}, \tag{5.16}$$

where $\nu(m)$ is given by Eq. (5.6) and

$$\begin{aligned}
\mathfrak{D}_{\nu(m)}^{(1)} &= \mathfrak{Im}[H_{\nu(m)}^{(2)}(kR_2) - H_{\nu(m)}^{(1)}(kR_2)]\cos 2\varphi, \\
\mathfrak{D}_{\nu(m)}^{(2)} &= \mathfrak{Im}[H_{\nu(m)}^{(1)}(kR_2)H_{\nu(m)}^{(2)}(kR_1) + H_{\nu(m)+1}^{(1)}(kR_2)H_{\nu(m)+1}^{(2)}(kR_1)], \\
\mathfrak{D}_{\nu(m)}^{(3)} &= \mathfrak{Im}[H_{\nu(m)+1}^{(1)}(kR_2)H_{\nu(m)}^{(2)}(kR_1) - H_{\nu(m)}^{(1)}(kR_2)H_{\nu(m)+1}^{(2)}(kR_1)], \\
\mathfrak{D}_{\nu(m)}^{(4)} &= \big(1+\nu(m)\big)\left(\frac{1}{kR_2} - \frac{1}{kR_1}\right)\cos 2\varphi\,\mathfrak{Im}[H_{\nu(m)}^{(1)}(kR_1)H_{\nu(m)}^{(2)}(kR_2) - H_{\nu(m)}^{(1)}(kR_2)H_{\nu(m)}^{(2)}(kR_1)], \\
\mathfrak{D}_{\nu(m)}^{(5)} &= \frac{\nu(m)^2\cos^2 2\varphi}{(kR_1)(kR_2)}\mathfrak{Im}[H_{\nu(m)+1}^{(1)}(kR_2)H_{\nu(m)}^{(2)}(kR_1) - H_{\nu(m)}^{(1)}(kR_2)H_{\nu(m)+1}^{(2)}(kR_1)].
\end{aligned} \tag{5.17}$$

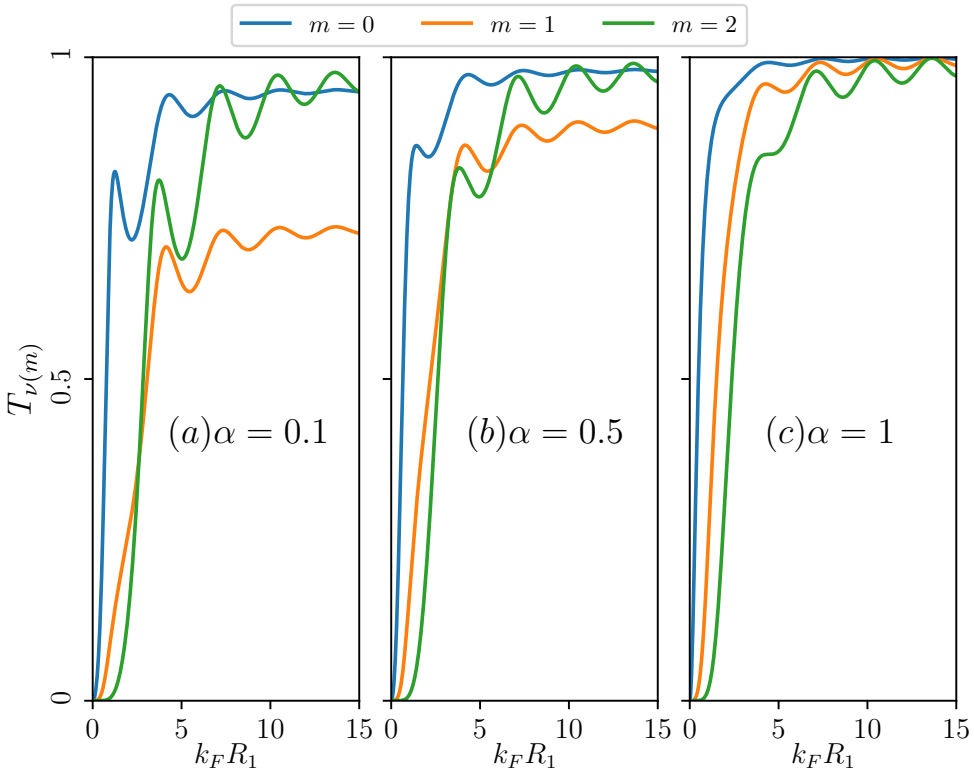

Figure 5.2: The transmission $T_{\nu(m)}$ ($m = 0, 1, 2$) as a function of the doping parameter, $k_F R_1$ for a radii ratio $R_2/R_1 = 5$, $\Phi/\Phi_0 = 1/2$, for (a) $\alpha = 0.1$, (b) $\alpha = 0.5$, and (c) $\alpha = 1$.

5.3 Transmission and Conductance Properties

We study the transmission $T_{\nu(m)}(m = 0, 1, 2)$, the conductance G, and the Fano factor F numerically for the α-T_3 Corbino disk with an annular region at the center ($R_1 < r < R_2$) and threading a flux through it as shown in Fig. 5.1. We show our results as a function of a dimensionless quantity, $k_F R_1$, which essentially controls the electron doping (through k_F). Fig. 5.2 represents the transmission as a function of $k_F R_1$ for three different values of α, namely, $\alpha = 0.1$, 0.5, and 1 in Figs. (a), (b), and (c) respectively, for a particular width of the α-T_3 disk denoted by $R_2/R_1 = 5$ and for a certain flux $\Phi/\Phi_0 = 1/2$. The transmission characteristics are shown for three different values of the angular momentum quantum number (corresponding to J_z) m, namely, $m = 0$, 1, and 2 each represented by different color as shown in the figure (see Fig. 5.2). We observe that the transmission strongly depends upon m, α, and the value of the magnetic flux. The transmission curves show a sharp increase for small values of $k_F R_1$. In Fig. 5.2(a), for $\alpha = 0.1$ (low values of α) the curves display oscillatory behaviour before they converge toward a saturation. This indicates that a small non-zero value of α introduces additional effects, possibly interference or resonance phenomena. The transmission for $m = 0$ (blue curve) increases more rapidly, while for $m = 1$ and $m = 2$, the oscillations are more

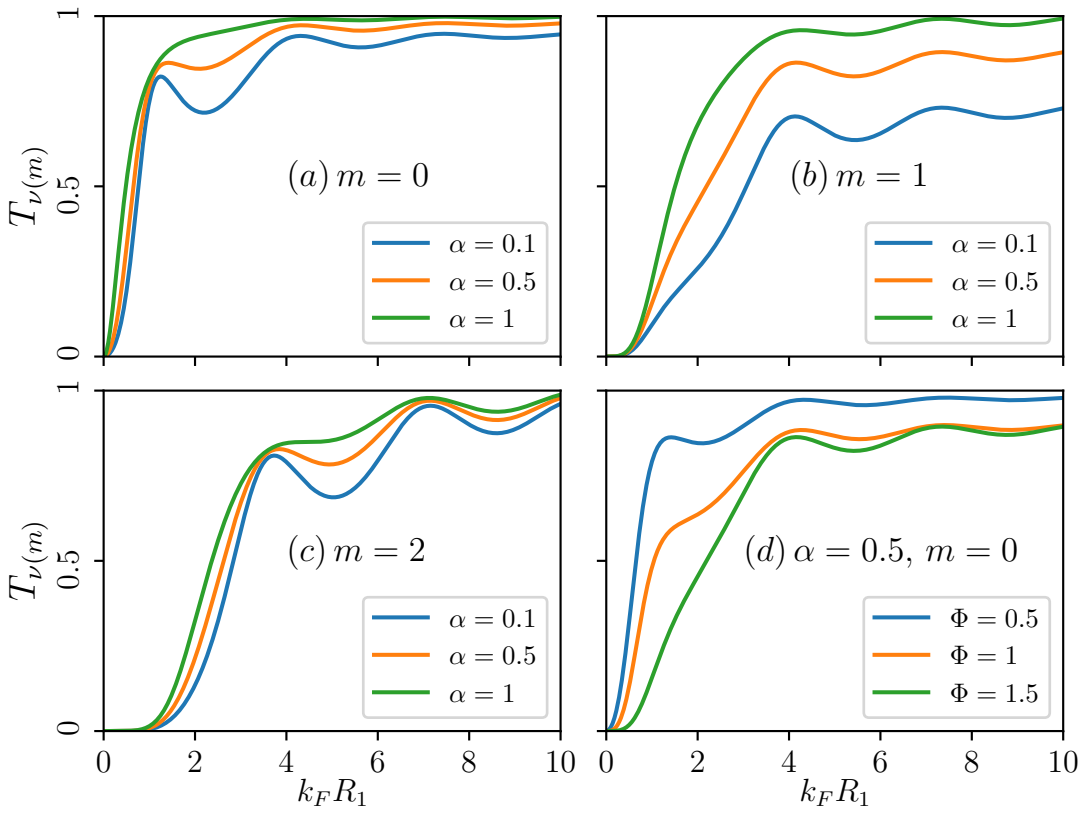

Figure 5.3: (The transmission $T_{\nu(m)}$ as a function of the doping $k_F R_1$ for a radii ratio $R_2/R_1 = 5$, $\Phi/\Phi_0 = 1/2$, and for different values of α (different colors correspond to different values of α) for $(a) m = 0$, $(b) m = 1$, and $(c) m = 2$. (d) Showing the transmission $T_{\nu(m)}$ as a function of the doping $k_F R_1$ for a radii ratio $R_2/R_1 = 5$, for a fixed value of the angular momentum quantum number, m (namely, $m = 0$), for a particular value of α (say, $\alpha = 0.5$), and for different Φ/Φ_0 ratio as shown by different colors in the plot.

gradual, and they converge slower than the $m = 0$ case. In Fig. 5.2(b) for $\alpha = 0.5$, the oscillatory behaviour becomes slightly more prominent compared to $\alpha = 0.1$ (Fig. 5.2(a)). The curves for larger doping saturate, however the oscillations for higher m values (especially $m = 2$) are more discernible. This suggest that the effect of increasing α is to minimize these oscillations, while still maintaining the overall trend of increasing transmission with doping. In Fig. 5.2(c), for $\alpha = 1$, the transmission smoothes compared to the lower values of α. While some oscillations are still visible, particularly for $m = 1$ and $m = 2$, they are less pronounced. For $m = 0$, the transmission reaches its saturation faster than for $m = 1$ and $m = 2$ curves. As α increases, the transmission for a particular m value increases which is shown in Figs. 5.3 (a), (b), and (c) for $m = 0$, 1, and 2 respectively for $\alpha = 0.1$, 0.5, and 1. However, as α increases, the transmission curves become less oscillatory, particularly for higher m values. The saturation of transmission occurs for large $k_F R_1$, indicating that large doping eventually results in a maximum transmission that does not significantly change with further increases in $k_F R_1$. The saturation occurs due to the fact that the energy levels nearly form a continuous

spectrum at large doping. Further, we have a full transmission (Klein tunneling) for larger α with $m = 0$. Larger the magnetic flux, the transmission decreases as shown in Fig. 5.3(d) for a fixed m and for particular α (namely, $\alpha = 0.5$). Fig. 5.4 shows the transmission $T_{\nu(m)}$ as

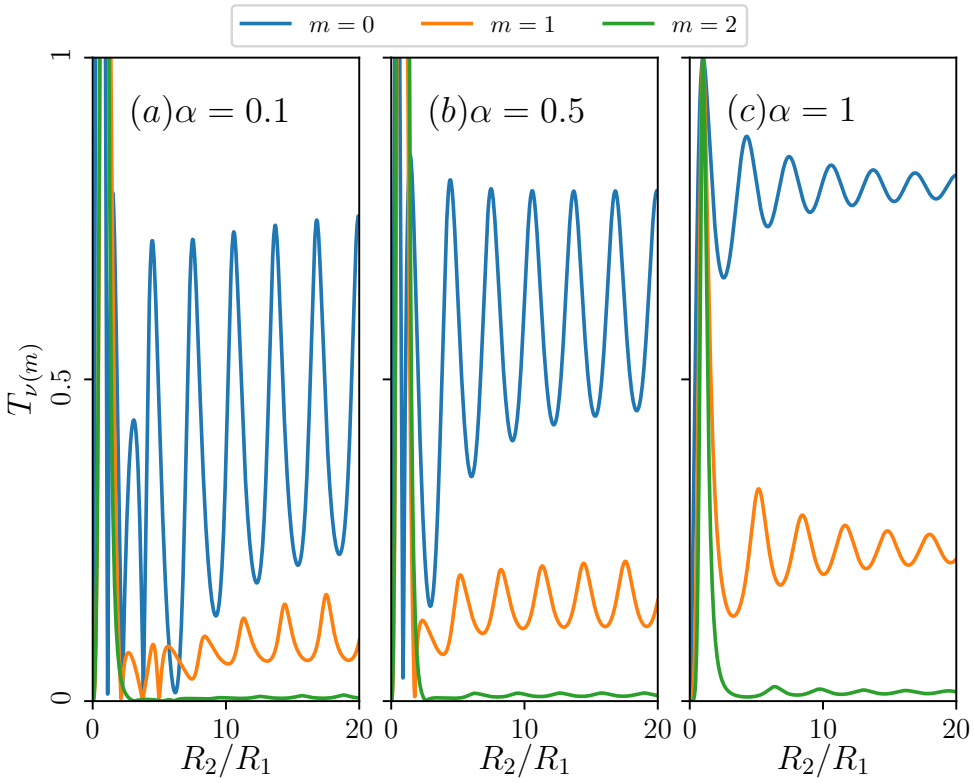

Figure 5.4: The transmission $T_{\nu(m)}$ ($m = 0, 1, 2, 3$) as a function of radii ratio R_2/R_1 for the doping $k_F R_1 = 1$, $\Phi/\Phi_0 = 1/2$, (a) for $\alpha = 0.1$, (b) for $\alpha = 0.5$, and (c) for $\alpha = 1$.

a function of the ratio of the outer and inner radii, namely, R_2/R_1 for a fixed doping value, namely, $k_F R_1 = 1$, with $\Phi/\Phi_0 = 1/2$ for $\alpha = 0.1, 0.5$, and 1. The transmissions are plotted for three different values of $m(= 0, 1, 2)$. The transmission curves exhibit an oscillatory behaviour as R_2/R_1 increases. The curves corresponding to $m = 0$ (blue lines) show largest transmission and are characterized by more prominent oscillations, with the transmission reaching close to 1 (complete transmission) at specific (lower) values of R_2/R_1. As α increases, the amplitudes and the frequency of these oscillation decrease. For $0 < \alpha < 1$ and higher m values the transmission at $R_2/R_1 \simeq k_F R_1$ is forbidden which is evident due to occurance of a singularity at that value of doping. Higher m values demonstrate much smaller transmission values and fewer oscillations. As α increases, higher m curves exhibit more pronounced oscillations. The oscillatory behaviour suggests that increasing α enhances the resonance effects. For $\alpha = 1$, the transmission oscillations smoothen, particularly for $m = 0$, where the transmission reaches a nearly constant value after some initial oscillations. For higher values of m and all values of

α, the transmission decreases exponentially. We notice that the amplitudes of these oscillation decreases when the ratio R_2/R_1 is increased and further they depends on the value of α.

Now we compute certain physical quantities related to the transmission coefficient. The conductance at the linear-response level is calculated via the Landauer-Büttiker formula [217, 220]

$$G = \frac{I}{V} = g_0 \sum_{m=\pm1,\pm2,\ldots} T_{\nu(m)}, \tag{5.18}$$

where the conductance quantum $g_0 = 4e^2/h$, with the factor 4 accounting for the spin and valley degeneracy, and the summation is performed over all the modes. In addition, the particle-hole symmetry, $T_{\nu(m)}(-k_F R_1) = T_{\nu(m)}(k_F R_1)$ allows us to limit the discussion only positive values of $k_F R_1$, that is, $k_F R_1 > 0$. Our numerical results are presented in the Fig. 5.5.

The asymptotic properties of the Hankel functions [329] in Eq. (5.16) lead to $T_{\nu(m)} \approx 1$ for $k_F R_1 - \nu(m) \gg 1$, with $\nu(m)$ given by Eq. (5.6), or to $T_{\nu(m)} \approx 0$ for $\nu(m) - k_F R_1 \gg 1$. With these, the conductivity can be approximated as $G \approx 2 g_0 k_F R_1$ for $k_F R_1 \gg 1$ and $R_2 \gg R_1$.

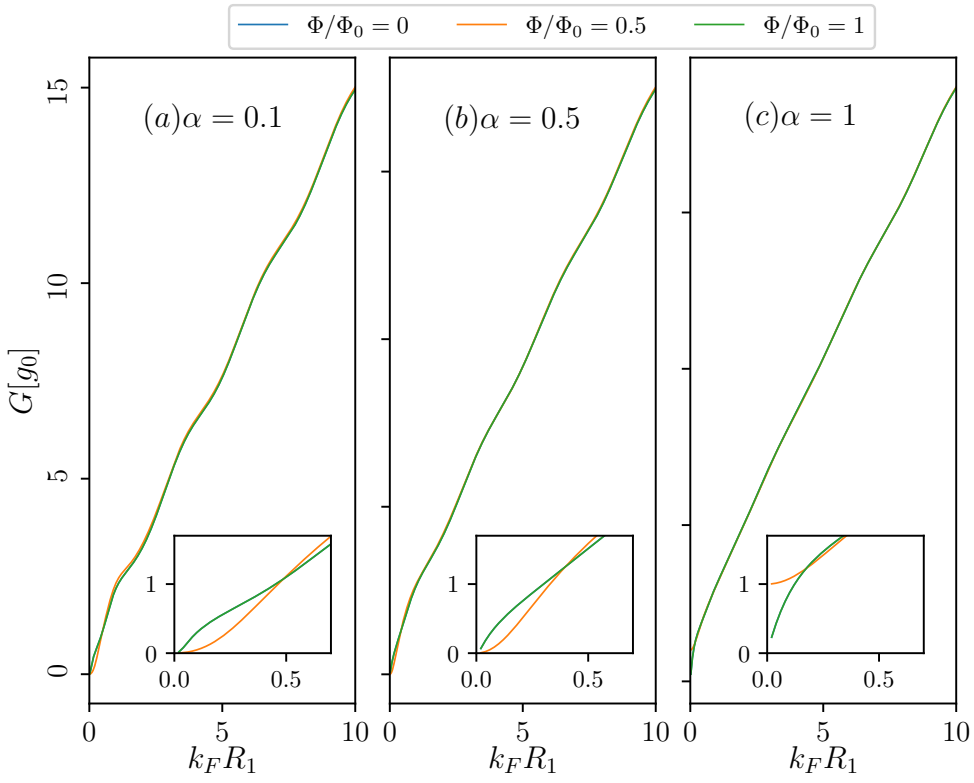

Figure 5.5: Conductance G as a function of the doping $k_F R_1$ for the radii ratio $R_2/R_1 = 5$. Different lines corresponding to $\Phi = 0$ (blue line), $\Phi = 1/2$ (orange line), and $\Phi = 1$ (green line) Φ is measured in unit of Φ_0. Different plots correspond to (a) $\alpha = 0.1$, (b) $\alpha = 0.5$, and (c) $\alpha = 1$. In the insets, zoomed in views are shown.

Let us put the ongoing discussion in perspective by mentioning some of the interesting results in graphene, and their relevance to those for the α-T_3 Corbino disk. Previously, the conductance quantization with steps of $4e^2/h$ was predicted for a graphene strip with a moderate aspect ratio (width/length $\leq$ 1) [330–333]. Quantization in unit of $8e^2/h$ was theoretically found in a bipolar junction in graphene, which exhibits the Goos-Hänchen effect [334]. The absence of conductance quantization observed in a graphene Corbino disk [77, 78] highlights the role of the evanescent modes, which decay slowly with distance (following a power law) and remain significant far from the Dirac point, illustrating a striking consequence of angular momentum conservation [75, 77, 78, 326, 327]. A similar behaviour in the conductance profile is also observed here for the α-T_3 Corbino disk as we see below.

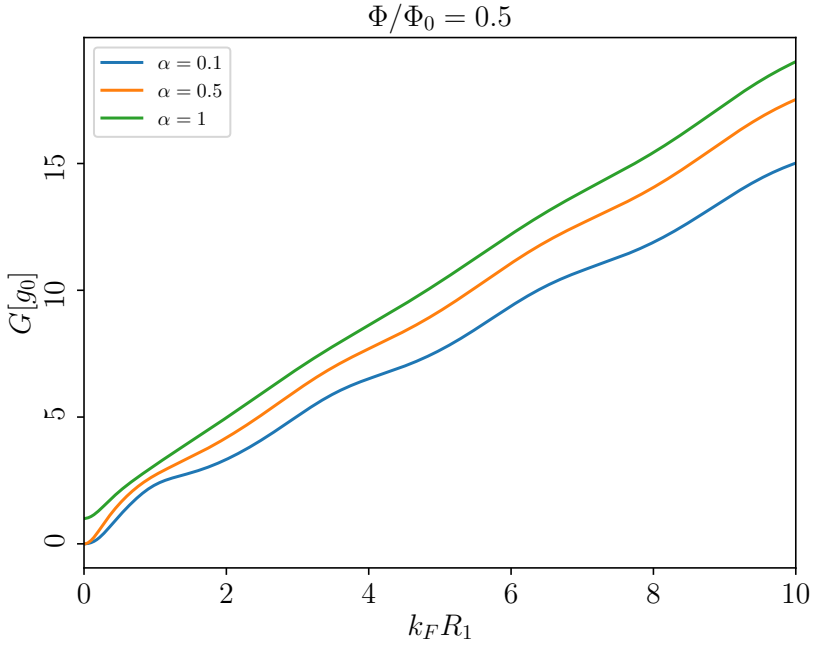

Figure 5.6: Conductance G as a function of the doping $k_F R_1 = 1$ for the radii ratio $R_2/R_1 = 5$ and $\Phi/\Phi_0 = 0.5$. Different lines corresponding to $\alpha = 0.1$ (blue line), $\alpha = 0.5$ (orange line), and $\alpha = 1$ (green line).

Fig. 5.5 shows the conductance $G[g_0]$ as a function of doping ($k_F R_1$) for $\Phi/\Phi_0 = 0$, 0.5, and 1 with the same α values as earlier, namely, 0.1, 0.5, and 1 in Figs. 5.5(a), (b), and (c) respectively. It is evident that the conductance G increases with increase in doping, showing nearly step like behaviour as a function of $k_F R_1$. However, the sharpness of the steps diminishes as α increases. This suggests that conductance is (nearly) proportional to doping for higher values of α. Additionally, for higher $k_F R_1$, all the three curves for $\Phi/\Phi_0 = 0, 0.5$, and 1 overlap significantly, showing very little dependence on the flux enclosed by the α-T_3 disk. This also suggests that, except at very low doped regimes, the conductance becomes independent of the magnetic flux. In contrast, for very low $k_F R_1$ values, the differences between the curves for

different Φ values are somewhat noticeable (see insets of Fig. 5.5), with even those becoming somewhat unnoticeable for larger α. Furthermore, the $\Phi/\Phi_0 = 0$ and $\Phi/\Phi_0 = 1$ curves are same, reminiscent of the AB effect in this disk-like geometry. Moreover, Fig. 5.6 shows that increasing α leads to higher conductance at any doping level. When $\alpha = 1$ (dice lattice), the conductance is most sensitive to the magnetic flux and demonstrates large conductance.

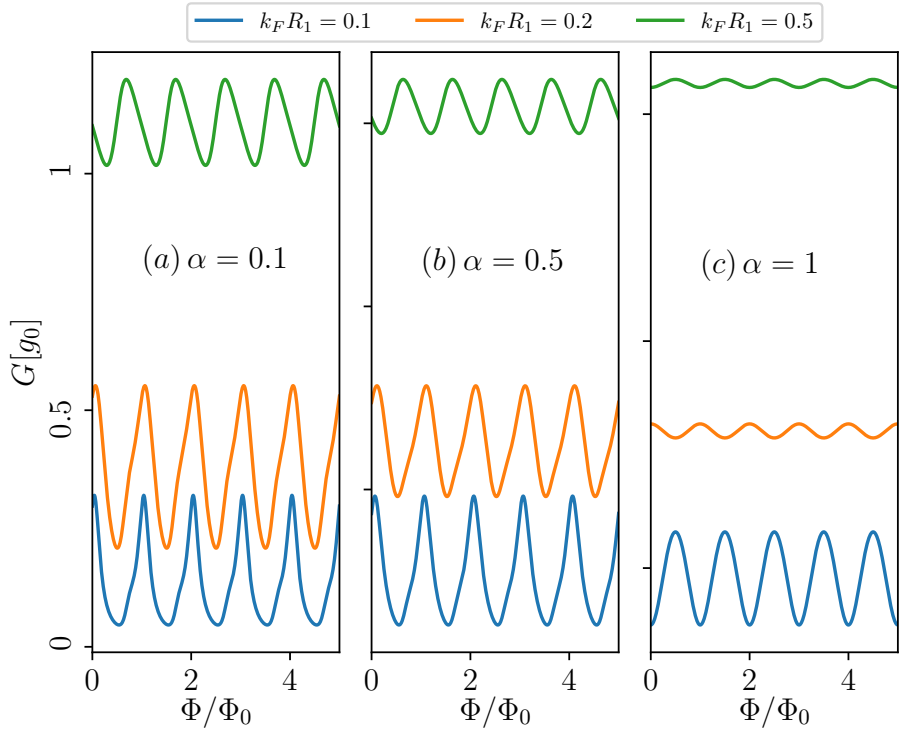

Figure 5.7: Conductance G as a function of the flux piercing the annular region (Φ/Φ_0) for the radii ratio $R_2/R_1 = 5$. The doping varies from $k_F R_1 = 0.1$ to 0.5 and specified for each lines on the plot. (a) for $\alpha = 0.1$, (b) for $\alpha = 0.5$, and (c) for $\alpha = 1$.

The structure of the Eqs. (5.6), (5.16), and (5.18) leads to a perfectly periodic functional dependence of $G(\Phi)$ at any arbitrary level of doping. In Figs. 5.7, 5.8, and 5.9, we show the conductance $G[g_0]$ as a function of the magnetic flux. It is clearly evident that the conductance oscillations are of the AB type with an oscillation period of one flux quantum, Φ_0. The amplitudes of these oscillations depend on $k_F R_1$, α, and the R_2/R_1 ratio. These results align well with the previously studied results for graphene [75, 326, 327]. The oscillations depict the quantum interference effects on the electron transport in mesoscopic disk structures, where the flux Φ through the disk modulates the conductance due to the AB effect. Here, the phase of the electronic wavefunction is affected by the presence of the magnetic flux (or the line integral of the vector potential), even if the electron travels through a region where the magnetic field is zero. The different panels illustrate the evolution of conductance oscillations with increasing α. As α increases, the oscillations become less pronounced (a general trend seen throughout), and

the amplitudes of the oscillations decrease for a particular value of $k_F R_1$ (here, $k_F R_1 = 0.5$) as shown in Fig. 5.8. This suggests that α influences certain aspects pertaining to the system geometry (or equivalently, the symmetry of the underlying α-T_3 lattice), which in turn affects the quantum interference pattern. Further, increasing α softens the oscillations. The data points in each plot of Fig. 5.7 represent different doping levels ($k_F R_1$). Doping affects the Fermi wavelength of the electrons, and consequently has implications on their interference pattern. Higher doping tends to reduce the prominence of the conductance modulation, as seen from the diminished oscillations corresponding to larger values of $k_F R_1$.

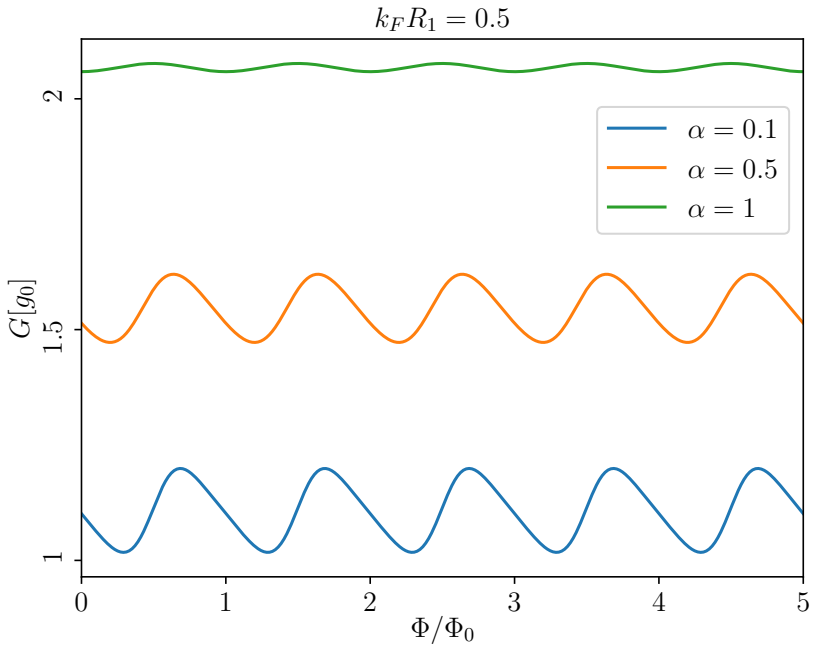

Figure 5.8: Conductance G as a function of the doping $k_F R_1 = 1$ for the radii ratio $R_2/R_1 = 5$ and $\Phi/\Phi_0 = 0.5$. Different lines corresponding to $\alpha = 0.1$ (blue line), $\alpha = 0.5$ (orange line), and $\alpha = 1$ (green line).

Fig. 5.9 illustrates the conductance $G[g_0]$ as a function of the flux Φ/Φ_0, with $k_F R_1 = 0.5$ (moderate doping), while varying the ratio of the radii R_2/R_1 (we have considered two limits, namely the *thin* limit ($R_2/R_1 = 5$) and the *thick* limit ($R_2/R_1 = 25$)), for different values of the hopping parameter α. For a particular value of α, as R_2/R_1 increases (as shown by the different curves in the plot), the amplitudes of the oscillations decrease. Additionally, for cases where $\alpha < 1$, there is a noticeable phase difference between different radius ratios. However, when $\alpha = 1$, the oscillations are in phase for both values R_2/R_1. Increasing the outer radius, R_2, expands the effective area of the disk region, which subsequently alters the interference patterns in the system.

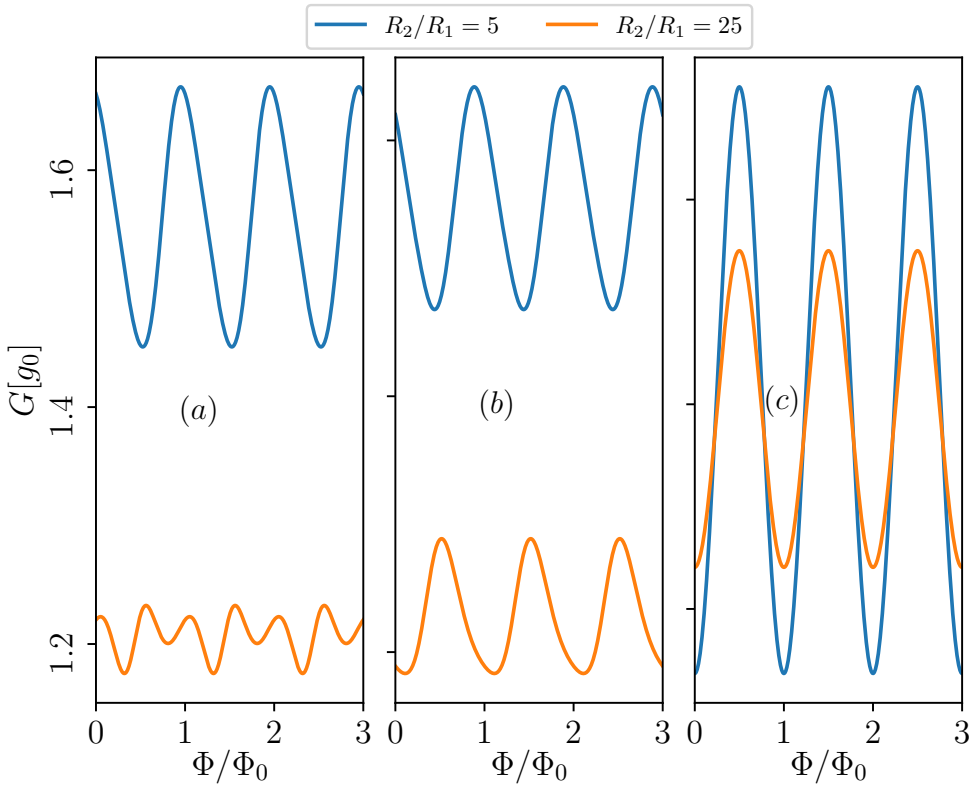

Figure 5.9: Conductance G as a function of the flux piercing the annular region (Φ/Φ_0) for doping $k_F R_1 = 0.5$. The radii ratio taken as, $R_2/R_1 = 5$ (thin limit) and 25 (thick limit), and specified for each lines on the plot with (a) for $\alpha = 0.1$, (b) for $\alpha = 0.5$, and (c) for $\alpha = 1$.

The $\alpha = 0$ (graphene) case, as discussed in the Refs. [75, 326, 327], demonstrates the conductance oscillations to be more regular, with a uniform amplitude and frequency with no asymmetry produced due to the absence of the central atom[1], yielding ideal AB oscillations. With the inclusion of the central atom ($\alpha \neq 0$) especially for small values of α and large R_2/R_1 ratio, the oscillations cease to be smooth and become irregular (see Fig. 5.9(a)). Instead, one can observe a double peak (or humps) in the conductance profile for each oscillation cycle, implying that there is an interference between different periodicities or frequencies.

This multi-harmonic contribution to the conductance oscillation may occur due to the availability of multiple pathways for the electrons contributing to the interference phenomena, such as the electron can traverse in both clockwise and anticlockwise paths around the flux. The hopping parameter α introduces a generic asymmetry in the system due to different coordination numbers for different sublattice sites, while $\alpha = 0$ represents a fully symmetric case. Even an infinitesimal value of α disturbs this symmetry, resulting in mixing of different modes leading

[1]Even with the central atom present, the α-T_3 lattice is still bipartite. As shown in Fig. 5.1, A, B, and C atoms represent the three basis sites of a unit cell. The coordination number is 3 for the A and C sublattices, while it is 6 for the B sublattice. The coordination number of one subset of sites is distinct than the other. We refer to this as an asymmetry.

to interference between them. As a result, we see a single peak turning complex and eventually evolving into a double-peak (split-peak) feature. Further, large R_2/R_1 implies larger area of the disk with larger number of sites and hence larger number of modes being involved. This may lead to different effective path lengths, resulting in a phase difference between them. This phase difference could result in a constructive interference at any two points within a single oscillation cycle, thereby producing the double-peak pattern.

Another possibility is that a larger outer radius (or larger R_2/R_1) induces higher harmonic contributions to the conductance oscillations. These higher harmonics have shorter periods and may interfere with the fundamental AB oscillation periods to produce the observed double-hump structure. Further, the magnetic flux enclosed by different electron paths in the system could also vary due to large disk area, causing the effective flux experienced by electrons to differ depending on their paths. This difference can lead to superposition of more than one oscillation frequencies, producing two peaks within a single oscillation period. This behaviour is typical in mesoscopic systems where the geometry and the confinement phenomenon conspire to yield complex interference effects between electron paths.

As α increases, the double-peak feature in the conductance oscillations gradually disappears, even at *thick* limit. Further, as α increases, the system becomes progressively more asymmetric [157]. This larger asymmetry is likely to disrupt the coherent interference between different electron paths that produces the double-peak feature at lower values of α. In the more asymmetric case (or a *thick* disk), the phase difference between the paths becomes more pronounced, and the interference effects that once contributed to the double-peak may cease to exist. Instead, the system possibly favours a more uniform interference pattern with regular AB-like oscillations. At higher α, the interference from the higher harmonics diminishes or the additional modes become weaker such that they no longer constructively interfere with the primary oscillations. As a result, the primary modes (fundamental AB oscillations) begin to dominate, and the conductance oscillations tend to have more uniform periodicity. This simplifies the oscillation pattern and eliminates the double-peak structure. However, even at high R_2/R_1, the same feature disappears for all values of α. This implies that the effect of increasing α is strong enough to suppress the complex (repeated) interference effects, regardless the size of the system. Further, the symmetry with respect to the direction of the flux has the consequence that the conductance is symmetric, that is, $G(-\Phi) = G(\Phi)$.

We study the magnitude of conductance oscillations ΔG. It is defined as the difference between $G(\Phi_0/2)$ and $G(0)$ as [75, 327]

$$\Delta G = G(\Phi_0/2) - G(0). \tag{5.19}$$

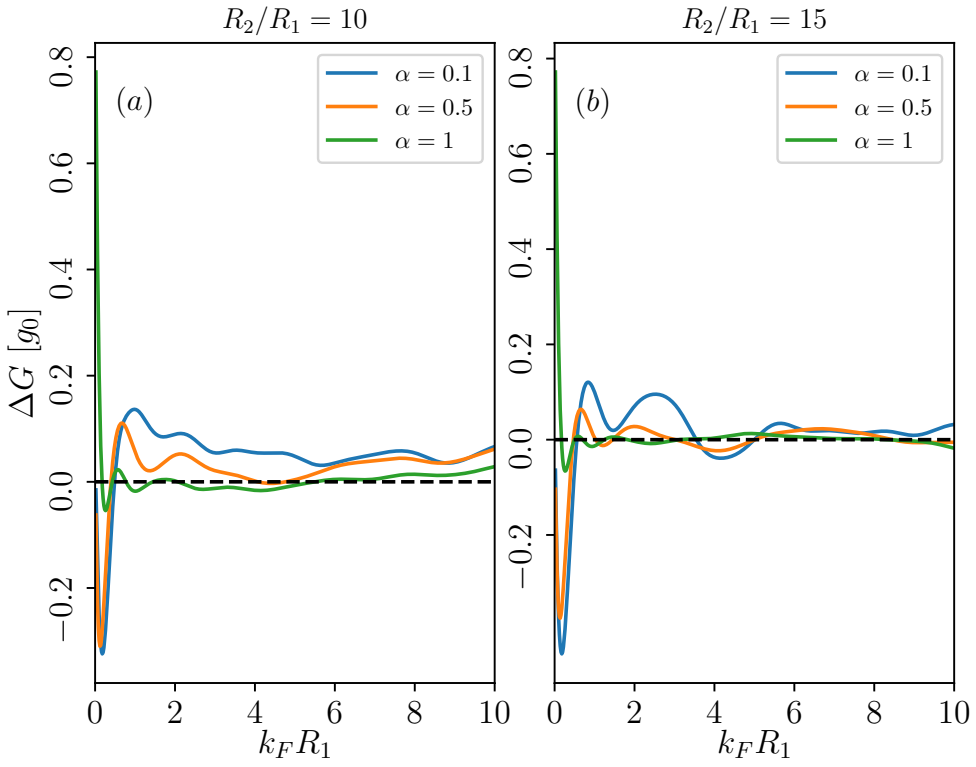

Figure 5.10: Magnitude of the conduction oscillations, $\Delta G = G(\Phi_0/2) - G(0)$, depicted as a function of the doping for selected values of α (specified for each line). Black dashed line shows the actual $\Delta G = 0$. (a) for $R_2/R_1 = 10$ and (b) for $R_2/R_1 = 15$.

Fig. 5.10 shows the magnitude of the conductance oscillations ΔG as a function of the doping $k_F R_1$ for two different radii ratios, namely $R_2/R_1 = 10$ (see Fig. 5.10(a)) and $R_2/R_1 = 15$ (see Fig. 5.10(b)). The absolute values of ΔG are relatively large not only in small vicinity of the charge neutrality point (zero doping), but also at larger doping. This means that for low Fermi wave vectors, the conductance oscillations are strong and more sensitive irrespective the value of α, signaling the importance of transport via the evanescent waves. This feature has a similarity to that in graphene [75, 327]. Notice that ΔG (Eq. (5.19)), is governed by only a few modes for which $k_F R_1 \approx \nu(m)$ (see Eq. (5.6)) and thus T_m's are neither ≈ 0 nor ≈ 1. A systematic growth of ΔG with the ratio R_2/R_1 is visible for $k_F \to 0$ for $\alpha < 1$ cases, which is consistent with the corresponding results for graphene as shown in Refs. [75, 77, 78, 327]. ΔG shows oscillates around the zero value (black dashed line). Positive or negative values indicate increase or decrease in the conductance relative to the flux-free state. As $k_F R_1$ increases, the oscillations gradually dampen, becoming smaller and more stable at large $k_F R_1$ for all values of α. This suggests that at higher values of Fermi energy, the quantum interference effects diminish. Further, the geometry (the ratio of radii) has a strong influence on the oscillation magnitudes, with larger ratios damping the oscillations more quickly. This implies that changing the geometry (tuning the disk region) of the system alters the sensitivity of the conductance to

the external magnetic flux, doping, and α.

For each values of the R_2/R_1 ratio, there is a unique series of discrete doping values where ΔG crosses the zero line, resulting in $G(\Phi_i)$ being constant (that is equal to $G[0]$). Moreover, for a given R_2/R_1, increasing α leads to an increase in the number of nodes. As shown in Fig. 5.10(a), for $R_2/R_1 = 10$, $\alpha = 0.1$ has only one node, while $\alpha = 0.5$ and 1 exhibit 3 and 6 nodes, respectively. Similarly, for $R_2/R_1 = 15$, the number of nodes increases to 3, 6, and 7 corresponding to $\alpha = 0.1$, 0.5, and 1, respectively (see Fig. 5.10(b)). For example, when $R_2/R_1 = 10$ and 15, the nodes of ΔG correspond to certain specific values of $(k_F R_1)_{\Delta G=0}$ are listed in table 5.1.

$R_2/R_1 = 10$							
α	1st	2nd	3rd	4th	5th	6th	7th
0.1	0.49	-	-	-	-	-	-
0.5	0.40	4.09	4.82	-	-	-	-
1	0.172	0.43	0.775	1.455	2.074	5.534	-
$R_2/R_1 = 15$							
α	1st	2nd	3rd	4th	5th	6th	7th
0.1	0.56	3.55	5.00	-	-	-	-
0.5	0.467	1.028	1.46	3.014	5.00	8.445	-
1	0.174	0.504	0.701	1.251	1.796	3.194	8.149

Table 5.1: Values of $k_F R_1$ for which $\Delta G = 0$ for $R_2/R_1 = 10$ and $R_2/R_1 = 15$.

Prior to the first node, for $\alpha < 1$, we have $\Delta G < 0$, however, for $\alpha = 1$, $\Delta G > 0$. Beyond that, the sign of ΔG alternates with growing values of $k_F R_1$ for each node, as indicated in Figs. 5.10(a) and (b). It is also visible in Fig. 5.10 that the occurance of the nodal points is irregular, as one can expect since ΔG can be regarded as originating from the behaviour of the Bessel function. For example, the typical separation between the first node of ΔG for $\alpha = 0.1$ (see Table I) can be approximated as $\Delta k_F R_1 \approx 0.5$, which corresponds to $R_1 \approx 80$ nm, (nearly consistent with the results of graphene [75]), to the energy interval of $\Delta E_f/k_B \approx 50$K (with the Boltzmann constant k_B). In turn, the conductance oscillations should be observable in comparable or higher temperatures then the standard AB effect in graphene rings [29, 335].

5.4 Fano Factor

In general, the electrical current through nanostructures exhibits time-dependent fluctuations due to the discrete nature of electric charge [336]. These fluctuations, known as the shot noise, and the ratio of the shot noise power to the average electrical current is known as the Fano factor [337]. The Fano factor assumes universal values depending on the electronic transport regime in tunnel junctions, such as, it corresponds to a Poissonian noise with $F = 1$ [338], for diffusive transport, it is $F = 1/3$ [339, 340], and in ballistic transport, $F = 0$ [336]. With the rise of graphene electronics, it was found that the conductivity of a graphene strip reaches its minimum at zero bias condition, causing the shot noise power to peak. Further, Ref. [341] demonstrated that the Fano factor for a graphene strip is $1/3$, matching the value for a diffusive transport. This result stems from the non-classical transport in graphene, governed by the Dirac equation, and has been experimentally verified in Refs. [342, 343]. Further, it was conceived that the energy of the Fano factor peaks track the locations of the Dirac points in the Brillouin zone [344].

In our case, the dominant contribution to the conductance fluctuation is due to the external magnetic flux. It would be interesting to explore how the conductance of an α-T_3 disk responds to the external flux by examining the Fano factor, which defined as the following ratio,

$$F = \frac{\sum_m [T_{\nu(m)}(1 - T_{\nu(m)})]}{\sum_m T_{\nu(m)}}. \tag{5.20}$$

where $\sum_m$ denotes the sum over all conducting modes and $T_{\nu(m)}$ is the transmission probability as defined in Eq. (5.16) The results obtained so far can be numerically analyzed under suitable choices for the physical parameters. The results are shown in Fig. 5.11 with two different values of the flux, namely, $\Phi/\Phi_0 = 0.5$ (see Fig. 5.11(a)) and 1 (see Fig. 5.11(b)). Similar to the strip geometry [341], the conductance minimum at $k_F R_1 \to 0$ corresponds to a maximum (for $\alpha < 1$) or a minimum (for $\alpha = 1$) value for the Fano factor, F. Further, F acquires high values near $k_F R_1 \to 0$, which decreases sharply followed a series of oscillations as $k_F R_1$ increases. The amplitudes of the oscillations diminishes as α increases, and the curves for higher α (towards the dice limit) tend to flatten more. The black dashed line corresponds to $F = 1/3$, which denotes a value, where the transport is fully diffusive. Our results shows that for all α and higher $k_F R_1$, we obtain the Fano factor assuming values closer to the diffusive limit. However, for the small $k_F R_1$ and $\alpha < 1$, we get $F \sim 1$ that underscores a Poissonian transport regime [338] dominated by independent tunneling events, with either little or no correlation between the electron transmissions. The above result ($F \sim 1$) contrasts with the regime where $F < 1$, which denotes diffusive (or sub-Poissonian) transport, where the electron correlations or

scattering play a more significant role. Small values of $k_F R_1$ mean that the size of the system is smaller compared to the Fermi wavelength, thereby leading to a regime where the quantum effects dominate, and the transport is primarily dominated by random tunneling events.

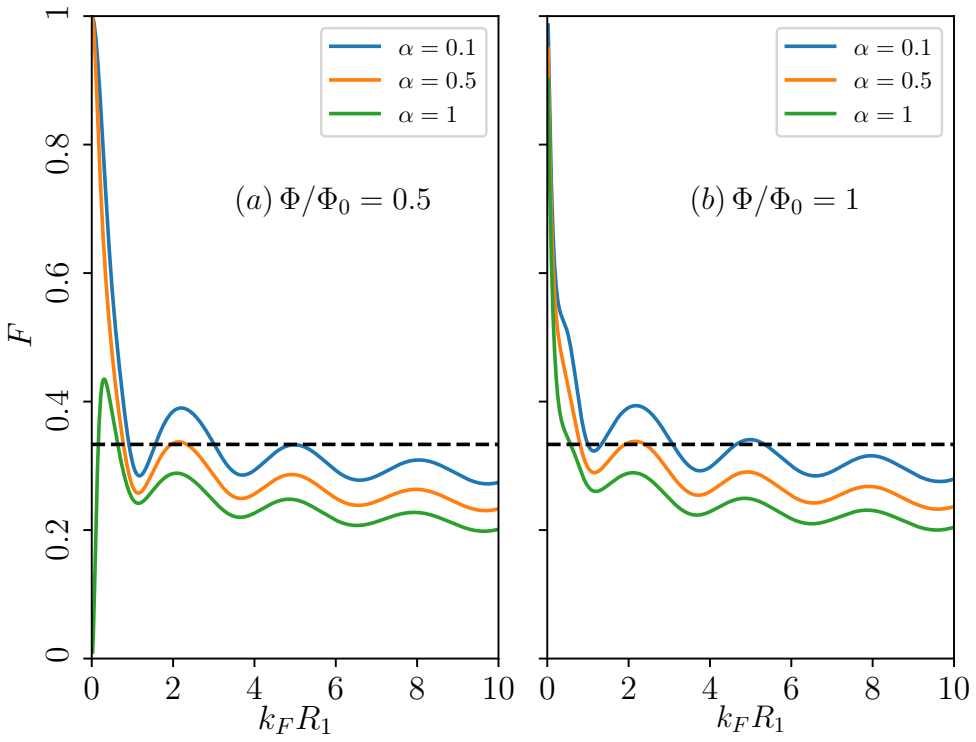

Figure 5.11: Fano factor F as a function of the doping $k_F R_1$ for the radii ratio $R_2/R_1 = 10$ and (a) for $\Phi/\Phi_0 = 0.5$ and (b) for $\Phi/\Phi_0 = 1$ (Φ being the threaded flux). Different lines corresponding to $\alpha = 0.1$ (blue line), $\alpha = 0.5$ (orange line), and $\alpha = 1$ (green line). The black dashed line denotes diffusive transport regime.

Further, different flux ratios threaded, for example $\Phi/\Phi_0 = 0.5$ with $\alpha < 1$, the system is likely to be weakly coupled, which contributes to the random (uncorrelated) nature of the transport. However, this is not the case for $\alpha = 1$, where the Fano factor changes from $F \sim 0$ to nonzero values with increasing $k_F R_1$. This indicates a departure from the ballistic regime to a pseudo-diffusive transport ($F \to 1/3$) for large values of $k_F R_1$ as shown in Fig. 5.11(a). Moreover, for $\Phi/\Phi_0 = 1$, we observe a transition from Poissonian transport ($F \sim 1$) to a pseudo-diffusive regime with increasing doping, for all values of α, as shown in Fig. 5.11(b). These results differ from those in graphene, where transport is ballistic in high-purity, mesoscopic samples [141, 345] and diffusive or pseudo-diffusive when disorder and impurities come into play [341, 346–348]. Here, by tuning the doping level and the external flux, we can modulate the transport properties and the correlations between electrons involved in the transport process.

The magnetic flux alters the phase of the electronic wavefunctions via the AB effect. At $\Phi/\Phi_0 = 0.5$, phase interference can either enhance or suppress the transport channels, depending on the

value of α. For $\alpha = 1$ and low doping, transport suppression is significant, resulting in nearly a noiseless transport ($F \sim 0$). In contrast, other values of α lead to a larger noise due to the following reasons. This happens because, when $\alpha = 1$, the path lengths between the A to B and A to C sublattices are equal, causing the flat band to become localized and preventing it from carrying current. As a result, the transport is dominated by the Dirac cones, which exhibit ballistic behavior, similar to that of graphene. When $\alpha < 1$, the differing path lengths between the A to B and A to C sublattices diminish flat-band the localization, causing higher fluctuations in the current due to less coherent transport. This leads to higher noise levels and the Fano factor approaches the Poissonian limit.

5.5 Comparison Between Graphene and α-T_3 Corbino Disks

While studies on graphene Corbino disks exist in literature, its generalization in terms of an α-T_3 structure has so far been ignored. In this section, we compare and contrast the properties of a graphene and the α-T_3 Corbino disks, thereby emphasizing the highlights of our work. In a particular setup, the magnetoconductance studies of a graphene Corbino disk in presence of a uniform magnetic field reveals conductance oscillations with the flux threading the disk area (denoted by Φ_d) with a period of $\Phi_0 = \frac{2h}{e} ln(\frac{R_{out}}{R_{in}})$ (where R_{out} and R_{in} are the outer and inner radii of the disk), the result clearly differs from the usual oscillations with one flux quantum. Additionally, at low but finite doping, these oscillations persist upto a limit of $|\Phi_d| \leq \Phi_d^{\max}$, beyond which the oscillatory behaviour vanishes and the conductance gets suppressed. In addition to observation of diffusive transport, ballistic transport has also been observed in this graphene Corbino disk configuration [73, 78]. In an alternate scenario, when the disk subjected to a solenoidal magnetic potential (similar to our setup), the graphene Corbino disk configuration exhibits smooth Aharonov-Bohm type conductance oscillations in the ballistic transport regime, and the conductance displays step-like features with increasing doping [75, 327, 349, 350].

Moving to the α-T_3 Corbino disk, where an additional atom is located at the center of each hexagon connected via tunable hopping with one of the neighbours possesses a zero-energy flat band that may play a decisive role in shaping the transport characteristics. Enroute to the perfect dice limit ($\alpha = 1$), in contrast to graphene ($\alpha = 0$), the step-like conductance feature diminishes as α increases. In certain parameter regime, namely, the *'thick'* disk limit (large R_2/R_1) and small values of α, higher harmonic contributions emerge in the conductance profile. The physical explanations of which are provided in the preceding section. It turns out that the presence of the zero-energy flat band significantly alters the transport characteristics compared to graphene. This result may be counter intuitive as the carriers pertaining to the flat band have

zero velocity and should have negligible role in transport. Finally, a statistical analysis yields the Fano factor to vary with both α and the magnetic flux, indicating emergence of distinct transport characteristics. These differences open up possibilities for fabricating novel transport devices in flat-band systems, such as hydrodynamic electron magnetotransport and enhanced (and tunable) thermoelectric properties of the α-T_3 Corbino disk.

5.6 Summary

We have studied the α-T_3 lattice in the form of a disk with inner radius R_1 and outer radius R_2, subjected to a magnetic flux Φ which perceived as an electron pump by Laughlin and should demonstrate quantum Hall effect at the low temperature. Utilizing the unique geometry of the Corbino disk, we have conducted analytical calculations leading to exact solution to the stationary Dirac equation. Also, we determined the transmission probability of an electron with a given value of angular momentum tunneling through the α-T_3 Corbino disk. Further, we have computed a few relevant physical quantities, such as, the conductance G and the Fano factor F.

Our numerical results were expressed in terms of the doping level $k_F R_1$, ratio of the outer to inner radii R_2/R_1, magnetic flux Φ, and α. The conductance as a function of the magnetic flux threading the disk shows periodic oscillation of the AB kind. However, the oscillation patterns and the amplitudes hugely depend upon the system parameters (α, $k_F R_1$ etc.). Additionally, we observe higher harmonic modes at lower α values and larger radii ratio.

Notably, away from the charge-neutrality point ($k_F R_1 = 0$), the conductance oscillations exhibit a substantial magnitude. Regardless of the value of α, these oscillations are strong and highly sensitive, highlighting the role of the evanescent waves in the mechanism leading to electron transport. Moreover, the conductance oscillates around zero, reflecting the influence of the geometry, magnetic flux, doping, and α. We have also computed the Fano factor, which reveals distinct behavior for $\alpha < 1$ (α-T_3) and $\alpha = 1$ (dice). For $\alpha < 1$, the transport shifts from Poissonian to pseudo-diffusive as the doping increases. In contrast, for $\alpha = 1$, the Fano factor transitions from the ballistic regime to pseudo-diffusive transport at large $k_F R_1$.

Chapter 6

Chern Insulating Phase of an α-T_3 Haldane-Holstein Model

In this chapter, we present impelling evidence of topological phase transitions induced by electron-phonon (e-ph) coupling in an α-T_3 Haldane-Holstein model. The e-ph coupling has been incorporated via the Lang-Firsov transformation which adequately captures the polaron physics in the high frequency regime, and yields an effective Hamiltonian through zero phonon averaging at $T = 0$. We explore the signature of phase transitions driven by polaron and its interplay with the parameter α.

6.1 Introduction

The study of topology in multiband systems has emerged as one of the fundamental areas that has reshaped the overall scenario of modern condensed matter physics [110, 195, 351–358]. With the advent of two-dimensional (2D) graphene-like materials, immense interest has been drawn to studying electronic and transport properties in honeycomb lattices and its variants [141, 143]. However, the role of many-body correlations like electron-electron and electron-phonon interactions in inducing the topological phase transition in an α-T_3 lattice has been

largely unnoticed. The previous proposals of topological phase transition are mainly in non-interacting systems (single-particle picture) where the topology is solely described by the properties of the electronic bands [102, 183, 186, 359] or by other external means [184, 360]. Nevertheless, attempts were made to investigate the topological phase transitions driven by many-body interactions in the past [96, 288, 361–370], most of which are devoted to explaining the effects of electronic correlations on the topological phases of matter. On the contrary, the role of electron-phonon (e-ph) interaction in such contexts has been scarce. We shall include the 'polaron' physics in a non-trivially gapped system. Breaking the time reversal symmetry (TRS) via complex next nearest neighbour (NNN) hopping is a starting point for our study. Specifically, we demonstrate that this polaronic 'impurity' moving in an α-T_3 lattice and interacting with the lattice vibrations, gives rise to the non-trivial spectral gap arising due to the polarons formed in a Haldane (Chern) insulator.

Since the parent α-T_3 possesses non-trivial topology, it remains to be seen whether the polarons aid or hinder the topological phases. If yes, whether these transitions are accompanied by the conventional wisdom, such as (dis)appearance of conducting edge modes, abrupt change in the topological invariant, the behaviour of the anomalous Hall conductivity etc. This interaction-driven topology may serve to connect the correlated phenomena in physics with topology. There are a few studies which describe the importance of e-ph coupling in determining the nontrivial phases in the Haldane Chern insulator [371, 372], graphene nanoribbons [373], topological superconductivity [374], and in other two-dimensional materials [370, 375–377]. Cangemi *et al.* [371] have proposed a topological quantum transition in a Haldane Chern insulator driven by the e-ph coupling, where they have shown the system undergoes a nontrivial to trivial transition with increasing e-ph coupling strength, where the average number of fermions shows a sharp discontinuity at the transition point indicating a topological transition. Along the same line, Camacho *et al.* [372] have investigated a phonon-induced transverse Hall effect through the "composite Berry phase" and shown the conductance jumps from zero to a finite value, where the latter is evidently accompanied by a nonzero Chern number. Using a diagrammatic technique in the continuum Dirac model, Pimenov [375] have reported a similar observation as in Ref. [372]. These studies largely encourage looking for systems that exhibit a nontrivial phase and possible phase transitions upon suitably tuning the strength of the e-ph coupling.

However, there is hardly any study revealing the effects of e-ph interaction in a multi-band α-T_3 system in the presence of a topological gap. Particularly, how the presence of a flat band, lying in between the conduction and the valence bands is impacted and whether it reveals emergence of a topological transition. Therefore, in this study, we aim to explore the role of e-ph coupling in stimulating the nontrivial topological phases in the α-T_3 lattice (see Fig. 6.1), which may

provide a fruitful prescription to understand the interaction-driven topology in other multi-band systems.

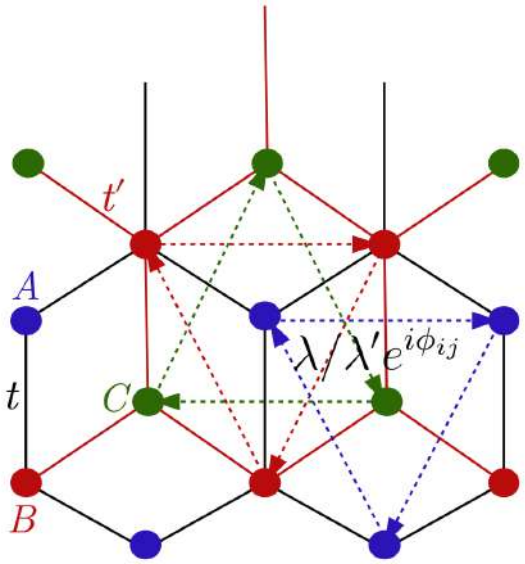

Figure 6.1: The schematic diagram of an α-T_3 lattice is shown, where the blue, red, and green circles represent the sublattices A, B, and C sublattices, respectively. The nearest neighbour (NN) hopping strength between A and B sublattices (solid black line) is t, while it is $t' = \alpha t$ between B and C sublattices (solid red line). The NNN hopping between A-B-A (dashed blue) or B-A-B (dashed red) is $\lambda e^{i\phi_{ij}}$, while through C, it is $\lambda' e^{i\phi_{jk}}$ between B-C-B (dashed red) and C-B-C (dashed green). Here $\lambda' = \alpha\lambda$ and the phase ϕ_{ij} $(-\phi_{ij})$ denotes the clockwise (anticlockwise) direction. The figure is repeated for the convenience of our ongoing discussion.

The chapter is organized in the following manner. In Sec. 6.2, we describe our system and present the model Hamiltonian of a polaronic α-T_3 lattice under the framework of the Haldane model modified by a Holstein term accounting for the e-ph coupling. In Sec. 6.2.1, we show the polaron formation in our system employing the Lang-Firsov technique, which works well for the high-frequency (anti-adiabatic) optical phonons. Sec. 6.2.2 deals with the momentum space representation of the model Hamiltonian. Sec. 6.3 is devoted to studying the topological phase transition driven by polarons, where we present our numerical results of the bulk and edge spectra in Sec. 6.3.1 and Sec. 6.3.2, respectively. In Sec. 6.4, we present the topological transitions induced by polaron via numerically computing the polaronic Chern number and the Berry curvature. Further support of the above, such as the quantized Hall plateaus below the critical value of e-ph coupling obtained in Sec. 6.5, also signifies the topological transition driven by e-ph interaction in our system. Finally, in Sec. 6.6, we conclude our results and briefly summarize our findings.

6.2 Haldane-Holstein Model for α-T_3 Lattice

We formulate our system in the spirit of a tight-binding Haldane-Holstein Hamiltonian, which is written as,

$$\begin{aligned}\mathcal{H} &= \left[-t\sum_{\langle i,j\rangle} c_i^\dagger c_j - \alpha t\sum_{\langle j,k\rangle} c_j^\dagger c_k - \frac{\lambda}{3\sqrt{3}}\sum_{\langle\langle i,j\rangle\rangle} e^{i\phi_{ij}} c_i^\dagger c_j - \frac{\alpha\lambda}{3\sqrt{3}}\sum_{\langle\langle j,k\rangle\rangle} e^{i\phi_{jk}} c_j^\dagger c_k + H.C.\right] \\ &\quad + \mathcal{M}\sum_i c_i^\dagger S_z c_i + \hbar\omega_0\left[\sum_i\left(b_i^\dagger b_i + \frac{1}{2}\right) + \lambda_{eph}\sum_i c_i^\dagger c_i (b_i^\dagger + b_i)\right], \end{aligned} \tag{6.1}$$

where different notations appearing in the first four terms have been introduced earlier and hence skipped. The fifth term of Eq. (6.1) is the Samenoff mass term, $\mathcal{M}$ is the mass, and S_z is the z-component of the pseudospin-1 matrix. The effects of the phonon modes are incorporated in the sixth and the seventh terms. The sixth term is the total onsite energy of the phonons denoted by the phononic creation (annihilation) operators, $b_i^\dagger(b_i)$ of site i and the last term of this modified Haldane model is the Holstein term that describes the onsite coupling between electrons and the longitudinal optical (LO) phonons with a coupling strength λ_{eph}, $\hbar\omega_0$ being the energy scale of phonons with a dispersionless LO frequency, ω_0.

6.2.1 Polaronic Hamiltonian: Lang-Firsov approach

The quasiparticles formed by the interaction between a bosonic lattice field (a phonon) and a fermionic charge carrier (an electron) undergo emission and absorption of virtual phonons by the electrons at $T = 0$. Owing to such an interaction, a net polarization potential is generated in which the electrons may get trapped. These quasiparticles dressed with virtual phonon clouds are known as polarons. For a tight-binding system, the size of a polaron is usually less compared to the lattice constant and is known as a small Holstein polaron. Here, we have only considered the onsite e-ph interaction, and neglecting the interactions of electrons with the NN and NNN site phonons, these being weak enough. To study the effects of the e-ph coupling, we first employ the much celebrated Lang-Firsov transformation (LFT), namely,

$$\tilde{\mathcal{H}} = e^R \mathcal{H} e^{-R}, \tag{6.2}$$

where the generator of the transformation is given by [260],

$$R = \lambda_{eph}\sum_i c_i^\dagger c_i (b_i^\dagger - b_i). \tag{6.3}$$

This is a coherent transformation of a displaced harmonic oscillator that eliminates the phonon degrees of freedom and transforms the Hamiltonian into an effective electronic Hamiltonian. We must assert that this unitary transformation works well in the high-frequency (non-adiabatic) regime, meaning the LO frequency of the phonons is much larger than the other electronic parameters of the system, that is, when $\omega_0 \gg t, t', \lambda, \lambda', \mathcal{M}$ and λ_{eph}. The LFT transforms the total Hamiltonian (6.1) as (see Appendix E for the derivation),

$$\begin{aligned}\tilde{\mathcal{H}} = -t\Big[\sum_{\langle i,j\rangle} c_i^\dagger c_j e^{[X_i - X_j]} + \alpha \sum_{\langle j,k\rangle} c_j^\dagger c_k e^{[X_j - X_k]}\Big] - \frac{\lambda}{3\sqrt{3}}\Big[\sum_{\langle\langle i,j\rangle\rangle} e^{i\phi_{ij}} c_i^\dagger c_j e^{[X_i - X_j]} + \alpha \sum_{\langle\langle j,k\rangle\rangle} e^{i\phi_{jk}} c_j^\dagger c_k e^{[X_j - X_k]}\Big] \\ + \sum_i c_i^\dagger(\mathcal{M}S_z - \lambda_{eph}^2 \hbar\omega_0 I_3)c_i + \hbar\omega_0 \sum_i b_i^\dagger b_i,\end{aligned} \tag{6.4}$$

where I_3 is a 3×3 identity matrix. The X-terms in the exponent contain the phonon operators as,

$$X_i = \lambda_{eph}(b_i^\dagger - b_i), \tag{6.5}$$

where i being the site index. At this stage, to eliminate the phonon degrees of freedom, one can obtain a zero-phonon average (at $T = 0$), which reads for the exponents as,

$$\langle 0|e^{[X_i - X_j]}|0\rangle \quad = \quad e^{-\lambda_{eph}^2}. \tag{6.6}$$

The quantity in RHS of Eq. (6.6) is known as the Holstein reduction factor which causes the band narrowing. The last term in Eq. (6.4) becomes zero after zero-phonon averaging. Therefore, in the transformed Hamiltonian (6.4), all the parameters are modified by the e-ph coupling and the effective Hamiltonian becomes,

$$\begin{aligned}\tilde{\mathcal{H}}_{eff} = \langle 0|\tilde{\mathcal{H}}|0\rangle \quad = \quad -\tilde{t}\left[\sum_{\langle i,j\rangle} c_i^\dagger c_j + \alpha \sum_{\langle j,k\rangle} c_j^\dagger c_k\right] - \frac{\tilde{\lambda}}{3\sqrt{3}}\left[\sum_{\langle\langle i,j\rangle\rangle} e^{i\phi_{ij}} c_i^\dagger c_j + \alpha \sum_{\langle\langle j,k\rangle\rangle} e^{i\phi_{jk}} c_j^\dagger c_k\right] \\ + \sum_i c_i^\dagger(\mathcal{M}S_z - \lambda_{eph}^2 \hbar\omega_0 I_3)c_i,\end{aligned} \tag{6.7}$$

where the reduced Holstein and Haldane amplitudes are renormalized as,

$$\tilde{t} = te^{-\lambda_{eph}^2} \quad \text{and} \quad \tilde{\lambda} = \lambda e^{-\lambda_{eph}^2}. \tag{6.8}$$

It is clear from Eq. (6.7) that the signatures of polaron in our system are captured through $\tilde{t}$ and $\tilde{\lambda}$, with both containing λ_{eph}. As the e-ph interaction modifies system parameters, it will be interesting to see how polaron induces a topological phase transition at certain critical e-ph coupling strength. To investigate the same, we need to transform the Hamiltonian (6.7) to the momentum ($\mathbf{k}$) space and calculate the band structures along with the relevant topological properties.

6.2.2 The continuum α-T_3 Haldane-Holstein Hamiltonian

The modified $\mathbf{k}$-space version of an α-T_3 lattice in the presence of e-ph interaction can be obtained by Fourier transforming the effective Haldane-Holstein Hamiltonian (6.7) in a tri-atomic sublattice basis as,

$$\tilde{\mathcal{H}}(\mathbf{k}) = -\tilde{t}\,(h_x S_x + h_y S_y) - \frac{2\tilde{\lambda}\Im\mathfrak{m}(f_{\mathbf{k}})}{3\sqrt{3}\,\cos\varphi} S_{zH} + \mathcal{M} S_z - \lambda_{eph}^2 \hbar\omega_0 I_3, \tag{6.9}$$

with

$$S_x = \nu \begin{pmatrix} 0 & \cos\varphi & 0 \\ \cos\varphi & 0 & \sin\varphi \\ 0 & \sin\varphi & 0 \end{pmatrix}, S_y = -i \begin{pmatrix} 0 & \cos\varphi & 0 \\ -\cos\varphi & 0 & \sin\varphi \\ 0 & -\sin\varphi & 0 \end{pmatrix}, S_z = \begin{pmatrix} 1 & 0 & 0 \\ 0 & 0 & 0 \\ 0 & 0 & -1 \end{pmatrix}, S_{zH} = \begin{pmatrix} -\cos\varphi & 0 & 0 \\ 0 & \cos\varphi - \sin\varphi & 0 \\ 0 & 0 & \sin\varphi \end{pmatrix}, \tag{6.10}$$

where $\varphi = \tan^{-1}\alpha$. Specifically, S_{zH} arises due to the presence of the NNN Haldane term. The parameter $\nu(=\pm 1)$ denotes the valleys K and K$'$ located at K$= (4\pi/3\sqrt{3}a, 0)$ and K$' = (-4\pi/3\sqrt{3}a, 0)$. The polaronic contributions to Eq. (6.9) enter through $\tilde{t}$, $\tilde{\lambda}$ (defined in Eq. (6.8)) and the last term in Eq. (6.9). h_x, h_y, and $f_{\mathbf{k}}$ in Eq. (6.9) are given as,

$$h_x = \sum_{i=1}^{3} \cos(\mathbf{k}.\mathbf{d_i}), \quad h_y = \sum_{i=1}^{3} \sin(\mathbf{k}.\mathbf{d_i}), \quad \text{and} \quad \mathbf{f_k} = \sum_{\mathbf{i=1}}^{\mathbf{3}} \mathbf{e}^{(\mathbf{ik}.\mathbf{a_i})}, \tag{6.11}$$

where the coordinates of the NN and NNN sites are,

$$\begin{aligned} \mathbf{d_1} &= (\sqrt{3}a/2, a/2), & \mathbf{a_1} &= (\sqrt{3}a/2, 3a/2), \\ \mathbf{d_2} &= (-\sqrt{3}a/2, a/2), & \mathbf{a_2} &= (-\sqrt{3}a/2, 3a/2), \\ \mathbf{d_3} &= (0, -a), & \mathbf{a_3} &= (\sqrt{3}a, 0), \end{aligned}$$

a being the lattice constant. Henceforth, we shall use the $\mathbf{k}$-space Haldane-Holstein Hamiltonian in Eq. (6.9) extensively for the rest of the chapter.

To obtain the low-energy limit of the above Bloch Hamiltonian, we must expand Eq. (6.9) in the vicinity of the Dirac points K and K$'$ and linearize it which takes the form of a pseudospin-1 Dirac-Weyl Hamiltonian for the polaronic α-T_3 lattice as,

$$\tilde{\mathcal{H}}(\mathbf{q}) = \hbar\tilde{v}_f \begin{pmatrix} \mathcal{M} - \lambda_{eph}^2\hbar\omega_0 & (\nu q_x - i q_y)\cos\varphi & 0 \\ (\nu q_x + i q_y)\cos\varphi & -\lambda_{eph}^2\hbar\omega_0 & (\nu q_x - i q_y)\sin\varphi \\ 0 & (\nu q_x + i q_y)\sin\varphi & -\mathcal{M} - \lambda_{eph}^2\hbar\omega_0 \end{pmatrix} - \frac{\tilde{\lambda}\nu}{\cos\varphi} \begin{pmatrix} -\cos\varphi & 0 & 0 \\ 0 & \cos\varphi - \sin\varphi & 0 \\ 0 & 0 & \sin\varphi \end{pmatrix}, \tag{6.12}$$

with $\hbar\tilde{v}_f = 3a\tilde{t}/2\cos\varphi$ and $\mathbf{q} = (q_x, q_y) = \mathbf{k} - \text{K}$ or $(\mathbf{k} - \text{K}')$.

It is well known that the Dirac-Weyl Hamiltonian (6.12) represents two dispersive bands, namely the valance band (VB) and the conduction band (CB), along with a dispersionless flat band (FB) for graphene ($\alpha = 0$) and dice ($\alpha = 1$) lattices, and a distorted FB for $0 < \alpha < 1$. In our case, all of these are modified by the polaronic factors through $\tilde{t}$ and $\tilde{\lambda}$ defined in Eq. (6.8).

6.3 Polaron Induced Topological Features in an α-T_3 Lattice

6.3.1 Bulk spectral properties

In our study, all the energy parameters are taken in units of t, which is set to unity. Further, we fix $a = 1$ (lattice constant), $\phi_{ij} = \pi/2$ (the Haldane flux) and $\hbar = 1$, for convenience. Before delving into the specifics of the e-ph interaction, let us briefly explore the bare Haldane α-T_3 lattice. In the absence of e-ph interaction and the mass term, and solely due to the breaking of the time-reversal symmetry by the Haldane term, the original zero-energy FB may get distorted. Additionally, the electronic band structure experiences valley splitting. Fig. 6.2 illustrates the low-energy bands for various values of α within the first BZ. The red, green, and blue colours denote the CB, the distorted FB (dFB) and the VBs, respectively. In three-band systems, there can be two distinct band gaps at the Dirac points: the gaps between (i) the CB and the distorted FB ($\Delta_{cf}^{\mathrm{K/K'}}$), and (ii) the distorted FB and VBs ($\Delta_{vf}^{\mathrm{K/K'}}$) at the K/K′ points. We consider three distinct values of α, at and either sides of a gap closing scenario. The middle band exhibits no dispersion at $\alpha = 0$ (not depicted here), but it gets more dispersive with increasing α. We see a mild dispersive nature of the FB at $\alpha = 0.4$ as shown in Fig. 6.2(a). In Fig. 6.2(b), where $\alpha = 0.5$, the distorted FB now connects with the VB by closing the gap between them at the K valley, while in the other valley (K′), the distorted FB connects to the CB. With further increase in α, the gap re-opens, as depicted in Fig. 6.2(c) for $\alpha = 0.6$. In case of $\alpha = 1$ (not shown here), the spectral gap attains its maximum value, and the distorted FB regains its dispersionless behaviour. Notably, at $\alpha = 0.5$ one finds that, $\Delta_{cf}^{\mathrm{K}} \neq 0$, but $\Delta_{vf}^{\mathrm{K}} = 0$, and further $\Delta_{cf}^{\mathrm{K'}} = 0$, whereas $\Delta_{vf}^{\mathrm{K'}} \neq 0$.

Let us include e-ph interaction in the ongoing discussion. We set the mass as $\mathcal{M} = 0.05t$, NNN hopping as $\lambda = 0.1t$, and the phonon-frequency as $\omega_0 = 3t$ which is greater than t, $\mathcal{M}$, λ for the non-adiabatic condition to be valid. In order to study the topological phases and transitions therein, we first present the bulk spectrum of the α-T_3 system for a few chosen values of α in Fig. 6.3 and examine the closing and opening of bulk gaps at the valleys via tuning the e-ph interaction strength λ_{eph}. As the bulk properties vary with the parameter α, we segregate them into two classes of α, namely, (i) $0 < \alpha \lesssim 0.6$ (from close to the bare graphene to moderate

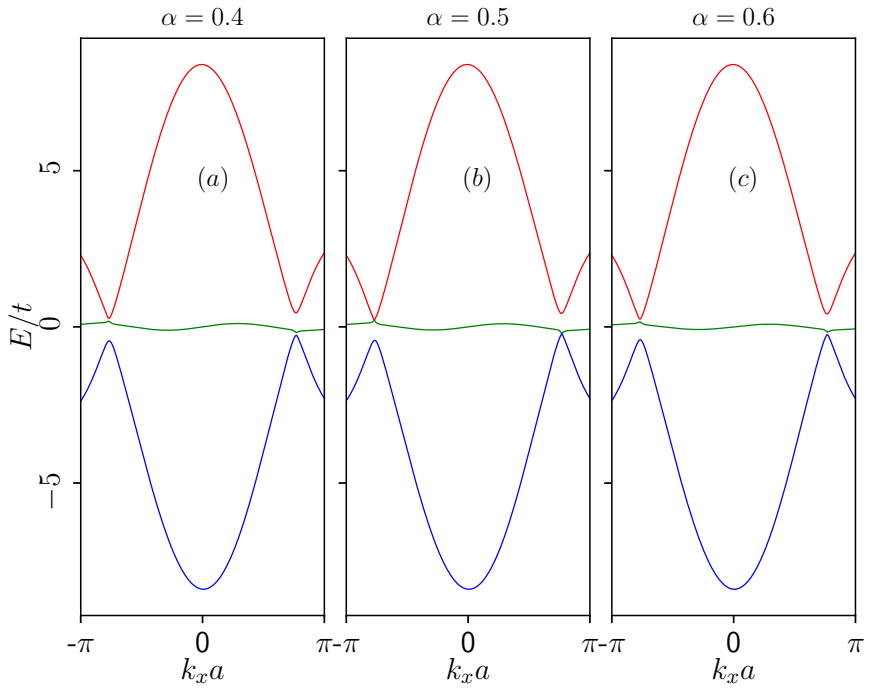

Figure 6.2: The bulk band structures with energy E (in the units of t) of the bare Haldane model are shown as a function of dimensionless momenta, k_x (multiplied by the lattice constant) at $k_y = 0$ for various values of α: (a) $\alpha = 0.4$, (b) $\alpha = 0.5$, and (c) $\alpha = 0.6$. The red, green, and blue colours represent the CB, the dFB and the VBs, respectively. Bands are no longer symmetric under the exchange of valleys (K and K′). The Haldane term is taken as $\lambda = 0.1t$.

α cases), (ii) $0.6 \lesssim \alpha < 1$ (from moderate α to Dice lattice). The purpose of making such distinctions will be clear in a moment. First of all, in Fig. 6.3, we show the bulk energy bands for lower α values, namely, for $\alpha = 0.1$, $\alpha = 0.2$ and $\alpha = 0.3$. As expected, we get three different spectra, namely the VB (shown in blue), the dFB (in green), and the CB (in red) as a function of the dimensionless momentum $k_x a$ (k_y is set to be zero). The FBs are dispersive (especially for $\alpha > 0$ cases) due to the presence of the NNN hopping λ and $\mathcal{M}$. Further, we notice a semi-Dirac dispersion, i.e., linear along k_y and quadratic along the k_x direction. The variations of the bands are shown in three different regimes of λ_{eph} i.e. when $\lambda_{eph} < \lambda_c$ (left panel), at $\lambda_{eph} = \lambda_c$ (middle panel) and then when $\lambda_{eph} > \lambda_c$ (right panel), where λ_c is the critical e-ph coupling strength at which the gap closes ($\Delta_{vf}^{\mathrm{K}} = 0$). These critical points (λ_c) for different α values are listed in Table 6.1.

Let us consider the $\alpha = 0.1$ case (Figs. 6.3$(a$-$c)$). As mentioned earlier, the mass term lifts the valley degeneracy. Also, the overall band spectrum is shifted vertically down as we increase λ_{eph} further (the dFB not being at $E = 0$). Interestingly, at the two valleys, K and K′, the e-ph interaction makes the behaviour of the dFBs contradictory (which otherwise looks symmetric when $\lambda_{eph} = 0$ (see Fig. 6.2)), especially when $\lambda_{eph} = \lambda_c$. We clearly notice that in the $\lambda_{eph} < \lambda_c$ regime (Fig. 6.3(a)), the dFB almost touches the CB at both the K and K′ valleys. Although,

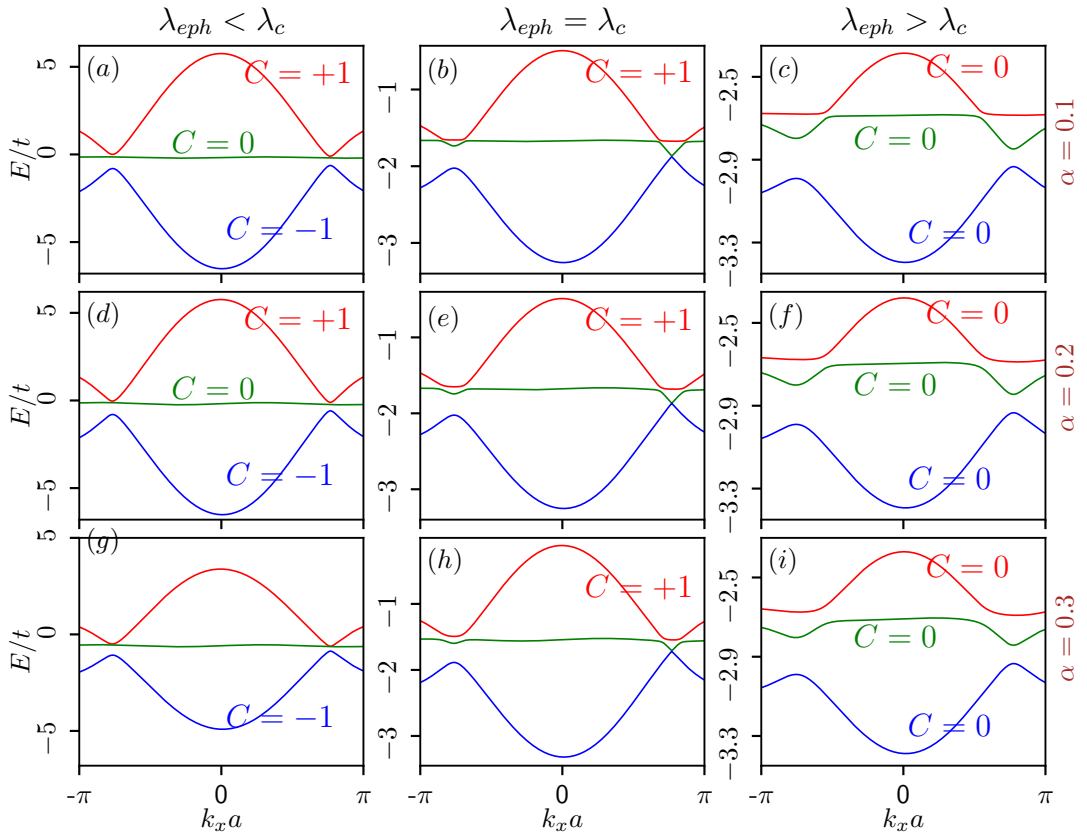

Figure 6.3: Plots of polaronic bulk band structure with energy E (in the units of t) for lower α values are shown as a function of dimensionless momenta, k_x (multiplied by the lattice constant) at $k_y = 0$. (Left column) The dispersions are plotted in the $\lambda_{eph} < \lambda_c$ regime for (a) $\alpha = 0.1$, (d) $\alpha = 0.2$, and (g) $\alpha = 0.3$, at $\lambda_{eph} = 0.3$. (Middle column) Those are plotted at the critical λ_{eph} $(= \lambda_c)$ for (b) $\alpha = 0.1$, $\lambda_c = 0.49$, (e) $\alpha = 0.2$, $\lambda_c = 0.48$, and (h) $\alpha = 0.3$, $\lambda_c = 0.47$. (Right column) The same are shown in the $\lambda_{eph} > \lambda_c$ regime for (c) $\alpha = 0.1$, (f) $\alpha = 0.2$, and (i) $\alpha = 0.3$, at $\lambda_{eph} = 0.6$. The red, green, and blue colours represent the CB, the dFB and the VBs, respectively. The parameters are taken as $\lambda = 0.1t$ and $\mathcal{M} = 0.05t$. Further, t and λ values are modified as $\tilde{t}$ and $\tilde{\lambda}$ as mentioned in the text. The Chern number, C (calculated in Sec. 6.4) corresponding to each band (however, ill-defined for those exhibiting zero bulk gap) is shown. The values of λ_c are mentioned in Table 6.1.

a prominent gap between VB and dFB is maintained in the $\lambda_{eph} < \lambda_c$ regime. However, as soon as λ_{eph} reaches a critical value, i.e., when $\lambda_{eph} = \lambda_c = 0.49$, the dFB touches the VB (Fig. 6.3(b)) at one of the valleys (K) and the band gap closes ($\Delta^{\mathrm{K}}_{vf} = 0$), while at the other valley (K′), the spectrum remains gapped ($\Delta^{\mathrm{K}}_{vf} \neq 0$). The band gap re-opens and the gap persists if we further increase λ_{eph}. Beyond λ_c ($\lambda_{eph} > \lambda_c$), the behaviour of the dFB is almost similar at both the valleys (Fig. 6.3(c)), especially for larger values of α. Therefore, both for $\lambda_{eph} < \lambda_c$ and $\lambda_{eph} > \lambda_c$, the spectrum remains gapped, implying it to be an insulator, and at $\lambda_{eph} = \lambda_c$ the bands touch, signifying a semi-metallic (SM) behaviour.

Now, we need to compute the topological properties for different λ_{eph} regimes to confirm the topological nature of the phase, which we shall show in the later sections (6.3.2 and 6.4). This

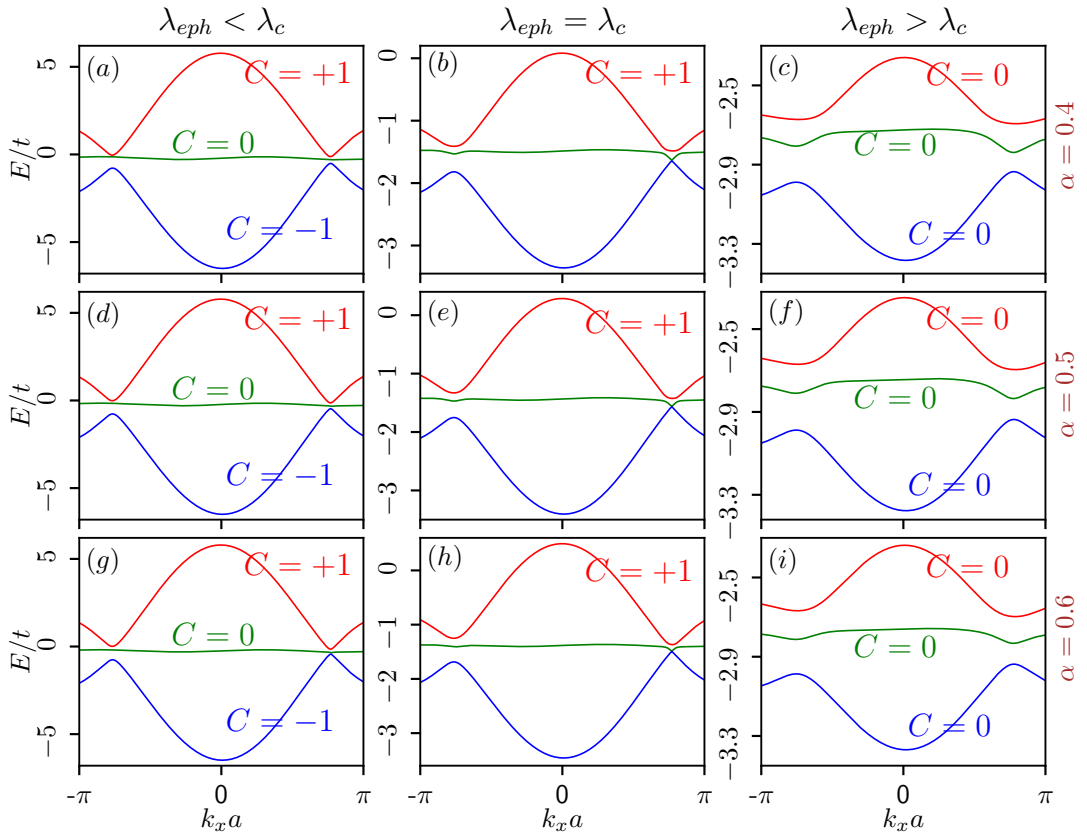

Figure 6.4: Plots of polaronic bulk band structure with energy E (in the units of t) for intermediate α values are shown as a function of dimensionless momenta, k_x (multiplied by the lattice constant) at $k_y = 0$. (Left column) The dispersions are plotted in the $\lambda_{eph} < \lambda_c$ regime for (a) $\alpha = 0.4$, (d) $\alpha = 0.5$, and (g) $\alpha = 0.6$, at $\lambda_{eph} = 0.3$. (Middle column) Those are plotted at the critical λ_{eph} $(= \lambda_c)$ for (b) $\alpha = 0.4$, $\lambda_c = 0.46$, (e) $\alpha = 0.5$, $\lambda_c = 0.45$, and (h) $\alpha = 0.6$, $\lambda_c = 0.43$. (Right column) The same are shown in the $\lambda_{eph} > \lambda_c$ regime for (c) $\alpha = 0.4$, (f) $\alpha = 0.5$, and (i) $\alpha = 0.6$, at $\lambda_{eph} = 0.6$. The red, green, and blue colours represent the CB, the dFB and the VBs, respectively. The parameters are taken as $\lambda = 0.1t$ and $\mathcal{M} = 0.05t$. Further, t and λ values are modified as $\tilde{t}$ and $\tilde{\lambda}$ as mentioned in the text. The values of λ_c are mentioned in Table 6.1.

phenomenon of band closing and opening at the Dirac points may give rise to a topological phase transition that is solely caused by tuning the e-ph interaction strength. This is the central result of this chapter. Smaller values of α in the range $[0.1 : 0.3]$ demonstrate similar behaviour (Fig. 6.3) with different λ_cs (listed in Table 6.1).

The intermediate α cases ($0.4 \leq \alpha \leq 0.6$) are shown in Fig. 6.4 where we observe the same phenomena, except that one notices for $\alpha = 0.6$ case, the dFB and the VB nearly touch each other even when $\lambda_{eph} < \lambda_c$ (the values of λ_c are mentioned in Table 6.1) region (can be seen clearly if we zoom in Fig. 6.4(g)). This feature persists for larger values of α ($\alpha > 0.6$) and it needs to be addressed carefully. To do so, we plot the band structure in Fig. 6.5 for $\alpha = 0.7$, where it is clearly shown that the VB and the dFB touch each other below a certain critical value,

$\boldsymbol{\alpha}$	$\boldsymbol{\lambda_c}$
0.1	0.49
0.2	0.48
0.3	0.47
0.4	0.46
0.5	0.45
0.6	0.43

Table 6.1: Table of λ_c points for α in the range $0.1 < \alpha \leq 0.6$.

$\boldsymbol{\alpha}$	$\boldsymbol{\lambda_{c_1}}$	$\boldsymbol{\lambda_{c_2}}$
0.7	0.28	0.43
0.8	0.20	0.44
0.9	0.26	0.39

Table 6.2: Table of λ_{c_1} and λ_{c_2} points for higher values of α.

namely, $\lambda_{c_1} = 0.28$ which may describe a SM phase in the $\lambda_{eph} < \lambda_{c_1}$ regime (Fig. 6.5(b)), and will hold even when $\lambda_{eph} = 0$ (Fig. 6.5(a)). Then, in the vicinity of $\lambda_{eph} = \lambda_{c_1}$, the gap between VB and dFB opens for the first time (can be seen clearly in the inset of Fig. 6.5(c)), signalling an insulating behaviour, and the gap stays intact in the $\lambda_{c_1} < \lambda_{eph} < \lambda_{c_2}$ regime (can be seen clearly in the inset of Fig. 6.5(d)) up to a second critical point, namely, $\lambda_{c_2} = 0.43$, at which the gap closes (Fig. 6.5(e)), referring to a re-onset of a SM phase. The bulk spectrum is gapped beyond λ_{c_2} (Fig. 6.5(f)). For other large values of α, namely, $\alpha = 0.8$ and $\alpha = 0.9$, the scenario is a bit more interesting. Unlike $\alpha = 0.7$, for $\alpha = 0.8$, we observe in Fig. 6.6$(a$-$b)$ that the bulk bands remain gapped (can be seen clearly in the insets of Fig. 6.6) in $\lambda_{eph} < \lambda_{c_1}$ regime (including $\lambda_{eph} = 0$), signifying an insulating (not SM as for $\alpha = 0.7$) phase till $\lambda_{eph} = \lambda_{c_1} = 0.2$, where the dFB and VB touch each other for the first time (Fig. 6.6(c)) and the insulating to the SM transition takes place. As we tune λ_{eph} above λ_{c_1}, we observe the same phenomena as it is shown for $\alpha = 0.7$ case (Fig. 6.5), that is, in $\lambda_{c_1} < \lambda_{eph} < \lambda_{c_2}$ regime (Fig. 6.6(d)), the dFB and VB remain gapped (can be seen clearly in the insets) denoting an insulating phase till $\lambda_{eph} = \lambda_{c_2} = 0.44$ at which the system again shows a SM (Fig. 6.6(e)) nature and for $\lambda_{eph} > \lambda_{c_2}$ (Fig. 6.6(f)) it behaves like an insulator, alike it does for $\alpha = 0.7$ case. Similar observations hold for $\alpha = 0.9$ (not shown here). The values of λ_{c_1} and λ_{c_2} for 0.7, 0.8, and 0.9 are listed in Table 6.2. We wish to mention that for $0.8 \leq \alpha < 1$, this feature of multiple phase transition becomes more prominent as we approach the dice lattice ($\alpha = 1$). Therefore, for higher α cases ($\alpha > 0.6$), we encounter two situations, one is for $0.6 < \alpha < 0.8$ and another

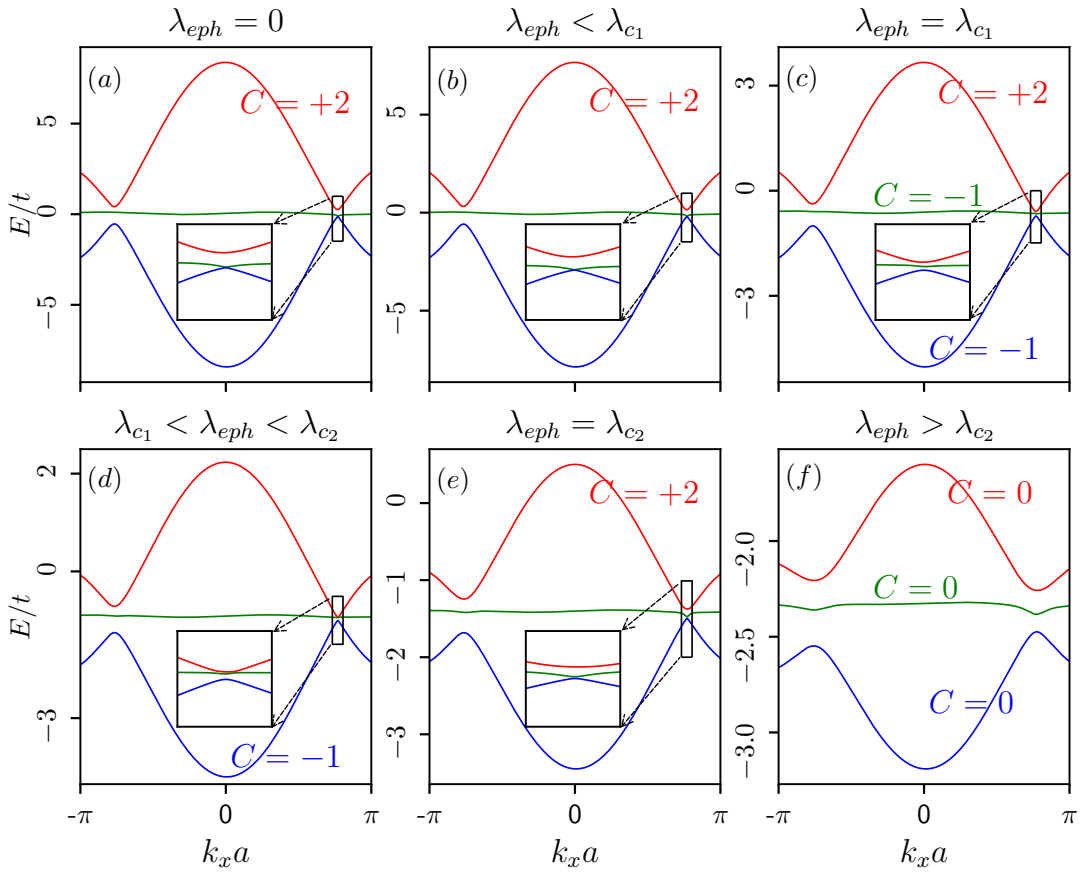

Figure 6.5: Plots of polaronic bulk band structure with energy E (in the units of t) for $\alpha = 0.7$ are shown as a function of dimensionless momenta, k_x (multiplied by the lattice constant) at $k_y = 0$ for (a) $\lambda_{eph} = 0$, (b) $\lambda_{eph} < \lambda_{c_1}$ ($\lambda_{eph} = 0.2$), (c) $\lambda_{eph} = \lambda_{c_1} = 0.28$, (d) $\lambda_{c_1} < \lambda_{eph} < \lambda_{c_2}$ ($\lambda_{eph} = 0.35$), (e) $\lambda_{eph} = \lambda_{c_2} = 0.43$, and (f) $\lambda_{eph} > \lambda_{c_2}$ ($\lambda_{eph} = 0.6$). The red, green, and blue colours represent the CB, the dFB and the VBs, respectively. In the insets, a zoomed in view of the regions near the band minima (Dirac) point is shown. The parameters are taken as $\lambda = 0.1t$ and $\mathcal{M} = 0.05t$. Further, t and λ values are modified as $\tilde{t}$ and $\tilde{\lambda}$ as mentioned in the text. The values of λ_{c_1} and λ_{c_2} are mentioned in Table 6.2.

is for $0.8 \leq \alpha < 1$. In the former case, we get two critical λ_c points, namely λ_{c_1} and λ_{c_2}, below (even when $\lambda_{eph} = 0$) and above which the system remains semi-metallic and insulating respectively. In between λ_{c_1} and λ_{c_2}, it behaves like an insulator. So, the system undergoes an SM-insulator-SM-insulator transition in the former case, while in the latter case, the system inherits an insulator-SM-insulator-SM-insulator transition. The nature of the gap (topological or trivial), will be ascertained in Sec. 6.3.2 and Sec. 6.4. Hence, the band topology in our study is substantially modified by the polaron formation, which is influenced by two factors, namely, the renormalized amplitudes $\tilde{t}$ and $\tilde{\lambda}$ (Eq. (6.8)) and the interplay between MS_z and $\lambda_{eph}^2 \hbar\omega_0$ (last two terms of Eq. (6.9)). The former causes the band narrowing and the latter is responsible for the competitive effects between the mass term and the polaron shift energy. Moreover, these polaronic markers make the variations of the band spectra (especially those of the dFB and the

VBs) different for different ranges of α. Specifically, for higher values of α, the correlation between M, α and λ_{eph} becomes stronger, giving rise to multiple phase transitions. In the case of the dice lattice ($\alpha = 1$), the flat band remains flat without any distortion and there is no occurrence of band gap closing phenomena for all values of the e-ph coupling λ_{eph} (not shown here). It is worth mentioning that the values of λ_c are different for different α cases (see Table 6.1 and Table 6.2), which ensures that we shall have a phase transition for all α values between $\alpha = 0$ to 1, albeit with different λ_c values.

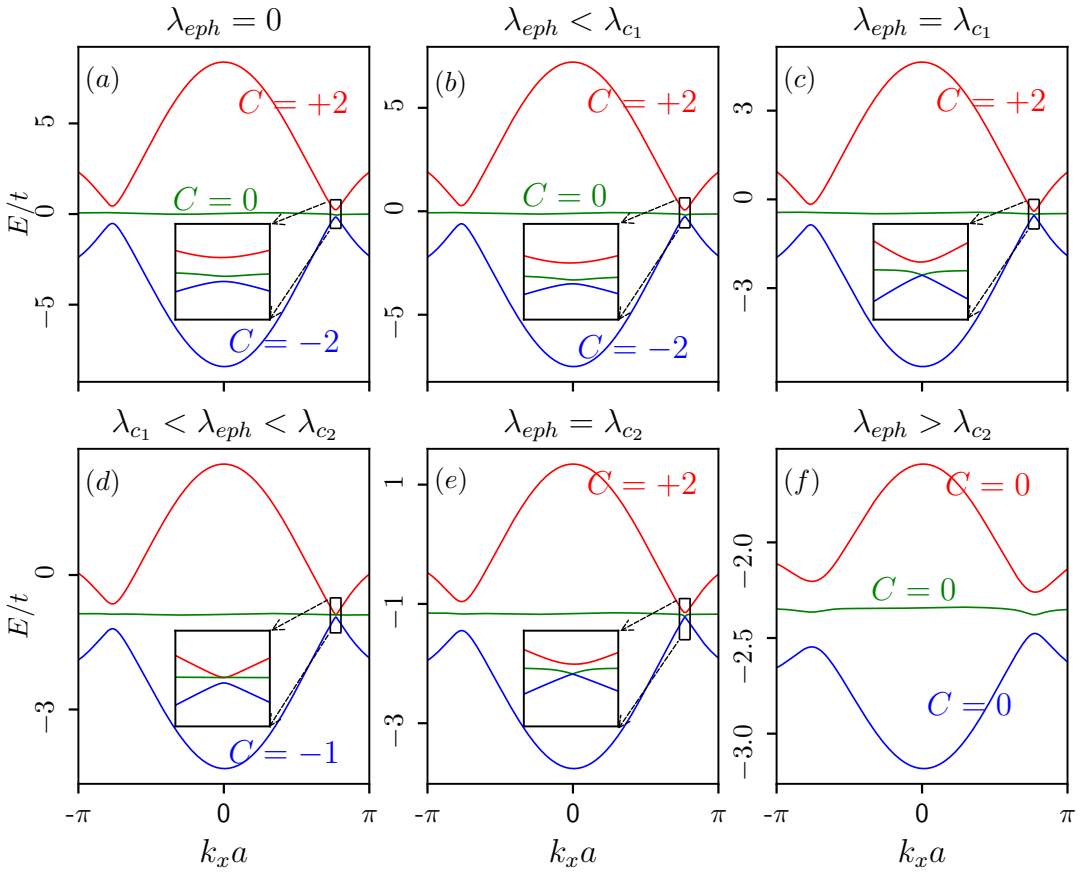

Figure 6.6: Plots of polaronic bulk band structure with energy E (in the units of t) for $\alpha = 0.8$ are shown as a function of dimensionless momenta, k_x (multiplied by the lattice constant) at $k_y = 0$ for (a) $\lambda_{eph} = 0$, (b) $\lambda_{eph} < \lambda_{c_1}$ ($\lambda_{eph} = 0.15$), (c) $\lambda_{eph} = \lambda_{c_1} = 0.2$, (d) $\lambda_{c_1} < \lambda_{eph} < \lambda_{c_2}$ ($\lambda_{eph} = 0.35$), (e) $\lambda_{eph} = \lambda_{c_2} = 0.44$, and (f) $\lambda_{eph} > \lambda_{c_2}$ ($\lambda_{eph} = 0.6$). The red, green, and blue colours represent the CB, the dFB and the VBs, respectively. In the insets, a zoomed in view of the regions near the band minima (Dirac) point is shown. The parameters are taken as $\lambda = 0.1t$ and $\mathcal{M} = 0.05t$. Further, t and λ values are modified as $\tilde{t}$ and $\tilde{\lambda}$ as mentioned in the text. The values of λ_{c_1} and λ_{c_2} are mentioned in Table 6.2.

6.3.2 Edge modes of a semi-infinite α-T_3 ribbon

In this section, to provide support to the topological properties, we discuss the edge state characteristics of a semi-infinite α-T_3 ribbon in the presence of e-ph coupling. In order to envisage whether the bulk band gap is topologically nontrivial, we inspect the crossings of the edge modes between CB and VB through the dFB. The ribbon geometry that exhibits zigzag edges is considered here [194]. Thus, it is infinite along the x-direction, while finite along the y-direction, breaking the translational symmetry along one direction (k_y in this case), while the same is protected along the other direction (k_x). We have taken the width of the nanoribbon as $N = 37$, which satisfies the condition of width $N = 3q + 1$ (q is an integer), and ensures both the edges are composed of A and C sublattices only. The nontrivial topological signatures are reflected in the edge state spectra, and the details depend upon the values of α. We begin by referring to Fig. 6.7, where we show the edge states for lower α values ($\alpha = 0.1$ and $\alpha = 0.2$ marked on the right edge). As stated above in Sec. 6.3.1, the bulk gap closes at a critical λ_c and it remains

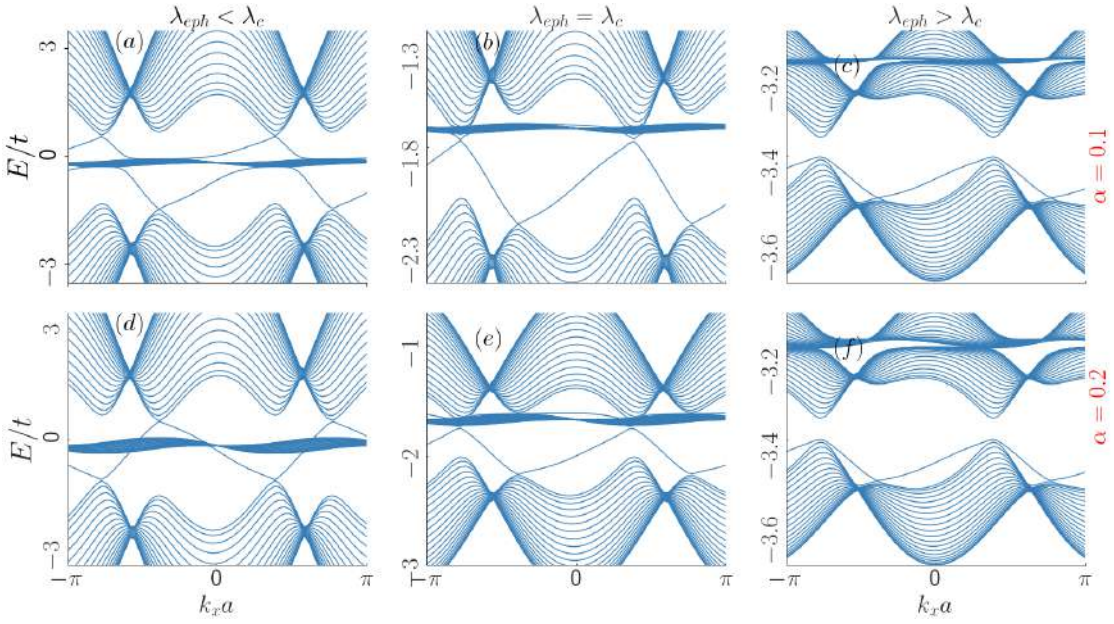

Figure 6.7: Energy spectra (in units of t) of the edge states are shown for a zigzag edged semi-infinite ribbon as a function of dimensionless momenta, k_x (multiplied by the lattice constant) of $\alpha = 0.1$ for (a) $\lambda_{eph} = 0.3$ ($\lambda_{eph} < \lambda_c$), (b) $\lambda_{eph} = \lambda_c = 0.49$, and (c) $\lambda_{eph} = 0.6$ ($\lambda_{eph} > \lambda_c$), and of $\alpha = 0.2$ for (d) $\lambda_{eph} = 0.3$ ($\lambda_{eph} < \lambda_c$), (e) $\lambda_{eph} = \lambda_c = 0.48$, and (f) $\lambda_{eph} = 0.6$ ($\lambda_{eph} > \lambda_c$). Other parameters are the same as those in Fig. 6.3. The values of λ_c are mentioned in Table 6.1.

gapped as long as to $\lambda_{eph} < \lambda_c$ and $\lambda_{eph} > \lambda_c$. We wish to ascertain the existence of edge states that distinguishes a topologically nontrivial phase from a trivial one in both scenarios. Below a critical λ_c, Figs. 6.7 (a) and (d) display a prominent set of edge states traversing from CB to VB through dFB (and vice versa) for $\alpha = 0.1$ and $\alpha = 0.2$, respectively for the $\lambda_{eph} < \lambda_c$

regime. We notice that a pair of edge states emerge from different valleys in the bulk, gather at the dFBs and hence cross over to the CBs. By looking at the slope of the edge states, that is, $\partial E/\partial k$, which is a measure of the velocity of the electron, we infer that the flow of the edge currents is counterpropagating, as it should be. These edge states are the chiral edge states of a Chern insulator, appearing in the regime of $\lambda_{eph} < \lambda_c$. The nature of the edge states for the $\alpha = 0.2$ case are distinct, in the sense that they are crossing the dFB at different points. It is also visible in Figs. 6.7 (b) and (e) that these chiral edges persist up to $\lambda_{eph} = \lambda_c$ and disappear beyond that. These are presented in Figs. 6.7 (c) and (f), that for values above λ_c, the edge states completely disappear and bulk spectra become gapped, signifying the transition of the system to a trivial phase. The critical values of λ_{eph} corresponding to the transitions for the $\alpha = 0.1$ and $\alpha = 0.2$ cases are listed in Table 6.1. Therefore, in α-T_3 systems (with smaller α values), one can generate topological insulating phases via only tuning λ_{eph} for a particular value of α below a certain λ_c, beyond which the system goes into a trivial insulating phase.

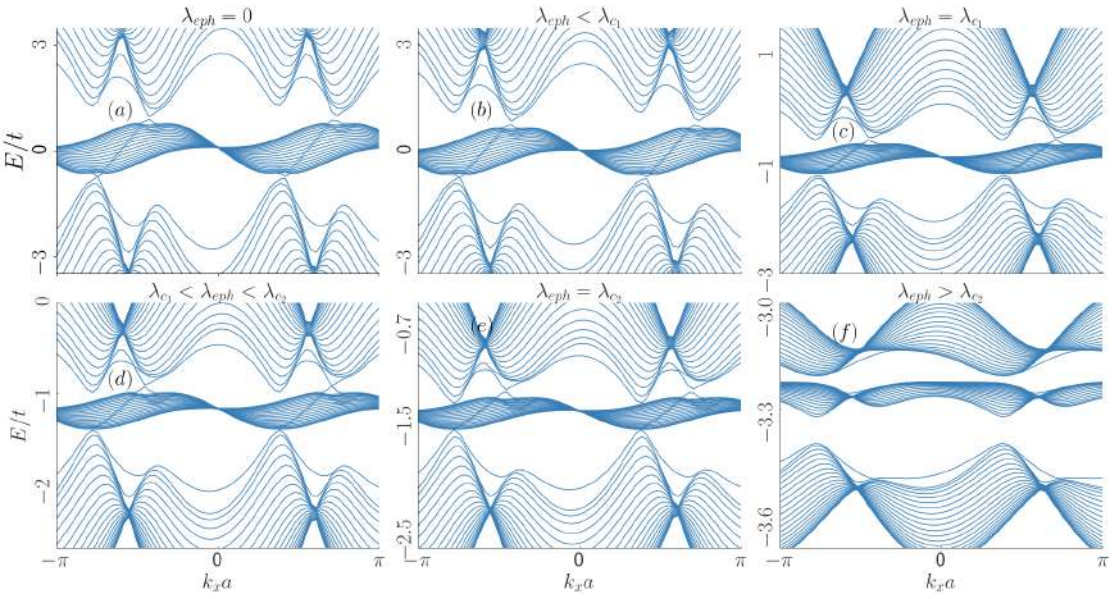

Figure 6.8: Energy spectra (in units of t) of the edge states are shown for a zigzag edged semi-infinite ribbon as a function of dimensionless momenta, k_x (multiplied by the lattice constant) of $\alpha = 0.7$ for (a) $\lambda_{eph} = 0$, (b) $\lambda_{eph} = 0.2$ ($\lambda_{eph} < \lambda_{c_1}$), (c) $\lambda_{eph} = \lambda_{c_1} = 0.28$, (d) $\lambda_{eph} = 0.35$ ($\lambda_{c_1} < \lambda_{eph} < \lambda_{c_2}$), (e) $\lambda_{eph} = \lambda_{c_2} = 0.43$, and (f) $\lambda_{eph} = 0.6$ ($\lambda_{eph} > \lambda_{c_2}$). Other parameters are the same as those in Fig. 6.5. The values of λ_{c_1} and λ_{c_2} are mentioned in Table 6.2.

Next, let us study the characteristics of the edge states for higher α values, and as a specific case, consider $\alpha = 0.7$, presented in Fig. 6.8. In reference to its bulk properties displayed in Fig. 6.5, we shall examine the edge states for different regimes of λ_{eph}. As discussed in Figs. 6.5$(a$-$b)$, the bulk dFB and VB remain in contact with each other for the $\lambda_{eph} \lesssim \lambda_{c_1}$ region, we notice its signature in Figs. 6.8$(a$-$b)$, where a pair of counterpropagating edge states emerge near each K valley, passing through the dFB for the $\lambda_{eph} \lesssim \lambda_{c_1}$ regime. However, in this regime of λ_{eph},

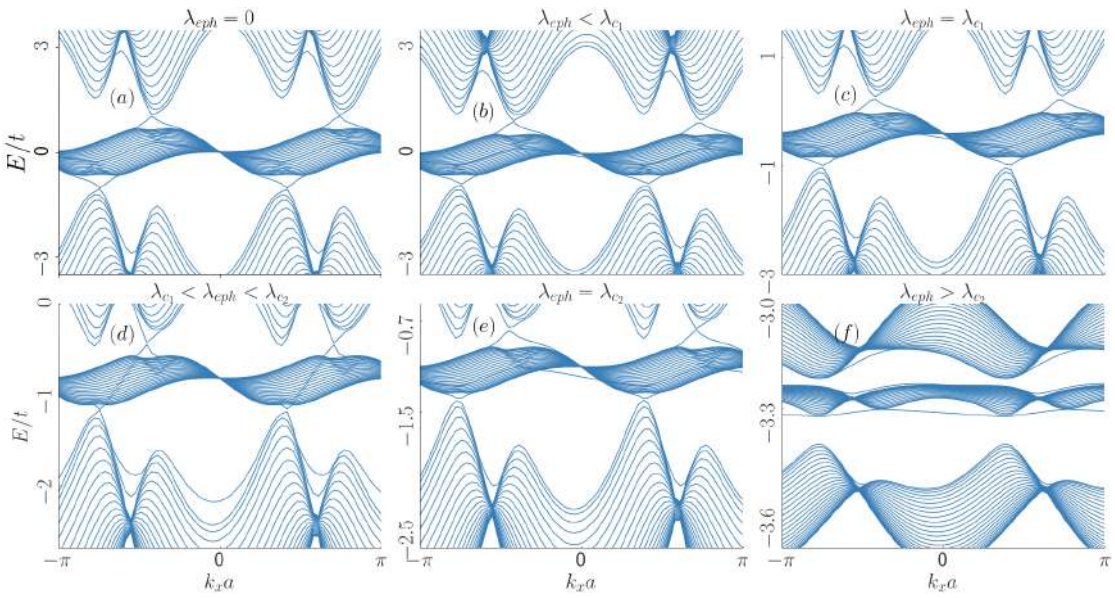

Figure 6.9: Energy spectra (in units of t) of the edge states are shown for a zigzag edged semi-infinite ribbon as a function of dimensionless momenta, k_x (multiplied by the lattice constant) of $\alpha = 0.8$ for (a) $\lambda_{eph} = 0$, (b) $\lambda_{eph} = 0.15$ ($\lambda_{eph} < \lambda_{c_1}$), (c) $\lambda_{eph} = \lambda_{c_1} = 0.2$, (d) $\lambda_{eph} = 0.35$ ($\lambda_{c_1} < \lambda_{eph} < \lambda_{c_2}$), (e) $\lambda_{eph} = \lambda_{c_2} = 0.44$, and (f) $\lambda_{eph} = 0.6$ ($\lambda_{eph} > \lambda_{c_2}$). Other parameters are the same as those in Fig. 6.6. The values of λ_{c_1} and λ_{c_2} are mentioned in Table 6.2.

the notion of the edge states is not important as the system does not have any bulk gap, inferring it to be a usual semi-metal. The edge states connecting the VB and CB through the dFB are gapped till $\lambda_{eph} = \lambda_{c_1}$ at which the edge states at one K valley touch for the first time (can be seen clearly if we zoom in Fig. 6.8(c)), thereby generating a conducting edge mode. In the intermediate region (see Fig. 6.8(d)), that is, for $\lambda_{c_1} < \lambda_{eph} < \lambda_{c_2}$, the system clearly exhibits the presence of edge states indicating a topologically nontrivial (Chern insulating) phase. It is evident in Fig. 6.8(d) that the edge states are counterpropagating, and they cross the dFB at the two edges for $\lambda_{c_1} < \lambda_{eph} < \lambda_{c_2}$. Therefore, for $\alpha = 0.7$, there seems to be a re-entrant mechanism to the SM phase, which may be achieved entirely by tuning the e-ph coupling strength. Around $\lambda_{eph} = \lambda_{c_2}$, the edge states start fading out (shown in Fig. 6.8(e)) at one K valley and is completely disappear above λ_{c_2} (see Fig. 6.8(f)). Undoubtedly, the $\lambda_{eph} > \lambda_{c_2}$ region refers to a trivial insulator with no sign of edge states. As suggested in the discussion of the bulk spectra (Sec. 6.3.1) that multiple phase transitions (insulator-SM-insulator-SM-insulator) can occur for $\alpha > 0.7$, we explicitly plot the edge states for $\alpha = 0.8$ in Fig. 6.9 which ascertains whether the insulating phases are topological. In Fig. 6.9(a) we notice that in the absence of e-ph coupling, a pair of prominent edge states cross the dFB at the K or the K$'$ valley, signifying a topologically nontrivial Chern insulating phase (unlike for $\alpha = 0.7$ where it is a SM phase), which remain intact in the $\lambda_{eph} < \lambda_{c_1}$ regime (Fig. 6.9(b)) till $\lambda_{eph} = \lambda_{c_1}$. At this value, one pair of edge states becomes gapped at one valley, while in the other valley it remains

gapless (Fig. 6.9(c)). However, such as for the $\alpha > 0.7$ case, it is vividly seen in Figs. 6.9$(d$-$f)$ that the counterpropagating edge states resurface in the $\lambda_{c_1} < \lambda_{eph} < \lambda_{c_2}$ regime, persist up to $\lambda_{eph} = \lambda_{c_2}$ and completely vanish beyond λ_{c_2}. So, for $\alpha = 0.8$ as well, the re-entrant scenario to the SM phase still holds (also true for $\alpha = 0.9$, not shown here). To confirm that the edge modes indeed correspond to a Chern insulating phase, we compute the topological properties and discuss them for each of the regions of λ_{eph} (as indicated above) in the following section (Sec. 6.4). The phase transition points, namely λ_{c_1} and λ_{c_2} for $\alpha = 0.7, 0.8$ and 0.9 are listed in Table 6.2.

6.4 Berry Curvature and Chern Number

To ascertain the topological signatures in the α-T_3 induced by the e-ph coupling, we numerically compute the topological ingredients, namely, the Berry curvature and the Chern number. We also obtain the phase diagram containing the Chern number and e-ph coupling strength. In a usual α-T_3 lattice, due to the TRS breaking NNN Haldane term, the system exhibits a nonzero Chern number. The onsite Samenoff mass term that breaks the valley degeneracy also plays a crucial role in opening of a band gap at high symmetry Dirac points.

However, our main aim is to investigate how e-ph interaction mediates a nonzero Chern number in the system for a fixed set of other system parameters, namely, λ and $\mathcal{M}$. We expect that there should exist an interplay between the mass term and the e-ph coupling. Therefore, we may achieve a topological transition only by tuning the strength of e-ph coupling, λ_{eph}.

The Chern number (C) can be calculated as,

$$C = \frac{1}{2\pi} \iint_{BZ} \Omega(k_x, k_y) dk_x dk_y, \tag{6.13}$$

where $\Omega(k_x, k_y)$ is the Berry curvature of our system expressed as,

$$\Omega(k_x, k_y) = -2i\mathfrak{Im}\left[\left\langle \frac{\partial\psi(k_x, k_y)}{\partial k_x} \middle| \frac{\partial\psi(k_x, k_y)}{\partial k_y} \right\rangle\right], \tag{6.14}$$

where $\psi(k_x, k_y)$ refers to the eigenstate of the modified Haldane model, which is the polaronic bulk band and $\mathfrak{Im}$ denotes the imaginary part. The topological phase transition is characterized by a topological invariant. In our study, it is the (polaronic) Chern number, C, displayed in Eq. (6.13). In order to calculate so, we first compute the Berry curvature, $\Omega(k_x, k_y)$ using Eq. (6.14) corresponding to the VB and integrate it over the entire BZ. We plot $\Omega(k_x, k_y)$ in

Figs. 6.10-6.12 and C in Fig. 6.14 to investigate the topological phase transition explicitly mediated through the e-ph coupling.

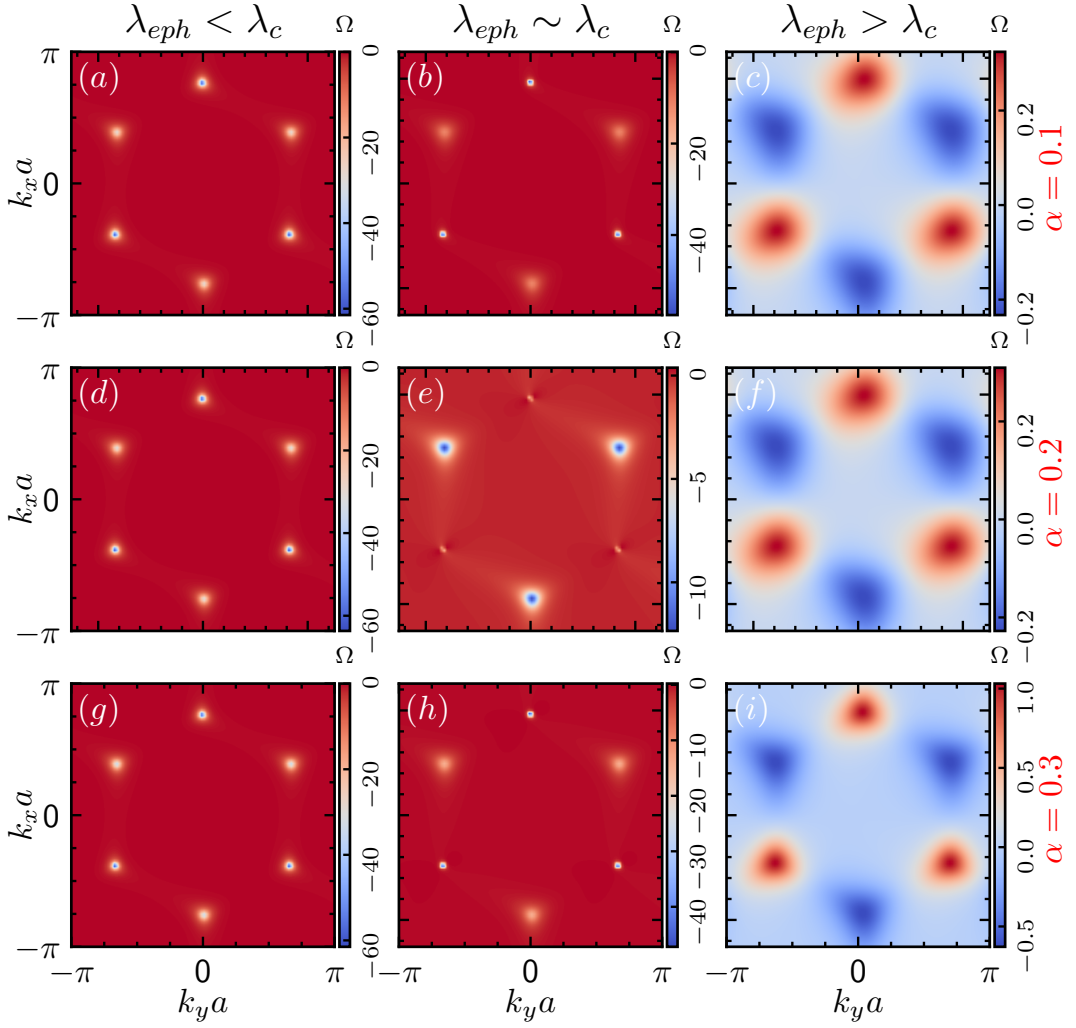

Figure 6.10: The Berry curvature corresponding to the VB is presented for lower α values in different regimes of λ_{eph}. (Left column) Those are plotted in the $\lambda_{eph} < \lambda_c$ regime for (a) $\alpha = 0.1$, (d) $\alpha = 0.2$, and (g) $\alpha = 0.3$, at $\lambda_{eph} = 0.3$. (Middle column) At the critical λ_{eph} $(= \lambda_c)$ for (b) $\alpha = 0.1$, $\lambda_c = 0.49$, (e) $\alpha = 0.2$, $\lambda_c = 0.48$, and (h) $\alpha = 0.3$, $\lambda_c = 0.47$. (Right column) The same are shown in the $\lambda_{eph} > \lambda_c$ regime for (c) $\alpha = 0.1$, (f) $\alpha = 0.2$, and (i) $\alpha = 0.3$, at $\lambda_{eph} = 0.6$. Other parameters are mentioned in Fig. 6.3. The values of λ_c are mentioned in Table 6.1.

In Fig. 6.10, we show the Berry curvatures in three different regions of λ_{eph} i.e., $\lambda_{eph} < \lambda_c$, $\lambda_{eph} \sim \lambda_c$ ('$\sim$' sign refers to values close to it, but not at it), and $\lambda_{eph} > \lambda_c$ in left, middle and right panels, respectively for smaller values of α, namely, $\alpha = 0.1$, $\alpha = 0.2$, and $\alpha = 0.3$ (marked on the right edge). It is generally true that a nonzero Berry curvature is a direct consequence of a nontrivial topology present in the system. The corresponding values seen to be

concentrated at the high symmetry points, K and K′. However, the change in the concentration of the Berry curvatures shown by colourmaps in Figs. 6.10-6.12 sets the precursor for any topological transition happening in the system. For $\alpha = 0.1$ (Fig. 6.10(a)), we clearly observe that below the critical λ_c (i.e., $\lambda_{eph} < \lambda_c$ regime) the Berry curvatures are equally distributed in the six corners of the hexagon which defines a topologically nontrivial phase with a nonzero Chern number. But as λ_{eph} is increased, the concentration changes. As the Berry curvature is singular at the critical point, we plot it in the vicinity of the critical point ($\lambda_{eph} \sim \lambda_c$) shown in Fig. 6.10$(b)$. Interestingly, as λ_{eph} approaches λ_c, we notice a clear distinction in the concentration of the Berry curvatures at K and K′ points. At the K point, the concentrations are predominantly higher compared to those at the K′ point. This observation can also be explained via Fig. 6.3(b) where at $\lambda_{eph} = \lambda_c$, we see a sharp mismatch in the behaviour of the bulk bands at K and K′ points, where at one K point, the dFB and VB touch each other, while they remain gapped at the K′ point, displaying the contrasting effects of the e-ph coupling on the dFB at two valleys. For other α values ($\alpha = 0.2$ and $\alpha = 0.3$) that are plotted in Figs. 6.10 (e) and (h), the distinction between the Berry curvatures at K and K′ points is much more prominent. In Fig. 6.10(c), we show that the Berry curvatures above the critical e-ph coupling strength are almost equal and opposite at K and K′ points thereby cancelling each other resulting in a topologically trivial phase with a zero Chern number. Hence, till the critical λ_c, the system remains in the topologically nontrivial phase exhibiting a nonzero Chern number. We wish to mention that we have also observed almost similar variations of the Berry curvature by varying the e-ph coupling for the intermediate range of α, namely, $\alpha = 0.4$, 0.5, and 0.6 (not shown here).

Further, to show the variations of the Berry curvature of $\alpha = 0.7$, we plot Fig. 6.11 that can be explained with the help of the bulk and edge spectra displayed in Fig. 6.5 and Fig. 6.8, respectively. Let us first look at Figs. 6.11 (a) and (b) which is for $\lambda_{eph} = 0$ and $\lambda_{eph} < \lambda_{c_1}$, respectively. In this regime, as we have discussed, the spectral gap between the dFB and VB vanishes even at $\lambda_{eph} = 0$, and remains so till $\lambda_{eph} = \lambda_{c_1}$, manifesting the presence of chiral edge states (see Figs. 6.8$(a$-$b)$) at the boundaries. However, in this regime, the Berry curvature shows singular behaviour as there is no bulk gap, and consequently, the Chern number is ill-defined. But as we tune λ_{eph} further, a bulk gap opens up for the first time at around $\lambda_{eph} \sim \lambda_{c_1}$ (see Fig. 6.5 (c)), where we see that the concentrations at the K points start behaving differently than that at K′ points and are shown in Fig. 6.11(c). Beyond λ_{c_1}, this signature is much more noticeable (can be seen in Fig. 6.11(d)) and the edge states are prominent (see Fig. 6.8(d)) in $\lambda_{c_1} < \lambda_{eph} < \lambda_{c_2}$ regime. In the vicinity of $\lambda_{eph} = \lambda_{c_2}$, the bulk gap closes and high values for the Berry curvature are noted (see Fig. 6.11(e)). Finally beyond λ_{c_2} (Fig. 6.11(f)), the variation of the Berry curvature is reminiscent of Figs. 6.10 (c), (f) and (i) enunciates the onset of a

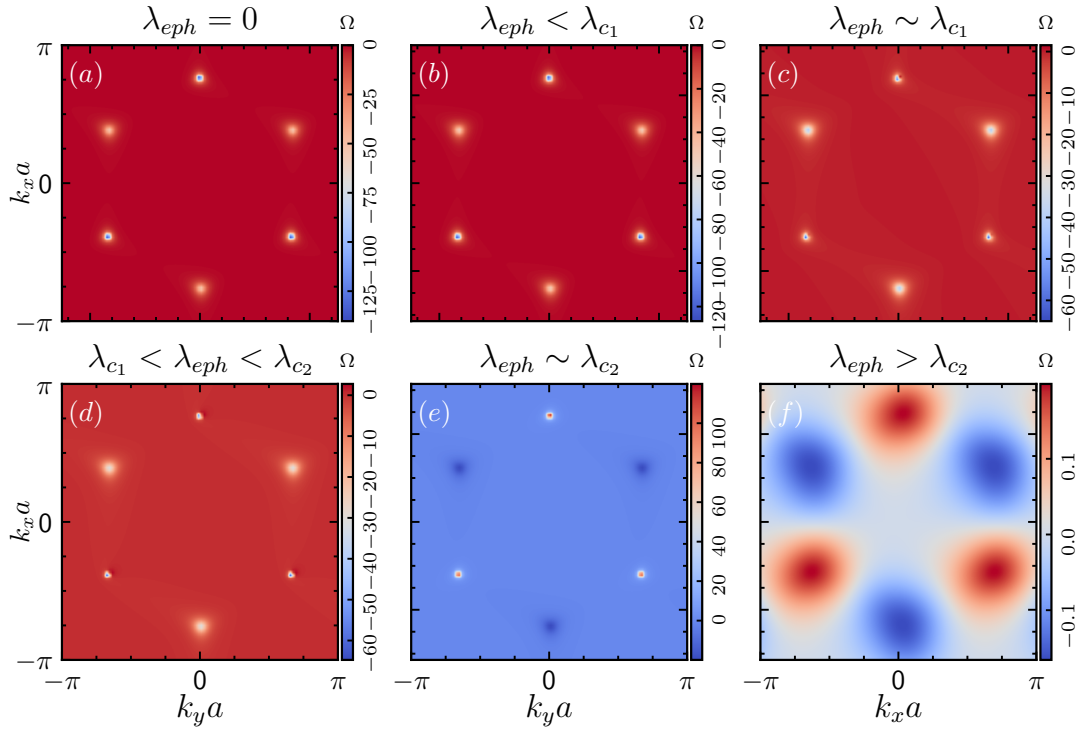

Figure 6.11: The Berry curvature corresponding to the VB is presented for $\alpha = 0.7$ in different regimes of λ_{eph} for (a) $\lambda_{eph} = 0$, (b) $\lambda_{eph} < \lambda_{c_1}$ ($\lambda_{eph} = 0.2$), (c) $\lambda_{eph} \sim \lambda_{c_1}$ ($\lambda_{eph} = 0.26$), (d) $\lambda_{c_1} < \lambda_{eph} < \lambda_{c_2}$ ($\lambda_{eph} = 0.35$), (e) $\lambda_{eph} \sim \lambda_{c_2}$ ($\lambda_{eph} = 0.41$), and (f) $\lambda_{eph} > \lambda_{c_2}$ ($\lambda_{eph} = 0.6$). Other parameters are mentioned in Fig. 6.5. The values of λ_{c_1} and λ_{c_2} are mentioned in Table 6.2.

trivial insulating phase.

The Berry curvature plots for $\alpha = 0.8$ are displayed in Fig. 6.12. Although the variations in the $\lambda_{eph} < \lambda_{c_1}$ regime (Fig. 6.12(b)) may look similar to those for $\alpha = 0.7$ showing higher values of the Berry curvatures even for $\lambda_{eph} = 0$ (Fig. 6.12(a)), but with the support of the findings of Fig. 6.6 and Fig. 6.9 described in Sec. 7.3 and 7.5 respectively, it is ensured that in the $0 \leq \lambda_{eph} < \lambda_{c_1}$ regime, they may correspond to some topological phase (unlike the usual SM phase for $\alpha = 0.7$) with conducting edge modes (see Figs. 6.9$(a$-$b)$) associated with higher Chern numbers. The observations of Figs. 6.12$(c$-$f)$ are almost same as $\alpha = 0.7$ case. However, a noticeable dissimilarity with the $\alpha = 0.7$ variation in the Berry curvature can be observed for the $\lambda_{c_1} < \lambda_{eph} < \lambda_{c_2}$ regime (Fig. 6.12(d)), where the disparity between the concentrations of the Berry curvature at two valleys is much more significant compared to that for $\alpha = 0.7$. This makes the variation of Fig. 6.12(d) distinguishable from Figs. 6.12$(a$-$b)$ denoting different topological phases.

To confirm the topological phase transition induced by the polaronic interaction in the system, we numerically compute the Chern number, C using Eq. (6.13) and examine the variation with

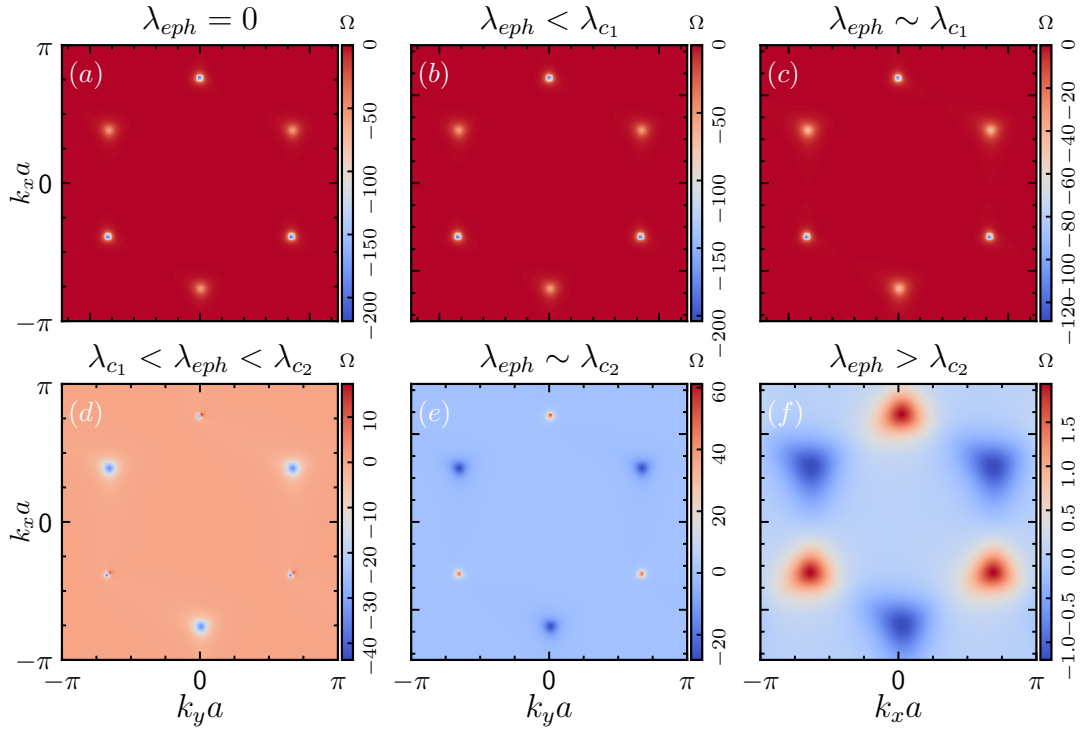

Figure 6.12: The Berry curvature corresponding to the VB is presented for $\alpha = 0.8$ in different regimes of λ_{eph} for (a) $\lambda_{eph} = 0$, (b) $\lambda_{eph} < \lambda_{c_1}$ ($\lambda_{eph} = 0.15$), (c) $\lambda_{eph} \sim \lambda_{c_1}$ ($\lambda_{eph} = 0.18$), (d) $\lambda_{c_1} < \lambda_{eph} < \lambda_{c_2}$ ($\lambda_{eph} = 0.35$), (e) $\lambda_{eph} \sim \lambda_{c_2}$ ($\lambda_{eph} = 0.42$), and (f) $\lambda_{eph} > \lambda_{c_2}$ ($\lambda_{eph} = 0.6$). Other parameters are mentioned in Fig. 6.6. The values of λ_{c_1} and λ_{c_2} are mentioned in Table 6.2.

the e-ph coupling strength, λ_{eph}. Before going into the intricacies of the e-ph interaction, let us take a moment to briefly examine the topological phase transition of the bare Haldane α-T_3 lattice. In Fig. 6.13, we illustrate how a Haldane term on an α-T_3 lattice renders the system a Chern insulating phase, that is characterized by a nonzero Chern number. Tuning the parameter α, a topological phase transition occurs at $\alpha = 0.5$. This transition alters the Chern number of the VB (CB) from $C = -1(1)$ to a larger Chern number, $C = -2(2)$.

Now let us examine the dependency of the Chern number on α in the presence of the e-ph interaction. Fig. 6.14 displays the variations of the Chern number as a function of λ_{eph}. Here, we display the variations of C separately in two diagrams for lower to intermediate values of α ($\alpha = 0.1, 0.2, ..., 0.6$) (see Fig. 6.14$(i)$) and larger values of α ($\alpha = 0.7, 0.8, 0.9$) (see Fig. 6.14(ii)). Starting from the $\alpha = 0.1$ case and shifting towards to the intermediate values, such as $\alpha = 0.6$, we notice that $C = -1$ up to a critical λ_c, at which C abruptly falls to $C = 0$ showing a sharp discontinuity. Therefore, for lower to intermediate cases of α (Fig. 6.14(i)), the system initially behaves like a Chern insulator designated by a nonzero Chern number until the e-ph coupling reaches a certain critical value, λ_c (λ_c's are listed in Table 6.1) at which the system undergoes a topological transition accompanied by the closing of the bulk gap and emerging

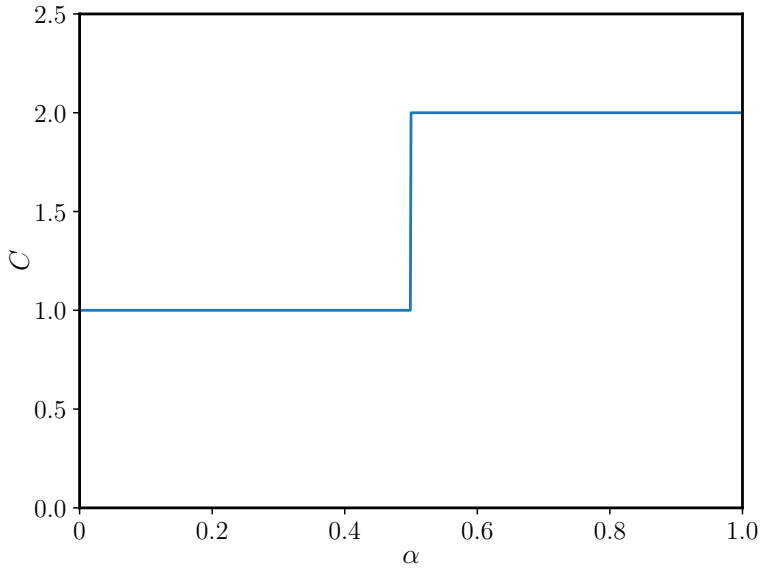

Figure 6.13: Chern number, C as a function of α for the bare (without e-ph coupling and mass term) Haldane model of an α-T_3 lattice.

signatures of the edge states. While, beyond λ_c, the system ceases to host edge states which is a typical signature of a trivial insulator for which $C = 0$. We display a zoomed in picture of the transition points in the inset (a) of Fig. 6.14(i) and (ii). In the inset (b) of Fig. 6.14(i), we depict the variation of the critical λ_c with respect to α, illustrating a nearly linear decrease with increasing α.

It is understood by now that such variations at higher α values are in contrast to those at lower values of α. Let us first consider the variation corresponding to $\alpha = 0.7$ which is represented via a solid blue line in Fig. 6.14(ii). Unlike the lower α values, there exist two transition points, namely, λ_{c_1} and λ_{c_2} for higher α values (listed in Table 6.2). Below the former, the system inherits a conventional SM phase (where C is ill-defined), and above the latter, the system becomes a trivial insulator. Understandably, the $\lambda_{c_1} < \lambda_{eph} < \lambda_{c_2}$ region is our main interest for $\alpha = 0.7$, where we find that the Chern number is fixed at $C = -1$ that underscores the emergence of a topologically nontrivial insulating phase, driven entirely by the e-ph coupling. As expected, beyond λ_{c_2}, C becomes zero confirming the onset of a trivial phase. Thus, the e-ph coupling favours a transition from a semi-metal to a topological insulator, and to a trivial insulator for $\alpha = 0.7$. However, the $0 \leq \lambda_{eph} < \lambda_{c_1}$ regime becomes interesting for $\alpha > 0.7$ as described earlier in the findings of Figs. 6.9 (a) and (b) that the conducting edge modes exist (specifically for $0.8 \leq \alpha < 1$) in that regime of λ_{eph} indicating a topologically nontrivial insulating phase. In Fig. 6.14(ii), we plot C as a function of λ_{eph} for $\alpha = 0.8$ denoted by the solid orange line, where higher Chern number, namely, $C = -2$ in $0 \leq \lambda_{eph} < \lambda_{c_1}$ regime is noted, confirming emergence of a distinct (other than $C = -1$) topological phase. Nevertheless,

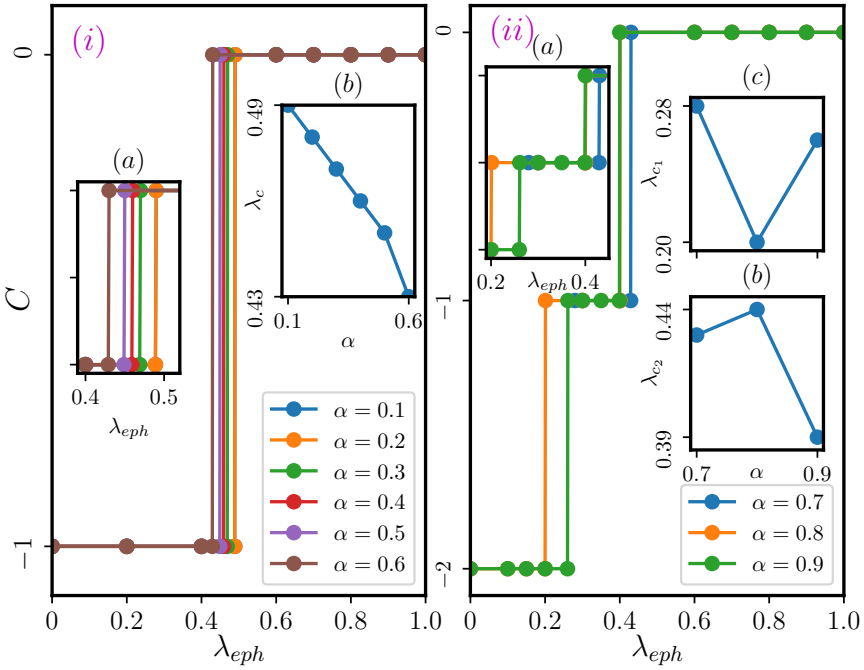

Figure 6.14: The Chern number, C corresponding to the VB as a function of e-ph coupling strength, λ_{eph} for (i) lower to intermediate α values ($0 < \alpha \leq 0.6$) is shown, while in the inset (a) a zoomed in picture of the transition regions, and in the inset (b), the variation of λ_c as a function of α is shown. In (ii), the variations of C for larger α values ($0.6 < \alpha \leq 0.9$) are shown. The inset (a) represents a zoomed in picture of the transition regions, while the insets (b) and (c), respectively, display the variations of λ_{c_2} and λ_{c_1} as a function of α. The values of λ_c are mentioned in Table 6.1 and 6.2.

as we tune λ_{eph} further, the scenario becomes exactly the same as $\alpha = 0.7$, that is, C changes from $C = -2$ to $C = -1$ at $\lambda_{eph} = \lambda_{c_1}$ signifying a distinct topological phase (owing to different values of the Chern number) that persists in the $\lambda_{c_1} < \lambda_{eph} < \lambda_{c_2}$ regime, which finally vanishes beyond λ_{c_2}. A similar observation is also shown for $\alpha = 0.9$ (marked by the solid green line). Therefore, for the $0.7 < \alpha < 1$ regime, the system undergoes a transition from one topological phase ($C = -2$) to another ($C = -1$) and hence transits to a trivial ($C = 0$) phase, purely mediated all the while by the e-ph coupling. The emergence of $|C| = 2$ topological phase in an α-T_3 is a familiar phenomenon obtained by others [102, 184, 186] in the absence of e-ph interaction. For our case, the results completely match with those in Ref. [186] corresponding to $\lambda_{eph} \to 0$ and $\mathcal{M} \to 0$ (shown in Fig.6.13). Moreover, due to the e-ph interaction, we obtain a $|C| = 2$ topological phase for lower values of λ_{eph}, even at $\lambda_{eph} = 0$ (in $0 \leq \lambda_{eph} < \lambda_{c_1}$ regime) for $0.8 \leq \alpha < 1$, that is for α values close to the dice lattice limit ($\alpha = 1$). As earlier, in the inset (b) and (c) of Fig. 6.14(ii), we show the variation of the critical λ_{c_2} and λ_{c_1}, respectively as a function of α. We observe that λ_{c_1} initially decreases and then increases with increasing α, whereas an opposite trend is observed for λ_{c_2}, namely, it increases first and hence decreases with increasing α. We should mention that the findings of Chern

number plots are completely consistent with those of bulk and edge spectra for different regimes of λ_{eph}. As stated in Sec. 6.3.1, although we have shown a few cases of α, it is also important to note that this kind of transition can occur for any value of α ($0 < \alpha < 1$). Therefore, it seems robust that the polaron formation in α-T_3 lattices induces a topological phase transition generated solely due to the presence of e-ph coupling.

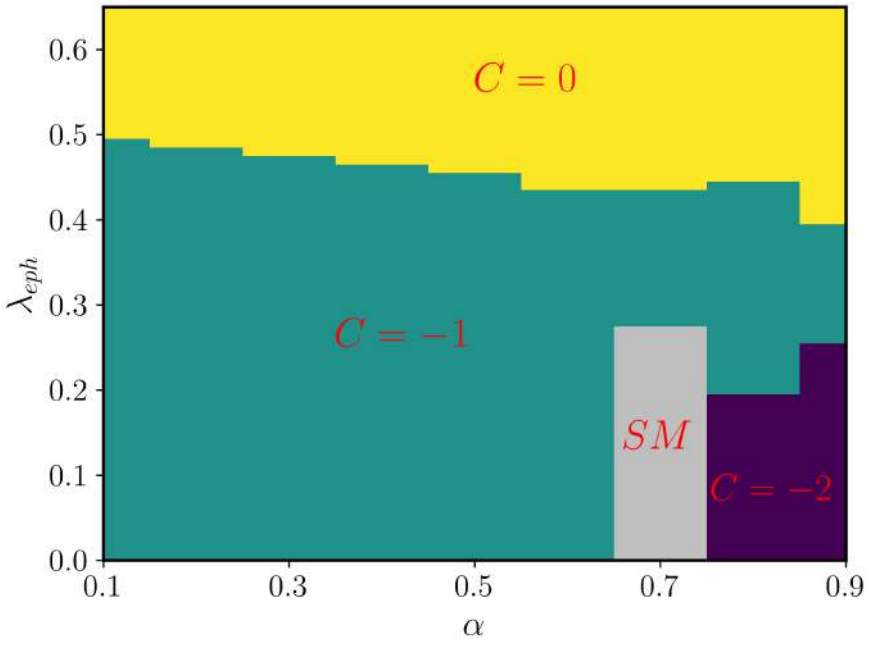

Figure 6.15: The topological phase diagram based on the Chern number (C) corresponding to the VB in the $\lambda_{eph} - \alpha$ plane. The nonzero C corresponding to the teal region is denoted as $C = -1$, while the yellow region represents the vanishing Chern number ($C = 0$), signifying a topologically trivial phase. The grey region denotes the SM phase for $0.65 \lesssim \alpha \lesssim 0.75$, while the deep purple region stands for a distinct topological phase with $C = -2$ for $0.75 \lesssim \alpha < 1$. Other parameters remain the same as mentioned in Fig. 6.3.

So far we have discussed the topological transitions for different α-T_3 lattices taking discrete values of α in the range $[0 : 1]$. A phase diagram is hence computed in the $\lambda_{eph} - \alpha$ plane to show the exact locations of different (topological/SM/trivial) phases in the parameter space. The phase diagram containing the Chern number (C) corresponding to the VB, in the parameter space defined by e-ph interaction (λ_{eph}) and α for fixed values of λ and $\mathcal{M}$, is depicted in Fig. 6.15. It is evident that the teal area represents a topological phase of the system with a Chern number as $C = -1$ in the $\lambda_{eph} < \lambda_c$ regime for $0 < \alpha \lesssim 0.65$ and in the $\lambda_{c_1} \leq \lambda_{eph} \leq \lambda_{c_2}$ regime for $0.65 \lesssim \alpha < 1$. Furthermore, for $0.65 \lesssim \alpha \lesssim 0.75$ regime, there exists an SM region (where C is ill-defined due to the closing of the bulk band gap) denoted by the grey colour corresponding to λ_{eph} values in the $0 \leq \lambda_{eph} \leq \lambda_{c_1}$ regime, signifying that the system behaves like a conventional semi-metal. While in the same regime of λ_{eph}, an α-T_3 lattice with $0.75 \lesssim \alpha < 1$ exhibits a distinct topological phase with $C = -2$ (the deep purple region).

The yellow region denotes a trivial phase with $C = 0$ for all values of α ($0 < \alpha < 1$) above their respective critical λ_c points (listed in Table 6.1 and 6.2). It may be noted that varying the parameters λ and M can significantly alter the phase diagram. However, we do not show them here for brevity.

6.5 Anomalous Hall Conductivity

In this section, we numerically compute the polaronic Hall conductivity using the following expression,

$$\sigma_{xy} = \frac{e^2}{2\pi h} \sum_{\gamma} \int \frac{dk_x dk_y}{4\pi^2} f(E^{\gamma}_{k_x,k_y}) \Omega(k_x, k_y), \tag{6.15}$$

where $e^2/h = \sigma_0$ is the scale in which σ_{xy} is measured, $E^{\gamma}_{k_x,k_y}$ is the energy band with the band index $\gamma = -1, 0$ and $+1$ corresponding to the VB, dFB and the CB, respectively, f denotes the Fermi-Dirac distribution function: $f(E) = [1 + e^{(E-E_F)/k_BT}]^{-1}$, E_F and T being the Fermi energy and the absolute temperature, respectively, $\Omega(k_x, k_y)$ being the Berry curvature. Fig. 6.16 display the variations of the polaronic Hall conductivities at $T = 0$ as a function of E_f for different values of e-ph interaction strength, λ_{eph} for $\alpha = 0.1$ (see Fig. 6.16(a)), $\alpha = 0.3$ (Fig. 6.16(b)), $\alpha = 0.7$ (Fig. 6.16(c)), and $\alpha = 0.8$ (Fig. 6.16(d)).

As shown in Fig. 6.16(a), the Hall conductivity (σ_{xy}) is plotted as a function of the Fermi energy (E_f) for $\lambda_{eph} = 0.3, 0.4$ and 0.5 marked by solid blue, black and red colours, respectively. It is observed for $\alpha = 0.1$, the Hall conductivities initially increase and show tiny plateaus (can also be seen in Fig. 6.16(b) and Fig. 6.16(c) for $\alpha = 0.3$ and $\alpha = 0.7$, respectively), which are quantized at a value e^2/h for the $\lambda_{eph} < \lambda_c$ regime. In other words, these quantized plateaus occurring at $|C|e^2/h$ (here, $|C| = 1$) presented in Fig. 6.16(a) re-confirm that up to a critical e-ph coupling $\lambda_c = 0.49$, the system behaves like a topological insulator. Beyond the critical λ_c (denoted by solid red), it becomes a trivial insulator with $\sigma_{xy} = 0$ (that is, $C = 0$). Similar observation is noted in Fig. 6.16(c) for $\alpha = 0.7$ where the plateaus at values $|C|e^2/h$ exist for λ_{eph} values that are in the $\lambda_{c_1} < \lambda_{eph} < \lambda_{c_2}$ regime.

In a scenario where $\lambda_{eph} = 0 = \mathcal{M}$, the Hall conductivity shows plateaus (but with small kinks on the plateaus due to the presence of the dFB) as long as the Fermi level lies in between the bulk gap. However, in our case (with $\lambda_{eph} \neq 0$ and $\mathcal{M} \neq 0$), the nature of the Hall conductivity deviates significantly as there exists a cumulative effect arising from the interplay of the three parameters, namely the Fermi energy (E_f), the mass term ($\mathcal{M}$) and the e-ph coupling strength (λ_{eph}). The reason for the plateaus to become tinier can be explained with the help of the bulk spectra, which are mainly affected by $\mathcal{M}$ and λ_{eph} for different α values. It is understandable

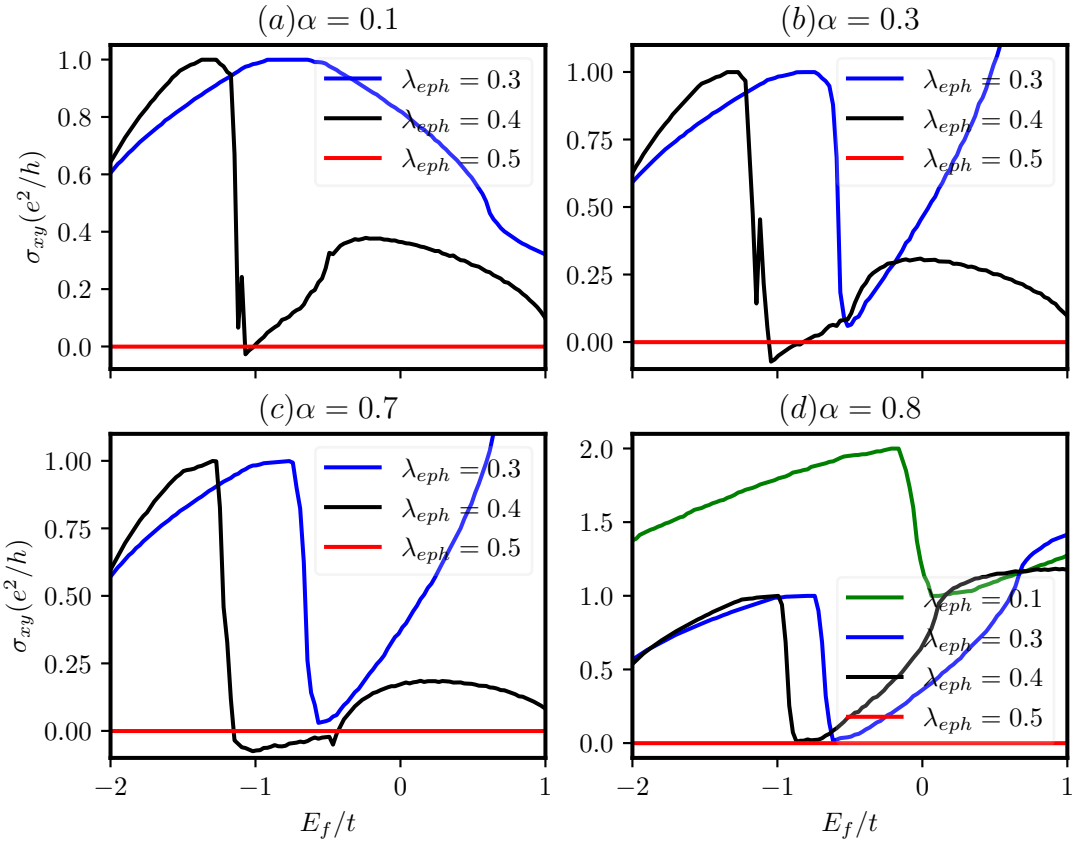

Figure 6.16: The Hall conductivity, σ_{xy} as a function of Fermi energy, E_f is presented for various values of α: (a) $\alpha = 0.1$, (b) $\alpha = 0.3$, (c) $\alpha = 0.7$, and (d) $\alpha = 0.8$ for different λ_{eph} values that are shown in the inset. Other parameters are the same as mentioned in Fig. 6.3.

that a significant width of the plateau is dependent on how accurately we fix the Fermi level in the bulk gap. As discussed in Sec. 6.3.1, the individual bulk bands shrink due to the Holstein factor (Eq. (6.8)), and the whole band structure shifts vertically down by the polaron shift energy ($\lambda_{eph}^2\hbar\omega_0$). Due to the band narrowing caused by the Holstein factor, the gap between the distorted (because of the Haldane term, λ) FB and VB decreases, makes it difficult for the Fermi level to lie *'properly'* in between the bulk gap, making the plateaus less prominent, especially for higher values of λ_{eph}. Additionally, we find that the increase in σ_{xy} as a function of E_f can be explained as follows. As observed in Sec. 6.3.1, $\mathcal{M}$ breaks the valley degeneracy and the interplay between $\mathcal{M}$ and λ_{eph} renders contrasting behaviour of the bulk bands at two valleys, that is, well-gapped at one valley and almost gapless at the other for $\lambda_{eph} < \lambda_c$. As E_f is increased, it is possible that at one valley, E_f may lie well in the gap, while it may lie in the CB as well at the other valley, which will contribute to higher σ_{xy}. The unusual behaviour of the Hall conductivity due to the presence of a dFB has also been reported by Singh [378] (in the absence of e-ph coupling). Certainly, all of the above discussions become unimportant for $\lambda_{eph} > \lambda_c$, where we have a trivial insulator.

Interestingly, for $\alpha = 0.8$, the quantized (tiny) Hall plateaus in Fig. 6.16(d) are located at e^2/h (where, $|C| = 1$) and $2e^2/h$ (where, $|C| = 2$) for $\lambda_{c_1} < \lambda_{eph} < \lambda_{c_2}$ (shown for $\lambda_{eph} = 0.3$ and 0.4, denoted by solid blue and black, respectively) and $0 \leq \lambda_{eph} < \lambda_{c_1}$ regimes (shown for $\lambda_{eph} = 0.1$, denoted by solid green), respectively, confirm existence of two distinct topological insulating phases with a nonzero σ_{xy} (also true for any α in $0.75 \lesssim \alpha < 1$ regime), while these plateaus vanish beyond λ_{c_2}, ascertaining emergence of a trivial insulating phase ($C = 0$) with $\sigma_{xy} = 0$. Thus, the polaronic Hall conductivity ensures that the system undergoes a transition from a nontrivial insulating phase with quantized plateaus at $|C|e^2/h$ in the $\lambda_{eph} \lesssim \lambda_c$ regime to a trivial insulating phase with zero Hall conductivity in the $\lambda_{eph} > \lambda_c$ regime.

6.6 Summary

To summarize, we have studied the effect of e-ph interaction on inducing a topological phase transition in a Haldane-Holstein model on an α-T_3 lattice. The NN and the complex NNN Haldane hopping amplitudes get renormalized by the Holstein reduction factor showing the signature of polaron formation in the system. The cases of our study are majorly divided into two scenarios, namely lower to intermediate α $(0 < \alpha \leq 0.6)$ and higher $(0.6 < \alpha < 1)$ values of α. With the help of the effective Hamiltonian in $\mathbf{k}$ space, we have computed the bulk and the edge spectra where it is observed that for the first case, as we increase the e-ph coupling strength λ_{eph}, the bulk gap between the distorted flat and valance bands closes at a critical coupling strength, namely λ_c at one K valley and re-opens beyond λ_c. This feature explains that the system is characterized by two distinct insulating states below and above $\lambda_{eph} = \lambda_c$. Consequently, the conducting edge modes emerge in the $\lambda_{eph} < \lambda_c$ regime, which are preserved up to $\lambda_{eph} = \lambda_c$, and disappear for $\lambda_{eph} > \lambda_c$, signifying a topologically nontrivial to trivial phase transition. In the second case, we encounter a different scenario where the distorted flat and valance bands in the bulk remain gapless for the $0.65 \lesssim \alpha \lesssim 0.75$ regime and gapped for $0.75 \lesssim \alpha < 1$, till λ_{eph} reaches a first critical value, namely λ_{c_1} and become gapped till λ_{eph} assumes another critical value, namely λ_{c_2} where similar gap closing transition takes place. The explicit emergence of conducting edge modes in the $\lambda_{c_1} < \lambda_{eph} < \lambda_{c_2}$ regime both for $0.65 \lesssim \alpha \lesssim 0.75$ and $0.75 \lesssim \alpha < 1$, and also in $0 \leq \lambda_{eph} < \lambda_{c_1}$ regime for $0.75 \lesssim \alpha < 1$ that traverse through the dFB around the K and K$'$ valleys makes the latter case more intriguing. It indicates that for $0.65 \lesssim \alpha \lesssim 0.75$ $(0.75 \lesssim \alpha < 1)$, the system re-enters from a conventional (topological) SM phase (in the $\lambda_{eph} < \lambda_{c_1}$ regime) to a (another) topological one (in the $\lambda_{c_1} < \lambda_{eph} < \lambda_{c_2}$ regime) upon tuning the e-ph coupling strength. The above discussions for both the cases, either with a unique λ_c or with two λ_cs, namely λ_{c_1} and

λ_{c_2}, strongly indicate possibilities of inducing topological phase transition via e-ph coupling in an α-T_3 Haldane-Holstein model. Furthermore, we have numerically computed the Berry curvature and the topological invariant, namely the (polaronic) Chern number (C), for different values of α. In our study, the evidence of a discontinuous change in C from $|C| = 1$ to $|C| = 0$ for $0 < \alpha \lesssim 0.75$ regime, and from $|C| = 2$ to $|C| = 1$ and finally to $|C| = 0$ for $0.75 \lesssim \alpha < 1$ regime exhibiting a jump in the C vs λ_{eph} diagram at different critical values of the e-ph coupling for different values of α directly confirms the topological phase transition solely caused by the e-ph interaction, while interpolating α between corresponding lattice structures of graphene to a dice lattice. More specifically, the system under investigation possesses a topological insulating phase accompanied by $|C| = 1$ or $|C| = 2$ (depending on the range of α) below certain critical values of the e-ph coupling strength, and becomes a trivial insulator ($C = 0$) above the critical point. We, furthermore, incorporate the above observations in a phase diagram plotted for C in the $\lambda_{eph} - \alpha$ plane. To confirm such phases, and phase transitions from one phase to another, we have calculated the Hall conductivity for a few values of α (both small and large) as a function of λ_{eph}. The existence (vanishing) of Hall plateaus at $|C|e^2/h$ below (above) a certain critical λ_c for a particular value of α further substantiates the evidence of topological phase transitions induced by e-ph coupling in our α-T_3 Haldane-Holstein model. We wish to motivate that our study may serve as a powerful tool for understanding the interaction-driven topology in novel quantum systems.

Chapter 7

Polaron Induced Phase Transitions in an α-T_3 Quantum Spin Hall System

In this chapter, we investigate the effects of Holstein polarons arising from the electron-phonon (e-ph) coupling on the quantum spin Hall phase (and phase transition therein) of a pseudospin-1 fermionic α-T_3 lattice. The parameter α and the e-ph coupling strength λ_{eph} have an interesting interplay, which demonstrates that at smaller values of α, there is a single transition from a topological to a trivial phase as a function of λ_{eph}, while the larger α values host two gap closing transitions, namely, trivial-topological-trivial transitions, accompanied by a narrow semi-metallic phase in between. These results are confirmed via computing the $\mathbb{Z}_2$ invariant.

7.1 Introduction

The discovery of symmetry-protected topological phases has stimulated enormous attention, where a continuous phase transition is possible between states with the same underlying symmetry but different topology [89, 91, 379, 380]. The nontrivial features of the topological insulators (TIs) are characterized by a d-dimensional insulating bulk and a $(d-1)$-dimensional gapless

surface or edge which are topologically robust against disorder. These TIs are classified into several categories, each of which is designated by a distinct topological index. One of them is the Chern insulator, where the topological invariant known as the Chern number (C) hosts chiral edge modes. Unlike the Chern insulators, which validate the breaking of time reversal symmetry (TRS), there exists another class of TIs, called the $\mathbb{Z}_2$ topological insulators, also commonly known as the quantum spin Hall (QSH) insulators, which endorse helical edge states protected by the TRS [91, 248]. In contrast to the Chern insulators, these QSH insulators, characterized by a $\mathbb{Z}_2$ invariant [244, 245, 248, 259, 381–384] (which takes values 0 or 1 denoting equivalently "$\mathbb{Z}_2$-even" (trivial) or "$\mathbb{Z}_2$-odd" (topological) insulators) demonstrate a zero (charge) Hall current, while carry a quantized spin Hall current owing to two counter-propagating (left and right mover) edge channels for two opposite spins per edge. Moreover, the role of spin-orbit coupling (SOC) that preserves TRS becomes important for a QSH insulator. As TRS is preserved, one can associate a $\mathbb{Z}_2$ invariant with the Kramers pairs [248, 259, 381–383] that are formed by the occupied states at the Dirac points across the Brillouin zone (BZ). A prototypical model for such $\mathbb{Z}_2$ insulators was proposed by Kane and Mele [257] in their seminal paper, where they have considered equal and opposite Haldane flux for the up and down spins of the particles, and thus this spinful version of the Haldane model restores the TRS in the system. In accordance with the TRS, the spinful bands add up to a net zero Chern number (contributing zero charge Hall current), with them being equal and opposite for up ($C_\uparrow$) and down-spin ($C_\downarrow$) bands. However, a spin dependent Chern number, namely C_σ (or the difference between $C_\uparrow$ and $C_\downarrow$) may act as an effective topological invariant giving rise to a finite spin Hall conductivity [89, 91, 248, 257, 385, 386]. Nevertheless, for a more realistic $\mathbb{Z}_2$ TI, this picture fails upon the inclusion of an extrinsic SOC, for example, the Rashba SOC (RSOC). Although it protects the TRS, it mixes the spins, destroying the conservation of the z component of the spin. Therefore, $\mathbb{Z}_2$ invariant becomes necessary for such mixed spin systems to encode the topological characterization.

In continuation of the study in the previous chapter on Chern insulator, here we shall take the effect of polaronic physics induced via the electron-phonon (e-ph) coupling in a spin Hall insulator. Conventionally, the e-ph interaction leaves the parent symmetries of the system and hence the topological properties unaltered, therefore making it possible to treat the electronic and phononic degrees of freedom independently. Here, we come up with a scheme which yields that if the polarons are formed in a tight binding system by local lattice distortion [112, 113], then the electron and phonon degrees of freedom become correlated and this strong e-ph coupling significantly affects the band topology [371], which may induce a gap closing transition at the Dirac points. As phonons are intrinsically present in a real crystal, the motivation behind

incorporating e-ph interaction effects in our model is to see how a nontrivial phase and its relative transitions can be engineered solely through the interaction between the fermionic charge carriers and the lattice vibrational modes.

The remainder of the chapter is structured as follows. In Sec. 7.2, we describe the e-ph coupling and the corresponding model Hamiltonian of our system are given in Sec. 7.2.1, formulated under the framework of the Kane-Mele model with the Rashba coupling modified by a Holstein term accounting for the e-ph coupling. The polaron formation in our system is employed in Sec. 7.2.2 through the Lang-Firsov technique. Sec. 7.3 deals with the numerical analysis of the bulk gap closing transitions indicating a plausible occurrence of topological phase transition (TPT). Hence, Sec. 7.4 and Sec. 7.5 respectively describe the formulation of the $\mathbb{Z}_2$ invariant and the edge states. Furthermore, a phase boundary is presented in Sec. 7.7 that summarizes our results for the TPT interpolating between graphene and a dice lattice. Finally, we conclude with a description of our main findings in Sec. 7.8.

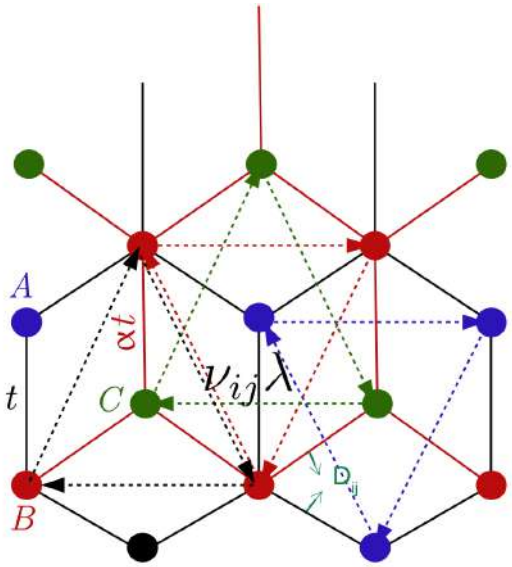

Figure 7.1: The schematic model of an α-T_3 lattice is shown, where the blue, red, and green circles represent the sublattices A, B, and C, respectively. The NN hopping strength between A and B sublattices (solid black line) is t, while it is αt between B and C sublattices (solid red line). The NNN hopping strength between A-B-A (dashed blue) or B-A-B (dashed black) is λ, while through C, it is $\alpha\lambda$ via B-C-B (dashed red) and C-B-C (dashed green). $\nu_{ij} = -1(+1)$ denotes the clockwise (anticlockwise) direction of hopping. The unit vector $\hat{D}_{ij}$ pointing perpendicular to the NN bonds represents the direction of RSOC. The coordinates of the NN sites are $\mathbf{d_1} = (\sqrt{3}a_0/2, a_0/2)$, $\mathbf{d_2} = (-\sqrt{3}a_0/2, a_0/2)$ and $\mathbf{d_3} = (0, -a_0)$, while those of the NNN sites are $\mathbf{a_1} = (\sqrt{3}a_0/2, 3a_0/2)$, $\mathbf{a_2} = (-\sqrt{3}a_0/2, 3a_0/2)$ and $\mathbf{a_3} = (\sqrt{3}a_0, 0)$, a_0 being the distance between two neighbouring atoms.

7.2 Quantum Spin Hall Effect via Polarons in an α-T_3 Lattice

In this section, we discuss the TPT mediated through e-ph coupling in a pseudospin-1 fermionic system on an α-T_3 Kane-Mele (KM) QSH insulator. We schematically represent an α-T_3 lattice in Fig. 7.1 (this figure is intentionally repeated in each chapter to provide convenience to readers). A typical hexagonal unit cell of an α-T_3 lattice constitutes A (blue) and B (red) lattice sites constructing a regular honeycomb lattice with nearest-neighbour (NN) hopping strength t between them and an additional C (green) atoms placed at the center of each hexagon connecting to only B atoms (hopping between C and A atom is forbidden) via a hopping strength αt ($\alpha \in [0:1]$). Therefore, the two limiting cases of our study are the results for graphene ($\alpha = 0$) and dice ($\alpha = 1$) lattices. We introduce our model Hamiltonian as follows.

7.2.1 Rashba coupled Kane-Mele-Holstein Hamiltonian

In order to study the effects of the e-ph coupling on an α-T_3 QSH insulator of Kane-Mele type [186, 309] in the presence of a Semenoff mass [179, 387] and the RSOC [157], we model our system under the framework of a tight-binding Kane-Mele-Holstein Hamiltonian, which can be written as $\mathcal{H} = \mathcal{H}_{\rm KM} + \mathcal{H}_{\rm R} + \mathcal{H}_{\mathcal{M}} + \mathcal{H}_{\rm ep}$ with,

$$\mathcal{H}_{\rm KM} = -t\sum_{\langle ij\rangle\sigma} c^{\dagger}_{i\sigma}c_{j\sigma} - \alpha t\sum_{\langle jk\rangle\sigma} c^{\dagger}_{j\sigma}c_{k\sigma} - \frac{i\lambda}{3\sqrt{3}}\sum_{\langle\langle ij\rangle\rangle\sigma\sigma'}\nu_{ij}c^{\dagger}_{i\sigma}\sigma_z c_{j\sigma'} - \frac{i\alpha\lambda}{3\sqrt{3}}\sum_{\langle\langle jk\rangle\rangle\sigma\sigma'}\nu_{jk}c^{\dagger}_{j\sigma}\sigma_z c_{k\sigma'}, \tag{7.1a}$$

$$\mathcal{H}_{\rm R} = -i\lambda_R\sum_{\langle ij\rangle\sigma\sigma'} c^{\dagger}_{i\sigma}(\hat{D}_{ij}\cdot\vec{\sigma})_{\sigma\sigma'}c_{j\sigma'} - i\alpha\lambda_R\sum_{\langle jk\rangle\sigma\sigma'} c^{\dagger}_{j\sigma}(\hat{D}_{jk}\cdot\vec{\sigma})_{\sigma\sigma'}c_{k\sigma'}, \tag{7.1b}$$

$$\mathcal{H}_{\mathcal{M}} = \mathcal{M}\sum_{i\sigma} c^{\dagger}_{i\sigma}S_z c_{i\sigma}, \tag{7.1c}$$

$$\mathcal{H}_{\rm ep} = \hbar\omega_0\left[\sum_i\left(b^{\dagger}_i b_i + \frac{1}{2}\right) + g\sum_{i\sigma} c^{\dagger}_{i\sigma}c_{i\sigma}(b^{\dagger}_i + b_i)\right], \tag{7.1d}$$

where $\mathcal{H}_{\rm KM}$, $\mathcal{H}_{\rm R}$, $\mathcal{H}_{\mathcal{M}}$ and $\mathcal{H}_{\rm ep}$, respectively represent the Hamiltonian for the bare Kane-Mele model, RSOC, Semenoff mass and e-ph interaction present in the system. $c^{\dagger}_{i\sigma}(c_{i\sigma})$ denotes the creation (annihilation) operator for electrons corresponding to A, B, and C sublattice with i, j, and k indices, respectively and σ_z is the z-component of the Pauli spin matrix, σ and σ' are the up ($\uparrow$) and down ($\downarrow$) spin indices, respectively. The descriptions of the first two terms

($\mathcal{H}_{\rm KM}$ and $\mathcal{H}_{\rm R}$) appear elsewhere and hence are not repeated for brevity. Further, the inclusion of the Semenoff mass ($\mathcal{M}$) breaks the sublattice (inversion) symmetry, which is written in Eq. (7.1c), where $S_z = \begin{pmatrix} 1 & 0 & 0 \\ 0 & 0 & 0 \\ 0 & 0 & -1 \end{pmatrix}$ is the z-component of the pseudospin-1 matrix. Since, the staggered mass term S_z is well known for generating a non-zero Berry phase and hence a nontrivial topology of the valence band in an α-T_3 lattice system (unlike a certain U term considered in the Hamiltonian of Ref. [387] that entails a distinct flat band topology) which correspondingly leads to the formation of edge states in our system, we restrict ourselves to the inclusion of only S_z in our Hamiltonian. The effect of e-ph coupling is represented by the Holstein Hamiltonian [139] written in Eq. (7.1d), where the first term signifies the total phononic onsite (at site i) energy in terms of the creation (annihilation) operators, $b_i^\dagger(b_i)$ of the longitudinal optical (LO) phonons which oscillate with a dispersionless LO frequency, ω_0 and interact with the electrons with a coupling strength g ($(\equiv \sqrt{\lambda_{eph} t/\omega_0})$), denoted by the second term of Eq. (7.1d). To obtain an effective electronic Hamiltonian that characterizes the bulk and edge spectra and the suitable topological invariant of our system, we proceed as follows.

7.2.2 Effective electronic Hamiltonian - Lang-Firsov transformation

Intending to investigate the effects of the (small) 'Holstein polaron' on the spectral properties, we first decouple the electron and phonon degrees of freedom by employing the well-known Lang-Firsov transformation (LFT) [260]. This is a coherent state transformation of a displaced harmonic oscillator that captures the polaron physics adequately well in the high-frequency (anti-adiabatic) regime, meaning the LO frequency of the phonons (highest energy scale) is much larger than the other parameters of the system, namely, when ω_0 to be much greater than t, t', λ, λ', λ_R, λ'_R, and $\mathcal{M}$ [371, 377]. In this limit, the electrons are unable to follow the motion of the phonons perfectly (due to the rapid motion of the phonons), leading to an anti-adiabatic coupling between electrons and phonons [112, 113]. Thus, electronic densities at the lattice sites are left undisturbed. In a tight binding (narrow-band) lattice (where the electrons are tightly bound to their host sites), due to the strong coupling between the electrons and phonons, the polarons get confined to a particular site and do not spread over to the neighbouring sites. In general, the size of the polaron, r_p is related to the electronic parameters as $r_p \sim a_0 t/g^2\hbar\omega_0$ [388]. Hence, for a strong coupling ($g^2 > 1$) and high frequency ($\hbar\omega_0 > t$) limit, the size of the polaron shrinks owing to the strong localization effects satisfying $r_p < a_0$, which implies that the size of the polaron becomes smaller than the lattice constant leading to the formation of

the small Holstein polaron [112, 113]. Due to this strong confinement effect of the polarons at the same site where the electrons are bound, the onsite strength of the e-ph interaction becomes much stronger compared to those at the neighbouring sites. Therefore, the couplings between the electrons with the phonons belonging to the NN and NNN sites are negligibly small as the e-ph interaction is weaker on the neighbouring sites, and hence they can possibly be neglected. The LFT with $\mathcal{S}$ being the generator of the transformation can be expressed as,

$$\tilde{\mathcal{H}} = e^{\mathcal{S}}\mathcal{H}e^{-\mathcal{S}}, \quad \mathcal{S} = g\sum_{i\sigma} c^{\dagger}_{i\sigma}c_{i\sigma}(b^{\dagger}_{i} - b_{i}), \tag{7.2}$$

which transforms the total Hamiltonian as,

$$\begin{aligned}
\tilde{\mathcal{H}} &= -t\Bigg[\sum_{\langle i,j\rangle\sigma} c^{\dagger}_{i\sigma}c_{j\sigma}e^{[X_i - X_j]} + \alpha\sum_{\langle j,k\rangle\sigma} c^{\dagger}_{j\sigma}c_{k\sigma}e^{[X_j - X_k]}\Bigg] - \frac{\lambda}{3\sqrt{3}}\Bigg[\sum_{\langle\langle i,j\rangle\rangle\sigma\sigma'} \nu_{ij}c^{\dagger}_{i\sigma}\sigma_z c_{j\sigma'}e^{[X_i - X_j]} \\
&+ \alpha\sum_{\langle\langle j,k\rangle\rangle\sigma\sigma'} \nu_{jk}c^{\dagger}_{j\sigma}\sigma_z c_{k\sigma'}e^{[X_j - X_k]}\Bigg] - i\lambda_R\Bigg[\sum_{\langle i,j\rangle\sigma\sigma'} c^{\dagger}_{i\sigma}(\hat{D}_{ij}\cdot\vec{\sigma})_{\sigma\sigma'}c_{j\sigma'}e^{[X_i - X_j]} \\
&+ \alpha\sum_{\langle j,k\rangle\sigma\sigma'} c^{\dagger}_{j\sigma}(\hat{D}_{jk}\cdot\vec{\sigma})_{\sigma\sigma'}c_{k\sigma'}e^{[X_j - X_k]}\Bigg] + \sum_{i\sigma} c^{\dagger}_{i\sigma}(\mathcal{M}S_z - g^2\hbar\omega_0 I_3)c_{i\sigma} \\
&+ \hbar\omega_0\sum_{i} b^{\dagger}_{i}b_{i},
\end{aligned} \tag{7.3}$$

where the X_is in the exponent contain the phonon operators of the i-th site as $X_i = g(b^{\dagger}_{i} - b_i)$ and I_3 is a 3×3 identity matrix. In the last step, we neglect the constant '1/2' factor in the onsite phonon energy term.

During the formation of the polarons, the electrons undergo continuous emission and absorption of virtual phonons at $T = 0$. While the slow electrons with energy less than the longitudinal optical phonons cannot emit real phonons. Hence, virtual processes do not require any conservation of energy. At $T = 0$, while the real phonons are absent, the lattice still possesses a non-zero energy (quantum mechanically) known as zero-point energy owing to which the formation of virtual phonons (which are associated with the quantum fluctuations of the lattice) takes place, even when there are no thermal excitations [112, 113]. Thus, slow electrons can emit and absorb virtual phonons at $T = 0$, and one would expect that they constitute a cloud of phonons surrounding the electron forming a polaron. Hence, the presence of virtual phonons induces an e-ph interaction effect, which significantly renormalizes the electronic band structure, even at zero temperature. Hence, to obtain an effective electronic Hamiltonian by eliminating phonon

modes from our system, we perform a zero-phonon averaging at $T = 0$, which results in,

$$\begin{aligned}
\tilde{\mathcal{H}}_{\text{eff}} &= \langle 0|\tilde{\mathcal{H}}|0\rangle \\
&= -\tilde{t}\Big[\sum_{\langle i,j\rangle\sigma} c^{\dagger}_{i\sigma}c_{j\sigma} + \alpha\sum_{\langle j,k\rangle\sigma} c^{\dagger}_{j\sigma}c_{k\sigma}\Big] - \frac{\tilde{\lambda}}{3\sqrt{3}}\Big[\sum_{\langle\langle i,j\rangle\rangle\sigma\sigma'} \nu_{ij}c^{\dagger}_{i\sigma}\sigma_z c_{j\sigma'} + \alpha\sum_{\langle\langle j,k\rangle\rangle\sigma\sigma'} \nu_{jk}c^{\dagger}_{j\sigma}\sigma_z c_{k\sigma'}\Big] \\
&- i\tilde{\lambda}_R\Big[\sum_{\langle i,j\rangle\sigma\sigma'} c^{\dagger}_{i\sigma}(\hat{D}_{ij}\cdot\vec{\sigma})_{\sigma\sigma'}c_{j\sigma'} + \alpha\sum_{\langle j,k\rangle\sigma\sigma'} c^{\dagger}_{j\sigma}(\hat{D}_{jk}\cdot\vec{\sigma})_{\sigma\sigma'}c_{k\sigma'}\Big] \\
&+ \sum_{i\sigma} c^{\dagger}_{i\sigma}(\mathcal{M}S_z - g^2\hbar\omega_0 I_3)c_{i\sigma},
\end{aligned} \tag{7.4}$$

where the hopping amplitudes are renormalized by the Holstein reduction factor, namely,

$$\langle 0|e^{[X_i - X_j]}|0\rangle = e^{-g^2} \tag{7.5}$$

via,

$$\tilde{t} = te^{-g^2}, \quad \tilde{\lambda} = \lambda e^{-g^2}, \quad \tilde{\lambda}_R = \lambda_R e^{-g^2}. \tag{7.6}$$

The last term of Eq. (7.3) drops out due to zero-phonon averaging. Within such an anti-adiabatic ($\hbar\omega_0 \gg t, t', \lambda, \lambda', \lambda_R, \lambda'_R, \mathcal{M}$, and g) decoupling scheme, the electronic and phonon modes do not affect each other any longer because the fast LO phonons possess larger energy gap between different phononic excitations than the electronic hopping strengths so that the phonons easily follow the electronic motion without altering their distributions. It is evident from Eq. (7.4) that the phonon degrees of freedom are removed from the system and the polaronic signatures are well inculcated through the Holstein factors (Eq. (7.6)) in the modified electronic hopping strengths, $\tilde{t}$, $\tilde{\lambda}$, and $\tilde{\lambda}_R$ which gives rise to the band narrowing effect and also through the polaron shift energy $-g^2\hbar\omega_0$ (last term of Eq. (7.4)). As these polaronic factors significantly influence the bands, one can tune the band topology accompanied by a bulk gap closing transition via changing the e-ph interaction strength.

7.2.3 k-space polaronic Hamiltonian

In the continuum limit, the Fourier transformed Hamiltonian can be obtained in a spinful triatomic sublattice basis, that is, in $(A_\uparrow\ B_\uparrow\ C_\uparrow\ A_\downarrow\ B_\downarrow\ C_\downarrow)$ basis as,

$$\tilde{\mathcal{H}}_{\text{eff}}(\mathbf{k}) = \begin{pmatrix} \rho^{11}_{\sigma\sigma}(\mathbf{k}) & \rho^{12}_{\sigma\sigma}(\mathbf{k}) & 0 & 0 & \gamma^{12}_{\sigma\sigma'}(\mathbf{k}) & 0 \\ \rho^{21}_{\sigma\sigma}(\mathbf{k}) & \rho^{22}_{\sigma\sigma}(\mathbf{k}) & \rho^{23}_{\sigma\sigma}(\mathbf{k}) & \gamma^{21}_{\sigma\sigma'}(\mathbf{k}) & 0 & \gamma^{23}_{\sigma\sigma'}(\mathbf{k}) \\ 0 & \rho^{32}_{\sigma\sigma}(\mathbf{k}) & \rho^{33}_{\sigma\sigma}(\mathbf{k}) & 0 & \gamma^{32}_{\sigma\sigma'}(\mathbf{k}) & 0 \\ 0 & \gamma^{12}_{\sigma'\sigma}(\mathbf{k}) & 0 & \rho^{11}_{\sigma'\sigma'}(\mathbf{k}) & \rho^{12}_{\sigma'\sigma'}(\mathbf{k}) & 0 \\ \gamma^{21}_{\sigma'\sigma}(\mathbf{k}) & 0 & \gamma^{23}_{\sigma'\sigma}(\mathbf{k}) & \rho^{21}_{\sigma'\sigma'}(\mathbf{k}) & \rho^{22}_{\sigma'\sigma'}(\mathbf{k}) & \rho^{23}_{\sigma'\sigma'}(\mathbf{k}) \\ 0 & \gamma^{32}_{\sigma'\sigma}(\mathbf{k}) & 0 & 0 & \rho^{32}_{\sigma'\sigma'}(\mathbf{k}) & \rho^{33}_{\sigma'\sigma'}(\mathbf{k}) \end{pmatrix}, \tag{7.7}$$

where ρ-blocks stand for the NN and NNN hopping (for bare KM model) elements, while γ-blocks refer to the RSOC terms which can be explicitly expressed as,

$$\rho^{11}_{\sigma\sigma(\sigma'\sigma')}(\mathbf{k}) = \mathcal{M} - g^2\omega_0 \pm \frac{2\tilde{\lambda}\mathfrak{Im}(f_{\mathbf{k}})}{3\sqrt{3}}\cos\varphi, \tag{7.8a}$$

$$\rho^{12}_{\sigma\sigma(\sigma'\sigma')}(\mathbf{k}) = -\tilde{t}(h^{\mathbf{k}}_x - ih^{\mathbf{k}}_y)\cos\varphi = \left[\rho^{21}_{\sigma\sigma(\sigma'\sigma')}(\mathbf{k})\right]^*, \tag{7.8b}$$

$$\rho^{22}_{\sigma\sigma(\sigma'\sigma')}(\mathbf{k}) = -g^2\omega_0 \mp \frac{2\tilde{\lambda}\mathfrak{Im}(f_{\mathbf{k}})}{3\sqrt{3}}(\cos\varphi - \sin\varphi), \tag{7.8c}$$

$$\rho^{23}_{\sigma\sigma(\sigma'\sigma')}(\mathbf{k}) = -\tilde{t}(h^{\mathbf{k}}_x - ih^{\mathbf{k}}_y)\sin\varphi = \left[\rho^{32}_{\sigma\sigma(\sigma'\sigma')}(\mathbf{k})\right]^*, \tag{7.8d}$$

$$\rho^{33}_{\sigma\sigma(\sigma'\sigma')}(\mathbf{k}) = -\mathcal{M} - g^2\omega_0 \mp \frac{2\tilde{\lambda}\mathfrak{Im}(f_{\mathbf{k}})}{3\sqrt{3}}\sin\varphi, \tag{7.8e}$$

and

$$\gamma^{12}_{\sigma\sigma'}(\mathbf{k}) = -i\tilde{\lambda}_R u_{\mathbf{k}}\cos\varphi = \left[\gamma^{21}_{\sigma'\sigma}(\mathbf{k})\right]^*, \tag{7.9a}$$

$$\gamma^{21}_{\sigma\sigma'}(\mathbf{k}) = i\tilde{\lambda}_R v_{\mathbf{k}}\cos\varphi = \left[\gamma^{12}_{\sigma'\sigma}(\mathbf{k})\right]^*, \tag{7.9b}$$

$$\gamma^{23}_{\sigma\sigma'}(\mathbf{k}) = i\tilde{\lambda}_R u_{\mathbf{k}}\sin\varphi = \left[\gamma^{32}_{\sigma'\sigma}(\mathbf{k})\right]^*, \tag{7.9c}$$

$$\gamma^{32}_{\sigma\sigma'}(\mathbf{k}) = -i\tilde{\lambda}_R v_{\mathbf{k}}\sin\varphi = \left[\gamma^{23}_{\sigma'\sigma}(\mathbf{k})\right]^*, \tag{7.9d}$$

where σ (σ') stands for the up (down) spin index, and $\varphi = \tan^{-1}\alpha$. The ij components of the $\rho_{\sigma\sigma}$-block differ only by a relative sign in $\tilde{\lambda}$ terms to those of the $\rho_{\sigma'\sigma'}$-block, while the ij components of the $\gamma_{\sigma\sigma'}$-block are complex conjugate to the ji components of the $\gamma_{\sigma'\sigma}$-block. The reduced hopping strengths (Holstein amplitudes), namely, $\tilde{t}$, $\tilde{\lambda}$, and $\tilde{\lambda}_R$ are expressed in Eq. (7.6) in terms of $g(\equiv \sqrt{\lambda_{eph}t/\omega_0})$. h_x^k, h_y^k and f_k in Eq. (7.8) and u_k and v_k in Eq. (7.9) are given as

$$h_x^{\mathbf{k}} = \sum_{i=1}^{3} \cos(\mathbf{k}.\mathbf{d_i}),\ h_y^{\mathbf{k}} = \sum_{i=1}^{3} \sin(\mathbf{k}.\mathbf{d_i}),\ f_{\mathbf{k}} = \sum_{i=1}^{3} e^{i\mathbf{k}.\mathbf{a_i}}, \tag{7.10a}$$

$$u_{\mathbf{k}}(v_{\mathbf{k}}) = -e^{-ik_y a_0} + \left[\cos\left(\frac{\sqrt{3}a_0k_x}{2}\right) \mp \sqrt{3}\sin\left(\frac{\sqrt{3}a_0k_y}{2}\right)\right] e^{\frac{ik_y a_0}{2}}, \tag{7.10b}$$

where the NN $\mathbf{d}$-vectors and the NNN $\mathbf{a}$-vectors have been mentioned in the caption of Fig. 7.1.

7.3 Bulk Spectra and Gap Closing Transitions

To study the spectral properties of the QSH α-T_3 lattice, we Fourier transform Eq. (7.4) to the momentum ($\mathbf{k}$) space. Subsequent discussions simplify that we shall divide the Eq. (7.7) by the NN hopping strength, t (all the parameters will be renormalized in the units of t) and use the same as our model Hamiltonian for the rest of the chapter. Therefore, we introduce a dimensionless parameter (renormalized e-ph coupling strength) as $\lambda_{eph} = \frac{g^2\omega_0}{t}$ which we henceforth call the e-ph coupling constant for our system.

For convenience, we consider $a_0 = \hbar = 1$. To perform the numerical analysis for the topological phase transition in a Kane-Mele α-T_3 lattice in the presence of RSOC, we fix the hopping strengths as $t = -2.7$ eV, $\lambda = 0.1t$, $\lambda_R = 0.02t$, and the Semenoff mass as $\mathcal{M} = 0.02t$. The rationale behind choosing these values is inspired by the corresponding quantities in graphene [257]. Our system having similar structure as the hexagonal graphene lattice (for $\alpha = 0$), we keep the ratios of these essential parameters fairly similar to Ref. [257], so that at $\alpha = 0$, the system lies within the well known QSH phase. We also set the LO frequency of the phonons, ω_0 as $\omega_0 = 3t \gg t, \alpha t, \lambda, \lambda', \lambda_R, \lambda_R'$, and $\mathcal{M}$ (for anti-adiabaticity to be valid).

The distinction of an α-T_3 lattice from bare graphene ($\alpha = 0$) lies in the appearance of the flat band (FB) for $\alpha \neq 0$, thus justifying pseudospin-1 fermions. Hence, the role of FB needs to be ascertained carefully in the context of TPT. A conventional α-T_3 lattice is identified with a dispersionless FB at zero-energy for graphene ($\alpha = 0$) and dice ($\alpha = 1$) lattices and a distorted FB (dFB) for $0 < \alpha < 1$ along with two dispersive bands, namely the conduction and the valence bands which touch each other at the Dirac cones located at K $= (2\pi/3\sqrt{3}a_0, 2\pi/3a_0)$

and K$'$ $= (-2\pi/3\sqrt{3}a_0, 2\pi/3a_0)$. For our case, due to the presence of the intrinsic SOC (KM) term, the FB becomes largely dispersive, while the valley degeneracy is preserved due to the TRS present, unlike the α-T_3 Haldane lattice. The dFB favours the transport of the system as the band electrons are associated with a non-zero group velocity. As the bulk band properties are different for different values of α, we segregate the whole range of $\alpha \in [0:1]$ into two regimes, namely (i) the lower to intermediate $(0 < \alpha \leq 0.5)$ and (ii) intermediate to higher $(0.5 < \alpha < 1.0)$ values and present the spectral properties for a particular α from each of the two regimes. The results for lower values of α are close to those of bare graphene $(\alpha = 0)$, while those for higher α agree with the dice $(\alpha = 1)$ lattice. Therefore, we encompass the entire range of α interpolating between the graphene and the dice lattice.

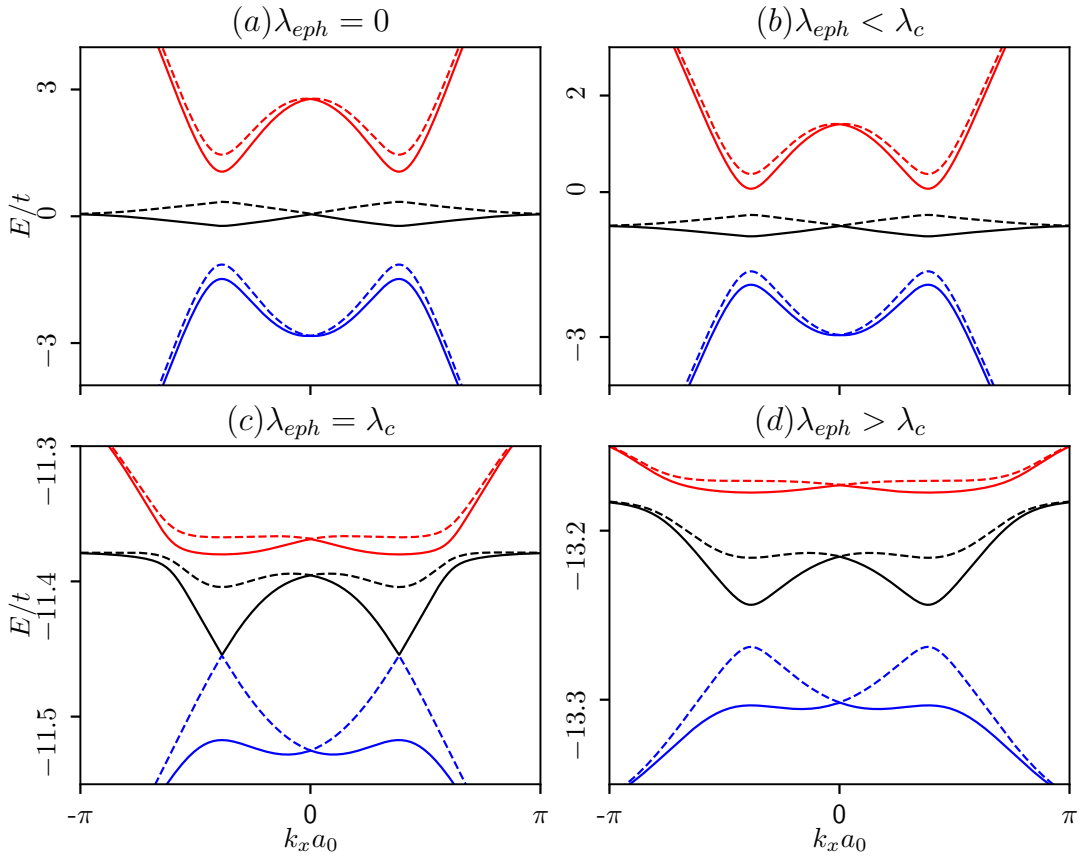

Figure 7.2: The bulk band structures with energy E (in units of t) are shown as a function of dimensionless momenta, k_x (multiplied by a_0) at $k_y = 2\pi/3a_0$ for $\alpha = 0.2$. The red, black, and blue colours represent the CB, the dFB and the VBs, respectively. In (a) and (b) the dispersion is plotted in the $0 \leq \lambda_{eph} < \lambda_c$ regime at $\lambda_{eph} = 0$ and $\lambda_{eph} = 0.5$, respectively, where the bulk is gapped. (c) The plot is shown at the critical $\lambda_{eph} = \lambda_c = 1.95$ where the bulk gap closing between the dFB and the VB occurs. (d) The same is shown in the $\lambda_{eph} > \lambda_c$ regime at $\lambda_{eph} = 2.2$ where the spectrum is again gapped. The parameters are taken as $\lambda = 0.1t$, $\mathcal{M} = 0.02t$ and $\lambda_R = 0.02t$.

At first, let us consider the bulk spectra for $\alpha = 0.2$ which are presented in Fig. 7.2. The

spectra are plotted as a function of dimensionless momentum, $k_x a_0$ (k_y is fixed at $\frac{2\pi}{3a_0}$), where the solid and the dotted lines represent those for two different spin subbands belonging to the Kramer's pair, respectively. We denote the conduction band (CB), distorted flat band (dFB) and the valence band (VB) by the red, black and blue colours, respectively. One may notice that the dispersions of the bands are of semi-Dirac type, which means they are linear along k_y, while quadratic along the k_x direction. The low energy spectrum of the Hamiltonian (7.7) obeys the Dirac-Weyl dispersion, which can be achieved by linearizing Eq. (7.7) in the vicinity of the two valleys K and K$'$. As the RSOC breaks the spin-degeneracy, the bulk bands are split for the $\uparrow$-spins and the $\downarrow$-spins giving rise to six distinct bands (three for each spin orientation). However, we cannot distinguish them as $\uparrow$ or $\downarrow$-spin bands as the spin-polarization is lost due to the presence of RSOC. Hence, we call them Kramer's pair of subbands as the TRS is preserved even upon inclusion of the RSOC. The bulk bands corresponding to each of the Kramer's pairs cross each other only at the $\mathcal{M}$ $(0, 2\pi/3a_0)$ point, resulting in a zero splitting. Moreover, the TRS validates identical behaviour of the bulk bands at the two valleys, namely K and K$'$. To investigate the different topological phases and the TPT therein mediated via polaron, we must vary the e-ph coupling (λ_{eph}) and examine possible gap closing transitions at $\lambda_{eph} = \lambda_c$, λ_c being the e-ph coupling at the TPT. The different regimes of λ_{eph} are entitled as $0 \leq \lambda_{eph} < \lambda_c$ (before the transition), $\lambda_{eph} = \lambda_c$ (at the transition) and $\lambda_{eph} > \lambda_c$ (beyond the transition). We can clearly see from Fig. 7.2(a) that the bulk bands are gapped at both valleys when $\lambda_{eph} = 0$, which implies that the system for small α, for example, $\alpha = 0.2$ behaves as an insulator in the absence of e-ph coupling. Further, as λ_{eph} increases, the overall spectrum shifts downward (because of the polaronic shift energy $-g^2\hbar\omega_0$), and the dFB is no longer fixed at $E = 0$ in the $\lambda_{eph} < \lambda_c$ regime (Fig. 7.2(b)). However, the gap in the spectrum still remains intact. As λ_{eph} reaches a critical value, namely $\lambda_{eph} = \lambda_c = 1.95$, we find that the bulk gap between the dFB and the VB closes (shown in Fig. 7.2(c)) at both the valleys, which indicates a bulk gap closing transition. Beyond, $\lambda_{eph} = \lambda_c$ (i.,e., in $\lambda_{eph} > \lambda_c$ regime), there exists a noticeable gap in the bulk spectrum (shown in Fig. 7.2(d)). Hence, for the lower values of α, the bulk bands are gapped in the $0 \leq \lambda_{eph} < \lambda_c$ and $\lambda_{eph} > \lambda_c$ regimes, resulting in an insulating behaviour, while at $\lambda_{eph} = \lambda_c$ they are gapless, implying a semi-metallic (SM) point. The explicit dependence of the band gap, ΔE on λ_{eph} is shown in Fig. 7.5. It should be mentioned here that the gapless condition of the Hamiltonian and the corresponding values of α and the e-ph coupling strength, λ_{eph} at which the VB and the dFB touch each other are obtained numerically via tuning these values with high degree of precision. We diagonalize the Hamiltonian (expressed in Eq. 7.7) to obtain the band energy and then plot the variations of the bands by tuning λ_{eph} for different cases of α. As shown in Fig. 7.5 for $\alpha = 0.2$ (a representative for the lower regime case), $\alpha = 0.52$ (a representative for $\alpha \in [0.51 : 0.54]$), and $\alpha = 0.7$ (a representative for the higher regime

case) marked by solid blue, solid green, and solid black, respectively the band gap (between VB and dFB), namely ΔE, and hence the touching of the bands (ΔE being zero) are observed very carefully imposing high precision conditions (within an accuracy of 10^{-6} or lower (in limit of t)) in the numerical algorithm by which we have computed these critical points, namely λ_c, λ_{c_1}, and λ_{c_2}. Similarly, the transition point(s) for any value of α in range $[0 : 1]$ can be obtained which are listed in Table 7.1. The explicit dependence of ΔE on λ_{eph} ascertains that for the lower values of α the system hosts two distinct insulating phases (exhibiting a finite gap, ΔE) for $0 \leq \lambda_{eph} < \lambda_c$ and $\lambda_{eph} > \lambda_c$, whereas for the higher values of α there exist three distinct insulating regions for $0 \leq \lambda_{eph} < \lambda_{c_1}$, $\lambda_{c_1} < \lambda_{eph} < \lambda_{c_2}$, and $\lambda_{eph} > \lambda_{c_2}$ accompanied by an SM phase ($\Delta E = 0$) for $\alpha \in [0.51 : 0.54]$ in the $0 \leq \lambda_{eph} < \lambda_{c_1}$ regime. As our system is modeled by the Kane-Mele Hamiltonian, one of the gapped phases may carry the signature of a QSH insulating phase.

To ascertain whether a certain gapped phase corresponds to a topological one, we calculate the topological invariant, namely the $\mathbb{Z}_2$ invariant, in the subsequent section. Therefore, a TPT is possible for an α-T_3 QSH lattice solely induced by the e-ph coupling, which is one of the pivotal points of this chapter. We must specify that similar findings hold true for the other values of α in the $0 < \alpha \leq 0.5$ range (however, not shown here). The scenarios become

$\boldsymbol{\alpha}$	$\boldsymbol{\lambda_c}$	$\boldsymbol{g_c}$	$\boldsymbol{\lambda_{c_1}}$	$\boldsymbol{\lambda_{c_2}}$	$\boldsymbol{g_{c_1}}$	$\boldsymbol{g_{c_2}}$
0.1	1.97	0.81	-	-	-	-
0.2	1.95	0.81	-	-	-	-
0.3	1.92	0.80	-	-	-	-
0.4	1.90	0.79	-	-	-	-
0.5	1.90	0.79	-	-	-	-
0.52	-	-	1.00	1.88	0.57	0.79
0.6	-	-	1.28	1.85	0.65	0.78
0.7	-	-	1.46	1.82	0.69	0.78
0.8	-	-	1.60	1.78	0.73	0.77
0.9	-	-	1.67	1.73	0.75	0.76

Table 7.1: Table of transition points, namely λ_c, corresponding to the bare e-ph coupling strengths at the transitions, namely g_c, related as $\lambda_c = \frac{g_c^2 \omega_0}{t}$, for different α cases. While g_c is always less than 1, λ_c acquires values greater than 1 due to scaling by ω_0/t.

contrasting for intermediate to higher values of α ($0.5 < \alpha < 1.0$) which are shown in Figs. 7.3 and 7.4. While deriving the band spectra for the intermediate α values, we come across a very interesting observation in the $0.51 \leq \alpha \leq 0.54$ regime where the bulk band gap is zero even

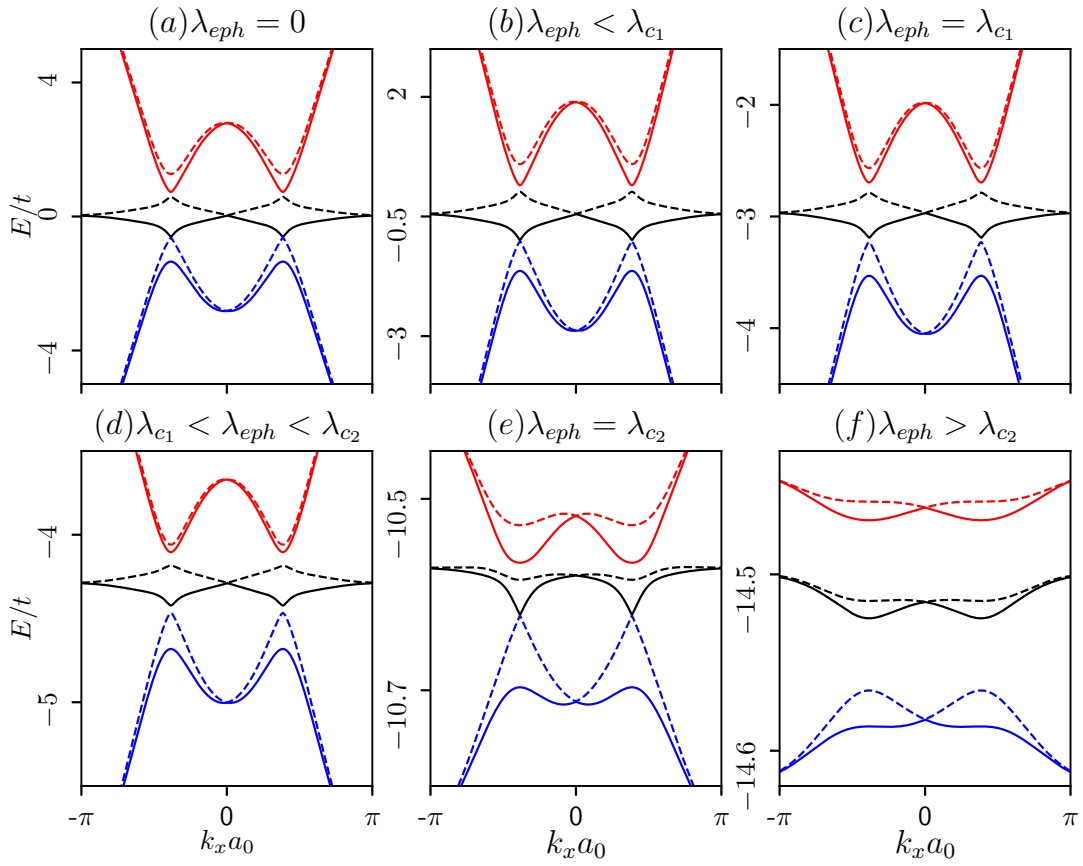

Figure 7.3: The bulk band structures with energy E (in units of t) are shown as a function of dimensionless momenta, k_x (multiplied by a_0) at $k_y = 2\pi/3a_0$ for $\alpha = 0.52$. The red, black, and blue colours represent the CB, the dFB and the VBs, respectively. In (a) and (b) the dispersion is plotted in the $0 \leq \lambda_{eph} < \lambda_c$ regime at $\lambda_{eph} = 0$ and $\lambda_{eph} = 0.5$, respectively, where the bulk gap is zero. (c) The plot is shown at the critical $\lambda_{eph} = \lambda_{c_1} = 1.00$ where the bulk gap between the dFB and the VB is seen. (d) The same is shown in the $\lambda_{c_1} < \lambda_{eph} < \lambda_{c_2}$ regime at $\lambda_{eph} = 1.2$ where the spectrum is sufficiently gapped. (e) The bulk closing transition occurs at $\lambda_{eph} = \lambda_{c_1} = 1.88$. (f) Again the spectrum becomes gapped in the $\lambda_{eph} > \lambda_{c_2}$ regime at $\lambda_{eph} = 2.2$. The parameters are kept the same as those in Fig. 7.2.

when $\lambda_{eph} = 0$, which corresponds to an SM phase of the α-T_3 lattice. Earlier studies suggest that a TPT in the vicinity of $\alpha = 0.5$ [186] exists in the absence of any interaction, supported by a gap closing transition in the bulk spectra of the α-T_3 lattice. We present the variations for $\alpha = 0.52$ as a sample case in this regime of α in Fig. 7.3(a). Here, the dFB becomes more distorted (as it should be) for larger values of α. The SM phase for $\alpha = 0.52$ remains unchanged for $\lambda_{eph} < \lambda_{c_1}$ (Fig. 7.3(b)) up to $\lambda_{eph} = \lambda_{c_1} = 1$, where we observe a very small gap (may be zoomed in for better visualization) for the first time between the dFB and the VB, shown in Fig. 7.3(c). Consequently, in the $\lambda_{c_1} < \lambda_{eph} < \lambda_{c_2}$ regime (Fig. 7.3(d)), a noticeable gap appears in the bulk spectrum which closes again at $\lambda_{eph} = \lambda_{c_2} = 1.88$ (Fig. 7.3(e)), beyond which the dFB and the VB are again gapped referring it to an insulating state (Fig. 7.3(f)). The gapless/gapped conditions can also be observed in Fig. 7.5. Similar observations are true for

any value of α in the range $[0.51 : 0.54]$ where the system undergoes an SM-insulator-insulator transition as the e-ph coupling is enhanced. As pointed out earlier, we shall investigate the topological characterizations of these phases later by computing the $\mathbb{Z}_2$ invariant.

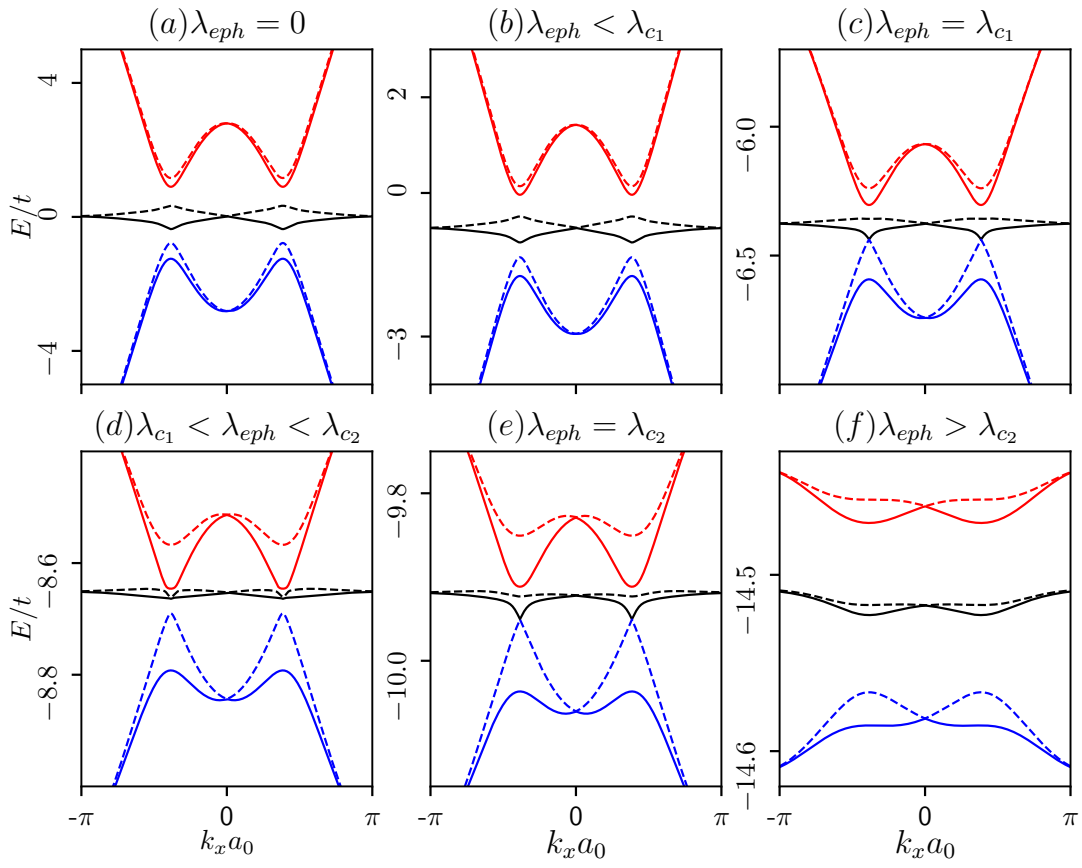

Figure 7.4: The bulk band structures with energy E (in units of t) are shown as a function of dimensionless momenta, k_x (multiplied by a_0) at $k_y = 2\pi/3a_0$ for $\alpha = 0.7$. The red, black, and blue colours represent the CB, the dFB and the VBs, respectively. In (a) and (b) the dispersion is plotted in the $0 \leq \lambda_{eph} < \lambda_c$ regime at $\lambda_{eph} = 0$ and $\lambda_{eph} = 0.5$, respectively, where the bulk is gapped. (c) The plot is shown at the critical $\lambda_{eph} = \lambda_{c_1} = 1.46$ where the bulk gap between the dFB and the VB is closed. (d) The same is shown in the $\lambda_{c_1} < \lambda_{eph} < \lambda_{c_2}$ regime at $\lambda_{eph} = 1.70$ where the spectrum is sufficiently gapped. (e) Again bulk closing transition occurs at $\lambda_{eph} = \lambda_{c_1} = 1.82$. (f) The spectrum becomes gapped in the $\lambda_{eph} > \lambda_{c_2}$ regime at $\lambda_{eph} = 2.2$. The parameters are kept the same as those in Fig. 7.2.

However, for higher range of α $(0.6 \leq \alpha < 1.0)$, the existence of the SM phase for the $\lambda_{eph} < \lambda_{c_1}$ regime is not certain. To clarify that, we present the results for $\alpha = 0.7$ as a sample case of the higher α regime. Interestingly, for $\alpha = 0.7$, a band gap is again seen between the dFB and the VB (Fig. 7.4(a)) for $\lambda_{eph} = 0$ as well as in the $\lambda_{eph} < \lambda_{c_1}$ region (Fig. 7.4(b)) till λ_{eph} becomes $\lambda_{c_1} = 1.46$ (Fig. 7.4(c)). Beyond this value the system enters into another gapped phase in the $\lambda_{c_1} < \lambda_{eph} < \lambda_{c_2}$ (Fig. 7.4(d)) and finally remains gapped in the $\lambda_{eph} > \lambda_{c_2}$ regime (Fig. 7.4(f)) accompanied by a gap closing transition at $\lambda_{eph} = \lambda_{c_2} = 1.82$ (Fig. 7.4(e)). As mentioned earlier, the variation of the gap with λ_{eph} can be seen in Fig. 7.5.

The findings of $\alpha = 0.7$ are also valid for any value of α in range $0.6 \leq \alpha < 1.0$, albeit with different λ_{c_1} and λ_{c_2}. It is to be noted that as we sufficiently increase α, the difference between λ_{c_1} and λ_{c_2} reduces, merging into a single transition point, as observed for the lower α ($0 < \alpha \leq 0.5$) regime, especially for $0.9 < \alpha < 1.0$ (close to the dice lattice). Hence, for $0.6 \leq \alpha < 1.0$, the system facilitates a re-entrant mechanism to multiple insulating phases accompanied by two gap closing transitions mediated through e-ph coupling, while the lower ($0 < \alpha \leq 0.5$) α values show an insulator-insulator transition. The bulk gap closing phenomena can be explained by the two main artefacts of our study: one is the polaronic effects which results in the narrowing of bands (Eq. (7.6)), and the other can be seen from the matrix elements of ρ-block (Eqs. (7.8)) which demonstrates the interplay between the three quantities, namely the parameter α (that accounts for the behaviour of the dFB), the Semenoff mass $\mathcal{M}$ (that acts as a staggered sublattice potential) and the e-ph coupling parameter λ_{eph}. Furthermore, these factors affect the dFB and the VB and thereby manipulate the gap between them, predominantly for higher values of α, which gives rise to a more complex nature of transition in this regime of α (namely, $0.5 < \alpha < 1.0$). Thus, we may encompass various (topologically different) kinds of nontrivial phases and the relative phase transitions induced by the e-ph coupling for all values of α in range $[0 : 1]$, albeit with different transition points (the values of λ_cs listed for each α value in Table 7.1). The data contained therein can be broadly divided into two categories: (i) lower α cases with one gap closing point, namely λ_c and (ii) intermediate to higher α cases accompanied by two transition points, namely λ_{c_1} and λ_{c_2}. Some of the spectral properties are similar to the ones obtained in the context of a Haldane-Holstein model.

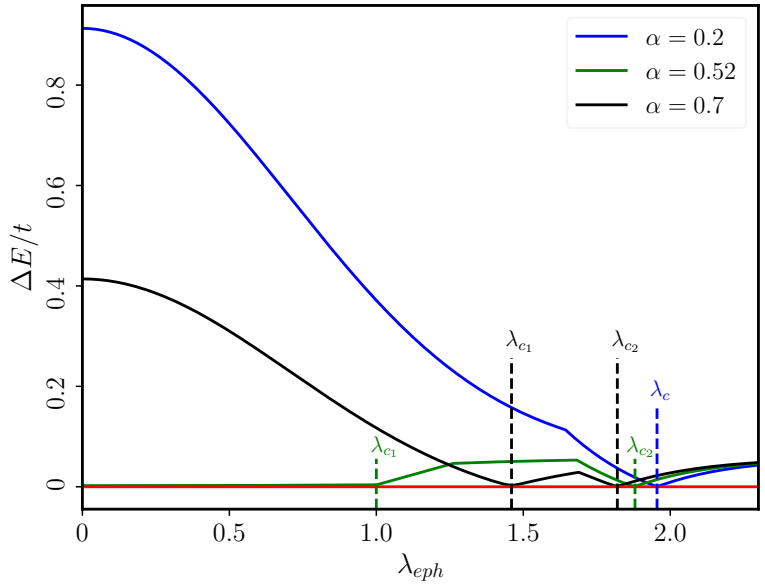

Figure 7.5: The band gap, ΔE (in the units of t) as a function of the e-ph coupling, λ_{eph} for $\alpha = 0.2$, $\alpha = 0.52$ and $\alpha = 0.7$ is shown. The parameters are kept the same as those in Fig. 7.2.

The plausible topological invariant to characterize a QSH phase (exhibiting a topological gap in the bulk spectrum) is the $\mathbb{Z}_2$ invariant [244, 245, 248, 259, 382–384] (especially, when spins are mixed), which we discuss below. Hence, to confirm the existence of a spin-mixed QSH phase in our system, we consider the evolution of the Wannier charge center (WCC) that determines the $\mathbb{Z}_2$ invariant.

7.4 $\mathbb{Z}_2$ Invariant: Evolution of the Wannier Charge Center

In this section, we study how the evolution of the Wannier charge center (WCC) (which is known as the center of charge in a unit cell) in different regimes of λ_{eph} that indicate topologically trivial or non-trivial characteristics for different values of α. As discussed earlier, the notion of the Chern number fails (being odd under TR) for a TR invariant (TRI) QSH insulator, and the topological properties are guaranteed both by the evolution of WCCs and the surface/edge energy spectra. The relevant discussions on mathematical construction of the WCC are presented in Chapter 1 Sec. 1.8.5. Since our 2D model lies in the x-y plane, we can define a general k-vector in the momentum space as $\mathbf{k} = k_{\hat{b}_1}\hat{b}_1 + k_{\hat{b}_2}\hat{b}_2$ and characterize the $\mathbb{Z}_2$ invariant by employing the hybrid Wannier transformation [244, 245, 384] along $\hat{b}_1$ and studying its evolution as a function of the remaining momentum, that is $k_{\hat{b}_2}$, where $\mathbf{b_1}$ and $\mathbf{b_2}$ are the reciprocal lattice vectors and are given as $\mathbf{b_1} = (-\frac{2\pi}{\sqrt{3}a_0}, \frac{2\pi}{3a_0})$ and $\mathbf{b_2} = (\frac{2\pi}{\sqrt{3}a_0}, \frac{2\pi}{3a_0})$. The hybrid WCC (HWCC) in the direction a_1 can be mathematically represented in terms of the Berry phase $\phi_n(k_{\hat{b}_2})$ as [244, 245, 384],

$$\langle r_{n,\hat{a}_1}(k_{\hat{b}_2})\rangle = \frac{\phi_n(k_{\hat{b}_2})}{2\pi} = \frac{1}{2\pi}\oint A_n^{\hat{b}_1}(k_{\hat{b}_1}, k_{\hat{b}_2})dk_{\hat{b}_1}, \tag{7.11}$$

with $A_n^{\hat{b}_1}(k_{\hat{b}_1}, k_{\hat{b}_2}) = -i\langle u_{n\mathbf{k}}|\frac{\partial}{\partial k_{\hat{b}_1}}|u_{n\mathbf{k}}\rangle$ being the Berry connection. The above definition is valid only when the bulk spectra exhibit a finite gap as the Berry connection is ill-defined for a gapless situation. The interpretation of the $\mathbb{Z}_2$ invariant in terms of the HWCC goes as follows. It is defined as the number of individual HWCC crossed by an arbitrary line traversing half the BZ, modulo 2 [384]. If the line intersects an even (odd) number of HWCCs while traversing through half the BZ, the $\mathbb{Z}_2$ invariant is zero (non-zero), assuring a topologically trivial (nontrivial) phase [384]. For a TRS-preserved system, the WCCs obey all the symmetries that are found in the energy bands. Particularly, the existence of the Kramers doublets at the two TRI momenta in the BZ also leads to a double degeneracy in the WCCs. Here, we consider only the first half of the BZ ($[0, \pi/a]$) as the TRS imposes the behaviour of the WCCs and the surface energy bands to be identical to those in the other half of the BZ. To envisage the existence of nontrivial phases

followed by a TPT, we thoroughly investigate the evolution of the HWCCs represented in Eq. (7.11) for different regimes of λ_{eph} vis-à-vis the bulk spectra presented in Sec. 7.3.

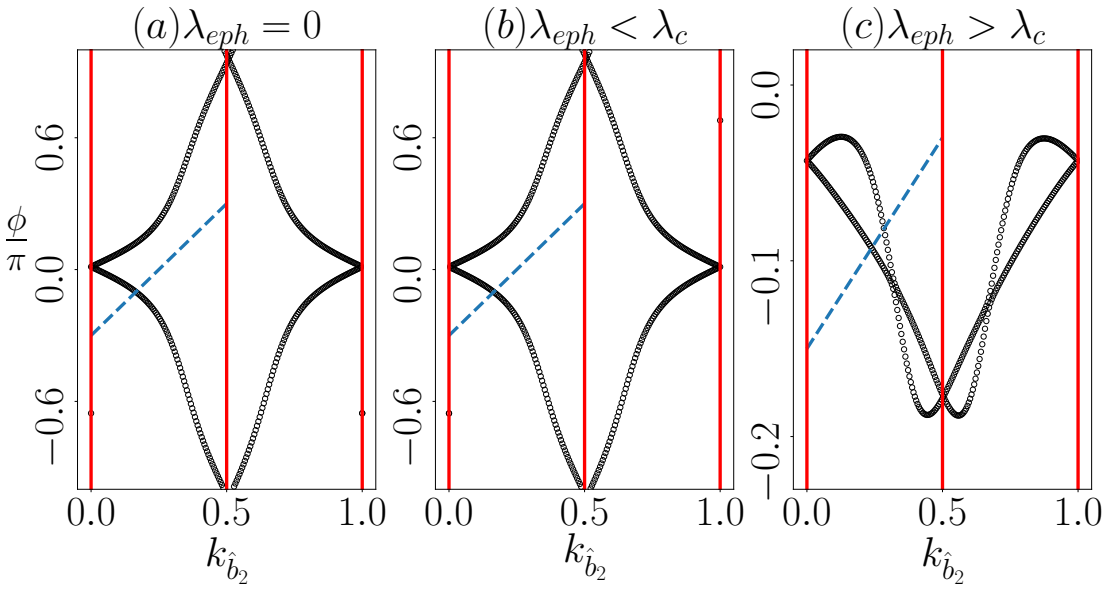

Figure 7.6: The evolution of the HWCCs in terms of the Berry phase ϕ (scaled by π) is shown as a function of dimensionless momenta, $k_{\hat{b}_2}$ for $\alpha = 0.2$ in different regimes of λ, namely (a) $\lambda_{eph} = 0$ and (b) $\lambda_{eph} < \lambda_c$ ($\lambda_{eph} = 0.5$) where the arbitrary line (dashed blue) cuts through odd number of HWCCs referring to a $\mathbb{Z}_2$-odd topological insulator, while (c) describes the $\lambda_{eph} > \lambda_c$ regime ($\lambda_{eph} = 2.2$) where the line crosses even number of HWCCs denoting a $\mathbb{Z}_2$-even trivial insulator. The parameters are kept the same as those in Fig. 7.2. The values of λ_c are mentioned in Table 7.1.

We present the evolution of the HWCCs for three values of α, one in the lower regime ($\alpha = 0.2$), one corresponding to the special case at $\alpha = 0.52$, and the other in the higher regime ($\alpha = 0.7$) of α. Consider a 2D $\mathbb{Z}_2$-insulator in the x-y plane whose evolution of the HWCCs as a function of the momentum, $k_{\hat{b}_2}$ is displayed in Fig. 7.6, Fig. 7.7, and Fig. 7.8 for $\alpha = 0.2$, $\alpha = 0.52$, and $\alpha = 0.7$, respectively. In Fig. 7.6, we plot the variations of $\mathbb{Z}_2$ for $\alpha = 0.2$ in the regimes $0 \leq \lambda_{eph} < \lambda_c$ and $\lambda_{eph} > \lambda_c$ where the bulk shown in Figs. 7.2 (a), (b) and (d) possesses a finite gap between VB and dFB. It is clearly visible from Figs. 7.6(a) and (b) that for $\alpha = 0.2$, the arbitrary (dashed blue) line in the half-BZ cuts through odd (one) number of HWCCs in the $0 \leq \lambda_{eph} < \lambda_c$ regime, which makes the $\mathbb{Z}_2$ invariant non-zero. For a TRS-preserved system, the non-zero $\mathbb{Z}_2$ invariant demonstrates that an HWCC switches its TRI partner as $k_{\hat{b}_2}$ evolves from 0 to π/a, and consequently the TR polarization changes sign. Alternatively, it describes that one HWCC jumps from one unit cell to the other (often referred to as *TR polarization pumping*), signifying a finite conduction on the surface or the edges, which is a typical signature of a $\mathbb{Z}_2$-odd topological (QSH) insulator. However, for $\lambda_{eph} > \lambda_c$ (Fig. 7.6(c)), the line crosses even (two) number of HWCCs implying no conduction along the edges, which proclaims a trivial ($\mathbb{Z}_2$-even) insulator. These findings are a direct consequence of the bulk band spectra found in

(Fig. 7.2). Although we only show the results for $\alpha = 0.2$, the above observations hold for any value in range $0 < \alpha \leq 0.5$. Therefore, it is confirmed that in the lower regime of α, the system undergoes a topological-trivial transition induced by the e-ph coupling. It is worth mentioning that studying the variations of the $\mathbb{Z}_2$ invariant as a function of λ_{eph} for $\alpha = 0.52$ needs special attention as the bulk spectrum is gapless in the $\lambda_{eph} < \lambda_{c_1}$ regime even at $\lambda_{eph} = 0$ (unlike the other values of α not in the range $[0.51 : 0.54]$ where it is gapped). Therefore, for $\alpha = 0.52$, the $\mathbb{Z}_2$ invariant is ill-defined for $\lambda_{eph} < \lambda_{c_1}$ (including at $\lambda_{eph} = 0$) which allows us to compute the $\mathbb{Z}_2$ invariant only for $\lambda_{c_1} < \lambda_{eph} < \lambda_{c_2}$ and $\lambda_{eph} > \lambda_{c_2}$ where the bulk is gapped (Figs. 7.3(d) and (f)) denoting the two insulating regions. Fig. 7.7(a) reveals that the arbitrary line passes though odd (one) number of HWCCs in the $\lambda_{c_1} < \lambda_{eph} < \lambda_{c_2}$ regime which demonstrates a topologically nontrivial insulating phase, while we notice an even (two) number of crossings in the HWCCs in the $\lambda_{eph} > \lambda_{c_2}$ regime (Fig. 7.7(b)) which confirms the insulating phase in this regime of λ_{eph} to be a trivial one.

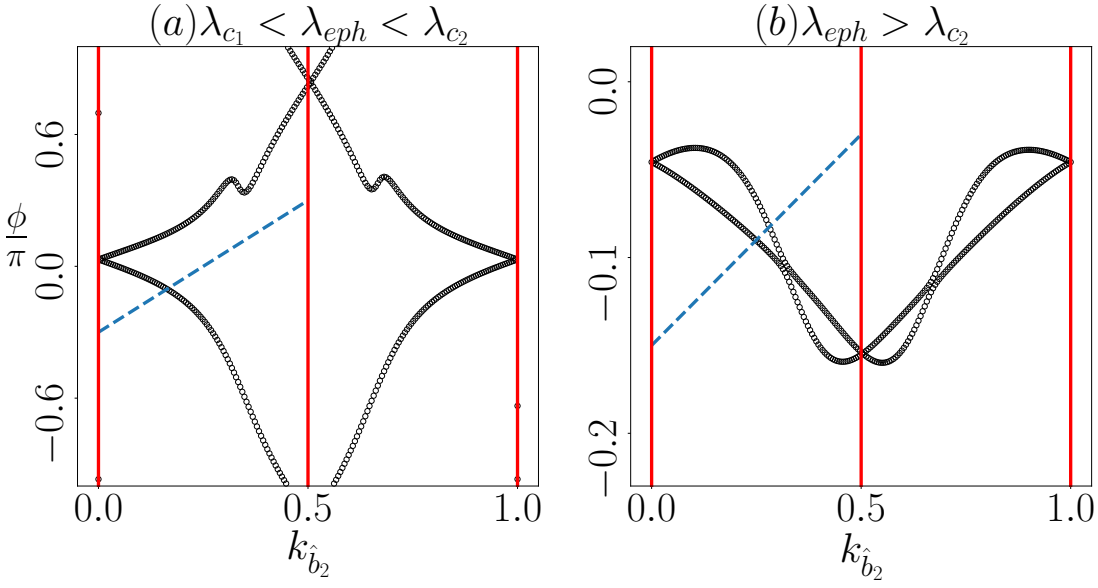

Figure 7.7: The evolution of the HWCCs (in terms of the Berry phase ϕ) is shown as a function of dimensionless momenta, $k_{\hat{b}_2}$ for $\alpha = 0.52$ in different regimes of λ_{eph}, namely (a) $\lambda_{c_1} < \lambda_{eph} < \lambda_{c_2}$ ($\lambda_{eph} = 1.2$) where the arbitrary line (dashed blue) cuts through odd number of HWCCs referring to a $\mathbb{Z}_2$-odd topological insulator, and (b) $\lambda_{eph} > \lambda_{c_2}$ ($\lambda_{eph} = 2.2$) where the same crosses even number of HWCCs denoting a $\mathbb{Z}_2$-even trivial insulator. The parameters are kept the same as those in Fig. 7.3. The values of λ_{c_1} and λ_{c_2} are mentioned in Table 7.1.

As suggested by the variations of the bulk spectra, the scenario becomes more interesting in the higher regime ($0.6 \leq \alpha < 1.0$) of α where the system accompanies two bulk gap closing transitions at λ_{c_1} and λ_{c_2} (for λ_c values see Table 7.1), associated with three gapped phases for $0 \leq \lambda_{eph} < \lambda_{c_1}$, $\lambda_{c_1} < \lambda_{eph} < \lambda_{c_2}$, and $\lambda_{eph} > \lambda_{c_2}$ (see Fig. 7.5). We evaluate the results for $\alpha = 0.7$ as a representative case for the $0.6 \leq \alpha < 1.0$ regime whose bulk spectra are discussed in Fig. 7.4. Fig. 7.8(a) is plotted for $\alpha = 0.7$ in the regime $0 \leq \lambda_{eph} < \lambda_{c_1}$ (where

the bulk spectra are widely gapped and are represented in Figs. 7.4(a) and (b)). They display an even (two) number of crossings in the HWCCs refereeing to a non-topological phase, while the gapped phase (see the bulk spectrum in Fig. 7.4(d)) in the $\lambda_{c_1} < \lambda_{eph} < \lambda_{c_2}$ regime denotes a topological one (accompanied by finite conduction along the edges) as the line intersects through only one HWCC, shown in Fig. 7.8(b). Hence, for higher α ($0.6 \leq \alpha < 1.0$) cases, nontrivial topological phases emerge in the $\lambda_{c_1} < \lambda_{eph} < \lambda_{c_2}$ regime solely by the e-ph coupling as we moderately tune λ_{eph} beyond $\lambda_{eph} = \lambda_{c_1}$ (till $\lambda_{eph} = \lambda_{c_2}$), which are otherwise absent in range $0 \leq \lambda_{eph} < \lambda_{c_1}$. As expected, the regime $\lambda_{eph} > \lambda_{c_2}$ describes a trivial phase (Fig. 7.8(c)) for the higher α cases. All the other α cases in range $0.6 \leq \alpha < 1.0$ show similar results as that for $\alpha = 0.7$, albeit with different λ_{c_1} and λ_{c_2} (not shown here). Thus, the evolution of the HWCCs ascertains that the system for higher values of α ($0.6 \leq \alpha < 1.0$) facilitates trivial-topological-trivial TPT upon suitably varying the strength of the e-ph interaction, λ_{eph}.

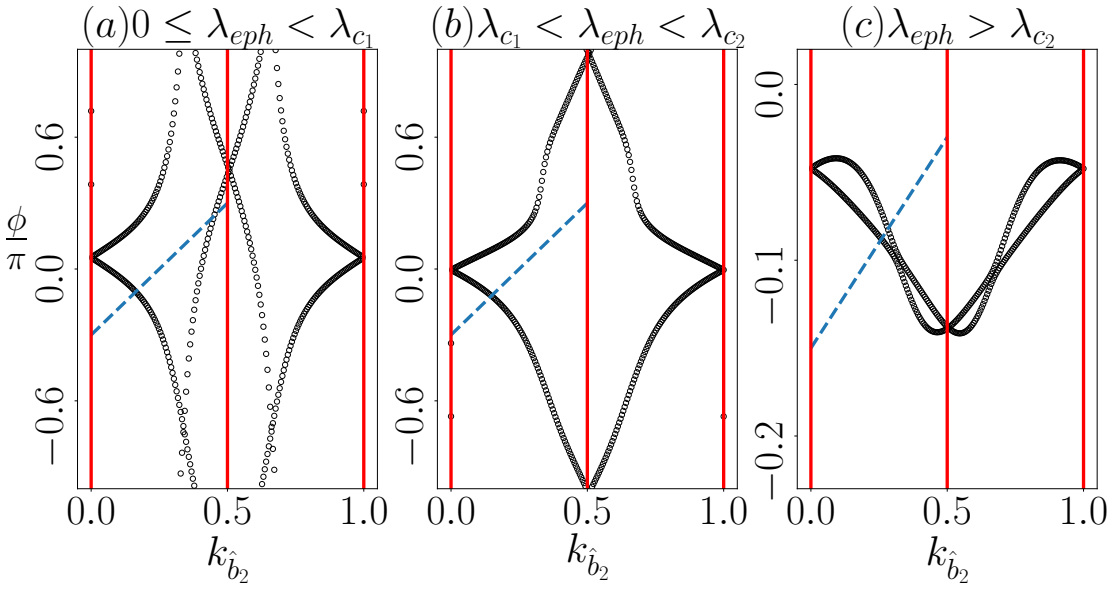

Figure 7.8: The evolution of the HWCCs (in terms of the Berry phase ϕ) is shown as a function of dimensionless momenta, $k_{\hat{b}_2}$ for $\alpha = 0.7$ in different regimes of λ_{eph}, namely (a) $0 \leq \lambda_{eph} < \lambda_{c_1}$ ($\lambda_{eph} = 0$) where the arbitrary line (dashed blue) cuts through even number of HWCCs denoting a $\mathbb{Z}_2$-even trivial insulator, (b) $\lambda_{c_1} < \lambda_{eph} < \lambda_{c_2}$ ($\lambda = 1.65$) where it crosses odd number of HWCCs signifying a $\mathbb{Z}_2$-odd topological insulator, and (c) $\lambda_{eph} > \lambda_{c_2}$ ($\lambda_{eph} = 2.2$) where the same intersects even number of HWCCs referring a trivial insulator. The parameters are kept the same as those in Fig. 7.4. The values of λ_{c_1} and λ_{c_2} are mentioned in Table 7.1.

In order to support the evidence of a TPT mediated through polaronic interactions, we also study the variations of the edge spectra of an α-T_3 semi-infinite zigzag ribbon, which we discuss next. We expect the $\mathbb{Z}_2$-odd topological phases (accompanied by an odd number of HWCCs crossings) to exhibit a pair of helical QSH edge modes per edge of the 2D α-T_3 lattice, with them vanishing for the topologically trivial phases.

7.5 Edge State Properties

This section is devoted to studying the effect of e-ph coupling on the edge state characteristics of a semi-infinite α-T_3 ribbon with zigzag edges [194]. In our case, the nanoribbon is infinite (protecting translational symmetry) along the x-direction, while finite along the y-direction (breaking the translational symmetry). We have constructed zigzag edges with the termination consisting of A-B sublattices. It is useful to mention that the topology in our system being robust topological non-triviality persists regardless of the kind of termination used for the construction of the ribbon. Thus, similar scenario should persist for an armchair ribbon as well. Here, we investigate the appearance (vanishing) of the edge states in different regimes of λ_{eph} for the same three α cases as earlier, whose bulk spectra and $\mathbb{Z}_2$ invariant are inspected in Sec. 7.3 and Sec. 7.4, respectively. The distinction between a topological and non-topological phase relies on the crossings of the edge modes between CB and VB through the dFB. We look for a direct correspondence between the evolution of HWCCs ($\mathbb{Z}_2$ invariant) and the edge states. Conventionally, if an arbitrary line intersects the HWCCs an odd number of times in the half-BZ, the Fermi level also crosses an odd number of edge states per edge during this half-BZ evolution.

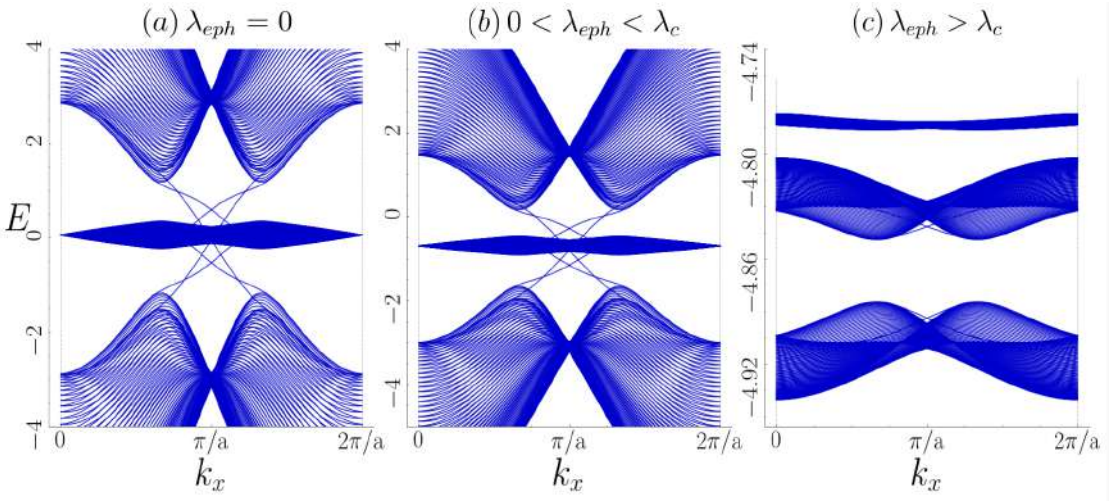

Figure 7.9: Edge state spectra (in units of t) of a zigzag semi-infinite ribbon for $\alpha = 0.2$ are shown as a function of dimensionless momenta, k_x for (a) $\lambda_{eph} = 0$, (b) $\lambda_{eph} = 0.5$ $(0 < \lambda_{eph} < \lambda_c)$, and (c) $\lambda_{eph} = 2.2$ $(\lambda_{eph} > \lambda_c)$. We consider a as $a = \sqrt{3}a_0$ throughout. Other parameters are the same as those in Fig. 7.2. The values of λ_c are mentioned in Table 7.1.

We begin by referring to Fig. 7.9(a), where we vividly notice the emergence of two pairs of the edge states traversing from the VB to CB through the dFB at $\lambda_{eph} = 0$ for $\alpha = 0.2$. These are helical QSH edge states of a $\mathbb{Z}_2$ topological insulator protected by TRS, which counterpropagate for two different Kramer's subbands with a velocity, $v = \partial E/\partial k$ (slope of the bands and $\hbar$ is

set to unity). However, we cannot distinctly designate them as the $\uparrow$-spin or the $\downarrow$-spin bands as the spins are mixed by the presence of the RSOC. These helical modes continue to persist in the $0 < \lambda_{eph} < \lambda_c$ regime, displayed in Fig. 7.9(b). Therefore, for $0 \leq \lambda_{eph} < \lambda_c$, an energy lying between the dFB and the VB (the 'so called' Fermi level) intersects the edge states odd (one) number of times per edge for a particular spin component (giving rise to two in total) and in an argument with an odd crossing in HWCCs (non-zero $\mathbb{Z}_2$ invariant) during the half-BZ evolution. We can reconcile this by the concept of *TR polarization pumping* [259]. *TR polarization pumping* is defined as follows. As one unit of spin corresponding to one subband of the Kramer's pair is pumped relative to that of the other subband along the edge while HWCCs evolve through half-BZ, giving rise to a finite conduction along the two edges. The existence of these helical edge modes in the $0 \leq \lambda_{eph} < \lambda_c$ regime directly corresponds to the gapped (topologically nontrivial) phase in the bulk (Figs. 7.2(a) and (b)) for which the $\mathbb{Z}_2$ invariant is found to be (odd) non-zero (Fig. 7.6(a) and (b)) clarifying the system to be a $\mathbb{Z}_2$ topological insulator. As anticipated earlier, both by the bulk diagrams and the $\mathbb{Z}_2$ invariants, beyond $\lambda_{eph} = \lambda_c$, these edge states disappear (Fig. 7.9(c)) completely (even cut in the HWCCs in Fig. 7.6(c)), inferring the system to be a trivial insulator. It is evident by the bulk spectra (Fig. 7.3(b)) that there is

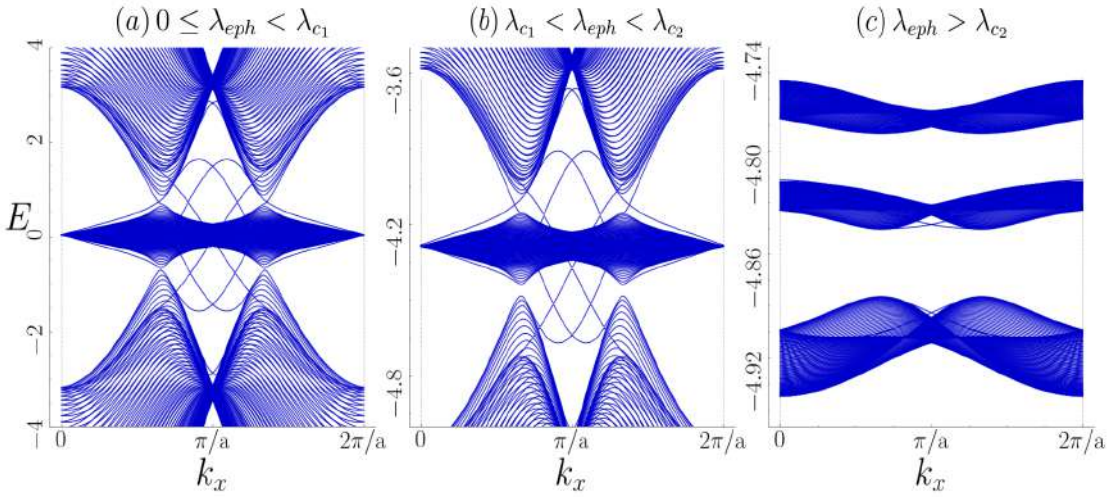

Figure 7.10: Edge state spectra (in units of t) of a zigzag semi-infinite ribbon for $\alpha = 0.52$ are shown as a function of dimensionless momenta, k_x for (a) $\lambda_{eph} = 0$ $(0 \leq \lambda_{eph} < \lambda_{c_1})$, (b) $\lambda_{eph} = 1.2$ $(\lambda_{c_1} < \lambda_{eph} < \lambda_{c_2})$, and (c) $\lambda_{eph} = 2.2$ $(\lambda_{eph} > \lambda_{c_2})$. Other parameters are the same as those in Fig. 7.3. The values of λ_{c_1} and λ_{c_2} are mentioned in Table 7.1.

an SM point at $\alpha = 0.52$ for the $0 \leq \lambda_{eph} < \lambda_{c_1}$ (including $\lambda_{eph} = 0$ shown in Fig. 7.3(a)) regime which also reflects in the edge spectrum, presented in Fig. 7.10(a). The concept of edge states is, therefore, not so important for this regime of λ_{eph} as the bulk bands are gapless. However, as we tune λ_{eph} further, the two pairs of the helical edge states emerge which traverse from the dFB to the VB (Fig. 7.10(b)) and thus yield the signature of a topological QSH insulator (also seen through an odd number of cut in HWCCs shown in Fig. 7.6(a)). Nevertheless,

the vanishing of edge states in the $\lambda_{eph} > \lambda_{c_2}$ (Fig. 7.10(c)) confirms this phase to be a trivial insulator. For a specific case of higher α value, say $\alpha = 0.7$, it is shown in Fig. 7.11(a) that although edge states exist in the $0 \leq \lambda_{eph} < \lambda_{c_1}$ regime (where the bulk is gapped represented in Fig. 7.4(a) and (b)), however, a total of four pairs appear, which essentially implies two pairs of 'copropagating' edge modes along a particular edge. Each of the two pairs may be denoted by the two spin orientations (they are infact superposition of $\uparrow$ and $\downarrow$ states), giving rise to a possibility of backscattering between the same spin states, which destroys the robustness of a topological phase. Consequently, the 'Fermi level' crosses them eight times which manifests a non-topological phase with zero conduction along edges (also confirmed by an even cut in the HWCCs (Fig. 7.8(a))). Interestingly, the gapped spectrum in the $\lambda_{c_1} < \lambda_{eph} < \lambda_{c_2}$ regime comprises of two pairs of helical edge states (Fig. 7.11(b)) which carries a trait of a $\mathbb{Z}_2$ QSH insulator characterized by an odd number of crossing in the HWCCs (Fig. 7.8(b)). As these edge states are susceptible to the e-ph coupling, we further enhance λ_{eph} and find that they entirely vanish (agreeing with an even cut in the HWCCs (Fig. 7.8(b))) for $\lambda_{eph} > \lambda_{c_2}$ (Fig. 7.11(c)) where the system behaves as a trivial insulator. We want to assert that the results for lower ($0 < \alpha \leq 0.5$) and higher ($0.6 \leq \alpha < 1.0$) values of α are identical to those for $\alpha = 0.2$ and $\alpha = 0.7$, respectively. We do not show all of them here for brevity. Hence, the evolution of the HWCCs giving rise to a $\mathbb{Z}_2$-odd (even) invariant consistent with the emergence (vanishing) of the edge states corroborates that a pseudospin-1 fermionic system, such as, an α-T_3 lattice goes through a topological-trivial and a trivial-topological-trivial phase transition for the $0 < \alpha \leq 0.5$ and $0.6 \leq \alpha < 1.0$ regimes, respectively, with an intervening SM-topological-trivial transition occurring at $\alpha = 0.52$.

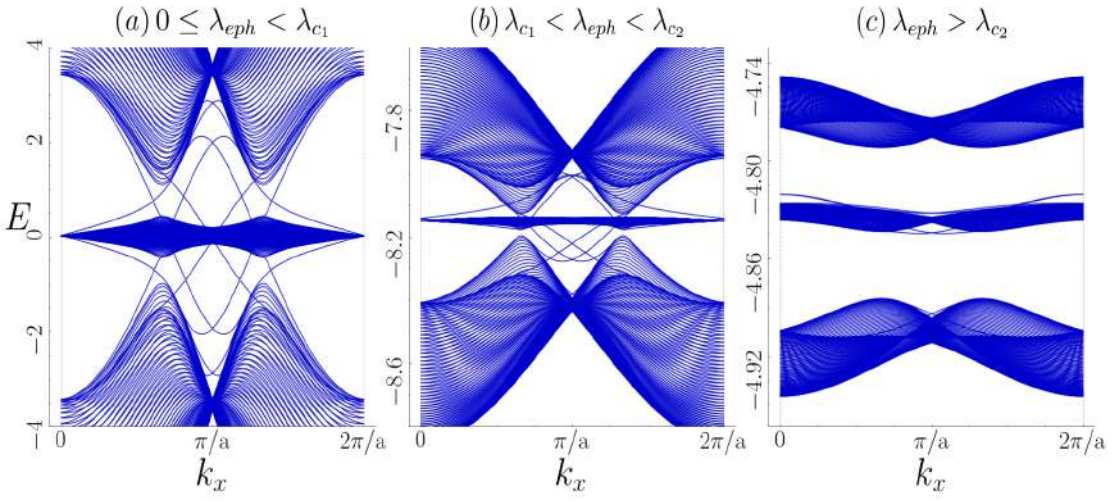

Figure 7.11: Edge state spectra (in units of t) of a zigzag semi-infinite ribbon for $\alpha = 0.7$ are shown as a function of dimensionless momenta, k_x for (a) $\lambda_{eph} = 0$ ($0 \leq \lambda_{eph} < \lambda_{c_1}$), (b) $\lambda_{eph} = 1.65$ ($\lambda_{c_1} < \lambda_{eph} < \lambda_{c_2}$), and (c) $\lambda_{eph} = 2.2$ ($\lambda_{eph} > \lambda_{c_2}$). Other parameters are the same as those in Fig. 7.4. The values of λ_{c_1} and λ_{c_2} are mentioned in Table 7.1.

7.6 Spin Hall Conductivity

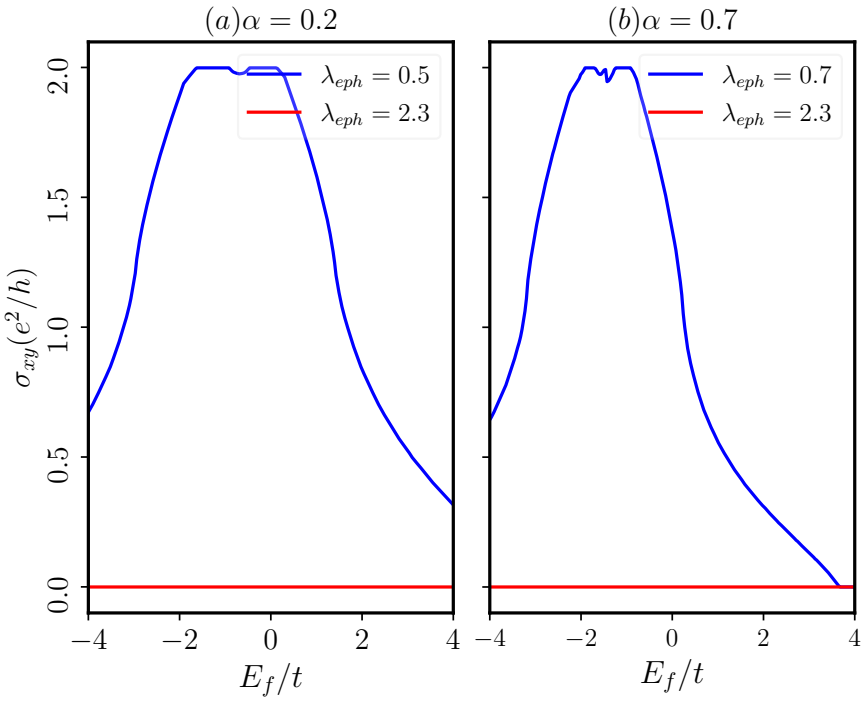

Figure 7.12: The spin-Hall conductivity, σ_{xy} (in the units of e^2/h) as a function of the Fermi energy, E_f (in the units of t). (a) For $\alpha = 0.2$, the results are presented for $\lambda_{eph} = 0.5$ ($0 \leq \lambda_{eph} < \lambda_c$ regime) and $\lambda_{eph} = 2.3$ ($\lambda_{eph} > \lambda_c$ regime). (b) For $\alpha = 0.7$, the results are shown for $\lambda_{eph} = 0.7$ (in the $0 \leq \lambda_{eph} < \lambda_c$ regime) and $\lambda_{eph} = 2.3$ (in the$\lambda_{eph} > \lambda_c$ regime). In both cases, λ_R has been set to zero.

It is now important to discuss the prospects of investigating the transport properties of our system. Although various proposals exist on investigating the transport properties of an α-T_3 lattice [163, 164, 173, 182, 360, 378, 389–392], one may study the anomalous spin Hall conductivity to detect the topological phases for a spin-orbit coupled α-T_3 lattice. To detect the topologically trivial/nontrivial phases, we present observations on anomalous spin Hall conductivity for $\alpha = 0.2$ and $\alpha = 0.7$ in Fig. 7.12. The other parameters are fixed as $\lambda = 0.1t$, $\mathcal{M} = 0.02t$. The spin Hall conductivity, σ_{xy} in the plot is defined as $\sigma_{xy} = \sigma_{xy,\uparrow} - \sigma_{xy,\downarrow}$. It is clear from the above picture that for $0 \leq \lambda_{eph} < \lambda_c$ regime (blue curve) the conductivity initially increases, reaches a plateau and finally falls as we increase the Fermi energy, E_f. To have a nonzero σ_{xy} the Fermi level should be suitably placed in between the valance and the flat bands (where the bulk spectrum is gapped). The finite spin Hall conductivity for our case is expected since the TRS is preserved in our model, which also manifests in zero "charge" conductivity and a finite "spin" Hall conductivity. Therefore, the fall in σ_{xy} for higher E_f suggests that as the Fermi level does not lie inside the gap, the conductivity diminishes. The more intriguing feature of the spin Hall conductivity can be derived from the plateau where it is quantized at $2e^2/h$ that

carries the signature of a TRS protected topological spin Hall phase. The factor "2" is coming from the pair of helical (conducting) edge modes obtained in our system (where the $\mathbb{Z}_2$ invariant is nonzero accompanied by an odd cut in WCC). As expected, the conductivity vanishes throughout the range of E_f for the e-ph coupling $\lambda_{eph} > \lambda_c$ ($\mathbb{Z}_2$ invariant being zero), which determines a trivial (insulating) phase with zero spin Hall conductivity. Thus, the topological invariant, namely the $\mathbb{Z}_2$ invariant for our system captures these features adequately and confirms a direct correspondence with the Hall conductivity measurements. We should also assert that similar observations hold true for other values of α (only two are shown here). Hence, the topological nature of the phases for different regimes of α and λ_{eph} for our system can be detected by the measurement of spin Hall conductivity.

7.7 The Phase Boundary

At this stage, it may be a good idea to depict all the distinct phases, namely, the topological, SM, and the trivial phases in the form of a phase diagram which encapsulates our findings in different regimes of e-ph coupling (λ_{eph}) for all values of α in the range $[0 : 1]$. To do the same, we show the $\mathbb{Z}_2$ invariant in the α-λ_{eph} plane, presented in Fig. 7.13. The phase boundaries are basically the coordinates of the critical transition points λ_c which demarcate the topological characteristics of the phases for different combinations of α and λ_{eph}. In the figure, the black boundary denotes that below a critical λ_{eph} (see Table 7.1 for λ_c values), the system with lower values of α ($0 < \alpha \leq 0.5$) possesses a $\mathbb{Z}_2$-odd topological phase which ceases to exist above values of λ_c where the system acquires a $\mathbb{Z}_2$-even trivial phase. Beyond $\alpha = 0.5$, there exists a narrow region (for $0.51 < \alpha < 0.54$) where the system behaves like SM accompanied by a gapless dispersion ($\mathbb{Z}_2$ being ill-defined) below a certain λ_{c_1} marked by the blue line. Above λ_{c_1}, it enters into a $\mathbb{Z}_2$-odd topological phase (the region between the blue and black boundaries) which remains unaltered till λ_{eph} reaches another critical point λ_{c_2} beyond which the system becomes an ordinary ($\mathbb{Z}_2$-even) insulator. As encountered in the preceding subsections, the higher α cases demonstrate two bulk closing transitions at λ_{c_1} and λ_{c_2}, which are shown by red and black boundaries, respectively in Fig. 7.13 as a function of α (however, no gap closing transition occurs beyond $\alpha = 0.99$ marked by the dotted green line). The regions enclosed by these boundaries of the phase diagram reveal that our system, for higher α values ($0.54 < \alpha \leq 0.99$) acts as a trivial insulator below $\lambda_{eph} = \lambda_{c_1}$ (region beneath the red curve) which is designated by the $\mathbb{Z}_2$-even region, while it shows the fingerprints of a topological insulator in the $\lambda_{c_1} < \lambda_{eph} < \lambda_{c_2}$ regime, labeled by the $\mathbb{Z}_2$-odd region. It is obvious that for $\lambda_{eph} > \lambda_{c_2}$ the system turns out to be a trivial ($\mathbb{Z}_2$-even) insulator for any value of α in the range

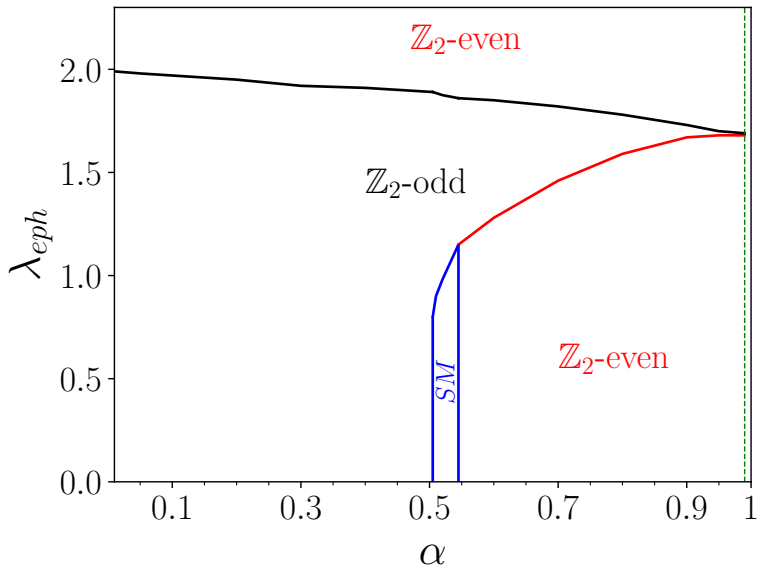

Figure 7.13: The phase boundary of $\mathbb{Z}_2$ invariant in the $\alpha - \lambda_{eph}$ plane. Various phases with even (trivial) and odd (topological) $\mathbb{Z}_2$ values and an SM phase are shown.

$0.54 < \alpha \leq 0.99$. It is also evident from Fig. 7.13 that as we increase α, the λ_c values (black line) decrease in the range $0 < \alpha \leq 0.5$, and also the difference between λ_{c_1} and λ_{c_2} (width of the region bounded by the red and black curves) diminishes for $0.5 < \alpha \leq 0.99$.

Let us now comment on plausible experimental realizations of these (topological) phases via tuning the e-ph interaction strength λ_{eph}. By engineering the uniaxial [393] and biaxial [394] strain effects in graphene-like hexagonal lattices, the strength of the e-ph coupling can be substantially enhanced which may show up in resonance and phonon softening effects of the optical phonon modes in the Raman spectroscopy experiments [395, 396]. In analogy to the substrate effects in graphene, similar mechanism to induce the effect of e-ph coupling in the α-T_3 lattice is possible via mounting it on a hexagonal boron nitride (h-BN) or SiO_2 substrate where the surface optical phonons can interact with the electrons giving rise to polaronic effects [397] that eventually impact the topological bandstructure and transport signatures [398].

7.8 Summary

To conclude, we study the effects of e-ph interaction to induce TPT in a pseudospin-1 fermionic system on an α-T_3 lattice. We formulate our model Hamiltonian in the spirit of the Kane-Mele model modified by the Holstein term accounting for the e-ph interaction and also include the effects of RSOC. The Lang-Firsov approach is employed to obtain the effective electronic

Hamiltonian, which is used later on throughout the study to compute the spectral and topological properties. As we tune the e-ph coupling, the system shows a topological-trivial insulator transition for $0 < \alpha \leq 0.5$ and a trivial-topological-trivial transition for $0.54 < \alpha < 1.0$ associated with an SM-topological-trivial transition for $0.51 < \alpha < 0.54$. The formation of these topologically distinct phases is accompanied by bulk gap closing transitions at critical e-ph coupling strengths, namely λ_c, λ_{c_1}, and λ_{c_2}. Nevertheless, there exists a gap in the bulk spectra below (topological) and above (trivial) λ_c for $0 < \alpha \leq 0.5$, while for $0.54 < \alpha < 1.0$, the same sustains in $\lambda_{eph} < \lambda_{c_1}$ (trivial), $\lambda_{c_1} < \lambda_{eph} < \lambda_{c_2}$ (topological), and $\lambda_{eph} > \lambda_{c_2}$ (trivial) regimes, whereas it provides similar scenarios for $0.51 < \alpha < 0.54$ in the last two regimes of λ_{eph}. Hence, apart from executing a TPT, the e-ph interaction has been able to generate topologically nontrivial phases in the $\lambda_{c_1} < \lambda_{eph} < \lambda_{c_2}$ regime for intermediate to higher range of α ($0.5 < \alpha < 1.0$), which are already present for lower range of α ($0 < \alpha \leq 0.5$) in the absence of e-ph coupling. These nontrivial phases induced by polarons are the QSH phases of an α-T_3 lattice protected by TRS. The signature of the topological (trivial) phase is assured by the emergence (disappearance) of the QSH helical edge modes characterized by a non-zero (zero) $\mathbb{Z}_2$ invariant (or equivalently an odd/even number of crossings in HWCCs evolving through the half-BZ). Finally, we summarize our findings for TPT in the form of a phase diagram which certifies that an α-T_3 lattice hosts QSH phases and relative transitions caused solely by the e-ph coupling.

Chapter 8

Conclusions and Future Prospects

8.1 Summary of the Chapters

Studies of physical properties of different systems have been drawing a wide attention in the Condensed matter community due to their possible future applications in fabricating nano-electronics devices. Since the discovery of graphene (pseudospin-1/2) in 2004, the fermions which can be governed by the relativistic Dirac-Weyl Hamiltonian with much lower velocity gained a lot of attention due to its unconventional electronic properties. On the other hand, higher pseudospin fermions which may be paraphrased as multi-band systems are found to have similar space group symmetry of the honeycomb structure and hence possess similar behaviour as that of graphene. One of such pseudospin-1 2D material is known as α-T_3 lattice, which can interpolate between graphene and the dice limits at the two extreme cases, namely, 0 and 1. Further, the study of topological properties in systems has been a fascinating area of research among the scientific community. It all started with the discovery of quantum Hall effect in electron gas and hence in graphene and its derivatives. However, gained importance after Haldane's groundbreaking work on a complex and chiral next neighbour hopping inducing topological phases in the honeycomb lattice without an external magnetic field. The spin-orbit coupling (SOC) is the main ingredient here to produce their own magnetic fields through internal interactions between the spin and orbital degrees of freedom. In 2D materials due to the confinement

of the electrons within a layer thereby violating the inversion symmetry, the SOC plays a significant role. Additionally, in such a 2D scenario, the Rashba spin-orbit coupling (RSOC) becomes salient and hence cannot be ignored. The ability to tune the strength of RSOC using an external field provides an additional boost to the exploration of tunable spintronic devices. Motivated by above we have extensively studied transport and topological properties of α-T_3 ring and ribbon systems respectively in presence of an external magnetic field that threads the plane of the ring perpendicularly (for transport properties) and the spin-orbit couplings (for transport and topological properties). An elaborate introduction is enclosed in the ***first chapter*** where various ingredients of the thesis and topological invariants to characterize the topological phase have been included. It also shows a detailed explanation of the method to compute those invariants and the calculation of Hall conductivity.

In the ***second chapter***, we have studied the electronic properties of a quantum ring (QR) build from a sheet of an α-T_3 lattice. With the help of proper coordinate mapping onto a ring geometry we solve its spectral properties in absence and presence of an external magnetic field. In the absence of an external field, the energy spectra consist of conduction band (CB), valence band (VB), and an infinitely degenerate zero energy flat band (FB), with the CB and VB being conditionally degenerate. The degeneracy of the CB and VB very much depends on the value of α. The inclusion of an external magnetic field hugely changes the nature of the CB and VB, while the FB remains flat. These non-monotonicity in the energy bands leads to the generation of persistent current, which circulates within the ring without any dissipation and exhibits quantum oscillations as a function of magnetic flux with period of one flux quantum. Further, we studied the electronic properties as well as persistent current of the massive (of the form δS_z) α-T_3 QR, focusing particularly on the non-trivial role of the distorted flat band (dFB).

The third chapter deals with the spin-orbit coupled α-T_3 QR in presence of an external perpendicular magnetic field. In particular, we have considered effects of intrinsic (ISOC) as well as Rashba spin-orbit couplings (RSOC) that may both be inherent to two dimensional quantum structures and yield interesting transport consequences. Further, it is noted that the flat bands demonstrate dispersive behavior, and hence is able to contribute to the transport properties only for finite ISOC. Moreover, the RSOC yields spin-split bands, thereby contributing to the spin-resolved currents. The charge and the spin-polarized persistent currents are hence computed which exhibit oscillatory behaviour as a function of the magnetic flux with a period equal to the flux quantum, as they should be; although they now depend upon the SOC parameters. Interestingly, the ISOC distorts the current profiles, owing to the distribution of the flat band caused by it, whereas RSOC alone preserves the flat band and hence a perfect periodicity of the current

characteristic is maintained. Further, we have explored the role played by the parameter α in our entire analyse.

In the ***fourth chapter***, we investigate the effect of a topological defect, such as a screw dislocation in an α-T_3 QR and scrutinized the cumulative effects of an external transverse magnetic field and Rashba spin-orbit coupling therein. The screw dislocation yields an effective flux which reshapes the periodic oscillations in the persistent current in both charge and spin sectors. Moreover, they suffer a phase shift that is proportional to the degree of the dislocation, and include scattering effects due to the dislocation present in the system. Such tunable oscillation of the spin persistent current again highlights applications of our system in presence of a topological defect as potential spintronic devices. Additionally, the presence of the screw dislocation induces a chirality effect, giving rise to an additional chiral current even without of an external field, suggesting two spin currents moving in opposite direction within the ring. The chiral current may hold important applications to spintronics.

In the ***fifth chapter***, the study focuses on the α-T_3 lattice configured as a Corbino disk, exploring its behavior under magnetic flux and its demonstration as a prototype of quantum Hall bar at low temperatures. Analytical solutions to the stationary Dirac equation were derived, enabling the determination of the electron transmission probability with angular momentum through the disk. Key physical quantities, such as conductance and the Fano factor were computed. The results indicate that conductance oscillates periodically with the magnetic flux, influenced by parameters such as the doping level and the ratio of the inner and outer radii, with notable sensitivity to these parameters. Additionally, conductance oscillations are more pronounced away from the charge-neutrality point (high doping), highlighting the significance of evanescent waves in the electron transport phenomena. The Fano factor shows differing behaviors for $\alpha < 1$ and $\alpha = 1$ (dice), indicating a shift from Poissonian to pseudo-diffusive transport as doping increases for $\alpha < 1$, while it transitions from ballistic to pseudo-diffusive for $\alpha = 1$ at high doping.

The next chapter, that is, ***sixth chapter*** is based on the electron-phonon (e-ph) coupled α-T_3 lattice, incorporating the Haldane term and distinct onsite potentials for different sublattices. We specifically focus on the topological properties, that is, the evolution of the electronic band properties and hence the topological characteristics associated with them. By considering the non-adiabatic high frequency longitudinal optical phonon, we achieve tunable dispersion behaviour. In our study, we observe a topological phase transition from a Chern insulating regime to a trivial insulating phase as the strength of the e-ph coupling is tuned beyond a certain critical value. Additionally, we investigate the evolution of the Berry curvature, which supports our observed phase transition induced solely by the e-ph coupling. Furthermore, we have explored

the behavior of the edge modes, which are localized states at the edges of the nanoribbon. Our findings indicate the existence of chiral edge modes as long as the non-trivial phase is maintained. Finally, our calculations of anomalous Hall conductivity demonstrate the existence of quantized plateaus, although narrow, below the critical e-ph coupling limit. The subsequent complete vanishing of these plateaus further supports the observed topological phase transition.

Finally, we focus on the other class of topological insulators, specifically the quantum spin Hall (QSH) insulators. In the ***seventh chapter***, we explored the topological properties of these spin Hall insulators using the electron-phonon (e-ph) coupled Kane-Mele model on the α-T_3 lattice. Our analysis of the spin-resolved band dispersions revealed a band closing phenomenon at specific points in the Brillouin zone. In this context, the Chern number is zero due to time-reversal symmetry. We calculated the $\mathbb{Z}_2$ topological invariant by examining the evolution of the hybrid Wannier charge center, which appropriately characterizes the topological properties of the system. We identified edge states in a ribbon geometry, which exhibit helical modes in the topological phase. Although the system shows no charge Hall conductivity, it possesses a finite spin Hall conductivity. We observed a quantized plateau at $2e^2/h$ for the non-trivial phase. This plateau disappears for the trivial phase due to a phase transition occurring at $\lambda_{eph} = \lambda_c$. Finally, we presented a comprehensive phase diagram that encompasses all possible phases in the $\alpha - \lambda_{eph}$ plane. This demonstrates that the system undergoes a topological phase transition from a QSH insulator to a trivial insulator at the critical e-ph coupling, supported by our computations of the helical edge modes, the $\mathbb{Z}_2$ invariant, and the spin Hall conductivity.

8.2 Future Prospects

There are numerous avenues for exploration in the study of thermoelectric effects such as the Seebeck, Nernst, and Peltier effects within α-T_3 ring, disk, and nanoribbon systems. The influence of the (distorted) flat band on thermoelectric and thermal transport coefficients is likely to be of interest in future theoretical and experimental studies. Additionally, the role of optical probes in these ring or disk geometries presents an intriguing area of research. In this context, the vector potential of incident photons couples with the band electrons through Peierls' coupling. The scenario becomes more complex in the presence of an external magnetic field, which causes the kinetic energy of the carriers to transform into macroscopically degenerate Landau levels. Consequently, the magneto-optical (MO) transport properties of these systems will attract considerable attention. Many fascinating MO phenomena could be discovered, including giant Faraday rotation, gate-tunable magnetoplasmons, and non-linear transport driven by light

radiation. Furthermore, the transport study of an α-T_3 quantum dot within a Josephson junction could be a captivating area of study in the near future.

This thesis examines the zero-temperature Hall conductivity for the α-T_3 model. The thermoelectric Hall effect (transverse response) in the presence of a magnetic field presents an interesting phenomenon. Additionally, interaction effects such as long-range and short-range interactions can be investigated by introducing an on-site Hubbard interaction term in a Kane-Mele model. Electron correlation effects may play a crucial role in topological phase transitions. Moreover, the behavior of surface modes, band deformation, the effects of spin-orbit coupling, and magnetic fields need deeper scrutiny for flat band topological insulators.

The role of spin-orbit coupling (SOC) in multi-band or flat-band systems represents an exciting frontier in condensed matter physics, particularly in its potential application to spintronics and spin-torque technologies. The unique interplay between SOC and the (dispersive) flat-band properties in these systems may unlock new mechanisms for controlling spin dynamics, offering opportunities to design innovative devices with enhanced efficiency and functionality. This area presents a broad spectrum of research possibilities, ranging from theoretical modeling to experimental validation, aiming to harness the intriguing properties of flat bands for practical applications.

Moreover, the analytic frameworks developed in this thesis for multi-band systems lay a foundation for extending these studies to other complex lattices, such as the kagome lattice, kagome rings, and ribbon structures. These systems, known for their exotic electronic properties, including flat bands and unconventional magnetic phenomena, present an avenue for deeper exploration. Understanding the interplay of geometry, symmetry, and electronic correlations in these lattices could provide insights into emergent phases of matter and novel quantum phenomena. This line of inquiry promises to contribute significantly to the broader understanding of multi-band systems and their applications in future quantum and nanoscale technologies.

Appendix A

Classification of Topological Insulators and Superconductors

Symmetry				d							
AZ	Θ	Ξ	Π	1	2	3	4	5	6	7	8
A	0	0	0	0	$\mathbb{Z}$	0	$\mathbb{Z}$	0	$\mathbb{Z}$	0	$\mathbb{Z}$
AIII	0	0	1	$\mathbb{Z}$	0	$\mathbb{Z}$	0	$\mathbb{Z}$	0	$\mathbb{Z}$	0
AI	1	0	0	0	0	0	$\mathbb{Z}$	0	$\mathbb{Z}_2$	$\mathbb{Z}_2$	$\mathbb{Z}$
BDI	1	1	1	$\mathbb{Z}$	0	0	0	$\mathbb{Z}$	0	$\mathbb{Z}_2$	$\mathbb{Z}_2$
D	0	1	0	$\mathbb{Z}_2$	$\mathbb{Z}$	0	0	0	$\mathbb{Z}$	0	$\mathbb{Z}_2$
DIII	-1	1	1	$\mathbb{Z}_2$	$\mathbb{Z}_2$	$\mathbb{Z}$	0	0	0	$\mathbb{Z}$	0
AII	-1	0	0	0	$\mathbb{Z}_2$	$\mathbb{Z}_2$	$\mathbb{Z}$	0	0	0	$\mathbb{Z}$
CII	-1	-1	1	$\mathbb{Z}$	0	$\mathbb{Z}_2$	$\mathbb{Z}_2$	$\mathbb{Z}$	0	0	0
C	0	-1	0	0	$\mathbb{Z}$	0	$\mathbb{Z}_2$	$\mathbb{Z}_2$	$\mathbb{Z}$	0	0
CI	1	-1	1	0	0	$\mathbb{Z}$	0	$\mathbb{Z}_2$	$\mathbb{Z}_2$	$\mathbb{Z}$	0

Table A.1: The table displaying the classification of topological insulators and superconductors is outlined. The ten symmetry classes are represented using the Altland-Zirnbauer notation [261]. This classification is influenced by time-reversal symmetry (TRS), particle-hole symmetry, and chiral symmetry, which are indicated by the operators Θ, Ξ, and Π, respectively. A designation of ± 1 indicates the presence of symmetry, while 0 signifies its absence; these values are derived from squaring the operators. The variable d represents the system dimension, and the topological invariants are $\mathbb{Z}$ and $\mathbb{Z}_2$, which recur in intervals of $d + 8$. This information is sourced from Ref. [89].

Appendix B

Justification of $\big[J_z, H\big] = 0$

The Hamiltonian is $H = \hbar v_F\big[(p_x + eA_x)S_x + (p_y + eA_y)S_y\big]$ and $J_z = L_z + S_z$. We shall now compute $[J_z, H] = [L_z, H] + [S_z, H]$.

Now,

$$\begin{aligned}[L_z, H] &= \hbar v_F\big[(xp_y - yp_x), \{S_x(p_x + eA_x) + S_y(p_y + eA_y)\}\big] \\ &= \hbar v_F\Big\{\big[(xp_y - yp_x), S_x(p_x + eA_x)\big]\Big\} + \Big\{\big[(xp_y - yp_x), S_y(p_y + eA_y)\big]\Big\}.\end{aligned} \tag{B.1}$$

Taking the first term we get,

$$\begin{aligned}&\big[(xp_y - yp_x), S_x(p_x + eA_x)\big] \\ &= \big[xp_y, S_xp_x\big] + \big[xp_y, eS_xA_x\big] - \big[yp_x, S_xp_x\big] - \big[yp_x, eS_xA_x\big] \\ &= i\hbar S_xp_y + \frac{ie\hbar xBS_x}{2}.\end{aligned} \tag{B.2}$$

Similarly, the second term becomes,

$$\begin{aligned}&\big[(xp_y - yp_x), S_y(p_y + eA_y)\big] \\ &= -i\hbar S_yp_x + \frac{ie\hbar yBS_y}{2}.\end{aligned} \tag{B.3}$$

Also,

$$\begin{aligned}
&[S_z, H] \\
&= \hbar v_F \big[S_z, \{S_x(p_x + eA_x) + S_y(p_y + eA_y)\}\big] \\
&= \hbar v_F \Big\{ \big[S_z, S_x p_x\big] + \big[S_z, S_y p_y\big] + \big[S_z, eS_x A_x\big] + \big[S_z, eS_y p_y\big] \Big\} \\
&= i\hbar v_F \big\{ S_y p_x - S_x p_y + eA_x S_y - eA_y S_x \big\} \\
&= i\hbar v_F \Big\{ S_y p_x - S_x p_y - \frac{eyBS_y}{2} - \frac{exBS_x}{2} \Big\}.
\end{aligned} \tag{B.4}$$

Finally, we obtain,

$$\begin{aligned}
[J_z, H] &= [L_z, H] + [S_z, H] \\
&= \hbar v_F \Big\{ \cancel{i\hbar S_x p_y} + \cancel{\frac{ie\hbar xBS_x}{2}} - \cancel{i\hbar S_y p_x} + \cancel{\frac{ie\hbar yBS_y}{2}} + \cancel{i\hbar S_y p_x} - \cancel{i\hbar S_x p_y} - \cancel{\frac{ie\hbar yBS_y}{2}} - \cancel{\frac{ie\hbar xBS_x}{2}} \Big\} \\
&= 0.
\end{aligned} \tag{B.5}$$

Appendix C

Justification of the Substitution $\frac{\partial}{\partial r} \rightarrow -\frac{1}{2R}$

The problem of the non-hermiticity of the quantum ring Hamiltonian appears when the 2D Hamiltonian contains a term linearly proportional to the momentum. To bypass such an ambiguity, the substitution $\frac{\partial}{\partial r} \rightarrow -\frac{1}{2R}$ is necessary as mentioned earlier. However, there is a nice argument in support of that substitution. This is based on the appropriate form of the radial momentum operator in 2D.

Note that the operator $\mathcal{P}_r = \frac{\boldsymbol{r}\cdot\boldsymbol{p}}{r}$ is not hermitian i.e. $\mathcal{P}_r^\dagger \neq \mathcal{P}_r$. Therefore, the radial momentum operator can be written in the symmetric form,

$$p_r = \frac{1}{2}(\mathcal{P}_r + \mathcal{P}_r^\dagger) = \frac{1}{2}\Big(\frac{1}{r}\boldsymbol{r}\cdot\boldsymbol{p} + \boldsymbol{p}\cdot\boldsymbol{r}\frac{1}{r}\Big). \tag{C.1}$$

Let us examine the action of p_r on a differentiable function of $\boldsymbol{r}$, say, $g(\boldsymbol{r})$. One obtains,

$$p_r g(\boldsymbol{r}) = -\frac{i\hbar}{2}\left[\frac{\partial g}{\partial r} + \boldsymbol{\nabla}\cdot\Big(\frac{\boldsymbol{r}g}{r}\Big)\right] = -i\hbar\left[\frac{\partial}{\partial r} + \frac{1}{2r}\right]g(\boldsymbol{r}).$$

Therefore, the radial momentum operator in 2D is identified as

$$p_r = -i\hbar\Big(\frac{\partial}{\partial r} + \frac{1}{2r}\Big). \tag{C.2}$$

For the case of a 1D quantum ring, the radial motion is essentially frozen, that is, $p_r = 0$. Therefore, the substitution $\frac{\partial}{\partial r} \rightarrow -\frac{1}{2R}$ is justified.

Appendix D

Phase Shift Due to Scattering

The scattering of an electron by a screw dislocation is analogous to the scattering by an Aharanov-Bohm flux, β in the quantum ring. The same is applicable to any gauge field, such as the one that we have in our system, namely, the field arising due to the screw dislocation. Let us elaborate it as follows. Consider an incident plane wave with a wave vector k propagating along the z-direction and is parallel to the external magnetic flux. The wave undergoes a phase shift due to the presence of the Aharonov-Bohm flux. In polar coordinates, the scattering phenomenon in two dimensions is described by the Schrödinger equation [310–312],

$$\left[\frac{\partial^2}{\partial r^2}+\frac{1}{r}\frac{\partial}{\partial r}+\frac{1}{r^2}\left(\frac{\partial}{\partial\theta}+i\beta\right)^2+k^2\right]\psi(r)=0. \tag{D.1}$$

The general solution of Eq. (D.1) is given by,

$$\psi(r)=\sum_{m=-\infty}^{\infty}a_m e^{im\theta}J_{|m+\beta|}(kr) \tag{D.2}$$

where $J_{|m+\beta|}(kr)$ is the Bessel function. Prior to scattering, we have to match the incoming wave (before scattering) with the incoming asymptotic polar component of the solution. Let the incoming wave is,

$$\psi_{inc}\sim\sqrt{\frac{1}{2\pi kr}}\sum_{m=-\infty}^{\infty}(-i)^m e^{im\theta}e^{-ikr}e^{im\pi/2}e^{i\pi/4}. \tag{D.3}$$

The polar component of the incoming wave which is useful for our purpose, is given by,

$$\left(\psi_{inc}\right)_\theta\sim\sqrt{\frac{1}{2\pi kr}}\sum_{m=-\infty}^{\infty}a_m e^{im\theta}e^{-ikr}e^{i|m+\beta|\pi/2}e^{i\pi/4}e^{i\beta\theta_k} \tag{D.4}$$

where θ_k is the angle of propagation. The matching condition requires that,

$$a_m = e^{-i|m+\beta|\pi/2} e^{-i\beta\theta_k}. \tag{D.5}$$

The same is true for the outgoing wave as well which is expressed as,

$$\psi_{out} \sim \sqrt{\frac{1}{2\pi kr}} \sum_{m=-\infty}^{\infty} (-i)^m e^{im\theta} e^{ikr} e^{-im\pi/2} e^{-i\pi/4} + f(\phi)\frac{e^{ikr}}{\sqrt{r}}. \tag{D.6}$$

Again, the polar component of the outgoing wave is,

$$\big(\psi_{out}\big)_\theta \sim \sqrt{\frac{1}{2\pi kr}} \sum_{m=-\infty}^{\infty} e^{im\theta} e^{ikr} e^{-i|m+\beta|\pi/2} e^{-i\pi/4} e^{-i\beta\theta_k}. \tag{D.7}$$

The outgoing wave is the superposition of the incoming (unscattered) wave and of the one with a scattering amplitude $f(\phi)$. The phase shift, δ_m, in the scattering is obtained by comparing the two outgoing plane waves of Eqs. (D.6) and (D.7) and has a form,

$$\delta_m = -\frac{\pi}{2}\Big(|m+\beta| - |m|\Big) \tag{D.8}$$

β in Eq. (D.8) contains the scattering effects. For the screw dislocation, we have used $\beta = k\eta$ in our calculations.

Appendix E

Derivation of the Modified Haldane-Holstein Hamiltonian for an α-T_3 Lattice

Here we briefly derive the major steps to obtain the Hamiltonian (Eq. (7.3) of Sec. 7.2.2) modified by the e-ph coupling, employing LFT via the generator of the transformation mentioned in Eq. (6.3). The transformed Hamiltonian in Eq. (7.2) can equivalently be expressed by the Baker–Campbell–Hausdorff formula as,

$$\tilde{\mathcal{H}} \;=\; e^{R}\mathcal{H}e^{-R} = \mathcal{H} + [R,\mathcal{H}] + \frac{1}{2!}[R,[R,\mathcal{H}]] + \frac{1}{3!}[R,[R,[R,\mathcal{H}]]] + ... \;. \tag{E.1}$$

Let us label the terms of Hamiltonian (6.1) as $\mathcal{H}^{(1)}, \mathcal{H}^{(2)}$, ..., etc. for the first till the seventh term of Hamiltonian (6.1), respectively. Now, we transform each individual term as in the following. Combining the NN ($\langle ...\rangle$) terms that are symbolized as $\mathcal{H}^{(1)}$ and $\mathcal{H}^{(2)}$ we can calculate the commutator for $\mathcal{H}^{(12)} \equiv \mathcal{H}^{(1)} + \mathcal{H}^{(2)}$ as,

$$\begin{aligned}
[R,\mathcal{H}^{(12)}] &= \Big[\lambda_{eph}\sum_{i} c_i^{\dagger}c_i(b_i^{\dagger}-b_i), [-t\sum_{\langle i',j'\rangle} c_{i'}^{\dagger}c_{j'} - \alpha t \sum_{\langle j',k'\rangle} c_{j'}^{\dagger}c_{k'}]\Big] \\
&= -(1+\alpha)t\sum_{i,\delta} c_i^{\dagger}c_{i+\delta}\Big[\lambda_{eph}[(b_i^{\dagger}-b_i)-(b_{i+\delta}^{\dagger}-b_{i+\delta})]\Big],
\end{aligned} \tag{E.2}$$

and consequently the successive commutators can be obtained as,

$$\begin{aligned}[R,[R,\mathcal{H}^{(12)}]] &= -(1+\alpha)t\sum_{i,\delta} c_i^\dagger c_{i+\delta}[X_i - X_{i+\delta}]^2,\\ [R,[R,[R,\mathcal{H}^{(12)}]]] &= -(1+\alpha)t\sum_{i,\delta} c_i^\dagger c_{i+\delta}[X_i - X_{i+\delta}]^3.\end{aligned} \tag{E.3}$$

where $X_i \equiv \lambda_{eph}(b_i^\dagger - b_i)$ and δ is the NN index, that is, $j = i+\delta$. Therefore, collecting terms in Eq. (E.2) and Eq. (E.3) and using Eq. (E.1) the NN terms are transformed as,

$$\begin{aligned}\tilde{\mathcal{H}}^{(12)} &= -(1+\alpha)t\sum_{i,\delta} c_i^\dagger c_{i+\delta}\left[1 + [X_i - X_{i+\delta}] + \frac{1}{2!}[X_i - X_{i+\delta}]^2 + \frac{1}{3!}[X_i - X_{i+\delta}]^3 + ...\right]\\ &= -(1+\alpha)t\sum_{i,\delta} c_i^\dagger c_{i+\delta}\, e^{[X_i - X_{i+\delta}]}.\end{aligned} \tag{E.4}$$

The NNN ($\langle\langle ... \rangle\rangle$) Haldane terms denoted by $\mathcal{H}^{(3)}$ and $\mathcal{H}^{(4)}$ can be transformed in a similar fashion with the NNN index, η as,

$$\tilde{\mathcal{H}}^{(34)} = -(1+\alpha)\frac{\lambda}{3\sqrt{3}}\sum_{i,\eta} c_i^\dagger c_{i+\eta}\, e^{[X_i - X_{i+\eta}]} e^{i\phi_{i,i+\eta}}, \tag{E.5}$$

while the onsite mass term, $\mathcal{H}^{(5)}(\equiv \sum_i c_i^\dagger M S_z c_i)$ remains unchanged by the transformation, that is,

$$\tilde{\mathcal{H}}^{(5)} = \sum_i c_i^\dagger M S_z c_i. \tag{E.6}$$

The phonon energy, $\mathcal{H}^{(6)}(\equiv \hbar\omega_0 \sum_i b_i^\dagger b_i)$ and the e-ph interaction term, $\mathcal{H}^{(7)}(\equiv \lambda_{eph}\hbar\omega_0 \sum_i c_i^\dagger c_i (b_i^\dagger + b_i))$ can respectively be transformed by Eq. (E.1) as,

$$\tilde{\mathcal{H}}^{(6)} = \hbar\omega_0 \sum_i \left[b_i^\dagger b_i - \lambda_{eph} c_i^\dagger c_i (b_i^\dagger + b_i) + \lambda_{eph}^2 c_i^\dagger c_i\right], \tag{E.7}$$

$$\tilde{\mathcal{H}}^{(7)} = \hbar\omega_0 \sum_i \left[\lambda_{eph} c_i^\dagger c_i (b_i^\dagger + b_i) - 2\lambda_{eph}^2 c_i^\dagger c_i\right], \tag{E.8}$$

where in Eqs. (E.7) and (E.8), we have used the identity, namely $n_i^2 = n_i (\equiv c_i^\dagger c_i)$ for the fermionic number operator. Hence, performing a sum of Eqs. (E.4)-(E.8), we obtain Eq. (7.3).

Bibliography

[1] R. García G., "Atomic-scale manipulation in air with the scanning tunneling microscope," *Appl. Phys. Lett.*, vol. 60, no. 16, pp. 1960–1962, 1992.

[2] M. A. McCord and R. F. W. Pease, "Lithography with the scanning tunneling microscope," *J. Vac. Sci. Technol. B*, vol. 4, no. 1, pp. 86–88, 1986.

[3] R. J. Colton, D. DiLella, R. L. Mowery, A. Snow, J. H. Wandass, and C. R. K. Marrian, "Surface chemical analysis of polydiacetylene films exposed to electron beam and ultraviolet irradiation," *J. Vac. Sci. Technol. A*, vol. 6, no. 3, pp. 933–935, 1988.

[4] E. A. Dobisz, C. R. K. Marrian, and R. J. Colton, "High resolution electron beam lithography with a polydiacetylene negative resist at 50 kV," *J. Appl. Phys.*, vol. 70, no. 3, pp. 1793–1799, 1991.

[5] P. Harrison and A. Valavanis, *Quantum wells, wires and dots: theoretical and computational physics of semiconductor nanostructures*. John Wiley & Sons, 2016.

[6] M. Büttiker, Y. Imry, and R. Landauer, "Josephson behavior in small normal one-dimensional rings," *Phys. Lett. A*, vol. 96, no. 7, pp. 365–367, 1983.

[7] R. Landauer and M. Büttiker, "Resistance of small metallic loops," *Phys. Rev. Lett.*, vol. 54, no. 18, p. 2049, 1985.

[8] L. P. Levy, G. Dolan, J. Dunsmuir, and H. Bouchiat, "Magnetization of mesoscopic copper rings: Evidence for persistent currents," *Phys. Rev. Lett.*, vol. 64, no. 17, p. 2074, 1990.

[9] V. Chandrasekhar, R. A. Webb, M. J. Brady, M. B. Ketchen, W. J. Gallagher, and A. Kleinsasser, "Magnetic response of a single, isolated gold loop," *Phys. Rev. Lett.*, vol. 67, no. 25, p. 3578, 1991.

[10] S. Tarucha, D. G. Austing, T. Honda, R. J. Van der Hage, and L. P. Kouwenhoven, "Shell filling and spin effects in a few electron quantum dot," *Phys. Rev. Lett.*, vol. 77, no. 17, p. 3613, 1996.

[11] K. Mullen, D. Loss, and H. T. C. Stoof, "Resonant phenomena in compact and extended systems," *Phys. Rev. B*, vol. 47, no. 5, p. 2689, 1993.

[12] K. L. Hobbs, P. R. Larson, G. D. Lian, J. C. Keay, and M. B. Johnson, "Fabrication of nanoring arrays by sputter redeposition using porous alumina templates," *Nano Letters*, vol. 4, no. 1, pp. 167–171, 2004.

[13] A. Lorke, R. J. Luyken, A. O. Govorov, J. P. Kotthaus, J. M. Garcia, and P. M. Petroff, "Spectroscopy of nanoscopic semiconductor rings," *Phys. Rev. Lett.*, vol. 84, no. 10, p. 2223, 2000.

[14] R. A. Webb, S. Washburn, C. P. Umbach, and R. B. Laibowitz, "Observation of h/e aharonov-bohm oscillations in normal-metal rings," *Phys. Rev. Lett.*, vol. 54, no. 25, p. 2696, 1985.

[15] G. Timp, A. M. Chang, J. E. Cunningham, T. Y. Chang, P. Mankiewich, R. Behringer, and R. E. Howard, "Observation of the Aharonov-Bohm effect for $\omega_c\tau > 1$," *Phys. Rev. Lett.*, vol. 58, no. 26, p. 2814, 1987.

[16] C. J. B. Ford, T. J. Thornton, R. Newbury, M. Pepper, H. Ahmed, D. C. Peacock, D. A. Ritchie, J. E. F. Frost, and G. A. C. Jones, "Electrostatically defined heterojunction rings and the Aharonov–Bohm effect," *Appl. Phys. Lett.*, vol. 54, no. 1, pp. 21–23, 1989.

[17] K. Ismail, S. Washburn, and K. Y. Lee, "Conductance in very clean quantum wires and rings," *Appl. Phys. Lett.*, vol. 59, no. 16, pp. 1998–2000, 1991.

[18] D. Mailly, C. Chapelier, and A. Benoit, "Experimental observation of persistent currents in GaAs-AlGaAs single loop," *Phys. Rev. Lett.*, vol. 70, no. 13, p. 2020, 1993.

[19] A. F. Morpurgo, J. P. Heida, T. M. Klapwijk, B. J. Van Wees, and G. Borghs, "Ensemble-average spectrum of Aharonov-Bohm conductance oscillations: evidence for spin-orbit-induced Berry's phase," *Phys. Rev. Lett.*, vol. 80, no. 5, p. 1050, 1998.

[20] S. Fuhrer, A .and Lüscher, T. Ihn, T. Heinzel, K. Ensslin, W. Wegscheider, and M. Bichler, "Energy spectra of quantum rings," *Nature*, vol. 413, no. 6858, pp. 822–825, 2001.

[21] S. M. Reimann and M. Manninen, "Electronic structure of quantum dots," *Rev. Mod. Phys.*, vol. 74, no. 4, p. 1283, 2002.

[22] A. Lorke and R. J. Luyken, "Many-particle ground states and excitations in nanometer-size quantum structures," *Phys. B: Cond. Matt.*, vol. 256, pp. 424–430, 1998.

[23] H. Pettersson, R. J. Warburton, A. Lorke, K. Karrai, J. P. Kotthaus, J. M. Garcia, and P. M. Petroff, "Excitons in self-assembled quantum ring-like structures," *Physica E*, vol. 6, no. 1-4, pp. 510–513, 2000.

[24] R. J. Warburton, C. Schäflein, D. Haft, F. Bickel, A. Lorke, K. Karrai, J. M. Garcia, W. Schoenfeld, and P. M. Petroff, "Optical emission from a charge-tunable quantum ring," *Nature*, vol. 405, no. 6789, pp. 926–929, 2000.

[25] M. J. Yang, C. H. Yang, and Y. B. Lyanda-Geller, "Quantum beating in ring conductance: Observation of spin chiral states and Berry's phase," *Euro Phys. Lett.*, vol. 66, no. 6, p. 826, 2004.

[26] M. Zarenia, J. M. Pereira, A. Chaves, F. M. Peeters, and G. A. Farias, "Erratum: Simplified model for the energy levels of quantum rings in single layer and bilayer graphene [Phys. Rev. B 81, 045431 (2010)]," *Phys. Rev. B*, vol. 82, no. 11, p. 119906, 2010.

[27] M. Zarenia, J. M. Pereira, F. M. Peeters, and G. A. Farias, "Electrostatically confined quantum rings in bilayer graphene," *Nano Lett.*, vol. 9, no. 12, pp. 4088–4092, 2009.

[28] N. Bolívar, E. Medina, and B. Berche, "Persistent charge and spin currents in the long-wavelength regime for graphene rings," *Phys. Rev. B*, vol. 89, no. 12, p. 125413, 2014.

[29] S. Russo, J. B. Oostinga, D. Wehenkel, H. B. Heersche, S. S. Sobhani, L. M. K. Vandersypen, and A. F. Morpurgo, "Observation of Aharonov-Bohm conductance oscillations in a graphene ring," *Phys. Rev. B*, vol. 77, no. 8, p. 085413, 2008.

[30] M. Huefner, F. Molitor, A. Jacobsen, A. Pioda, C. Stampfer, K. Ensslin, and T. Ihn, "Investigation of the Aharonov–Bohm effect in a gated graphene ring," *Phys. Stat. Soli. B*, vol. 246, no. 11-12, pp. 2756–2759, 2009.

[31] M. Huefner, F. Molitor, A. Jacobsen, A. Pioda, C. Stampfer, K. Ensslin, and T. Ihn, "The Aharonov–Bohm effect in a side-gated graphene ring," *New Journal of Physics*, vol. 12, no. 4, p. 043054, 2010.

[32] J. L. Zhu, X. Wang, and N. Yang, "Confined electronic states and their modulations in graphene nanorings," *Phys. Revi. B*, vol. 86, no. 12, p. 125435, 2012.

[33] A. De Martino, L. Dell'Anna, and R. Egger, "Magnetic confinement of massless Dirac fermions in graphene," *Phys. Rev. Lett.*, vol. 98, no. 6, p. 066802, 2007.

[34] F. D. M. Haldane, "Model for a quantum Hall effect without Landau levels: Condensed-matter realization of the "parity anomaly"," *Phys. Rev. Lett.*, vol. 61, no. 18, p. 2015, 1988.

[35] P. Recher, B. Trauzettel, A. Rycerz, Y. M. Blanter, C. W. J. Beenakker, and A. F. Morpurgo, "Aharonov-Bohm effect and broken valley degeneracy in graphene rings," *Phys. Rev. B*, vol. 76, no. 23, p. 235404, 2007.

[36] D. Faria, A. Latgé, S. E. Ulloa, and N. Sandler, "Currents and pseudomagnetic fields in strained graphene rings," *Phys. Rev. B*, vol. 87, no. 24, p. 241403, 2013.

[37] D. S. L. Abergel, V. M. Apalkov, and T. Chakraborty, "Interplay between valley polarization and electron-electron interaction in a graphene ring," *Phys. Rev. B*, vol. 78, no. 19, p. 193405, 2008.

[38] D. R. Da Costa, A. Chaves, M. Zarenia, J. M. Pereira Jr., G. A. Farias, and F. M. Peeters, "Geometry and edge effects on the energy levels of graphene quantum rings: A comparison between tight-binding and simplified Dirac models," *Phys. Rev. B*, vol. 89, no. 7, p. 075418, 2014.

[39] M. M. Ma, J. W. Ding, and N. Xu, "Odd-even width effect on persistent current in zigzag hexagonal graphene rings," *Nanoscale*, vol. 1, no. 3, pp. 387–390, 2009.

[40] T. Luo, A. P. Iyengar, H. A. Fertig, and L. Brey, "Effective time-reversal symmetry breaking and energy spectra of graphene armchair rings," *Phys. Rev. B*, vol. 80, no. 16, p. 165310, 2009.

[41] J. Wurm, M. Wimmer, H. U. Baranger, and K. Richter, "Graphene rings in magnetic fields: Aharonov–Bohm effect and valley splitting," *Semicond. Sci. Technol.*, vol. 25, no. 3, p. 034003, 2010.

[42] C. H. Yan and L. F. Wei, "Size effects in Aharonov–Bohm graphene rings," *J. Phys.: Cond. Matt.*, vol. 22, no. 29, p. 295503, 2010.

[43] B. L. Huang, M. C. Chang, and C. Y. Mou, "Persistent currents in a graphene ring with armchair edges," *J. Phys.: Cond. Matt.*, vol. 24, no. 24, p. 245304, 2012.

[44] M. Omidi and E. Faizabadi, "Energy spectrum and persistent current in an armchair hexagonal graphene ring in the presence of vacancies, Rashba and Zeeman interactions," *Euro. Phys. Jour. B*, vol. 88, pp. 1–6, 2015.

[45] F. R. V. Araújo, D. R. da Costa, A. J. C. Chaves, F. E. B. de Sousa, and J. M. Pereira, "Modulation of persistent current in graphene quantum rings," *J. Phys.: Cond. Matt.*, vol. 34, no. 12, p. 125503, 2022.

[46] M. Mirzakhani, D. R. da Costa, and F. M. Peeters, "Isolated and hybrid bilayer graphene quantum rings," *Phys. Rev. B*, vol. 105, no. 11, p. 115430, 2022.

[47] M. Samal, N. Barange, D.-H. Ko, and K. Yun, "Graphene quantum rings doped PEDOT:PSS based composite layer for efficient performance of optoelectronic devices," *J. Phys. Chem. C*, vol. 119, no. 34, pp. 19 619–19 627, 2015.

[48] D. J. P. de Sousa, A. Chaves, J. M. Pereira, and G. A. Farias, "Interferometry of Klein tunnelling electrons in graphene quantum rings," *J. Appl. Phys.*, vol. 121, no. 2, 2017.

[49] H. F. Cheung, Y. Gefen, and E. K. Riedel, "Isolated rings of mesoscopic dimensions. quantum coherence and persistent currents," *IBM J. Res. Dev.*, vol. 32, no. 3, pp. 359–371, 1988.

[50] H. F. Cheung, Y. Gefen, E. K. Riedel, and W. H. Shih, "Persistent currents in small one-dimensional metal rings," *Phys. Rev. B*, vol. 37, no. 11, p. 6050, 1988.

[51] E. M. Q. Jariwala, P. Mohanty, M. B. Ketchen, and R. A. Webb, "Diamagnetic persistent current in diffusive normal-metal rings," *Phys. Rev. Lett.*, vol. 86, no. 8, p. 1594, 2001.

[52] E. I. Rashba, "Spin-orbit coupling in condensed matter physics," *Sov. Phys. Solid State*, vol. 2, p. 1109, 1960.

[53] E. A. d. A. e Silva, G. C. La Rocca, and F. Bassani, "Spin-split subbands and magneto-oscillations in III-V asymmetric heterostructures," *Phys. Rev. B*, vol. 50, no. 12, p. 8523, 1994.

[54] E. A. d. A. e Silva, G. C. La Rocca, and F. Bassani, "Spin-orbit splitting of electronic states in semiconductor asymmetric quantum wells," *Phys. Rev. B*, vol. 55, no. 24, p. 16293, 1997.

[55] J. Nitta, T. Akazaki, H. Takayanagi, and T. Enoki, "Gate control of spin-orbit interaction in an inverted $In_{0.53}Ga_{0.47}$ As/$In_{0.52}Al_{0.48}$ as heterostructure," *Phys. Rev. Lett.*, vol. 78, no. 7, p. 1335, 1997.

[56] G. Engels, J. Lange, T. Schäpers, and H. Lüth, "Experimental and theoretical approach to spin splitting in modulation-doped $In_xGa_{1-x}As$/InP quantum wells for B$\rightarrow$ 0," *Phys. Rev. B*, vol. 55, no. 4, p. R1958, 1997.

[57] D. Liang and X. P. A. Gao, "Strong tuning of Rashba spin-orbit interaction in single InAs nanowires," *Nano Lett.*, vol. 12, no. 6, pp. 3263–3267, 2012.

[58] S. Datta and B. Das, "Electronic analog of the electro-optic modulator," *Appl. Phys. Lett.*, vol. 56, no. 7, pp. 665–667, 1990.

[59] D. Frustaglia and K. Richter, "Spin interference effects in ring conductors subject to Rashba coupling," *Phys. Rev. B*, vol. 69, no. 23, p. 235310, 2004.

[60] R. Ionicioiu and I. D'Amico, "Mesoscopic Stern-Gerlach device to polarize spin currents," *Phys. Rev. B*, vol. 67, no. 4, p. 041307, 2003.

[61] C. Furtado and F. Moraes, "On the binding of electrons and holes to disclinations," *Phys. Lett. A*, vol. 188, no. 4-6, pp. 394–396, 1994.

[62] C. Furtado, B. G. C. da Cunha, F. Moraes, E. R. B. de Mello, and V. B. Bezzerra, "Landau levels in the presence of disclinations," *Phys. Lett. A*, vol. 195, no. 1, pp. 90–94, 1994.

[63] C. Furtado, A. Rosas, and S. Azevedo, "Landau quantization and curvature effects in a two-dimensional quantum dot," *Euro Phys. Lett.*, vol. 79, no. 5, p. 57001, 2007.

[64] A. A. Lima, C. Filgueiras, and F. Moraes, "Torsion effects on condensed matter: like a magnetic field but not so much," *Eur. Phys. J. B*, vol. 90, pp. 1–8, 2017.

[65] K. V. Klitzing, G. Dorda, and M. Pepper, "New method for high-accuracy determination of the fine-structure constant based on quantized Hall resistance," *Phys. Rev. Lett.*, vol. 45, pp. 494–497, 1980.

[66] A. H. MacDonald and P. Středa, "Quantized Hall effect and edge currents," *Phys. Rev. B*, vol. 29, no. 4, p. 1616, 1984.

[67] V. P. Mineev, "de Haas–Van Alphen effect versus integer quantum Hall effect," *Phys. Rev. B*, vol. 75, no. 19, p. 193309, 2007.

[68] B. I. Halperin, "Quantized Hall conductance, current-carrying edge states, and the existence of extended states in a two-dimensional disordered potential," *Phys. Rev. B*, vol. 25, no. 4, p. 2185, 1982.

[69] J. Yan and M. S. Fuhrer, "Charge transport in dual gated bilayer graphene with Corbino geometry," *Nano Lett.*, vol. 10, no. 11, pp. 4521–4525, 2010.

[70] E. C. Peters, A. J. M. Giesbers, M. Burghard, and K. Kern, "Scaling in the quantum Hall regime of graphene Corbino devices," *Appl. Phys. Lett.*, vol. 104, no. 20, 2014.

[71] M. Kumar, A. Laitinen, and P. Hakonen, "Unconventional fractional quantum Hall states and wigner crystallization in suspended Corbino graphene," *Nat. Comm.*, vol. 9, no. 1, p. 2776, 2018.

[72] Y. Zeng, J. Li, S. Dietrich, O. Ghosh, K. Watanabe, T. Taniguchi, J. Hone, and C. Dean, "High-quality magnetotransport in graphene using the edge-free Corbino geometry," *Phys. Rev. Lett.*, vol. 122, no. 13, p. 137701, 2019.

[73] Z. Khatibi, H. Rostami, and R. Asgari, "Valley polarized transport in a strained graphene based Corbino disc," *Phys. Rev. B*, vol. 88, no. 19, p. 195426, 2013.

[74] G. W. Jones, D. A. Bahamon, A. H. Castro Neto, and V. M. Pereira, "Quantized transport, strain-induced perfectly conducting modes, and valley filtering on shape-optimized graphene Corbino devices," *Nano Lett.*, vol. 17, no. 9, pp. 5304–5313, 2017.

[75] A. Rycerz and D. Suszalski, "Graphene disk in a solenoid magnetic potential: Aharonov-Bohm effect without a two-slit-like setup," *Phys. Rev. B*, vol. 101, no. 24, p. 245429, 2020.

[76] M. I. Katsnelson, "Graphene: carbon in two dimensions," *Materials today*, vol. 10, no. 1-2, pp. 20–27, 2007.

[77] A. Rycerz, P. Recher, and M. Wimmer, "Conformal mapping and shot noise in graphene," *Phys. Rev. B*, vol. 80, no. 12, p. 125417, 2009.

[78] A. Rycerz, "Magnetoconductance of the Corbino disk in graphene," *Phys. Rev. B*, vol. 81, no. 12, p. 121404, 2010.

[79] M. I. Katsnelson, "Aharonov-Bohm effect in undoped graphene: Magnetotransport via evanescent waves," *Euro Phys. Lett.*, vol. 89, no. 1, p. 17001, 2010.

[80] E. H. Hall, "On a new action of the magnet on electric currents," *American Journal of Science*, vol. 3, no. 111, pp. 200–205, 1880.

[81] D. C. Tsui, H. L. Stormer, and A. C. Gossard, "Two-dimensional magnetotransport in the extreme quantum limit," *Phys. Rev. Lett.*, vol. 48, no. 22, p. 1559, 1982.

[82] R. B. Laughlin, "Quantized Hall conductivity in two dimensions," *Phys. Rev. B*, vol. 23, no. 10, p. 5632, 1981.

[83] S. A. Trugman, "Localization, percolation, and the quantum Hall effect," *Phys. Rev. B*, vol. 27, no. 12, p. 7539, 1983.

[84] D. J. Thouless, M. Kohmoto, M. P. Nightingale, and M. den Nijs, "Quantized Hall conductance in a two-dimensional periodic potential," *Phys. Rev. Lett.*, vol. 49, no. 6, p. 405, 1982.

[85] C. Z. Chang, J. Zhang, X. Feng, J. Shen, Z. Zhang, M. Guo, K. Li, Y. Ou, P. Wei, L. L. Wang *et al.*, "Experimental observation of the quantum anomalous Hall effect in a magnetic topological insulator," *Science*, vol. 340, no. 6129, pp. 167–170, 2013.

[86] C. Z. Chang, W. Zhao, D. Y. Kim, H. Zhang, B. A. Assaf, D. Heiman, S. C. Zhang, C. Liu, M. H. W. Chan, and J. S. Moodera, "High-precision realization of robust quantum anomalous Hall state in a hard ferromagnetic topological insulator," *Nat. Mat.*, vol. 14, no. 5, pp. 473–477, 2015.

[87] Y. Deng, Y. Yu, M. Z. Shi, Z. Guo, Z. Xu, J. Wang, X. H. Chen, and Y. Zhang, "Quantum anomalous Hall effect in intrinsic magnetic topological insulator $MnBi_2Te_4$," *Science*, vol. 367, no. 6480, pp. 895–900, 2020.

[88] N. Nagaosa, J. Sinova, S. Onoda, A. H. MacDonald, and N. P. Ong, "Anomalous Hall effect," *Rev. Mod. Phys.*, vol. 82, no. 2, pp. 1539–1592, 2010.

[89] M. Z. Hasan and C. L. Kane, "Colloquium: topological insulators," *Rev. Mod. Phys.*, vol. 82, no. 4, pp. 3045–3067, 2010.

[90] Y. Ando, "Topological insulator materials," *J. Phys. Soc. Japan*, vol. 82, no. 10, p. 102001, 2013.

[91] X. L. Qi and S. C. Zhang, "Topological insulators and superconductors," *Rev. Mod. Phys.*, vol. 83, no. 4, pp. 1057–1110, 2011.

[92] J. E. Moore, "The birth of topological insulators," *Nature*, vol. 464, no. 7286, pp. 194–198, 2010.

[93] C. Weeks and M. Franz, "Topological insulators on the Lieb and perovskite lattices," *Phys. Rev. B*, vol. 82, no. 8, p. 085310, 2010.

[94] N. Goldman, D. F. Urban, and D. Bercioux, "Topological phases for fermionic cold atoms on the Lieb lattice," *Phys. Rev. A*, vol. 83, no. 6, p. 063601, 2011.

[95] W. F. Tsai, C. Fang, H. Yao, and J. Hu, "Interaction-driven topological and nematic phases on the Lieb lattice," *New J. Phys.*, vol. 17, no. 5, p. 055016, 2015.

[96] K. Sun, H. Yao, E. Fradkin, and S. A. Kivelson, "Topological insulators and nematic phases from spontaneous symmetry breaking in 2D fermi systems with a quadratic band crossing," *Phys. Rev. Lett.*, vol. 103, no. 4, p. 046811, 2009.

[97] K. Ohgushi, S. Murakami, and N. Nagaosa, "Spin anisotropy and quantum Hall effect in the Kagomé lattice: Chiral spin state based on a ferromagnet," *Phys. Rev. B*, vol. 62, no. 10, p. R6065, 2000.

[98] Y. Xiao, V. Pelletier, P. M. Chaikin, and D. A. Huse, "Landau levels in the case of two degenerate coupled bands: Kagomé lattice tight-binding spectrum," *Phys. Rev. B*, vol. 67, no. 10, p. 104505, 2003.

[99] H. M. Guo and M. Franz, "Topological insulator on the Kagomé lattice," *Phys. Rev. B*, vol. 80, no. 11, p. 113102, 2009.

[100] A. R. Wright, "Realising Haldane's vision for a Chern insulator in buckled lattices," *Sci. Rep.*, vol. 3, no. 1, p. 2736, 2013.

[101] Y. Ding, Y. Peng, Y. Zhu, X. Fan, J. Yang, B. Liang, X. Zhu, X. Wan, and J. Cheng, "Experimental demonstration of acoustic Chern insulators," *Phys. Rev. Lett.*, vol. 122, no. 1, p. 014302, 2019.

[102] S. Mondal and S. Basu, "Topological features of the Haldane model on a dice lattice: Flat-band effect on transport properties," *Phys. Rev. B*, vol. 107, no. 3, p. 035421, 2023.

[103] B. Dey, P. Kapri, O. Pal, and T. K. Ghosh, "Unconventional phases in a Haldane model of dice lattice," *Phys. Rev. B*, vol. 101, no. 23, p. 235406, 2020.

[104] H. S. Kim and H. Y. Kee, "Realizing Haldane model in Fe-based honeycomb ferromagnetic insulators," *npj Quantum Materials*, vol. 2, no. 1, p. 20, 2017.

[105] K. F. Garrity and D. Vanderbilt, "Chern insulator at a magnetic rocksalt interface," *Phys. Rev. B*, vol. 90, no. 12, p. 121103, 2014.

[106] L. B. Shao, S. L. Zhu, L. Sheng, D. Y. Xing, and Z. D. Wang, "Realizing and detecting the quantum Hall effect without Landau levels by using ultracold atoms," *Phys. Rev. Lett.*, vol. 101, no. 24, p. 246810, 2008.

[107] E. Alba, X. F. Gonzalvo, J. M. Petit, J. K. Pachos, and J. J. G. Ripoll, "Seeing topological order in time-of-flight measurements," *Phys. Rev. Lett.*, vol. 107, no. 23, p. 235301, 2011.

[108] L. Tarruell, D. Greif, T. Uehlinger, G. Jotzu, and T. Esslinger, "Creating, moving and merging Dirac points with a fermi gas in a tunable honeycomb lattice," *Nature*, vol. 483, no. 7389, pp. 302–305, 2012.

[109] G. Jotzu, M. Messer, R. Desbuquois, M. Lebrat, T. Uehlinger, D. Greif, and T. Esslinger, "Experimental realization of the topological Haldane model with ultracold fermions," *Nature*, vol. 515, no. 7526, pp. 237–240, 2014.

[110] T. Andrijauskas, E. Anisimovas, M. Račiūnas, A. Mekys, V. Kudriašov, I. B. Spielman, and G. Juzeliūnas, "Three-level Haldane-like model on a dice optical lattice," *Phys. Rev. A*, vol. 92, no. 3, p. 033617, 2015.

[111] J. T. Devreese and A. S. Alexandrov, "Fröhlich polaron and bipolaron: recent developments," *Rep. Prog. Phys.*, vol. 72, no. 6, p. 066501, 2009.

[112] A. S. Alexandrov and J. T. Devreese, *Advances in polaron physics*. Springer, 2010, vol. 159.

[113] A. Chatterjee and S. Mukhopadhyay, *Polarons and bipolarons: an introduction*. CRC Press, 2018.

[114] M. Tinkham, *Introduction to superconductivity*. Courier Corporation, 2004, vol. 1.

[115] H. Fröhlich, "Theory of the superconducting state. I. the ground state at the absolute zero of temperature," *Phys. Rev.*, vol. 79, no. 5, p. 845, 1950.

[116] J. Bardeen, "Electron-vibration interactions and superconductivity," *Rev. Mod. Phys.*, vol. 23, no. 3, p. 261, 1951.

[117] J. M. Ziman, *Electrons and phonons: the theory of transport phenomena in solids*. Oxford university press, 2001.

[118] J. A. Yan, R. Stein, D. M. Schaefer, X. Q. Wang, and M. Y. Chou, "Electron-phonon coupling in two-dimensional silicene and germanene," *Phys. Rev. B*, vol. 88, no. 12, p. 121403, 2013.

[119] G. G. Samsonidze, E. B. Barros, R. Saito, J. Jiang, G. Dresselhaus, and M. S. Dresselhaus, "Electron-phonon coupling mechanism in two-dimensional graphite and single-wall carbon nanotubes," *Phys. Rev. B*, vol. 75, no. 15, p. 155420, 2007.

[120] S. Mukhopadhyay and A. Chatterjee, "Rayleigh-Schroedinger perturbation theory for electron-phonon interaction effects in polar semiconductor quantum dots with parabolic confinement," *Phys. Lett. A*, vol. 204, no. 5-6, pp. 411–417, 1995.

[121] L. Challis, *Electron-Phonon Interactions in Low-Dimensional Structures*. Oxford University Press, 2003.

[122] Y. Xie, Y. Li, P. Bourges, A. Ivanov, Z. Ye, J. X. Yin, M. Z. Hasan, A. Luo, Y. Yao, Z. Wang *et al.*, "Electron-phonon coupling in the charge density wave state of CsV_3Sb_5," *Phys. Rev. B*, vol. 105, no. 14, p. L140501, 2022.

[123] M. Campetella, G. Marini, J. S. Zhou, and M. Calandra, "Electron-phonon driven charge density wave in CuTe," *Phys. Rev. B*, vol. 108, no. 2, p. 024304, 2023.

[124] H. Luo, Q. Gao, H. Liu, Y. Gu, D. Wu, C. Yi, J. Jia, S. Wu, X. Luo, Y. Xu *et al.*, "Electronic nature of charge density wave and electron-phonon coupling in Kagomé superconductor KV_3Sb_5," *Nat. Comm.*, vol. 13, no. 1, p. 273, 2022.

[125] M. Koschorreck, D. Pertot, E. Vogt, B. Fröhlich, M. Feld, and M. Köhl, "Attractive and repulsive fermi polarons in two dimensions," *Nature*, vol. 485, no. 7400, pp. 619–622, 2012.

[126] A. Schirotzek, C. H. Wu, A. Sommer, and M. W. Zwierlein, "Observation of fermi polarons in a tunable fermi liquid of ultracold atoms," *Phys. Rev. Lett.*, vol. 102, no. 23, p. 230402, 2009.

[127] F. Scazza, G. Valtolina, P. Massignan, A. Recati, A. Amico, A. Burchianti, C. Fort, M. Inguscio, M. Zaccanti, and G. Roati, "Repulsive fermi polarons in a resonant mixture of ultracold Li_6 atoms," *Phys. Rev. Lett.*, vol. 118, no. 8, p. 083602, 2017.

[128] J. R. Senna and S. D. Sarma, "Electron-phonon interaction, Kohn anomalies, and the Peierls transition in semiconductor quantum wires," *Phys. Rev. B*, vol. 48, no. 7, p. 4552, 1993.

[129] K. Luo and X. Dai, "Transverse Peierls transition," *Phys. Rev. X*, vol. 13, no. 1, p. 011027, 2023.

[130] L. Zhang, U. Bhattacharya, A. Bachtold, S. Forstner, M. Lewenstein, F. Pistolesi, and T. Grass, "Steady-state Peierls transition in nanotube quantum simulator," *npj Quantum Information*, vol. 9, no. 1, p. 7, 2023.

[131] I. Garate, "Phonon-induced topological transitions and crossovers in Dirac materials," *Phys. Rev. Lett.*, vol. 110, no. 4, p. 046402, 2013.

[132] Z. Li and J. P. Carbotte, "Conductivity of Dirac fermions with phonon-induced topological crossover," *Phys. Rev. B*, vol. 88, no. 19, p. 195133, 2013.

[133] R. Heid, I. Y. Sklyadneva, and E. V. Chulkov, "Electron-phonon coupling in topological surface states: The role of polar optical modes," *Sci. Rep.*, vol. 7, no. 1, p. 1095, 2017.

[134] R. Schmidt and T. Enss, "Self-stabilized Bose polarons," *SciPost Physics*, vol. 13, no. 3, p. 054, 2022.

[135] M. G. Hu, M. J. V. de Graaff, D. Kedar, J. P. Corson, E. A. Cornell, and D. S. Jin, "Bose polarons in the strongly interacting regime," *Phys. Rev. Lett.*, vol. 117, no. 5, p. 055301, 2016.

[136] N. B. Jørgensen, L. Wacker, K. T. Skalmstang, M. M. Parish, J. Levinsen, R. S. Christensen, G. M. Bruun, and J. J. Arlt, "Observation of attractive and repulsive polarons in a Bose-Einstein condensate," *Phys. Rev. Lett.*, vol. 117, no. 5, p. 055302, 2016.

[137] S. Chaudhary, A. Haim, Y. Peng, and G. Refael, "Phonon-induced floquet topological phases protected by space-time symmetries," *Phys. Rev. R*, vol. 2, no. 4, p. 043431, 2020.

[138] H. Hübener, U. De Giovannini, and A. Rubio, "Phonon driven floquet matter," *Nano letters*, vol. 18, no. 2, pp. 1535–1542, 2018.

[139] T. Holstein, "Studies of polaron motion: Part II. the "small" polaron," *Annals of physics*, vol. 8, no. 3, pp. 343–389, 1959.

[140] J. Bonča, S. A. Trugman, and I. Batistić, "Holstein polaron," *Phys. Rev. B*, vol. 60, no. 3, p. 1633, 1999.

[141] K. S. Novoselov, A. K. Geim, S. V. Morozov, D. Jiang, Y. Zhang, S. V. Dubonos, I. V. Grigorieva, and A. A. Firsov, "Electric field effect in atomically thin carbon films," *Science*, vol. 306, no. 5696, pp. 666–669, 2004.

[142] K. S. Novoselov, A. K. Geim, S. V. Morozov, D. Jiang, M. I. Katsnelson, I. V. Grigorieva, S. V. Dubonos, and A. A. Firsov, "Two-dimensional gas of massless Dirac fermions in graphene," *Nature*, vol. 438, no. 7065, pp. 197–200, 2005.

[143] A. H. Castro Neto, F. Guinea, N. M. R. Peres, K. S. Novoselov, and A. K. Geim, "The electronic properties of graphene," *Rev. Mod. Phys.*, vol. 81, no. 1, pp. 109–162, 2009.

[144] N. Stander, B. Huard, and D. Goldhaber-Gordon, "Evidence for Klein tunneling in graphene p-n junctions," *Phys. Rev. Lett.*, vol. 102, no. 2, p. 026807, 2009.

[145] A. F. Young and P. Kim, "Quantum interference and Klein tunnelling in graphene heterojunctions," *Nat. Phys.*, vol. 5, no. 3, pp. 222–226, 2009.

[146] B. Huard, J. A. Sulpizio, N. Stander, K. Todd, B. Yang, and D. Goldhaber-Gordon, "Transport measurements across a tunable potential barrier in graphene," *Phys. Rev. Lett.*, vol. 98, no. 23, p. 236803, 2007.

[147] S. V. Morozov, K. S. Novoselov, M. I. Katsnelson, F. Schedin, L. A. Ponomarenko, D. Jiang, and A. K. Geim, "Strong suppression of weak localization in graphene," *Phys. Rev. Lett.*, vol. 97, no. 1, p. 016801, 2006.

[148] Y. Zheng and T. Ando, "Hall conductivity of a two-dimensional graphite system," *Phys. Rev. B*, vol. 65, no. 24, p. 245420, 2002.

[149] V. P. Gusynin and S. G. Sharapov, "Unconventional integer quantum Hall effect in graphene," *Phys. Rev. Lett.*, vol. 95, no. 14, p. 146801, 2005.

[150] Y. Zhang, Y. W. Tan, H. L. Stormer, and P. Kim, "Experimental observation of the quantum Hall effect and Berry's phase in graphene," *Nature*, vol. 438, no. 7065, pp. 201–204, 2005.

[151] K. S. Novoselov, Z. Jiang, Y. Zhang, S. V. Morozov, H. L. Stormer, U. Zeitler, J. C. Maan, G. S. Boebinger, P. Kim, and A. K. Geim, "Room-temperature quantum Hall effect in graphene," *Science*, vol. 315, no. 5817, pp. 1379–1379, 2007.

[152] B. Sutherland, "Localization of electronic wave functions due to local topology," *Phys. Rev. B*, vol. 34, no. 8, p. 5208, 1986.

[153] J. Vidal, R. Mosseri, and B. Douçot, "Aharonov-Bohm cages in two-dimensional structures," *Phys. Rev. Lett.*, vol. 81, no. 26, p. 5888, 1998.

[154] D. F. Urban, D. Bercioux, M. Wimmer, and W. Häusler, "Barrier transmission of Dirac-like pseudospin-one particles," *Phys. Rev. B*, vol. 84, no. 11, p. 115136, 2011.

[155] J. D. Malcolm and E. J. Nicol, "Frequency-dependent polarizability, plasmons, and screening in the two-dimensional pseudospin-1 dice lattice," *Phys. Rev. B*, vol. 93, no. 16, p. 165433, 2016.

[156] D. Bercioux, D. F. Urban, H. Grabert, and W. Häusler, "Massless dirac-weyl fermions in a T_3 optical lattice," *Phys. Rev. A*, vol. 80, no. 6, p. 063603, 2009.

[157] F. Wang and Y. Ran, "Nearly flat band with Chern number C = 2 on the dice lattice," *Phys. Rev. B*, vol. 84, no. 24, p. 241103, 2011.

[158] B. Dóra, J. Kailasvuori, and R. Moessner, "Lattice generalization of the Dirac equation to general spin and the role of the flat band," *Phys. Rev. B*, vol. 84, no. 19, p. 195422, 2011.

[159] J. D. Malcolm and E. J. Nicol, "Magneto-optics of general pseudospin-s two-dimensional Dirac-Weyl fermions," *Phys. Rev. B*, vol. 90, no. 3, p. 035405, 2014.

[160] Z. Lan, N. Goldman, A. Bermudez, W. Lu, and P. Öhberg, "Dirac-Weyl fermions with arbitrary spin in two-dimensional optical superlattices," *Phys. Rev. B*, vol. 84, no. 16, p. 165115, 2011.

[161] E. Illes, "Properties of the α-T_3 model," Ph.D. dissertation, University of Guelph, 2017.

[162] J. D. Malcolm and E. J. Nicol, "Magneto-optics of massless Kane fermions: Role of the flat band and unusual Berry phase," *Phys. Rev. B*, vol. 92, no. 3, p. 035118, 2015.

[163] E. Illes, J. P. Carbotte, and E. J. Nicol, "Hall quantization and optical conductivity evolution with variable Berry phase in the α-T_3 model," *Phys. Rev. B*, vol. 92, no. 24, p. 245410, 2015.

[164] T. Biswas and T. K. Ghosh, "Magnetotransport properties of the α-T_3 model," *J. Phys.: Cond. Matt.*, vol. 28, no. 49, p. 495302, 2016.

[165] B. Gulácsi, M. Heyl, and B. Dóra, "Geometrical quench and dynamical quantum phase transition in the α- T_3 lattice," *Phys. Rev. B*, vol. 101, no. 20, p. 205135, 2020.

[166] J. Wang, J. F. Liu, and C. S. Ting, "Recovered minimal conductivity in the α-T_3 model," *Phys. Rev. B*, vol. 101, no. 20, p. 205420, 2020.

[167] A. Filusch, A. R. Bishop, A. Saxena, G. Wellein, and H. Fehske, "Valley filtering in strain-induced α-T_3 quantum dots," *Phys. Rev. B*, vol. 103, no. 16, p. 165114, 2021.

[168] N. Weekes, A. Iurov, L. Zhemchuzhna, G. Gumbs, and D. Huang, "Generalized WKB theory for electron tunneling in gapped α-T_3 lattices," *Phys. Rev. B*, vol. 103, no. 16, p. 165429, 2021.

[169] J. Sun, T. Liu, Y. Du, and H. Guo, "Strain-induced pseudo magnetic field in the α-T_3 lattice," *Phys. Rev. B*, vol. 106, no. 15, p. 155417, 2022.

[170] R. Khomeriki and S. Flach, "Landau-Zener Bloch oscillations with perturbed flat bands," *Phys. Rev. Lett.*, vol. 116, no. 24, p. 245301, 2016.

[171] A. Fang, Z. Q. Zhang, S. G. Louie, and C. T. Chan, "Klein tunneling and supercollimation of pseudospin-1 electromagnetic waves," *Phys. Rev. B*, vol. 93, no. 3, p. 035422, 2016.

[172] M. A. Mojarro, V. G. Ibarra-Sierra, J. C. Sandoval-Santana, R. Carrillo-Bastos, and G. G. Naumis, "Electron transitions for Dirac hamiltonians with flat bands under electromagnetic radiation: Application to the α-T_3 graphene model," *Phys. Rev. B*, vol. 101, no. 16, p. 165305, 2020.

[173] E. Illes and E. J. Nicol, "Magnetic properties of the α-T_3 model: Magneto-optical conductivity and the hofstadter butterfly," *Phys. Rev. B*, vol. 94, no. 12, p. 125435, 2016.

[174] S. F. Islam and P. Dutta, "Valley-polarized magnetoconductivity and particle-hole symmetry breaking in a periodically modulated α-T_3 lattice," *Phys. Rev. B*, vol. 96, no. 4, p. 045418, 2017.

[175] B. Dey and T. K. Ghosh, "Photoinduced valley and electron-hole symmetry breaking in α-T_3 lattice: The role of a variable Berry phase," *Phys. Rev. B*, vol. 98, no. 7, p. 075422, 2018.

[176] T. Louvet, P. Delplace, A. A. Fedorenko, and D. Carpentier, "On the origin of minimal conductivity at a band crossing," *Phys. Rev. B*, vol. 92, no. 15, p. 155116, 2015.

[177] R. Shen, L. B. Shao, B. Wang, and D. Y. Xing, "Single Dirac cone with a flat band touching on line-centered-square optical lattices," *Phys. Rev. B*, vol. 81, no. 4, p. 041410, 2010.

[178] E. Illes and E. J. Nicol, "Klein tunneling in the α-T_3 model," *Phys. Rev. B*, vol. 95, no. 23, p. 235432, 2017.

[179] Y. Betancur-Ocampo, G. Cordourier-Maruri, V. Gupta, and R. De Coss, "Super-Klein tunneling of massive pseudospin-one particles," *Phys. Rev. B*, vol. 96, no. 2, p. 024304, 2017.

[180] E. V. Gorbar, V. P. Gusynin, and D. O. Oriekhov, "Electron states for gapped pseudospin-1 fermions in the field of a charged impurity," *Phys. Rev.B*, vol. 99, no. 15, p. 155124, 2019.

[181] E. V. Gorbar, V. P. Gusynin, and D. O. Oriekhov, "Gap generation and flat band catalysis in dice model with local interaction," *Phys. Rev. B*, vol. 103, no. 15, p. 155155, 2021.

[182] L. Chen, J. Zuber, Z. Ma, and C. Zhang, "Nonlinear optical response of the α-T_3 model due to the nontrivial topology of the band dispersion," *Phys. Rev. B*, vol. 100, no. 3, p. 035440, 2019.

[183] D. Bercioux, N. Goldman, and D. F. Urban, "Topology-induced phase transitions in quantum spin Hall lattices," *Phys. Rev. A*, vol. 83, no. 2, p. 023609, 2011.

[184] B. Dey and T. K. Ghosh, "Floquet topological phase transition in the α-T_3 lattice," *Phys. Rev. B*, vol. 99, no. 20, p. 205429, 2019.

[185] S. Cheng, H. Yin, Z. Lu, C. He, P. Wang, and G. Xianlong, "Predicting large-Chern-number phases in a shaken optical dice lattice," *Phys. Rev. A*, vol. 101, no. 4, p. 043620, 2020.

[186] J. Wang and J. F. Liu, "Quantum spin Hall phase transition in the α-T_3 lattice," *Phys. Rev. B*, vol. 103, no. 7, p. 075419, 2021.

[187] A. Iurov, G. Gumbs, and D. Huang, "Peculiar electronic states, symmetries, and Berry phases in irradiated α-T_3 materials," *Phys. Rev. B*, vol. 99, no. 20, p. 205135, 2019.

[188] A. Iurov, L. Zhemchuzhna, D. Dahal, G. Gumbs, and D. Huang, "Quantum-statistical theory for laser-tuned transport and optical conductivities of dressed electrons in α- T_3 materials," *Phys. Rev. B*, vol. 101, no. 3, p. 035129, 2020.

[189] T. Biswas and T. K. Ghosh, "Dynamics of a quasiparticle in the α-T_3 model: role of pseudospin polarization and transverse magnetic field on zitterbewegung," . *Phys.: Cond. Matt.*, vol. 30, no. 7, p. 075301, 2018.

[190] A. Balassis, D. Dahal, G. Gumbs, A. Iurov, D. Huang, and O. Roslyak, "Magnetoplasmons for the α-T_3 model with filled Landau levels," *J. Phys.: Cond. Matt.*, vol. 32, no. 48, p. 485301, 2020.

[191] A. Iurov, L. Zhemchuzhna, G. Gumbs, D. Huang, D. Dahal, and Y. Abranyos, "Finite-temperature plasmons, damping, and collective behavior in the α-T_3 model," *Phys. Rev. B*, vol. 105, no. 24, p. 245414, 2022.

[192] D. O. Oriekhov and V. P. Gusynin, "RKKY interaction in a doped pseudospin-1 fermion system at finite temperature," *Phys. Rev. B*, vol. 101, no. 23, p. 235162, 2020.

[193] O. Roslyak, G. Gumbs, A. Balassis, and H. Elsayed, "Effect of magnetic field and chemical potential on the RKKY interaction in the α-T_3 lattice," *Phys. Rev. B*, vol. 103, no. 7, p. 075418, 2021.

[194] M. W. Alam, B. Souayeh, and S. F. Islam, "Enhancement of thermoelectric performance of a nanoribbon made of α-T_3 lattice," *J. Phys.: Cond. Matt.*, vol. 31, no. 48, p. 485303, 2019.

[195] E. Tang, J. W. Mei, and X. G. Wen, "High-temperature fractional quantum Hall states," *Phys. Rev. Lett.*, vol. 106, no. 23, p. 236802, 2011.

[196] K. Sun, Z. Gu, H. Katsura, and S. D. Sarma, "Nearly flatbands with nontrivial topology," *Phys. Rev. Lett.*, vol. 106, no. 23, p. 236803, 2011.

[197] J. W. McClure, "Diamagnetism of graphite," *Phys. Rev.*, vol. 104, no. 3, p. 666, 1956.

[198] X. Zhou, "Andreev reflection and Josephson effect in the α-T_3 lattice," *Phys. Rev. B*, vol. 104, no. 12, p. 125441, 2021.

[199] M. Islam and P. Kapri, "Electrical and thermal transport through α-T_3 NIS junction," *J. Phys.: Cond. Matt.*, vol. 35, no. 10, p. 105301, 2022.

[200] W. Zeng and R. Shen, "Pure crossed Andreev reflection assisted transverse valley currents in α-T_3 lattices," *Phys. Rev. B*, vol. 106, no. 9, p. 094503, 2022.

[201] L. Tamang, T. Nag, and T. Biswas, "Floquet engineering of low-energy dispersions and dynamical localization in a periodically kicked three-band system," *Phys. Rev. B*, vol. 104, no. 17, p. 174308, 2021.

[202] L. Tamang and T. Biswas, "Probing topological signatures in an optically driven α-T_3 lattice," *Phys. Rev. B*, vol. 107, no. 8, p. 085408, 2023.

[203] F. E. Meijer, A. F. Morpurgo, and T. M. Klapwijk, "One-dimensional ring in the presence of rashba spin-orbit interaction: Derivation of the correct hamiltonian," *Phys. Rev. B*, vol. 66, no. 3, p. 033107, 2002.

[204] Y. Aharonov and D. Bohm, "Significance of electromagnetic potentials in the quantum theory," *Phys. Rev.*, vol. 115, no. 3, p. 485, 1959.

[205] J. J. Sakurai, S. Fu T., and R. G. Newton, "Modern quantum mechanics," 1986.

[206] S. H. Simon, "Topological quantum: Lecture notes and proto-book," *Unpublished prototype.[online] Available at: http://www-thphys. physics. ox. ac. uk/people/SteveSimon*, vol. 26, p. 35, 2020.

[207] M. O. Katanaev and I. V. Volovich, "Theory of defects in solids and three-dimensional gravity," *Annals of Physics*, vol. 216, no. 1, pp. 1–28, 1992.

[208] M. V. Entin and L. I. Magarill, "Spin-orbit interaction of electrons on a curved surface," *Phys. Rev. B*, vol. 64, no. 8, p. 085330, 2001.

[209] K. Kawamura, "Scattering of a tight-binding electron off an edge dislocation," *Z. Phys. B Cond. Matt.*, vol. 48, no. 3, pp. 201–207, 1982.

[210] R. Bausch, R. Schmitz, and L. A. Turski, "Single-particle quantum states in a crystal with topological defects," *Phys. Rev. Lett.*, vol. 80, no. 11, p. 2257, 1998.

[211] A. Turski, R. Bausch, and R. Schmitz, "Gauge theory of sound propagation in crystals with dislocations," *J. Phys.: Cond. Matt.*, vol. 19, no. 9, p. 096211, 2007.

[212] S. Azevedo and F. Moraes, "Topological Aharonov-Bohm effect around a disclination," *Phys. Lett. A*, vol. 246, no. 3-4, pp. 374–376, 1998.

[213] S. Azevedo and J. Pereira, "Double Aharonov-Bohm effect in a medium with a disclination," *Phys. Lett. A*, vol. 275, no. 5-6, pp. 463–466, 2000.

[214] C. A. de L. Ribeiro, A. M. de M. Carvalho, and C. Furtado, "Quantum scattering of an electric dipole by a charged screw dislocation," *Prog. Theo. Phys.*, vol. 124, no. 4, pp. 547–553, 2010.

[215] E. Aurell, "Torsion and electron motion in quantum dots with crystal lattice dislocations," *J. Physics A: Math. Gen.*, vol. 32, no. 4, p. 571, 1999.

[216] D. S. Fisher and P. A. Lee, "Relation between conductivity and transmission matrix," *Phys. Rev. B*, vol. 23, no. 12, p. 6851, 1981.

[217] Y. Büttiker, M .and Imry, R. Landauer, and S. Pinhas, "Generalized many-channel conductance formula with application to small rings," *Phys. Rev. B*, vol. 31, no. 10, p. 6207, 1985.

[218] M. Y. Azbel, "Generalized Landauer formula," *Phys. Lett. A*, vol. 78, no. 4, pp. 410–412, 1980.

[219] P. W. Anderson, D. J. Thouless, E. Abrahams, and D. S. Fisher, "New method for a scaling theory of localization," *Phys. Rev. B*, vol. 22, no. 8, p. 3519, 1980.

[220] R. Landauer, "Spatial variation of currents and fields due to localized scatterers in metallic conduction," *IBM J. Res. Dev.*, vol. 1, no. 3, pp. 223–231, 1957.

[221] R. Landauer, "Electrical resistance of disordered one-dimensional lattices," *Philos. Mag.*, vol. 21, no. 172, pp. 863–867, 1970.

[222] M. Büttiker, "Symmetry of electrical conduction," *IBM J. Res. Dev.*, vol. 32, no. 3, pp. 317–334, 1988.

[223] M. Büttiker, "Voltage fluctuations in small conductors," *Phys. Rev. B*, vol. 35, no. 8, p. 4123, 1987.

[224] S. Datta, *Electronic transport in mesoscopic systems*. Cambridge university press, 1997.

[225] Y. Imry, "Physics of mesoscopic systems," in *Directions in Condensed Matter Physics: Memorial Volume in Honor of Shang-keng Ma*. World Scientific, 1986, pp. 101–163.

[226] R. Landauer, "Conductance determined by transmission: probes and quantised constriction resistance," *J. Phys. Cond. Matt.*, vol. 1, no. 43, p. 8099, 1989.

[227] Y. Imry and R. Landauer, "Conductance viewed as transmission," *Rev. Mod. Phys.*, vol. 71, no. 2, p. S306, 1999.

[228] D. Thouless, *Topological Quantum Numbers In Nonrelativistic Physics*. World Scientific Publishing Company, 1998.

[229] J. E. Avron, J. Sadun, L.and Segert, and B. Simon, "Topological invariants in fermi systems with time-reversal invariance," *Phys. Rev. Lett.*, vol. 61, no. 12, p. 1329, 1988.

[230] M. V. Berry, "Quantal phase factors accompanying adiabatic changes," *Proceedings of the Royal Society of London. A. Mathematical and Physical Sciences*, vol. 392, no. 1802, pp. 45–57, 1984.

[231] D. Xiao, M.-C. Chang, and Q. Niu, "Berry phase effects on electronic properties," *Reviews of modern physics*, vol. 82, no. 3, pp. 1959–2007, 2010.

[232] A. Bohm, A. Mostafazadeh, H. Koizumi, Q. Niu, and J. Zwanziger, *The Geometric phase in quantum systems: foundations, mathematical concepts, and applications in molecular and condensed matter physics*. Springer Science & Business Media, 2013.

[233] A. Shapere and F. Wilczek, *Geometric phases in physics*. World scientific, 1989, vol. 5.

[234] R. Y. Chiao and Y.-S. Wu, "Manifestations of Berry's topological phase for the photon," *Physical review letters*, vol. 57, no. 8, p. 933, 1986.

[235] B. Simon, "Holonomy, the quantum adiabatic theorem, and Berry's phase," *Physical Review Letters*, vol. 51, no. 24, p. 2167, 1983.

[236] B. A. Bernevig, *Topological insulators and topological superconductors*. Princeton university press, 2013.

[237] R. Shankar and H. Mathur, "Thomas precession, Berry potential, and the meron," *Phys. Rev. Lett.*, vol. 73, no. 12, p. 1565, 1994.

[238] T. Kato, "On the adiabatic theorem of quantum mechanics," *Journal of the Physical Society of Japan*, vol. 5, no. 6, pp. 435–439, 1950.

[239] C.-X. Liu, S.-C. Zhang, and X.-L. Qi, "The quantum anomalous Hall effect: theory and experiment," *Annual Review of Condensed Matter Physics*, vol. 7, no. 1, pp. 301–321, 2016.

[240] N. Marzari and D. Vanderbilt, "Maximally localized generalized Wannier functions for composite energy bands," *Phys. Rev. B*, vol. 56, no. 20, p. 12847, 1997.

[241] C. Sgiarovello, M. Peressi, and R. Resta, "Electron localization in the insulating state: Application to crystalline semiconductors," *Phys. Rev. B*, vol. 64, no. 11, p. 115202, 2001.

[242] J. Zak, "Berry's phase for energy bands in solids," *Phys. Rev. Lett.*, vol. 62, no. 23, p. 2747, 1989.

[243] E. I. Blount, "Formalisms of band theory," in *Solid state physics*. Elsevier, 1962, vol. 13, pp. 305–373.

[244] A. A. Soluyanov and D. Vanderbilt, "Wannier representation of $\mathbb{Z}_2$ topological insulators," *Phys. Rev. B*, vol. 83, no. 3, p. 035108, 2011.

[245] M. Taherinejad, K. F. Garrity, and D. Vanderbilt, "Wannier center sheets in topological insulators," *Phys. Rev. B*, vol. 89, no. 11, p. 115102, 2014.

[246] D. Gresch, G. Autès, O. V. Yazyev, M. Troyer, D. Vanderbilt, B. A. Bernevig, and A. A. Soluyanov, "Z2pack: Numerical implementation of hybrid Wannier centers for identifying topological materials," *Phys. Rev. B*, vol. 95, p. 075146, 2017.

[247] Y. Chen, Y. Xie, X. Yan, M. L. Cohen, and S. Zhang, "Topological carbon materials: A new perspective," *Phys. Rep.*, vol. 868, pp. 1–32, 2020.

[248] C. L. Kane and E. J. Mele, "$\mathbb{Z}_2$ topological order and the quantum spin Hall effect," *Phys. Rev. Lett.*, vol. 95, no. 14, p. 146802, 2005.

[249] D. J. Griffiths, *Introduction to quantum mechanics*. Cambridge university press, 2018.

[250] W. Greiner, *Relativistic quantum mechanics*. Springer, 2000, vol. 2.

[251] G. Dresselhaus, "Spin-orbit coupling effects in zinc blende structures," *Phys. Rev.*, vol. 100, no. 2, p. 580, 1955.

[252] R. Winkler, S. Papadakis, E. De Poortere, and M. Shayegan, *Spin-orbit coupling in two-dimensional electron and hole systems*. Springer, 2003, vol. 41.

[253] N. A. Sinitsyn, E. M. Hankiewicz, W. Teizer, and J. Sinova, "Spin Hall and spin-diagonal conductivity in the presence of Rashba and Dresselhaus spin-orbit coupling," *Phys. Rev. B*, vol. 70, no. 8, p. 081312, 2004.

[254] D. Bercioux and P. Lucignano, "Quantum transport in Rashba spin-orbit materials: a review," *Rep. Prog. Phys.*, vol. 78, no. 10, p. 106001, 2015.

[255] D. Culcer, A. MacDonald, and Q. Niu, "Anomalous Hall effect in paramagnetic two-dimensional systems," *Phys. Rev. B*, vol. 68, no. 4, p. 045327, 2003.

[256] S. Murakami, N. Nagaosa, and S. C. Zhang, "Dissipationless quantum spin current at room temperature," *Science*, vol. 301, no. 5638, pp. 1348–1351, 2003.

[257] C. L. Kane and E. J. Mele, "Quantum spin Hall effect in graphene," *Phys. Rev. Lett.*, vol. 95, no. 22, p. 226801, 2005.

[258] C. L. Kane, "Topological band theory and the $\mathbb{Z}_2$ invariant," in *Cont. Conc. Cond. Matt. Sci.* Elsevier, 2013, vol. 6, pp. 3–34.

[259] L. Fu and C. L. Kane, "Time reversal polarization and a $\mathbb{Z}_2$ adiabatic spin pump," *Phys. Rev. B*, vol. 74, no. 19, p. 195312, 2006.

[260] I. G. Lang and Y. A. Firsov, "Kinetic theory of semiconductors with low mobility," *Sov. Phys. JETP*, vol. 16, no. 5, p. 1301, 1963.

[261] A. Altland and M. R. Zirnbauer, "Nonstandard symmetry classes in mesoscopic normal-superconducting hybrid structures," *Phys. Rev. B*, vol. 55, no. 2, p. 1142, 1997.

[262] U. F. Keyser, C. Fühner, S. Borck, R. J. Haug, M. Bichler, G. Abstreiter, and W. Wegscheider, "Kondo effect in a few-electron quantum ring," *Phys. Rev. Lett.*, vol. 90, no. 19, p. 196601, 2003.

[263] J. Appenzeller, T. Schäpers, H. Hardtdegen, B. Lengeler, and H. Lüth, "Aharonov-Bohm effect in quasi-one-dimensional $In_{0.77}Ga_{0.23}As$/InP rings," *Phys. Rev. B*, vol. 51, no. 7, p. 4336, 1995.

[264] A. Yacoby, M. Heiblum, D. Mahalu, and H. Shtrikman, "Coherence and phase sensitive measurements in a quantum dot," *Phys. Rev. Lett.*, vol. 74, no. 20, p. 4047, 1995.

[265] J. A. Stroscio and D. M. Eigler, "Atomic and molecular manipulation with the scanning tunneling microscope," *Science*, vol. 254, no. 5036, pp. 1319–1326, 1991.

[266] V. D. Pham, K. Kanisawa, and S. Fölsch, "Quantum rings engineered by atom manipulation," *Phys. Rev. Lett.*, vol. 123, no. 6, p. 066801, 2019.

[267] P. Földi, B. Molnár, M. G. Benedict, and F. M. Peeters, "Spintronic single-qubit gate based on a quantum ring with spin-orbit interaction," *Phys. Rev. B*, vol. 71, no. 3, p. 033309, 2005.

[268] S. K. Maiti, "Electron transport in a double quantum ring: Evidence of an and gate," *Phys. Lett. A*, vol. 373, no. 48, pp. 4470–4474, 2009.

[269] W. H. Lin, M. Y. Lin, S. Y. Wu, and S. Y. Lin, "Room-temperature electro-luminescence of type-II GaSb/GaAs quantum rings," *IEEE Photon. Technol. Lett.*, vol. 24, no. 14, pp. 1203–1205, 2012.

[270] J. Wu, Z. Li, D. Shao, M. O. Manasreh, V. P. Kunets, Z. M. Wang, G. J. Salamo, and B. D. Weaver, "Multicolor photodetector based on gaas quantum rings grown by droplet epitaxy," *Appl. Phys. Lett.*, vol. 94, no. 17, 2009.

[271] M. Lee and C. Bruder, "Spin filter using a semiconductor quantum ring side coupled to a quantum wire," *Phys. Rev. B*, vol. 73, no. 8, p. 085315, 2006.

[272] M. Grujić, M. Tadić, and F. M. Peeters, "Antiferromagnetism in hexagonal graphene structures: Rings versus dots," *Phys. Rev. B*, vol. 87, no. 8, p. 085434, 2013.

[273] H. A. Fertig and L. Brey, "Nanophysics in graphene: neutrino physics in quantum rings and superlattices," *Philo. Trans. Royal Society A: Mathematical, Physical and Engineering Sciences*, vol. 368, no. 1932, pp. 5483–5497, 2010.

[274] L. J. P. Xavier, D. R. Da Costa, A. Chaves, J. M. Pereira, and G. A. Farias, "Electronic confinement in graphene quantum rings due to substrate-induced mass radial kink," *J. Phys.: Cond. Matt.*, vol. 28, no. 50, p. 505501, 2016.

[275] J. A. Neto, M. J. Bueno, and C. Furtado, "Two-dimensional quantum ring in a graphene layer in the presence of a Aharonov–Bohm flux," *Ann. Phys.*, vol. 373, pp. 273–285, 2016.

[276] B. Molnár, F. M. Peeters, and P. Vasilopoulos, "Spin-dependent magnetotransport through a ring due to spin-orbit interaction," *Phys. Rev. B*, vol. 69, no. 15, p. 155335, 2004.

[277] K. Novoselov, "Mind the gap," *Nat. Mat.*, vol. 6, no. 10, pp. 720–721, 2007.

[278] G. W. Semenoff, "Condensed-matter simulation of a three-dimensional anomaly," *Phys. Rev. Lett.*, vol. 53, no. 26, p. 2449, 1984.

[279] B. Hunt, J. D. S. Yamagishi, A. F. Young, M. Yankowitz, B. J. LeRoy, K. Watanabe, T. Taniguchi, P. Moon, M. Koshino, P. J. Herrero *et al.*, "Massive Dirac fermions and hofstadter butterfly in a van der Waals heterostructure," *Science*, vol. 340, no. 6139, pp. 1427–1430, 2013.

[280] M. Kindermann, B. Uchoa, and D. L. Miller, "Zero-energy modes and gate-tunable gap in graphene on hexagonal boron nitride," *Phys. Rev. B*, vol. 86, no. 11, p. 115415, 2012.

[281] G. Giovannetti, P. A. Khomyakov, G. Brocks, P. J. Kelly, and J. Van Den Brink, "Substrate-induced band gap in graphene on hexagonal boron nitride: Ab initio density functional calculations," *Phys. Rev. B*, vol. 76, no. 7, p. 073103, 2007.

[282] Y. Fan, M. Zhao, Z. Wang, X. Zhang, and H. Zhang, "Tunable electronic structures of graphene/boron nitride heterobilayers," *Appl. Phys. Lett.*, vol. 98, no. 8, 2011.

[283] G. W. Semenoff, V. Semenoff, and F. Zhou, "Domain walls in gapped graphene," *Phys. Rev. Lett.*, vol. 101, no. 8, p. 087204, 2008.

[284] X. Ye, S. S. Ke, X. W. Du, Y. Guo, and H. F. Lü, "Quantum tunneling in the α-T_3 model with an effective mass term," *J. Low Temp. Phys.*, vol. 199, no. 5, pp. 1332–1343, 2020.

[285] G. Autès and O. V. Yazyev, "Engineering quantum spin Hall effect in graphene nanoribbons via edge functionalization," *Phys. Rev. B*, vol. 87, no. 24, p. 241404, 2013.

[286] H. Min, J. E. Hill, N. A. Sinitsyn, B. R. Sahu, L. Kleinman, and A. H. MacDonald, "Intrinsic and Rashba spin-orbit interactions in graphene sheets," *Phys. Rev. B*, vol. 74, no. 16, p. 165310, 2006.

[287] K. Shakouri, B. Szafran, M. Esmaeilzadeh, and F. M. Peeters, "Effective spin-orbit interaction hamiltonian for quasi-one-dimensional quantum rings," *Phys. Rev. B*, vol. 85, no. 16, p. 165314, 2012.

[288] R. Soni, N. Kaushal, S. Okamoto, and E. Dagotto, "Flat bands and ferrimagnetic order in electronically correlated dice-lattice ribbons," *Phys. Rev. B*, vol. 102, no. 4, p. 045105, 2020.

[289] R. Soni, A. B. Sanyal, N. Kaushal, S. Okamoto, A. Moreo, and E. Dagotto, "Multitude of topological phase transitions in bipartite dice and Lieb lattices with interacting electrons and Rashba coupling," *Phys. Rev. B*, vol. 104, no. 23, p. 235115, 2021.

[290] L. Brey and H. A. Fertig, "Electronic states of graphene nanoribbons studied with the Dirac equation," *Phys. Rev. B*, vol. 73, no. 23, p. 235411, 2006.

[291] X. Xu, W. Yao, D. Xiao, and T. F. Heinz, "Spin and pseudospins in layered transition metal dichalcogenides," *Nat. Physics*, vol. 10, no. 5, pp. 343–350, 2014.

[292] M. Ezawa, "Spin-valley optical selection rule and strong circular dichroism in silicene," *Phys. Rev. B*, vol. 86, no. 16, p. 161407, 2012.

[293] A. C. Bleszynski-Jayich, W. E. Shanks, B. Peaudecerf, E. Ginossar, F. Von Oppen, L. Glazman, and J. G. E. Harris, "Persistent currents in normal metal rings," *Science*, vol. 326, no. 5950, pp. 272–275, 2009.

[294] L. Ci, Z. Xu, L. Wang, W. Gao, F. Ding, K. F. Kelly, B. I. Yakobson, and P. M. Ajayan, "Controlled nanocutting of graphene," *Nano Research*, vol. 1, pp. 116–122, 2008.

[295] J. Balakrishnan, G. Kok Wai Koon, M. Jaiswal, A. H. Castro Neto, and B. Özyilmaz, "Colossal enhancement of spin–orbit coupling in weakly hydrogenated graphene," *Nat. Physics*, vol. 9, no. 5, pp. 284–287, 2013.

[296] V. Grinenko, R. Sarkar, S. Ghosh, D. Das, Z. Guguchia, H. Luetkens, I. Shipulin, A. Ramires, N. Kikugawa, Y. Maeno, K. Ishida, C. W. Hicks, and H. H. Klauss, "μSR measurements on Sr_2RuO_4 under <110> uniaxial stress," *Phys. Rev. B*, vol. 107, no. 2, p. 024508, 2023.

[297] N. Zhang, P. Carrez, and R. Shahsavari, "Screw-dislocation-induced strengthening–toughening mechanisms in complex layered materials: the case study of tobermorite," *ACS Appl. Mat. Inter.*, vol. 9, no. 2, pp. 1496–1506, 2017.

[298] X. Sun, X. Feng, X. Y. Yan, J. Luo, R. Zhang, T. Li, H. Li, J. Chen, F. Liu, E. Raee, S. Z. D. Cheng, and T. Liu, "Screw dislocation-induced pyramidal crystallization of dendron-like macromolecules featuring asymmetric geometry," *Chem. Sci.*, vol. 12, no. 36, pp. 12 130–12 137, 2021.

[299] H. Xue, D. Jia, Y. Ge, Y. Guan, Q. Wang, S. Yuan, H. Sun, Y. D. Chong, and B. Zhang, "Observation of dislocation-induced topological modes in a three-dimensional acoustic topological insulator," *Phys. Rev. Lett.*, vol. 127, no. 21, p. 214301, 2021.

[300] V. Atanasov, R. Dandoloff, and A. Saxena, "Geometry-induced charge separation on a helicoidal ribbon," *Phys. Revi. B*, vol. 79, no. 3, p. 033404, 2009.

[301] R. Dandoloff, A. Saxena, and B. Jensen, "Geometry-induced potential on a two-dimensional section of a wormhole: Catenoid," *Phys. Revi. A*, vol. 81, no. 1, p. 014102, 2010.

[302] O. Mustafa and Z. Algadhi, "Position-dependent mass schrödinger particles in space-like screw dislocation: associated degeneracies and magnetic and Aharonov–Bohm flux fields effects," *Quant. Stud.: Math. Foun.*, vol. 10, no. 2, pp. 263–277, 2023.

[303] M. K. Bahar and P. Başer, "Nonlinear optical specifications of the Mathieu quantum dot with screw dislocation," *Eur. Phys. Jour. Plus*, vol. 138, no. 8, p. 724, 2023.

[304] M. K. Bahar and F. Ungan, "Magneto-optical specifications of Rosen-Morse quantum dot with screw dislocation," *Inter. Jour. Quan. Chem.*, vol. 120, no. 11, p. e26186, 2020.

[305] E. Schafler, M. Zehetbauer, and T. Ungar, "Measurement of screw and edge dislocation density by means of x-ray Bragg profile analysis," *Mat. Sci. Eng.: A*, vol. 319, pp. 220–223, 2001.

[306] P. Castany, F. Pettinari-Sturmel, J. Crestou, J. Douin, and A. Coujou, "Experimental study of dislocation mobility in a Ti–6Al–4V alloy," *Acta Materialia*, vol. 55, no. 18, pp. 6284–6291, 2007.

[307] Z. Li and L. R. Ram-Mohan, "Quantum mechanics on a Möbius ring: Energy levels, symmetry, optical transitions, and level splitting in a magnetic field," *Phys. Rev. B*, vol. 85, no. 19, p. 195438, 2012.

[308] W. C. F. da Silva and K. Bakke, "Topological effects of a spiral dislocation on quantum rings," *Annals of Physics*, vol. 421, p. 168277, 2020.

[309] S. Q. Lin, H. Tan, P. H. Fu, and J. F. Liu, "Interaction-driven Chern insulating phases in the α-T_3 lattice with Rashba spin-orbit coupling," *Iscience*, vol. 26, no. 9, 2023.

[310] C. R. Hagen, "Aharonov-Bohm scattering of particles with spin," *Phys. Rev. Lett.*, vol. 64, no. 5, p. 503, 1990.

[311] C. R. Hagen, "Aharonov-Bohm scattering amplitude," *Phys. Rev. D*, vol. 41, no. 6, p. 2015, 1990.

[312] V. Parente, G. Campagnano, D. Giuliano, A. Tagliacozzo, and F. Guinea, "Topological defects in topological insulators and bound states at topological superconductor vortices," *Materials*, vol. 7, no. 3, pp. 1652–1686, 2014.

[313] E. I. Rashba, "Spin currents in thermodynamic equilibrium: The challenge of discerning transport currents," *Phys. Rev. B*, vol. 68, no. 24, p. 241315, 2003.

[314] I. V. Tokatly, "Equilibrium spin currents: Non-abelian gauge invariance and color diamagnetism in condensed matter," *Phys. Rev. Lett.*, vol. 101, no. 10, p. 106601, 2008.

[315] A. Droghetti, I. Rungger, A. Rubio, and I. V. Tokatly, "Spin-orbit induced equilibrium spin currents in materials," *Phys. Rev. B*, vol. 105, no. 2, p. 024409, 2022.

[316] L. Yang, C. H. Park, Y. W. Son, M. L. Cohen, and S. G. Louie, "Quasiparticle energies and band gaps in graphene nanoribbons," *Phys. Rev. Lett.*, vol. 99, no. 18, p. 186801, 2007.

[317] J. R. Williams, L. DiCarlo, and C. M. Marcus, "Quantum Hall effect in a gate-controlled pn junction of graphene," *Science*, vol. 317, no. 5838, pp. 638–641, 2007.

[318] L. A. Ponomarenko, F. Schedin, M. I. Katsnelson, R. Yang, E. W. Hill, K. S. Novoselov, and A. K. Geim, "Chaotic Dirac billiard in graphene quantum dots," *Science*, vol. 320, no. 5874, pp. 356–358, 2008.

[319] J. Y. Vaishnav, J. Q. Anderson, and J. D. Walls, "Intravalley multiple scattering of quasiparticles in graphene," *Phys. Rev. B*, vol. 83, no. 16, p. 165437, 2011.

[320] J. M. Caridad, S. Connaughton, C. Ott, H. B. Weber, and V. Krstić, "An electrical analogy to Mie scattering," *Nat. Commun.*, vol. 7, no. 1, p. 12894, 2016.

[321] D. Gunlycke, D. A. Areshkin, J. Li, J. W. Mintmire, and C. T. White, "Graphene nanostrip digital memory device," *Nano Lett.*, vol. 7, no. 12, pp. 3608–3611, 2007.

[322] P. Zhao and J. Guo, "Modeling edge effects in graphene nanoribbon field-effect transistors with real and mode space methods," *J. Appl. Phys.*, vol. 105, no. 3, 2009.

[323] C. I. Liu, D. S. Scaletta, D. K. Patel, M. Kruskopf, A. Levy, H. M. Hill, and A. F. Rigosi, "Analysing quantized resistance behaviour in graphene Corbino pn junction devices," *J. Phys. D: Appl. Phys.*, vol. 53, no. 27, p. 275301, 2020.

[324] B. Abdollahipour and E. Moomivand, "Magnetopumping current in graphene Corbino pump," *Physica E*, vol. 86, pp. 204–209, 2017.

[325] D. Suszalski, G. Rut, and A. Rycerz, "Mesoscopic valley filter in graphene Corbino disk containing a p–n junction," *J. Phys.: Materials*, vol. 3, no. 1, p. 015006, 2019.

[326] A. B. Cheikh, A. Bouhlal, A. Jellal, and E. H. Atmani, "Tunneling effect in gapped graphene disk in magnetic flux and electrostatic potential," *Phys. Scri.*, vol. 96, no. 12, p. 125863, 2021.

[327] A. Bouhlal, A. Jellal, and M. Mansouri, "Quantum tunneling in graphene Corbino disk in a solenoid magnetic potential with wedge disclination," *Physica B*, vol. 639, p. 413904, 2022.

[328] A. Filusch and H. Fehske, "Electronic properties of α-T_3 quantum dots in magnetic fields," *Euro. Phys. Jour. B*, vol. 93, pp. 1–11, 2020.

[329] G. Nemes, "Error bounds for the large-argument asymptotic expansions of the Hankel and Bessel functions," *Acta Appl. Math.*, vol. 150, pp. 141–177, 2017.

[330] A. Rycerz, J. Tworzydlo, and C. W. J. Beenakker, "Valley filter and valley valve in graphene," *Nat. Phys.*, vol. 3, no. 3, pp. 172–175, 2007.

[331] W. Yao, S. A. Yang, and Q. Niu, "Edge states in graphene: From gapped flat-band to gapless chiral modes," *Phys. Rev. Lett.*, vol. 102, no. 9, p. 096801, 2009.

[332] G. Tkachov and M. Hentschel, "Coupling between chirality and pseudospin of Dirac fermions: Non-analytical particle-hole asymmetry and a proposal for a tunneling device," *Phys. Rev. B*, vol. 79, no. 19, p. 195422, 2009.

[333] A. Rycerz, "Nonequilibrium valley polarization in graphene nanoconstrictions," *Phys. Stat. Soli.*, vol. 205, no. 6, pp. 1281–1289, 2008.

[334] C. W. J. Beenakker, R. A. Sepkhanov, A. R. Akhmerov, and J. Tworzydlo, "Quantum Goos-hänchen effect in graphene," *Phys. Rev. Lett.*, vol. 102, no. 14, p. 146804, 2009.

[335] C. Stampfer, E. Schurtenberger, F. Molitor, J. Güttinger, T. Ihn, and K. Ensslin, "Transparency of narrow constrictions in a graphene single electron transistor," *Inter. Jour. Mod. Phys. B*, vol. 23, no. 12n13, pp. 2647–2654, 2009.

[336] Y. M. Blanter and M. Büttiker, "Shot noise in mesoscopic conductors," *Phys. Rep.*, vol. 336, no. 1-2, pp. 1–166, 2000.

[337] C. Beenakker and C. Schönenberger, "Quantum shot noise," *Physics Today*, vol. 56, no. 5, pp. 37–42, 2003.

[338] U. T. Eden and M. A. Kramer, "Drawing inferences from fano factor calculations," *J. Neuro. Meth.*, vol. 190, no. 1, pp. 149–152, 2010.

[339] K. E. Nagaev, "On the shot noise in dirty metal contacts," *Phys. Lett. A*, vol. 169, no. 1-2, pp. 103–107, 1992.

[340] C. W. J. Beenakker, "Sub-poissonian shot noise in nondegenerate diffusive conductors," *Phys. Rev. Lett.*, vol. 82, no. 13, p. 2761, 1999.

[341] J. Tworzydlo, B. Trauzettel, M. Titov, A. Rycerz, and C. W. J. Beenakker, "Sub-poissonian shot noise in graphene," *Phys. Rev. Lett.*, vol. 96, no. 24, p. 246802, 2006.

[342] R. Danneau, F. Wu, M. F. Craciun, S. Russo, M. Y. Tomi, J. Salmilehto, A. F. Morpurgo, and P. J. Hakonen, "Shot noise in ballistic graphene," *Phys. Rev. Lett.*, vol. 100, no. 19, p. 196802, 2008.

[343] L. DiCarlo, J. R. Williams, Y. Zhang, D. T. McClure, and C. M. Marcus, "Shot noise in graphene," *Phys. Rev. Lett.*, vol. 100, no. 15, p. 156801, 2008.

[344] J. R. F. Lima, A. L. R. Barbosa, C. G. Bezerra, and L. F. C. Pereira, "Tuning the fano factor of graphene via fermi velocity modulation," *Physica E*, vol. 97, pp. 105–110, 2018.

[345] F. Miao, S. Wijeratne, Y. Zhang, U. C. Coskun, W. Bao, and C. N. Lau, "Phase-coherent transport in graphene quantum billiards," *Science*, vol. 317, no. 5844, pp. 1530–1533, 2007.

[346] X. Du, I. Skachko, A. Barker, and E. Y. Andrei, "Approaching ballistic transport in suspended graphene," *Nat. Nano.*, vol. 3, no. 8, pp. 491–495, 2008.

[347] S. V. Morozov, K. S. Novoselov, M. I. Katsnelson, F. Schedin, D. C. Elias, J. A. Jaszczak, and A. K. Geim, "Giant intrinsic carrier mobilities in graphene and its bilayer," *Phys. Rev. Lett.*, vol. 100, no. 1, p. 016602, 2008.

[348] E. R. Mucciolo and C. H. Lewenkopf, "Disorder and electronic transport in graphene," *J. Phys. Cond. Matt.*, vol. 22, no. 27, p. 273201, 2010.

[349] M. Kamada, V. Gall, J. Sarkar, M. Kumar, A. Laitinen, I. Gornyi, and P. Hakonen, "Strong magnetoresistance in a graphene Corbino disk at low magnetic fields," *Phys. Rev. B*, vol. 104, no. 11, p. 115432, 2021.

[350] G. Rut and A. Rycerz, "Magnetoconductance of the Corbino disk in graphene: chiral tunneling and quantum interference in the bilayer case," *J. Phys. Cond. Matt.*, vol. 26, no. 48, p. 485301, 2014.

[351] W. Beugeling, E. Kalesaki, C. Delerue, Y. M. Niquet, D. Vanmaekelbergh, and C. M. Smith, "Topological states in multi-orbital HgTe honeycomb lattices," *Nat. Commun.*, vol. 6, no. 1, p. 6316, 2015.

[352] H. Hu and Q. Si, "Coupled topological flat and wide bands: Quasiparticle formation and destruction," *Sci. Adv.*, vol. 9, no. 29, p. eadg0028, 2023.

[353] Z. Huang, J. H. Wu, Y. Huang, C. Liu, C. Chen, and F. Ma, "Multi-band selective acoustic valley transport through band separation of topological interface states," *J. Phys. D: Appl. Phys.*, vol. 55, no. 4, p. 045301, 2021.

[354] G. F. Zhang, Y. Li, and C. Wu, "Honeycomb lattice with multiorbital structure: Topological and quantum anomalous Hall insulators with large gaps," *Phys. Rev. B*, vol. 90, no. 7, p. 075114, 2014.

[355] S. Okamoto, N. Mohanta, E. Dagotto, and D. N. Sheng, "Topological flat bands in a Kagomé lattice multiorbital system," *Commun. Phys.*, vol. 5, no. 1, p. 198, 2022.

[356] R. Liu, W. C. Chen, Y. F. Wang, and C. D. Gong, "Topological quantum phase transitions and topological flat bands on the Kagomé lattice," *J. Phys.: Cond. Matt.*, vol. 24, no. 30, p. 305602, 2012.

[357] M. Trescher and E. J. Bergholtz, "Flat bands with higher Chern number in pyrochlore slabs," *Phys. Rev. B*, vol. 86, no. 24, p. 241111, 2012.

[358] B. Jaworowski, A. Manolescu, and P. Potasz, "Fractional Chern insulator phase at the transition between checkerboard and Lieb lattices," *Phys. Rev. B*, vol. 92, no. 24, p. 245119, 2015.

[359] B. Bradlyn, L. Elcoro, J. Cano, M. G. Vergniory, Z. Wang, C. Felser, M. I. Aroyo, and B. A. Bernevig, "Topological quantum chemistry," *Nature*, vol. 547, no. 7663, pp. 298–305, 2017.

[360] Y. R. Chen, Y. Xu, J. Wang, J. F. Liu, and Z. Ma, "Enhanced magneto-optical response due to the flat band in nanoribbons made from the α-T_3 lattice," *Phys. Rev. B*, vol. 99, no. 4, p. 045420, 2019.

[361] N. Mohanta, R. Soni, S. Okamoto, and E. Dagotto, "Majorana corner states on the dice lattice," *Commun. Phys.*, vol. 6, no. 1, p. 240, 2023.

[362] S. Rachel, "Interacting topological insulators: a review," *Rep. Prog. Phys.*, vol. 81, no. 11, p. 116501, 2018.

[363] A. S. Sørensen, E. Demler, and M. D. Lukin, "Fractional quantum Hall states of atoms in optical lattices," *Phys. Rev. Lett.*, vol. 94, no. 8, p. 086803, 2005.

[364] S. Raghu, X. L. Qi, C. Honerkamp, and S. C. Zhang, "Topological mott insulators," *Phys. Rev. Lett.*, vol. 100, no. 15, p. 156401, 2008.

[365] M. Hohenadler and F. F. Assaad, "Correlation effects in two-dimensional topological insulators," *J. Phys.: Cond. Matt.*, vol. 25, no. 14, p. 143201, 2013.

[366] C. Wang, A. C. Potter, and T. Senthil, "Classification of interacting electronic topological insulators in three dimensions," *Science*, vol. 343, no. 6171, pp. 629–631, 2014.

[367] C. N. Varney, K. Sun, M. Rigol, and V. Galitski, "Interaction effects and quantum phase transitions in topological insulators," *Phys. Rev. B*, vol. 82, no. 11, p. 115125, 2010.

[368] X. Y. Dong, A. G. Grushin, J. Motruk, and F. Pollmann, "Charge excitation dynamics in bosonic fractional Chern insulators," *Phys. Rev. Lett.*, vol. 121, no. 8, p. 086401, 2018.

[369] C. Repellin, T. Yefsah, and A. Sterdyniak, "Creating a bosonic fractional quantum Hall state by pairing fermions," *Phys. Rev. B*, vol. 96, no. 16, p. 161111, 2017.

[370] S. Julià-Farré, M. Müller, M. Lewenstein, and A. Dauphin, "Self-trapped polarons and topological defects in a topological mott insulator," *Phys. Rev. Lett.*, vol. 125, no. 24, p. 240601, 2020.

[371] L. M. Cangemi, A. S. Mishchenko, N. Nagaosa, V. Cataudella, and G. De Filippis, "Topological quantum transition driven by charge-phonon coupling in the Haldane Chern insulator," *Phys. Rev. Lett.*, vol. 123, no. 4, p. 046401, 2019.

[372] A. Camacho-Guardian, N. Goldman, P. Massignan, and G. M. Bruun, "Dropping an impurity into a Chern insulator: A polaron view on topological matter," *Phys. Rev. B*, vol. 99, no. 8, p. 081105, 2019.

[373] H. L. Calvo, J. S. Luna, V. D. Lago, and L. E. F. Foa Torres, "Robust edge states induced by electron-phonon interaction in graphene nanoribbons," *Phys. Rev. B*, vol. 98, no. 3, p. 035423, 2018.

[374] S. Li, L. H. Hu, R.-X. Zhang, and S. Okamoto, "Topological superconductivity from forward phonon scatterings," *Commun. Phys.*, vol. 6, no. 1, p. 235, 2023.

[375] D. Pimenov, A. Camacho-Guardian, N. Goldman, P. Massignan, G. M. Bruun, and M. Goldstein, "Topological transport of mobile impurities," *Phys. Rev. B*, vol. 103, no. 24, p. 245106, 2021.

[376] J. Medina Dueñas, H. L. Calvo, and L. E. F. Foa T., "Copropagating edge states produced by the interaction between electrons and chiral phonons in two-dimensional materials," *Phys. Rev. Lett.*, vol. 128, no. 6, p. 066801, 2022.

[377] C. Lu, M. Zhang, H. Wang, Q. Ai, and T. Liu, "Topological quantum transition driven by charge-phonon coupling in higher-order topological insulators," *Phys. Rev. B*, vol. 107, no. 12, p. 125118, 2023.

[378] A. Singh and G. Sharma, "Geometrical transport in pseudospin-1 fermions," *Phys. Rev. B*, vol. 107, no. 24, p. 245150, 2023.

[379] J. M. Kosterlitz and D. J. Thouless, "Ordering, metastability and phase transitions in two-dimensional systems," in *Basic Notions Of Condensed Matter Physics*. CRC Press, 2018, pp. 493–515.

[380] T. Senthil, "Symmetry-protected topological phases of quantum matter," *Annu. Rev. Condens. Matter Phys.*, vol. 6, no. 1, pp. 299–324, 2015.

[381] J. E. Moore and L. Balents, "Topological invariants of time-reversal-invariant band structures," *Phys. Rev. B*, vol. 75, no. 12, p. 121306, 2007.

[382] L. Fu and C. L. Kane, "Topological insulators with inversion symmetry," *Phys. Rev. B*, vol. 76, no. 4, p. 045302, 2007.

[383] R. Roy, "$\mathbb{Z}_2$ classification of quantum spin Hall systems: An approach using time-reversal invariance," *Phys. Rev. B*, vol. 79, no. 19, p. 195321, 2009.

[384] D. Gresch, G. Autes, O. V. Yazyev, M. Troyer, D. Vanderbilt, B. A. Bernevig, and A. A. Soluyanov, "Z2pack: Numerical implementation of hybrid Wannier centers for identifying topological materials," *Phys. Revi. B*, vol. 95, no. 7, p. 075146, 2017.

[385] B. A. Bernevig, T. L. Hughes, and S. C. Zhang, "Quantum spin Hall effect and topological phase transition in HgTe quantum wells," *Science*, vol. 314, no. 5806, pp. 1757–1761, 2006.

[386] X. L. Qi, Y. S. Wu, and S. C. Zhang, "Topological quantization of the spin Hall effect in two-dimensional paramagnetic semiconductors," *Phys. Rev. B*, vol. 74, no. 8, p. 085308, 2006.

[387] X. H. Wang, J. J. Wang, J. Wang, and J. F. Liu, "Flat band assisted topological charge pump in the dice lattice," *Phys. Rev. B*, vol. 103, no. 19, p. 195442, 2021.

[388] J. T. Devreese, "Fröhlich polarons. lecture course including detailed theoretical derivations–," *arXiv preprint arXiv:1611.06122*, 2016.

[389] Á. D. Kovács, G. Dávid, B. Dóra, and J. Cserti, "Frequency-dependent magneto-optical conductivity in the generalized α-T_3 model," *Phys. Rev. B*, vol. 95, no. 3, p. 035414, 2017.

[390] C. D. Han and Y. C. Lai, "Optical response of two-dimensional Dirac materials with a flat band," *Phys. Rev. B*, vol. 105, no. 15, p. 155405, 2022.

[391] D. O. Oriekhov and V. P. Gusynin, "Optical conductivity of semi-Dirac and pseudospin-1 models: Zitterbewegung approach," *Phys. Rev. B*, vol. 106, no. 11, p. 115143, 2022.

[392] J. J. Wang, S. Liu, J. Wang, and J. F. Liu, "Integer quantum Hall effect of the α-T_3 model with a broken flat band," *Phys. Rev. B*, vol. 102, no. 23, p. 235414, 2020.

[393] M. E. Cifuentes-Quintal, O. de la Peña-Seaman, R. Heid, R. de Coss, and K. P. Bohnen, "Uniaxial strain-induced Kohn anomaly and electron-phonon coupling in acoustic phonons of graphene," *Phys. Rev. B*, vol. 94, no. 8, p. 085401, 2016.

[394] C. Si, Z. Sun, and F. Liu, "Strain engineering of graphene: a review," *Nanoscale*, vol. 8, no. 6, pp. 3207–3217, 2016.

[395] A. C. Ferrari, "Raman spectroscopy of graphene and graphite: Disorder, electron–phonon coupling, doping and nonadiabatic effects," *Solid State commun.*, vol. 143, no. 1-2, pp. 47–57, 2007.

[396] T. Venanzi, L. Graziotto, F. Macheda, S. Sotgiu, T. Ouaj, E. Stellino, C. Fasolato, P. Postorino, V. Mišeikis, M. Metzelaars *et al.*, "Probing enhanced electron-phonon coupling in graphene by infrared resonance Raman spectroscopy," *Phys. Rev. Lett.*, vol. 130, no. 25, p. 256901, 2023.

[397] E. H. Hwang and S. D. Sarma, "Surface polar optical phonon interaction induced many-body effects and hot-electron relaxation in graphene," *Phys. Rev. B*, vol. 87, no. 11, p. 115432, 2013.

[398] B. S. Kandemir and S. Atag, "Substrate-limited helical edge states," *Phys. Rev. B*, vol. 100, no. 24, p. 245408, 2019.